UNIVERSITAT POLITÈCNICA DE CATALUNYA
BARCELONATECH
Escola Tècnica Superior d'Enginyeria
Industrial de Barcelona

Design and Bioapplication of Nanointerfaces Based on Conducting Polymers

Presented by

Maria M. Pérez-Madrigal

Supervisors:

Dr. Elaine Armelin

Prof. Carlos Alemán

Thesis submitted to obtain the degree Doctor of Philosophy in *Polymers and Biopolymers* at Universitat Politècnica de Catalunya

Barcelona, May 2015

Departament d'Enginyeria Química
Grup d'Innovació en Materials i Enginyeria Molecular

A Mercè

Little darling, it's been a long cold lonely winter.
Little darling, it feels like years since it's been here.
Here comes the sun.
Here comes the sun, and I say it's all right
(The Beatles)

Abstract

Global search on conducting polymers (CPs) during the last decades has confirmed their feasibility as innovative bioactive materials which are able to induce electrical, electrochemical and electromechanical stimulation of cell tissues. However, their application is limited by their non-biodegradable properties or poor mechanical integrity.

This Thesis reports the fabrication and characterization of interfaces based on CPs, which are designed with at least one dimension in the nanometric scale, for bioapplications such as scaffolds for promoting electro-active tissue regeneration, drug delivery systems or passive ion transport membranes. In particular, the development of such platforms is addressed to overcome CPs limitations without compromising their electrochemical and electrical properties. Special attention is placed on evaluating those properties that are known to determine cell-biointerface interactions (*i.e.* surface chemistry, topology and mechanical features) in addition to biocompatibility and biodegradability. Concretely, CP-based biointerfaces are designed as free-standing nanomembranes (FsNM), fibrous substrates or electropolymerized ultra-thin interfaces.

In the first approach, spin-coating is used to prepare robust and flexible nanofilms by blending a chemically synthesized PTh derivative (P3TMA), which is soluble in THF, $CHCl_3$ and DMSO, with an insulating polymer (*i.e.* polyester (PE44) or thermoplastic polyurethane (TPU)), which is crucial to provide mechanical integrity to P3TMA. Fully characterization of the resulting FsNM reveals that both systems, P3TMA:PE44 and TPU:P3TMA interfaces, retain features coming from each of the homopolymers: electrochemical activity and electrical response on the one hand, and biodegradability on the other. Moreover, they behave as potent cellular biointerfaces because they are biocompatible, electrobioactive and adequate substrates for type I collagen adsorption.

Secondly, P3TMA is further used to obtain hybrid fibrous scaffolds. In this case, polylactide (PLA) or poly(ester urea)-*co*-poly(ester amide) (PEU-*co*-PEA) are chosen as biodegradable polymers. After the optimization of the electrospinning process, a study is carried out to investigate the electrochemical properties (electroactivity and electrostability) of both PLA:P3TMA and PEU-*co*-PEA:P3TMA hybrid samples, and their bioapplication. P3TMA displays a good doping level, and retains its electrochemical features in the hybrid fibrous samples, which are electroactive and electrostable. Again, P3TMA improves the cellular proliferation of cells cultured on the hybrid fibrous interfaces, thus enabling their use as suitable scaffolds for cell

regeneration. Furthermore, PLA:P3TMA fibrous interface can perform as a drug-delivery platform since it combines suitable wetting behaviour, biocompatibility and good electrical features. Matrices loaded with antibacterial drugs are active, and thus the drug is feasible to be released from the fibrous biointerface by electrical stimulation.

Finally, CP-based biointerfaces are prepared by electrochemical polymerization adopting specific strategies. Hence, Omp2a, an outer membrane protein which forms trimeric pores, is entrapped in a poly(*N*-methylpyrrole) (PNMPy) matrix, preserving its native structure, which ensures its operative and functional state as passive ion channel. Similarly, a bioactive platform is prepared based on the *co*-electropolymerization of a specially synthesized bis-thienyl monomer, AzbT, which contains carboxyl and Schiff base functionalities, and 2,2':5',2''-therthiophene (Th_3). Such interfaces display good optical and electrochemical properties depending on the AzbT:Th_3 molar ratio in the electrpolymerization medium. Furthermore, the copolymer with the highest AzbT content shows enhanced cell adhesion and proliferation results, with cells cultured on their surface homogeneously spread. Such behaviour has been interpreted as the combination effect of the minor release of harmful Th_3 monomer entrapped into the polymeric matrix and the presence of the AzbT's distinctive groups.

Keywords: conducting polymer, biodegradable blend, nanomembranes, fibrous scaffolds, tissue engineering, drug-delivery, funtional biointerfaces, electrochemical polymerization.

Acknowledgements

Cuando la gratitud es tan absoluta, las palabras sobran; dijo el poeta y novelista colombiano Álvaro Mutis. Así que acogiéndome a su consejo, intentaré ser breve, aunque no será fácil ya que las personas que han puesto su granito de arena en este proyecto (profesional y personal) son numerosas…

A mis directores de tesis, la Dra. Elaine Armelin y el Prof. Carlos Alemán, por brindarme la oportunidad de realizar la tesis en el grupo IMEM. Pero sobretodo, por su constante apoyo, buen criterio y acertados consejos. He podido hacer y deshacer, equivocarme y aprender, he llenado mi maleta de viaje de conocimientos y buenas prácticas. Por todo, les estoy sinceramente agradecida.

Los ensayos *bio* y el rumbo de la tesis no hubieran sido posibles sin la inestimable contribución (a todos los niveles) del Dr. Luis Javier del Valle; Lucho, has dejado huella, gracias.

Agradezco al Prof. Fausto Sanz el poder haber desarrollado parte de la tesis en su grupo (*Nanoprobes and nanoswitches,* IBEC). La experiencia me enriqueció con creces. A la Dra. Marina I. Giannotti, por su excelente supervisión. He aprendido mucho trabajando contigo. Gracias por tu cercanía y paciencia.

Al Prof. Dr. David Díaz-Díaz, cuya pasión por la ciencia es genuinamente única. Gracias por acogerme en tu grupo (*The DDD Research Group,* at Universität Regensburg) y enseñarme algunos de los intríngulis de la síntesis orgánica y de los hidrogeles. Fue una estancia muy productiva.

Al hacer balance, te das cuenta de que gracias a la aportación y conocimiento específico de mucha gente las cosas han salido adelante: al Dr. Alex L. Gomes, de quien tomé el relevo en el mundillo de las FsNM; al Dr. Francesc Estrany, per les estones compartides al AFM, i per estar sempre disposat a aclarir-me tots els dubtes electroquímics sense perdre el bon humor; als membres del grup PSEP: el Prof. Jordi Puiggalí, la Dra. Lourdes Franco, la Dra. Elena Llorens i el Dr. Marc Planelles, ha estat un plaer treballar amb vosaltres; al equipo de *Mecwins S.L.*; to Dr. Ioan Cianga and Dr. Luminita Cianga, for synthesizing the famous AzbT monomer, and enrich this dissertation; to Dr. Catherine Michaux, Dr. Guillaume Roussel and Dr. Eric A. Perpète, working in the Omp2a project has been quite a challenge; a la Dra. Denise S. Azambuja y a la Dra. Núria Ferrer-Anglada, gracias por compartir vuestra experiencia.

Gracias a los técnicos del "centro de nano" (*CRnE,* UPC), Trifon Trifonov y Montse Domínguez; y a los dels "serveis" (*Centres Científics i Tecnològics,* UB), Dr. Gerard Oncins y Jordi Díaz.

Un agraïment molt especial a les persones del grup IMEM per haver fet de la tesi una aventura encara més inoblidable. Gràcies, a la Dra. Georgina Fabregat, ets tot un exemple, no cal dir res més; a la Dra. Esther Córdova-Mateo, gràcies per contestar amb ∞ paciència totes les meves preguntes! (sobretot pels consells de format per la tesi); al Dr. Daniel E. López-Pérez, empezamos juntos, y espero que nuestros caminos se crucen de nuevo; a Neudys González, a Silvana Maione, a Jordi Triguero, a l'Anna Puiggalí, a l'Enric Mayans, i a Marcele Arais, molts ànims amb el doctorat (si al final, mereix la pena i tot!); al Dr. David Zanuy, per les nostres converses al mig del passadís, amb molt bons consells; i als que hi vau formar part, el Dr. Guillem Revilla, el Dr. Bruno Teixeira-Dias, el Dr. David Aradilla, la Dra. Viviane Dalmoro, la Dra. Franciélli Müller, i el Dr. Rafael Peres.

También, hago extensivo mi agradecimiento a los compañeros del departamento de Ingeniería Química.

In Regensburg, I met incredibly nice people who made my stay there even more worth it. To my lab mates, Marleen, Judith and Toby; to my corridor mates, Mercedes and Samuel; and to my flatmate, Silvia, the warmest thank you. I wish you all the best.

Els anys de tesi sempre aniran inevitablement vinculats a l'Ari i als nostres dinars/cafè, per fer que cada migdia fos diferent. Bruna, què són 1640 km?? Res! Gràcies per estar sempre, sempre al meu costat, aquí, allà, on sigui…. Als amics, els de la uni i la colla de Sarrià.

Con la familia es con quien en horas bajas y cuando no sale nada te desahogas. Buenas noticias: esto ya se acaba. Gracias por aguantar el chaparrón, por vuestro ánimo constante e incondicional. A mis padres y hermanos, a Asun y a Chema; y en especial a Javi, por estar a mi lado cada día.

The author of this thesis thanks financial support to Universitat Politècnica de Catalunya through a FPI-UPC grant (2010-2014).

Table of Contents

List of Figures and Schemes

Chapter 1. Introduction

Chapter 2. Literature Review

Chapter 3. Objectives

Chapter 4. Bioactive Nanomembranes of Polythiophene Derivative and Biodegradable Polyester

Chapter 5. Bioactive Nanomembranes of Polythiophene Derivative and Thermoplastic Polyurethane

Chapter 6. Sensitive Thermal Transitions of Nanoscale P3TMA Interface Using the Bimetallic Effect

Chapter 7. Fibrous Biointerfaces Based on Polythiophene Derivative and Biodegradable Polylactide

Chapter 8. Fibrous Biointerfaces Based con Polythiophene Derivative and Biodegradable Poly(ester urea)-*co*-Poly(ester amide)

Chapter 9. Polypyrrole-Membrane Protein Supported Interface: Bioinspired Channels

List of Tables

Chapter 10. Bioactive Interface Containing Terthiophene, Carboxyl and Schiff Base Functionalitites

List of Abbreviations

Abbreviation	Meaning
^{1}H-NMR	Proton nuclear magnetic resonance
3TAA	3-thiophene acid acetic
AC	Alternating current
AFM	Atomic force microscopy
APS	Ammonium persulfate
ATRP	Atom radical polymerization
AzbT	3,5-Bis([2-thienylmethylene]amino)benzoic acid monomer
BP	Bulk powder model
C-AFM	Conductive AFM
CA	Chronoamperometry
CD	Circular dichroism
CE	Counter electrode
CHX	Chlorhexidine dihydrochloride
CIP	Ciprofloxacin
CNT	Carbon nanotubes
CNT-Fn	Carbon nanotubes-fibronectin composite
Cos-7	African green monkey kidney fibroblast cell line
CP(s)	Conducting polymer(s)
CPE	Constant phase element
CP−MP	Conducting polymer-membrane protein composite
CREKA	Biologically active linear pentapeptide
CSA	Camphorsulfonic acid
CV	Cyclic voltammetry
DABA	3,5-diamonobenzoic acid
DBSA	Dodecylbenzene sulfonic acid
DC	Direct current
DEAD	Diethyl diazenedicarboxylate
DGI	Dodecylglyceryl itaconate
DL	Doping level
DMEM	Dulbecco's modified Eagle medium
DMLPEI	N,N-dodecylmethyl-polyethylenimine
DMSO	Dimethyl sulfoxide

DMT	Derjaguin-Muller-Toropov contact mechanics model
DNA	Deoxyribonucleic acid
DSC	Differential scanning calorimetry
DTGA	Derivative thermogravimetric analysis
Du-145	Human prostate cancer cell line
EC-AFM	Electrochemical atomic force microscopy
ECD	Electron capture detector
ECM	Extra cellular matrix
EDTA	Ethylenedinitrilo-tetraacetic acid
EDX	Energy-dispersive X-ray spectroscopy
EEC	Electrical equivalent circuit
EF	Electric field
EIS	Electrochemical impedance spectroscopy
EoS	Equation of State
ES	Electrical stimulation
F-AP15	Lipase F-AP15 (from *Rhizopus oryzae*)
FBS	Fetal bovine serum
FC	Fibrous collagen
FIP	Freezing interfacial polymerization
FsNM	Free-standing nanomembrane
FTIR-ATR	Fourier transform infrared - attenuated total reflection
GC	Gas chromatograph
GPC	Gel permeation chromatography
HA	Hyaluronic acid
HEp-2	Human laryngeal epidermoid carcinoma cell line
HOMO	Highest occupied molecular orbital
HPLC	High performance liquid chromatography
IBU	Ibuprofen sodium salt
IP	Interface polymerization
IPOM	Intraperitoneal polypropylene overlaid mesh
ITO	Indium tin oxide
KAS	Kissinger−Akahira−Sunose isoconversional method
LB	Langmuir-Boldgett
LbL	Layer-by-layer
LEA	Loss of electroactivity

LUMO	Lowest unoccupied molecular orbital
MD	Molecular dynamics
MDCK	Madin Darby canine kidney cell line
MDI	Methylene diphenyl diisocyanate
MG-63	Human osteosarcoma cell line
MPC	2-Methacryloyloxyethyl phosphorylcholine
MPD	2-methyl-2,4-pentanediol
MPs	Membrane proteins
MSCs	Mesenchymal stem cells
MTT	3-(4,5-dimethylthiazol- 2-yl)-2,5-diphenyltetrazolium bromide
Na-alginate	Sodium alginate
NBPT	4′-Nitro-1,1′-biphenol-4-thiol
NFC	Non fibrous collagen
NGF	Nerve growth factors
NMPy	*N*-Methylpyrrole
OCP	Open circuit potential
Omp2a	Outer membrane protein OMP2a
OWRK	Owens-Wendt-Rabel-Kaelble
P3AA	Poly(3-thiophene acetic acid)
P3HT	Poly(3-hexylthiophene)
P3OTh	Poly(3-octylthiohene)
P3TMA	Poly(3-thiophene methyl acetate)
P4VPPS	Poly(4-vinylpyridine propylsulfobetaine)
PAA	Poly(acrylic acid)
PAH	Poly(allylamine hydrochloride)
PAH-D	Poly(allylamine hydrochloride)−dextran
PAni	Polyaniline
PBS	Phosphate buffered saline
PCL	Poly(ε-caprolactone)
PDA	Polydopamine
PDI	Polydispersity
PDDA	Poly(diallyldimethylammonium)
PDLA	Poly(D,L-lactide)
PDMS	Poly(dimethyl siloxane)
PE44	Poly(tetramethylene succinate)

PEDOT	Poly(3,4-ethylenedioxythiophene)
PEG	Poly(ethylene glycol)
PEO	Poly(ethylene oxide)
PEU-*co*-PEA	Poly(ester urea)-*co*- poly(ester amide)
PGA	Polyglycolic acid
PHEMA	Poly(2-Hydroxyethyl methacrylate)
PHS	Poly(4-hydroxysytrene)
PLA	Poly(lactic acid) or polylactide
PLGA	Poly(lactic-*co*-glycolic acid)
PMMA	Poly(methyl methacrylate)
PMPC	Poly(2-methacryloyloxyethyl phosphorylcholine)
PMSF	Phenylmethanesulfonyl fluoride
PNIPAM	Poly(N-isopropylacrylamide)
PNMPy	Poly(N-methylpyrrole)
PPy	Polypyrrole
PS	Polystyrene
PSS	Poly(sodium-4-styrenesulfonate)
PTh	Polythiophene
PU	Polyurethane
PVA	Poly(vinyl alcohol)
Py	Pyrrole
QNM	Quantitative nanomechanical
RCS	Refrigerated cooling system
RGD	Tripeptidyl sequence: Arg-Gly-Asp
RMS	Root mean square
SAM	Self-assembled monolayers
sCA	Static contact angle measurement
SCALA	Scanning laser analyzer
SDS	Sodium dodecyl sulfate
SDS–PAGE	Sodium dodecyl sulfate-Polyacrylamide gel electrophoresis
SEC	Size exclusion chromatography
SEM	Scanning electron microscopy
SPION	Superparamagnetic iron oxide nanoparticles
SWCNT	Single-walled carbon nanotube
TBATFB	Tetrabutylammonium tetrafluoroborate

TC	Tetracycline
TCS	Triclosan
TCPS	Tissue culture polystyrene
TDI	Toluene diisocyanate
TEM	Transmission electron microscopy
TEP	Transepithelial Potential
TGA	Thermogravimetry analysis
Th	Thiophene
Th_3	Terthiophene
THF	Tetrahydrofuran
TPU	Thermoplastic polyurethane
Tris	2-Amino-2-hydroxymethyl-propane-1,3-diol
TSA	*p*-Toluenesulfonic acid
UTC	Ultra-thin coating model
Vero	African green monkey kidney epithelial cell line
WE	Working electrode
WL	Weight loss
WU	Water uptake
XPS	X-ray photoelectron spectroscopy

List of Symbols

Symbol	Meaning
A	Area
c	Speed of light
C or C_{dl}	Ideal double layer capacitance
CPE	Constant phase element (imperfect double layer capacitance)
CPE_M	Membrane constant phase element
CPE_{ST}	Steel constant phase element
E	Young's modulus
E_a	Activation energy
E_g	Lowest π-π^* transition energy /band gap energy
E_p^a	Oxidation/anodic peak potential
E_p^c	Reduction/cathodic peak potential
E^0	Offset potential

F	Faraday constant
F_{adh}	Adhesion force between AFM tip and sample surface
h	Plank's constant
I_{av}	Average current
j	Current density
k_s	AFM tip nominal spring constant
ℓ or t	Thickness
Lc	Critical load related to the adhesion force
LC	Critical device dimension
m	Sample weight
M_n	Number-average molecular weight
M_w	Weigth-average molecular weight
MW_{MU}	Molecular weight of the monomeric unit
Q_M	Membrane double layer capacitance
Q_i	Oxidation voltammetric charge corresponding to a CV cycle
Q_{pol}	Polymerization charge
Q_{ST}	Steel double layer capacitance
R	Electrical resistance
RMS R_q	Root mean square roughness
R_s or R_{soln}	Electrolyte resistance
T_c	Crystallization temperature
T_f / T_m	Melting temperature
T_g	Glass transition temperature
V	Voltage
W	Warburg impedance
W_A	Work of adhesion
Z'	Impedance: real component
-Z''	Impedance: imaginary component
Δ	Porosity
ΔH_c	Crystallization enthalpy
ΔH_f / ΔH_m	Melting enthalpy
ΔQ	Difference of oxidation voltammetric charge
α	Deviation from the vertical in the Nyquist plot
γ_L	Surface energy of the liquid-gas interface
γ_S	Surface energy of the solid-gas interface

γ_{SL}	Surface energy of the solid-liquid interface
$\gamma_L^d;\ \gamma_L^p$	Dispersive and polar components of γ_L
$\gamma_S^d;\ \gamma_S^p$	Dispersive and polar components of γ_S
ε_{max}	Ultimate tensile elongation
θ	Polymerization time
θ	Contact angle
λ_{max}	Maximum absorbance peak
λ_{onset}	Cut off wavelength for the absorption spectra
ρ	Density
σ	Conductivity
σ_{max}	Ultimate tensile strength
ω	Frequency
χ	Dihedral angle
$\langle \bar{x}_a^2 \rangle$	Averaged atomic mean square displacement

CHAPTER 1

INTRODUCTION

1.1. Motivation of the Thesis Research

Without electricity our brain would not work, our muscles would not contract, we would not sense or the rhythm of our heartbeat and the movement of blood through our circulatory system would not be controlled. The human body is a complex bioelectrical system and, at the end, those electrical signals are responsible for the correct internal function of our body. Biological processes are driven by charge transport phenomena: transport of ions across the cell membranes and of electrons along biomolecules. There are measurable electric potentials that exist at the cellular level (cell membrane), the interstitial level (between layers), and the epidermis (transepithelial potential, TEP).

A great example of how electricity takes part directly in some body functions is the role it plays as the driving force in the correct wound healing process.[1] This is a systematic and yet not fully understood process. In a normal state, the TEP, which varies from 10 mV to 60 mV (average 23 mV), is caused by the imbalance of negative chlorine ions and positive sodium and potassium ions in the tissues. When a wound is formed, this seal is broken and the TEP collapses to 0 mV, thus establishing a movement of ions, referred to "injury current" (ca. 10 – 100 μA), and also a physiological electric field (EF) of ca. 140 mV/mm. Only 2 – 3 mm away from the wound edge, the EF decreases to 0 mV/mm. Therefore, both the EF and the injury current start a cascade of events that results in healthy cells being attracted or repelled to induce wound healing, and thus close the wounded gap. Current will continue until the defect is fixed, and the TEP value restored.

Therefore, it is not surprising that since the invention of electricity, electrical current has been used for medical and therapeutic applications: in the treatment of skin wounds,[1] to accelerate bone fracture healing,[2] and also to prevent muscle atrophy and pain relief during rehabilitation.

Generally, electrical stimulation (ES) is used for wound healing purposes because it can mimic the natural "injury current".[3,4] Rouabhia *et al.* showed how ES promotes skin fibroblast growth and migration, increases growth factor secretion, and enhances wound healing.[5]

Apart from that, research has evidenced how electrical stimuli induce other cellular responses such as stem cell differentiation,[6] specifically in electrically excitable tissues, like skeletal, muscle, nerve or cardiac tissues, and bone. Thus electric signals are able to regulate cell growth and function.[7] As it was reviewed by Meng *et al.*, there is no standardized methodology or setup for ES, as it can be delivered in many modalities depending on the final purpose it accomplishes.[8]

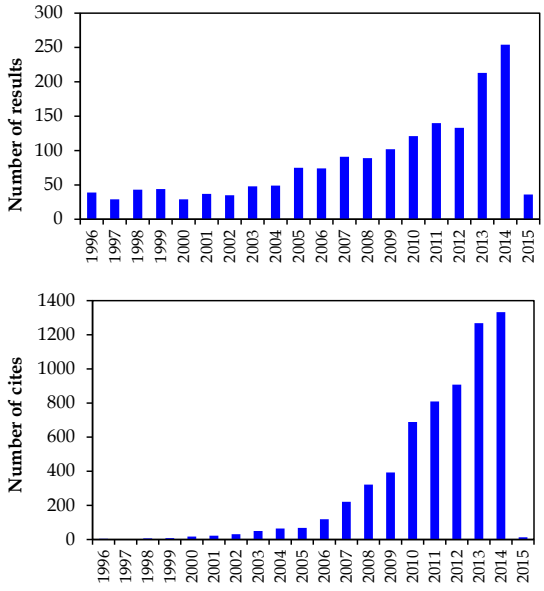

Figure 1.1.1. Result of the search under the key words: "electrical stimulation" and "conducting polymers" until January, 2015. Top: scientific papers and patents found at ScienceDirect. Bottom: number of cites each year (Source: Web of Science).

Hence, the optimization of the overall process is quite complex since a lot of variables are involved (*e.g.* electrical voltage, duration, electrical pulse sequence, frequency, and the selection of appropriate electrodes in terms of geometry, position and material).[9]

Conventional biomaterials do not result in appropriate biointerfaces to conduct ES since they lack of electrical conductivity properties. And recently, standard materials (*i.e.* stainless steel, platinum or titanium) are being replaced by non-metallic materials which are biocompatible and also display conductive properties.[10-13] Figure 1.1.1 shows how research on both "electrical stimulation" and "conducting polymers (CPs)" has been increasing considerably during the last 5 years. A new and exciting area of research has emerged, in which CPs are the key biomaterial component not only because of their tuneable ability for electron/ion transport, but also because of their biocompatibility, softness and easy of blending, self-assembly ability, environmental stability and processability.

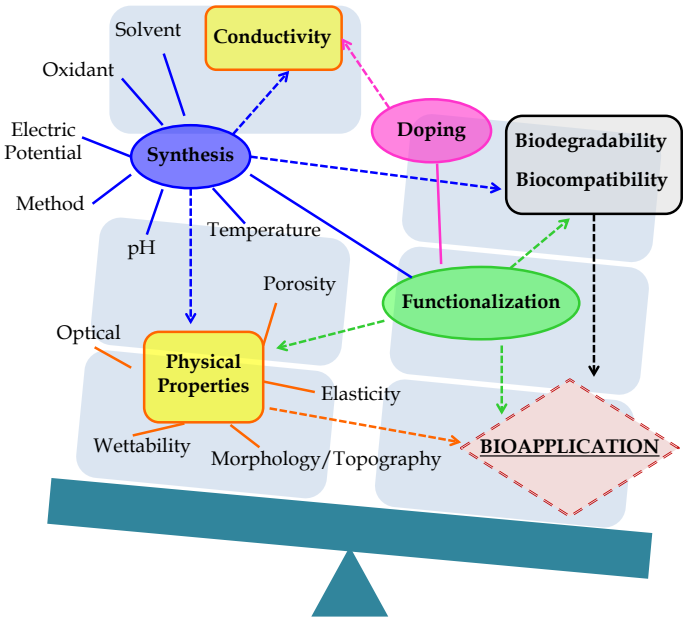

Figure 1.1.2. Parameters and factors connected in the design of CPs. [Adapted with permission.[20] - Open Acces article under a Creative Commons license (CC. BY 3.0)].

Consequently, CPs represent an excellent choice to support cell adhesion, migration and proliferation.[12] Moreover, their ability to electrically stimulate local tissue is of great potential.[13]

In contrast, their application is limited by their non-biodegradable properties, low porosity, hydrophobicity and poor mechanical integrity. Among the different strategies to overcome such limitations, a common one is based on the combination of CPs with other biopolymers and the processing of the mixtures into membranes or fibers. The homogeneous distribution of the CP phase in the blend ensures electrical signals to be effectively transmitted throughout the biointerface, reaching all seeded cells. Even without the effect of ES, the respond of cells towards CP-based biointerfaces depends on its features: wettability,[14] mechanical stiffness,[15,16] elasticity,[17] and surface topography.[18,19] It is not the effect of one specific property, but the combination of all that influences significantly the behaviour of seeded cells, including their proliferation, migration, differentiation and structural reorganization.

Accordingly, CP-based scaffolds can effectively interface biological systems and act as cell-instructive platforms, thus contributing enormously to the field of tissue

engineering and regenerative medicine. Taking advantage of CPs unique properties, research efforts are aimed to produce a suitable scaffold with enhanced biocompatibility and biodegradation properties, as well as tailored topological, mechanical, electrical and electrochemical features which can be relevant to satisfy the specific biomaterial requirement. Finally, it is important to bear in mind that, due to CPs vast versatility, a lot of variables are interconnected in the design steps (Figure 1.1.2). In consequence, the challenge remains in balancing all these characteristics, and still obtaining a functional biointerface, which is the aim of this work.

1.2. Background and Overview of Key Concepts

1.2.1. Biomaterials: from Bioinertness to Biointeractivity

It was in the late 1940s and early 1950s when the first medical devices based on biomaterials were used in humans.[21] Since then, the biomaterials field has gained widespread scientific and technological attention, and the list of commonly used applications has been growing considerably. Just to cite a few, the list of key applications of biomaterials include cardiovascular prostheses, intraocular lenses, joint replacements, dental implants, scaffolds for *in vivo* and *in vitro* cell growth, skin substitutes, sutures, blood bags, bone cement, *etc.*, and the field is continuously updating with the design of novel biomaterials and emerging technologies.[22]

As it is defined by the International Union of Pure and Applied Chemistry (IUPAC), a biomaterial is any material exploited in contact with living tissues, organism or microorganism.[23] Traditionally, biomaterials science has focused on the study of the physical and chemical interactions that arise when complex biological systems and entities interact with either synthetic or modified natural materials.[24] However, the progress achieved during the last decades in areas such as medicine, cell and molecular biology, chemistry, materials science and engineering has undoubtedly contributed to biomaterials research, which has been continuously evolving and adapting through three generations now (Figure 1.2.1). Each generation differs from the previous one by the specific purpose it tries to accomplish, thus enlarging the field of applications, and temporal overlapping can occur.[21]

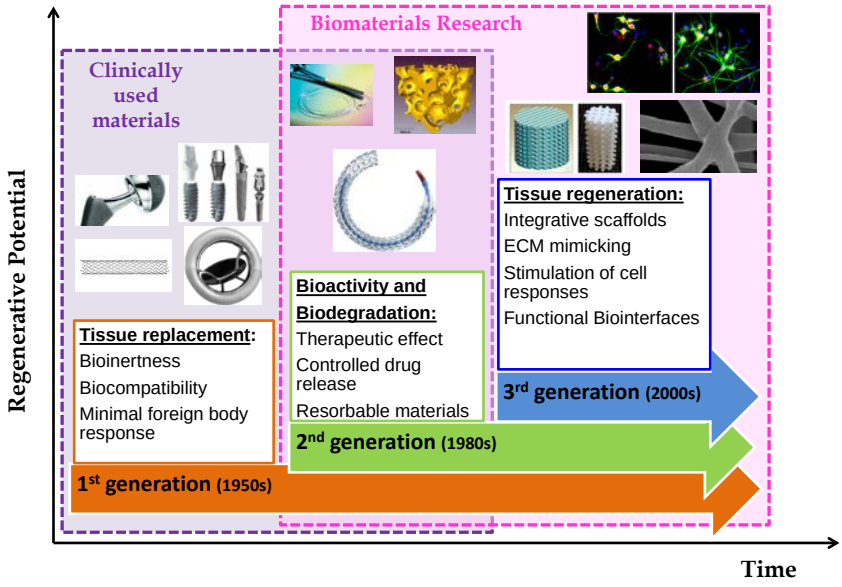

Figure 1.2.1. Evolution of biomaterials. Classical biomaterials, such as solid metallic implants, pursue the objective to be biocompatible, to replace damaged tissue and to provide structural support. However, more and more biological approaches focusing on repair rather than on replacement are pursued in experimental research. Smart biomaterials are biodegradable and actively participate in the regeneration process of damaged tissue by stimulating specific cellular responses at the molecular level. Adapted with permission from [25] (Copyright 2002, Elsevier) and [22] (Copyright 2013, Elsevier).

The **1st generation** of biomaterials (1950s and 1960s) was developed by using widely available industrial materials which, although not being designed for a specific medical application, resulted in excellent candidates for tissue replacement because they were bioinert (*i.e.* their suitable chemical and physical properties induced minimal foreign body response).[26] For example, silicone rubber used in medical components and assemblies or pyrolitc carbon for mechanical heart valves are examples of 1st generation biomaterials.

During the **2nd generation** (1980s-1990s), the goal is not aimed to achieve bioinertness anymore, but bioactivity.[27] That is, biomaterials features are tailored to obtain a desired therapeutic effect at the biointerface they contact. Hence, biomaterials are conceptualized as systems for controlled drug release and gene therapy, delivering pharmacologic agents such as drugs, active proteins, growth factors, and other macromolecules of interest to localized areas.

For such purposes, bioactive glasses and ceramics are widely used in orthopedic and dental procedures.[28] Drug-eluting stent coatings designed to prevent endovascular restenosis (blood vessel closure) or biodegradable sutures are also found among this group.[29]

Finally, **3rd generation** biomaterials research (2000s-onwards) focuses on developing innovative systems to support functional tissue regeneration as opposed to replacement (1st generation), or either resorbability or bioactivity (2nd generation).[26] On the contrary, at the present time, these last two properties are combined to help the body heal itself.[30] Renovation of living tissue is accomplished by designing biocompatible matrices (scaffolds) which resemble the complexity of natural tissue assemblages (*i.e.* the native extracellular matrix, ECM), and stimulate specific cellular responses at the biointerface to promote cell adhesion, proliferation, migration and differentiation processes.[31] Figure 1.2.2 illustrates the tissue engineering paradigm: various cell types are seeded on porous scaffolds, possibly proliferated in a bioreactor, and finally implanted in various tissue sites to restore or regenerate damaged or missing tissue.[21,32]

Eventually, when this biointerface is able to actively guide and control specific adhesion and recognition events it is defined as a functional biointerface, and its development is of particular interest for tissue engineering applications and regenerative therapeutics.[33] This new concept of scaffold, which is also referred as smart interface or proactive cell-instructive material,[34] is designed to display a series of chemical, biochemical and biophysical signals that actively guide the whole tissue repairing process.[35] Furthermore, smart biomaterials which are able to interact with the surrounding environment and respond accordingly are also included in this 3rd generation, regardless the biomedical application.

Taking into account the interdisciplinary component of the biomaterials field, it is not surprising that nanotechnological concepts and procedures,[36-37] as well as biomimicry-inspired design[40-42] are being applied to obtain advanced biointerface structures that will interact with the *in vivo* system in the desired way. On the one hand, techniques such as molecular and nanoparticles self-assembly,[43] nanopatterning,[44] electrospinning[45-48] or nanotemplating[49,50] approaches are introduced to control with nanometric precision the spatial organization of the biointerface to resemble the fibrillar structure of the ECM, which is vital for enabling effective cell guidance.[51] On the other, the biological response is also influenced by the mechanical,[17,52] physico-chemical,[53] electrical[54,55] and morphological[56,57] properties of biointerfaces.

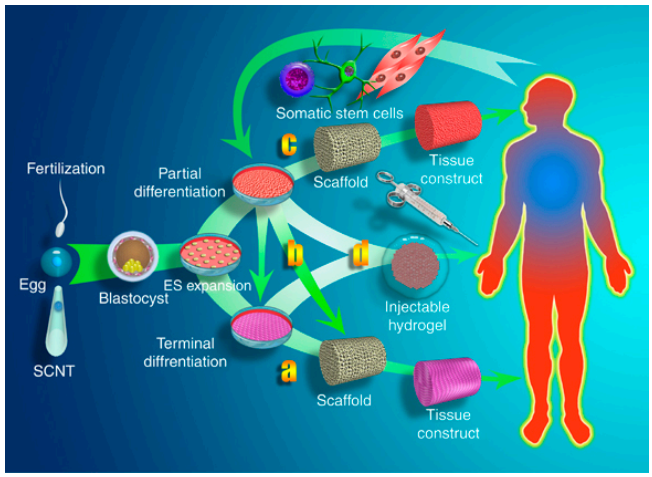

Figure 1.2.2. The tissue engineering paradigm: multiple roles for biomaterials. Reproduced with permission.[32] Copyright 2007, Nature Publishing Group.

Thus, all these features are tailored at the nanoscale in an effort to mimic the complex and dynamic signalling processes that induce cell recognition, adhesion, cytoskeleton assembly, differentiation and migration processes.[58,59]

1.2.2. Conducting Polymers in Biomaterials Research

Throughout these three generations, metals (titanium, stainless steel, platinum, platinum-iridium), ceramics (calcium phosphates), glasses, carbons, polymers (polyester, poly(lactic acid), polyurethane, silicone, polypropylene, Teflon®, poly(methyl methacrylate), nylon) and biopolymers have been used as biomaterials.[21] Generally, polymeric biomaterials are distinctive since they can be modelled and processed into a wide range of forms, such as coatings, fibers, films, membranes, foams, nanoparticles or hydrogels. This versatility results in materials able to accommodate a greater number of clinical contexts because it is possible to precisely tune their structural, mechanical and surface properties, fulfilling the requirements set for each specific biomedical application. Global search on CPs during the last decades has confirmed their feasibility as innovative bioactive materials or functional biointerfaces. CP-based electroactive biomaterials are important in that they are able to induce electrical, electrochemical and electromechanical stimulation of cell tissues.[20, 60-62]

Introduction to CPs

The first inherently CP was recognized in 1977 when Shirakawa, MacDiarmid, Heeger and co-workers reported the change in polyacetylene conductivity for many orders of magnitude after being doped with iodine.[63] The fact that under oxidation such property could be tuned in that range has attracted the interest of the scientific world. Since then, research on organic semiconductors has resulted in a wide range of technological applications,[64] such as optoelectronics (organic light-emitting diodes and field-effect transistors), [65-68] energy storage devices[69] (supercapacitors[70,71] and solar cells[72]), electromechanical actuators,[73,74] electronic textile,[75,76] and anticorrosive coatings.[77-79]

These polymers are special in that they consist of long polymeric chains in which alternation of double and single-bonded sp^2 hybridized atoms is present. This conjugation results in an extended π-orbital system that allows charge mobility along the polymer backbone and between adjacent chains, thus endowing the polymer with semiconductive properties, both electrical and optical.[80] Besides, CPs also exhibit the attractive properties associated with conventional polymers, such as ease of synthesis and flexibility in processing. Figure 1.2.3 presents the most commonly used CPs.

In addition to the conjugated alternation of double bonds, application of a doping process is also a requirement for CPs conduction. CPs with low ionization potentials are oxidized when submitted to an anodic potential, thus undergoing p-doping. Radical cations (chemical term), or polarons (physical term) are generated in the polymer backbone delocalized generally over several repeating units, while counter-anions from the solution are also introduced to balance the charge. The intercalation of these mobile dopant ions is reversible. On the other hand, CPs with high electronic affinity are reduced at cathodic potential (n-doping) from the neutral state and store negative charges. In this case, counter-cations are needed to maintain electroneutrality. It is the ordered movement of these charge carriers along the conjugated CP backbone that results in high electrical conductivity. Moreover, the chemical nature, size and steric properties of the mobile dopant ions affect the electroactivity of CPs as well as their surface and bulk structural properties. Another important concept when talking about CPs is the electrochemical band gap, that is the energy difference between the ionization potential (valence band, HOMO value) and electroaffinity (conductance band, LUMO value) of a CP. Whenever this value is below 3 eV, the polymer can be referred as semiconductive.

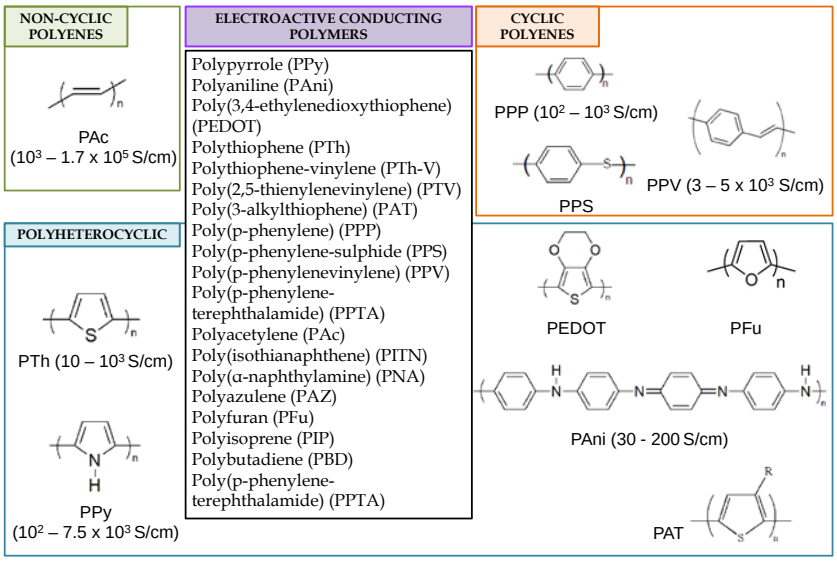

Figure 1.2.3. List of CPs and their abbreviations. Chemical structure and conductivity values for some of the representative CP of each family. [Adapted with permission.[20] - Open Acces article under a Creative Commons license (CC. BY 3.0)].

The accepted mechanism to synthesize CPs is the coupling of radical-ions generated by electrochemical, chemical, or photochemical oxidation of the monomer. Thus, the energy required to extract one electron from the monomer and initiate polymerization is provided in each case by an anodic potential, an electron acceptor (oxidizing agent) or by photons, respectively. In addition to the monomer, a solvent and the doping agent are also required.[80]

CPs biomedical applications

After the assessment that CPs were compatible with biological systems,[81,82] their use for biomedical applications increased considerably. Basically, the combination of their outstanding properties (good stability, high conductivities and easy of synthesis) with features such as biocompatibility, high sensitivity/selectivity for specific analytes, reproducibility of the electrode response and redox stability turned them into potential components in biosensors,[83-86] tissue engineering scaffolds,[87,88] neural probes,[89-91] drug-delivery systems,[92] or bio-actuators devices.[93,94] Practical applications in such fields have been typically developed using polypyrrole (PPy),[95-98] polyaniline (PAni)[99-101], polythiophene (PTh)[102] and its derivatives, specially poly(3,4-ethylenedioxythiophene) (PEDOT.)[103-105]

Nevertheless, as reported by Green *et al.*,[106] there are three main factors which can influence CPs toxicity, and thus have to be carefully controlled: unreacted monomers and oligomers, the mobility and toxicity of dopant ions and, finally, residual solvent used during the chemical or electrochemical polymerization process. Monomers tend to display higher toxicity than dopants, although both are slightly-moderately toxic. Therefore, complete removal of leachable components during the purification step is of vital importance to obtain high purity CP with reduced cytotoxicity.[81] Besides, the unique properties exhibited by CPs when structured at the nanoscale,[107] such as high electrical conductivity, electrochemical stability and quantum effects, can induce adverse biological effects (*i.e.* the surface area of nanomaterials increases exponentially with decreasing size, resulting in an enhanced interaction with biological tissues). Therefore, it is essential to run systematic cytotoxicity tests when working with CP nanomaterials to ensure the safety of these devices for biomedical applications.[62]

1.2.3. CPs Biointerfaces: Modification Strategies

For biomedical applications, the optimized design of CPs bioactive surfaces is crucial since the first contact established between biological systems and biomaterials is done at this interface. Commonly, CPs require specific modifications, which are done through four major approaches (physical adsorption, entrapment, doping or covalent linkage methods), to tune their properties (electrical, chemical or physical), and achieve an optimized performance.[108] Again, this flexibility of synthesis and adaptation to better suit the needs of each application is a great advantage (Figure 1.2.4).

In the physical adsorption approach, the interaction between the molecule and the CP interface is established by static forces and, although it is the most direct and simple route, loss of activity can occur if adsorbed molecules detach from the CP by external factors (*e.g.* pH changes). In the entrapment option, the molecule of interest is present in the polymerization solution during the CP synthesis and its incorporation in the growing CP occurs without any chemical reaction. These two routes have been widely used to prepare CP-based biosensors.[109,110] For instance, biofunctionalization with large biomolecules, such as enzymes or DNA, prevents their leakage from the CP matrix once entrapped.[111-113]

Similarly, if the entrapped molecule is charged, it can act as dopant and accomplish a two-fold purpose: it induces conductivity and a CP bioactive surface with new properties is obtained.[114]

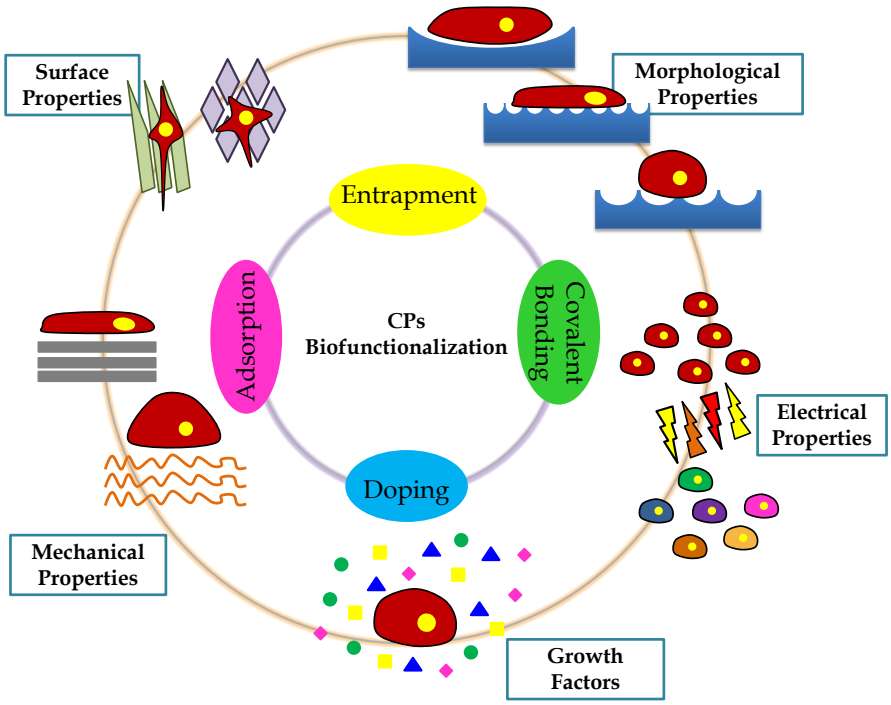

Figure 1.2.4. Scaffold properties. Surface properties: the surface topography could drive cell adhesion, proliferation, migration and differentiation. Mechanical properties: cells respond to the mechanical properties of the substrate on which they are growing, thus changing their fate. Morphological properties: scaffold morphologies for cell biomaterial interaction may vary in terms of interconnectivity, pore-size and shape. Electrical properties of the substrates are important issues for biomaterial-cell interaction. Adapted with permission.[117] Copyright 2012, Elsevier.

It is highly important to note that the CP performance, in terms of electrochemical activity, electrical conductivity, stability and biocompatibility, is significantly influenced by the properties of the dopants.[115]

Lastly, molecules can be strongly bounded to the CP backbone by covalently linkage, thus preventing their release from the biointerface.[116] Even though covalent functionalization can be achieved both during the synthesis of the monomer or after its polymerization, CP tend to be insoluble in most common organic solvents, which is an obstacle to post-polymerization covalent modification. Moreover, after functionalization, CP chains can adopt new conformations that alter the conjugation system and hinder their conductivity.

1.2.4. CP-based Scaffolds: Biomimetic Properties

When designing CP-based interfaces, it is of the outmost importance to incorporate well-defined features that mimic the native ECM. By applying all the strategies described in the previous section, the list of properties susceptible to modify and thus obtain a tissue scaffold with biomimetic chemical, topological and mechanical properties include: surface roughness, porosity, hydrophobicity, three-dimensional geometry, redox stability, biomolecule functionalization, degradability and elasticity, among other (Figure 1.2.4).[117]

Chemical properties

Biological activity and biodegradation are two of the most important features exhibited by the natural ECM. Regarding the former, cell adhesive sequences (*i.e* protein, peptide and synthetic peptidomimetic ligands) stimulate cells via receptor signalling.[118] On the other hand, ECM biodegradability ensures its constant regulation when it is replaced by functional tissue during natural wound healing. Hence, CP-based scaffolds are required to mimic these biochemical cues since both influence to a great extend cell adhesion behaviour.[119]

Biological activity:

Chemical biomimicry is achieved by the incorporation of bio-regulative cues. Many research groups have biofunctionalized CP by adding type I collagen,[120-122] gelatin,[123] laminin,[124,125] lysozyme,[126,127] polysaccharides,[128] dextrin molecules,[129] or doping with heparin,[130,131] hyaluronic acid (HA) and chondroitin sulphate A[132] to promote cellular adhesion, while nerve growth factors (NGF) have been used to improve compatibility with neural cells.[133-135] In addition to that, it is well-known that cellular adhesion mechanisms proceed via the RGD (Arg-Gly-Asp) ligand-receptor interaction, in which the RGD tripeptidyl sequence is the minimal amino acid sequence common to adhesive proteins.[136,137] Therefore, RGD has been used in many research studies to enhance the cytocompatibility of the CP interface.[138-140]

Another approach to add biological activity to the CP biointerface is based on the covalently modification of monomers to bear biological molecules, generally peptides, that promote cell-material interactions.[141-143] Furthermore, the use of functionalized monomers allows the precise control of the functional group density. This is the case of an electroactive polymer–amino acid hybrid material synthesized by conjugating PEDOT with a synthetic aminoacid as a new method to prepare CPs with cell adhesive functions. The final material successfully retained the morphological and structural characteristics of PEDOT as well as electrical

conductivity, electroactivity and electrochemical stability, while supporting cell adhesion and proliferation.[144] Similarly, Fabregat *et al.* reported the design of a new biocomposite based on a PEDOT matrix and a pentapeptide (CREKA), which recognizes and binds clotted plasma proteins.[145] One CREKA molecule per six PEDOT repeating units was entrapped during the electrochemical polymerization in basic aqueous solution. Results evidenced that the presence of CREKA favoured cellular proliferation by binding fibrin molecules from the culture medium, without negative impact on the CP electrochemical activity.

Finally, surface energy, wetting and adhesion properties of biointerfaces, which can be assessed by contact angle measurements, determine protein and biomolecular interactions.[14,146] CPs are exposed to acid-base and hydrophobic interactions because of their organic polymer backbone and the presence of radical cations and negatively charged dopants. When in contact with biological entities, such as cell adhesion proteins (*i.e.* integrins, selectins or cadherins), the non-specific adsorption of these biomolecules can be enhanced or prevented by controlling the redox state of the CP and its interaction with the dopant agent since both determine surface properties.[147] For instance, Li *et al.* adjusted easily the hydrophobicity of polythiophene films with different alkyl side chains by controlling their chain length, which in turn affected protein adsorption.[148] Atomic force microscopy (AFM) is an interesting tool to explore how CP interfaces interact with specific biomolecules at the molecular and nanoscale level after chemical functionalization of the AFM tip.[149-151]

Biodegradation:

CPs inability to biodegrade (degradation due to the scission of the backbone of the polymer caused by enzymatic or hydrolytic bond cleavage) is still a great challenge: inflammatory responses can occur if biomaterials are kept *in vivo* for long periods of time. Recently, Guo *et al.* published an excellent review on the different fabrication methods followed to obtain degradable CPs, while retaining electrical conductive properties.[152] Three major approaches were described: (1) blends and composites of CPs with conventional insulating polymeric biomaterials,[153,154] (2) erodible CPs[155,156] or (3) degradable CPs with conducting oligomers.[157] The first one is the most commonly used and, although it combines the positive properties of both polymers, the CP still has to be removed from the body after the degradation of the insulating polymer. In the last case, the CP is modified by adding ionisable or hydrolysable bonds that render it degradable. Therefore, the future design and study of CPs should be oriented to optimize simultaneously both their biodegradation rate and conductivity properties. Several groups (notably those of

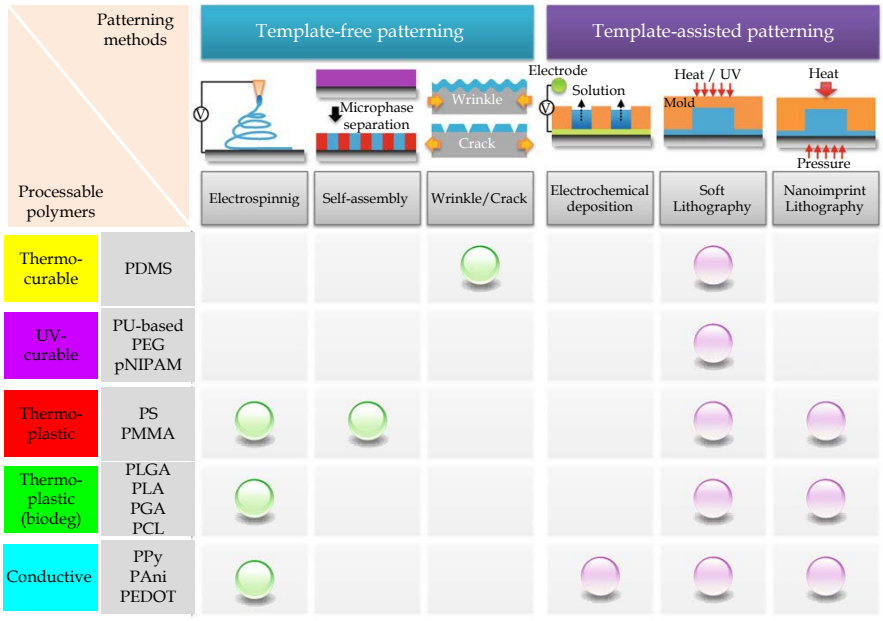

Figure 1.2.5. Classification of patterning methods with template-free and template-assisted principles and their availability with the existing various synthetic polymers. Reproduced with permission.[59] Copyright 2012, Spinger.

Schmidt, Albertsson, Wei and Langer) have reported the preparation of biodegradable CP-scaffolds that are suitable candidates for cell attachment and proliferation.[158-161]

Topological properties

The studies described in the previous section have shown how surface chemistry affects cell response toward biointerfaces.[162] However, the topological arrangement of these functionalities also controls and directs cell function.[163] Some natural tissues (*i.e.* cardiac, ligament, nervous or musculoskeletal) exhibit anisotropic response and morphology when in contact with the scaffold.[164] Therefore, its topological features, such as scale-length (micro- and nanoscopic structure[165,166]), type (*i.e.* ridges or grooves), distribution (randomly or distributed in pits or spikes) and surface roughness,[167] can regulate cellular behaviour (adhesion, proliferation, differentiation, and apoptosis), even without the effect of traditional growth factors.[168] For this reason, biomimetic topological properties and physical guidance cues are induced in tissue engineering platforms by patterning the surface.[169,170]

Besides, the use of biodopants when polymerizing CP is not only intended to improve their compatibility with biological systems, but they can also alter the physical surface properties of CPs. For instance, Gelmi *et al.* studied the physical surface properties of PPy substrates doped with ECM and non-biological molecules using AFM and Electrochemical AFM (EC-AFM) techniques. Results showed how these parameters correlated with the differing ability of the PPy biointerfaces to support cell growth.[122]

CP biointerfaces are topologically patterned[171] by electrospinning,[172] electrochemical deposition, soft lithography[173] and printing[174-176] methods (Figure 1.2.5).[59] From all these approaches, electrospinning is one of the most popular methods, since it allows the design of 3D-matrices with tuneable fiber features, such as the degree of fiber density, size and alignment.[177] Moreover, interconnecting porosity can be also controlled through experimental parameters. This results in large surface areas to exchange nutrients and wastes, and promote cell attachment and cell in-growth. Recently, J. Y. Lee reviewed the progress achieved so far in the fabrication of electrically CP based nanofibers biointerfaces, as well as their applications as potential tissue engineering scaffolds.[178] A more extensive insight on this topic is addressed in Chapter 2.

Mechanical properties

As it has been discussed, the design of scaffolds with optimal microenvironment conditions for cell tissues is based on maintaining the chemical, physical and biological similarity to the native ECM. Moreover, mechanical properties are also a key factor in controlling the response of cells towards the biointerface.[179,180] Recently, Evans *et al.* reviewed the role that material structure and mechanical features play in cell-matrix interactions: cells must sense and understand the mechanical context of the material in which they reside to perform their correct physiological function.[52] However, in addition to respond towards an applied force, cells also exert a mechanical force on the substrate, thus gauging feedback and making cell-fate decisions.

Specifically, processes such as cell growth, differentiation, shape changes and cell death are regulated by cycles of mechanosensing, mechanotransduction and mechanoresponse, all three mechanisms influencing cell behaviour thorough mechanical stimuli. Therefore, local sensing of force, geometry or substrate stiffness is transduced into biochemical signals.[181] As an example of that, back in 1977 Emerman e*t al.* showed how mammary epithelial cells proliferate on rigid substrates, while they were able to differentiate on softer substrates.[182]

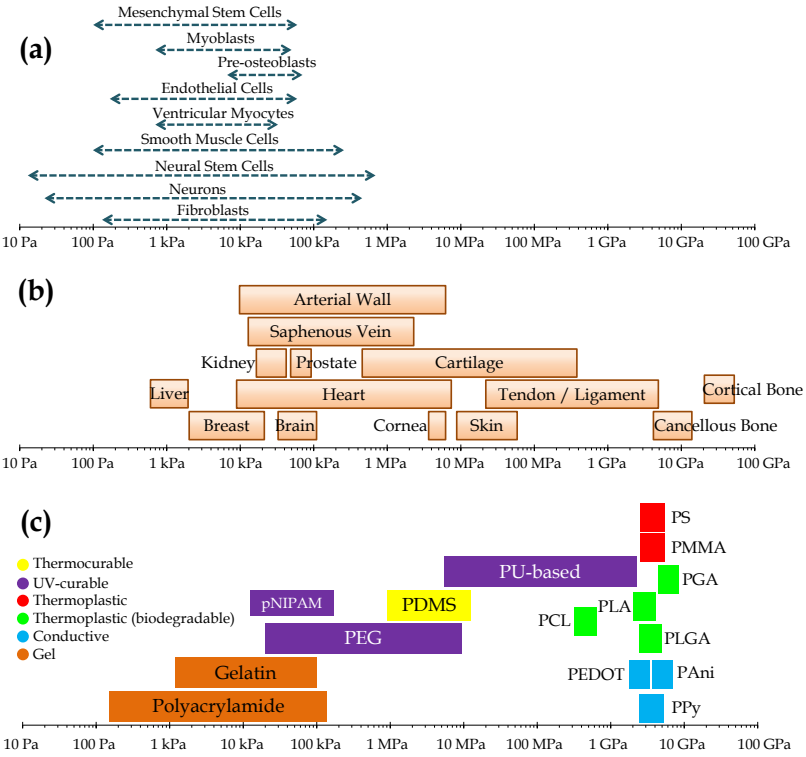

Figure 1.2.6. Range of the elastic modulus of various (a) cell types, (b) natural tissues in human body and (c) synthetic polymers. Adapted and reproduced with permission.[59] Copyright 2012, Spinger.

Similarly, Engler *et al.* showed that the stiffness of the substrate has a direct correlation with the differentiation of mesenchymal stem cells (MSCs).[183] Furthermore, each biological tissue displays a characteristic elastic modulus and rigidity based on the cell type and structural organization (Figure 1.2.6), ranging from hundreds of Pa for soft tissue (brain and fat), tens of kPa for stiffer tissues (muscle), and modulus in the order of MPa and GPa for bone tissue.[184] Recent research has evidenced that the mechanical characteristics of the biomaterial have to match those displayed by the tissue it is going to interface or replace to avoid undesired side effects like inflammation or scarring processes.[185]

In general, CPs display poor mechanical integrity and they lack flexibility. Their limited conformational freedom leads to brittle materials, which are not easily handled. Therefore, their blending with insulating materials (*i.e.*

polycaprolactone,[186] polyurethane,[154,187] poly(styrene-β-isobutylene-β-styrene[188], poly(lactic acid)[188-191] or poly(glycerol-sebacate)[192]) is aimed to achieve a two-fold purpose. First, the non-conductive matrix supports the CP, thus resulting in a flexible biointerface with electroactive features. Secondly, the elastic modulus of the scaffold can be tailored to equal that of the cell tissue of interest (*i.e.* tuneable mechanical and physicochemical properties).

Finally, complex CP-based tissue scaffolds have been developed by using hydrogels as the polymeric matrix since they exhibit excellent properties for tissue engineering applications: high water content, porosity and mechanical features similar to those displayed by soft tissues.[193,194] Excellent research work which addresses the challenges derived from the development of electrically conductive hydrogels can be found in the literature.[195-199] For example, an electrically conductive hydrogel consisting of oligo(polyethylene glycol) fumarate and PPy was developed and successfully applied to regenerate nerve cells[200] Similarly, a single component CP hydrogel was developed and combined both electrical properties and hydrogel characteristics.[201] It also promoted cell adhesion and proliferation, opening the way for the development of new tissue engineering scaffolds that have potential applications for nerve and muscle regeneration.

1.2.5. CP-based Scaffolds: Electrical Stimulation

Electrical stimulation (ES) is one of the agents that modulate cell-biointerface interaction in CP-based biointerfaces.[202] In particular, scaffolds made of PPy,[97] PAni[99] or PTh[102] derivatives are the most commonly used when applying ES, specifically when delivered to enhance neurite outgrowth in nerve cells.[203-205] Beneficial effects from ES have been theorized as the result of the release and uptake of negative/positive ions from/by the polymer, as well as electrophoretic redistribution of cell surface receptors and the increase in ECM molecules adsorption (*i.e.* fibronectin) onto the CP surface.[206,207] However, the ES set up has to be carefully designed since CP experience an increase in their resistivity as the ES proceeds, thus limiting their useful time, while long-term exposure of cells to high electrical currents (above 1 mA) can lead to a cytotoxic effect. Table 1.2.1 summarizes some of the most recent studies in which ES has been applied to CP-based scaffolds made of PAni and PPy.

Table 1.2.1. Summary of some of the most recent studies in which ES has been applied to CP-based scaffolds made of PAni and PPy.

Conductive Scaffold	Cell line tested	ES parameters	Outcome	Ref
Thin films of PAni	Human mesenchymal stem cells (hMSCs)	DC EF of 100 mV/cm during 10 min every 24h during 7 days	ES triggered the expression of early neural phenotypic markers Distinctive morphological change towards neural-like cells with enhanced cytoskeletal elongation	[208]
PAni-poly(lactic-*co*-glycolic acid) blend	Neonatal cardiomyocytes	Trains of electrical pulses (1.25 Hz, 5 V/cm)	Cardiomyocytes synchronized their beating as a result of ES	[209]
Sulfonated PAni micropattern electrodes	Mouse bone marrow stromal cells (BMSCs) Pre-osteoblast cells (MC3T3-E1)	ES with a sine wave generator at 1 kHz and 500 mV	Both BMSC and MC3T3-E1 cells grew faster than control	[210]
PPy films	Schwann cell (SC)	ES for 2h at 0.1 V, 0.5 V, and 1.0 V	Increased average SC displacement and enhanced levels of adsorbed proteins	[211]
PPy films	Rat bone marrow stromal cells (rBMSCs)	DC EF of 3.5, 0.35, and 0.035 V/cm during 2, 4, and 12h	ES accelerated the osteo-differentiation of rBMSCs and improved their mineralization	[212]
PPy deposited onto ITO glass slides	Mouse retinal progenitor cells (mRPC)	100 μA pulse trains, 5 s in duration, once per minute, for 4 days	Stimulated cells developed pronounced neuronal morphologies with significantly longer dendritic processes and larger cell bodies	[213]

Conductive Scaffold	Cell line tested	ES parameters	Outcome	Ref
PPy inkjet printed on polyarylate film	Rat pheochromocytoma 12 cells (PC12)	Pulsed current signal at 1 mA	ES promoted neurite outgrowth and orientation of neurites	[214]
PPy-poly(D,L-lactic acid) nerve conduits	PC12 cells	DC of 100 mV for 2 h	ES promoted nerve regeneration *in vivo:* cells exhibited more and longer neurites	[215]
PPy-block-polycaprolactone with poly(lactic-*co*-glycolic acid)	Dorsal root ganglia (DRG)	DC/AC EF of 100 mV/cm for 2 h	Increased axon growth for peripheral nerve repair	[216]
Nanoporous cellulose gels + PPy nanoparticles	PC12 cells	Rectangular peak-to-peak potential of 100 mV centering around a rest potential with a frequency of 100 Hz for 30 min every 24 h, repeated 3 times	PC12 cells attached and extended longer neurites when electrically stimulated	[217]
PPy coated polylactide scaffolds	Human adipose stem cells (hASCs)	0.2 V symmetric biphasic pulsed DC voltage at 1 or 100 Hz for 4h/day	ES promoted proliferation and osteogenic differentiation of hASCs	[218]

1.3. References

[1] *Wounds International* **2013**, *4(Suppl.)*, 1-12. Available at: www.woundsinternational.com
[2] C. A. L. Bassett, R. J. Pawluk, R. O. Becker, *Nature* **1964**, *204*, 652.
[3] M. A. Messerli, D. M. Graham, *Biol. Bull.* **2011**, *221*, 79.
[4] L. C. Kloth, *Int. J. Lower Extremity Wounds* **2005**, *4*, 23.
[5] M. Rouabhia, H. Park, S. Meng, H. Derbali, Z. Zhang, *PLoS One* **2013**, *8*, e71660.
[6] G. Jin, K. Li, *Mater. Sci. Eng., C* **2014**, *45*, 671.
[7] P. W. Luther, H. B. Peng, J. J.-C. Lin, *Nature* **1983**, *303*, 61.
[8] S. Meng, M. Rouabhia, Z. Zhang, in *Electrical Stimulation in Tissue Regeneration, Applied Biomedical Engineering,* (Ed: G. Gargiulo) InTech, Rijeka, Croatia **2011**, pp. 37-62.
[9] A. K. Dubey, S. D. Gupta, B. Basu, *J. Biomed. Mater. Res., Part* B **2011**, *98B*, 18.
[10] L. Ghasemi-Mobarakeh, M. P. Prabhakaran, M. Morshed, M. H. Nasr-Esfahani, H. Baharvand, S. Kiani, S. S. Al-Deyab, S. Ramakrishna, *J. Tissue Eng. Regener. Med.* **2011**, *5*, e17.
[11] H.-C. Tian, J.-Q. Liu, D.-X. Wei, X.-Y. Kang, C. Zhang, J.-C. Du, B. Yang, X. Chen, H.-Y. Zhu, Y.-N. NuLi, C.-S. Yang, *Biomaterials* **2014**, *35*, 2120.
[12] P. R. Bidez, S. Li, A. G. MacDiarmid, E. C. Venancio, Y. Wei, P. I. Lelkes, *J. Biomater. Sci., Polym. Ed.* **2006**, *17*, 199.
[13] I. Jun, S. Jeong, H. Shin, *Biomaterials* **2009**, *30*, 2038.
[14] K. M. Sivaraman, B. Özkale, O. Ergeneman, T. Lühmann, G. Fortunato, M. A. Zeeshan, B. J. Nelson, S. Pané, *Adv. Healthcare Mater.* **2013**, *2*, 591.
[15] D. E. Discher, P. Janmey, Y.-l. Wang, *Science* **2005**, *310*, 1139.
[16] C.-M. Lo, H.-B. Wang, M. Dembo, Y.-l. Wang, *Biophys. J.* **2000**, *79*, 144.
[17] A. J. Engler, S. Sen, H. L. Sweeney, D. E. Discher, *Cell* **2006**, *126*, 677.
[18] M. M. Stevens, J. H. George, *Science* **2005**, *310*, 1135.
[19] Y. Xia, S.-S. Peng, L.-Z. Xie, X.-J. Lian, X.-J. Zhang, H. Cui, T.-X. Song, F.-M. Zhang, N. Gu, F.-Z. Cui, *J. Biomater. Appl.* **2014**, *29*, 59.
[20] R. Balint, N. J. Cassidy, S. H. Cartmell, *Acta Biomater.* **2014**, *10*, 2341.
[21] B. D. Ratner, A. S. Hoffman, F. J. Schoen, J. E. Lemons, in *Biomaterials Science* (Third Edition), *Introduction – Biomaterials Science: An Evolving, Multidisciplinary Endeavor* (Eds: B. D. Ratner, A. S. Hoffman, F. J. Schoen, J. E. Lemons), Academic Press, **2013**, pp. xxv-xxxix.
[22] B. M. Holzapfel, J. C. Reichert, J.-T. Schantz, U. Gbureck, L. Rackwitz, U. Nöth, F. Jakob, M. Rudert, J. Groll, D. W. Hutmacher, *Adv. Drug Delivery Rev.* **2013**, *65*, 581.
[23] M. Vert, Y. Doi, K.-H. Hellwich, M. Hess, P. Hodge, P. Kubisa, M. Rinaudo, F. Schué, *Pure Appl. Chemistry* **2012**, *84*, 377.
[24] D. F. Williams, "Definitions in Biomaterials. Proceedings of a Consensus Conference of the European Society of Biomaterials.", Chester, England, March 3-5 1986, in *Progress in Biomedical engineering*, Vol. 4 (Ed: Elsevier), Amsterdam, Holand 1987, p. 54.
[25] E. Rabkin, F. J. Schoen, *Cardiovasc. Pathol.* **2002**, *11*, 305.
[26] R. J. Narayan, *Phil. Trans. R. Soc. A.* **2010**, *368*, 1831.
[27] L. L. Hench, I. Thompson, *J. R. Soc., Interface* **2010**, *7*, S379.
[28] G. Kaur, O. P. Pandey, K. Singh, D. Homa, B. Scott, G. Pickrell, *J. Biomed. Mater. Res., Part A* **2014**, *102*, 254.
[29] J. Daemen, P. W. Serruys, *Circulation* **2007**, *116*, 961.
[30] L. L. Hench, J. M. Polak, *Science* **2002**, *295*, 1014.
[31] L. Moroni, J. R. de Wijn, C. A. van Blitterswijk, *J. Biomater. Sci., Polym. Ed.* **2008**, *19*, 543.
[32] C. Chai1, K. W Leong, *Mol. Ther.* **2007**, *15*, 467.
[33] P. A. Netti, *Interface Focus* **2014**, 4, 20130065.

[34] E. S. Place, N. D. Evans, M. M. Stevens, *Nat. Mater.* **2009**, *8*, 457.
[35] M. Wu, J. He, X. Ren, W.-S. Cai, Y.-C. Fang, X.-Z. Feng, *Colloids Surf., B* **2014**, *116*, 700.
[36] S. Fleischer, T. Dvir, *Curr. Opin. Biotechnol.* **2013**, *24*, 664.
[37] T. Cohen-Karni, R. Langer, D. S. Kohane, *ACS Nano* **2012**, *6*, 6541.
[38] C. N. R. Rao, A. K. Cheetham, in *Nanomaterials Handbook*, Chapter 1. Materials Science at the Nanoscale (Ed: Y. Gogotsi) CRC Press – Taylor & Francis, Boca Raton, US, **2006**
[39] S. Choi, A. Tripathi, D. Singh, *J. Biomed. Nanotechnol.* **2014**, *10*, 3162.
[40] N. F. Huang, J. Okogbaa, J. C. Lee, A. Jha, T. S. Zaitseva, M. V. Paukshto, J. S. Sun, N. Punjya, G. G. Fuller, J. P. Cooke, *Biomaterials* **2013**, *34*, 4038.
[41] P. Viswanathan, S. Chirasatitsin, K. Ngamkham, A. J. Engler, G. Battaglia, *J. Am. Chem. Soc.* **2012**, *134*, 20103.
[42] S. Sartori, V. Chiono, C. Tonda-Turo, C. Mattu, C. Gianluca, *J. Mater. Chem. B* **2014**, *2*, 5128.
[43] E. Tejeda-Montes, K. H. Smith, M. Poch, M. J. López-Bosque, L. Martín, M. Alonso, E. Engel, A. Mata, *Acta Biomater.* **2012**, *8*, 998.
[44] P. Reemann, T. Kangur, M. Pook, M. Paalo, L. Nurmis, I. Kink, O. Porosaar, K. Kingo, E. Vasar, S. Kõks, V. Jaks, M. Järvekülg, *J. Mater. Sci.: Mater. Med.* **2013**, *24*, 783.
[45] C. P. Grey, S. T. Newton, G. L. Bowlin, T. W. Haas, D. G. Simpson, *Biomaterials* **2013**, *34*, 4993.
[46] S. Lyu, C. Huang, H. Yang, X. Zhang, *J. Orthop. Res.* **2013**, *31*, 1382.
[47] E. Llorens, L. Valle, R. Ferrán, A. Rodríguez-Galán, J. Puiggalí, *J. Polym. Res.* **2014**, *21*, 360.
[48] D. Sundaramurthi, U. M. Krishnan, S. Sethuraman, *Polym. Rev.* **2014**, *54*, 348.
[49] S. L. Bechara, A. Judson, K. C. Popat, *Biomaterials* **2010**, *31*, 3492.
[50] S. Bechara, L. Wadman, K. C. Popat, *Acta Biomater.* **2011**, *7*, 2892.
[51] I. Wheeldon, A. Farhadi, A. G. Bick, E. Jabbari, A. Khademhosseini, *Nanotechnology* **2011**, *22*, 212001.
[52] N. D. Evans, E. Gentleman, *J. Mater. Chem. B* **2014**, *2*, 2345.
[53] I. Ilie, R. Ilie, T. Mocan, D. Bartos, L. Mocan, *Int. J. Nanomed.* **2012**, *7*, 2211.
[54] T.-I. Chao, S. Xiang, J. F. Lipstate, C. Wang, J. Lu, *Adv. Mater.* **2010**, *22*, 3542.
[55] M. C. Serrano, S. Nardecchia, C. García-Rama, M. L. Ferrer, J. E. Collazos-Castro, F. del Monte, M. C. Gutiérrez, *Biomaterials* **2014**, *35*, 1543.
[56] A. M. Higgins, B. L. Banik, J. L. Brown, *J. Biomater. Tissue Eng.* **2013**, *3*, 396.
[57] W. Chen, L. G. Villa-Diaz, Y. Sun, S. Weng, J. K. Kim, R. H. W. Lam, L. Han, R. Fan, P. H. Krebsbach, J. Fu, *ACS Nano* **2012**, *6*, 4094.
[58] E. K. F. Yim, E. M. Darling, K. Kulangara, F. Guilak, K. W. Leong, *Biomaterials* **2010**, *31*, 1299.
[59] H. N. Kim, D.-H. Kang, M. S. Kim, A. Jiao, D.-H. Kim, K. Y. Suh, *Ann. Biomed. Eng.* **2012**, *40*, 1339. And reference within: S. Nemir, J. L. West, *Ann. Biomed. Eng.* **2010**, 38, 2.
[60] N. K. Guimard, N. Gomez, C. E. Schmidt, *Prog. Polym. Sci.* **2007**, *32*, 876.
[61] J. Jagur-Grodzinski, *e-Polym.* **2012**, *12*, 722.
[62] W.-K. Oh, O. S. Kwon, J. Jang, *Polym. Rev.* **2013**, *53*, 407.
[63] H. Shirakawa, E. J. Louis, A. G. MacDiarmid, C. K. Chiang, A. J. Heeger, *J. Chem. Soc., Chem. Commun.* **1977**, *578*.
[64] C. Li, H. Bai, G. Shi, *Chem. Soc. Rev.* **2009**, *38*, 2397.
[65] Y. Sun, X. Lu, S. Lin, J. Kettle, S. G. Yeates, A. Song, *Org. Electron.* **2010**, *11*, 351.
[66] B. Kumar, B. K. Kaushik, Y. S. Negi, *Polym. Rev.* **2014**, *54*, 33.
[67] S. Ouyang, Y. Xie, D. Wang, D. Zhu, X. Xu, T. Tan, J. DeFranco, H. H. Fong, *J. Polym. Sci., Part B: Polym. Phys.* **2014**, *52*, 1221.
[68] A. N. Aleshin, *Polym. Sci., Ser. C* **2014**, *56*, 47.
[69] J. F. Mike, J. L. Lutkenhaus, *J. Polym. Sci., Part B: Polym. Phys.* **2013**, *51*, 468.

[70] J. F. Mike, J. L. Lutkenhaus, *ACS Macro Lett.* **2013**, *2*, 839.
[71] Y. Shi, L. Pan, B. Liu, Y. Wang, Y. Cui, Z. Bao, G. Yu, *J. Mater. Chem. A* **2014**, *2*, 6086.
[72] Z. Zhang, X. Li, G. Guan, S. Pan, Z. Zhu, D. Ren, H. Peng, *Angew. Chem., Int. Ed.* **2014**, *53*, 11571.
[73] W. Zheng, G. Alici, P. R. Clingan, B. J. Munro, G. M. Spinks, J. R. Steele, G. G. Wallace, *J. Polym. Sci., Part B: Polym. Phys.* **2013**, *51*, 57.
[74] I. S. Romero, N. P. Bradshaw, J. D. Larson, S. Y. Severt, S. J. Roberts, M. L. Schiller, J. M. Leger, A. R. Murphy, *Adv.Funct. Mater.* **2014**, *24*, 3866.
[75] J. A. Lee, M. K. Shin, S. H. Kim, H. U. Cho, G. M. Spinks, G. G. Wallace, M. D. Lima, X. Lepró, M. E. Kozlov, R. H. Baughman, S. J. Kim, *Nat. Commun.* **2013**, *4*, Art. Number 1970.
[76] M. J. Biglari, J. Mokhtari, M. Nouri, A. A. Sarabi, *J. Appl. Polym. Sci.* **2014**, 131. DOI: 10.1002/app.40673
[77] P. Fu, H. Li, J. Sun, Z. Yi, G.-c. Wang, *Prog. Org. Coatings* **2013**, *76*, 589.
[78] A. C. C. de Leon, R. B. Pernites, R. C. Advincula, *ACS Appl. Mater. Interfaces* **2012**, *4*, 3169.
[79] M. Martí, L. Molina, C. Alemán, E. Armelin, *ACS Sustainable Chem. Eng*. **2013**, *1*, 1609.
[80] J. Roncali, in *Handbook of Conducting Polymers*, (Eds: T. A. Skotheim, R. L. Elsenbaumer, J. R. Reynolds) CRC Press– Taylor & Francis, Boca Raton, US **2007**.
[81] P. Humpolicek, V. Kasparkova, P. Saha, J. Stejskal, *Synth. Met.* **2012**, *162*, 722.
[82] X. Wang, X. Gu, C. Yuan, S. Chen, P. Zhang, T. Zhang, J. Yao, F. Chen, G. Chen, *J. Biomed. Mater. Res., Part A* **2004**, *68A*, 411.
[83] W. Lei, W. Si, Y. Xu, Z. Gu, Q. Hao, *Microchim. Acta* **2014**, *181*, 707.
[84] J. Travas-Sejdic, N. Aydemir, B. Kannan, D. E. Williams, J. Malmstrom, *J. Mater. Chem. B* **2014**, *2*, 4593.
[85] S. Radhakrishnan, C. Sumathi, A. Umar, S. J. Kim, J. Wilson, V. Dharuman, *Biosens. Bioelectron.* **2013**, *47*, 133.
[86] G. Fabregat, E. Córdova-Mateo, E. Armelin, O. Bertran, C. Alemán, *J. Phys. Chem. C* **2011**, *115*, 14933.
[87] J. G. Hardy, J. Y. Lee, C. E. Schmidt, *Curr. Opin. Biotechnol*. **2013**, *24*, 847.
[88] Z. Shi, Y. Li, X. Chen, H. Han, G. Yang, *Nanoscale* **2014**, *6*, 970.
[89] D. Khodagholy, T. Doublet, P. Quilichini, M. Gurfinkel, P. Leleux, A. Ghestem, E. Ismailova, T. Hervé, S. Sanaur, C. Bernard, G. G. Malliaras, *Nat. Commun.* **2013**, *4*, 1575.
[90] P. Fattahi, G. Yang, G. Kim, M. R. Abidian, *Adv. Mater.* **2014**, *26*, 1846.
[91] D. Bennet, S. Kim, *J. Mater. Sci.* **2011**, *46*, 4723.
[92] V. Pillay, T.-S. Tsai, Y. E. Choonara, L. C. du Toit, P. Kumar, G. Modi, D. Naidoo, L. K. Tomar, C. Tyagi, V. M. K. Ndesendo, *J. Biomed. Mater. Res., Part A* **2014**, *102*, 2039.
[93] T. F. Otero, J. G. Martinez, J. Arias-Pardilla, *Electrochim. Acta* **2012**, *84*, 112.
[94] K. Svennersten, M. Berggren, A. Richter-Dahlfors, E. W. H. Jager, *Lab Chip* **2011**, *11*, 3287.
[95] A. Vaitkuviene, V. Ratautaite, L. Mikoliunaite, V. Kaseta, G. Ramanauskaite, G. Biziuleviciene, A. Ramanaviciene, A. Ramanavicius, *Colloids Surf., A* **2014**, *442*, 152.
[96] M. Sharma, G. I. N. Waterhouse, S. W. C. Loader, S. Garg, D. Svirskis, *Int. J. Pharm.* **2013**, *443*, 163.
[97] Z.-B. Huang, G.-F. Yin, X.-M. Liao, J.-W. Gu, *Front. Mater. Sci.* **2014**, *8*, 39.
[98] S. Naficy, N. Stobi, P. G. Whitten, G. M. Spinks, G. G. Wallace, *Smart Mater. Struct.* **2013**, *22*, 075005.
[99] T. H. Qazi, R. Rai, A. R. Boccaccini, *Biomaterials* **2014**, *35*, 9068.
[100] V. Guarino, M. A. Alvarez-Perez, A. Borriello, T. Napolitano, L. Ambrosio, *Adv. Healthcare Mater.* **2013**, *2*, 218.

[101] H. Cui, J. Shao, Y. Wang, P. Zhang, X. Chen, Y. Wei, *Biomacromolecules* **2013**, *14*, 1904.
[102] P. Sista, K. Ghosh, J. S. Martinez, R. C. Rocha, *J. Nanosci. Nanotechnol.* **2014**, *14*, 250.
[103] L. Sui, X. J. Song, J. Ren, W. J. Cai, L. H. Ju, Y. Wang, L. Y. Wang, M. Chen, *J. Biomed. Mater. Res., Part A* **2014**, *102*, 1681.
[104] Z. Baghmanli, K. B. Sugg, B. Wei, B. S. Shim, D. C. Martin, P. S. Cederna, M. G. Urbanchek, *Plast. Reconstr. Surg.* **2013**, *132*, 374.
[105] L. Jin, T. Wang, Z.-Q. Feng, M. K. Leach, J. Wu, S. Mo, Q. Jiang, *J. Mater. Chem. B* **2013**, *1*, 1818.
[106] R. A. Green, N. H. Lovell, G. G. Wallace, L. A. Poole-Warren, *Biomaterials* **2008**, *29*, 3393.
[107] G. W. Wang, Y. N. Lu, L. P. Wang, H. J. Wang, J. Y. Wang, *J. Nanosci. Nanotechnol.* **2014**, *14*, 596.
[108] Z. Ma, Z. Mao, C. Gao, *Colloids Surf., B* **2007**, *60*, 137.
[109] S. Cosnier, *Biosens. Bioelectron.* **1999**, *14*, 443.
[110] T. Ahuja, I. A. Mir, D. Kumar, Rajesh, *Biomaterials* **2007**, *28*, 791.
[111] N. Prabhakar, K. Arora, S. P. Singh, H. Singh, B. D. Malhotra, *Anal. Biochem.* **2007**, *366*, 71.
[112] P.-C. Nien, T.-S. Tung, K.-C. Ho, *Electroanalysis* **2006**, *18*, 1408.
[113] S. K. Jha, M. Kanungo, A. Nath, S. F. D'Souza, *Biosens. Bioelectron.* **2009**, *24*, 2637.
[114] C. Vallejo-Giraldo, A. Kelly, M. J. P. Biggs, *Drug Discovery Today* **2014**, *19*, 88.
[115] H.-C. Tian, J.-Q. Liu, X.-Y. Kang, D.-X. Wei, C. Zhang, J.-C. Du, B. Yang, X. Chen, C.-S. Yang, *RSC Adv.* **2014**, *4*, 47461.
[116] X. Strakosas, M. Sessolo, A. Hama, J. Rivnay, E. Stavrinidou, G. G. Malliaras, R. M. Owens, *J. Mater. Chem. B* **2014**, *2*, 2537.
[117] S. Martino, F. D'Angelo, I. Armentano, J. M. Kenny, A. Orlacchio, *Biotechnol. Adv.* **2012**, *30*, 338.
[118] K. G. Sreejalekshmi, P. D. Nair, *J. Biomed. Mater. Res., Part A* **2011**, *96A*, 477.
[119] D. L. Elbert, J. A. Hubbell, *Annu. Rev. Mater. Sci.* **1996**, *26*, 365.
[120] Y. Xiao, C. M. Li, S. Wang, J. Shi, C. P. Ooi, *J. Biomed. Mater. Res., Part A* **2010**, *92A*, 766.
[121] X. Liu, Z. Yue, M. J. Higgins, G. G. Wallace, *Biomaterials* **2011**, *32*, 7309.
[122] A. Gelmi, M. J. Higgins, G. G. Wallace, *Biomaterials* **2010**, *31*, 1974.
[123] E. Stavrinidou, O. Winther-Jensen, B. S. Shekibi, V. Armel, J. Rivnay, E. Ismailova, S. Sanaur, G. G. Malliaras, B. Winther-Jensen, *Phys. Chem. Chem. Phys.* **2014**, *16*, 2275.
[124] R. A. Green, N. H. Lovell, L. A. Poole-Warren, *Biomaterials* **2009**, *30*, 3637.
[125] L. Zhang, W. R. Stauffer, E. P. Jane, P. J. Sammak, X. T. Cui, *Macromol. Biosci.* **2010**, 10, 1456.
[126] B. Teixeira-Dias, L. J. del Valle, D. Aradilla, F. Estrany, C. Alemán, *Macromol. Mater. Eng.* **2012**, 297, 427.
[127] D. E. López-Pérez, D. Aradilla, L. J. del Valle, C. Alemán, *J. Phys. Chem. C* **2013**, *117*, 6607.
[128] R. Lv, Y. Sun, F. Yu, H. Zhang, *J. Appl. Polym. Sci.* **2012**, *124*, 855.
[129] B. Teixeira-Dias, L. J. del Valle, F. Estrany, J. F. Mano, R. L. Reis, C. Alemán, *Macromol. Mater. Eng.* **2012**, *297*, 359.
[130] E. Shamaeli, N. Alizadeh, *Int. J. Pharm.* **2014**, *472*, 327.
[131] H. Ding, M. Zhong, Y. J. Kim, P. Pholpabu, A. Balasubramanian, C. M. Hui, H. He, H. Yang, K. Matyjaszewski, C. J. Bettinger, *ACS Nano* **2014**, *8*, 4348.
[132] K. J. Gilmore, M. Kita, Y. Han, A. Gelmi, M. J. Higgins, S. E. Moulton, G. M. Clark, R. Kapsa, G. G. Wallace, *Biomaterials* **2009**, *30*, 5292.
[133] D. H. Kim, S. M. Richardson-Burns, J. L. Hendricks, C. Sequera, D. C. Martin, *Adv. Funct. Mater.* **2007**, *17*, 79.

[134] J. Y. Lee, C. A. Bashur, C. A. Milroy, L. Forciniti, A. S. Goldstein, C. E. Schmidt, *IEEE Trans. NanoBiosci.* **2012**, *11*, 15.
[135] J. Y. Lee, J.-W. Lee, C. E. Schmidt, *J. R. Soc., Interface* **2009**, *6*, 801.
[136] Y. Takemoto, T. Matsuda, T. Kishimoto, M. Maekawa, T. Akutsu, *ASAIO Trans. Am. Soc. Artif. Intern. Organs* **1989**, *35*, 354.
[137] T.-W. Chung, D.-M. Lai, S.-D. Chen, Y.-I. Lin, *J. Biomed. Mater. Res., Part A* **2014**, *102*, 315.
[138] Y. Guo, M. Li, A. Mylonakis, J. Han, A. G. MacDiarmid, X. Chen, P. I. Lelkes, Y. Wei, *Biomacromolecules* **2007**, *8*, 3025.
[139] J.-W. Lee, F. Serna, C. E. Schmidt, *Langmuir* **2006**, *22*, 9816.
[140] J. Y. Lee, E.-D. Jeong, C. W. Ahn, J.-W. Lee, *Synth. Met.* **2013**, *185–186*, 66.
[141] X. Wang, R. Gong, Y. Song, M. Li, Y. Mu, Z. Guo, X. Wan, W. Jiang, *Supramol. Chem.* **2013**, *25*, 842.
[142] R. Gong, Z. Guo, F. Li, Y. Song, Y. Mu, M. Li, X. Wan, *Macromol. Chem. Phys.* **2014**, *215*, 906.
[143] L. K. Povlich, J. C. Cho, M. K. Leach, J. M. Corey, J. Kim, D. C. Martin, *Biochim. Biophys. Acta, Gen. Subj.* **2013**, *1830*, 4288.
[144] G. Fabregat, G. Ballano, E. Armelin, L. J. del Valle, C. Cativiela, C. Alemán, *Polym. Chem.* **2013**, *4*, 1412.
[145] G. Fabregat, B. Teixeira-Dias, L. J. del Valle, E. Armelin, F. Estrany, C. Alemán, *ACS Appl. Mater. Interfaces* **2014**, *6*, 11940.
[146] J. M. Pelto, S. P. Haimi, A. S. Siljander, S. S. Miettinen, K. M. Tappura, M. J. Higgins, G. G. Wallace, *Langmuir* **2013**, *29*, 6099.
[147] J. Liao, C. Ning, Z. Yin, G. Tan, S. Huang, Z. Zhou, J. Chen, H. Pan, *ChemPhysChem* **2013**, *14*, 3891.
[148] D.-F. Li, H.-J. Wang, J.-X. Fu, W. Wang, X.-S. Jia, J.-Y. Wang, *J. Phys. Chem. B* **2008**, *112*, 16290.
[149] M. J. Higgins, G. G. Wallace, *Polym. Rev.* **2013**, *53*, 506.
[150] P. Knittel, M. J. Higgins, C. Kranz, *Nanoscale* **2014**, *6*, 2255.
[151] A. Gelmi, M. J. Higgins, G. G. Wallace *Biochim. Biophys. Acta, Gen. Subj.* **2013**, *1830*, 4305.
[152] B. Guo, L. Glavas, A.-C. Albertsson, *Prog. Polym. Sci.* **2013**, *38*, 1263.
[153] J. Huang, X. Hu, L. Lu, Z. Ye, Q. Zhang, Z. Luo, *J. Biomed. Mater. Res., Part A* **2010**, *93A*, 164.
[154] C. R. Broda, J. Y. Lee, S. Sirivisoot, C. E. Schmidt, B. S. Harrison, *J. Biomed. Mater. Res., Part A* **2011**, *98A*, 509.
[155] A. N. Zelikin, D. M. Lynn, J. Farhadi, I. Martin, V. Shastri, R. Langer, *Angew. Chem., Int. Ed.* **2002**, *41*, 141.
[156] D. Mawad, K. Gilmore, P. Molino, K. Wagner, P. Wagner, D. L. Officer, G. G. Wallace, *J. Mater. Chem.* **2011**, *21*, 5555.
[157] N. K. E. Guimard, J. L. Sessler, C. E. Schmidt, *Macromolecules* **2008**, *42*, 502.
[158] T. J. Rivers, T. W. Hudson, C. E. Schmidt, *Adv. Funct. Mater.* **2002**, *12*, 33.
[159] B. Guo, Y. Sun, A. Finne-Wistrand, K. Mustafa, A.-C. Albertsson, *Acta Biomater.* **2012**, *8*, 144.
[160] H. Cui, Y. Liu, M. Deng, X. Pang, P. Zhang, X. Wang, X. Chen, Y. Wei, *Biomacromolecules* **2012**, *13*, 2881.
[161] C. J. Bettinger, J. P. Bruggeman, A. Misra, J. T. Borenstein, R. Langer, *Biomaterials* **2009**, *30*, 3050.
[162] J. M. Curran, R. Chen, J. A. Hunt, *Biomaterials* **2006**, *27*, 4783.
[163] D. V. Bax, R. S. Tipa, A. Kondyurin, M. J. Higgins, K. Tsoutas, A. Gelmi, G. G. Wallace, D. R. McKenzie, A. S. Weiss, M. M. M. Bilek, *Acta Biomater.* **2012**, *8*, 2538.

[164] D. Langheinrich, E. Yslas, M. Broglia, V. Rivarola, D. Acevedo, A. Lasagni, *J. Polym. Sci., Part B: Polym. Phys.* **2012**, *50*, 415.
[165] M. J. Dalby, N. Gadegaard, R. Tare, A. Andar, M. O. Riehle, P. Herzyk, C. D. W. Wilkinson, R. O. C. *Oreffo, Nat.* Mater. **2007**, *6*, 997.
[166] R. J. McMurray, N. Gadegaard, P. M. Tsimbouri, K. V. Burgess, L. E. McNamara, R. Tare, K. Murawski, E. Kingham, R. O. C. Oreffo, M. J. Dalby, *Nat. Mater.* **2011**, *10*, 637.
[167] H.-W. Liu, W.-C. Huang, C.-S. Chiang, S.-H. Hu, C.-H. Liao, Y.-Y. Chen, S.-Y. Chen, *Adv. Funct. Mater.* **2014**, *24*, 3715.
[168] M. Ventre, C. F. Natale, C. Rianna, P. A. Netti, *J. R. Soc., Interface* **2014**, *11*, 20140687.
[169] N. Gomez, J. Y. Lee, J. D. Nickels, C. E. Schmidt, *Adv. Funct. Mater.* **2007**, *17*, 1645.
[170] E. K. Purcell, Y. Naim, A. Yang, M. K. Leach, J. M. Velkey, R. K. Duncan, J. M. Corey, *Biomacromolecules* **2012**, *13*, 3427.
[171] L. Jiang, X. Wang, L. Chi, *Small* **2011**, *7*, 1309.
[172] B. K. Gu, M. S. Kim, C. M. Kang, J.-I. Kim, S. J. Park, C.-H. Kim, *J. Nanosci. Nanotechnol.* **2014**, *14*, 7621.
[173] V. Strong, Y. Wang, A. Patatanyan, P. G. Whitten, G. M. Spinks, G. G. Wallace, R. B. Kaner, *Nano Lett.* **2011**, *11*, 3128.
[174] B. Weng, R. L. Shepherd, K. Crowley, A. J. Killard, G. G. Wallace, *Analyst* **2010**, *135*, 2779.
[175] C. A. Mire, A. Agrawal, G. G. Wallace, P. Calvert, M. in het Panhuis, *J. Mater. Chem.* **2011**, *21*, 2671.
[176] B. Weng, X. Liu, M. J. Higgins, R. Shepherd, G. Wallace, *Small* **2011**, *7*, 3434.
[177] N. G. Rim, C. S. Shin, H. Shin, *Biomed. Mater.* **2013**, *8*, 014102.
[178] J. Y. Lee, *Polym. Rev.* **2013**, *53*, 443.
[179] G. C. Reilly, A. J. Engler, *J. Biomech.* **2010**, *43*, 55.
[180] B. Trappmann, J. E. Gautrot, J. T. Connelly, D. G. T. Strange, Y. Li, M. L. Oyen, M. A. C. Stuart, H. Boehm, B. Li, V. Vogel, J. P. Spatz, F. M. Watt, W. T. S. Huck, *Nat. Mater.* **2012**, *11*, 642.
[181] V. Vogel, M. Sheetz, *Nat. Rev. Mol. Cell Biol.* **2006**, *7*, 265.
[182] J. T. Emerman, D. R. Pitelka, *In Vitro* **1977**, 13, 316.
[183] A. J. Engler, S. Sen, H. L. Sweeney, D. E. Discher, *Cell*, **2006**, *126*, 677.
[184] S. Nemir, J. West, *Ann. Biomed. Eng.* **2010**, *38*, 2.
[185] B. N. Mason, in *Engineering Biomaterials for Regenerative Medicine*, Chapter "Matrix Stiffness: A Regulator of Cellular Behavior and Tissue Formation" (Eds: S. K. Bhatia) Springer, New York, US **2012**, pp. 19-37.
[186] X. Lu, Z. Qiu, Y. Wan, Z. Hu, Y. Zhao, *Composites, Part A* **2010**, *41*, 1516.
[187] P. K. Prabhakar, S. Raj, P. R. Anuradha, S. N. Sawant, M. Doble, *Colloids Surf., B* **2011**, *86*, 146.
[188] Y. Liu, X. Liu, J. Chen, K. J. Gilmore, G. G. Wallace, *Chem. Commun.* **2008**, 3729.
[189] L. Jin, Z.-Q. Feng, M.-L. Zhu, T. Wang, M. K. Leach, Q. Jiang, *J. Biomed. Nanotechnol.* **2012**, *8*, 779.
[190] N. A. Rahman, M. Gizdavic-Nikolaidis, S. Ray, A. J. Easteal, J. Travas-Sejdic, *Synth. Met.* **2010**, *160*, 2015.
[191] P. H. S. Picciani, E. S. Medeiros, Z. Pan, D. F. Wood, W. J. Orts, L. H. C. Mattoso, B. G. Soares, *Macromol. Mater. Eng.* **2010**, *295*, 618.
[192] T. H. Qazi, R. Rai, D. Dippold, J. E. Roether, D. W. Schubert, E. Rosellini, N. Barbani, A. R. Boccaccini, *Acta Biomater.* **2014**, *10*, 2434.
[193] N. Annabi, A. Tamayol, J. A. Uquillas, M. Akbari, L. E. Bertassoni, C. Cha, G. Camci-Unal, M. R. Dokmeci, N. A. Peppas, A. Khademhosseini, *Adv. Mater.* **2014**, *26*, 85.
[194] A. L. Butcher, G. S. Offeddu, M. L. Oyen, *Trends Biotechnol.* **2014**, *32*, 564.

[195] M. R. Abidian, E. D. Daneshvar, B. M. Egeland, D. R. Kipke, P. S. Cederna, M. G. Urbanchek, *Adv. Healthcare Mater.* **2012**, *1*, 762.
[196] R. A. Green, R. T. Hassarati, J. A. Goding, S. Baek, N. H. Lovell, P. J. Martens, L. A. Poole-Warren, *Macromol. Biosci.* **2012**, *12*, 494.
[197] J. Thiele, Y. Ma, S. M. C. Bruekers, S. Ma, W. T. S. Huck, *Adv. Mater.* **2014**, *26*, 125.
[198] D. Zhai, B. Liu, Y. Shi, L. Pan, Y. Wang, W. Li, R. Zhang, G. Yu, *ACS Nano* **2013**, *7*, 3540.
[199] S. Sirivisoot, R. Pareta, B. S. Harrison, *Interface Focus* **2014**, 4, 20130050.
[200] M. B. Runge, M. Dadsetan, J. Baltrusaitis, T. Ruesink, L. Lu, A. J. Windebank, M. J. Yaszemski, *Biomacromolecules* **2010**, *11*, 2845.
[201] D. Mawad, E. Stewart, D. L. Officer, T. Romeo, P. Wagner, K. Wagner, G. G. Wallace, *Adv. Funct. Mater.* **2012**, *22*, 2692.
[202] G. G. Wallace, S. E. Moulton, G. M. Clark, *Science* **2009**, *324*, 185.
[203] Z. Zhang, M. Rouabhia, Z. Wang, C. Roberge, G. Shi, P. Roche, J. Li, L. H. Dao, *Artif. Organs* **2007**, *31*, 13.
[204] R. T. Richardson, B. Thompson, S. Moulton, C. Newbold, M. G. Lum, A. Cameron, G. G. Wallace, R. Kapsa, G. Clark, S. O'Leary, *Biomaterials* **2007**, *28*, 513.
[205] M. P. Prabhakaran, L. Ghasemi-Mobarakeh, G. Jin, S. Ramakrishna, *J. Biosci. Bioeng.* **2011**, *112*, 501.
[206] A. Kotwal, C. E. Schmidt, *Biomaterials* **2001**, *22*, 1055.
[207] Y. Li, K. G. Neoh, E.-T. Kang, *J. Colloid Interface Sci.* **2004**, *275*, 488.
[208] G. Thrivikraman, G. Madras, B. Basu, *Biomaterials* **2014**, *35*, 6219.
[209] C.-W. Hsiao, M.-Y. Bai, Y. Chang, M.-F. Chung, T.-Y. Lee, C.-T. Wu, B. Maiti, Z.-X. Liao, R.-K. Li, H.-W. Sung, *Biomaterials* **2013**, *34*, 1063.
[210] Y. Min, Y. Liu, Y. Poojari, J.-C. Wu, B. E. Hildreth III, T. J. Rosol, A. J. Epstein, *Synth. Met.* **2014**, *198*, 308.
[211] L. Forciniti, J. Ybarra III, M. H. Zaman, C. E. Schmidt, *Acta Biomater.* **2014**, *10*, 2423.
[212] W.-W. Hu, Y.-T. Hsu, Y.-C. Cheng, C. Li, R.-C. Ruaan, C.-C. Chien, C.-A. Chung, C.-W. Tsao, *Mater. Sci. Eng., C* **2014**, *37*, 28.
[213] R. Saigal, E. Cimetta, N. Tandon, J. Zhou, R. Langer, M. Young, G. Vunjak-Novakovic, S. Redenti, "Electrical stimulation via a biocompatible conductive polymer directs retinal progenitor cell differentiation", presented at Engineering in Medicine and Biology Society (EMBC), 35th Annual International Conference of the IEEE, 3-7 July 2013.
[214] B. Weng, X. Liu, R. Shepherd, G. G. Wallace, *Synth. Met.* **2012**, *162*, 1375.
[215] H. Xu, J. M. Holzwarth, Y. Yan, P. Xu, H. Zheng, Y. Yin, S. Li, P. X. Ma, *Biomaterials* **2014**, *35*, 225.
[216] H. T. Nguyen, S. Sapp, C. Wei, J. K. Chow, A. Nguyen, J. Coursen, S. Luebben, E. Chang, R. Ross, C. E. Schmidt, *J.Biomed. Mater. Res., Part A* **2014**, *102*, 2554.
[217] Z. Shi, H. Gao, J. Feng, B. Ding, X. Cao, S. Kuga, Y. Wang, L. Zhang, J. Cai, *Angew. Chem., Int. Ed.* **2014**, *53*, 5380.
[218] J. Pelto, M. Björninen, A. Pälli, E. Talvitie, J. Hyttinen, B. Mannerström, R. S. Seppanen, R., M. Kellomäki, S. Miettinen, S. Haimi, *Tissue Eng., Part A* **2013**, *19*, 882.

CHAPTER 2

LITERATURE REVIEW

CP-BASED BIOINTERFACES: NANOMEMBRANES AND NANOFIBERS

Summary

Development of advanced biointerfaces that are able to combine electroactive and biodegradable features is currently considered a promising field of study for biomedical applications such as tissue engineering or drug delivery systems.

On one hand, the electrical response of CP enables the local stimulation of desired tissue, time controlled drug release and stimulation of either proliferation or differentiation of various cell tissues. On the other, this new class of functional platforms should not pose any long-term health risk. Nevertheless, as one polymer does not meet all the necessary requirements, it remains a considerable challenge to combine all the requisites and still minimize the inflammatory reaction in the host tissue. Hence, important efforts have been focused on developing biocompatible CP-based biointerfaces by combining conducting and degradable units.

Nanotechnology approaches assist in this purpose, and nanostructured blends are designed to result in smart platforms with tuned properties. Biomaterials scientists design functional scaffolds at the nanometer scale to better control the cell-biointerface interaction based on appropriate surface chemistry, topography and mechanical features.

This chapter reviews the latest research conducted on CP-based biointerfaces arranged as free-standing nanomenbranes and nanofibrous mats. The content and cited references have been adapted from:

(1) Review: Nanomembranes and Nanofibers from Biodegradable Conducting polymers [E. Llorens, E. Armelin, M. M. Pérez-Madrigal, L. J. del Valle, C. Alemán, J. Puiggalí, *Polymers* **2013**, *5*, 1115].

(2) From Insulating to Semiconducting Polymeric Free Standing Nanomembranes for Biomedical Applications [M. M. Pérez-Madrigal, E. Armelin, J. Puiggalí, C. Alemán, Submitted work to *J. Mater. Chem. B*].

2.1. Free-standing Nanomembranes (FsNM)

Over the past decades, biomaterials science has been increasingly evolving into a more interdisciplinary field combining elements of medicine, chemistry, biology, engineering and materials science. Recently, nanotechnological concepts and procedures have also been applied to obtain and improve devices with very different applications in biomedicine and biotechnology.[1-3] Specifically, there is a growing interest in the fabrication of nanomembranes (also known as ultra-thin films or nanosheets) since their distinctive features make them suitable for designing sensors,[4,5] nanobiological reactors,[6] biomotors,[7] biointerfaces for cellular matrices,[8] antimicrobial surfaces,[9,10] or drug release devices.[11,12]

In practice, the term *nanomembrane* refers to quasi-2D structures with macroscopic surface area and thickness values ranging from 10 to a few hundreds of nm. A few years ago, Kunitake *et al*., pioneers in this field, coined the term "*giant nanomembrane*" to denote self-supporting (also named free-standing) membranes with thickness from 1 to 100 nm and an aspect ratio of size and thickness greater than 10^6.[13] Such a high aspect ratio facilitates the macroscopic handling of these nanomembranes, while the self-supporting property, which enables the nanosheet to be removed from its supporting substrate retaining the mechanical integrity, is required to physically separate two spaces. Besides, free-standing nanomenbranes (hereafter denoted FsNM) are characterized by other special properties, such as low weight, high flexibility, robustness and, in some cases, transparency.[14]

Typically, FsNM are produced by depositing nanofilms on solid substrates, or via the fluid-fluid interface (either liquid-liquid or liquid-air). In addition, some other approaches, including layer-by-layer (LbL) assembly, Langmuir-Blodgett transfer (LB), spin-coating, electrophoretic deposition and cross-linking of self-assembled monolayers (SAM) techniques, also often are employed. These methods differ in two general aspects: (1) the degree of control over the final FsNM thickness, composition and stability; and (2) the step in which the nanomembrane is removed, transferred or extracted from the solid surface or the fluid-fluid interface.[15]

In the LbL technique, which was developed by Decher *et al*.[16-18] in the early 1990s, the formation of the FsNM is achieved by depositing on a solid surface alternating layers of oppositely charged materials (Figure 2.1.1a), such as polyions, metals, nanoparticles, ceramics or biological molecules.

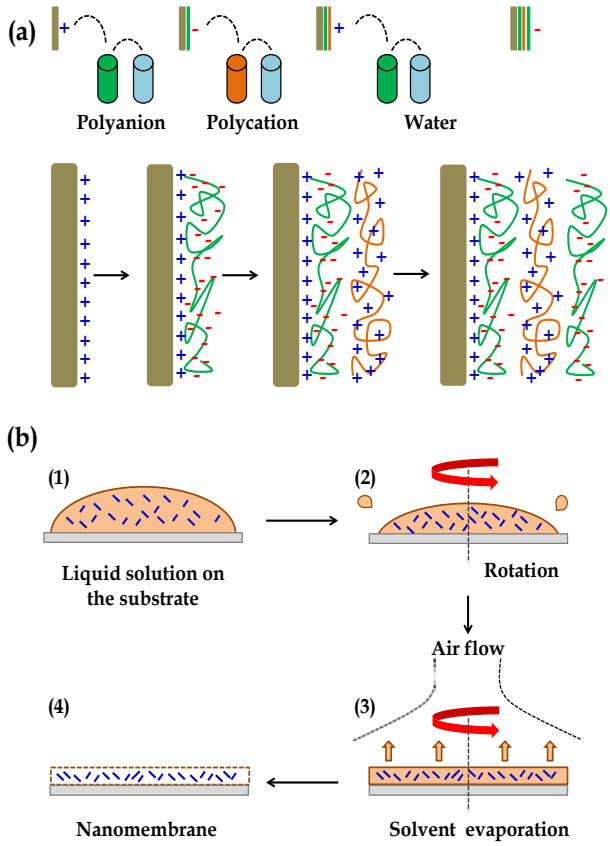

Figure 2.1.1. Schematic illustration of the (a) LbL and (b) spin-coating processes.

Accordingly, FsNM stability arises from primary or secondary interactions between those layers. This approach stands out because of its simplicity and the high degree of control over the FsNM thickness. Furthermore, the precise guidance exerted over the chemical composition of the layers results in a tremendous versatility for their assembly when designing FsNM.[19] Regarding the SAM technique, in 2003, Stroock *et al.*[20] extensively described the synthesis of polymeric FsNM with 10-15 nm in thickness and well-defined lateral size and shape.

On the other hand, spin-coating (Figure 2.1.1b) is another interesting approach that allows the preparation of single- or multi-layered FsNM in a few steps. In this case, the optimization of the spin-coating parameters (*e.g.* spinning speed and time, and the solution concentration) leads to ultra-thin films with controlled features,

thickness and homogeneity. In this procedure, which seems to be the most versatile and easy-going, the liquid polymeric solution is spin-coated onto a solid substrate, previously coated with a sacrificial layer. Hence, by dissolving the sacrificial layer in an appropriated solvent, the FsNM is detached from the substrate and released into a liquid environment where it can be easily handled with syringes or pipettes. Most of the FsNM described in this review were fabricated using a combination of both the LbL assembly and spin-coating procedures.

2.1.1. Insulating and Electrochemically Inactive FsNM

Generally, FsNM for biomedical applications are made using synthetic or naturally derived polymers. Among the synthetic ones, linear aliphatic polyesters, such as poly(lactic acid) (PLA) and poly(lactic-*co*-glycolic acid) (PLGA), have been extensively chosen since their biodegradation rate and mechanical properties can be easily controlled through variations in their molecular weight.[21] Also, poly(ether ester) copolymers have been successfully employed due to their excellent properties (*e.g.* elasticity, toughness, strength and easy processability), which arise from the combination of both soft and hard segments along their chemical structure.[22] In regard to biopolymers, the most frequently used are collagen and polysaccharides, such as alginate and chitosan, their applications being usually focused in tissue engineering.[23,24]

In the biomedical context, FsNM have been frequently reported as novel substrates/biointerfaces to promote cell adhesion, migration, proliferation and differentiation. For this purpose, specific requirements such as biocompatibility and, in some cases, also biodegradability and/or bioresorbability need be met. Furthermore, by successfully controlling the chemical composition and the fabrication process, it is possible to tune and adjust the physicochemical, mechanical, chemical and morphological properties of FsNM to promote cell-substrate interaction, which is particularly relevant in regenerative medicine (*i.e.* cellular organization can be directly regulated through the cellular microenvironment).[25,26] Threfore, FsNM can be used for different therapeutic uses (*e.g.* treatment of microbial infections, control of cell adhesion and repair of tissue defects). Their structure and flexibility allow them to coat the surface devices that interact with biological systems or, alternatively, FsNM can be introduced in a needle by aspiration and then be moved and released/injected in liquid environments (*e.g.* finely positioned on surgical incisions or directly used for wound treatments).

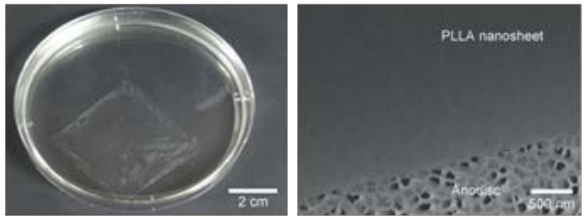

Figure 2.1.2. (a) PLA FsNM with a thickness of 23 ± 5 nm: macroscopic image of the nanosheet suspended in water (left) and SEM image of the nanosheet on an anodisc membrane (right). Reproduced with permission.[27] Copyright 2009, John Wiley and Sons.

This chapter is focused on reviewing CP-based FsNM. Nevertheless, Table 2.1.1 summarizes the most important characteristics (*i.e.* preparation method, thickness, properties and potential biomedical application) of FsNM made of insulating and electrochemically inactive polymers reported to date. As representative examples, two of the cited works are described in more detail.

First, Okamura *et al*.[27] developed PLA FsNM (Figure 2.1.2) with a thickness of 23 ± 5 nm by spin-coating a PLA solution (5 mg/mL) at 4000 rpm for 20 s onto a poly(vinyl alcohol) (PVA) sacrificial film. The mechanical properties and adhesion strength of the resulting transparent films, which exhibited a flat and uniform surface without cracks, were evaluated using the bulging test and micro-scratch test, respectively. These PLA-based FsNM showed low elastic modulus (1.7 ± 0.1 GPa) and high adhesiveness, which encouraged the analysis of their feasibility as a wound dressing in an *in vivo* experimental gastrostomy model test. Results were extremely positive, showing an excellent sealing efficacy that did not require adhesive agents. Moreover, the incision healed completely without scars and tissue adhesion. In an effort to investigate the possible biomedical application of these PLA FsNM, their antiadhesive and fixative characteristics were further investigated: an intraperitoneal polypropylene mesh (IPOM) overlaid with PLA nanosheets was placed on an intact peritoneum.[28] Results evidenced that PLA FsNM are feasible to induce adhesion prophylaxis in IPOM, having a beneficial effect as an atraumatic fixation tool.

Later, Fujie, Okamura and Takeoka[29] constructed what they called a "nano-adhesive plaster", a multilayered FsNM (nano-scale thickness: 30.2 ± 4.3 nm) made of chitosan and sodium alginate (Na alginate) that was deposited onto a PVA-silicone rubber substrate using the spin-coating assisted LbL approach. More

specifically, the layers of each polyelectrolyte were spin-coated on the silicone rubber (millimetre scale thickness: 1.0 mm) previously covered with a sacrificial PVA layer (micrometer scale thickness: 1.2 μm). As a result, the nano-adhesive plaster consists of the superposition of three different types of free-standing sheets. Chitosan and Na alginate contain amino and carboxylic groups, respectively, as cationic and anionic polyelectrolytes at ambient pH, which enormously facilitated their assembly in the FsNM. The elastic modulus, which was determined by the bulge test, was found to be 1.3 GPa. The good adhesiveness and flexibility of the nano-adhesive plaster was evidenced by transferring it, after modification with a luminescent pigment for ease of visibility, not only onto the skin of the arm of a human subject[29] but also onto a tissue (rat cecum) surface.[30]

Table 2.1.1. Summary of the most important characteristics (*i.e.* preparation method, thickness, properties and potential biomedical applications) of FsNM made of insulating and electrochemically inactive polymers.

Material	Preparation	Thickness (nm)	Properties[a]	Biomedical applications	Reference
PLA	Spin-coating	23±5	*E*: 1.7±0.1 GPa, L_c= (1.7±0.3–1.8±0.2) $\cdot 10^{-5}$ N/m. Transparency	Wound dressing	[27,28,31]
	Spin-coating assisted multilayering	60±6	Transparency	Barrier against burn wound infection	[32]
	Spin-coating	320±27	*E*: 136±44 MPa. Transparency	Bone/tendon repair: healing, adhesive bioactive matrix	[33,34]
PLA-mesh	Spin-coating	From 29±1 to 703±4.4	*E*: from 3.5±1.3 to 7-10 GPa. Transparency. Weak adhesiveness for higher thickness nanosheets	Anisotropic cell proliferation/differentiation	[35]
PLA coated with collagen at one side	Spin-coating	59.5±9.5 (PLA) and 5-10 (collagen)	Weak adhesiveness	Scaffold with different discrete functions: anti-adhesive and pro-healing	[36]
PLA + SPION	Spin-coating	From 33±3 to 245±9	*E* similar to PLA. Magnetically responsive and colored	Magnetically controllable support	[37]

Material	Preparation	Thickness (nm)	Properties[a]	Biomedical applications	Reference
PLA / PAH-D / HA	Spin-coating + LbL	~500	Robust and flexible	Drug delivery	[38]
PLGA	Thermal fusion	-	-	Platelet substitute, carrier	[39]
Chitosan / Na-alginate	Spin-coating assisted LbL	From 30.2±4.3 to ~75	*E*= 1.3 / 9.6 GPa. Pressure resistance, high flexibility adhesiveness, transparency, biodegradability	Nano-adhesive plaster Tissue defect repair. Multi-overlapping therapy for venous hemorrhage.	[29,30,40-43]
PVA / TC / (chitosan / Na-alginate)	Spin-coating assisted LbL	177	High flexibility, adhesive strength, transparency	Overlapping therapy, treatment of burn wound infections, antimicrobial/drug-loading	[44-45]
HA / collagen	LbL	42±4 (fibrous collagen, FC) and 62±7 (non-fibrous collagen, NFC)	FC: *E*= 12.5±1.5 GPa, σ_{max}= 289±9 MPa, ε_{max}= 1.0±0.1%. NFC: E= 4.3±0.6 GPa, σ_{max}= 227±10 MPa and ε_{max}= 1.7±0.3%	Scaffolds for regenerative medicine	[46]

Material	Preparation	Thickness (nm)	Properties[a]	Biomedical applications	Reference
Cell / gelatin / (chitosan / Na-alginate)$_3$	LbL onto cultured cells on PNIPAM-grafted surfaces	-	-	Fabrication of complex artificial soft tissues substitutes	[47]
PEO / PAA	LbL	80 nm per bilayer	Elastomeric properties, smooth, transparent	Biosubstrates, drug delivery devices and pH-sensitive sensors	[48]
PAA / PEG – PAH / PSS	Spraying polymer solutions	55 to several hundreds	Biocompatible. Transparent, pH responsive	Therapeutic devices and aids	[49]
NBPT-PEG	Spin-coating	~5	Mechanical stability, biocompatibility, high transparency. Protein-repelling behavior	Support in TEM studies	[50]
PEG hydrogel	Chemical crosslinking	10-350	Mechanical stability, high flexibility (E= ~ 2MPa), hydrophylicity, biorepulsion	Highly sensitive support Sensor element for biological samples	[51]
PAH / PAA	LbL dipping	253-688	Pores size: 300 nm-2 μm	Drug-delivery systems	[11]

Material	Preparation	Thickness (nm)	Properties[a]	Biomedical applications	Reference
PDDA / P4VPPS	LbL	~29 per bilayer	pH-dependent	Sacrificial layer for biological templates	[52]
PHEMA	Surface-initiated ATRP on a PDA layer	16-75	Good chemical stability, low mechanical strength, transparency	Multi-stimuli responsive sensors after functionalizing the surface of the films	[53]
PMPC / (PS, PAH, PAA)	ATRP of MPC and spin-coating assisted LbL	11 (PMPC) + 85±2 (PS, PAH, PAA)	Physiological stability, surface wettability, anti-biofouling	Biointerface for tissue-engineering scaffolds	[54]
PMMA	Spin-coating	199±20	High flexibility and physiological stability	Platforms with space-selective cell culture. Cell-directed culture in muscular tissue engineering	[55]
PMMA	Spin-coating PMMA:PS mixtures	From 38.8±1.1 to 110.2±2.0	Porous and perforated structures	Cell culture devices, high flux biosensors, drug delivery systems	[56]
PS – (CNT-Fn)	Spin-coating (PS) + μcontact printing (CNT-Fn)	From tens (~40) to hundreds (~360)	High flexibility, cell adhesiveness +tailored morphology	Flexible platforms to direct the cellular organization	[57]

Material	Preparation	Thickness (nm)	Properties[a]	Biomedical applications	Reference
$(PAH/PSS)_n$PAH-Au-$(PAH/PSS)_n$-PAH	Spin-coating assisted LbL	25-70	E= 30-40 GPa, σ_{max}> 100 MPa and ε_{max}= 2%. Light blue color. Long life, extraordinary sensitivity, unique auto-recovering ability	No biomedical application directly examine. Outstanding mechanical and dynamical properties.	[4,58]
PAA / DMLPEI	LbL	< 100 (from 2 to 20 bilayers)	Mechanical robustness, pH responsive	Coatings with microbicide properties for airborne and waterborne bacteria	[10]
DGI	Free-radical polymerization under UV radiation	< 5	High mechanical strength, thermal stability.	Practical applications depend on the surface post-functionalization	[59]

[a]*E*: Elastic modulus. L_c: Critical load related to the adhesion. σ_{max}: Ultimate tensile strength. ε_{max}: Ultimate tensile elongation.

2.1.2. FsNM with Electroactive CP

CPs have been used as biocompatible materials which can support cell adhesion, migration and proliferation.[60] Their properties are of great potential since the can be used to electrically stimulate local tissue,[61-64] exchange ions reversibly with cells, thus promoting adhesion and proliferations of these living systems,[65] fabricate electronic devices (*e.g.* biobatteries) that can be implanted in the organism,[66] act as time controlled drug- or bactericidal-release devices,[67,68] detect biomolecules,[69-71] or recognize specific fragments of DNA.[72,73]

Nevertheless, one of the major drawbacks to obtain free-standing nanosheets composed exclusively of CPs is the lack of mechanical integrity, poor stability, brittleness and the restricted processability of many of these materials. These limitations, combined with their lack of degradability, affect the number of biomedical applications of all-CP FsNM.

In spite of the fact that the mechanical properties of CPs are in general poor, different strategies have been developed to produce free-standing membranes of micrometric thickness made of PPy,[74-78] PAni[79-81] and PTh[82-84] for their application in different fields, such as separation membranes, electrode materials, sensors and catalysts.

In 2010, Wang *et al.*[85] reported a novel one–pot procedure to prepare PPy FsNM which was based on an interface polymerization (IP) that occurred at the interface between air and a Cu^{2+}-containing ionic liquid (Figure 2.1.3a). Resulting films were compact and uniform, and exhibited finely controlled thickness, with values from tens to hundreds of nanometers (*i.e.* as low as 60 nm, Figure 2.1.3b-d). However, FsNM with a thickness under 50 nm were brittle and weak, and broke easily. PPy FsNM doped with p-toluenesulfonic acid (TSA) displayed good electrical properties. Specifically, the electrical conductivity of films with a thickness of ~230 nm was 1.14 S/cm, although this value was lower than that reported previously for PPy in other systems. Moreover, asymmetrical films with different smoothness and water wettability on each side of the film were also prepared by altering the concentration of Cu^{2+} ions in the liquid phase. Even though no biomedical application was proposed by the authors, it is highly promising for this field the development of a general methodology for the preparation of CP films with different hydrophilicity and roughness on each side.

Jeon *et al.*[86] fabricated PPy FsNM by the organic crystal surface-induced polymerization of the monomer in an aqueous suspension containing hydrated

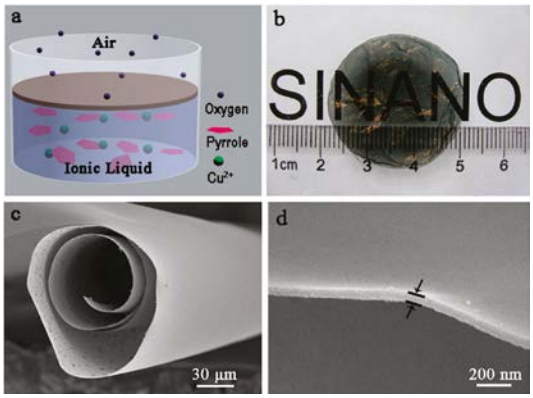

Figure 2.1.3. (a) Schematic illustration of the formation of a film at the air/ionic liquid interface. (b) Photograph of the film floating on water. (c) Low and (d) high magnification of the cross-sectional SEM images of the film. Reproduced with permission.[85] Copyright 2010, American Chemical Society.

crystals of sodium decylsulfonate below the Krafft temperature (*i.e.* temperature above which thermodynamic stable micelles are formed), and using $FeCl_3$ as oxidant. The main role of the crystals was to act as a template onto which the polymerization occurred. FsNM obtained using this procedure were composed of a unique CP domain with a thickness of ~21 nm, widths of 2-6 μm, and lengths greater than 10 μm. The electrical conductivity of these nanosheets was determined to be 30.6 S/cm, thus one order of magnitude higher than the value displayed by spherical PPy nanoparticles (diameters 30-50 nm) prepared by emulsion polymerization (2.9 S/cm). Besides, the feasibility of PPy FsNM to perform as HCl and NH_3 vapour detectors was evaluated: the system exhibited high sensitivity and a fast response with respect to PPy nanoparticles, which was attributed to the increased surface area and porosity of the former nanostructure. Despite the fact that the application studied for PPy FsNM was not biologically related, the methodology used is of relevant importance to successfully obtain FsNM.

More recently, Qi *et al.*[87] developed PPy FsNM by *in situ* freezing interfacial polymerization (FIP). This approach differs from the conventional interfacial polymerization in that the chemical reaction takes place at a solid/liquid interface. In this specific work, water and cyclohexane, which are immiscible, were used as the liquid and solid phase, respectively; solid cyclohexane being achieved upon crystallization. Special attention was paid to the following two issues: (1) proper choice of the reaction temperature, which should be lower than the freezing points of the organic solvent and water, but above that of the monomer; and (2)

minimizing the polymerization of pyrrole and the formation of PPy particles before the formation of solvent crystals. FsNM were very smooth and their thickness was about 100 nm. In this case, the electrical conductivity was determined to be 430 S/cm, whereas for the optimal synthetic conditions and doping parameters, the electrical conductivity reached peaks as high as 2000 S/cm, opening the door to potential biomedical applications.

Jha *et al*.[88] reported a novel strategy for the one-pot fabrication of PPy FsNM by dropping a dichloromethane solution that contained the monomer and a porphyrin derivative to an aqueous $FeCl_3$ solution kept in a beaker. Initially, a porphyrin/PPy bilayer formed spontaneously at the air/$FeCl_3$ interface, which after being washed rendered the PPy nanosheet. Follwoing this method, the nanosheet thickness can be tailored by changing the monomer concentration in the dropping solution. Hence, the thickness of PPy FsNM prepared by Jha et al.[88] increased from 50 to 250 nm when the pyrrole concentration augmented from 0.01 to 1 M. In addition, the conductivity of these PPy FsNM, which initially was of only ~10^{-5} S/cm, was enhanced after optimizing the doping parameters (*i.e.* the conductivity improved by ~ 30 and ~150 times on exposure to hydrochloric acid and iodine, respectively). Most importantly, the conductivity of these nanosheets showed no change when kept in air for more than 6 months, revealing a very noticeable stability in air. Although no specific application was examined, potential applications were mentioned (*e.g.* biosensors, scaffolds and artificial muscles).

On the other hand, the number of studies devoted to PAni-based nanosheets, which mainly consist of PAni/inorganic hybrid composites, is very scarce and their application in the biomedical field is practically inexistent. For example, very recently it was reported the fabrication of layered PAni/graphene/PAni nanosheets (the thickness of PAni and graphene layers was of 3.7 and 8.9 nm, respectively), which exhibited excellent gravimetric capacitance.[89] However, this sandwiched structure was essentially oriented towards applications in energy storage devices, solar cells, semiconducting devices, etc. Niu *et al*.[90] used a "skeleton/skin" strategy for the preparation of free-standing, thin and flexible single-walled carbon nanotube (SWCNT)/PAni hybrid films by a simple *in situ* electrochemical polymerization method. In this approach, directly grown SWCNT films with a continuous reticulate structure acted as the template, whereas PAni layers acted as the skin. The resulting hybrid films displayed a much higher conductivity compared to that of SWCNT/PAni composite films based on the post-deposition of the SWCNT film.

Regarding to PTh derivatives, PEDOT has also been used to prepare mechanically robust, electrically conductive and transparent hybrid FsNM. This

was achieved by Lee *et al*.[91] who coated densified carbon nanotube sheets with PEDOT by vapour phase polymerization. For FsNM with a thickness of ~66 nm, the main properties were high mechanical strength and modulus (135 MPa and 12.6 GPa, respectively), low resistance (below 200 Ω/sq), moderate optical transparency (56% at 550 nm wavelength), high flexibility and minor changes in resistance upon bending. Another interesting characteristic of these FsNM was their remarkable shape-recovery ability in a liquid and at the liquid/air interface, as opposed to previous carbon nanotube sheets. On the basis of these properties, these hybrid PEDOT-containing FsNM were proposed so far to be of potential interest in the design of sensors, actuators, optical devices, fuel cells, as well as for electrochemical capacitors. Unfortunately, their use for biomedical applications has not been considered yet.

As mentioned above, blending of CPs with insulating polymers is the most commonly followed approach to overcome the poor mechanical integrity of organic semiconductors. Accordingly, free-standing membranes have been fabricated by solvent casting mixtures of CPs with conventional insulating polymers, such as PVA[80] and nylon 66.[92] However, in all cases, such membranes were of micrometric thickness and their potential use (*e.g*. optical pH sensors[80] and conductive coatings[92]) was not related to the biomedical field, even though they were prepared by combining CPs with biopolymers derived from natural sources. For example, cellulose-PAni membranes of micrometric thickness, which were prepared by *in situ* polymerization of aniline in the presence of bacterial cellulose nanofibrils, were used as electromagnetic interference shielding materials despite the biological origin of the biopolymer.[93]

Greco *et al*.[94] reported the preparation of FsNM made of PEDOT and polystyrene sulfonate (PSS) complexes (PEDOT/PSS), where PSS acted as the dopant agent. In this sturdy, the Supporting Layer method, which enables the release and recovering of the free-standing nanosheet, was used (Figures 2.1.4 and 2.1.5). Firstly, a layer of water-soluble PVA is deposited as the sacrificial layer on a substrate (PDMS) by spin-coating. Then, the desired nanosheet is supported on that sacrificial layer. Later, once the bilayered film is dried, it is peeled off from the substrate. The thickness of those FsNM, which was controlled through the rotation speed, ranged from ~100 nm (rotation speed of 1000 rpm) to ~40 nm (rotation speed ≥ 4000 rpm).

Moreover, the mechanical and electrical properties of these PEDOT/PSS FsNM were extensively investigated as a function of their thickness. With decreasing thickness, the elastic modulus values, which were determined by the strain-induced

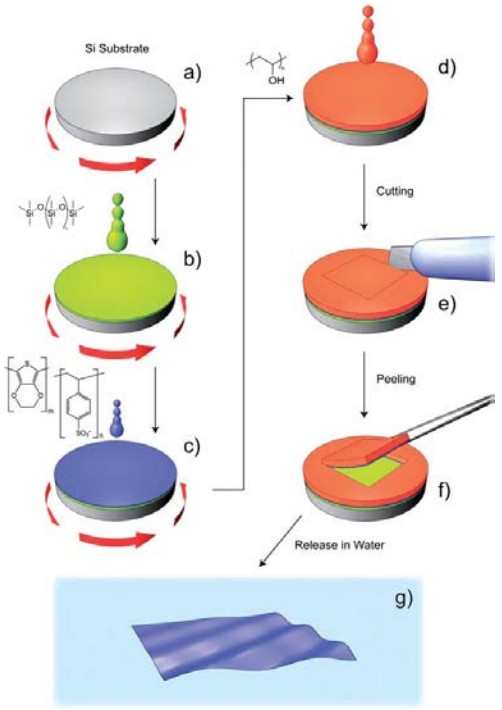

Figure 2.1.4. Schematic representation of the main steps of fabrication and release for obtaining PEDOT/PSS nanofilms by a Supporting Layer technique. (a) Si substrate; (b) spin-coating deposition of the PDMS substrate layer; (c) spin-coating deposition of the PEDOT/PSS nanofilm; (d) casting of a thick PVA supporting layer; (e) cutting and (f) peeling of the bilayer (PVA supporting layer + PEDOT/PSS nanofilm); (g) freestanding PEDOT/PSS nanofilm floating in water after dissolving PVA. Reproduced with permission.[94] Copyright 2011, Royal Society of Chemistry.

buckling test, varied between 0.81 and 1.02 GPa, while the electrical conductivity decreased from 1.44 to 0.88 S/cm. Interestingly, solvent casted PEDOT/PSS micrometric films (thickness of 7.5 μm) showed a conductivity of 1.38 S/cm. Therefore, a percolation threshold was reached based on the microscopic grain-like structure or the effect of residual water present in the FsNM.

Because of the proven biocompatibility of PEDOT,[65,95] PEDOT/PSS FsNM were considered as a first proof of concept towards the development of smart conductive substrates for cell growth and stimulation.[94] Although no cell culture study was reported in that work, PEDOT/PSS FsNM have been recently used to fabricate electrochemical microactuators in the form of microfingers of a variety of lengths.[96]

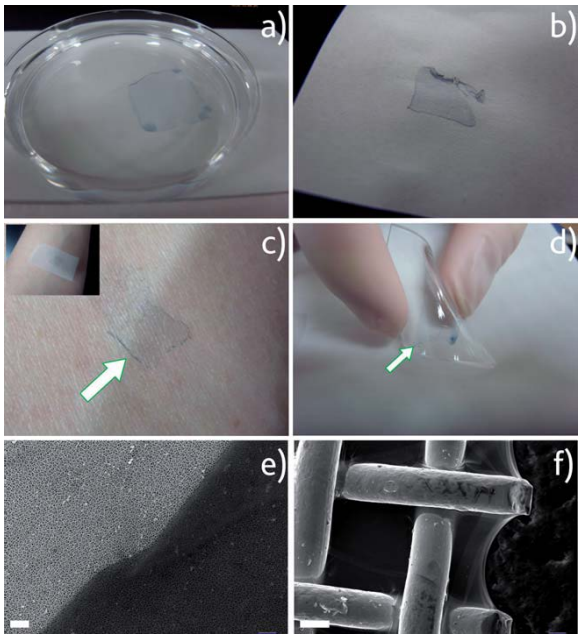

Figure 2.1.5. PEDOT/PSS nanofilms transferred to various substrates: (a) freestanding PEDOT/PSS nanofilms floating in water after PVA dissolving; nanofilms collected onto (b) paper, (c) human skin and (d) flexible PDMS. SEM micrographs showing the PEDOT/PSS nanofilm collected onto (e) the porous alumina substrate (scale bar 2 μm) and (f) steel mesh (scale bar 100 μm). Reproduced with permission.[94] Copyright 2011, Royal Society of Chemistry.

The reversible actuation of these microactuators, which consists in the bending of such microfingers, has been demonstrated by imposing electrochemical oxidation and reduction cycles on PEDOT/PSS supports. A number of possible applications can be envisaged for these small, soft actuators, such as microrobotics for cell manipulation.

The same group embedded iron oxide superparamagnetic nanoparticles into PEDOT/PSS FsNM using the Supporting Layer method described above.[97] More specifically, a stable colloidal dispersion of iron oxide nanoparticles added to the PEDOT:PSS mixture was used to prepare nanofilms through spin-coating. The thickness and surface roughness of the nanosheets depended on the amount of incorporated nanoparticles, ranging from 218 ± 13 to 269 ± 19 nm and from 1.5 to 8.5 nm, respectively. In this investigation, the attention was focused on the characterization of the morphological, electrical, magnetic and magneto-optical

properties, which also depended on the amount of entrapped iron oxide nanorparticles. The electrical conductivity was found to decrease from 1.96 ± 0.14 S/cm to 0.38 ± 0.06 S/cm with increasing concentration of nanoparticles. These FsNM open up new perspectives in technological fields (electronics, telecommunications and optics) rather than in biomedicine, even though no practical evidence for any application was provided.

PEDOT/PSS was also employed by Greco *et al.*[98] to prepare and characterize robust wrinkled conductive surfaces. This was achieved by following the simple two-step approach (metal deposition and subsequent heating) developed for the fabrication of nanowrinkles on shape-memory polymer sheets.[99] Specifically, the CP nanosheet (thickness ranging from 53.6 ± 1.2 to 120.9 ± 1.5 nm) was deposited onto a thermo-retractable polystyrene (PS) sheet by spin-coating an aqueous dispersion of PEDOT:PSS. A subsequent thermal treatment induced the substrate shrinking causing the microbuckling of the upper PEDOT:PSS layer due to compressive stress patterning. Adhesion and proliferation assays of C2C12 murine skeletal cells on uniaxial wrinkled samples indicated that cells preferentially aligned on low and narrow ridges (~1.5 μm height) rather than on high and wide ones (~2.5 μm height). This observation was corroborated when aligned myotubes in C2C12 differentiation stage were only formed on the former topology. Furthermore, the co-culturing of C2C12 cells with a fibroblast feeder layer improved the formation of aligned and mature myotubes. The achievement of tuneable conductive nanowrinkles interfaces represents a unique tool for the development of innovative biomedical devices.

A completely different strategy to obtain FsNM made of a CP and an insulating polymer is the one in which both components are arranged in a bilayered configuration. For instance, Greco *et al.* fabricated self-supported nanosheets with patterned conductivity using PEDOT/PSS and PLA, which acted as the mechanical support layer, thus maintaining continuity and robustness.[100] In a first step, the PEDOT/PSS layer (thickness of ~45 nm) was spin-coated onto a substrate. Then, in a second step, and after thermal treatment, the PLA layer (thickness of ~200 nm) was spin-coated onto the previous one. However, in order to obtain a patterned bilayer FsNM, an intermediate step (inject patterning) was introduced just before the deposition of the PLA layer. (*i.e.* localized over-oxidation of PEDOT/PSS nanofilm to provoke an irreversible loss of electrical conductivity at specific spots) of the PEDOT/PSS nanofilm Moreover, to enhance its electrical conductivity, which reached values of 180 S/cm, DMSO was added as a secondary doping agent. The resulting bilayered FsNM is of great interest as (bio)electrical interface and as thin

floating or ultraconformable circuits. In addition to that, the surface wettability of the bilayered FsNM was electrochemically switched through simple oxidation and reduction processes. This change was even more evident for nanosheets supported on a PS substrate. On the basis of this interesting ability, authors proposed the application of these nanofilms as smart conductive biointerfaces for directing cell adhesion and differentiation.[101]

Table 2.1.2 summarizes the most relevant examples of CP-containing FsNM discussed in this section.

Table 2.1.2. Summary of the most important characteristics (*i.e.* preparation method, thickness, properties and potential biomedical applications) of CP-containing FsNM.

Material	Preparation	Thickness (nm)	Properties[a]	Biomedical applications	Reference
PPy	Interface polymerization	From 60 to hundreds	σ= 1.14 S/cm for a thickness of 230 nm. Flexible, transparent, shiny, light-blue color.	Different roughness and water wettability on each side of film fit	[85]
	Organic crystal surface-induced polymerization	~21	σ= 30.6 S/cm. Smooth surface	Chemical sensor for HCl and NH_3 vapors	[86]
	In situ FIP	~100	Extremely high electrical conductivity σ= 2000 S/cm. Semi-transparency, smooth surface	Sensors	[87]
	Interface polymerization using porphyrin as *in situ* template	From 50 to 250	Low conductivity (σ≈ 10^{-5} S/cm) Mechanically strong, dense morphology	Biosensors and artificial muscles	[88]
PEDOT / PSS	Supporting Layer	From ~40 to ~100	σ= 0.88-1.44 S/cm *E*= 0.81-1.02 GPa. Flexibility.	Bioactive platforms. Electrochemical soft microactuators	[94,96]

Material	Preparation	Thickness (nm)	Properties[a]	Biomedical applications	Reference
PEDOT / PSS	Spin-coating +heat-shrinking	From 53.6±1.2 to 120.9±1.5	R= 199±11 - 586±16 Ω/sq	Scaffolds for functional cell alignment and ES	[98]
PEDOT-carbon nanotube sheet	Vapor phase polymerization	~66	R= 200 Ω/sq E= 12.6 GPa, σ_{max}= 135 MPa. Volumetric capacitance: ~40 F/cm^3 at 100 V/s. Flexibility and transparency. σ= 180 S/cm. Mechanical robustness	Sensors and actuators	[91]
(PEDOT/PSS) / PLA	Spin-coating	~45 (PEDOT/PSS layer) + ~200 (PLA layer)	Colors from dark blue to light blue or even transparent depending on the oxidation state. Electrochemical regulation of the surface wettability.	Smart conductive biointerfaces for directing cell adhesion and differentiation. Bioelectrodes.	[100]

[a] σ: Electrical conductivity. R: Electrical resistance. E: Elastic modulus. σ_{max}: Ultimate tensile strength. F_{adh}: Adhesion force between the AFM tip and the sample surface. E_g: Optical band gap energy.

2.2. Nanofibrous Biointerfaces

Electrospun nanofibers display promising features for biomedical purposes since they result in interconnected porous networks with increased surface area and abundant binding sites for absorbing proteins and cell membrane receptors. These features are interesting for applications such as drug gene/cell delivery, artificial blood vessels, wound dressings and substrates for tissue regeneration, immobilization of enzymes and development of catalyst systems. In addition to that, mats of electrospun nanofibers can mimic topographically the extracellular matrix (ECM): their architecture becomes similar to that of the ECM collagen (*i.e.* a 3D network of nanofibers with diameters between 50–500 nm).

Therefore, it is not surprising that the electrospinning technique has gained huge attention due to its advantages: (1) great accessibility to fabricate composites and incorporate drugs, (2) capability to prepare correct controllable topography (nanoscale size, alignment and orientation of nanofibers), (3) feasibility to render 3D scaffolds with the porosity required for effective tissue regeneration application, (4) encapsulation and local sustained release of drugs (*e.g.* growth factors, antioxidants, anti-inflammatory agents), and (5) surface functionalization.

Briefly, this electrostatic technique involves the use of a high voltage field to charge the surface of a polymer solution droplet, held at the end of a capillary tube, and induce the ejection of a liquid jet towards a grounded target (collector). The single jet initially formed is divided into multiple filaments by radial charge repulsion, which results in the formation of solidified ultra-thin fibers as the solvent is evaporating (Figure 2.2.1). The final morphology of fibers obtained onto the collector depends on (i) the molecular weight, molecular-weight distribution and architecture of the polymer, (ii) the solution properties (*e.g.* viscosity, dielectric constant, surface tension, concentration), (iii) operational parameters (*e.g.* applied electrical potential, deposition distance, flow rate, collector's size and motion), and finally (iv) ambient parameters (*e.g.* temperature or humidity).[101,102] Selection of the appropriate experimental conditions can lead to fibers with diameters that can range from several micrometers to few nanometers in an extremely rapid process (millisecond scale).[103]

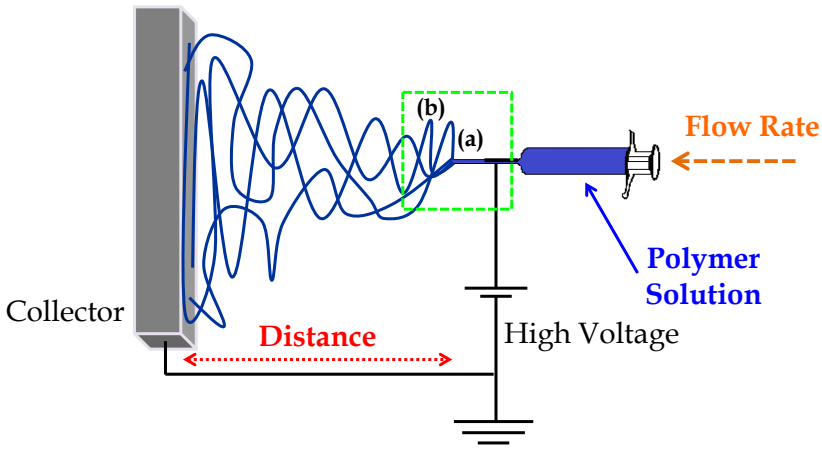

Figure 2.2.1. Typical electrospinning setup. Box shows fibers formation: (a) slow acceleration zone, (b) rapid acceleration (transition between liquid and solid).

In the last years, different reviews were concerned on the formation of biodegradable nanomats by electrospinning and their potential use for tissue engineering applications as functional smart scaffolds.[104-108] Specifically, Kai *et al.* reported advances for electrospun nanofibers that are based on natural proteins such as collagen, gelatin, silk, chitosan and alginate; synthetic polymers such as polyglycolide (PGA), poly(ε-caprolactone) (PCL), PLA and their copolymers, PLGA; and their blends.[109]

2.2.1. CP-based Nanofibrous Biointerfaces

Biopolymer-based conducting fibrous mats are of special interest for tissue engineering because they are able to stimulate specific cell functions or trigger cell responses in addition to the expected ability to physically support tissue growth.[110] Apart from that, several other properties are also desired when designing conducting fibrous mats: reversible oxidation, redox stability, conductivity, biocompatibility, controlling of the three-dimensional geometry and tunable surface topography.

However, the preparation of conductive nanofibers by electrospinning is not trivial and different strategies have been followed: (a) Incorporation of conductive particles (*e.g.* carbon nanotubes (CNT)) into the fibers, being usually necessary to submit the particles to surface treatment to increase their affinity for the polymeric matrix; (b) Direct electrospinning of CPs (in this case problems related to their high

stiffness and low solubility appear); (c) Blending of the CP with another electrospinnable polymer (used as a carrier), being the detriment of the electronic properties the major inconvenience (Figure 2.2.2a); and finally (d) Coating electrospun nanofibers with conductive materials (Figure 2.2.2b).

As it is stated in [111], MacDiarmid and his group firstly verified the possibility to electrospun fibers of CPs where no chain degradation was observed after electrical field application. Since then, many CPs such as PAni, PPy and PTh and its derivatives have been used to produce nanosized electrospun fibers.[112]

In the next subsections, some studies on CP-based nanofiber mats prepared by the electrospinning approach are described. In addition, Table 2.2.1 lists further examples.

PAni-based fibrous mats

One strategy to get conductive and biodegradable polymers is based on combining a biodegradable polymer (*e.g.* PLA or chitosan) with heterocyclic oligomers of aniline.[113] In fact, oligoanilines compounds with well-defined chain lengths have been used to model the electrical, magnetic, optical, and structural properties of PAni. Different approaches involve the use of aniline trimers,[114] tetramers,[115] and pentamers.[116]. However, nanofibers based on blending PAni and gelatin[117] resulted in the first novel conductive material with well suited properties as biocompatible scaffold. Both compounds were dissolved in 1,1,1,3,3,3-hexafluoroisopropanol and co-electrospun into nanofibers. PAni-gelatin blend

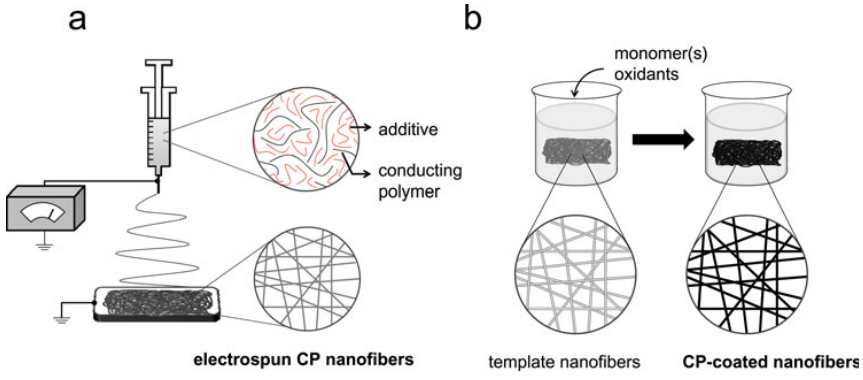

Figure 2.2.2. Fabrication of electrically conducting nanofibers using CPs: (a) electrospinning of CP containing blend, (b) nano-thick CP deposition onto a nanofiber template in a CP polymerizing solution. Reproduced with permission.[110] Copyright 2013, Taylor and Francis.

fibers supported H9c2 rat cardiac myoblast cell attachment and proliferation to a similar degree as positive controls (*i.e.* tissue culture-treated plastic).

Picciani *et al*.[118] considered the use of PLA as the support polymeric matrix for the preparation of PAni-based conducting nanofibers and evaluated the influence of some operational parameters, such as polymer concentration, applied voltage, and flow rate, on the morphology of electrospun fibers. Similarly, several PAni and poly(D,L-lactide) (PANi/PDLA) mixtures were successfully electrospun and their conductivity and biocompatibility evaluated.[119] Specifically, this scaffold was able to conduct a current of 5 mA and had an electrical conductivity of 0.0437 S/cm. Primary rat muscle cells were able to attach and proliferate over the entire new scaffold. The polymer degradation and shrinkage may prevent the blend from being used as the primary component of a biomedical device, but it was claimed useful as a biocompatible coating on devices such as sensors. In another example, composite substrates made of PAni doped with camphorsulfonic acid (CSA) and PCL electrospun fibers were investigated as platforms for cardiac tissue regeneration.[120] Finally, a biodegradable five-arm star-shaped polymer based on PCL was synthesized combining the advantages of star-shaped PCL with benefits of the electrospinning method to obtain uniform nanofibers with possible potential for use in tissue engineering.[121]

PPy-based fibrous mats

PPy is one of the most widely investigated CP because of the aqueous solubility of the monomer, its low oxidation potential and high conductivity, it is easily synthesized and displays long-term ambient stability. However, scarce work is concerned on the electrospinning of PPy alone. PPy fibers were firstly achieved using chloroform soluble samples chemically synthesized using ammonium persulfate (APS) as the oxidant and dodecylbenzene sulfonic acid (DBSA) as the dopant source.[122] Resulting PPy fibers exhibited circular cross-section, smooth surface and diameters about 3 μm. The electrical conductivity of the compressed PPy nonwoven web was about 0.5 S/cm, which was slightly higher than those of powder or cast films, possibly because of molecular orientation induced during the electrospinning.

Later, PPy conductive nanofibers (70-300 nm) were obtained by electrospinning organic solvent soluble PPy using PEO as the carrier.[123] Nanofibers were obtained with a well-defined morphology and physical stability. Moreover, the electrical conductivity increased with the PPy content, probably as a consequence of the

contact established between CP regions which remained 'less isolated', thus facilitating the electrical conduction.

Similarly, scaffolds constituted by PPy/PCL/gelatin nanofibres were obtained with balanced properties of conductivity, mechanical properties, and biodegradability, matching the requirements for regeneration of cardiac tissue. Furthermore, the scaffold promoted cell attachment, proliferation, interaction, and expression of cardiac-specific proteins.[124]

PTh-based fibrous mats

Electrospinning of CP has been scarcely carried out mainly because of their low solubility and fast crystallization, which easily blocks the nozzle. Among PTh derivatives, poly(3-hexylthiophene) (P3HT) has been considered the best candidate since it has very high field effect mobility (*i.e.* 0.1 cm^2/Vs can be attained). Nanofibers, with diameters of 100–500 nm, were deposited by electrospinning from chloroform solution onto electrodes on a SiO_2/Si substrate. However, the morphology of the P3HT nanofibers was poor since they were not continuously produced and contained lots of beads along the fibers.[125]

Lee *et al.*[126] studied the way to avoid P3HT crystallization and the block of the nozzle tip in order to obtain continuous nanofibers with uniform thickness. Experiments were performed using chloroform, which is the best solvent for P3HT, and a coaxial setup to continuously provide a small amount of additional solvent to the evaporating solution. This additional chloroform effectively maintained the concentration of P3HT low in the solution at the nozzle tip and consequently crystallization was late enough to allow continuous electrospinning without blocking the nozzle tip. Blends of P3HT and PCL were also electrospun into nanofibers to facilitate the production of continuous nanofibers even at low P3HT concentration (Figure 2.2.3).[126]

Later, a mixture of PLGA and poly(3-hexylthiophene) (P3HT) was electrospun into 2D random (196 nm) and 3D axially aligned nanofibers (200-80 nm).[127] Results of *in vitro* cell studies indicated that aligned PLGA–P3HT nanofibers had a significant influence on the adhesion and proliferation of Schwann cells.

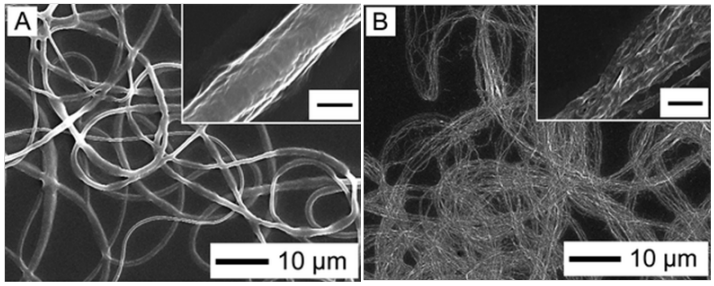

Figure 2.2.3. SEM images of electrospun blend fibers with 10% P3HT in PCL (P3HT:PCL 10:90, w/w): (A) as-electrospun fibers and (B) fibers after selectively removing PCL. Scale bar in insets indicates 500 nm. Reproduced with permission.[126] Copyright 2008, Royal Society of Chemistry.

The new electrically conducting axially aligned nanofibres provided both electrical and structural cues and could be potentially used as scaffolds for neural regeneration.

Table 2.2.1. Further examples of CP-based nanofiber mats prepared as tissue engineering scaffolds by the electrospinning approach.

CP	Insulating Polymer	Properties	Ref
PAni	Gelatin and PCL	PAni patterned on electrospun scaffold by inkjet printing	[128]
	PLA	Nanofibers prepared with a 3 wt% PLA/PAni solution were conducting. Diameters: 10 nm–300 nm	[129]
	PEG and PCL	The presence of $(PAni)_n$-*b*-PEG-*b*-$(PAni)_n$ terpolymers enhanced the spinnability of solution and significantly reduced the bead formation	[130]
	PEG and PCL	Low molecular weight copolymer with PAni segment resulted in fibers without any beads and average size of micrometer	[131]
	PLA	High porosity electrospun mats provided cells with comparably stiff, sub-micron sized fibres as anchoring points	[132]
P3HT	PLGA	*In vivo* experiments revealed the biocompatibility and biodegradability of PLGA-PHT nanofibers	[133]

2.3. References

[1] R. Langer, *J. Biomed. Mater. Res.* **2013**, *101A*, 2449.
[2] S. Fleischer, T. Dvir, *Curr. Opin. Biotechnol.* **2013**, *24*, 664.
[3] T. Cohen-Karni, R. Langer, D.S. Kohane, *ACS Nano* **2012**, *6*, 6541.
[4] C. Jiang, S. Markutsya, Y. Pikus, V. V. Tsukruk, *Nat. Mater.* **2004**, *3*, 721.
[5] J. D. Kittle, C. Wang, C. Qian, Y. Zhang, M. Zhang, M. Roman, J. R. Morris, R. B. Moore, A. R. Esker, *Biomacromolecules* **2012**, *13*, 714.
[6] M. G. Bellino, I. Tropper, H. Duran, A. E. Regazzoni, G. J. A. A. Soler-Illia, *Small* **2010**, *6*, 1221.
[7] J. A. Jaber, P. B. Chase, J. B. Schlenoff, *Nano Lett.* **2003**, *3*, 1505.

[8] C. S. Hajicharalambous, J. Lichter, W. T. Hix, M. Swierczewska, M. F. Rubner, P. Rajagopalan, *Biomaterials* **2009**, *30*, 4029.
[9] Z. Tai, H. Ma, B. Liu, X. Yan, Q. Xue, *Colloids Surf., B* **2012**, *89*, 147.
[10] S. Y. Wong, Q. Li, J. Veselinovic, B.-S. Kim, A. M. Klibanov, P. T. Hammond, *Biomaterials* **2010**, *31*, 4079.
[11] M. C. Berg, L. Zhai, R. E. Cohen, M. F. Rubner, *Biomacromolecules* **2006**, *7*, 357.
[12] K. C. Wood, J. Q. Boedicker, D. M. Lynn, P. T. Hammond, *Langmuir* **2005**, *21*, 1603.
[13] H. Watanabe, E. Muto, T. Ohzono, A. Nakao, T. Kunitake, *J. Mater. Chem.* **2009**, *19*, 2425.
[14] H. Watanabe, T. Kunitake, in Giant Nanomembrane, *Handbook of nanophysics. Functional nanomaterials,* Vol. 5 (Ed. K. D. Sattler), CRC Press, Taylor & Francis, Boca Raton, FL 2011, pp. 11-1.
[15] W. Cheng, M. J. Campolongo, S. J. Tan, D. Luo, *Nano Today* **2009**, *4*, 482.
[16] G. Decher, J. D. Hong, J. Schmitt, *Thin Solid Films* **1992**, *210–211, Part 2*, 831.
[17] G. Decher, *Science* **1997**, *277*, 1232.
[18] G. Decher, Y. Lvov, J. Schmitt, *Thin Solid Films* **1994**, *244*, 772.
[19] C. Jiang, V. V. Tsukruk, *Adv. Mater.* **2006**, *18*, 829.
[20] A. D. Stroock, R. S. Kane, M. Weck, S. J. Metallo, G. M. Whitesides, *Langmuir* **2002**, *19*, 2466.
[21] K. M. Nampoothiri, N. R. Nair, R. P. John, *Bioresource Technol.* **2010**, *101*, 8493.
[22] K. Odelius, P. Plikk, A.-C. Albertsson, *Biomacromolecules* **2005**, *6*, 2718.
[23] F. Khan, S. R. Ahmad, *Macromol. Biosci.* **2013**, *13*, 395.
[24]] R. Parenteau-Bareil, R. Gauvin, F. Berthod, *Materials* **2010**, *3*, 1863.
[25] S. Martino, F. D'Angelo, I. Armentano, J. M. Kenny, A. Orlacchio, *Biotechnol. Adv.* **2012**, *30*, 338.
[26] C. Zhao, A. Tan, G. Pastorin, H. K. Ho, *Biotechnol. Adv.* **2013**, *31*, 654.
[27] Y. Okamura, K. Kabata, M. Kinoshita, D. Saitoh, S. Takeoka, *Adv. Mater.* **2009**, *21*, 4388.
[28] K. Fujino, M. Kinoshita, A. Saitoh, H. Yano, K. Nishikawa, T. Fujie, K. Iwaya, M. Kakihara, S. Takeoka, D. Saitoh, Y. Tanaka, *Surg. Endosc.* **2011**, *25*, 3428.
[29] T. Fujie, Y. Okamura, S. Takeoka, *Adv. Mater.* **2007**, *19*, 3549.
[30] S. Takeoka, Y. Okamura, T. Fujie, Y. Fukui, *Pure Appl. Chem.* **2008**, *80*, 2259.
[31] H. Miyazaki, M. Kinoshita, A. Saito, T. Fujie, K. Kabata, E. Hara, S. Ono, S. Takeoka, D. Saitoh, *Wound Rep. Reg.* **2012**, *20*, 573.
[32] Y. Okamura, K. Kabata, M. Kinoshita, H. Miyazaki, A. Saito, T. Fujie, S. Ohtsubo, D. Saitoh, S. Takeoka, *Adv. Mater.* **2013**, *25*, 545.
[33] V. Pensabene, S. Taccola, L. Ricotti, G. Ciofani, A. Menciassi, F. Perut, M. Salerno, P. Dario, N. Baldini, *Acta Biomater.* **2011**, *7*, 2883.
[34] L. Ricotti, S. Taccola, V. Pensabene, V. Mattoli, T. Fujie, S. Takeoka, A. Menciassi, P. Dario, *Biomed. Microdevices* **2010**, *12*, 809.
[35] T. Fujie, L. Ricotti, A. Desii, A. Menciassi, P. Dario, V. Mattoli, *Langmuir* **2011**, *27*, 13173.
[36] D. Niwa, T. Fujie, T. Lang, N. Goda, S. Takeoka, *J. Biomater. Appl.* **2012**, *27*, 131.
[37] S. Taccola, A. Desii, V. Pensabene, T. Fujie, A. Saito, S. Takeoka, P. Dario, A. Menciassi, V. Mattoli, *Langmuir* **2011**, *27*, 5589.
[38] D. Chen, J. Chen, M. Wu, H. Tian, X. Chen, J. Sun, *Langmuir* **2013**, *29*, 8328.
[39] Y. Okamura, Y. Fukui, K. Kabata, H. Suzuki, M. Handa, Y. Ikeda, S. Takeoka, *Bioconjugate Chem.* **2009**, *20*, 1958.
[40] T. Fujie, N. Matsutani, M. Kinoshita, Y. Okamura, A. Saito, S. Takeoka, *Adv. Funct. Mat.* **2009**, *19*, 2560.
[41] T. Fujie, M. Kinoshita, S. Shono, A. Saito, Y. Okamura, D. Saitoh, S. Takeoka, *Surgery* **2010**, *148*, 48.

[42] K. Hagisawa, A. Saito, M. Kinoshita, T. Fujie, N. Otani, S. Shono, Y.-K. Park, S. Takeoka, *J. Vasc. Surg. Venous Lymphat. Disord.* **2013**, *1*, 289.
[43] N. Otani, M. Kinoshita, T. Fujie, A. Saito, S. Takeoka, D. Saitoh, K. Hagisawa, H. Nawashiro, K. Shima, *J. Clin. Neurosci.* **2013**, *20*, 301.
[44] T. Fujie, A. Saito, M. Kinoshita, H. Miyazaki, S. Ohtsubo, D. Saitoh, S. Takeoka, *Biomaterials* **2010**, *31*, 6269.
[45] A. Saito, H. Miyazaki, T. Fujie, S. Ohtsubo, M. Kinoshita, D. Saitoh, S. Takeoka, *Acta Biomater.* **2012**, *8*, 2932.
[46] T. Fujie, S. Furutate, D. Niwa, S. Takeoka, *Soft Matter*, **2010**, *6*, 4672.
[47] J. Chen, X. Qiu, L. Wang, W. Zhong, J. Kong, M. M. Q. Xing, *Adv. Funct. Mater.* **2014**, *24*, 2216.
[48] J. L. Lutkenhaus, K. D. Hrabak, K. McEnnis, P.T. Hammond, *J. Am. Chem. Soc.* **2005**, *127*, 17228.
[49] S. S. Ono, G. Decher, *Nano Lett.* **2006**, *6*, 592.
[50] N. Meyerbröker, Z.-A. Li, W. Eck, M. Zharnikov, *Chem. Mater.* **2012**, *24*, 2965.
[51] N. Meyerbröker, M. Zharnikov, *Adv. Mater.* **2014**, *26*, 3328.
[52] Z. Gui, J. Qian, B. Du, M. Yin, Q. An, *J. Colloid Interf. Sci.* **2009**, *340*, 35.
[53] M. Kohri, Y. Shinoda, H. Kohma, Y. Nannichi, M. Yamauchi, S. Yagai, T. Kojima, T. Taniguchi, K. Kishikawa, *Macromol. Rapid Commun.* **2013**, *34*, 1220.
[54] T. Fujie, H. Haniuda, S. Takeoka, *J. Mater. Chem.* **2011**, *21*, 9112.
[55] T. Fujie, A. Desii, L. Ventrelli, B. Mazzolai, V. Mattoli, *Biomed. Microdevices* **2012**, *14*, 1069.
[56] H. Zhang, S. Takeoka, *Macromolecules* **2012**, *45*, 4315.
[57] T. Fujie, S. Ahadian, H. Liu, H. Chang, S. Ostrovidov, H. Wu, H. Bae, K. Nakajima, H. Kaji, A. Khademhosseini, *Nano Lett.* **2013**, *13*, 3185.
[58] C. Jiang, S. Markutsya, V. V. Tsukruk, *Adv. Mater.* **2004**, *16*, 157.
[59] H. Qin, D. Wang, X. Xiong, J. Jin, *Macromol. Rapid Commun.* **2014**, *35,* 1055.
[60] P. R. Bidez, S. Li, A. G. MacDiarmid, E. C. Venancio, Y. Wei, P. I. Lelkes, *J. Biomater. Sci., Polym. Ed.* **2006**, *17*, 199.
[61] I. Jun, S. Jeong, H. Shin, *Biomaterials* **2009**, *30*, 2038.
[62] J. Huang, X. Hu, L. Lu, Z. Ye, Q. Zhang, Z. Luo, *J. Biomed. Mater. Res., Part A* **2010**, *93A*, 164.
[63] J. Y. Lee, C. A. Bashur, C. A. Milroy, L. Forciniti, A. S. Goldstein, C.E. Schmidt, *IEEE Trans. Nanobiosci.,* **2012**, *11*, 15.
[64] C. R. Broda, J. Y. Lee, S. Sirivisoot, C. E. Schmidt, B. S. Harrison, *J. Biomed. Mater. Res., Part A* **2011**, *98A*, 509.
[65] L. J. del Valle, F. Estrany, E. Armelin, R. Oliver, C. Alemán, *Macromol. Biosci.* **2008**, *8*, 1144.
[66] D. E. López-Pérez, D. Aradilla, L. J. del Valle, C. Alemán, *J. Phys. Chem. C* **2013**, *117*, 6607.
[67] B. Teixeira-Dias, L. J. del Valle, D. Aradilla, F. Estrany, C. Alemán, *Macromol. Mater. Eng.* **2012**, *297*, 427.
[68] G. Fabregat, B. Teixeira-Dias, L. J. del Valle, E. Armelin, F. Estrany, C. Alemán, *ACS Appl. Mater. Interfaces* **2014**, *6*, 11940.
[69] G. Fabregat, E. Armelin, C. Alemán, *J. Phys. Chem. B* **2014**, *118*, 4669.
[70] M. Martí, G. Fabregat, F. Estrany, E. Armelin, C. Alemán, *J. Mater. Chem.* **2010**, *20*, 10652.
[71] G. Fabregat, E. Córdova-Mateo, E. Armelin, O. Bertran, C. Alemán, *J. Phys. Chem. C* **2011**, *115*, 14933.
[72] S. Radhakrishnan, C. Sumathi, A. Umar, S. J. Kim, J. Wilson, V. Dharuman, *Biosens. Bioelectron.* **2013**, *47*, 133.

[73] B. Teixeiras-Dias, D. Zanuy, J. Poater, M. Solà, F. Estrany, L. J. del Valle, C. Alemán, *Soft Matter* **2011**, *7*, 9922.
[74] J. Lei, Z. Li, X. Lu, W. Wang, X. Bian, T. Zheng, Y. Xue, C. Wang, *J. Colloid Interface Sci.* **2011**, *364*, 555.
[75] T. F. Otero, M. J. Ariza, *J. Phys. Chem. B* **2003**, *107,* 13954.
[76] D. Chowdhury, A. Paul, A. Chattopadhyay, *Langmuir* **2005**, *21*, 4123.
[77] Y. Lu, G. Shi, C. Li, Y. Liang, *J. Appl. Polym. Sci.* **1998**, *70*, 2169.
[78] J. Song, H. Liu, M. Wan, Y. Zhu, L. Jiang, *J. Mater. Chem. A* **2013**, *1*, 1740.
[79] B. Zhao, K. G. Neoh, F. T. Liu, E. T. Kang, *Langmuir* **1999**, *15,* 8259.
[80] I. Mihai, F. Addiego, D. Ruch, V. Ball, *Sensors Actuat. B-Chem.* **2014**, *192*, 769.
[81] G.-W. Huang, H.-M. Xiao, H.-Q. Shi, S.-Y. Fu, *J. Polym. Sci, Part A: Polym. Chem.*, **2012**, *50*, 2794.
[82] R. Yue, S. Chen, B. Lu, C. Liu, J. Xu, *J. Solid State Electrochem.* **2011**, *15*, 539.
[83] H. Zhu, L. Gao, M. Li, H. Yin, D. Wang, *Electrochem. Commun.* **2011**, *13*, 1479.
[84] G. Shi, S. Jin, G. Xue, C. Li, *Science* **1995**, *267*, 994.
[85] D. Wang, Y.-X. Li, Z. Shi, H.-L. Qin, L. Wang, X.-F. Pei, J. Jin, *Langmuir* **2010**, *26*, 14405.
[86] S. S. Jeon, H. H. An, C. S. Yoon, S. S. Im, *Polymer* **2011**, *52*, 652.
[87] G. Qi, L. Huang, H. Wang, *Chem. Commun.* **2012**, *48*, 8246.
[88] P. Jha, S. P. Koiry, V. Saxena, P. Veerender, A. K. Chauhan, D. K. Aswal, S. K. Gupta, *Macromolecules* **2011**, *44*, 4583.
[89] Z. Tong, Y. Yang, J. Wang, J. Zhao, B.-L. Su, Y. Li, *J. Mater. Chem. A* **2014**, *2*, 4642.
[90] Z. Niu, P. Luan, Q. Shao, H. Dong, J. Li, J. Chen, D. Zhao, L. Cai, W. Zhou, X. Chen, S. Xie, *Energ. Environ. Sci.* **2012**, *5*, 8726.
[91] J. A. Lee, M. K. Shin, S. H. Kim, S. J. Kim, G. M. Spinks, G. G. Wallace, R. Ovalle-Robles, M. D. Lima, M. E. Kozlov, R. H. Baughman, *ACS Nano* **2012**, *6*, 327.
[92] R. A. Khalkhali, M. B. Keivani, *Asian J. Chem.* **2005**, *17*, 835.
[93] J. A. Marins, B. G. Soares, M. Fraga, D. Müller, G. M. O. Barra, *Cellulose* **2014**, *21*, 1409.
[94] F. Greco, A. Zucca, S. Taccola, A. Menciassi, T. Fujie, H. Haniuda, S. Takeoka, P. Dario, V. Mattoli, *Soft Matter* **2011**, *7*, 10642.
[95] K. Svennersten, M. H. Bolin, E. W. H. Jager, M. Berggren, A. Richter-Dahlfors, *Biomaterials* **2009**, *30*, 6257.
[96] S. Taccola, F. Greco, B. Mazzolai, V. Mattoli, E. W. H. Jager, *J. Micromech. Microeng.* **2013**, *23,* 117004.
[97] S. Taccola, F. Greco, A. Zucca, C. Innocenti, C. de Julián Fernández, G. Campo, C. Sangregorio, B. Mazzolai, V. Mattoli, *ACS App. Mater. Interfaces* **2013**, *5*, 6324.
[98] F. Greco, T. Fujie, L. Ricotti, S. Taccola, B. Mazzolai, V. Mattoli, *ACS Appl. Mater. Interfaces* **2013**, *5*, 573.
[99] C.-C. Fu, A. Grimes, M. Long, C. G. L. Ferri, B. D. Rich, S. Ghosh, S. Ghosh, L. P. Lee, A. Gopinathan, M. Khine, *Adv. Mater.* **2009**, 21, 4472.
[100] F. Greco, A. Zucca, S. Taccola, B. Mazzolai, V. Mattoli, *ACS Appl. Mater. Interfaces* **2013**, *5*, 9461.
[101] A. Frenot, I. S. Chronakis, *Curr. Opin. Colloid Interface Sci.* **2003**, *8*, 64.
[102] Q. P. Pham, U. Sharma, A. G. Mikos, *Tissue Eng.* **2006**, *12*, 1197.
[103] J. M. Deitzel, J. Kleinmeyer, D. Harris, N. C. Beck Tan, *Polymer* **2001**, *42*, 261.
[104] N. Ashammakhi, A. Ndreu, A. M. Piras, L. Nikkola, T. Sindelar, H. Ylikauppila, A. Harlin, M. E. Gomes, N. M. Neves, E. Chiellini, F. Chiellini, V. Hasirci, H. Redl, R. L. Reis, *J. Nanosci. Nanotechnol.* **2007**, *7*, 862.
[105] W.-E. Teo, W. He, S. Ramakrishna, *Biotechnol. J.* **2006**, *1*, 918.
[106] A. Di Martino, L. Liverani, A. Rainer, G. Salvatore, M. Trombetta, V. Denaro, *Musculoskelet Surg.* **2011**, *95*, 69.
[107] T. Wee-Eong, I. Ryuji, R. Seeram, *Sci. Technol. Adv. Mater.* **2011**, *12*, 013002.

[108] J. E. Trachtenberg, P. M. Mountziaris, J. S. Miller, M. Wettergreen, F. K. Kasper, A. G. Mikos, *J. Biomed. Mater. Res., Part A* **2014**, *102A*, 4326.
[109] D. Kai, S. S. Liow, X. J. Loh, *Mater. Sci. Eng., C* **2014**, *45*, 659.
[110] J. Y. Lee, *Polym. Rev.* **2013**, *53*, 443.
[111] A. G. MacDiarmid, W. E. Jones Jr, I. D. Norris, J. Gao, A. T. Johnson Jr, N. J. Pinto, J. Hone, B. Han, F. K. Ko, H. Okuzaki, M. Llaguno, *Synth. Met.* **2001**, *119*, 27.
[112] P. H. S. Piccini, E. S. Medeiros, W. J. Orts, L. H. C. Mattoso, in *Nanofibers - Production, Properties and Functional Applications*, Chapter 5: Advances in Electroactive Electrospun Nanofibers (Ed: T. Lin), InTech, Rijeka, Croatia, **2011**, pp. 85-116. Available from: http://www.intechopen.com/books/nanofibers-production-properties-and-functional-applications/advances-inelectroactive-electrospun-nanofibers]
[113] R. Alizadeh, M. Karimi, R. Mofrad, A. Entezami, *J. Polym. Res.* **2014**, *21*, 1.
[114] C.-J. Weng, Y.-S. Jhuo, C.-H. Chang, C.-F. Feng, C.-W. Peng, C.-F. Dai, J.-M. Yeh, Y. Wei, *Soft Matter* **2011**, *7*, 10313.
[115] X. Ma, J. Ge, Y. Li, B. Guo, P. X. Ma, *RSC Adv.* **2014**, *4*, 13652.
[116] Y. Liu, H. Cui, X. Zhuang, Y. Wei, X. Chen, *Acta Biomater.* **2014**, *10*, 5074.
[117] M. Li, Y. Guo, Y. Wei, A. G. MacDiarmid, P. I. Lelkes, *Biomaterials* **2006**, *27*, 2705.
[118] P. H. S. Picciani, E. S. Medeiros, Z. Pan, W. J. Orts, L. H. C. Mattoso, B. G. Soares, *J. Appl. Polym. Sci.* **2009**, *112*, 744.
[119] K. D. McKeon, A. Lewis, J. W. Freeman, *J. Appl. Polym. Sci.* **2010**, *115*, 1566.
[120] A. Borriello, V. Guarino, L. Schiavo, M. A. Alvarez-Perez, L. Ambrosio, *J. Mater. Sci.: Mater. Med.* **2011**, *22*, 1053.
[121] L. Shadi, M. Karimi, A. Entezami, *Colloid Polym. Sci.* **2015**, *293*, 481.
[122] T. S. Kang, S. W. Lee, J. Joo, J. Y. Lee, *Synth. Met.* **2005**, *153*, 61.
[123] Y. Cong, S. Liu, H. Chen, *J. Nanomater.* **2013**, *2013*, Article ID 148347.
[124] D. Kai, M. P. Prabhakaran, G. Jin, S. Ramakrishna, *J. Biomed. Mater. Res., Part A* **2011**, *99A*, 376.
[125] H. Sirringhaus, P. J. Brown, R. H. Friend, M. M. Nielsen, K. Bechgaard, B. M. W. Langeveld-Voss, A. J. H. Spiering, R. A. J. Janssen, E. W. Meijer, *Synth. Met.* **2000**, *111–112*, 129.
[126] S. Lee, G. D. Moon, U. Jeong, *J. Mater. Chem.* **2009**, *19*, 743.
[127] A. Subramanian, U. Krishnan, S. Sethuraman, *J. Mater. Sci.: Mater. Med.* **2012**, *23*, 1797.
[128] I. Rajzer, M. Rom, E. Menaszek, P. Pasierb, *Mater. Lett.* **2015**, *138*, 60.
[129] W. Serrano, A. Meléndez, I. Ramos, N. J. Pinto, *Polymer* **2014**, *55*, 5727.
[130] L. Shadi, M. Karimi, A. Entezami, K. Safa, *Polym. Bull.* **2013**, *70*, 3529.
[131] L. Shadi, M. Karimi, K. Asadpour-Zeynali, A. A. Entezami, K. D. Safa, *Polym. Plast. Technol. Eng.* **2013**, *53*, 254.
[132] N. Abdul Rahman, V. Feisst, M. E. Dickinson, J. Malmström, P. R. Dunbar, J. Travas-Sejdic, *Mater. Chem. Phys.* **2013**, *138*, 333.
[133] A. Subramanian, U. M. Krishnan, S. Sethuraman, *BioMed Res. Int.* **2013**, *2013*, Article ID 390518.

CHAPTER 3

OBJECTIVES

The review of the latest examples of nanostructured materials (free-standing nanomembranes (FsNM) and nanofibrous mats) for biomedical applications demonstrates the versatility of these systems, which relies on the variety of techniques available for their preparation and the concept that rational design can be used to tailor the relationship between desired properties and advanced applications (*e.g.* wound dressing, patches for bone or tendon repair, scaffolds for regenerative medicine and tissue engineering, drug delivery devices, artificial soft tissues, biosensors, artificial muscles and bioelectrodes).

On the one hand, research in FsNM for biomedical applications began about one decade ago, and investigations have been conducted considering basically a few groups of insulating and biodegradable polymeric materials: polyesters (*e.g.* poly(lactic acid) (PLA)), polysaccharides and other materials (*e.g.* poly(ethylene glycol), poly(acrylic acid) or poly(methyl methacrylate), among others). FsNM made of CPs have emerged with great interest in the last few years (*i.e.* first works appeared in 2010). Therefore, the number of CP-based FsNM studied so far, individually or combined with insulating polymers, is still limited. On the other hand, CP-based nanofibrous mats are of special interest for tissue engineering purposes because they are able to stimulate specific cell functions or trigger cell responses and physically support tissue growth.

Generally, the role played by the insulating polymer in these CP-based nanostructures is not only to provide mechanical robustness but also to protect any embedded biomolecule (*i.e.* drugs, growth factors, DNA, peptides and proteins, *etc.*) and to provide a matrix support for the CP, which in turn is responsible for the optical, electrochemical or electrical activity of such systems.

Still, as it has been appointed in the Introduction Chapter, the development of functional CP-based biointerfaces represents a tremendous challenge, in which decisive variables need to convergence. During the design step, the main difficulty is found in the limited solubility of CPs in common organic solvents, while their poor biodegradability hinders their practical use in *in vivo* tests.

Hence, the optimized performance of CP-based biointerfaces for bioapplications relies on the fact that CPs are able to deliver biological cues, and thus modulate the cell-biointerface interaction. This is based on the synergy among (1) physical stimulation (surface roughness, channels, or grooves), (2) biochemical stimulation, (3) mechanical stimulation and finally, (4) electrical stimulation (ES).

3.1. Aim of the Thesis

In this Thesis, the design and fully characterization of novel functional CP-based biointerfaces for biomedical applications is highlighted. Specifically, the development of such platforms is addressed to overcome the CPs limitations without compromising their electrochemical and electrical properties. In addition to that, the assessment of their biocompatibility and biodegradability features is also a main objective. Furthermore, special attention has been paid to evaluating those properties that are known to determine cell-biointerface interactions (*i.e.* surface chemistry, topology and mechanical features).

The obtained CP-based biointerfaces have been primary applied to function as scaffolds for promoting electro-active tissue regeneration. However, other applications such as drug delivery or passive ion transport have also been considered. Basically, this global purpose has been accomplished through three different approaches, which correspond to each one of the main parts of this dissertation, in which CP-based biointerfaces have been designed as FsNM, fibrous mats or electropolymerized ultra-thin interfaces. Specific objectives for each part are listed and described in detail in the next section.

3.2. Outline of the Thesis: Specific Objectives

This Thesis consists of ten chapters and, at the end, a summary which presents the general conclusions derived from the overall of the work.

In **Chapter 1**, the motivation of the Thesis is introduced. Moreover, a general overview of key concepts related to the topic of the dissertation is presented. **Chapter 2** consists on a review of the latest research conducted on CP-based biointerfaces which are produced as FsNM or nanofibrous mats. The current chapter, **Chapter 3**, summarizes the aim, objectives and outline of the Thesis.

PART A describes the experimental approach followed to develop FsNM as CP-based biointerfaces by blending a chemically synthesized PTh derivative with an insulating polymer (*i.e.* poly(tetramethylene succinate) (PE44) or thermoplastic polyurethane (TPU), Scheme 3.2.1). The choice of this specific PTh derivative is based on the fact that the incorporation of substituents into the 3-position of the thiophene ring enhances the solubility and processability of the CP. Therefore, the improved solubility of P3TMA in organic solvents enabled its blending with conventional polymers, thus improving its mechanical integrity.

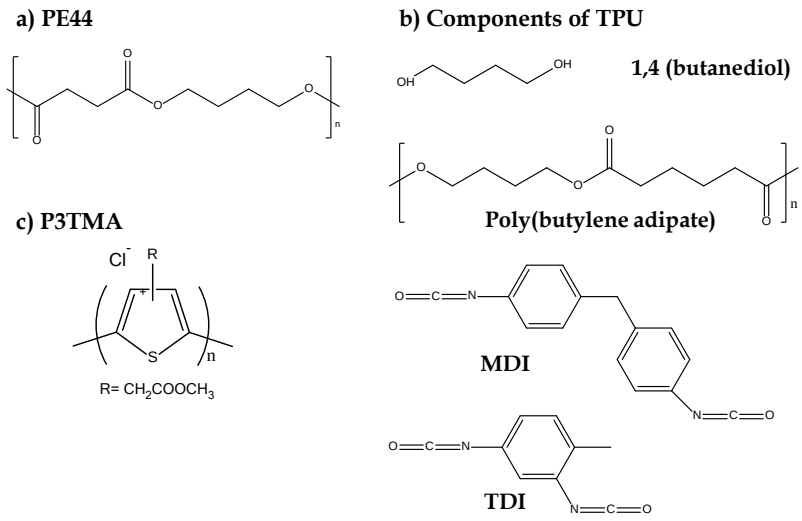

Scheme 3.2.1. Polymers used in Part A (MDI = Methylene diphenyl diisocyanate; TDI = Toluene diisocyanate).

Chapter 4 describes the preparation and characterization of PE44:P3TMA FsNM, while in **Chapter 5** PE44 is substituted by TPU to produce TPU:P3TMA FsNM. For both systems, their potential application as biointerfaces is explored. The specific objectives for these two Chapters can be summarized as follows:

- Optimize the experimental conditions (spin-coating speed and time, or solution concentration) required to obtain stable, flexible and robust FsNM with tunable thickness and roughness parameters by applying the spin-coating technique.
- Determine the miscibility of P3TMA and the insulating polymer in the corresponding blend by thermal and microscopic studies, and check their thermal stability.
- Analyse the doping state of P3TMA (in terms of band gap energy, E_g) in the blend from both the macroscopic (bulk properties) and nanoscopic scales.
- Evaluate the electrical semiconducting and electrochemical properties of P3TMA in each system to ensure that the CP retains its electroactivity after blending with PE44 or TPU, and determine if they produce a significant insulating effect.
- Study the influence of the TPU:P3TMA weight composition (20:80, 40:60 and 60:40) on the FsNM nanostructural features and nanomechanical response (Young's modulus and adhesion force).

- Investigate the influence of the P3TMA/insulating polymer interfaces composition on properties related to biomedical applications. This includes: swelling behaviour, hydrolytic and enzymatic degradability from both a quantitative and qualitative approach, biocompatibility towards different epithelial and fibroblast-like cell lines by cellular adhesion and proliferation studies, and finally the ability to adsorb extra cellular matrix proteins.
- Examine the electrobioactivity of the system: the influence of cell monolayers on the electrochemical response of P3TMA:PE44 biointerfaces.

Chapter 6 focuses on the characterization of P3TMA interfaces. Special interest is placed on the study of thermal properties (glass temperature transition, T_g). More specifically, the following aspects are explicitly addressed in this Chapter:

- Determine the T_g of ultra-thin P3TMA interfaces using a new technology (nanocalorimetric measurements based on the *bimetallic effect*), and compare the results with those obtained by conventional DSC thermal characterization (bulk sample).
- Correlate the morphological features of both systems (bulk and ultra-thin P3TMA) with the thermal results (T_g).
- Run atomistic molecular dynamics simulations on models that represent P3TMA bulk powder and ultra-thin films to evaluate the influence of the film-air interface on the density and conformation of P3TMA polymeric chains.

In **PART B**, the main goal is to characterize the electrochemical response and describe the bioapplication of CP-based fibrous interfaces made of P3TMA and biodegradable polymers (*i.e.* polylactide (PLA) (**Chapter 7)** or poly(ester urea)-*co*-poly(ester amide) PEU-*co*-PEA **(Chapter 8)**, Scheme 3.2.2). Special interest has been taken in determining the influence of the CP content on the features displayed by P3TMA-based hybrid fibrous interfaces. After optimizing their preparation, and evaluate their morphological and thermal properties, these studies have been focussed on the following specific objectives:

- Examine the electrochemical properties (electroactivity and electrostability) of both PLA:P3TMA and PEU-*co*-PEA:P3TMA hybrid samples.
- Assess the biocompatibility of PLA:P3TMA scaffolds toward Vero cells (epithelial-like) by cellular adhesion and proliferation studies.

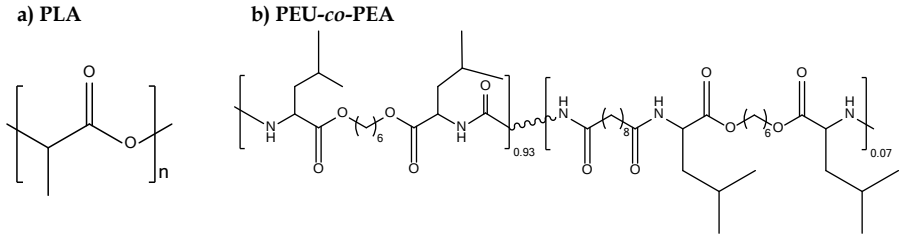

Scheme 3.2.2. Biodegradable polymers used in Part B

- Prepare PLA:P3TMA scaffolds to perform as drug-delivery interfaces by loading drugs with different hydrophobic/hydrophilic character (*i.e.* ciprofloxacin, chlorhexidine, triclosan and ibuprofen), and evaluate their release kinetics.

Finally, **PART C** consists on the preparation of new CP-based biointerfaces with nanometric thickness by electrochemical polymerization adopting specific modification strategies, as well as their characterization and bioapplication.

Chapter 9 is devoted to obtain a bioinspired interface formed by poly(*N*-methylpyrrole) (PNMPy) and Omp2a (Scheme 3.2.3a), an outer membrane protein which forms trimeric pores, by the entrapment method. The following issues are specifically approached in such investigation:

- Determination of the electrochemical polymerization conditions for the optimized immobilization of active Omp2a into the PNMPy matrix.
- Assessment of the influence of Omp2a on the morphological, topographical and electrochemical features of PNMPy-Omp2a biocomposites, comparing them with those of the control PNMPy.
- Regarding the bioapplication, three different targets have been addressed: (i) investigate the Omp2a response towards severe enzymatic degradation conditions; (ii) evaluate the cell adhesion and proliferation response of two cell lines (Vero and Cos-7) toward the PNMPy-Omp2a biointerface; and (iii) study of the passive ion transport of PNMPy-Omp2a biointerfaces by means of electrochemical impedance spectroscopy.

Chapter 10 has been focused on the development of a bioactive platform based on the *co*-electropolymerization of a specially synthesized bis-thienyl monomer, AzbT, which contains carboxyl and Schiff base functionalities (*i.e.* covalent linkage method), and 2,2′:5′,2′′-therthiophene (Th_3) (Scheme 3.2.3b). The specific objectives examined in this Chapter can be listed as follows:

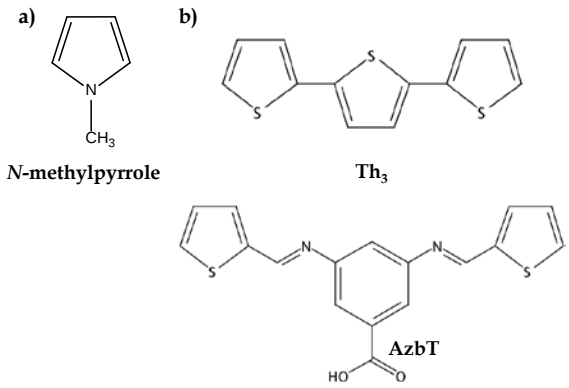

***N*-methylpyrrole** **Th_3**

Scheme 3.2.3. Monomers used in Part C to obtain CPs by electropolymerization.

- Confirm the correlation between the AzbT:Th_3 molar ratio of the electropolymerization medium with the final content of AzbT structural units in P(AzbT:Th_3) copolymers.
- Determine the dependence of the AzbT:Th_3 molar ratio with the morphology and topography, the electrochemical response and optical properties displayed by P(AzbT:Th_3) copolymers.
- Examine the cytotoxicity and biocompatible response of P(AzbT:Th_3) copolymers toward cell adhesion and proliferation tests, and infer the influence of AzbT and Th_3 content on the results.

CHAPTER 4

BIOACTIVE NANOMEMBRANES OF POLYTHIOPHENE DERIVATIVE AND BIODEGRADABLE POLYESTER

Summary

The present chapter reports the fabrication of free-standing nanomembranes (FsNM) with semiconducting and biodegradable properties. Specifically, nanomembranes have been prepared by spin-coating mixtures of a semiconducting polythiophene derivative, poly(3-thiophene methyl acetate), P3TMA, and a biodegradable polyester, poly(tetramethylene succinate), PE44, considering three different molar ratios.

Firstly, P3TMA:PE44 nanomembranes (80:20, 50:50 and 20:80) were evaluated by spectroscopic (FTIR), thermal, morphological and electrical studies (section 4.3). The biocompatibility response of this system was tested using P3TMA:PE44 (50:50) nanomembrane. As results were satisfactory, nanomembranes with composition 50:50 were chosen to be further characterized (section 4.4).

Materials and general methodology (*i.e*. P3TMA and PE44 synthesis, FsNM fabrication, and cell viability assays) are described in section 4.2, whereas experimental details of the characterization techniques used are found in sections 4.3.1 and 4.4.1.

PE44 was synthesized by Dr. A. L. Gomes[1], who also performed the determination of the viscosity and molecular weights of the obtained polymers, and the AFM microscopic studies described in section 4.3.1. Thermal measurements were run by Dr. L. Franco[2], while electrical characterization was performed under the guidance of Dr. N. Ferrer-Anglada[3]. Biological and biodegradation assays were done in collaborative working with Dr. L. J. del Valle[2].

Publications derived from this work:

E. Armelin, A.L. Gomes, M.M. Pérez-Madrigal, J. Puiggalí, L. Franco, L.J. del Valle, A. Rodríguez-Galán J.S. de C. Campos, N. Ferrer-Anglada, C. Alemán, *J. Mater. Chem.* **2012**, *22*, 585.

M.M. Pérez-Madrigal, E. Armelin, L.J. del Valle, F. Estrany, C. Alemán, *Polym. Chem.* **2013**, *3*, 979.

[1]Departamento de Tecnología de Polímeros, Faculdade de Engenharia Química, Universidade Estadual de Campinas, Brazil.
[2]Departament d'Enginyeria Química, E.T.S. d'Enginyers Industrials de Barcelona, UPC.
[3]Departament de Física Aplicada, UPC.

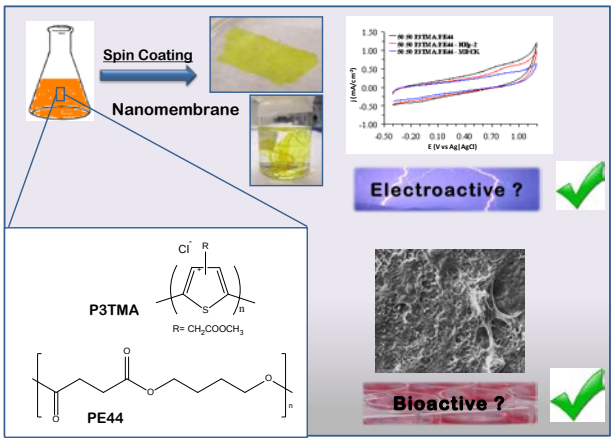

Graphical abstract

4.1. Introduction

Conjugated polymers (CPs) and their composites have attracted much attention because of their interesting electrical and optical properties. Indeed, these materials are currently used for a great variety of applications in different fields, like electronics, nanotechnology and biotechnology.[1–8] Among CPs, polythiophene (PTh) derivatives are particularly important since much progress has been made in the past two decades to solve their serious problems of solubility and processability.[9–11] A widely accepted strategy to overcome such problems is based on the incorporation of substituents into the 3-position of the thiophene ring. Specifically, it was found that the incorporation of long alkyl side chains increases the solubility in non-polar solvents,[12–14] whereas hydrophilic substituents produce PThs soluble in water and/or polar solvents.[15–20] For example, PThs bearing carboxylate groups, like poly(3-thiophene methyl acetate) (P3TMA), show easy solubility in different solvents and solution processability in films or fibers.[16,17,19–21]

In order to improve the mechanical integrity of CPs, in the last decade some studies have been focused on blending PTh derivatives with conventional polymers. Hsieh *et al.* studied the miscibility of poly(3-thiophene acetic acid) (P3AA) with poly(ethylene oxide) (PEO), films being obtained by solvent casting polymer solutions onto a glass plate.[22] Nicho *et al.* studied the morphological and physicochemical properties of thin film composites made of poly(3-octylthiophene) (P3OTh) and polystyrene (PS), which were spin-coated onto corning glass substrates from toluene.[23] Özgün *et al.* characterized blends and composites with

different molar ratios of PTh and polyoxymethylene.[24] More recently, Manna *et al.* fabricated new nanostructures of P3TMA within a poly(vinylidene fluoride) matrix using a reactive blending technique under melt-cooled conditions.[25] Finally, Mawad *et al.* prepared a multilayered system based on water soluble polymers with charges of opposite sign, poly[(3-thienyl) ethoxypropanesulfonate] and poly(ethyleneimine), electrostatically assembled by the LbL technique.[26]

Among CP applications, those related with both biotechnology and biomedicine have a very relevant impact. More specifically, CPs are biocompatible materials able to stimulate cell attachment, proliferation, regeneration and differentiation through electrical signals and/or simple ion-exchange in which the dopant agents embedded in the material play a crucial role.[27–33] Although these properties favour the use of CPs as scaffolds for tissue engineering, the biomedical use of these materials is still limited because of their lack of biodegradability. Combination of thiophene (Th) and pyrrole (Py) units with an aliphatic moiety, which acts as a linker, allowed Rivers *et al.* to obtain a biodegradable CP.[34]

The work summarized in this chapter focused on the fabrication of a new type of FsNM, which has been achieved by blending P3TMA and poly(tetramethylene succinate) (PE44), a biodegradable polyester. The major achievements of this study can be summarized as follows: (i) P3TMA:PE44 blends retain the semiconducting properties of P3TMA and the biodegradability of PE44; (ii) polyester matrices are good supports for CPs since they provide mechanical integrity to the latter; and (iii) P3TMA:PE44 FsNM enhance the cell adhesion and proliferation behaviour with respect to the individual homopolymers. In addition, both the biodegradability and the excellent behaviour as cellular substrates of P3TMA:PE44 nanomembranes allow us to conclude that they should be considered as bioactive platforms for tissue engineering applications.

4.2. Experimental Section

4.2.1 Materials

3-Thiophene acetic acid (3TAA, 98.0%), poly(4-hydroxysytrene) (PHS, M_w *ca.* 11 000), magnesium sulfate (97+%), 1,4-butane-diol (99.0%), succinic acid (≥99.0%) and titanium(IV) butoxide (97%) were purchased from Sigma-Aldrich, Germany. Iron(III) chloride anhydrous (97.0%), methanol (99.5%), ethanol (99.5%), diethyl ether stabilized with 6 ppm of BHT-QP (99.5%), trichloromethane dry stabilized

with 50 ppm of amylene DS-ACS (99.9%) and sulfuric acid (98.0%) were purchased from Panreac Quimica S.A.U. (Spain). Dichloroacetic acid solution (≥99.0%) used for intrinsic viscosity characterization and 1,1,1,3,3,3-hexafluoro-2-propanol (≥99.8%) used for size exclusion chromatography were both purchased from Sigma-Aldrich, Germany. All reagents were used as received without further purification.

For cell culture experiments, Madin Darby canine kidney (MDCK), human prostate cancer (Du-145), human laryngeal epidermoid carcinoma (HEp-2) and monkey kidney fibroblast (Cos-7) were purchased from ATCC (USA). Dulbecco's phosphate buffered saline (PBS) solution without calcium chloride and magnesium chloride, Dulbecco's modified Eagle's medium (DMEM, with 4500 mg of glucose per L, 110 mg of sodium pyruvate per L and 2 mM of L-glutamine), penicillin–streptomycin, 3-(3,5-dimethylthiazol-2-yl)-2,5-diphenyl-2H-tetrazolium bromide (MTT, 97.5%) and trypsin–EDTA solution (0.05% trypsin, 0.02% EDTA) were all purchased from Sigma, Germany. Fetal bovine serum (FBS) and trypan blue stain (0.4%) were purchased from Gibco, UK. Dimethyl sulfoxide (99.0%) was purchased from Panreac Quimica S.A.U. (Spain) and sodium azide (NaN_3, ≥99.5%) from Sigma-Aldrich, Germany. Finally, Lipase F-AP15 (from *Rhizopus oryzae*) was purchased from Sigma (USA) and used in the enzymatic degradation experiments.

4.2.2. Synthesis of Poly(3-thiophene methyl acetate)

Using 3TAA as starting monomer and $FeCl_3$ as oxidant, 3-thiophene methyl acetate (3TMA) was prepared and subsequently polymerized by oxidative coupling following the procedure described by Kim *et al.* (Scheme 4.2.1).[16] The purified 3TMA monomer was obtained with 82% yield, while the yield of P3TMA was 25% after removal of the residual oxidant and oligomers. Unfortunately, changes in the 3TMA:$FeCl_3$ ratio did not improve the low yield of the oxidative coupling polymerization. The ^{1}H-NMR characterization of the produced P3TMA (not shown) was in complete agreement with that previously reported.[16]

4.2.3. Synthesis of Poly(tetramethylene succinate)

The biodegradable polyester was prepared by bulk thermal polycondensation of 1,4-butanediol and succinic acid (diol/diacid molar ratio of 2.2/1).[35] The reaction was first performed in a nitrogen atmosphere at 150 °C for 6 hours, and then in vacuum at 180 °C for 18 hours (Scheme 4.2.1). Titanium tetrabutoxide was used as a

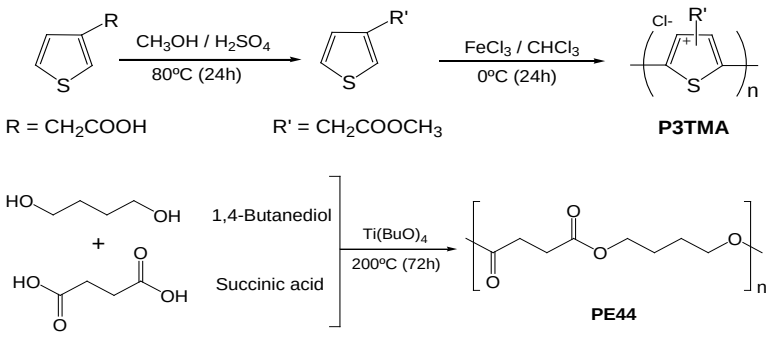

Scheme 4.2.1. Synthetic routes for obtaining P3TMA and PE44.

catalyst. The polymer was dissolved in chloroform and precipitated with ethanol. PE44 was obtained with a 72% yield after drying overnight under vacuum.

4.2.4. Viscosity and Molecular Weights Determination

The intrinsic viscosity of PE44, 0.80 dL/g, was determined using a Cannon-Ubbelohde microviscometer and a dichloroacetic acid solution at 25 ± 0.1 °C. The intrinsic viscosity of P3TMA was not evaluated due to the insolubility of this material in dichloroacetic acid. Molecular weights were estimated by size exclusion chromatography (SEC) using a liquid chromatograph (Shimadzu, model LC-8A) equipped with an Empower computer program (Waters). A PL HFIP gel column (Polymer Lab) and a refractive index detector (Shimadzu RID-10A) were employed. Polymers were dissolved and eluted in hexafluoroisopropanol at a flow rate of 0.5 mL/min (injected volume 100 mL, sample concentration 1.5 mg/mL) and using poly(methyl methacrylate) standards. The resulting number and weight average molecular weight were $\overline{M_n}$ = 10 500 g/mol and $\overline{M_w}$ = 22 500 g/mol, and $\overline{M_n}$ = 24 365 g/mol and $\overline{M_w}$ = 36 524 g/mol for PE44 and P3TMA, respectively.

4.2.5. Preparation of Free-standing Nanomembranes

The procedure described by Kunitake and co-workers[36,37] for the preparation of ultrathin films of epoxy resins has been followed in this work for the fabrication of P3TMA:PE44 nanomembranes. Poly(4-hydroxystyrene) in ethanol (50 mg/mL) was firstly spin-coated on an indium-tin oxide (ITO) glass slide (dimensions ranged from 2.5 × 2.5 to 5.0 × 10.0 cm^2) at 3000 rpm for 60 s to give a 0.1 mm thick sacrificial layer after two applications. On the other hand, sonicated powder of P3TMA and

PE44 were separately dissolved in chloroform (50 mg/mL) and then mixed. The resulting mixtures, which were prepared considering 80:20, 50:50 and 20:80 molar ratios, were subsequently stirred at room temperature for 4 hours. The dispersions were then diluted with chloroform (final concentration 10 mg/mL), filtered and subjected to spin-coating for film deposition. The thickness of the films was adjusted in the range of 15–100 nm by varying the spin-coater speed (from 1500 to 8000 rpm). Spin-coating was performed using a Spin Coater (WS-400BZ- 6NPP/A1/AR1, Laurell Technologies Corporation).

After coating, the samples were dried under vacuum at room temperature for 24 h to remove completely the solvent. Detachment of the nanomembranes from the ITO substrate was achieved by immersion into ethanol, which dissolved the sacrificial layer and induced the separation of the nanomembrane from the substrate. The edge of the specimens was cut to help penetration of ethanol into the sacrificial layer. Nanomembranes were also fabricated using steel AISI 316 sheets (dimensions 1.0 × 1.0 cm^2) as substrate using the same procedure.

Detachment of the nanomembranes from the substrate was not required for some assays (*i.e.* microscopic observations, contact angle, electrical and electrochemical measurements, qualitative biodegradation studies and cellular adhesion and proliferation tests), no sacrificial layer being necessary in such cases.

4.2.6. Cell Adhesion and Proliferation Tests

MDCK, Du-145, HEp-2 or Cos-7 cells were cultured in DMEM high glucose supplemented with 10% FBS, penicillin (100 units/mL), and streptomycin (100 µg/mL). The cultures were maintained in a humidified incubator with an atmosphere of 5% CO_2 and 95% O_2 at 37 °C. Culture media were changed every two days. When the cells reached 80–90%confluence, they were detached using 1–2 mL of trypsin (0.25%trypsin/EDTA) for 5 min at 37 °C, and centrifuged at 650g for 1 min. Finally, cells were re-suspended in fresh medium, their concentration being determined by counting in a Neubauer camera using 0.4% trypan blue as a dye vital.

Nanomembranes of PE44, P3TMA and 50:50 P3TMA:PE44 were prepared and deposited onto steel AISI 316 sheets of 1 cm^2. These samples were placed in plates of 24 wells and sterilized using UV-light for 15 min in a laminar flux cabinet. Controls were simultaneously performed by culturing cells on the surface of the tissue culture polystyrene (TCPS) plates and steel plates. For adhesion assays, an aliquot of 50 µL containing 5 × 10^4 cells was deposited on the nanomembrane of each well.

Then, cell attachment to the nanomembrane surface was promoted by incubating under culture conditions for 30 min. Finally, 500 µL of the culture medium were added to each well. After 24 h, non-attached cells were washed out, while attached cells were quantified. For proliferation assays, the 50 µL aliquots deposited on each well contained 2×10^4 cells, quantification of proliferated cells being performed after 7 days of culture.

Cell adhesion and proliferation were evaluated by the colorimetric MTT assay.[38] This assay measures the ability of the mitochondrial dehydrogenase enzyme of viable cells to cleave the tetrazolium rings of the MTT and form formazan crystals, which are impermeable to cell membranes and, therefore, are accumulated in healthy cells. This process is detected by a color change: the characteristic pale yellow of MTT transforms into the dark blue of formazan crystals. Specifically, 50 µL of MTT solution (5 mg/mL in PBS) were added to each well. After 3 h of incubation, samples were washed twice with PBS and stored in clean wells. In order to dissolve formazan crystals, 1 mL of DMSO/methanol/water (70/20/10% v/v) was added. Finally, the absorbance at 540 mm was measured after using an UV-vis spectrophotometer (UV-3600, Shimadzu). The resulting viability results were normalized to TCPS control as relative percentages. Results were derived from the average of four replicates (n = 4) for each independent experiment. ANOVA and Tukey's tests were performed to determine the statistical significance, which was considered at a confidence level of 95% ($p < 0.05$).

SEM observations of cell-coated samples were carried out using a Focused Ion Beam Zeiss Neon40 scanning electron microscope equipped with an energy dispersive X-ray (EDX) spectroscopy system and operating at 5 kV. All samples were coated with a carbon layer of 6 nm thickness using a K950X Turbo Evaporator to prevent sample charging problems. Before the carbon coating for examination by SEM, samples covered with cells were fixed in a 2.5% glutaraldehyde PBS solution (pH = 7.2) overnight at 4 °C. Then, they were dehydrated by washing in an alcohol battery (30°, 50°, 70°, 90°, 95° and 100°) at 4 °C for 30 min per wash. Finally, samples were air-dried, and sputter-coated with carbon before SEM observation.

4.3. First Approach to P3TMA:PE44 FsNM

This section covers the preparation and characterization results for P3TMA:PE44 nanomembranes considering three different molar ratios 80:20, 50:50 and 20:80. Furthermore, 50:50 P3TMA:PE44 has been taken as a representative sample for some characterization studies.

4.3.1. Characterization Methods

FTIR spectroscopy

IR absorption spectra were recorded on a FTIR Jasco 4100 spectrometer. Samples were placed in an attenuated total reflection accessory (top-plate) with a diamond crystal (Specac model MKII Golden Gate Heated Single Reflection Diamond ATR). PE44 and P3TMA:PE44 films were prepared by solvent casting from the corresponding chloroform solutions, while P3TMA was analyzed as a powder. For each sample 32 scans were performed between 4000 and 600 cm^{-1} with a resolution of 4 cm^{-1}.

Thermal analyses

Calorimetric data were obtained by differential scanning calorimetry (DSC) with a TA Instruments Q100 series equipped with a refrigerated cooling system (RCS) operating at temperatures from -90 °C to 600 °C. Experiments were conducted under a flow of dry nitrogen with a sample weight of approximately 5 mg, calibration being performed with indium. The T_{zero} calibration requested two experiments: the first was done without samples, while the second one was performed with sapphire disks. Hot crystallizations were performed at a cooling rate of 10 °C/min with melted samples previously heated until 200 °C to erase the thermal history. Heating runs were performed at 20 °C/min with samples previously quenched from the melt state by cooling at the maximum rate allowed by the equipment. Determination of T_g values from the calorimetric curves was carried out with the TA-Universal Analysis software furnished with the instrument. Thermal degradation was determined at a heating rate of 20 °C/min with around 5–8 mg samples in a Q50 thermogravimetric analyzer of TA Instruments and under a flow of dry nitrogen. The analysis was performed in the temperature range from 30 to 800 °C. For polymer kinetic analysis additional heating scans were carried out at rates ranging from 5 °C/min to 20 °C/min. In all cases deconvolution of the

derivative thermogravimetric curves was performed with the PeakFit v4 program by Jandel Scientific Software using an asymmetric double sigmoidal function.

Microscopy studies

Optical microscopy observations were performed using a Zeiss Axioskop 40 Pol light polarizing microscope equipped with a Linkam temperature control system configured by a THMS 60. Micrographs were taken with a Zeiss AxiosCam MRC5 digital camera. A first-order red tint plate was employed to determine the sign of spherulite birefringence under crossed polarizers.

Scanning electron microscopy (SEM) studies were carried out using a Focused Ion Beam Zeiss Neon40 scanning electron microscope equipped with an energy dispersive X-ray (EDX) spectroscopy system and operating at 30 kV. Samples were mounted on a double-sided adhesive carbon disc and sputter-coated with a thin layer of carbon to prevent sample charging problems. Atomic force microscopy (AFM) was employed to take topographic images of P3TMA:PE44 nanomembranes using the tapping mode. Images were obtained with a Molecular Imaging PicoSPM using a NanoScope IV controller under ambient conditions. The row scanning frequency was set to 1 Hz. The RMS roughness was determined using the statistical application of the Nanoscope software. The scan window size was 5 × 5 μm^2 in all cases.

Conductivity measurements

In order to measure the electrical properties, films of P3TMA:PE44 were spin-casted onto glass substrates, and dried under vacuum overnight. The nanofilms (thickness from 20 to 80 nm) were partially coated with silver paint to yield two electrodes for two-probe conductivity measurements. A direct voltage ranging from -20 to +20 V was applied, the current response being measured with a Keithley 6430 Sub-FemtoAmp Remote Sourcemeter. Conductivity (σ) was calculated as $\sigma = L/(R \times A)$, where L (cm) is the distance between the electrodes, R (Ω) is the membrane resistance, and A (cm^2) is the cross-sectional area of the membrane.

4.3.2. Results and Discussion

Many technological applications of organic CPs are seriously limited by their poor mechanical properties. Thus, many strategies to improve the mechanical integrity of these interesting materials have been proposed in the last few years.

In this work, we have prepared P3TMA:PE44 nanomembranes not only to enhance the mechanical integrity of this conducting polymer, but also to promote its use in biomedical applications. Specifically, the electron-withdrawing carboxylate groupof P3TMA (Scheme 4.2.1) have increased both the environmental stability and the solubility of the polythiophene, while the polyester matrix has provided mechanical integrity and biodegradability. The combination of these properties allows us to propose the use of P3TMA:PE44 as a new material with interesting biomedical applications.

P3TMA is highly soluble in chloroform, this behaviour being also showed by other polythiophenes bearing carboxylate substituents in the 3-position of the thiophene ring.[17,20-21,39] The Hildebrand solubility parameter of PE44,[35] which is also soluble in chloroform, is expected to be similar to that of P3TMA suggesting a partial miscibility between them. Thermal polycondensation of 1,4-butanediol and succinic acid yielded a polyester with high polydispersity (PD = 2.14), whereas the oxidative polymerization produced a CP with uniform size and almost homogeneous distribution (PD = 1.50). Therefore, P3TMA exhibits a stabilizing effect in the blend formation, avoiding the coagulation and agglomeration of P3TMA in the polyester matrix. In this sense, different segments of PE44 absorb P3TMA particles through attractive forces, resulting in a homogeneous distribution of nanoparticles. P3TMA:PE44 nanomembranes with 80:20, 50:50 and 20:80 molar ratios were prepared by spin-coating using an ITO substrate and a poly(4-hydroxystyrene) sacrificial layer.

The resulting FsNM (Figure 4.3.1a-b), which were detached from the substrate by dissolving the sacrificial layer, are flexible ultra-thin films with average thicknesses and areas ranging from ~20 to ~80 nm and from 4 to 50 cm^2, respectively.

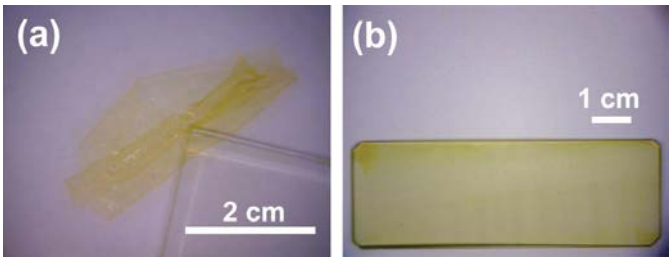

Figure 4.3.1. Digital camera images of a P3TMA:PE44 FsNM: (a) release in ethanol (*i.e.* after detachment from ITO) and (b) deposited on a glass substrate.

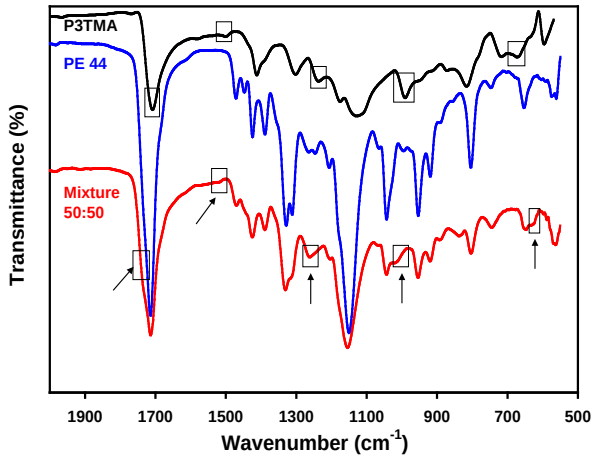

Figure 4.3.2. FTIR spectrum of P3TMA, PE44 and 50:50 P3TMA:PE44 in the range between 2000 cm^{-1} and 500 cm^{-1}. Absorption bands marked with boxes and arrows have been used to identify the CP in the mixture.

The thickness is controlled through both the speed applied to the spin-coater and the blend composition, while the area depends on the dimensions of the substrate. The nanomembranes are stable in air and in ethanol solution for their manipulation, such stability remaining more than a year after their preparation.

FTIR spectroscopy studies

Figure 4.3.2 shows the FTIR spectrum of P3TMA, PE44 and 50:50 P3TMA:PE44 in the range from 1800 to 550 cm^{-1}. Changes and shifts occurring at higher wavenumbers are not displayed but discussed for comparison. Absorption bands of the two individual polymers and the three blends (20:80, 50:50 and 80:20 P3TMA:PE44 compositions) are displayed in Table 4.3.1. Although CPs are difficult to identify by infrared spectroscopy, some assessments can be pointed out. The band for C–H aromatic stretching vibration is only observed in the P3TMA spectrum (3005 cm^{-1}), and it is associated with the benzonoid or quinonoid form. Other C–H stretching vibrations are identified for the aliphatic segment (2998, 2948, and 2843 cm^{-1}). The weak absorption intensity at 1522 cm^{-1} has been attributed to C=C stretching vibration of the thiophene ring, indicating the conjugation behaviour of P3TMA chains. Another C=C aromatic ring stretching (medium intensity) is observed at 1322 cm^{-1}. Asymmetric and symmetric stretching of ester groups in P3TMA are identified at 1146 cm^{-1} (C=O, broad and high intensity), 1196

cm^{-1} (R–CO–O–CH_3, weak intensity) and 1013 cm^{-1} (C–O–C, broad and medium intensity). Finally, the peak at 615 cm^{-1} has been attributed to the C–S bonds of the thiophene rings.

On the other hand, the main absorption bands corresponding to C–H aliphatic stretching of PE44 are observed at 2964, 2946 and 2857 cm^{-1}. Absorption bands characteristic of –$(CH_2)_n$– hydrocarbon chains are detected at 804 cm^{-1} (sharp) and 748 cm^{-1} (broad, CH_2 rock vibrations). Relevant bands related to the CH_2 asymmetric and symmetric bending are shown between 1470 and 1390 cm^{-1}. Three significant peaks are detected in the PE44 spectrum at 1150 cm^{-1} (sharp and strong absorption band), 1044 and 954 cm^{-1} (sharp and medium absorption bands), which have been assigned to the C=O and C–O–C vibrations. Other bands typically associated with the C–O component tend to be less pronounced, sometimes being overlapped with other fingerprint absorptions of the molecule. These bands are usually located in the 1320–1200 cm^{-1} (C–O stretch) interval. In the current case, they appear as sharp and strong doublet bands at 1329 and 1311 cm^{-1}; and also at 954 cm^{-1}, as discussed above.

Formation of the 50:50 P3TMA:PE44 nanomembranes is evidenced by some overlapped bands, which are marked in Figure 4.3.2, arising from the two individual polymers. The strong absorption at 1716 cm^{-1} and the broad shoulder at 1734 cm^{-1} have been attributed to the C=O stretching of ester units from PE44 and P3TMA, respectively. Furthermore, a very weak shoulder at 1508 cm^{-1} was also observed for the mixture, corresponding to the C=C stretching of thiophene ring. Other overlapped bands arising from the P3TMA contribution can be seen at: 1262, 1018, 837 and 620 cm^{-1}. Similar features are displayed in Table 4.3.1 for the 20:80 and 80:20 nanomembranes.

Table 4.3.1. Main infrared absorption bands (cm^{-1}) of P3TMA, PE44 and P3TMA:PE44 (50:50) blends studied in this work. Note: [a)]Band overlapped with C=O ester.

	Aromatic C-H in plane deform. β	**Aliphatic C-H stretch**	**C=O ester**	**C=C conjugated diene**	**CH_3 Asymmetric symmetric bending**	**CH_2 Asymmetric symmetric bending**	**C-O-C stretches**	**Aliphatic C-H out of plane bending**	**Aromatic C-H out of plane deform.** α/β
P3TMA	3005	2998, 2948, 2843	1726	1690 [a)], 1522, 1322	1431	1402	1196, 1148 (broad and strong), 1016	689	737/835
P3TMA:PE44 (80:20)	~3000	2937, 2836	1713	1510	1421	1422, 1381, 1312	1190, 1141, 1109	681	726/830
P3TMA:PE44 (50:50)	-	2948, 2919, 2858	1732 1713	1675 [a)]	1444	1470, 1424, 1389, 1331, 1314	1043, 1018, 1016		743/836
P3TMA:PE44 (20:80)	-	2934, 2904, 2896	1708	-	-	1460, 1418 1383, 1322, 1251	1147, 1036, 948	800, 642	738/837
PE44	-	2964, 2946, 2923, 2857	1714	-	-	1472, 1448, 1424, 1389	1329, 1311 (doublet) 1207,1150 (strong), 1044, 954	804, 748, 653	-/-

Thermal analyses

Calorimetric data reveal that P3TMA and PE44 are partially miscible. Specifically, DSC cooling runs from the melt state (Figure 4.3.3a) indicate that the crystallization of PE44 is hindered by the presence of P3TMA. Thus, both the temperature of the exothermic crystallization peak and the crystallization enthalpy decrease when the P3TMA content increases (Table 4.3.2). Heating runs of melt quenched samples show two glass transition temperatures (T_g), as expected from a phase separation (Figure 4.3.3b). Values corresponding to each phase were determined separately. It was clearly found that the determined glass transition temperatures depend on the composition, evidencing a partial miscibility. The T_g associated with the P3TMA decreases with the concentration of this polymer in the blend, while the T_g of PE44 increases when the concentration of polyester in the blend decreases (Table 4.3.2). The weight percentage of each polymer in the corresponding phase was determined from Eq. 4.3.1 (Table 4.3.2):

$$\frac{1}{T_g} = \frac{w_1}{T_{g,1}} + \frac{w_2}{T_{g,2}} \qquad (4.3.1)$$

where $T_{g,1}$ and $T_{g,2}$ correspond to the T_g of the pure components (*i.e.* -34 °C and 63 °C for PE44 and P3TMA, respectively) and, w_1 and w_2 are the weight fractions in the studied phase.

Table 4.3.2. Calorimetric data of P3TMA:PE44 system.[a]

	T_c (°C)	ΔH_c (J/g)[b]	Tg_1 (°C)	Tg_2 (°C)	w_1[c]	w_2[d]	T_f (°C)
PE44	93.2	75.0	-34	-	100	0	102, 112.8
P3TMA:PE44 20:80	73.5	73.8	-27	-	0.89	-	112.5
P3TMA:PE44 50:50	68.8	66.5	-20	38	0.79	0.89	111.8
P3TMA:PE44 80:20	62.0	33.4	-10	45	0.65	0.96	111.6
P3TMA	-	0	-	63	0	100	-

[a]Cooling and heating runs performed at 10 and 20 °C/min, respectively. [b]Referred to the PE44 content. [c]PE44 weight fraction in the PE44 phase. [d]P3TMA weight fraction in the P3TMA phase.

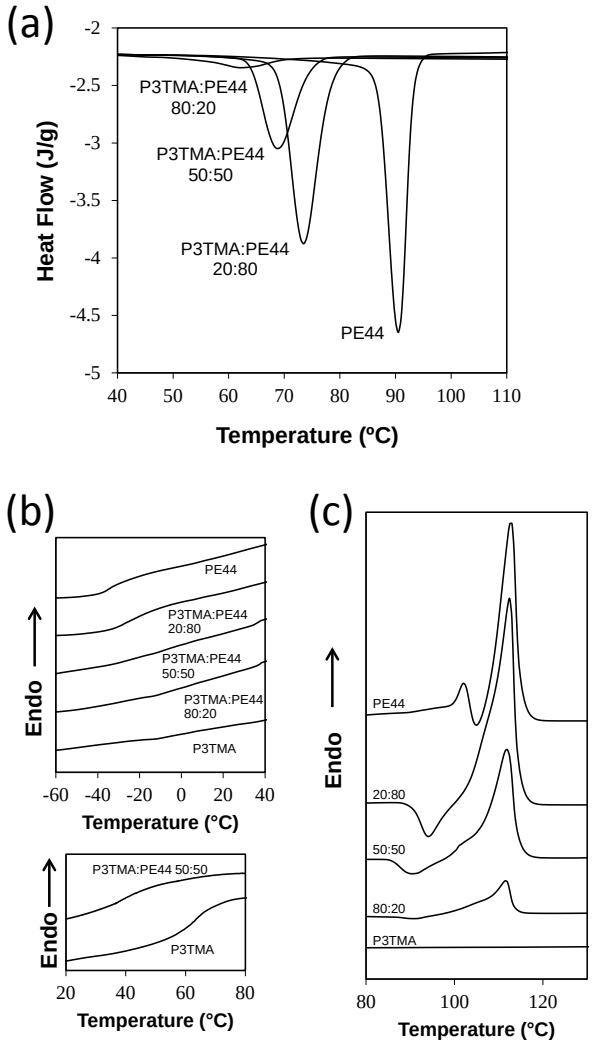

Figure 4.3.3. (a) Dynamic DSC curves (10 ºC/min) showing the exothermic crystallization peak of the different P3TMA:PE44 samples. (b) DSC heating traces (20 ºC/min) showing the glass transitions associated to PE44 (up) and P3TMA (down) domains for the indicated blends. (c) DSC heating traces (20 ºC/min) showing the melting behaviour of the indicated P3TMA:PE44 blends.

On the other hand, the fusion of the PE44 crystalline fraction is also affected by the incorporation of P3TMA (Figure 4.3.3c). The polyester has two well defined melting peaks that have been associated with the existence of two populations of lamellar crystals with different thickness.[40] The first peak corresponds to the melt of thinner crystals, which undergo a reorganization giving rise to the intermediate exothermic peak. This melt/reorganization process is less clear in the heating runs of the studied blends, the first melting process being only detected as a small shoulder of the main peak. Heating traces of all blends show also a small cold crystallization exothermic peak around 95 °C (*i.e.* before any fusion process). Finally, the melting peak of the thicker crystals slightly decreases when the content of P3TMA increases (Table 4.3.2). However, shifts are lower than 2 °C in all cases, evidencing that the contamination of PE44 crystals is very low.

Thermogravimetric scans show that the onset degradation temperature and the temperature corresponding to a given weight loss increase with the content of PE44 (Figure 4.3.4a). Table 4.3.3 indicates that the thermal stability of the blends is highly dependent on the P3TMA:PE44 composition (*i.e.* PE44 increases the thermal stability of P3TMA and decreases the char yield, which reaches practically constant values at 500 °C). Nevertheless, although the incorporation of P3TMA decreases the thermal stability of the aliphatic polyester, the blends are very stable with degradation temperatures ranging between 320 and 385 °C.

Table 4.3.3. Thermogravimetric data of P3TMA:PE44 system[a].

	T_{onset}	$T_{20\%}$[b]	$T_{50\%}$[b]	$T_{70\%}$[b]	T_{max}		
PE44	390	392	412	421	418		
P3TMA:PE44 20:80	385	391	412	424	415	321	
P3TMA:PE44 50:50	357	368	403	-	396	344	284
P3TMA:PE44 80:20	320	355	572	-	373		282
P3TMA	314	391	-	-	399	341	279

[a]Heating rate of 20 °C/min. [b]$T_{20\%}$, $T_{50\%}$ and $T_{70\%}$ correspond to the temperatures after 20%, 50% and 70% degradation, respectively.

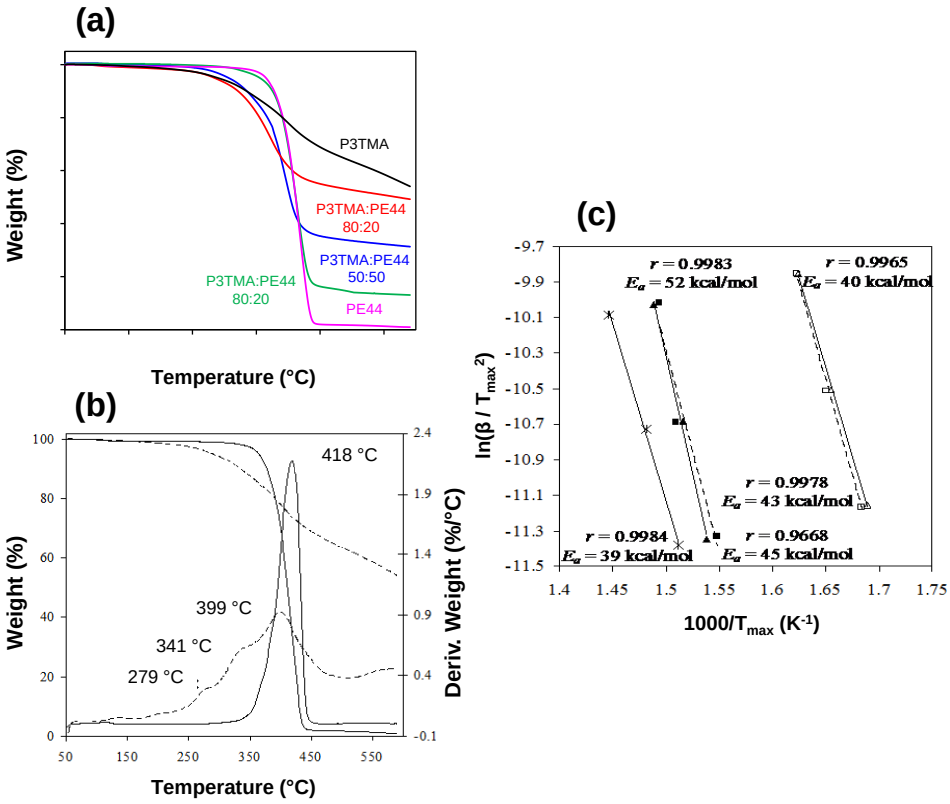

Figure 4.3.4. (a) Thermogravimetric curves obtained at a heating rate of 20 °C/min for the P3TMA:PE44 blends and the two individual polymers. (b) TGA and DTGA curves corresponding to the thermal decomposition of PE44 (solid lines) and P3TMA polymers (dashed lines). (c) Kissinger plots for the thermal decomposition of PE44 (✱) and the two main thermal decomposition steps observed for P3TMA (solid lines, ▲ symbols) and P3TMA:PE44 50:50 (dashed lines, ■ symbols) samples. Full and empty symbols correspond to the peaks appearing at the highest and the intermediate temperature, respectively.

The derivative thermogravimetry (DTG) curve of PE44 shows a single peak (418 °C), while the curve corresponding to the CP was characterized by three well differentiated shoulders (399, 341 and 279 °C), indicating a complex degradation behaviour (Figure 4.3.4b). DTG curves of P3TMA:PE44 blends (Table 4.3.3) also revealed a complex behaviour, which depends on the polymers ratio in the mixture. However, it is interesting to note that the blend with an intermediate composition (50:50) showed three DTG shoulders at temperatures close to those determined for P3TMA (Table 4.3.3). These results suggest that the degradation of P3TMA gives rise to radicals that favour the decomposition of the aliphatic polyester, the DTG shoulder of the latter appearing at practically the same temperature as that of the main decomposition step of P3TMA.

DTG curves obtained at different heating rates (5, 10 and 20 °C/min) were used to estimate the activation energies, E_a, associated with the single degradation step of PE44, and the two main decomposition steps of the individual P3TMA and the P3TMA:PE44 blend with a 50:50 molar ratio. For this purpose, the Kissinger method[41] was applied because of its simplicity:

$$\ln\frac{\beta}{T_{max}^2} = \ln\frac{AR}{E_a} + \ln[n(1-\alpha_{max})^{n-1}] - \frac{E_a}{RT_{max}} \qquad (4.3.2)$$

where β is the heating rate, T_{max} is the temperature at the maximum reaction rate associated with each degradation step, α_{max} is the conversion at this T_{max} temperature, n is the reaction order and A is the frequency factor.

The representation of $\ln \beta/T_{max}^2$ against $1/T_{max}$, which was fitted to a straight line using a simple linear regression, allowed us to determine the E_a from the slope of the resulting linear equation. It should be noted that this method is a rough approximation since it is not a rigorous isoconversional method. Thus, the peak temperature of each step is obtained at different heating rates, and the extent of conversion related to a given peak is known to change with the heating rate.[42,43] Moreover, the determined activation energies may lose sense if they vary throughout the degradation processes.

Figure 4.3.4c shows the Kissinger plots of the thermal decomposition steps of the three investigated samples. The linear plot of PE44, which showed the lowest activation energy (E_a = 39 ± 2 kcal/mol), was clearly shifted to the high temperature zone, whereas the two main decomposition steps of the 50:50 blend and the P3TMA samples provided very similar linear plots. In spite of this, the highest activation energy (E_a=52 ± 3 kcal/mol) was determined for the high temperature decomposition step of P3TMA, the activation energy of the equivalent

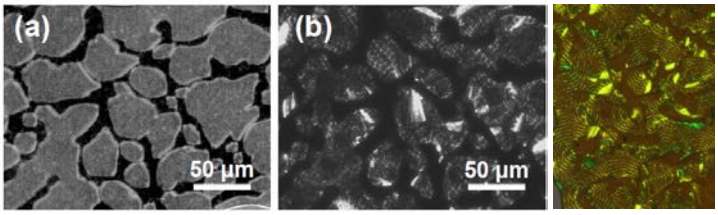

Figure 4.3.5. Optical micrographs of P3TMA:PE44 50:50 in (a) the melt state and (b) after isothermal crystallization at 70 ºC, black domains corresponding to the P3TMA phase.

decomposition step of the 50:50 P3TMA:PE44 blend (E_a = 45 ± 4 kcal/mol) being half way between those of individual PE44 and P3TMA. Finally, the activation energies for the second decomposition step of the 50:50 blend and the individual P3TMA were practically identical (E_a = 43 ± 3 and 40 ± 1 kcal/mol, respectively).

Microscopy studies

Optical micrographs of melted blends showed a phase separation, suggesting again a partial miscibility, which after keeping the samples at 70 °C became the amorphous and crystalline domains of P3TMA and PE44, respectively (Figure 4.3.5). Typical double ringed spherulites of PE44 were developed during these isothermal crystallizations. The P3TMA amorphous phase corresponds to the black domains in Figure 4.3.5. As it can be seen, the amorphous domains of P3TMA tend to preclude the formation of spherulites by the crystalline phases of PE44. Accordingly, the amount of double ringed spherulites on blends decreases when the concentration of CP increases.

SEM images indicated a completely homogeneous distribution of P3TMA and PE44, as it is evidenced in Figure 4.3.6a for the nanomembrane with a 50:50 molar ratio. According to the sulfur concentration detected by EDX spectroscopy, the embedded spherical nanoaggregates shown in such micrograph correspond to P3TMA trapped in the polyester matrix. Comparison of SEM micrographs obtained for the 20:80, 50:50 and 20:80 nanomembranes indicates that the number of spherical nanoaggregates increases with the concentration of CP, even though their distribution was homogeneous in all cases. SEM micrographs of P3TMA, like that displayed in Figure 4.3.6b, also evidence spherical nanoaggregates of small (40–70 nm) and medium (250–340 nm) size. Thus, P3TMA does not present good film-forming properties, bigger particles detaching from the polymer surface.

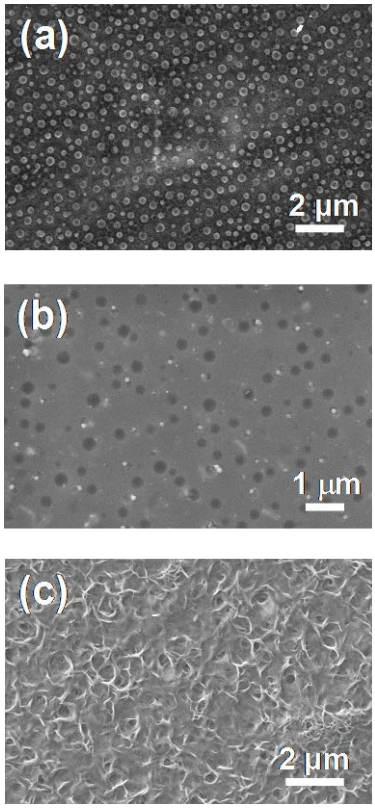

Figure 4.3.6. SEM micrographs of nanomembranes made of: (a) P3TMA:PE44 50:50, (b) individual P3TMA, and (c) individual PE44.

However, good mechanical integrity is obtained by blending the CP with PE44. On the other hand, PE44 nanomembranes showed lamellar aggregates with superficial porosity, as is clearly reflected in Figure 4.3.6c. The porosity induced by these microstructures is expected to facilitate the blending between the polyester and the CP.

The topography of the nanofilms depends on the speed used in the spin-coating process. The AFM image of the 50:50 nanomembrane deposited on a silicon wafer substrate using 3000 rpm (Figure 4.3.7a) shows a very smooth surface with some small pores randomly distributed. The measured RMS roughness ranged from 3 to 5 nm, this value being similar to that typically measured for the ITO substrate (~4 nm). The number and size of the pores, as well as the RMS roughness, are significantly higher for the nanomembranes prepared using small (1500 rpm) and

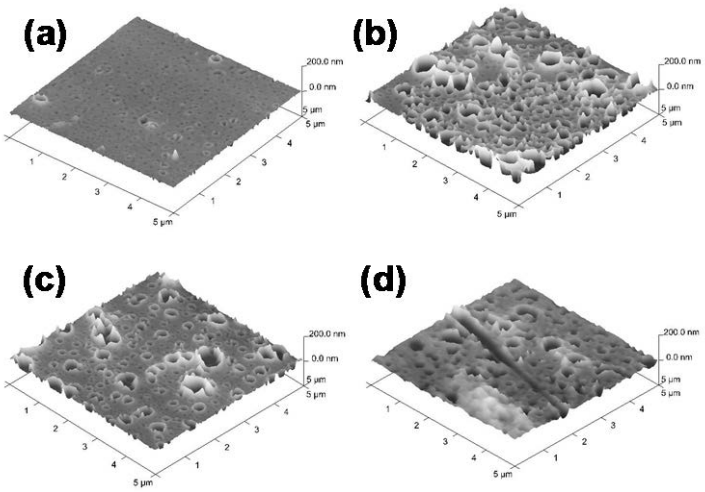

Figure 4.3.7. 3D AFM images of the nanomembranes prepared using the P3TMA:PE44 50:50 blend and spin-coating for 60 s at a speed of: (a) 3000 rpm; (b) 1500 rpm; (c) 5000 rpm; and (d) 8000 rpm. The thickness of the films was determined using AFM scratch, an example of scratch being displayed in (d).

large (5000 and 8000 rpm) spin-coater speeds. More specifically, the RMS roughness determined for the 1500, 5000 and 8000 rpm samples ranges within the following intervals: from 16 to 20 nm (Figure 4.3.7b), from 10 to 11 nm (Figure 4.3.7c), and from 12 to 13 nm (Figure 4.3.7d), respectively.

The thickness of the films was determined using the AFM scratch technique, an example of a scratch being displayed in Figure 4.3.7d. The average thickness determined by AFM scratch (Figure 4.3.8a) of the nanomembranes produced using 3000 rpm is ℓ = 15 nm, this value increases to ℓ = 71, 62 and 55 nm for 1500, 5000 and 8000 rpm, respectively. Thus, 3000 rpm has been found to be the optimum speed to produce 50:50 nanofilms with the smallest roughness and thickness. The ultrathin thickness of the films was corroborated by SEM, the average value measured for the 50:50 nanomembranes produced using 3000 rpm being 19 nm (Figure 4.3.8b).

Conductivity measurements

The electrical properties of the nanomembranes were studied on an insulating substrate using a Keithley 6430 Sourcemeter. The conductivity determined for the 80:20 P3TMA:PE44 nanomembranes ranged from ~10^{-4} to ~10^{-5} S/cm, depending on the thickness. These values are within the range typically found for semiconductor

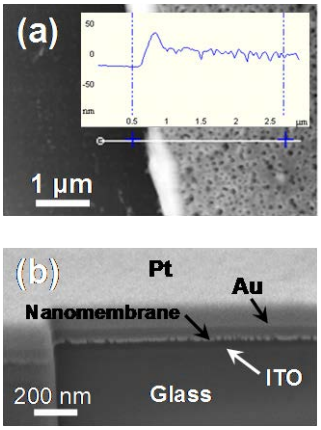

Figure 4.3.8. Thickness of the 50:50 nanomembrane prepared using a spin-coater speed of 3000 rpm for 60 s determined using (a) AFM scratch (the topographic image and the corresponding height profile (inset) are displayed) and (b) the SEM micrograph of a cross-sectional nanomembrane (the different material layers are displayed).

polythiophene derivatives bearing carboxylate groups.[22,44] Thus, the carboxylate side groups affect the electron transport through the π-conjugated backbone of the polymer. Unfortunately, measurements for the 50:50 and 20:80 were not possible indicating that the conductivity decreases when the concentration of P3TMA reduces.

Cellular adhesion and proliferation

Biological assays were performed to assess the biocompatibility of the system considering the HEp-2 cell line (human epithelial morphology) due to its highly adherent characteristics. A preliminary quantitative comparison between P3TMA, PE44 and P3TMA:PE44 50:50 nanomembranes as substrates for cellular adhesion and proliferation is displayed in Figure 4.3.9. Five samples were analysed for each group of nanomembranes, the standard deviation of the mean being small in all cases. Moreover, those cases in which the difference between the bioactive behaviour of the nanomembranes and the control TCPS plates is significant (confidence level of 95%) have been explicitly labelled in Figure 4.3.9 with an asterisk. Cellular adhesion is significantly lower on P3TMA than on the control (tissue culture polystyrene, TCPS), while the adhesion on the polyester and P3TMA:PE44 is similar to that on the TCPS (Figure 4.3.9a).

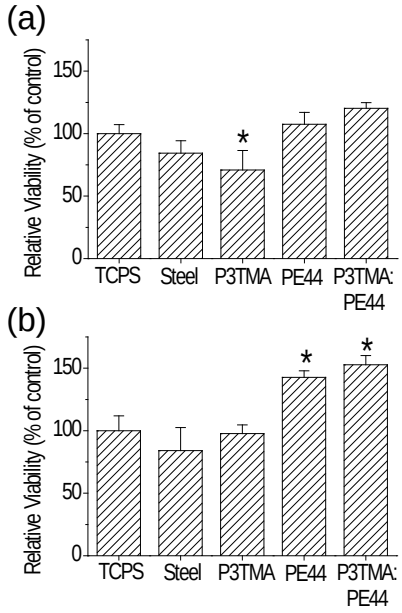

Figure 4.3.9. Cellular adhesion (a) and cellular proliferation (b) on the nanomembranes. *$p < 0.05$ *vs* TCPS. Five samples were analyzed for each group. Bars represent the mean ± standard deviation. The asterisk indicates a significant difference with the control, Tukey's test ($p < 0.05$).

After 7 days of culture in identical conditions, examination of the cellular viability shows a remarkable enlargement in the number of viable cells onto the PE44 and P3TMA:PE44 50:50 films but not onto the P3TMA substrate (Figure 4.3.9b).

The SEM micrograph displayed in Figure 4.3.10a shows the characteristics of cells cultured onto the surface of hybrid P3TMA:PE44 nanomembranes. As it can be seen, a cellular monolayer with cells having a broad spreading was formed on the surface, even though very small domains without cells are occasionally detected (see the inset of Figure 4.3.10a). In contrast, relatively large microdomains without cells are frequently identified on the surface of P3TMA, as it is reflected in the SEM micrograph displayed in Figure 4.3.10b. These observations suggest that, although the receptivity of the P3TMA surface to cellular adhesion is relatively poor, colonization of such material through proliferation of the adhered cells should be possible by considering more days of culture. Indeed, the biological behaviour of P3TMA has been found to be worse than that observed for other polythiophene

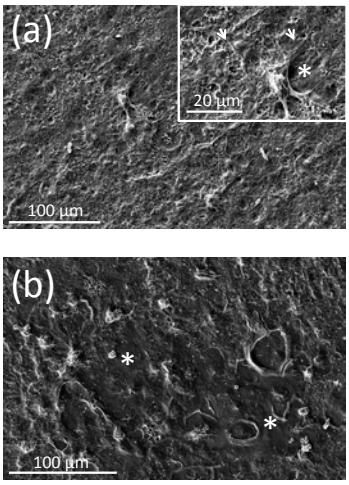

Figure 4.3.10. Micrographs of the HEp-2 cells cultured for seven days on the surfaces of the (a) P3TMA:PE44 50:50 and (b) individual P3TMA nanomembranes. Morphological details of the cellular adhesion (arrows) are displayed in the inset of (a). Asterisks indicate domains at the surface without cells.

derivatives with higher conductivities and doping levels, *e.g.* poly (3,4-ethylenedioxythiophene).[30,31]

In spite of the limitations of this CP to allow cell attachment, the P3TMA:PE44 50:50 blend has been identified as a potent cellular matrix showing the highest viability to support the cellular adhesion and proliferation. Thus, although the use of polyesters as biomaterials with biomedical applications is broadly accepted due to its very high biocompatibility, the combination of PE44 with the CP has allowed us to improve the behaviour of such polyester as bioactive platform. It should be noted that cell attachment to CPs, especially to polythiophene derivatives, has been found to be favoured because of the following two reasons:[30,31] (1) the morphology of these materials is suitable to establish an intimate interfacial contact with cells; and (2) the exchange of anions between the CP and the cells through the cellular membrane. Moreover, although PTh derivatives are usually biocompatible materials, monomers retained in the polymeric matrix are cytotoxic.[31] According to these observations, the poor bioactivity of P3TMA has been attributed to the toxicity of the 3TMA monomer, such damaging effect being minimized in the 50:50 blend. Thus, the reduction in the relative concentration of P3TMA to a half should be enough not only to eliminate the injurious effect of 3TMA, but also to take advantage of the morphological and anion-diffusion benefits typically associated with CPs (*i.e.* promoting the bioactivity of the blend with respect to the polyester).

4.4. 50:50 P3TMA:PE44 FsNM In Depth

FsNM made of P3TMA and PE44 were satisfactorily prepared by spin-coating blended solutions of the CP and the biodegradable polyester. The thickness of these ultra-thin films, which were stable in both air and ethanol solution for more than a year, ranged from 20 to 80 nm, while the area varied between 4 and 50 cm^2 depending on the dimensions of the substrate used in the spin-coating process. Thermal, morphological and electrical properties of the P3TMA:PE44 nanomembranes were described in the previous section (Section 4.3.2).

Motivated by the promising bioactive behaviour displayed by P3TMA:PE44 50:50, in this section the following items related to the P3TMA:PE44 50:50 nanomembrane are examined in depth: (i) the intrinsic electrochemical properties, which have remained completely unknown so far; (ii) the hydrolytic and enzymatic degradability, both from a qualitative and quantitative point of view; (iii) the response towards different fibroblast and epithelial cellular lines using both adhesion and proliferation studies; and (iv) the electrobioactivity, which has allowed us to determine the influence of cell monolayers in the electrochemical characteristics of the nanomembrane.

4.4.1. Characterization Methods

Electrochemical assays

The electrochemical behaviour of the nanomembranes was investigated by cyclic voltammetry (CV) using both acetonitrile and PBS (pH=7.4) solutions. Measurements were performed on ultra-thin films, which were deposited on steel sheets by spin-coating, before and after covering them with cells. All electrochemical assays were performed with a VersaStat II potentiostat–galvanostat (Princeton Applied Research) using a three-electrode compartment cell under nitrogen atmosphere (99.995% pure) at room temperature. The working compartment was filled with 50 mL of electrolyte solution (acetonitrile or PBS) with 0.1 M $LiClO_4$ as supporting electrolyte. Steel AISI 316 sheets of 1.0 × 1.0 cm^2 in area were used as working and counter electrodes. The reference electrode was an Ag|AgCl electrode containing a KCl saturated aqueous solution (offset potential *versus* the standard hydrogen electrode, E^0 = 0.222 V at 25 °C). The initial and final potentials were -0.40 V, whereas a reversal potential of 1.20 was considered for PBS and acetonitrile. Scan rates of 10 and 50 mV/s were used in this work. The

electroactivity (*i.e.* ability to store charge) increases with the similarity between the anodic and cathodic areas of the first control voltammogram, whereas the electrostability (*i.e.* electrochemical stability) decreases with the oxidation and reduction areas of consecutive control voltammograms.

Contact angle measurements

Contact angles were obtained using the water drop method. Images of water drops (0.3 μL) in the surface of the films were recorded with a contact angle meter (Dataphysics, Contact Angle System OCA15+) after stabilization (30 s). The images of the drop shapes were analysed, and the contact angle measures were carried out with the SCA20 software. Measurements were performed four times for each material.

Hydrolytic degradation studies

Degradation studies were carried out with films prepared by solvent casting and cut to approximately 1 cm×1 cm and nanomembranes deposited on steel substrates, the former and the latter being used for quantitative (weight loss) and qualitative (SEM studies) analyses, respectively. Both films and nanomembranes were placed in vials containing 10 mL of PBS solution supplemented with 0.1 mg/mL of sodium azide, and incubated at 37 °C in a shaking incubator set at 100 rpm for a total of eight weeks. Vials were closed and sealed with parafilm to avoid loss of solution by evaporation, even though the PBS solution was replaced every 48 h. Samples were analyzed after 4 days, 7 days, 2 weeks, 4 weeks and 8 weeks. After each immersion time, samples were removed from the solution and gently washed with distillate water. After drying under vacuum for several days at room temperature (24 h), films were weighed. Degradation was quantitatively monitored as weight loss (WL, in %) of the films by applying the following formula:

$$WL = \frac{m_0 - m_t}{m_0} \; x \; 100 \qquad (4.4.1)$$

where m_0 is the weight of the film before the degradation assay and m_t is the weight of the film after exposure to the degradation medium. The influence of the hydrolytic degradation on the morphology was evaluated by SEM. For SEM studies, nanomembranes were sputter-coated with carbon before observation.

Enzymatic degradation studies

The procedure was identical to that mentioned above for hydrolytic degradation studies with the exception of the solution contained in the vials, which was formed by 4 mg/mL of Lipase F-AP15 in a 10 mL of PBS solution supplemented with 0.1 mg/mL of sodium azide to prevent contamination. The variation of the weight loss against the exposure time was used to evaluate the enzymatic degradability from a quantitative point of view. Micrographs were taken with a Canon IXUS 40 digital camera.

4.4.2. Results and Discussion

Figure 4.4.1 shows a digital camera image of a nanomembrane immersed in ethanol, which was fabricated and detached using the procedure previously described. These self-standing P3TMA:PE44 nanomembranes are very flexible and robust, their folding into small shapes being an easy process. This is evidenced in Figure 4.4.1b–i, which shows optical images of the aspiration process of a nanofilm, with an area of 5 cm^2 floating in ethanol, into a pipette with a tip diameter of 1 mm. As can be seen, the nanomembrane is completely introduced into the pipette (Figure 4.4.1f) due to its outstanding flexibility. After releasing it into the solvent, the nanofilm adopts a folded appearance (Figure 4.4.1g) recovering rapidly its original shape when manipulated with a spatula (Figure 4.4.1i). This aspiration/release/shape recovery process can be repeated more than five times without producing any damage in the nanomembrane. A similar behaviour was reported for hybrid inorganic/organic hybrid nanomembranes made of zirconia and a crosslinked polymer,[45] their robustness and flexibility being essentially attributed to the combination of hard and soft networks in a single material. Thus, in that case two-dimensionally extended double interpenetrated networks were used to reinforce the mechanical properties of the hybrid nanomembrane. However, it should be emphasized that the 50:50 P3TMA:PE44 is a pure organic blend without crosslinking. Accordingly, the robustness and flexibility of the nanomembranes studied in this work are due to the excellent dispersion achieved between the two organic materials.

The contact angles of steel, P3TMA, PE44 and 50:50 P3TMA:PE44 have been determined to illustrate the morphological changes induced by the blending on the wettability of the films. The contact angle of P3TMA at room temperature is 93.8° ± 3.46°. This value indicates that the hydrophobicity at the surface of P3TMA is significantly higher than that observed for other polythiophene derivatives (*e.g.* θ =

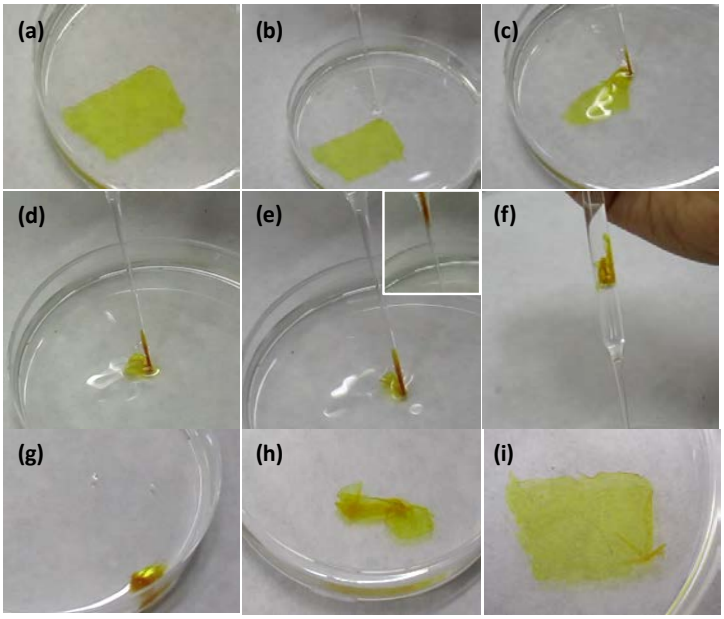

Figure 4.4.1. (a) Digital camera image of a P3TMA:PE44 FsNM immersed in ethanol; (b-f) aspiration of the nanomembrane floating in ethanol into a pipette; (g-h) release of the folded nanomembrane into the ethanol solution; and (i) aspect of the nanomembrane after recovery the shape.

54.0° ± 0.6° for poly(3,4-ethylenedioxythiophene)[46]). On the other hand, the contact angles of PE44 and steel are θ = 76.1° ± 2.5° and 31.2° ± 0.0°, indicating that the two materials, especially the latter, are considerably more hydrophilic than the CP. Finally, the contact angle of the P3TMA:PE44 50:50, θ = 91.9° ± 1.8°, is very close to that of the individual CP. This result is fully consistent with the SEM image of the blend displayed in Figure 4.3.6, which allows identification of spherical P3TMA nanoparticles trapped in the polyester matrix. Thus, the phase separation between the two components of the blend is the cause of the fundamental role played by the CP in the wettability of the film surface.

Electrochemical behaviour of the nanomembranes

The intrinsic electrochemical properties of the blend and the individual polymers were investigated in both PBS and acetonitrile solutions, 0.1 M $LiClO_4$ being added in both cases as supporting electrolyte. Control voltammograms recorded for P3TMA, PE44 and 50:50 P3TMA:PE44 in PBS and acetonitrile are

compared in Figure 4.4.2a-b, respectively. Voltammograms collected using scan rates of 10 and 50 mV/s are displayed to provide information about the definition of the peaks. In general, the oxidation and reduction peaks are more clear and intense in acetonitrile than in PBS indicating that polarons are formed at more specific positions of the polymer chains in the former environment than in the latter one.

The electroactivity of chemically produced P3TMA is significantly higher in the organic solvent than in PBS, which is consistent with preliminary investigations reported for the electrochemically polymerized material 3TMA.[47] In PBS, the CP shows an oxidation shoulder O_1 with anodic peak potential $E_p^a(O_1)$ = 0.84 V, and an oxidation peak O_2 that is expected to reach an anodic peak potential $E_p^a(O_2)$ ≈ 1.4 V (*i.e.* 0.20–0.25 V above the reversal potential). These two processes, which have been attributed to the formation of polarons and bipolarons in polymer chains, are highly irreversible. Thus, the cathodic scan shows a weak reduction shoulder R_1 with a cathodic peak potential of -0.14 V.

The anodic scan recorded for P3TMA in acetonitrile indicates that at potentials around 0.7 V begins a very clear oxidation peak, O_2, which is expected to show an anodic peak potential $E_p^a(O_2)$ ≈ 1.5 V (*i.e.* ~0.3 V above the reversal potential). An oxidation shoulder, O_1, partially overlapped with O_2 is detected at potentials close to 1.0 V. These results indicate the formation of polarons and bipolarons in the polymeric chains at ~1.0 and ~1.5 V, respectively. Moreover, comparison of the current densities indicates that the amount of oxidized molecules is significantly larger in acetonitrile than in PBS. Thus, in acetonitrile the current density at 1.20 V is 6.61 mA/cm², whereas in PBS the current density at 1.20 V is 0.91 mA/cm². The cathodic scan in acetonitrile reflects a reduction peak R_1 with $E_p^c(R_1)$ = 0.88 V (*i.e.* polarons and bipolarons reduce at the same potential). These features suggest the formation of a quasi-reversible redox pair in acetonitrile. Moreover, the voltammogram of the blank demonstrates that the identified shoulders and peaks are not perturbed by the organic solvent.

The voltammogram recorded for PE44 in PBS is similar to that recorded for P3TMA in the same medium. Thus, the oxidation shoulder O_1 with $E_p^a(O_1)$ = 0.90 V and the oxidation peak O_2 with an anodic peak potential higher than 1.20 V have been attributed to the formation of irreversible polarons and bipolarons, respectively. The cathodic scan shows a small reduction shoulder R_1 with cathodic peak potential $E_p^c(R_1)$ = 0.10 V, which corresponds to the reduction of PBS. The voltammogram recorded for PE44 in acetonitrile does not show oxidation or

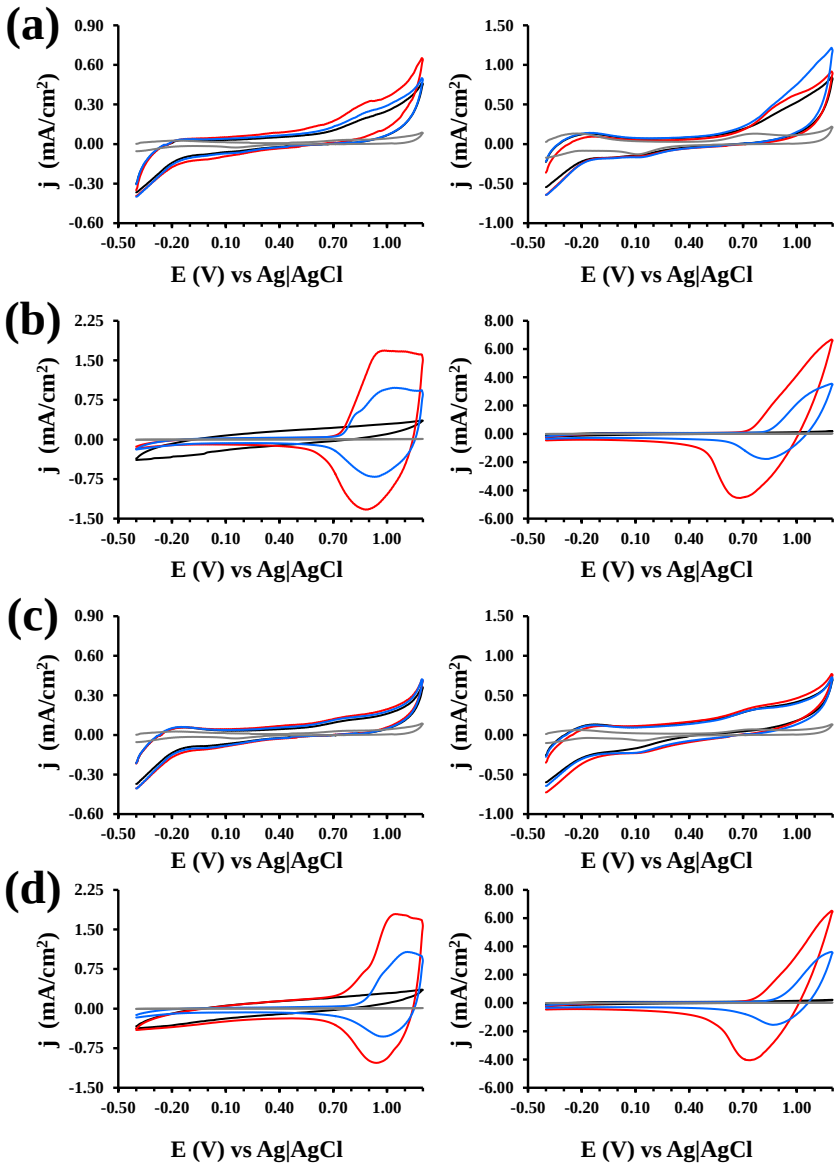

Figure 4.4.2. Control voltammograms collected using scan rates of 10 and 50 mV/s (left and right, respectively) of P3TMA (red line), PE44 (black line) and 50:50 P3TMA:PE44 (blue line) in (a) PBS and (b) acetonitrile solutions (grey lines) with 0.1 M $LiClO_4$. Control voltammograms of the same species after 10 consecutive oxidation-reduction cycles in (c) PBS and (d) acetonitrile solutions with 0.1 M $LiClO_4$.

reduction processes, indicating that no oxidized specie is formed in the potential range from -0.50 to 1.20 V.

The behaviour of the P3TMA:PE44 50:50 in both PBS and acetonitrile shares some of the characteristics discussed for the two individual components, even though some distinctive features are also reflected. In PBS the oxidation peak O_1 shows an anodic peak potential, $E_p^a(O_1)$ = 0.75 V, lower than those of the two individual polymers. However, the characteristics of O_2 and R_1 are similar to those described for P3TMA and PE44 in this medium, confirming that the irreversibility of the oxidation processes is maintained in the blend. The voltammogram recorded for the blend in acetonitrile presents an oxidation peak that begins at 0.80 V and is expected to present an anodic peak potential ~0.3 V higher than the reversal potential. This peak has been associated with the oxidation peak O_2 of P3TMA, even though the current density at 1.20 V is lower for the blend than for the individual CP (1.35 and 2.60 mA/cm^2, respectively). The cathodic scan of the blend presents a reduction peak with a cathodic peak potential of 0.90 V, which corresponds to the peak R_1 identified for the pure CP, indicating the formation of polarons in P3TMA molecules.

Figure 4.4.2c-d shows the voltammograms recorded for P3TMA, PE44 and 50:50 P3TMA:PE44 in PBS and acetonitrile, respectively, with 0.1 M $LiClO_4$ after ten consecutive oxidation–reduction cycles. As it can be seen, the integrated cathodic and anodic areas decrease, independently of the environment, after such amount of cycles indicating a reduction of the electroactivity. However, the electrochemical stability of the blend has been found to be similar in PBS and acetonitrile. The quantitative determination of the loss of electroactivity for the two electroactive species (*i.e.* P3TMA and 50:50 P3TMA:PE44) is around 40% and 30% in PBS and acetonitrile, respectively.

Hydrolytic degradation

Figure 4.4.3 compares the PE44 and 50:50 P3TMA:PE44 50:50 films after 4 days, 2 weeks and 8 weeks of immersion in PBS solution. As it can be seen, the mechanical integrity of the PE44 films was retained in all cases. However, the SEM micrographs of PE44 nanomembranes (Figure 4.4.4a-b) suggest that the influence of the PBS solution on the surface morphology is non-negligible after 4 and 8 weeks of exposure. Thus, degradation produces changes in the superficial texture of the polyester and numerous crevasses and thin grooves appear, their extension and proportion being more noticeable as the immersion time increases. When aliphatic polyester is submerged in an aqueous environment, the water only penetrates into

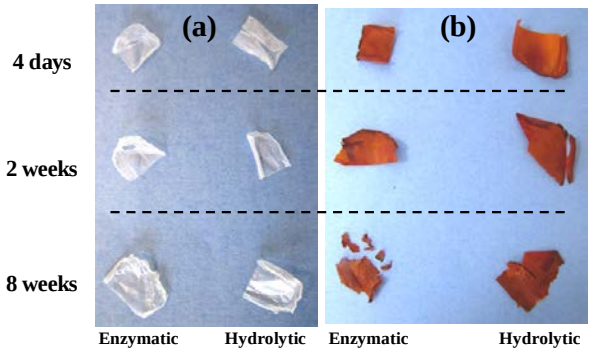

Figure 4.4.3. Optical photographs showing (a) PE44 and (b) 50:50 P3TMA:PE44 samples after 4 days, 4 weeks and 8 weeks of hydrolytic and enzymatic degradation.

the amorphous domains of the polymer chains; it cannot enter the crystalline regions, as reported elsewhere.[48] Amorphous domains can undergo surface erosion or bulk degradation. A theoretical model supported experimentally was developed[49] to predict the erosion mechanism of insoluble biodegradable polymer matrices by water. The model showed that the type of degradation depends on the diffusivity of water inside the matrix, the degradation rate of the polymer's functional groups and the matrix dimensions, these parameters allowing a critical device dimension *LC* to be calculated. If the matrix dimensions are larger than *LC* it will be subjected to surface erosion, otherwise it will undergo bulk erosion. The influence of *LC* on the degradation was experimentally confirmed using poly(*α*-hydroxy ester) matrices.[49] Experiments on other aliphatic polyesters also showed bulk erosion processes.[50-52] Koning and co-workers demonstrated that the main reaction in the degradation of aliphatic polyesters is the autocatalytic hydrolysis of ester bonds, which causes the molecular weight to decrease.[53,54] The reduction of the molecular weight has been measured using films prepared by solvent casting and determining the temporal evolution of the weight loss (WL). As it can be seen in Figure 4.4.5, the weight remains practically unaltered after 8 weeks of immersion in PBS (*i.e.* WL = 1.4%) indicating that the changes in superficial texture only correspond to the first stages of the degradation process.

Hydrolytic degradation underwent by 50:50 P3TMA:PE44 nanomembranes resembles that observed for the polyester. Thus, the appearance of abundant crevasses and thin grooves was detected after 4 weeks of immersion in PBS (Figure 4.4.4c-d), these effects becoming more pronounced after 8 weeks (Figure 4.4.4e-f). However, Figure 4.4.5 indicates that changes in the superficial texture are

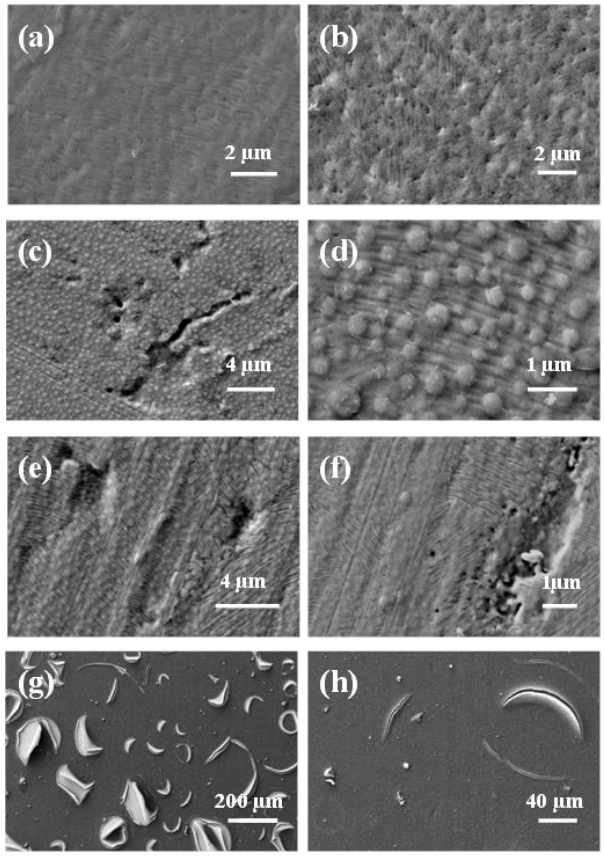

Figure 4.4.4. SEM micrographs of hydrolytically degraded nanomembranes: PE44 after 4 weeks (a) and 8 weeks of immersion (b); 50:50 P3TMA:PE44 after 4 weeks (c and d) and 8 weeks (e and f) of immersion; low (g) and high (h) magnification micrographs of P3TMA after 8 weeks of immersion.

accompanied by a significant increase of the weight loss (WL = 17.2%). Thus, we found that the degradation of the polyester in the blend produced the detachment of the P3TMA domains, the thin grooves observed after 4 weeks of degradation transform into large and deep cracks after 8 weeks. Moreover, the mechanical integrity of P3TMA:PE44 disappears after two weeks, hydrolytic degradation inducing the fragmentation of the films. These results indicate that the contribution of the polyester is essential not only to provide mechanical integrity but also to facilitate the hydrolytic degradation of the P3TMA:PE44 nanomembranes.

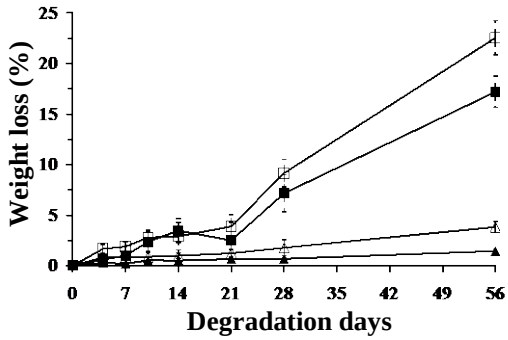

Figure 4.4.5. Plot of the WL (%) *versus* the degradation time (days) in hydrolytic (filled symbols) and enzymatic media (empty symbols) for PE44 (triangles) and 50:50 P3TMA:PE44 (squares) films.

Immersion of P3TMA in PBS produced a delamination process, which is evidenced in the SEM micrographs displayed in Figure 4.4.4g-h. This particular degradation process, which started after 2 weeks, was initially observed through the appearance of blisters and small cracks around them. However, inspection of the samples submerged during 8 weeks reflected significant growth of such cracks, which induced the above-mentioned delamination process. Thus, fragments of relatively large dimensions were released to the medium, leaving holes that are detectable at first glance (*i.e.* visible to the naked eye). The delamination process, which is not properly a degradation process, of P3TMA may be attributed to a corrosion process at the steel substrate, which was used to deposit the material. More specifically, molecules of water, which were absorbed by the nanofilm due to the hydrophilic carboxylate side groups, reached the steel/P3TMA interface. This absorption produced not only a swelling effect but also the corrosion of the anodic region (*i.e.* in the metal surface, under the P3TMA coating), which was activated by the dissolved salts. These features enabled the development of blisters and tensions on the surface, inducing the formation of crevasses in the nanomembrane. Interestingly, the delamination process described for P3TMA was not observed in P3TMA:PE44 nanomembranes. Due to the lack of film forming properties of the CP, no quantitative analysis of the degradation was carried out for P3TMA samples.

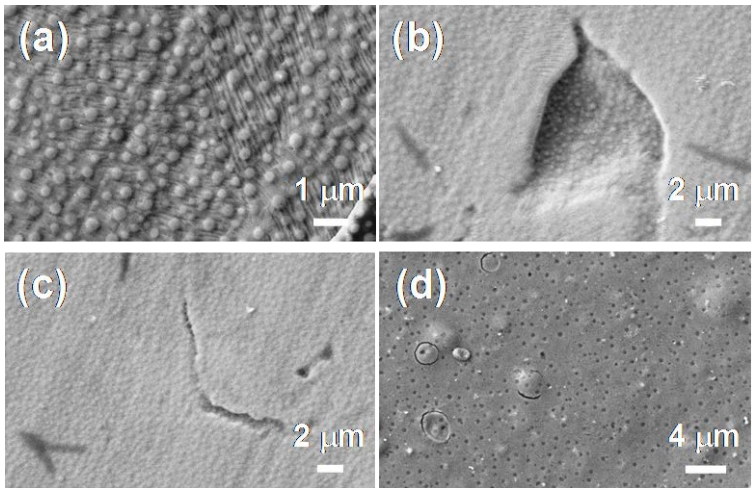

Figure 4.4.6. SEM micrographs of the 50:50 nanomembrane after (a) one week and (b and c) three weeks of exposure under enzymatic degradation conditions. (d) SEM micrograph of an ultrathin film of P3TMA after four weeks of incubation in the enzymatic medium.

Enzymatic degradation

Results derived from enzymatic degradation assays are qualitatively similar to those described above for hydrolytic degradation but quantitatively enhanced due to the action of the enzyme. This qualitative similarity is reflected in both the digital camera images displayed in Figure 4.4.3, which compares the effects of the two different degradation media in the PE44 and P3TMA:PE44 50:50 films, and the SEM micrographs (Figure 4.4.6). Thus, although PE44 films retain the mechanical integrity after 8 weeks, blend films start a fragmentation process after only two weeks. Moreover, the influence of the enzymatic degradation in the morphology of the individual polyester and the blend is also very similar to that displayed in Figure 4.4.4 for hydrolytic degradation assays. On the other hand, Figure 4.4.5 shows that the WL for the polyester and the blend after 8 weeks of immersion is 3.8%and 22.5%, respectively. These values confirm that the presence of the Lipase F-AP15 in the degradation medium produces an increment in the weight loss of 2.4% and 5.3% for the polyester and the blend, respectively, with respect to the PBS without enzyme.

Cell adhesion and proliferation

The responses of P3TMA:PE44 nanomembranes towards different cellular lines were compared with those of P3TMA and PE44. Cellular adhesion and proliferation assays were performed considering four different lines of eukaryotic cells: MDCK and Cos-7, which are fibroblast cells, and Du-145 and HEp-2, which are epithelial cells. These carcinogenic cells were selected due to their fast growth. Quantitative results of cellular adhesion assays are displayed in Figure 4.4.7, steel and TCPS being used as control substrates. As it can be seen, the number of cells by area of a given material is similar for the four cellular lines. Although the behaviour of P3TMA as a supportive matrix for cellular adhesion is significantly worse than that of PE44, the adhesion of fibroblast and epithelial cells on the surface of 50:50 nanomembranes is the most favoured in all cases.

After 7 days of culture, the cellular activity on the material was re-evaluated. Cellular proliferation results, which are included in Figure 4.4.7, show that the number of viable cells per area of material in the TCPS control substrate remains practically unaltered, while that in steel decreases slightly. In contrast, a significant increment in the number of viable cells is detected in both PE44 and 50:50 P3TMA:PE44. Indeed, the ability of the two substrates for cellular proliferation is the same for all cellular lines with exception of Cos-7 cells, which show a slight preference towards the blend with respect to the individual polyester. This is an amazing result since the comparison between adhered and proliferated cells reflects in all cases, with exception of HEp-2, the negative behaviour of P3TMA as a cellular matrix. Thus, the number of viable cells decreases after seven days of culture for the MCDK, Du-145 and Cos-7 lines. The cell proliferation inhibition exhibited by individual P3TMA should be attributed to the presence of the oxidizing agent ($FeCl_3$) in the matrix, which was in excess during the polymerization process. Thus, recent studies showed both the cytotoxicity effect produced by $FeCl_3$ in MCF-7 cells[55] and the lipid peroxidation induced by this oxidizing agent in the cell membranes.[56] The negative effect induced by $FeCl_3$ is eliminated when the CP is mixed with the polyester because of the reduction in its effective concentration.

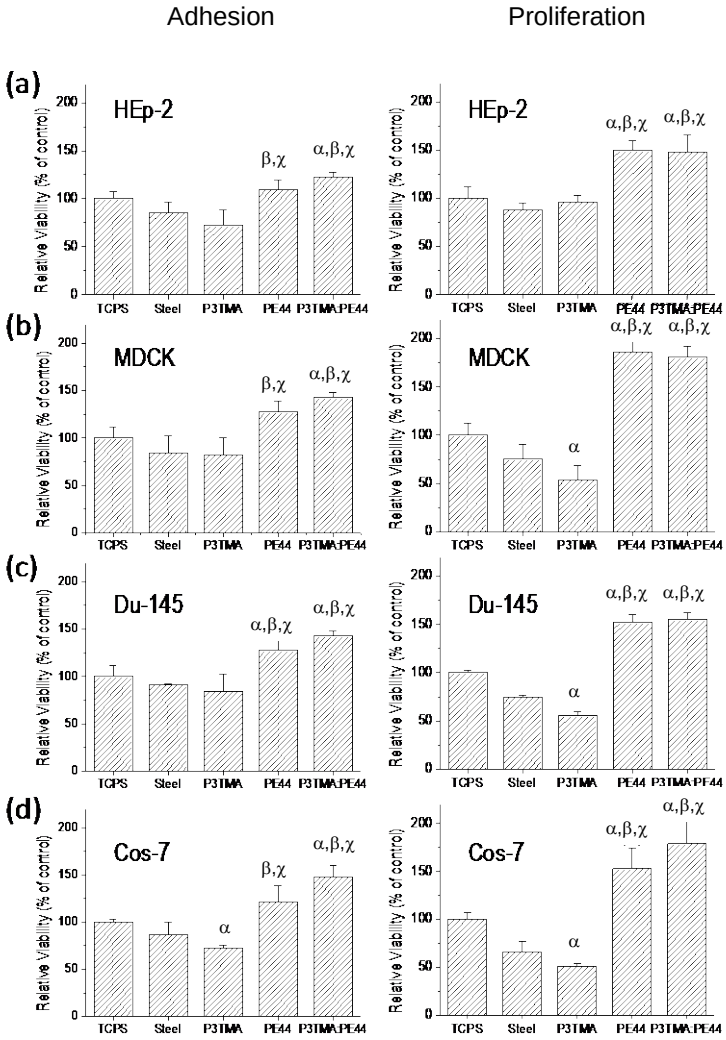

Figure 4.4.7. Cellular adhesion (right column) and proliferation (left column) on P3TMA, PE44 and 50:50 P3TMA:PE44 substrates. Assays were carried out using the following eukaryotic cell lines: a) HEp-2, b) MDCK, c) Du-145, and d) Cos-7. The relative viability was established in relation to the TCPS control (tissue culture polystyrene). Steel was also considered as control substrate because the individual polymers and the blend were deposited on this material. Greek letters on the columns refer to significant differences (p<0.05) using the ANOVA and Tukey's test: α *vs.* TCPS; β *vs.* steel; χ *vs.* P3TMA; and δ *vs.* PE44.

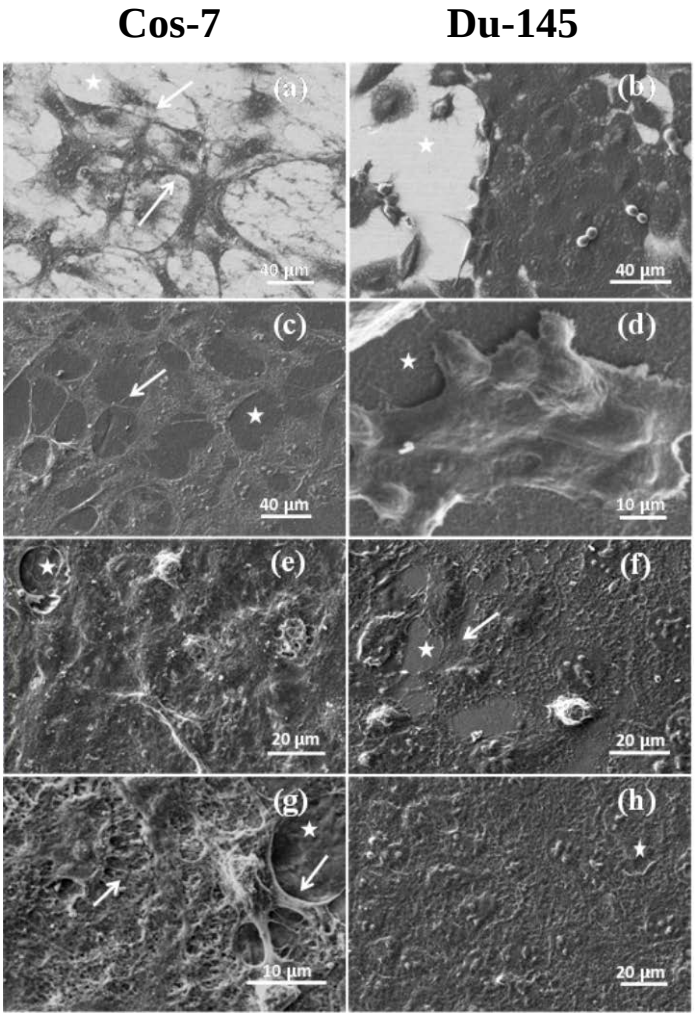

Figure 4.4.8. SEM micrographs of Cos-7 and Du-145 cells adhered on the surface of steel (a and b), and cultured on PE44 (c and d), P3TMA (e and f) and 50:50 P3TMA:PE44 (g and h). The substrates surfaces (domains without cells) are shown by asterisks (★), while the connections or interactions between the cell and the surface or between two cells are indicated by arrows.

Figure 4.4.8 displays SEM images of different cells cultured on steel, P3TMA, PE44 and 50:50 P3TMA:PE44 substrates. In general, there is a significant spreading of cells on the surface of steel and PE44 substrates. The connection sites between the cells and the surface of these substrates have been marked with arrows, details about the stress fibers formed by the cells to move along the substrates being also displayed. The latter correspond to the lamellipodia, which are delicate sheet-like extensions of cytoplasm that form transient adhesions with the substrate, and the actin filaments are known as filopodia (*i.e.* thin extensions of cytoplasm to focal adhesion). The formation of lamellipodia and fillopodia is less abundant on the P3TMA surface, which is consistent with the poor colonization of such a substrate. In contrast, the abundance of cells on the surface of the 50:50 sample was so high that it allowed us to identify thick monolayers involving different levels of cellular growth. Similarly, connections of cells to both the blend surface and the neighbouring cells are clearly evidenced in this substrate. Within this context, it should be remarked that Cos-7 cells present a star shape that grow side-by-side forming a very compact monolayer. Such a compact disposition is also observed for Du-145 cells, even though they present a round-like shape. The overall of these *in vitro* results support the fact that 50:50 P3TMA:PE44 nanomembranes should be considered as powerful bioactive platforms for tissue regeneration.

Electrobioactivity

The electrochemical behaviour of P3TMA:PE44 nanomembranes coated with MDCK and HEp-2 cell monolayers was investigated by CV in PBS with 0.1 M $LiClO_4$. Figure 4.4.9 compares the control voltammograms recorded for P3TMA, PE44 and 50:50 P3TMA:PE44 coated with cellular monolayers with those obtained for the uncovered materials. Although HEp-2 cell monolayers do not affect the profile of the voltammogram recorded for P3TMA and PE44, these epithelial cells produce a slight enhancement of the anodic current densities in both the anodic and cathodic scans. This feature suggests that HEp-2 cells facilitate the ionic diffusivity in the polymer–cells–solution interfaces but do not modify the almost irreversible behaviour of the oxidation processes. In contrast, MDCK cells proliferated on P3TMA and PE44 produce a reduction of the anodic current densities of oxidation and reduction profiles, which causes a loss in the definition of the oxidation peaks that is particularly remarkable for the CP. Accordingly, these cellular line reduces the mobility of the ions at the interface, even though as observed for HEp-2 monolayers the irreversible behaviour of the oxidation and reduction processes remains unaltered.

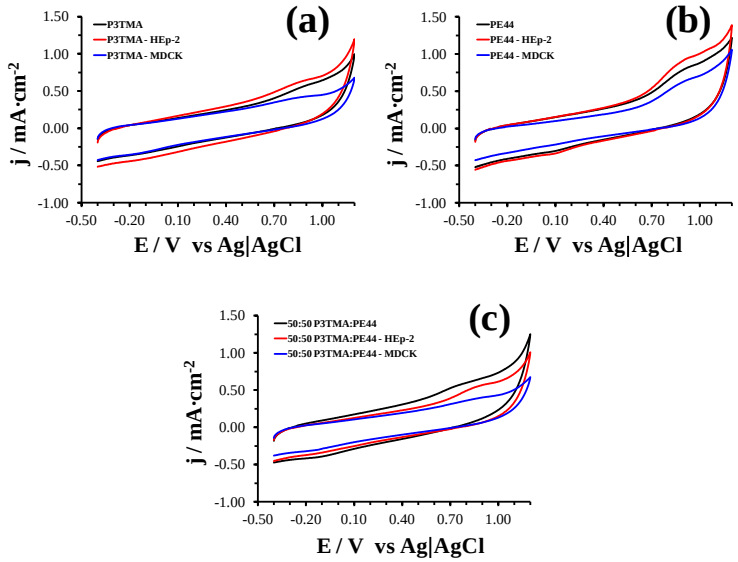

Figure 4.4.9. Control voltammograms of: (a) P3TMA; (b) PE44; and (c) 50:50 P3TMA:PE44 in PBS with 0.1 M $LiClO_4$ (scan rate 50 mV/s). For each material, control voltammograms for the oxidation of the uncoated sample (black lines) and samples coated with HEp-2 (red lines) and MDCK cells (blue lines) are displayed.

The most remarkable effect of the HEp-2 and MCDK cells on the 50:50 blend refers to the decrease of the anodic and cathodic intensities in the whole voltammogram, such a reduction being especially evident for the latter monolayers. This feature is particularly striking for the HEp-2 cells since they were found to enhance the anodic and cathodic intensities of the two individual polymers (Figure 4.4.9a-b). The overall of these results suggests that important differences exist in the interfaces of the blend and the individual polymers. Thus, the channels that allow the access and escape of the dopant ions are blocked by the two types of cells in the blends, whereas this effect is only detected for MDCK cells in the individual polymers.

Figure 4.4.10 displays the SEM micrographs of P3TMA and 50:50 P3TMA:PE44 coated with cellular monolayers after eight consecutive oxidation–reduction cycles. As it can be seen, cells are severely affected by the electric current, which produces their detachment from the substrate surface. Amazingly, the influence of the electric current in the cellular structure depends on both the substrate and the cellular line.

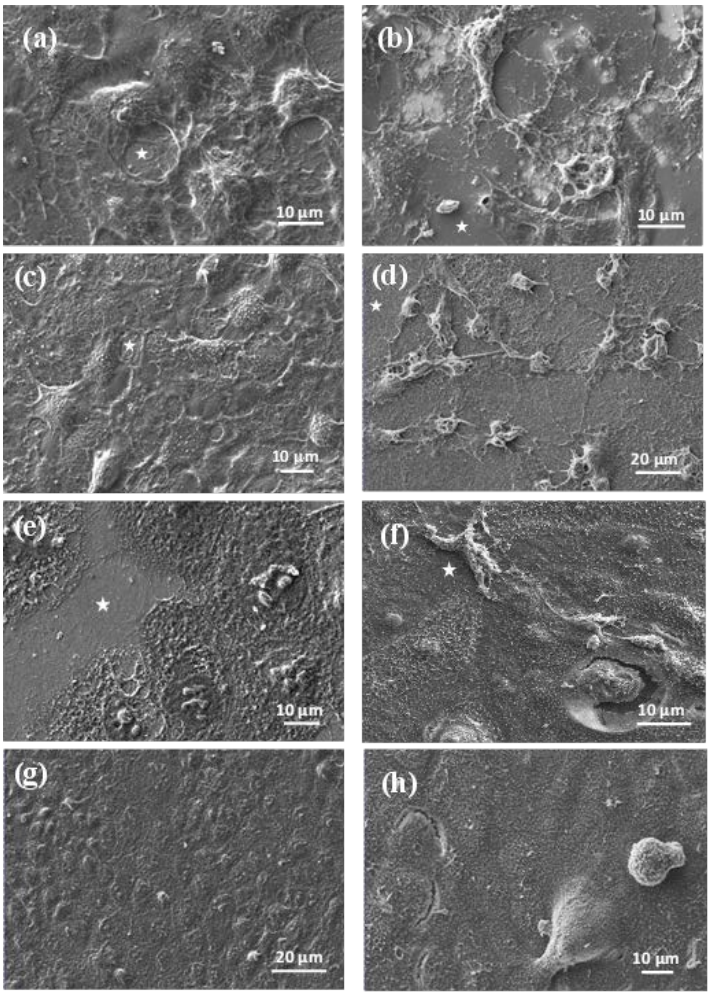

Figure 4.4.10. SEM micrographs of P3TMA and 50:50 P3TMA:PE44 samples coated with HEp-2 and MDCK cells before and after an electrochemical treatment consisting of eight consecutive oxidation-reduction cycles: P3TMA coated with HEp-2 cells (a) before and (b) after treatment; 50:50 blend coated with HEp-2 cells (c) before and (d) after treatment; P3TMA coated with MDCK cells (e) before and (f) after treatment; and 50:50 blend coated with MDCK cells (g) before and (h) after treatment. Stars indicate regions not covered by cells.

More specifically, the interconnections between the HEp-2 cells and the P3TMA surface (Figure 4.4.10a-b) were damaged by the eight redox processes, whereas damages were not so severe in the case of the 50:50 blend (Figure 4.4.10c-d). This result should be attributed to the fact that the initial distribution of cells was very

different for the two substrates. In opposition, MDCK cells were annihilated by the anodic current in all cases (Figure 4.4.10f and h). Thus, although a few isolated cells were detected on the substrates, the surfaces were essentially coated by denatured proteins (*i.e.* cell remainders). It is worth noting that in the initial samples, MDCK cells formed compact monolayers (Figure 4.4.10e and g). Therefore, detachment of some cells induced the detachment of neighbouring cells, which are in close contact, through a cascade effect. The scenario of HEp-2 cells is completely different since cells are more spread over the surface facilitating their resistance towards the anodic current.

4.5. Conclusions

The present work presents the fabrication of very stable FsNM by combining a polythiophene derivative bearing carboxylate substituents in the 3-position of the heterocyclic ring and a biodegradable polyester. The thickness and roughness of the nanomembranes are controlled through the spin-coater speed. Specifically, 50:50 P3TMA:PE44 obtained using a speed of 3000 rpm displayed values of 19 and 5 nm, respectively. The dimensions of these flexible films are only limited by the size of substrate used in the fabrication process. Moreover, their flexibility and robustness have been investigated by aspirating the nanomembrane floating in ethanol into a pipette and subsequently releasing it into the solvent. We found that the nanofilm rapidly recovers the original shape, this aspiration/release/shape recovery process being repeated more than five times without producing any damage to the nanofilm. The robustness and flexibility of the nanomembrane have been attributed to the good dispersion of the CP and the polyester in the blend.

The structure and wettability of the blend have been investigated and compared with those of the individual polymers using FTIR and contact angle measurements, respectively. Amazingly, both the blend and the individual CP show a very similar hydrophobicity, the contribution of the hydrophilic polyester to the wettability of the 50:50 nanomembrane being practically negligible.

Investigation of the electrochemical properties by CV in PBS and acetonitrile indicates that the oxidation and reduction processes found in the individual CP are also present in the blend. Thus, the polyester only affects the infrequent oxidation process detected for P3TMA at 0.22 V, which is blocked in the blend. The electroactivity of both the blend and the P3TMA is higher in acetonitrile than in PBS. Moreover, the definition of the oxidation and reduction peaks is more clear and intense in the organic solvent indicating that in this environment the formation

of polarons is more localized. However, the electrochemical stabilities of the blend are similar in the physiological and the organic environment.

Hydrolytic and enzymatic degradation produces changes in the superficial texture of the PE44 samples, which are evidenced by the appearance of crevasses and thin grooves. In spite of this, the weight loss was very low in both cases since the degradation media only penetrate into the amorphous domains of the polyester. In contrast, the weight loss grows significantly when the 50:50 blend is exposed to hydrolytic and, especially, enzymatic degradation media, which has been attributed to the fact that the degraded polyester facilitates the detachment of the P3TMA domains. Thus, the degradation rate is considerably higher for the blend than for the individual polyester.

Cellular adhesion and proliferation assays have been carried out using HEp-2, MDCK, Cos-7 and Du-145 lines. Results clearly evidence that P3TMA:PE44 50:50 behaves as a potent cellular matrix, the viability of the cultured cells being significantly higher in the blend than in the polyester and, especially, the CP. Indeed, cellular proliferation is inhibited by the P3TMA substrate, which has been attributed to the detrimental effects caused by an excess of $FeCl_3$.

Finally, analysis of the electrobioactivity of P3TMA, PE44 and the 50:50 blend coated with HEp-2 and MDCK monolayers has been carried out using CV. Comparison of the results obtained for uncoated and coated systems indicates that all three materials are electrocompatible with cellular monolayers, even though the anodic and cathodic intensities are in general smaller for the coated systems. On the other hand, inspection of the cellular connections after eight consecutive oxidation and reduction cycles indicates that the HEp-2 cells are more resistant towards the anodic current than the MDCK ones. The different electrobioactive behaviour found for HEp-2 and MDCK lines suggests a significant dependence on the interaction between cells and the substrate surface. In summary, the combination of P3TMA and PE44 to produce nanomembranes allows us to retain, or even to improve, the best properties of each individual material (*i.e.* the biodegradability and good behaviour as cellular matrix of PE44 on one side, and the electroactivity of P3TMA on the other).

4.6. References

[1] M. Mazzeo, V. Vitale, F. Della Salla, M. Anni, G. Barbarella, L. Favaretto, G. Sotgiu, R. Cingolani, G. Gigli, *Adv. Mater.* **2005**, *17*, 34.

[2] W. U. Huynh, J. J. Dittmer, A. P. Alivisatos, *Science* **2002**, *295*, 2425.

[3] P. Bjork, D. Thomsson, O. Mirzov, J. Wigenius, O. Inganas, I.Scheblykin, *Small* **2009**, *5*, 96.
[4] H. A. Ho, M. Leclerc, *J. Am. Chem. Soc.* **2004**, *126*, 1384.
[5] M. Hamedi, R. Forchheimer, O. Inganas, *Nat. Mater.* **2007**, *6*, 357.
[6] R. Berridge, S. P. Wright, P. J. Skabara, A. Dyer, T. Steckler, A. A. Argun, J. R. Reynolds, W. H. Ross, W. J. Clegg, *Mater. Chem.* **2007**, *17*, 225.
[7] R. A. Marsh, J. M. Hodgkiss, R. H. Firend, *Adv. Mater.* **2010**, *22*, 3672.
[8] N. K. Guimard, N. Gomez, C. E. Schmidt, *Prog. Polym. Sci.* **2007**, *32*, 876.
[9] A. Mishra, C. Q. Ma, P. Bäuerle, *Chem. Rev.* **2009**, *109*, 1141.
[10] H. S. O. Chan, S. C. Ng, *Prog. Polym. Sci.* **1998**, *23*, 1167.
[11] G. Barbarella, M. Melucci, G. Sotgiu, *Adv. Mater.* **2005**, *17*, 1581.
[12] T. A. Chen, X. Wu, R. D. Rieke, *J. Am. Chem. Soc.* **1995**, *117*, 233.
[13] C. Yang, F. P. Orfino, S. Holdcroft, *Macromolecules* **1996**, *29*, 6510.
[14] R. D. McCullough, *Adv. Mater.* **1998**, *10*, 93.
[15] M. Chayer, K. Faïd, M. Leclerc, *Chem. Mater.* **1997**, *9*, 2902.
[16] B. Kim, L. Chen, J. Gong, Y. Osada, *Macromolecules* **1999**, *32*, 3964.
[17] D. J. Liaw, B. Y. Liaw, J. P. Gong, Y. Osada, *Synth. Met.* **1999**, *99*, 53.
[18] P. C. Ewbank, R. S. Loewe, L. Zhai, J. Reddinger, G.Sauvé, R. D. McCullough, *Tetrahedron* **2004**, ***60***, 11269.
[19] O. Bertran, E. Armelin, J. Torras, F. Estrany, M. Codina, C. Alemán, *Polymer* **2008**, *49*, 1972.
[20] E. Armelin, O. Bertran, F. Estrany, R. Salvatella, C. Alemán, *Eur. Polym. J.* **2009**, *45*, 2211.
[21] O. Bertran, E. Armelin, F. Estrany, A. Gomes, J. Torras, C. Alemán, *J. Phys. Chem. B* **2010**, *114*, 6281.
[22] K. H. Hsieh, K. S. Ho, Y. Z. Wang, S. D. Ko, S. C. Fu, *Synth. Met.* **2001**, *123*, 217.
[23] M. E. Nicho, D. Peña-Salgado, P. Altuzar-Coello, *Thin Solid Films* **2010**, *518,* 1799.
[24] A. Özgün, B. Sari, A. Uygun, H. I. Ünal, Ç. Çakanyildirim, *Int. J. Polym. Anal. Charact.* **2009**, *14,* 469.
[25] S. Manna, A. Mandal, A. K. Nandi, *J. Phys. Chem. B* **2010**, *114*, 2342.
[26] D. Mawad, K. Gilmore, P. Molino, K. Wagner, P. Wagner, D. L. Officer, G. G. Wallace, *J. Mat. Chem.* **2011**, *21*, 5555.
[27] G. G.Wallace, L. A. P. Kane-Maguire *Adv. Mater.* **2002**, *14*, 953.
[28] J. Hu, L. Huang, X. Zhuang, P. Zhang, L. Lang, X. Chen, Y. Wei, X. Jing, *Biomacromolecules* **2008**, *9*, 2637.
[29] Q.-S. Zhang, Y.-H. Yan, S.-P. Li, T. Feng, *Biomed. Mater.* **2009**, *4*, 035008.
[30] L J. del Valle, D. Aradilla, R. Oliver, F. Sepulcre, A. Gamez, E. Armelin, C. Alemán, F. Estrany, *Eur. Polym. J.* **2007**, *43*, 2342.
[31] L. J. del Valle, F. Estrany, E. Armelin, R. Oliver, C. Alemán, *Macromol. Biosci.* **2008**, *8*, 1144.
[32] D.-F. Li, H.-J. Wang, J.-X. Fu, W. Wang, X.-S. Jia, J.-Y. Wang, *J. Phys. Chem. B* **2008**, *112*, 16290.
[33] R. D. Breukers, K. J. Gilmore, M. Kita, K. K. Wagner, M. J. Higgins, S. E. Moulton, G. M. Clark, D. L. Officer, R. M. I. Kapsa, G. G. Wallace, *J. Biomed. Mater. Res., Part A* **2010**, *95*, 256.
[34] T. J. Rivers, T. W. Hudson, C. E. Schmidt, *Adv. Funct. Mat.* **2002**, *12*, 33.
[35] T. Fujimaki, *Polym. Degr. Stab.* **1998**, *30*, 209.
[36] H. Watanabe, T. Ohzono, T. Kunitake, *Macromolecules* **2007**, *40*, 1369.
[37] H. Watanabe, T. Kunitake, *Adv. Mater.* **2007**, *19*, 909.
[38] T. Mosmann, *J. Immunol. Methods* **1983**, *65*, 55.

[39] O. Bertran, P. Pfeiffer, J. Torras, E. Armelin, F. Estrany, C. Alemán, *Polymer* **2007**, *48*, 6955.
[40] E. S. Yoo, S. S. Im, *J. Polym. Sci.: Part B: Polym. Phys.* **1999**, *37*, 1357.
[41] H. E. Kissinger, *Anal. Chem.* **1957**, *29*, 1702.
[42] N. Sbirrazzuoli, Y. Girault, L. Elégant, *Thermochim. Acta* **1997**, *293*, 25.
[43] S. Vyazovkin and N. Sbirrazzuoli, *Macromol. Rapid Commun.* **2006**, *27*, 1515.
[44] F. Zang, M. P. Srinivivasan, *Macromol. Chem. Phys.* **2008**, *112*, 223.
[45] R. Vendamme, S. Y. Onoue, A. Nakao, T. Kunitake, *Nat. Mater.* **2006**, *5*, 494.
[46] B. Teixeira-Dias, L. J. del Valle, F. Estrany, J. F. Mano, R. L. Reis, C. Alemán, Macromol. Mater. Eng. **2011**, *297*, 359.
[47] P. N. Bartlett, D. H. Dawson, *J. Mater. Chem.* **1994**, *4*, 1805.
[48] E. W. Fischer, H. J. Sterzel, G. Wegner and Z. Z. Kolloid, *Polymer* **1973**, *251*, 980.
[49] F. Von Burkersroda, L. Schedl, A. Göpferich, *Biomaterials* **2002**, *23*, 4221.
[50] J. A. Tamada, R. Langer, *Proc. Natl. Acad. Sci. U. S. A.* **1993**, *90*, 552.
[51] R. A. Kenley, M. O. Lee, T. R. Mahoney, L. M. Sanders, *Macromolecules* **1987**, *20*, 2398.
[52] M. Hakkarainen, A.-C. Albertsson, S. Karlsson, *Polym. Degrad. Stab.* **1996**, *52*, 283.
[53] H. Antheunis, J.-C. Van der Meer, M. De Geus, A. Heise, C. E. Koning, *Biomacromolecules* **2010**, *11*, 1118.
[54] H. Antheunis, J.-C. Van der Meer, M. De Geus, W. Kingma, C. E. Koning, *Macromolecules* **2009**, *42*, 2462.
[55] E. Laqué-Rupérez, M. J. Ruiz-Gómez, L. de la Peña, L. Gil, M. Martínez-Morillo, *Bioelectrochemistry* **2003**, *60*, 81.
[56] K. J. Woollard, S. Sturgeon, J. P. F. Chin-Dusting, H. H. Salem, S. P. Jackson, *J. Biol. Chem.* **2009**, *284*, 13110.

CHAPTER 5

BIOACTIVE NANOMEMBRANES OF POLYTHIOPHENE DERIVATIVE AND THERMOPLASTIC POLYURETHANE

Summary

The results described in Chapter 4 encouraged the further study of P3TMA-based FsNM. In an effort to improve the miscibility between the CP and the insulating matrix that supports it, PE44 was substituted by thermoplastic polyurethane (TPU), which was gently provided by *Merquinsa, A Lubrizol Company*. Again, spin-coating was the technique chosen to prepare these biointerfaces. Although TPU:P3TMA samples were processed as supported nanomembranes for most of the characterization tests, it should be noted that blends were also processed as films by solvent-casting due to experimental limitations of the techniques. Each approach will be specified when required.

Firstly, the thermal, nanostructural and nanomechanical properties of TPU:P3TMA FsNM were examined (Section 5.3). Secondly, a complete study of their electronic, electric and electrochemical features was performed (section 5.4). Finally, their feasibility as interfaces for biomedical and biotechnological applications was evaluated in terms of biocompatibility, biodegradability and protein adsorption response (section 5.5).

Following the structure of the previous chapter, common materials for sections 5.3-5.5, P3TMA synthesis and FsNM fabrication are described in Section 5.2.

This work is the result of a research collaboration stablished with Dr. M. I. Giannotti[1] and Prof. F. Sanz[1]. Thus, AFM measurements were performed at the Centres Científics i Tecnològics (UB). Thermal measurements were run by Dr. L. Franco[2], while biological and biodegradation assays were done in collaborative working with Dr. L. J. del Valle[2].

Publications derived from this work:

M. M. Pérez-Madrigal, M. I. Giannotti, G. Oncins, L. Franco, E. Armelin, J. Puiggalí, F. Sanz, L. J. del Valle, C. Alemán, *Polym. Chem.* **2013**, *4*, 568.

M. M. Pérez-Madrigal, M. I. Giannotti, E. Armelin, F. Sanz, C. Alemán, *Polym. Chem.* **2014**, *5*, 1248.

M. M. Pérez-Madrigal, M. I. Giannotti, L. J. del Valle, L. Franco, E. Armelin, J. Puiggalí, F. Sanz, C. Alemán, *ACS Appl. Mater. Interfaces* **2014**, *6*, 9719.

[1]Institut de Bioenginyeria de Catalunya (IBEC), Barcelona, Spain.
[2]Departament d'Enginyeria Química, E.T.S. d'Enginyers Industrials de Barcelona, UPC.

5.1. Introduction

Tissue engineering is a novel interdisciplinary field which focuses fundamentally on restoring or regenerating dysfunctional tissues and organs. In order to accomplish this purpose, biocompatible matrices or porous scaffolds are used as substrates/biointerfaces to promote cell adhesion, migration, proliferation and differentiation, thus mimicking the native extracellular matrix functions.[1] Scaffolds must exhibit specific requirements such as biocompatibility and, possibly, also biodegradability and/or bioresorbability. Besides, their mechanical integrity must offer adequate support for cells to attach and seed, thus integrating them with the surrounding tissue to restore the defect.

Biomaterials are usually made of either synthetic or naturally derived polymers. Linear aliphatic polyesters, such as poly(lactide) (PLA) and poly(glycolic acid), have been extensively used as synthetic biopolymers since their biodegradation rate and mechanical properties can be easily adjusted (*e.g.* by modifying the molecular weight).[2] Moreover, poly(ε-caprolactone) is another biocompatible polymer used extensively.[3] Polyether-ester co-polymers form another group of synthetic polymers that present excellent properties like elasticity, toughness, strength and easy processability that come from the combination of both soft and hard segments along the chemical structure.[4] Within naturally derived polymers, collagen and polysaccharides, like alginate and chitosan, have been studied for many tissue engineering applications.[5,6] Generally, all these biomaterials can be easily processed into films or fibers thus tuning precisely their structural, mechanical and surface properties.

Recently, CPs such as polythiophene (PTh) derivatives have been brought into focus.[7-9] The combination of their electrical response and their non-toxicity towards biological systems makes biocompatible PTh derivatives suitable candidates for interesting biomedical devices.[10] The use of PTh derivatives has been proposed for several biomedical applications like controlled release and drug delivery, DNA synthesis enhancement, protein secretion and biosensors and bioactive platforms/scaffolds for tissue engineering.[11-14] However, some chemical and physical characteristics of PTh derivatives (*e.g.* brittleness, low chemical stability, restricted processability into films and fibers and low solubility in common organic solvents), also showed by many other CPs, restrict their practical applications when used individually. In order to overcome these limitations, several approaches are followed, the one consisting in blending the CP with another polymer, generally insulating, that provides a polymeric matrix in which the CP is embedded being the

most usual. Although attenuation of the semiconductor performance of the CP can arise when blending with a non-conductive material, a great improvement in the mechanical stability and processability of the final product is achieved.

On the other hand, artificial nanomembranes are a very recent concept in nanotechnology. They may be defined as free-standing (self-supported) structures that have one nano-dimension (5–100 nm) and two macroscopic dimensions.[15] Robust and flexible nanomembranes were fabricated by Kunitake and co-workers using a variety of cross-linked synthetic materials, for example inorganic/organic hybrid,[16,17] thermosetting resins[18,19] and photopolymers.[20] Robust nanomembranes have also been obtained using biopolymers, such as polysaccharides[21,22] and silk,[23] and biodegradable polylactic acid.[24]

Within this context, P3TMA:PE44 nanomembranes (Chapter 4) were prepared by spin-coating mixed solutions of the two polymers, the thickness of the resulting ultra-thin films ranging from 20 to 80 nm depending on the spin-coater speed.[25] Nanometric P3TMA:PE44 blends were found to retain the intrinsic semiconducting and electrochemical properties (*i.e.* oxidation and reduction processes) of P3TMA.[25,26] Moreover, hydrolytic and enzymatic studies showed that the degradation of polyester domains produces the detachment of the P3TMA domains. Successful adhesion and proliferation assays using four different cellular lines allowed us to propose that P3TMA:PE44 free-standing nanomembranes are potential bioactive platforms for tissue regeneration. Thus, the viability of the cultured cells was significantly higher in the blend than in the individual polymers. In spite of the important benefits obtained from blending the polyester matrix with the semiconducting polymer, thermal and microscopy analyses revealed the presence of two phases in the mixture indicating that P3TMA and PE44 are only partially miscible. Thus, calorimetric data of melt quenched samples showed two glass transition temperatures, as expected from a phase separation, while both optical and scanning electron microscopy (SEM) micrographs evidenced phase separation.

In this work, FsNM have been prepared by blending P3TMA and thermoplastic polyurethane (TPU), which presents many useful applications and probed biodegradability.[27] The TPU used in this study is a block copolymer formed by the polymerization reaction of a diisocyanate, a short-chain diol and a macrodiol. The reaction of the diisocyanate and the short-chain diol produces hard segments with a high density of urethane groups of high polarity and capability to form intermolecular hydrogen bond interactions, while the reaction of diisocyanate and the long-chain diol results in soft segments of low polarity with a very low density

of urethane groups. Hard and soft segments are rigid and flexible, respectively, at room temperature. The polarity of hard segments produces a strong attraction between them and a high degree of aggregation, causing a phase separation between blocks (*i.e.* crystalline micro- or nanodomains formed by hard segments located in a soft and flexible matrix).[28] Semiconducting blends based on mixtures of polyurethanes and semiconducting polymers (*e.g.* polypyrrole and polythiophene derivatives) showed attractive mechanical, electrical, optical and thermal properties.[29-32] In particular, their excellent elasticity and mechanical behavior were found to reinforce the poor mechanical integrity of semiconducting polymers when processed into fibers and films. In this study, we combined P3TMA with an aromatic grade TPU, which is expected to show higher miscibility with the aromatic thiophene rings than the linear polyester used previously,[25,26] at the nanometric scale to fabricate robust free-standing nanomembranes.

5.2. Experimental Section

5.2.1. Materials

3-Thiophene acetic acid (3TAA) (98.0%) was purchased from Fluka (Poland) while poly(vinyl alcohol) (PVA, 87–89% hydrolyzed) was purchased from Sigma-Aldrich (USA). Iron chloride anhydrous (97.0%), dry methanol (99.5%), chloroform (99.9%) and tetrahydrofuran (THF) stabilized with 300 ppm of BHT-PRS (99.5%) were purchased from Panreac Quimica S.A.U. (Spain) and used as received, without further purification. TPU 12K85 of aromatic grade (ρ = 1.20 g/cm^3), which is a standard polyester-based TPU that combines hardness with excellent mechanical properties, was kindly supplied by *Merquinsa* (Spain).

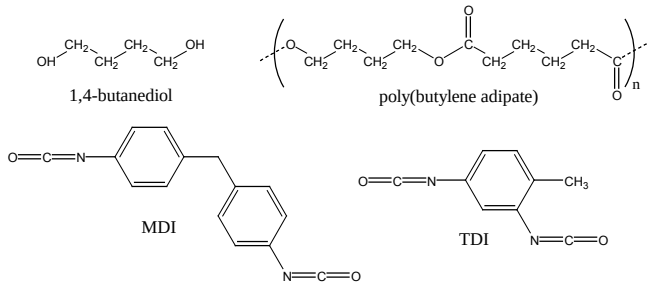

Scheme 5.2.1. Components of TPU (MDI = Methylene diphenyl diisocyanate; TDI = Toluene diisocyanate).

This material can be easily processed by cast film and blown film extrusions. The chemical structure of the components of the selected TPU is shown in Scheme 5.2.1., and corresponds to a copolymer sequence that involves two aromatic diisocyanates (MDI and TPI) and two aliphatic diols, specifically, 1,4-butanediol and a macrodiol based on poly(butylene adipate), which affords the degradable ester linkages. The melting range at which the melting flow index (MFI) equals 10 (10 g/10 min at 21.6 kg) is 155–165 °C.

5.2.2. Synthesis of Poly(3-thiophene methyl acetate)

Briefly, P3TMA can be prepared by chemical oxidative[11,33] and photochemical[34] polymerizations. In this work, we prepared P3TMA using 3TAA as the starting monomer and iron chloride ($FeCl_3$) as the oxidant and dopant. The polymerization process is summarized in Scheme 5.2.2., the details being described in the previous chapter (section 4.2.2). The purified 3TMA monomer was obtained with 74% of yield, while the yield of P3TMA was *ca.* 61% after removing the residual oxidant and oligomers.

5.2.3. Preparation of TPU:P3TMA FsNM

In order to obtain 5 mg/mL (0.5 wt.%) solutions, given amounts of neat TPU and P3TMA powder were separately dissolved in THF. P3TMA was sonicated for 10 minutes before (powder) and after its dissolution. After this, the solution was filtered with cotton as separation barrier. In contrast, TPU was dried at 120 °C under vacuum for 2 hours prior to its dissolution. The resulting TPU:P3TMA mixtures, which were prepared considering four different weight ratios (20:80, 40:60, 50:50, 60:40), were subsequently stirred at room temperature for 2 hours. The dispersions were then filtered and used for film deposition.

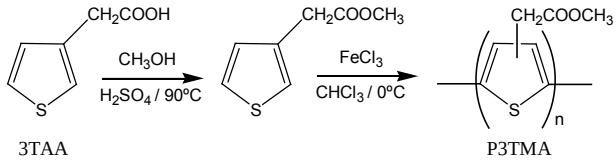

Scheme 5.2.2. Procedure used for the synthesis of P3TMA.

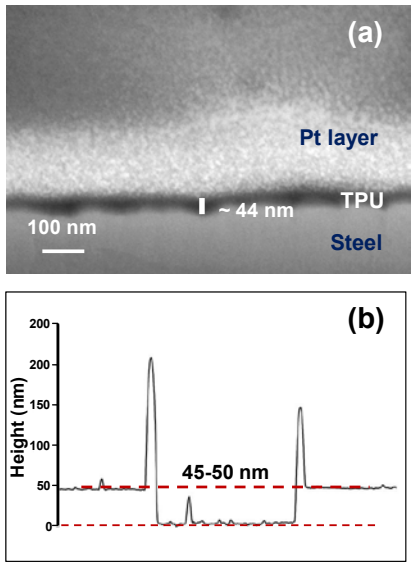

Figure 5.2.1. Thickness determination: (a) TPU nanomembrane (SEM); (b) TPU:P3TMA 40:60 (profilometer).

Supported nanomembranes of TPU, P3TMA and TPU:P3TMA were obtained by spin-coating at 4000 rpm for one minute, directly onto 0.5 × 1.0 cm^2 ITO substrates (40–60 Ω per square slide). Previous to the deposition, ITO substrates were cleaned in an ultrasonic bath using acetone, ethanol, de-ionized water, and isopropanol (5 minutes each), followed by acetone rinsing and drying under air flow.[35]

Free-standing TPU:P3TMA (40:60 and 60:40) ultrathin films were prepared by applying the procedure described by Kunitake and co-workers,[16] which was also used for P3TMA:PE44 FsNM. However, in this work the role of the sacrificial layer was played by poly(vinyl alcohol) (PVA) rather than by poly(4-hydroxystyrene) (PHS) since the latter is soluble in THF, which is the solvent used to prepare the TPU and P3TMA solutions. The process used to prepare the FsNM can be summarized in three stages. First, a PVA solution in water (2 wt. %) was spin-coated onto a glass slide (dimensions ranged from 2.5 × 2.5 to 2.0 × 6.0 cm^2) at 3000 rpm for 60 s. After this, the TPU:P3TMA solution in THF was spin-coated at speeds ranging from 1500 to 8000 rpm to obtain nanofilms with thicknesses varying between 15 and 100 nm. The spin-coating speed selected for this work was 4000 rpm for one minute, which resulted in films with suitable thickness and a uniform surface aspect when examined by optical microscopy. Sample thickness, which was determined by SEM (Figure 5.2.1a) and profilometry (Figure 5.2.1b), was about 40 –

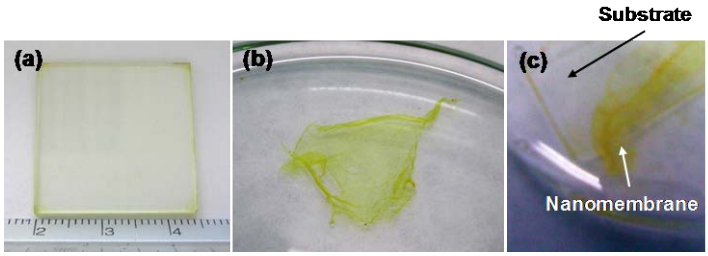

Figure 5.2.2. (a) TPU:P3TMA 60:40 nanomembrane deposited onto an ITO substrate. (b) TPU:P3TMA 60:40 nanomembrane released in water. (c) Releasing a TPU:P3TMA 40:60 nanomembrane from a glass substrate.

50 nm for films prepared at 4000 rpm. Finally, samples were immersed into water for the nanomembrane separation from the substrate (*i.e.* dissolution of the sacrificial layer). The edges of the specimens were cut to help penetration of water into the sacrificial layer. Supported and free-standing TPU:P3TMA nanomembranes are displayed in Figure 5.2.2. Manipulation of the free-standing nanomembranes revealed that the robustness of the membranes is higher for TPU:P3TMA than for P3TMA:PE44, which should be attributed to the combination of hard and soft segments in TPU.

5.3. Thermal, Nanostructural and Nanomechanical Properties

The first item investigated for this new system refers to the thermal properties of blends with different TPU:P3TMA weight ratios. After this, a comprehensive study based on atomic force microscopy (AFM) has been carried out to investigate the nanostructural (topography and morphology) and nanomechanical (Young's modulus (*E*) and adhesion energy) properties of the nanomembranes made of TPU:P3TMA 40:60, composition which showed the highest miscibility, and the two individual polymers. In order to make such exhaustive characterization possible, nanomembranes were supported on ITO substrates. Moreover, this AFM study has been complemented with a morphological investigation using scanning electron microscopy (SEM) and with a cellular proliferation study to compare the response of TPU:P3TMA and PE44:P3TMA against Cos-7 fibroblast cells, as a preliminary biocompatibility test. It should be mentioned that, although the peak force AFM method has been used to examine conventional polymers, this is the first application to ultrathin films made of conducting polymers.[36-40]

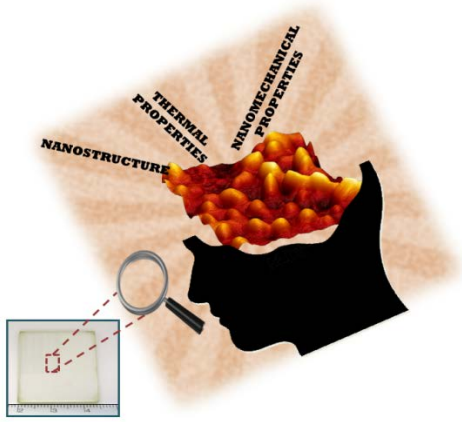

Graphical abstract

5.3.1. Experimental Section

FTIR Spectroscopy

IR absorption spectra were recorded on a FTIR Jasco 4100 spectrophotometer. Samples were placed in an attenuated total reflection accessory (Top-plate) with a diamond crystal (Specac model MKII Golden Gate Heated Single Reflection Diamond ATR). TPU and TPU:P3TMA films were solvent cast from the corresponding THF solutions, while P3TMA was analyzed as powder. For each sample 32 scans were performed between 4000 and 600 cm^{-1} with a resolution of 4 cm^{-1}.

Thermal analyses

The miscibility of the two components in TPU:P3TMA blends was studied by differential scanning calorimetry (DSC). Two different sets of samples were analyzed. First, films of TPU and TPU:P3TMA blends with 20:80, 40:60, 50:50 and 60:40 weight ratios were solvent cast from THF solutions onto Teflon® sheets, which were slowly dried under vacuum (48 h) at room temperature. The thickness of the resulting films, which were easily separated from the Teflon® sheets and cut into small pieces, was determined by profilometry as being around 3–4 mm. Second, FsNM of TPU and TPU:P3TMA with 40:60 weight ratio (around 20

nanomembranes for each species) were prepared by spin-coating, released in water, and dried under vacuum at room temperature for 48 h before being tested. These samples have been denoted as TPU-n and TPU:P3TMA 40:60-n, where the n refers to nanomembrane, so as to differentiate them from solvent cast thick films (bulk).

Calorimetric data were obtained with a TA Instruments Q100 series equipped with a refrigerated cooling system (RCS) operating at temperatures from -90 °C to 600 °C. Calorimetric results for P3TMA were reported in the previous chapter (section 4.3.2) and, therefore, have not been repeated in this secton. Experiments were conducted under a flow of dry nitrogen with a sample weight of approximately 3 mg, calibration being performed with indium. The T_{zero} calibration required two experiments: the first was done without samples, while the second one was performed with sapphire disks.

Samples were firstly heated up to 200 °C to erase the thermal history. Heating runs were performed at 20 °C/min with samples previously quenched from the melt state by cooling at the maximum rate allowed by the equipment. Determination of glass transition temperature (T_g) values from the calorimetric curves was carried out with the TA-Universal Analysis software furnished with the instrument.

For thermal degradation studies, TPU and TPU:P3TMA films were solvent cast from THF solutions onto Teflon® sheets and slowly dried under vacuum for 3 days. P3TMA was analyzed as powder. Thermal degradation was determined at heating rates of 5, 10, 20, 30, and 40 °C/min with around 5 mg samples in a Q50 thermogravimetric analyzer of TA Instruments under a flow of dry nitrogen and in the temperature range from 50 to 600 °C. Activation energies were determined by the Kissinger method[41] and the advanced isoconversional method provided by Kissinger−Akahira−Sunose (KAS).[41,42]

According to the non-isothermal kinetics theory, thermal degradation of a sample can be expressed by the following function:

$$\frac{d\alpha}{dt} = \frac{1}{\beta} A e^{\left(\frac{-E_a}{RT}\right)} f(\alpha) \qquad (5.3.1)$$

where β is the heating rate, T is the absolute temperature, R is the gas constant, $f(\alpha)$ is the differential conversion function, and A and E_a are the pre-exponential factor and the activation energy for the decomposition reaction step, respectively.

The Kissinger method gives the activation energy at the maximum of the derivative thermogravimetric curve (DTG) for each degradation step. The analysis is based on the following equation:

$$\ln\frac{\beta}{T_{max}^2} = \ln\frac{AR}{E} + \ln[n(1-\alpha_{max})^{n-1}] - \frac{E}{RT_{max}} \quad (5.3.2)$$

where T_{max} is the temperature at the maximum reaction rate, α_{max} is the conversion at this T_{max} temperature, n is the reaction order, and A is the frequency factor. From a plot of $\ln \beta/T_{max}^2$ versus $1/T_{max}$, the activation energy of the degradation step can be determined.

The activation energy during the whole degradation process can be calculated by the KAS method. This methodology is based on equation 5.3.2, which after reordering gives:

$$\ln\frac{\beta}{T^2} = \ln\left(\frac{AR}{g(\alpha)E_a}\right) - \frac{E_a}{RT} \quad (5.3.3)$$

where $g(\alpha)$ is the integral conversion function (*i.e.* $g(\alpha) = \int_0^\alpha \frac{d\alpha}{f(\alpha)}$).

For each degree of conversion and each step of the degradation process, the activation energy is obtained from the linear representation of $\ln \beta/T^2$ versus $1/T$.

Morphological and topographical characterization

The surface morphology and topography of TPU, P3TMA and TPU:P3TMA (40 : 60) nanomembranes supported onto ITO were studied by atomic force microscopy (AFM). Images were obtained with an AFM Dimension 3100 Microscope using a NanoScope IV controller. The AFM was operated in ambient conditions at a scan speed of 0.8–1 Hz, in tapping mode and using single-beam silicon cantilever probes with a nominal tip radius between 5 and 10 nm (T300 Vistaprobes, Phoenix, AZ). RMS roughness (R_q) and profile sections of the images were determined using the statistics application and tools of the NanoScope Analysis software version 1.20 (Bruker). The scan window sizes were 5 × 5 or 1 × 1 μm².

The AFM scratching technique was used to measure the thickness of the films. Specifically, contact mode AFM was used to intentionally scratch the film deposited on the ITO substrate. Thus, the force was set to completely remove the layer in a scratch area of 0.7 × 0.7 μm². After scratching, a topographic image was then obtained with tapping mode AFM and used to determine the film thickness from the depth of the scratch. It should be noted that such a topographic image was taken of a region bigger than the scratch area so as to accurately measure the step between the coated and the uncoated surfaces.

The surface morphology of TPU, P3TMA and TPU:P3TMA (40:60) supported nanomembranes was also carefully examined by SEM. Samples were mounted on a

double-side adhesive carbon disc and sputter-coated with a thin layer of carbon to prevent sample charging problems. Microscopy studies were carried out using a Focused Ion Beam Zeiss Neon40 scanning electron microscope equipped with an energy dispersive X-ray (EDX) spectroscopy system and operating at 5 kV.

Measurements of the electrical conductivity distribution over TPU:P3TMA (40:60) surface were performed with an AFM Dimension 3100 microscope equipped with an Extended TUNA unit and a NanoScope IV controller (Bruker) under ambient conditions. The cantilever used was a silicon rectangular lever coated with Pt–Ir (ANSCM-PC: f = 12 kHz and k_s = 0.2 N/m, Applied Nanostructures, Santa Clara, CA). During the measurements, a voltage difference was applied between the tip, which acted as the back electrode, and the ITO front electrode, while the current through the tip was measured. The ITO substrate was grounded during all the measurements.

Quantitative nanomechanical (QNM) characterization

QNM mapping of TPU, P3TMA and TPU:P3TMA (40:60) supported nanomembranes was performed using a Multimode 8 AFM in peak force tapping mode with ScanAsyst as feedback optimization technology (Bruker AXS Corporation, Santa Barbara, CA). Measurements were done under ambient conditions and cantilevers were carefully calibrated following the next procedure. First, the radius of the tip was experimentally evaluated by scanning a calibration grid with extremely sharp ridges (NioProbe, Aurora Nanodevices). Then, the obtained image was processed with SPIP software (Image Metrology, Denmark) in order to reconstruct the 3D shape of the tip apex. Afterwards, the Young's modulus of a reference sample (Bruker QNM toolkit) was experimentally obtained and compared with its nominal value. If the experimentally obtained Young's modulus value is ± 10% of the reference value, the calibration is considered as successful. Otherwise, the AFM probe is discarded. Finally, the spring constant was measured using the thermal noise method implemented in the Nanoscope 8.10 software (Bruker).

QNM allows quantitative nanomechanical mapping of the material properties, including mechanical modulus (Derjaguin-Muller-Toropov (DMT) contact mechanics model is applied) and adhesion forces, while simultaneously imaging the sample topography at high resolution. QNM imaging mode performs force curves at 2 kHz so as to provide the feedback loop with accurate topographic information, leading to applied vertical forces that can be in the pN range (depending on the chosen AFM probe).

The proper probe is chosen depending on the expected Young's modulus (*E*) value of the sample. However, as the real E value is unknown before testing the sample, the probe is tentatively selected, as every kind of probe can cover a fairly large range of E values. Thus, it is crucial to choose a probe that will be able to produce enough sample deformation but retain high force sensitivity. The E value for TPU is *ca.* 10 MPa, while that for P3TMA is of the order of several GPa.[43-45] As these values are separated by three orders of magnitude, supported nanomembranes were tested with three different probes. Their characteristics are displayed in Table 5.3.1. Furthermore, Table 5.3.1 lists the tip chosen for each sample and the assumed Poisson's ratio. The TAP525A probe was discarded because it was too stiff for all the samples, leading to deformations higher than 10 nm. Due to the same reason, the TPU nanomembrane could only admit the softest probe, SNL-10.

The peak-force set-point was adjusted to obtain a deformation of approximately 2 nm, which is the optimum deformation for the software to be able to fit the retraction region of the force curve with the DMT model, while remaining in the region of elastic deformation. The line scan rate was equal to 0.5–1.0 Hz. Image processing and data analysis were performed with the NanoScope software version 8.10, and NanoScope Analysis software version 1.20. QNM AFM measurements were performed several times using different samples, the results described in this work being reproducible.

Table 5.3.1. Probes tested in Peak Force QNM measurements.

Probe	Resonance Frequency (kHz)	Nominal Spring Constant (k_s, N/m)	Sample Modulus (*E*)	Supported nano-membrane	Poisson's ratio
TAP525A	448-468	200	1 GPa – 20 GPa	-	
RTESPA	255-374	20-80	200 MP – 2 GPa	P3TMA TPU:P3TMA (40:60)	0.4
SNL-10	50-80	0.35	0.7MPa - 20MPa	TPU	0.5

Cell proliferation tests

Cos-7 cells were cultured in DMEM high glucose supplemented with 10% FBS, penicillin (100 units/mL), and streptomycin (100 µg/mL). These carcinogenic cells were selected due to their fast growth. The cultures were maintained in a humidified incubator in an atmosphere of 5% CO_2 and 95% O_2 at 37 °C. Culture media were changed every two days. When the cells reached 80–90% confluence, they were detached using 1–2 mL of trypsin (0.25% trypsin/EDTA) for 5 min at 37 °C. Finally, cells were re-suspended in 5 mL of fresh medium, their concentration being determined by counting in a Neubauer camera using 0.4% trypan blue as a dye vital.

TPU, P3TMA and TPU:P3TMA 40:60 films of nanometric thickness were prepared and deposited onto steel AISI 316 sheets of 1 cm^2. These samples were placed in plates of 24 wells and sterilized using UV-light for 15 min in a laminar flux cabinet. Controls were simultaneously performed by culturing cells on the surface of the tissue culture polystyrene (TCPS) plates and steel plates. An aliquot of 50 µL containing 2×10^4 cells was deposited on the nanomembrane of each well. Then, cell attachment to the nanomembrane surface was promoted by incubating under culture conditions for 30 min. Finally, 500 µL of the culture medium were added to each well. After 24 h, non-attached cells were washed out. The quantification of proliferated cells was performed after 7 days of culture.

Cell proliferation was evaluated by the colorimetric MTT assay.[46] This assay measures the ability of the mitochondrial dehydrogenase enzyme of viable cells to cleave the tetrazolium rings of MTT and form formazan crystals, which are impermeable to cell membranes and, therefore, are accumulated in healthy cells. This process is detected by a color change: the characteristic pale yellow of MTT transforms into the dark-blue of formazan crystals. Specifically, 50 µL of MTT solution (5 mg/mL in PBS) were added to each well. After 3 h of incubation, the samples were washed twice with PBS and stored in clean wells. In order to dissolve formazan crystals, 1 mL of DMSO/methanol/water (70/20/10% v/v) was added. Finally, the absorbance at 540 mm was measured after using an UV-vis spectrophotometer (UV-3600, Shimadzu). The resulting viability results were normalized to TCPS control as relative percentages. Results were derived from the average of four replicates (n = 4) for each independent experiment. ANOVA and Tukey tests were performed to determine the statistical significance, which was considered at a confidence level of 95% ($p < 0.05$).

5.3.2. Results and Discussion

FTIR spectroscopy

Before assessing the thermal properties associated to the TPU:P3TMA system, a more general characterization was conducted. Concretely, it included the assessment of the chemical structure of the 20:80, 40:60, and 60:40 TPU:P3TMA samples. Figure 5.3.1 shows the FTIR spectra of P3TMA, TPU, and TPU:P3TMA blends in the range from 1800 to 900 cm^{-1}. Results evidence the formation of TPU:P3TMA blends by the overlapping of absorption bands coming from the two individual polymers, TPU and P3TMA. The bands observed for the P3TMA are fully consistent with those reported in our previous work,[26] and, therefore, their description has been omitted. As it is reported in Table 5.3.2, the presence of P3TMA in the blends is confirmed by the $-CH_3$ bending absorption at 1431 cm^{-1} (peak a in Figure 5.3.1) and the changes and shifts occurring at region e. Moreover, another band arising from the P3TMA contribution is observed between 1008 and 1017 cm^{-1} for the three composition blends (peak h).

The rest of peaks marked (from b to g) correspond to TPU groups present in the blends. First, the hydrogen bonded C=O stretching band coming from urethane carbonyl groups appears as a small shoulder in the blends spectra at 1701 cm^{-1} (peak b) in the C=O stretching band associated with the soft segment ester groups (1719 cm^{-1}, amide I region). Second, transmittance peaks observed at 1595 cm^{-1} (peak c) and 1526 cm^{-1} (peak d) are consistent with the TPU C=C stretching of the phenyl ring and the C—N stretching + N—H bending (amide II band), respectively. Other bands arising from TPU hard-segment groups (C—N stretching, amide III region) are identified at 1215 cm^{-1} (strong absorption) and 1308 cm^{-1} (weaker absorption). However, those bands are clearly detected only for 60:40 and 40:60 TPU:P3TMA compositions. Finally, the absorption bands seen in the blends at 1166 and 1138 cm^{-1} (peaks f) are attributed to the C—O—C stretching of TPU soft segments, while the peak observed at 1061 cm^{-1} (peak g) correspond to the C—O—C stretching of both TPU soft and hard segments. Overall, the position and intensity of the absorption bands in TPU:P3TMA blends spectra are in good agreement with their composition.

Table 5.3.2. Main infrared absorption bands (cm^{-1}) of TPU, P3TMA, 20:80, 40:60 and 60:40 TPU:P3TMA blends (labels are identified in Figure 5.3.1).

Absorption bands		**P3TMA**	**TPU:P3TMA**			**TPU**
			20:80	40:60	60:40	
CH_3 bending	*a*	1431	1430	1433	1435	
C=O ester	*b*	1730	1726	1723 1704	1723 1703	1724 1704
C=C Stretching phenyl ring (HS)	*c*		1593	1595	1595	1595
N–H bending C–N stretching	*d*		1526	1527	1527	1526
C–N stretching	*e*		1319[a)]	1308 1215	1308 1215	1308 1215
C–O–C stretching	*f,g*		1164 1067	1166 1138 1067	1168 1142 1067	1166[b)] 1138 1062

[a)] Shifted by conjugated diene C=C (1325 cm^{-1}). [b)] Band overlapped with C-O-C groups from P3TMA.

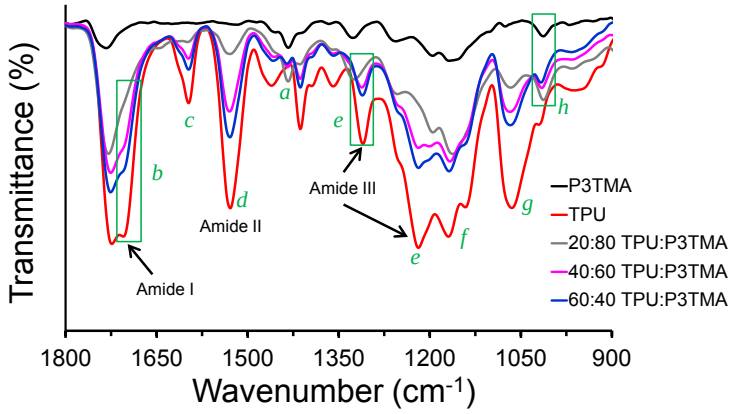

Figure 5.3.1. FTIR spectrum of P3TMA, TPU and (20:80, 40:60 and 60:40) TPU:P3TMA blends in the range 1800–900 cm^{-1}. Absorption bands are described in Table 5.3.2. Changes in the peaks marked with labels *a-h* (in green) have been used to identify the formation of blends.

Thermal analyses

DSC measurements were performed to characterize the thermal behavior of TPU and P3TMA as well as to determine their miscibility in the prepared TPU:P3TMA blends. Results obtained from DSC are shown in Figure 5.3.2. Figure 5.3.2a displays the heat flow for TPU films cast onto Teflon® and P3TMA powder, as the film forming properties of individual P3TMA are very limited. The glass transition temperature of P3TMA was assessed at T_g = 62.11 °C.[25] DSC heating runs of TPU allowed us to identify the glass transition temperature at T_g = -10.52 °C, which was attributed to the motion of the soft-segment domains. Furthermore, the crystallization of the hard-segment domains appeared at T_c=60.75 °C (ΔH_c =3.18 J/g), their corresponding melting peak being detected at T_f = 124.01 °C (ΔH_f =5.29 J/g). Although crystallization and melting peaks are weak, it should be mentioned that the difference between the enthalpies of crystallization and melting peaks indicates that a small TPU fraction crystallizes during the cooling. This feature suggests an underestimation of the TPU glass transition temperature because some crystallized rigid blocks were not present in the amorphous phase.

The miscibility of TPU and P3TMA in the TPU:P3TMA blends can be evaluated in terms of T_g (Table 5.3.3.). Figure 5.3.2b presents the DSC heating curves for the

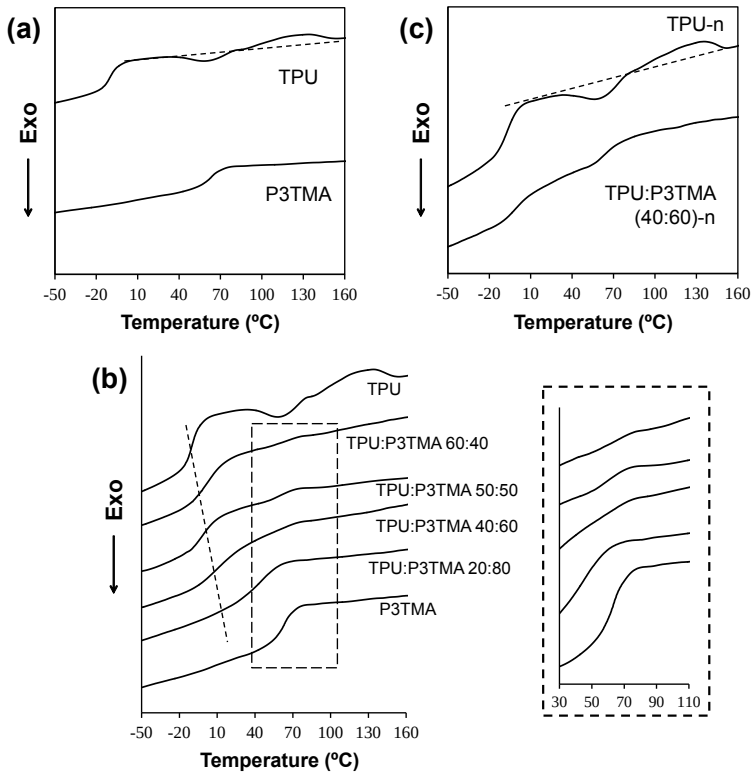

Figure 5.3.2. DSC heating traces of: (a) TPU solvent cast film and P3TMA powder; (b) TPU:P3TMA solvent cast films; and (c) TPU and TPU:P3TMA (40:60) spin-coated nanomembranes. In (b) the dashed lines and the box (magnification displayed in the right) show the glass transition temperatures associated with the TPU and the P3TMA domains.

solvent cast TPU:P3TMA films with 60:40, 50:50, 40:60 and 20:80 weight ratios. DSC scans show two different T_g values, which are attributed to the TPU soft-segment domains and to P3TMA. Furthermore, such T_g values depend on the composition, indicating a partial miscibility of TPU and P3TMA. The T_g value associated with TPU increases with the concentration of P3TMA, suggesting that the presence of P3TMA in the TPU phase reduces the mobility of the soft-segment domains. Besides, the T_g value related to P3TMA decreases with the content of P3TMA. However, the shifts in the T_g values are relatively small indicating a low partial miscibility between TPU and P3TMA. An exception to this behavior was found for the blend with a 20:80 weight ratio, in which the T_g value attributed to P3TMA was the only one detected because of the low TPU content in the blend.

Table 5.3.3. Calorimetric data of TPU, P3TMA and TPU:P3TMA blends.

Sample	$T_{g,1}$ (°C)	$T_{g,2}$ (°C)	w_1[a]	w_2[b]	T_c (°C)	ΔH_c (J/g)	T_f (°C)	ΔH_f (J/g)
TPU	-10.5	-	1	0	60.7	3.2	124.0	5.3
TPU-n [c]	-7.1	-	1	0	60.1	3.0	131.3	3.7
TPU:P3TMA 60:40	-0.9	56.5	0.84 (0.89)	0.94 (0.93)				
TPU:P3TMA 50:50	-1.1	56.3	0.84 (0.89)	0.94 (0.93)				
TPU:P3TMA 40:60	10.4	46.5	0.66 (0.70)	0.82 (0.81)				
TPU:P3TMA 40:60-n [c]	-1.5	60.5	0.85 (0.90)	0.98 (0.98)				
TPU:P3TMA 20:80	-	46.9	-	0.83 (0.82)				
P3TMA	-	62.1	0	1				

[a] TPU weight fraction in the TPU phase. Values outside and inside the parenthesis were obtained using the T_g values of TPU and TPU-n, respectively. [b] P3TMA weight fraction in the P3TMA phase. Values outside and inside the parenthesis were obtained using the T_g values of TPU and TPU-n, respectively. [c] TPU-n and TPU:P3TMA 40:60-n refer to samples derived from self-standing nanomembranes.

The weight percentage of each polymer in its corresponding phase was determined using:

$$\frac{1}{T_g} = \frac{w_1}{T_{g,1}} + \frac{w_2}{T_{g,2}} \tag{5.3.4}$$

where $T_{g,1}$ and $T_{g,2}$ correspond to the T_g of each of the two individual components (*i.e.* -10.52 °C and 62.11 °C for TPU and P3TMA, respectively), and w_1 and w_2 are the weight fractions in the studied phase.

In contrast, the crystallization and fusion processes of TPU are also affected by the presence of P3TMA since they do not appear in the heating scans. It seems that P3TMA molecules suppress the crystallization of the hard-segment domains of

TPU, providing additional evidence of the partial miscibility between the two materials.

In order to truly correlate the phase separation observed by both DSC and AFM (see next section), DSC heating runs were also performed with TPU and TPU:P3TMA 40:60 FsNM, these samples being denoted as TPU-n and TPU:P3TMA 40:60-n, respectively, in Table 5.3.3. The resulting heating scans, which are displayed in Figure 5.3.2c, indicate that TPU-n follows the same behavior as that of TPU as a bulk, even though the T_g value was slightly higher for the former (-7.14 °C). In contrast, TPU:P3TMA 40:60-n showed T_g values for TPU and P3TMA that were lower and higher, respectively, than those determined for the bulk TPU:P3TMA 40:60 blend. This result reflects a low degree of miscibility in TPU:P3TMA 40:60 nanomembranes, a fact that was corroborated by the existence of two phases in AFM images (see next section). According to these observations, the miscibility of TPU and P3TMA is better in thick films prepared by solvent evaporation than in ultra-thin films prepared by spin-coating. In any case, it should be noted that heating scans of TPU and TPU-n samples are significantly different when crystallization and melting peaks are compared. Thus, the nanomembrane was practically amorphous as the close values of the melting and crystallization enthalpies reflect (*i.e.* all hard blocks of TPU-n were located in the amorphous phase, which results in a higher T_g). As previously indicated, all blends are completely amorphous and consequently the composition of TPU and P3TMA phases was also calculated taking into account the new T_g value (Table 5.3.3).

Overall, all studied samples are amorphous with the exception of pure TPU, which exhibits a relatively low melting temperature in the 124−131 °C range depending on the processing conditions (*e.g.* solvent casting and spin coating). According to possible applications, it seems also highly interesting to evaluate their thermal stability and the thermal degradation processes.

Thermogravimetric scans (Figure 5.3.3) show that all P3TMA-containing samples started to decompose at a relatively low temperature (*ca.* 140 °C), 10% degradation requiring a temperature higher than 280 °C *(i.e.* far away from the melting temperature). Decomposition of blends was characterized by two main degradation steps as shown in the derivative thermogravimetric (DTG) curves (Figure 5.3.4a) for the 50:50 TPU:P3TMA representative sample. These steps are related with a low temperature degradation process, most probably due to the initiation of the P3TMA degradation, and a high temperature degradation process that could be associated mainly with decomposition of TPU.

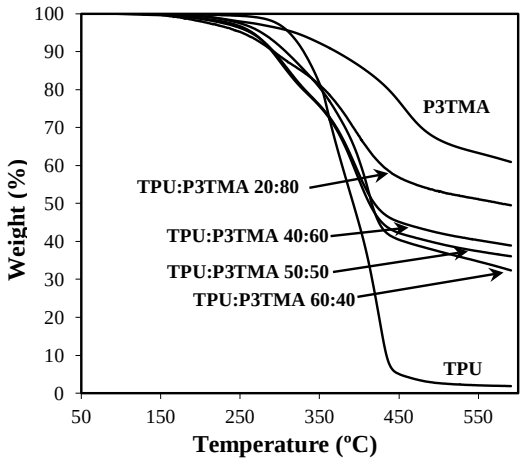

Figure 5.3.3. Thermogravimetric curves obtained at a heating rate of 20 ºC/min for the TPU:P3TMA blends and the two homopolymers.

The DTG curves of TPU and P3TMA samples (Figure 5.3.4a) reveal highly complex degradation processes with at least three steps. The main decomposition process occurred at the highest temperature for both polymers (*i.e.* 430 and 460 °C for TPU and P3TMA, respectively) and involved practically a 50% of the relative weight loss and gave rise to well-defined DTG peaks. Despite the complex decomposition process of TPU, its activation energy remained practically constant (*ca.* 124 kJ/mol) during degradation, as was revealed by the KAS isoconversional analysis (Figure 5.3.4b). On the contrary, a high variation was detected for P3TMA (*i.e.* from 65 to 298 kJ/mol; Figure 5.3.4b) as expected for well-differentiated degradation mechanisms.

Kissinger analysis became useful to discern the degradation processes of the polymer blends, although it can be considered a rough approximation since it is not a rigorous isoconversional method. As shown in Figure 5.3.4c, activation energies of 104 and 142 kJ/mol were obtained for the two degradation steps detected for the 50:50 TPU:P3TMA sample. The first step occurs, as explained before, at the temperature range where decomposition of P3TMA starts and the associated energy is in agreement with the low values determined for P3TMA at low conversions. The activation energy deduced from the second DTG peak of the blend (*i.e.* 142 kJ/mol) is in full agreement with the energy derived from the main peak of TPU (137 kJ/mol) and clearly deviates from the higher value (161 kJ/mol) obtained for

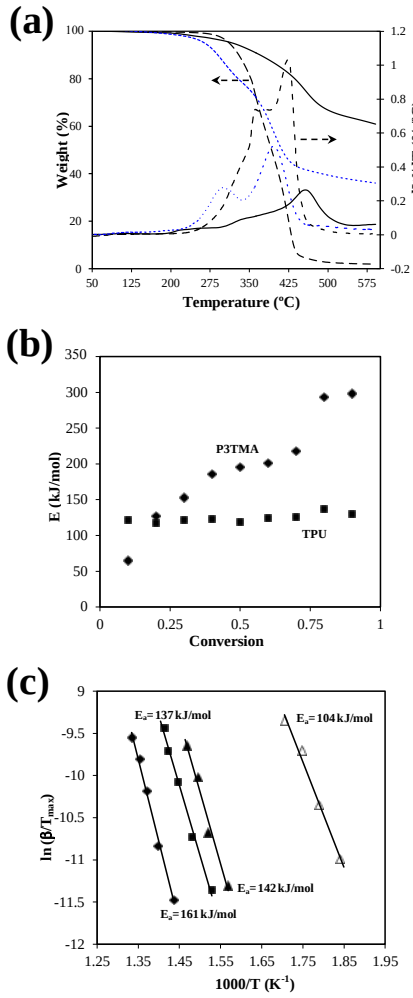

Figure 5.3.4. (a) Thermogravimetric and derivative thermogravimetric curves corresponding to the thermal decomposition of TPU (black and dashed lines), P3TMA (black and solid lines), and 50:50 TPU:P3TMA (blue and dotted lines). (b) Plots of the activation energy calculated by the KAS method as a function of the conversion degree for TPU (■) and P3TMA (◆) homopolymers. (c) Kissinger plots for the main decomposition step of the TPU (■) and P3TMA (◆) homopolymers, and the two degradation steps of the 50:50 TPU:P3TMA blend (▲, Δ). Full and empty symbols correspond to the peaks appearing at the higher and lower temperature, respectively.

P3TMA. In addition, it is also clear that thermal degradation of the blend is practically finished at a temperature lower than that associated with the main decomposition step of P3TMA (Figure 5.3.4a). In summary, thermal degradation of the blends is determined by the low energy processes associated with each individual polymer, namely, P3TMA at the beginning and TPU at the end.

Surface morphology and topography

AFM images of P3TMA, TPU, and 20:80, 40:60 and 60:40 TPU:P3TMA supported nanomembranes onto ITO and prepared by spin-coating are displayed in Figure 5.3.5. We examined the influence of the composition on the morphology and topography of the samples surface. As it can be seen, the characteristics of the 40:60 and 60:40 TPU:P3TMA samples consist of irregular distributions of relatively prominent and well-defined folds, the RMS roughness being very similar for the two compositions (*i.e.* 20 and 19 nm for 60:40 and 40:60 TPU:P3TMA, respectively). Therefore, both compositions are found in an intermediate position between TPU and P3TMA since the morphology of TPU consists of a smooth surface with multiple and well-localized folds homogeneously distributed (RMS roughness of only 6 nm), whereas the surface of P3TMA is significantly more irregular (RMS roughness of 28 nm). Finally, the irregular surface of 20:80 TPU:P3TMA is more similar to that of P3TMA, even though the RMS roughness (12 nm) is closer to that of TPU.

Table 5.3.4. Roughness and thickness of TPU, P3TMA and TPU:P3TMA 40:60 nanomembranes supported on ITO substrates.

	RMS Roughness (nm)		**Thickness (nm)**
	Mean	**Std. Dev.**	**Interval determined by AFM scratch**
TPU	16.3	0.8	11.4 – 70.7
P3TMA	47.0	4.9	26.2 – 141.6
TPU:P3TMA 40:60	17.4	2.2	10.8 – 92.8

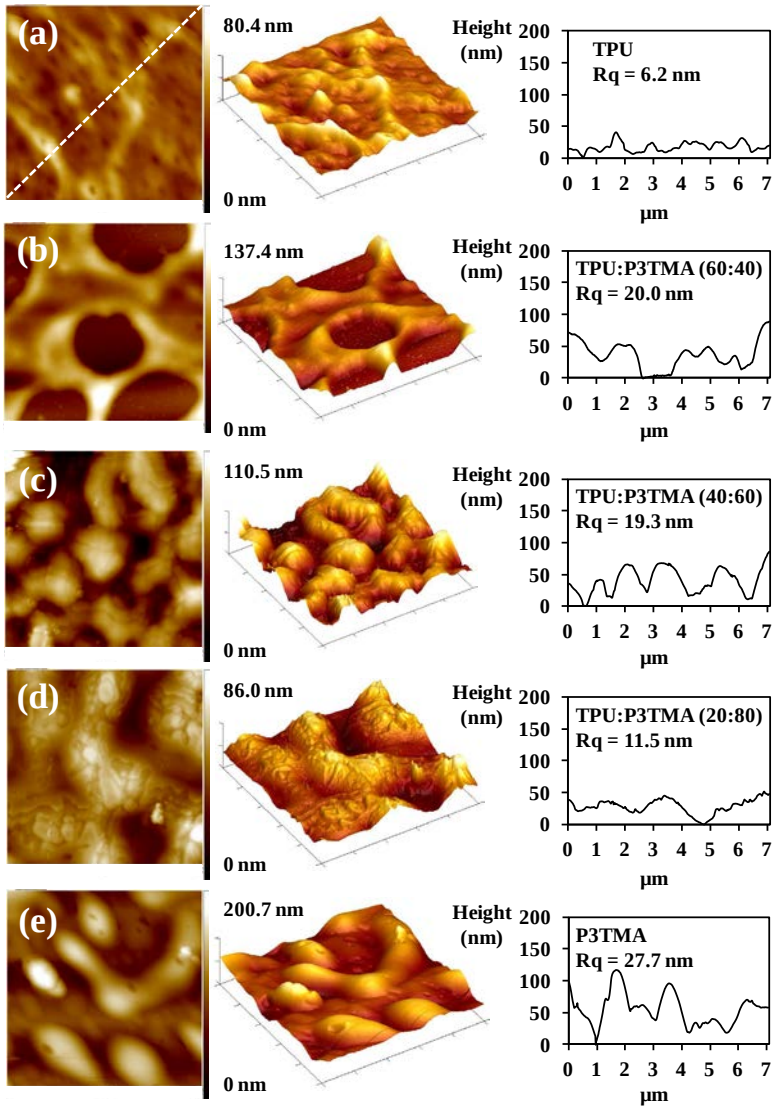

Figure 5.3.5. AFM topographic images of the ITO-supported nanomembranes: (a) TPU, (b) 60:40 TPU:P3TMA, (c) 40:60 TPU:P3TMA, (d) 20:80 TPU:P3TMA, and (e) P3TMA. 2D height images (left column), 3D height images (middle column) and cross-section profiles (right column) from the diagonal line for each sample as depicted in (a). RMS R_q values are also provided. In all cases the image window is 5.0 × 5.0 µm².

A closer inspection of topographical parameters has been performed for TPU, P3TMA and TPU:P3TMA 40:60 films supported on ITO. Hence, the surface parameters of the three investigated systems are summarized in Table 5.3.4., whereas AFM images are displayed in Figures 5.3.6– 5.3.10. The morphology of TPU nanomembranes (Figure 5.3.6a) can be described as a smooth surface with multiple, relatively prominent and well-localized folds homogeneously distributed onto it. The folds on the surface of these ultra-thin films have been attributed to artifacts produced during the spin-coating process. This hypothesis is supported by the lack of contrast in the phase image, which indicates that the TPU film entirely covers the ITO substrate, and by the fact that the contrast in the height images is the same for all the positions of the folds. The thickness determined by AFM scratching tests using the tip in contact mode, ranges from 11 to 71 nm. Figure 5.3.6a includes a topography image with the corresponding cross-sectional profiles. The height of the folds varies between ~20 and ~55 nm, while the mean RMS roughness of the whole film, which was measured considering several 5 × 5 μm^2 windows, is 16.3 ± 0.8 nm.

The surface of P3TMA films (Figure 5.3.6b) is significantly more irregular than that displayed by TPU. Thus, continuous and well-defined granules (islands) and "*ridges*" emerging from flat regions ("*valleys*") are detected. The diameter and height of the granules range from 314 to 490 nm and from 59 to 73 nm, respectively, while the height of the ridges varies between 123 and 146 nm. The low contrast observed in the phase image indicates that all the ITO substrate is completely covered by the polymer. The RMS roughness of P3TMA (47.0 ± 4.9 nm) is about three-folds higher than that of TPU, whereas the thickness ranges from 26 to 142 nm.

AFM topographic images of TPU:P3TMA 40:60 nanomembranes are displayed in Figure 5.3.7. As it can be seen, the surface of this blend can be described as the combination of the topographies of its individual components. Thus, it consists of a homogeneous distribution of granules that are smaller than those found for P3TMA, with diameters and heights ranging from 90 to 205 nm and from 12 to 40 nm, respectively. The RMS roughness was found to be 17.4 ± 2.2 nm, while the thickness ranged from 11 to 93 nm (Table 5.3.4). Moreover, the blend shows folds that are similar to those found for individual TPU samples. Inspection of the phase images allows us to distinguish between the two phases in the blend. The bright areas in Figure 5.3.7b correspond to the granules, which are associated with the P3TMA-rich phase (*i.e.* P3TMA with some dissolved TPU), whereas the dark areas represent the TPU-rich phase (*i.e*. TPU with some dissolved P3TMA).

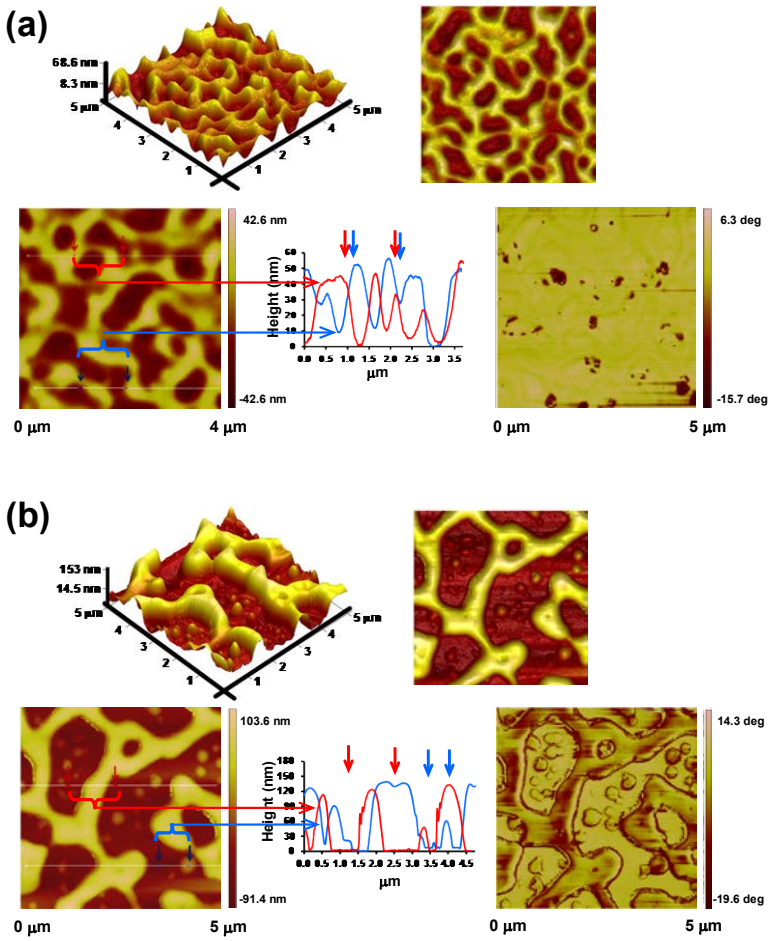

Figure 5.3.6. AFM micrographs (3D and 2D topography, height and phase images) of ultra-thin films of (a) TPU and (b) P3TMA supported on ITO. Illustrative cross-sectional profiles of the topography images are displayed.

The combination of composition and topographic information provided by the phase and the height images, respectively, indicates that the blend consists of a dispersion of granules essentially made up of P3TMA in a film mainly made of TPU, even though a small fraction of the second component is contained in each of such elements. In contrast, it should be mentioned that some TPU:P3TMA 40:60 nanomembranes did not present folds at the surface (an example is provided in Figure 5.3.10). However, the morphology of these ultra-thin films was very similar to that displayed in Figure 5.3.7, their RMS roughness being 15.6 ± 1.2 nm.

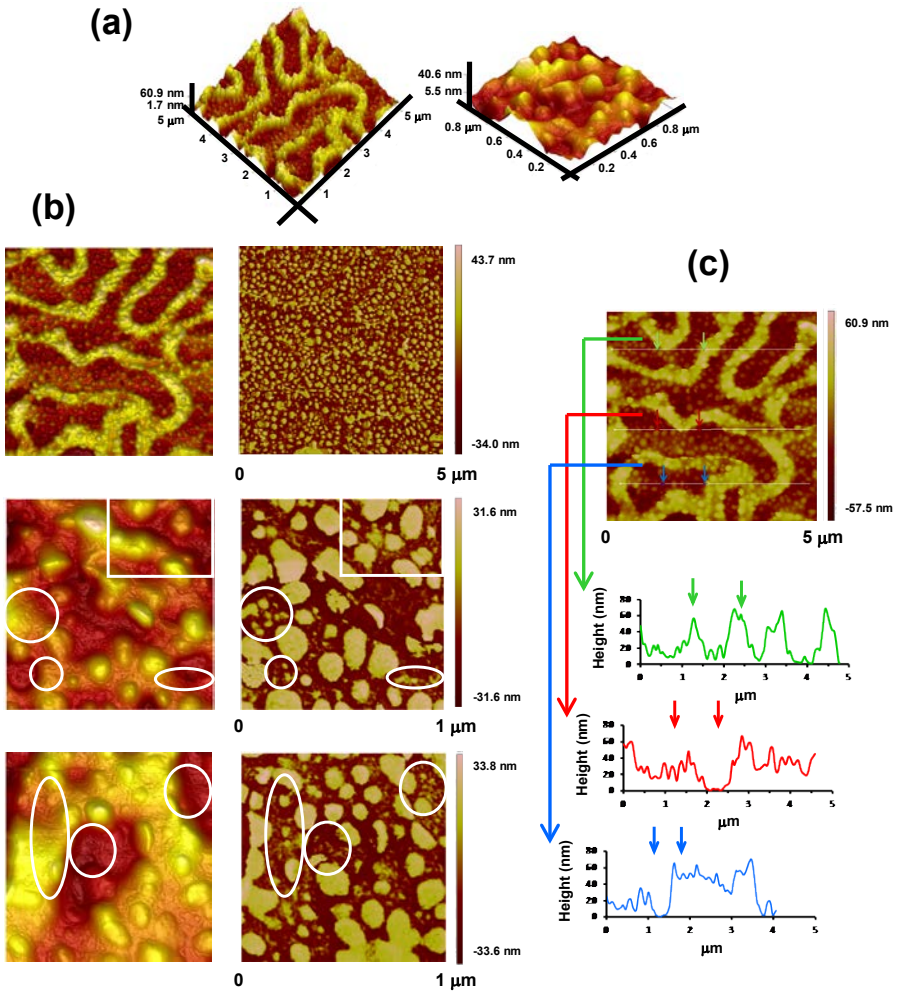

Figure 5.3.7. AFM micrographs of TPU:P3TMA 40:60 nanomembranes: (a) 3D height images; (b) 3D height (left) and phase (right) images; and (c) cross-sectional profiles.

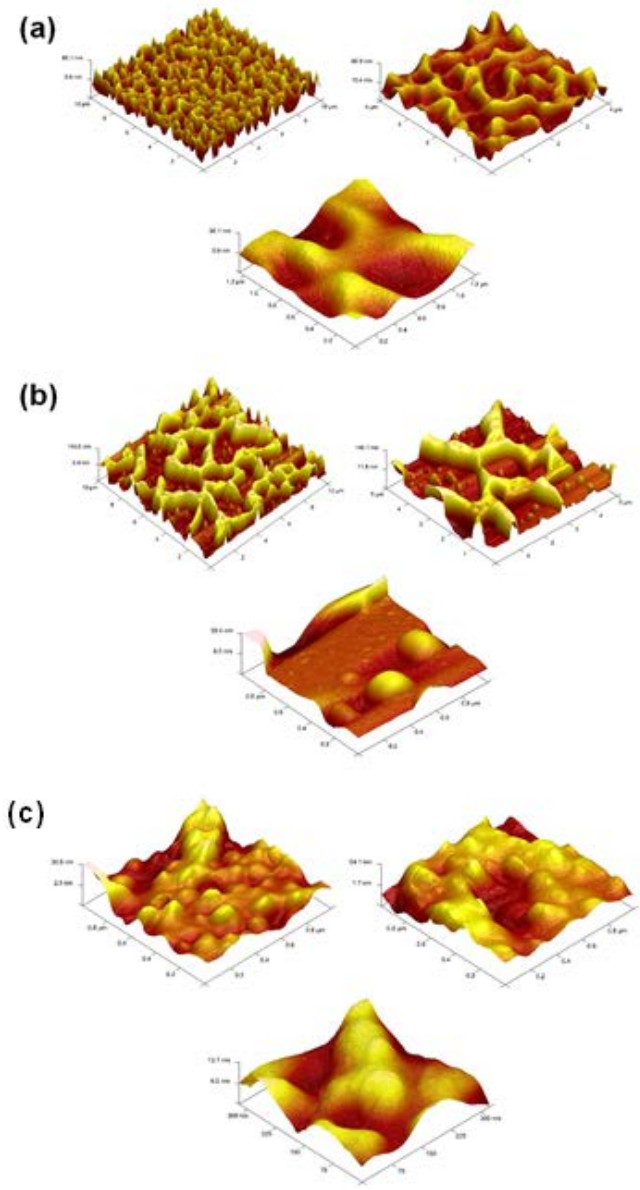

Figure 5.3.8. 3D AFM micrographs of ultra-thin films of (a) TPU, (b) P3TMA and TPU:P3TMA 40:60 supported on ITO.

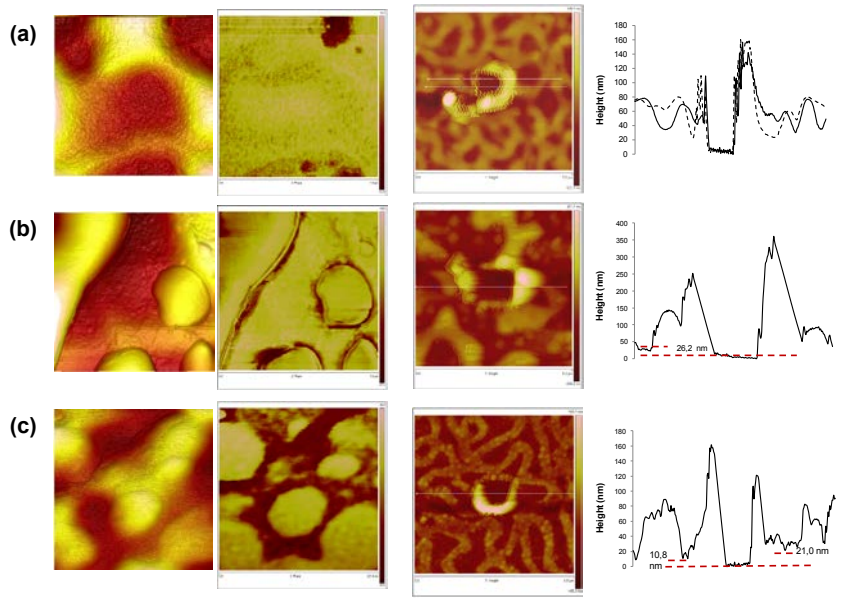

Figure 5.3.9. Height (left) and phase (middle) AFM images of ultra-thin films of (a) TPU, (b) P3TMA and (c) TPU:P3TMA 40:60 supported on ITO. On the right, AFM micrographs of supported ultra-thin film scratches with their cross-sectional profile to determine the ultra-thin film thickness.

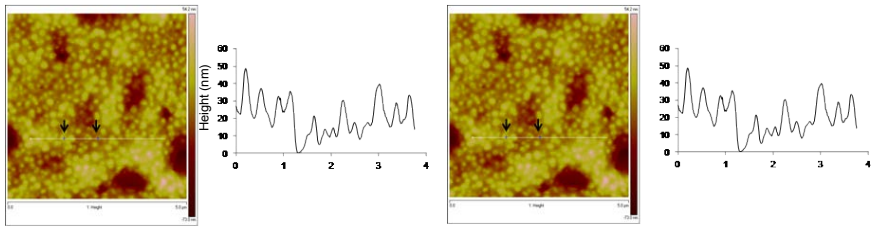

Figure 5.3.10. AFM micrographs of TPU:P3TMA 40:60 without folds. Scanning area: 5.0 μm x 5.0 μm (left) and 1.5 μm x 1.5 μm (right).

C-AFM measurements were carried out to corroborate both the distribution of phases in the TPU:P3TMA 40:60 films and the co-existence of the two components in the observed folds. Figure 5.3.11 reveals that the application of a voltage between the AFM tip and the ITO substrate provokes a current response in the P3TMA domains (*i.e.* the granules). Nevertheless, the response of the granules was not uniform, as it is evidenced by the fact that some granules appear in the topographic image but not in the current image (Figure 5.3.11: left and right, respectively). This indicates that, in some cases, the P3TMA path between the tip and the ITO substrate is interrupted by insulating TPU.

SEM images, which are displayed in Figure 5.3.12, are fully consistent with AFM observations. TPU exhibits a very smooth surface with no distinctive features (Figure 5.3.12a). As expected, TPU nano-folds detected by AFM were not observed in SEM micrographs because of their bidimensionality and resolution. The morphology of P3TMA (Figure 5.3.12b–d) can be described as a relatively smooth surface dotted by a homogeneous and dense distribution of round-like pits (or craters). The diameters of such craters range from 140 to 520 nm. This particular morphology is attributed to the combination of two well-known characteristics of individual P3TMA:[25] its poor film-forming properties and its tendency to form spherical aggregates of medium size. Thus, the abundant and well-defined particles formed by such aggregates detach from the polymer surface during the preparation of the film. Finally, TPU:P3TMA 40:60 (Figure 5.3.12e–h) shows a granular (island) morphology in which pseudo-spherical granules with diameters ranging from 85 to 180 nm are homogeneously distributed through the whole surface.

The formation of films by mixing solutions of two individual polymers in a common solvent can be described as a process with a ternary phase diagram of the polymer blend and the solvent.[47] Initially, the two polymers are solubilized by the solvent and the blend is in the intermixed or one-phase region of the phase diagram. As the evaporation of the solvent proceeds during the spin-coating process, the solution concentration increases rapidly, leading to a metastable or unstable state and inducing phase separation. This phase separation process was found to be sensitive to different parameters: the polymer blend ratio, the solubility of the individual polymers in the common solvent, the polymer–polymer interaction parameters, and the speed of the spin-coating process.[48-55] However, typical models used to explain the phase separation in the bulk or in thin films are probably not valid for the conditions used in the present study. This is because the thickness of the films prepared in this study is extremely small (40–50 nm) and, therefore, the substrate–film and film–air interfaces are expected to play a crucial role in the phase

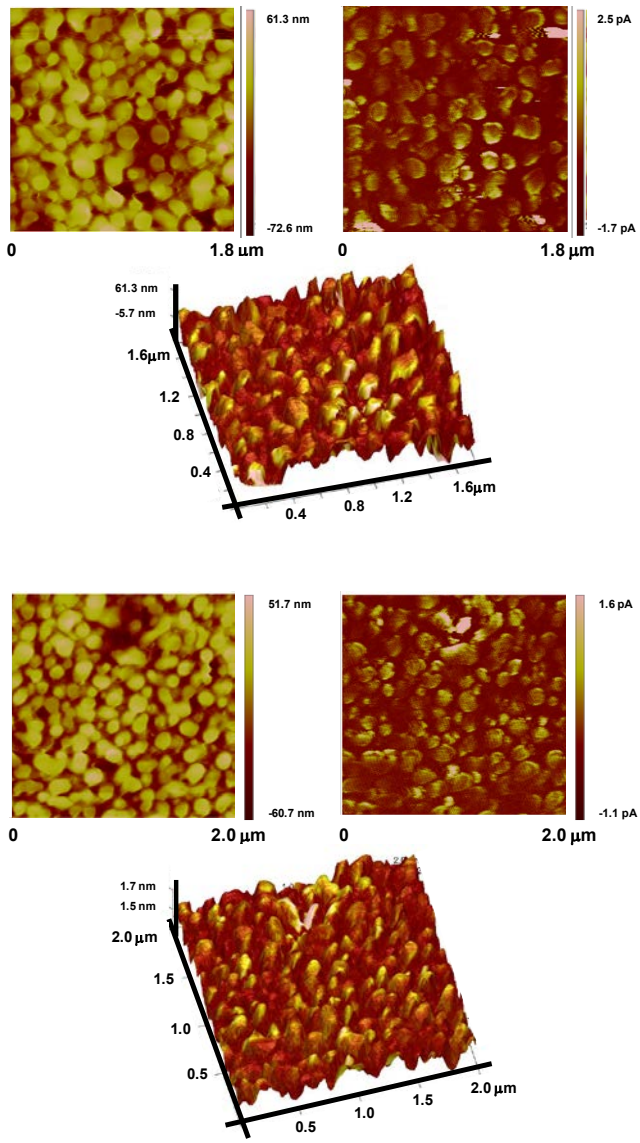

Figure 5.3.11. C-AFM micrographs of TPU:P3TMA 40:60 nanomembranes. The 2D topography height and current channel images are shown to the left and right, respectively, while the 3D corresponds to the superposition of both images.

separation. Thus, these interfaces may break the symmetry, imposing a direction to the phase separation process (*i.e.* the formation of wetting and capping layers in competition with bulk phase separation can lead to a vertical phase separation of the film).[56] A simultaneous vertical and lateral phase separation was recently observed in blends formed by mixing two polyfluorenes.[57] This behavior is analogous to that found in the present work for TPU:P3TMA 40:60, and it is attributed to the coexistence of the following two factors: (i) the actions of substrate–film and film–air interfaces, which provoke the vertical phase separation; and (ii) the spin-coating process, which is responsible for the lateral phase separation. Figure 5.3.13 schematizes the phase separation found in TPU:P3TMA 40:60 spin-coated ultra-thin films, illustrating the coexistence of vertical and lateral phase separation.

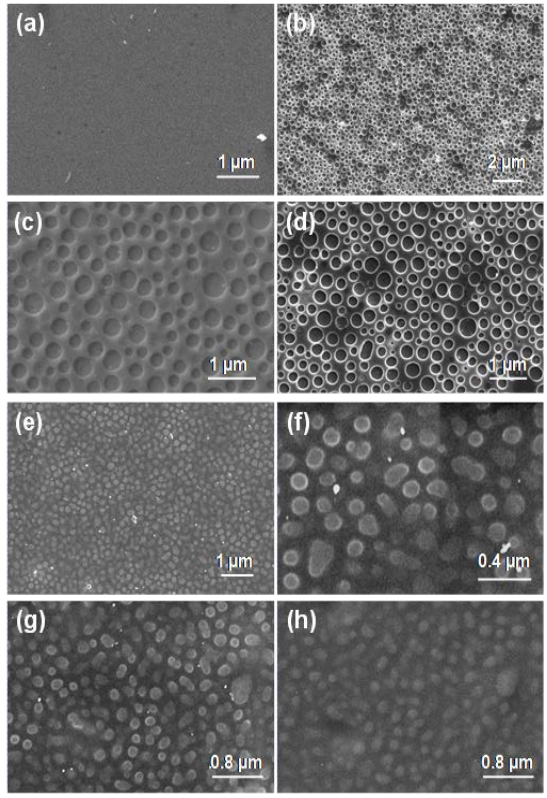

Figure 5.3.12. SEM micrographs of (a) TPU; (b–d) P3TMA; and (e–h) TPU:P3TMA 40:60 nanomembranes.

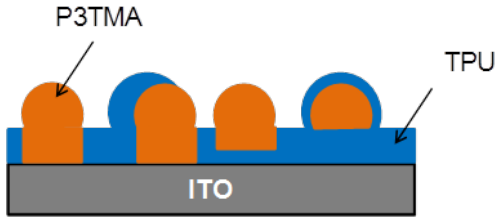

Figure 5.3.13. Scheme showing the cross-sectional view of the TPU:P3TMA 40:60 ultra-thin films obtained by spin-coating.

Nanomechanical properties

QNM mode was used to investigate the nanomechanical properties of the films in the elastic deformation regime and to qualitatively map the different phases found in the blends. The main advance of QNM mode is that it allows the simultaneous imaging and mechanical mapping of the sample. The E value (applying DMT model) and the adhesion force, which are both represented as maps, are obtained from the force–distance curves recorded in each pixel. The procedure is schematically indicated in the Figure 5.3.14. It should be noted that the DMT model, which is a modified Hertz model where adhesion between the probe and the sample surface is taken into account, is only appropriated for weak adhesive forces and tips with a small curvature radius.[58] In Figure 5.3.14, the green and dotted-red profiles (trace and retrace, respectively) represent the tip approaching process and the tip withdrawal, respectively. Part of the retrace curve (purple) is used to calculate the Derjaguin-Muller-Toropov (DMT) elastic modulus. The minimum force in the retrace curve is used for mapping the adhesion properties. (1) Little or no force on the tip. As the piezo expands and the separation decreases, the tip is pull down (2) by attractive forces (*i.e.* van der Waals, capillarity, electrostatic…) until it arrives to the surface (separation = 0). The tip is pushed into the sample until the peak force set point is reached (3). The tip is pulled up by the piezo and the force on the tip decreases to a minimum value (4), and the tip comes off the surface. Finally, forces on the tip decreases as the separation increases (5) and the piezo returns to its initial position.

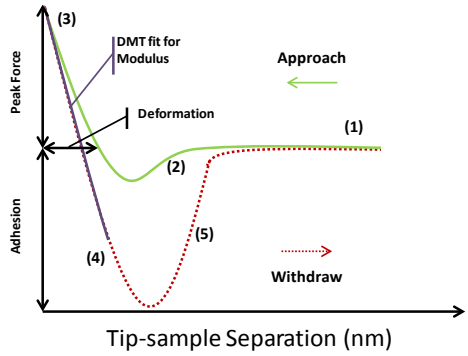

Figure 5.3.14. Force-separation curve obtained during the PeakForce AFM tip tapping.

Spin-coated TPU films were examined using a soft cantilever (*i.e.* its nominal spring constant, k_s, was 0.35 N/m), with the set point adjusted to get a sample deformation of ~2 nm. In spite of this, accurate control was not possible because of the heterogeneity of the sample thickness. Thus, the true deformation ranged from values lower than 2 nm in the thinner regions (*i.e.* thickness of 10–30 nm) to values higher than 2 nm in the creases (*i.e.* thicker regions with a thickness of ~80 nm). Minimal and maximal deformations are illustrated for a given scan in the Figure 5.3.15. Consequently, the *E* value varied between ~25 MPa (thicker regions) and ~35 MPa (thinner regions). This is reflected in Figure 5.3.16a, which clearly indicates that the *E* value increases when the thickness decreases (*i.e.* in Figure 5.3.16a creases are identified in boxes labeled 1 and 2, while thinner regions correspond to labels 3 and 4). These values are similar to those recently measured by nanoindentation for different kinds of polyurethane samples (60–70 MPa) with millimeter-scale thicknesses (0.5–1.2 mm).[59] Moreover, adhesion force is quite homogeneous through the whole surface, as is evidenced in Figure 5.3.16b, the mean value being 7.2 nN.

A similar behavior was obtained for P3TMA films, even though the nominal spring constant of the cantilever used for testing this material (k_s = 40 N/m) was higher than the one used for TPU. Again, the *E* value was found to vary with the thickness of the region. Specifically, values of ~12 and ~3.5 GPa were obtained for the thinner (*i.e.* thickness of ~26 nm; labels 2 and 3 in Figure 5.3.17a) and thicker regions (*i.e.* thickness of ~140 nm; label 1 in Figure 5.3.17a), respectively. These modules are significantly higher than those for TPU, which is fully consistent with the stiffer nature of P3TMA.

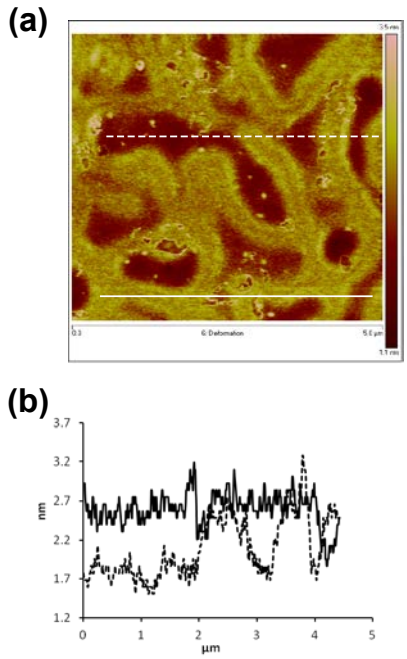

Figure 5.3.15. (a) Deformation mapping image for TPU and (b) its corresponding cross-profiles.

The average value of the adhesion force, which is homogeneous along the whole surface, was found to be 5 nN (Figure 5.3.17b). This value is one order of magnitude larger than that reported for poly(3-decyl thiophene) (0.45 nN).[60]

Results obtained for TPU:P3TMA 40:60 are displayed in Figure 5.3.18. As it is reflected by the contrast, thinner and thicker regions of the films present different *E* values. Moreover, small domains (*i.e.* pseudo-spherical protuberances) dispersed in the continuous phase also show contrast, resulting in a broad distribution of moduli. The mean values obtained for the thinner (labels 1 and 3 in Figure 5.3.18a) and thicker regions (labels 2 and 4 in Figure 5.3.18a) are 1.7 and 0.9 GPa, respectively. It is important to remark that the modulus values obtained for the blend sample have to be considered cautiously; the vertical force applied on the sample, while performing the nanomechanical experiments is constant and should be chosen in order to create a sample deformation of around 2 nm. This deformation is small enough to make sure that no plastic deformation is being induced on the sample and representative enough to be able to calculate the *E* value of the sample.

Nevertheless, because of the remarkable differences in the modulus for the two polymers present in the sample, it is not straightforward to set a suitable vertical force that ensures a minimum deformation of the stiffest polymer, while being low enough not to create plastic deformation on the softest one. Still, we can consider a general value for the modulus of the TPU:P3TMA 40:60 blend to be in the order of 1 GPa. This is lower than the *E* value derived from nanomechanical mapping for copolymers of 1,4-phenylene with benzoyl-1,4-phenylene (~10 GPa),[61] but higher than those obtained for poly(styrene-b-ethylene-co-butylene-b-styrene) block (SEBS), which was found to be highly dependent on the composition.[62] The modulus of the latter triblock copolymer was found to increase from 19 to 823 MPa with the polystyrene content.[62]

In contrast to the homogeneous distribution observed for individual TPU and P3TMA, the blend presents a high contrast in the adhesion force for the continuous phase and the segregated domains. Specifically, the adhesion force is higher for the TPU-rich domains than for the P3TMA-rich ones. In the P3TMA-rich phase, part of the measured adhesion force distribution falls in negative values. After studying individual force curves in this region of the sample, it is concluded that these adhesion values are an artifact which arises when there is no adhesion at all between the sample and the AFM tip. In fact, the software calculates the adhesive force as the force increment between the flat baseline of the trace signal prior to contact and the lowest point of the retrace curve, which corresponds to the maximum adhesion peak. Then, if there is no adhesive peak, and the trace and the retrace signals are overlapped, any small deviation from linearity in the trace signal can lead to negative adhesive forces. Because of that, it can be considered that the adhesive force on this part of the sample is close to 0 nN.

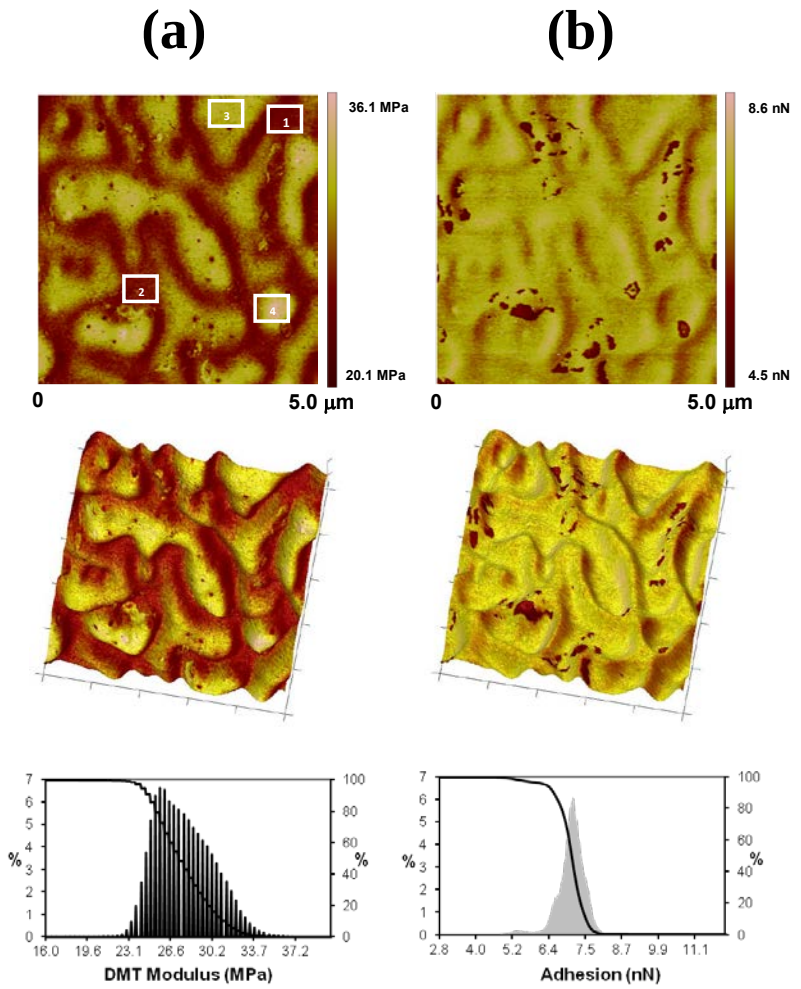

Figure 5.3.16. (a) DMT modulus and (b) adhesion force maps (two rows at the top), 3D-topography data (middle) and histograms (bottom) for TPU.

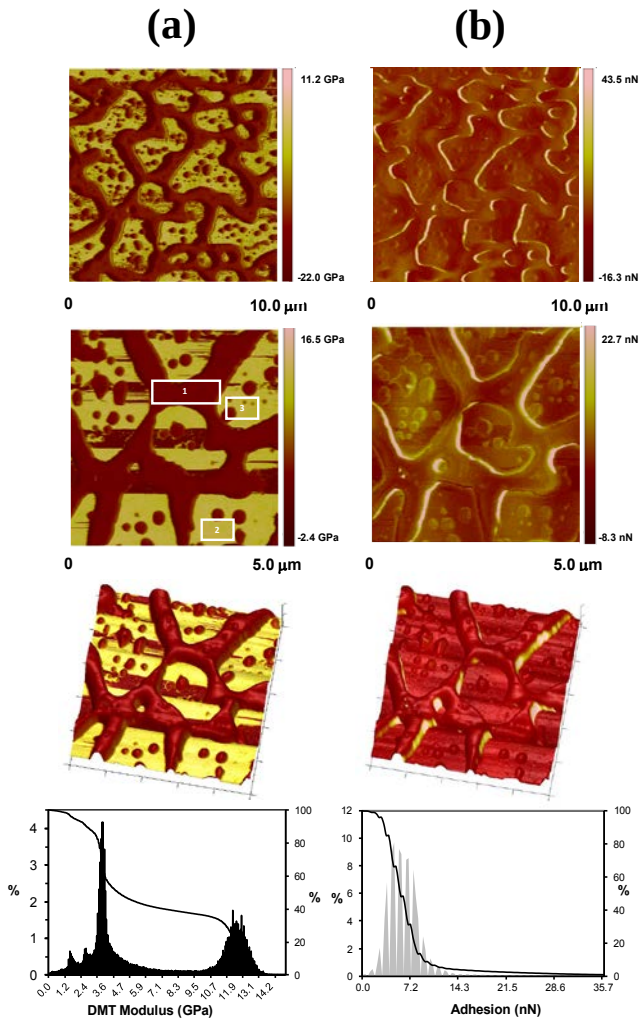

Figure 5.3.17. (a) DMT modulus and (b) adhesion force maps (first and second row), 3D-topography data (third row) and histograms (bottom) for P3TMA.

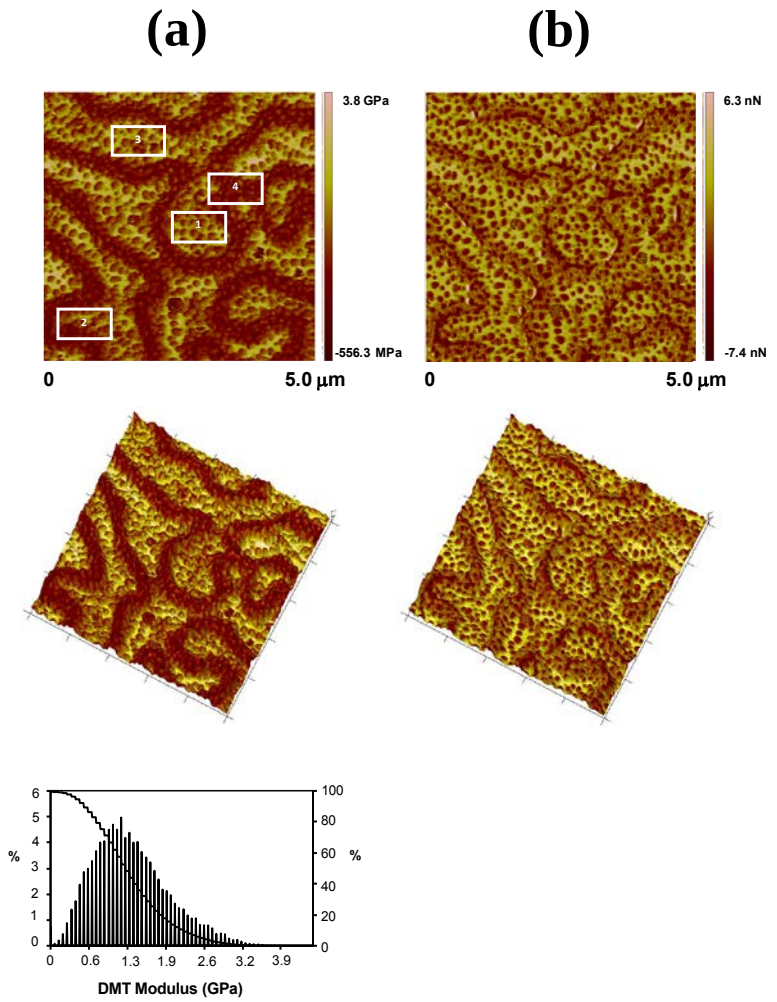

Figure 5.3.18. (a) DMT modulus and (b) adhesion force maps (top), 3D-topography data (middle) and histogram (bottom) for TPU:P3TMA 40:60.

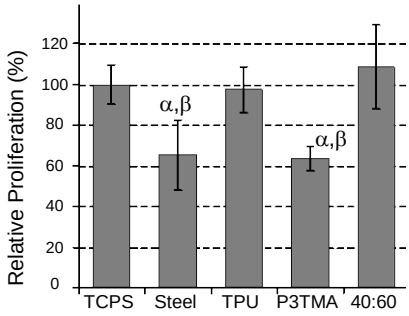

Figure 5.3.19. Cellular proliferation on P3TMA, TPU and TPU:P3TMA 40:60 substrates. Assays were carried out using the Cos-7 eukaryotic cell line. The relative viability was established in relation to TCPS control (tissue culture polystyrene). Steel was also considered as a control substrate because the individual polymers and the blend were deposited on this material. Greek letters on the columns refer to significant differences ($p < 0.05$) using the ANOVA and Tukey's tests: α *vs.* TCPS; β *vs.* steel.

Cell Proliferation

The response of the TPU:P3TMA 40:60 nanomembranes towards the Cos-7 fibroblast cells have been compared with those of individual P3TMA and TPU. Quantitative results for cellular proliferation assays are displayed in Figure 5.3.19, which displays the cellular activity of the materials after seven days of culture. Both steel and TCPS were used as control substrates, the number of viable cells per area of material being considerably higher in the latter than in the former. Moreover, the number of viable cells detected in P3TMA and TPU are similar to those found in steel and TCPS, respectively. This feature is evidence that the behavior of P3TMA as a cellular matrix is limited, which is a consequence of the cytotoxicity of the oxidizing agent ($FeCl_3$) contained in the matrix.[63,64] This negative effect is eliminated in the TPU:P3TMA 40:60 blend because of the reduction in the effective concentration of $FeCl_3$. Interestingly, the ability of the blend for cellular proliferation is slightly higher than that of individual TPU, indicating the positive effects of mixing P3TMA and TPU. Nevertheless, the latter effect is smaller than that found in P3TMA:PE44 nanomembranes.[25] Thus, the TPU:P3TMA blend shows better mechanical properties than P3TMA:PE44, even though the latter behaves better as a cellular matrix.[25,26] This is due to the fact that the cells interact more favorably with the PE44 substrate than with the TPU one. In spite of this, it should be mentioned that cell proliferation is higher in TPU:P3TMA than in the two individual polymers.

5.3.3. Conclusions

TPU:P3TMA blends with 60:40, 50:50, 40:60 and 20:80 weight ratios have been prepared and thermally characterized. The dependence of T*g* on the composition indicates a low partial miscibility between TPU and P3TMA. The highest miscibility has been obtained for the 40:60 weight ratio. Thermal analysis of samples prepared using TPU:P3TMA 40:60 nanomembranes evidence that the partial phase miscibility found in the solvent cast films decreases at the nanometric scale. This effect is attributed to the influence of the solvent casting and spin-coating processes on the crystallinity of TPU.

The topography and morphology of TPU:P3TMA nanomembranes present the same elements as the individual TPU and P3TMA samples. Thus, the blend films consist of a dispersion of granules, which are associated with the P3TMA-rich phase, throughout the rest of the film. The co-existence of the two components in some domains has been demonstrated by means of C-AFM measurements and detailed observation of AFM phase images. The phase separation has been rationalized in terms of both the conventional parameters typically found in thin films (*e.g.* polymer–polymer interactions, solubility of the polymers in the solvent and, especially, the spin-coating process) and the crucial role of the substrate–film–air interfaces due to the ultra-thin nature of the membranes.

Regarding nanomechanical properties, the *E* value, which depends on the thickness of the different regions comprised in the samples, is higher for P3TMA (~12.0 and ~3.5 GPa for thinner and thicker regions, respectively) than for TPU (~35 and ~25 MPa for thinner and thicker regions, respectively). In contrast, the adhesion force of the two individual components is homogeneous and higher for TPU than for P3TMA (7.2 and 5.0 nN, respectively). The *E* value determined for the 40:60 blend is half-way between those found for the individual components (1.7 and 0.9 GPa for the thinner and thicker regions, respectively), while the adhesion force depends on the composition of the domains, being higher for the TPU-rich domains.

Nanomembranes prepared by blending TPU and P3TMA are more active as a cellular matrix than each of the two individual materials. However, the response of the P3TMA:PE44 nanomembranes towards the cells is more positive than that of TPU:P3TMA. Thus, substitution of PE44 by TPU results in an improvement of the mechanical resistance and robustness of the nanomembranes, even though the bioactivity decreases. In spite of this, TPU:P3TMA nanomembranes have been found to be good substrates for applications related to tissue engineering.

5.4. Electronic, Electric and Electrochemical Properties

Human body tissues, such as neural, cardiac or skeletal muscle ones, respond to electrical stimulus, signals being able to regulate cell growth and behaviour. However, conventional biomaterials do not result in appropriate biointerfaces to conduct electrical stimulation since they lack electrical conductivity. Recently, in order to overcome this drawback, conducting polymers (CPs) have been used as biocompatible materials which can support cell adhesion, migration and proliferation,[10,65,66] or even act as substrates for tissue electrical stimulation.[67] Practical applications in such a field have been typically developed using polypyrrole (PPy) and polyaniline (PAni) CPs.[68-71]

Considering the previous described results (section 5.3), TPU:P3TMA 40:60 biointerface has been subjected to further studies to test its feasibility as a future platform for electrically stimulated cell growth. Bearing such biomedical application in mind, in the present study the electronic and electrical properties, and the electrochemical behaviour of these nanomembranes have been examined. Specifically, we focused on the determination of the doping state of P3TMA (band gap energy, E_g) from both the macroscopic (bulk properties of the blend) and the nanoscopic scales. Besides, P3TMA distribution in the blend (interconnected network), its electrical response and the insulating effect of the TPU matrix have been also analyzed. Finally, an electrochemical study has been performed on steel supported nanomembranes in order to determine their electroactivity and electrochemical stability.

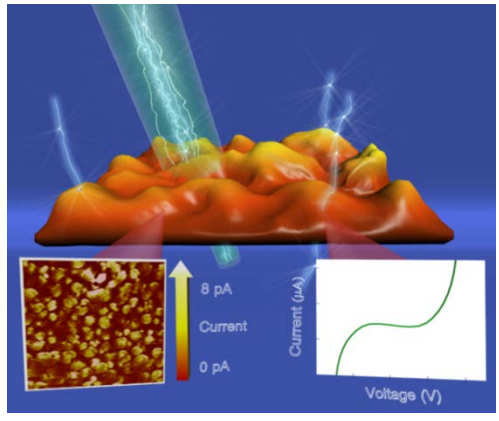

Graphical abstract

5.4.1. Experimental Section

UV-vis absorption spectroscopy

Absorption spectra for both polymer solutions and ITO-supported nanomembranes were obtained using a UV-vis-NIR Shimadzu 3600 spectrophotometer equipped with a tungsten halogen visible source, a deuterium arc UV source, a photo-multiplier tube UV-vis detector, and InGaAs photodiode and cooled PbS photocell NIR detectors. Spectra were recorded in the absorbance mode, with the wavelength range being 300–800 nm for both solution and supported nanomembrane samples. For analyzing ITO-supported nanomembranes, the integrating sphere accessory (model ISR-3100) was used. Its interior is coated with highly diffuse BaO reflectance standard. Single-scan spectra were recorded at a scan speed of 60 nm/min. Measurements, data collection and evaluation were controlled by the computer software UVProbe 2.31.

Conductive atomic force microscopy (C-AFM)

AFM Dimension 3100 microscope equipped with an Extended TUNA unit and a NanoScope IV controller (Bruker) was used in contact mode to simultaneously obtain topographic and current images of the analyzed samples. The study was carried out with two different current-sensing cantilevers. For imaging, a silicon rectangular lever coated with Pt–Ir (ANSCM-PC: resonant frequency 12 kHz and spring constant 0.2 N/m) was purchased from Applied Nanostructures (Santa Clara, CA). During all the imaging experiments, a bias voltage of 1 V was applied between the tip, which acted as the back electrode, and the ITO front electrode, while the current through the tip was measured. The ITO substrate was ground during all the measurements, which were conducted under ambient conditions. The load force was maintained below 10 nN to avoid damage on the film or the tip so contact could be reliable and reproducible. Current images of the 40:60 TPU:P3TMA supported nanomembranes were obtained using the most sensitive amplifier (0.01 nA per div; current upper limit detected 100 pA). Thus, the presence of TPU in some regions produced an insulating effect leading to small current signals only clearly detected by such amplifier. As a drawback, intensity values higher than 100 pA were not distinguishable.

In addition to C-AFM imaging, current/voltage (*I/V*) measurements were recorded at given spots by performing forward and reverse voltage scans between 3.0 V and + 3.0 V. In this case, a solid Pt probe (RMN-25PT300B: nominal resonant

frequency 20 kHz and spring constant 18 N/m) was purchased from Bruker Corporation (Santa Barbara, CA). These probes were chosen since they offer excellent conductivity and do not suffer from metal wear.

Electrochemical measurements

The electrochemical behaviour of TPU, P3TMA, and TPU:P3TMA nanomembranes supported on steel AISI316 was determined by cyclic voltammetry (CV). Phosphate buffer saline (PBS) (pH = 7.4) and acetonitrile (99.9%, Panreac Quimica Sau) with 0.1M $LiClO_4$ were used as electrolytes. All electrochemical experiments were performed with a Potentiostat Versastat II connected to a PC and controlled through the Electrochemistry Power Suite 2.58 (Princeton Applied Research) program using a three-electrode cell under a nitrogen atmosphere (99.995% in purity) at room temperature. The working compartment was filled with 50 mL of the electrolyte solution with 0.1 M $LiClO_4$. $LiClO_4$ worked as an electrolyte increasing the number of electrons able to interact with the polymer structure and maintained the total ionic force of the PBS solution stable. Steel AISI 316 sheets of 1 cm^2 were both used as the working and counter electrodes, and an Ag|AgCl electrode as the reference electrode which contained a KCl saturated aqueous solution (offset potential versus the standard hydrogen electrode, E^0 = 0.222 V at 25 °C). All potentials given in this report are referred to this electrode. Cyclic voltammograms were registered at a scan rate of 20, 50 and 100 mV/s in the potential range from −0.4 to +1.0 V.

The electroactivity, which indicates the ability to store charge, was evaluated by examining the similarity between the anodic and cathodic areas of the control voltammogram. The electrochemical stability (*i.e.* loss of electroactivity, LEA), which decreases with the oxidation and reduction areas of consecutive control voltammograms, was determined using the following expression:

$$LEA = \frac{\Delta Q}{Q_i} \times 100 \qquad (5.4.1)$$

where ΔQ is the difference of oxidation voltammetric charge between the first cycle and the last cycle and Q_i is the oxidation voltammetric charge corresponding to the first cycle. In this work all values of LEA were referenced to 10 consecutive oxidation−reduction cycles.

5.4.2. Results and Discussion

Electronic properties of P3TMA: doping state

The doping state of P3TMA and of the CP in the TPU:P3TMA blend has been compared in ITO-supported nanomembranes and in solution by UV-vis spectroscopy. Furthermore, UV-vis measurements have been used to examine the influence of the spin-coating process on the CP. The spectra displayed in Figure 5.4.1 show that TPU nanomembranes and TPU solutions at any concentration do not present any absorbance peak. As a control, the absorption spectrum for ITO was recorded in the range from 300 to 800 nm showing almost 0% of absorbance (not shown).

The absorbance peaks of P3TMA and TPU:P3TMA supported nanomembranes (Figure 5.4.1a) appear at λ_{max} = 410 and 413 nm, respectively, which corresponds to the π–π * transition of thiophene rings in P3TMA chains.[72,73] The optical π – π * lowest transition energy or band gap energy (E_g) was determined by considering the following expression:

$$E_g\,(eV) = \frac{hc}{1.6 \times 10^{-19}\,\lambda_{onset}} \qquad (5.4.2)$$

where h (Plank's constant) = 6.626×10^{-34} J · s, c (speed of light) = 3.0×10^{8} m/s and λ_{onset} (m) is the cut off wavelength for the absorption spectra.

E_g obtained for P3TMA and TPU:P3TMA ITO supported nanomembranes deposited from THF solutions (Table 5.4.1) is 2.35 and 2.32 eV, respectively. E_g of P3TMA supported nanomembranes deposited onto ITO from a $CHCl_3$ solution (5 mg/mL) was determined to be 2.17 eV (λ_{max} = 419 nm),[33] indicating a hypsochromic effect when the solvent changes from $CHCl_3$ to THF. The shift observed suggests a slightly different polymer chain conformation induced by the solvent. When chloroform is used a more planar conformation is obtained. The energy required for the π–π* transition decreases since the π-conjugation length increases.

UV-vis spectra of P3TMA and TPU:P3TMA in dilute (0.01 and 0.05 mg/mL) and concentrated (0.5 and 5 mg·/mL) THF solutions are compared in Figure 5.4.1b and c, respectively. Dilute solutions (0.01 mg/mL) showed absorbance peaks at λ_{max} = 383 and 399 nm (Figure 5.4.1b) and band gap energy values of 2.62 and 2.59 eV for P3TMA and TPU:P3TMA solutions, respectively. On the other hand, solutions with a concentration of 0.05 mg/mL presented a maximum absorbance peak at 401 nm for both P3TMA and TPU:P3TMA solutions, with E_g values of 2.46 eV for P3TMA

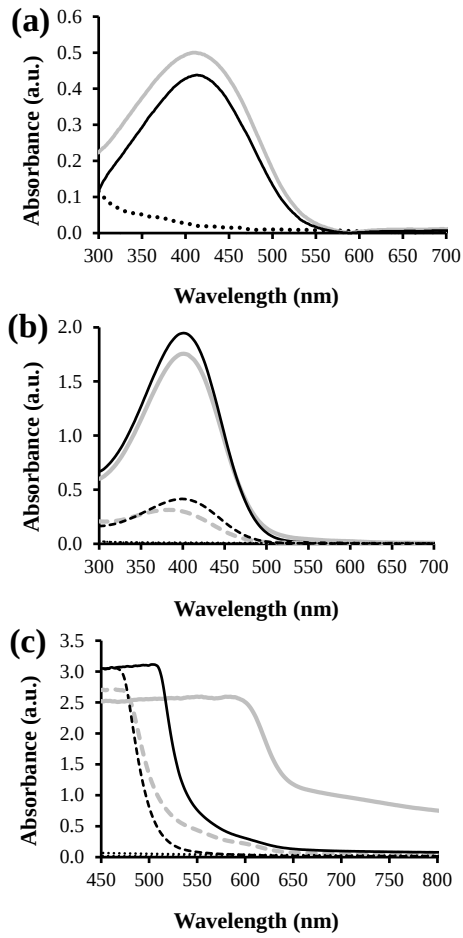

Figure 5.4.1. UV-vis absorption spectra for TPU (dotted line), P3TMA (gray line) and 40:60 TPU:P3TMA (black line): (a) ITO-supported nanomembranes; (b) dilute solutions with 0.01 and 0.05 mg/mL (dashed and solid lines, respectively); and (c) concentrated solutions with 0.5 and 5 mg/mL (dashed and solid lines, respectively).

and 2.53 eV for TPU:P3TMA (Table 5.4.1). The E_g values for dilute P3TMA solutions are similar to those obtained in our previous work despite having changed the solvent.[33] These results indicate that the effect of the solvent in the π–π^* transition band is almost negligible for dilute solutions, and thus, the influence in the π-electron delocalization is very small (Table 5.4.1).

Table 5.4.1. Values of λ_{max} (nm), λ_{onset} (nm) and E_g (eV) derived from UV-vis absorption spectra (Figure 5.4.1.) for P3TMA and 40:60 TPU:P3TMA in different conditions.

Conditions	λ_{max}	λ_{onset}	E_g
P3TMA nanomembrane spin-coating (5 mg/mL)	410	535	2.32
40:60 TPU:P3TMA nanomembrane spin-coating (5 mg/mL	413	528	2.35
P3TMA dilute solution (0.01 mg/mL)	383	475	2.62
P3TMA dilute solution (0.05 mg/mL)	401	505	2.46
P3TMA concentrated solution (0.5 mg/mL)	464	524	2.37
P3TMA concentrated solution (5 mg/mL)	584	657	1.89
40:60 TPU:P3TMA dilute solution (0.01 mg/mL)	399	480	2.59
40:60 TPU:P3TMA dilute solution (0.05 mg/mL	401	492	2.53
40:60 TPU:P3TMA concentrated solution (0.5 mg/mL)	464	505	2.46
40:60 TPU:P3TMA concentrated solution (5 mg/mL)	503	546	2.28

When increasing the concentration, the π–π^* transition exhibits a red shift with respect to the spectra recorded for dilute solutions, indicating that the energy required for such transition decreases since the π -conjugation length increases (Figure 5.4.1c). Concretely, λ_{max} increases from 401 nm (0.05 mg/mL) to 464 nm (0.5 mg/mL) for both P3TMA and TPU:P3TMA solutions, while for the solution at 5 mg/mL the maximum absorbance peak shifts up to 584 and 503 nm for P3TMA and TPU:P3TMA, respectively. Accordingly, E_g decreases to 1.89 and 2.28 eV for P3TMA and TPU:P3TMA solutions at 5 mg/mL, respectively (Table 5.4.1). Although they appear as shoulder peaks, bands observed at wavelengths of 600 nm in concentrated solutions may be associated with the polaron to π^* band transition in polymer chains evidencing the influence of the dopant agent ($FeCl_3$) during the chemical oxidative polymerization. In particular, these shoulders can be observed in the spectra of P3TMA (0.5 and 5 mg/mL) and TPU:P3TMA (5 mg/mL) THF solutions (Figure 5.4.1c).

As a general trend, the E_g values obtained in solution are higher for TPU:P3TMA than for P3TMA solutions regardless of the concentration (except for the most dilute solution, 0.01 mg/mL). These results indicate that the intermolecular interactions among polymer molecules and solute–solvent or solute–solute interactions affect the energy required for the π–π^* transition. The similarity between E_g values for the most dilute P3TMA and TPU:P3TMA solutions (0.01 mg/mL) evidences the low effect of solute–solute interactions on the π–π^* transition energy at that concentration level, as the P3TMA/solvent interactions prevail.

However, this consideration does not apply to the supported nanomembranes since the E_g values for both P3TMA and TPU:P3TMA ITO-supported nanomembranes are similar and, in fact, slightly higher than those determined for the solution used in the spin-coating process (5 mg/mL). This can be possibly ascribed to the spin-coating process in which alterations in the polymer chains take place. Polymer molecules are not able to adopt their equilibrium conformation since the solvent is completely evaporated and, therefore, conformational effects in the molecular π-conjugation length and the packing of the π-conjugated backbone influence negatively the E_g values.

According to the E_g results obtained from UV-vis spectra, TPU:P3TMA nanomembranes still exhibit a partial semiconductor behaviour (*i.e.* $E_g < 3$ eV). Therefore, a current response is expected when voltage is applied.

P3TMA distribution and electrical response by C-AFM

C-AFM was chosen as an interesting tool to assess the interfacial electrical characterization because of the possibility of taking simultaneously topographical and current images for the same scanned region, allowing the correlation between topographic features and the electrical response. Besides, this relationship could also be evaluated by performing *I/V* curves at specific points throughout the sample.

C-AFM: conductivity determination. Figure 5.4.2 presents typical height and current images simultaneously obtained by C-AFM for the surface of the TPU:P3TMA ITO-supported nanofilm. The topography of the TPU:P3TMA surface is similar to the one shown in the previous section. It was described as the combination of the topographies of the two individual components, resulting in a homogeneous distribution of granules throughout the surface.

As is depicted in Figure 5.4.2, the application of a voltage between the tip and the ITO substrate in the TPU:P3TMA supported nanomembrane results in a current response: bright (high current-flowing) regions which essentially correspond to the P3TMA-rich regions (*i.e.* granules) and dark (low current-flowing) regions that correspond to the insulating TPU-rich areas. Still, some of the P3TMA-rich regions show lower current values indicating that either the conducting path is somehow interrupted by the insulating TPU in those zones or the electrical conductivity is reduced by the conformation adopted by the P3TMA polymer chains.

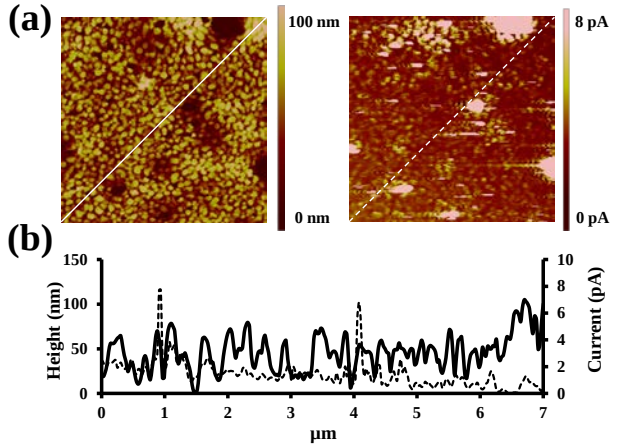

Figure 5.4.2. Simultaneous 5 µm × 5 µm topographical image (left) and C-AFM current image (right) for 40:60 TPU:P3TMA. (b) Dual cross-section profile of the above images indicating variations in height (solid line) and current (dashed line).

These results evidence that the electron conduction across the nanomembrane is not homogeneous since localized areas of varying extension were found to show a different intensity response while being embedded in an insulating matrix of TPU. Accordingly, conductivity is not totally dependent on the topography or roughness parameters. It is worth noting that although P3TMA is not completely doped, it exhibits conductive spots (bright regions). A closer look reveals that some P3TMA granules do not conduct at all, as it can be observed in the 1 µm × 1 µm region of the TPU:P3TMA ITO-supported nanomembrane displayed in Figure 5.4.3 (see also Figures 5.4.4-5.4.6). Dual cross-section profiles confirm this remark since almost no current is detected when measuring granules of 70 nm height (cross-section H1). These results suggest that these localized spots have the electron path between ITO and tip blocked by the presence of TPU. Furthermore, in order to assess quantitatively the conductivity of the supported nanomembranes, the minimum and maximum current values obtained after averaging 256 points taken from the current profiles shown below each current image are 1.85 ± 1.32 pA for profile V in Figure 5.4.3 and 0.43 ± 0.21 pA for profile H in Figure 5.4.4., respectively. The line and total area average current values for different zones (imaged areas) are summarized in Table 5.4.2.

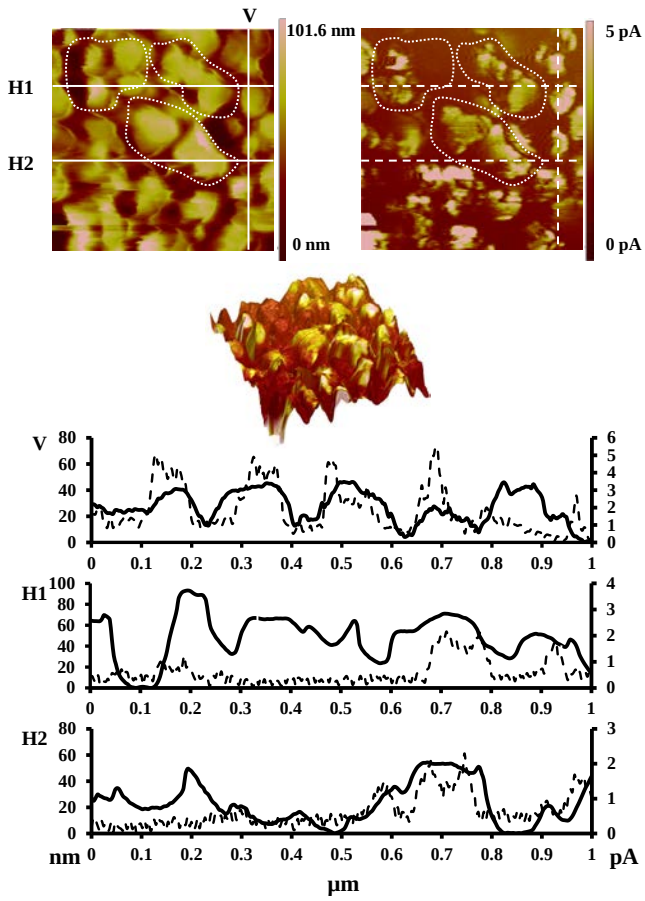

Figure 5.4.3. Top: simultaneous 1 µm × 1 µm topographical image (left) and C-AFM current image (right) for 40:60 TPU:P3TMA. Middle: super-imposition of both images. Bottom: dual cross-section profile of the above images indicating variations in height (solid line) and current (dashed line) for the vertical line (top, V) and horizontal lines (bottom, H1 and H2).

Table 5.4.2. Data for 40:60 TPU:P3TMA regions shown in Figures 5.4.2 – 5.4.6: RMS roughness, average current and average conductivity obtained from topography and current images and calculated as described in the text.

40:60 TPU:P3TMA	Roughness (nm)	Av. Current (pA)	Av. Conductivity (S/cm)
Figure 5.4.2 D	22.2	1.44 ± 1.03	$1.74\times10^{-5} \pm 1.24\times10^{-5}$
Figure 5.4.3 V	21.6	1.85±1.32	$2.23\times10^{-5} \pm 1.59\times10^{-5}$
Figure 5.4.3 H1		0.59±0.49	$7.12\times10^{-6} \pm 5.91\times10^{-6}$
Figure 5.4.3 H2		0.63±0.47	$7.60\times10^{-6} \pm 5.67\times10^{-6}$
Figure 5.4.4 D	19.1	0.66±0.46	$7.97\times10^{-6} \pm 5.55\times10^{-6}$
Figure 5.4.4 H		0.66±0.44	$7.97\times10^{-6} \pm 5.31\times10^{-6}$
Figure 5.4.5 D	17.4	0.54±0.27	$6.52\times10^{-6} \pm 3.26\times10^{-6}$
Figure 5.4.5 H		0.43±0.21	$5.19\times10^{-6} \pm 2.53\times10^{-6}$
Figure 5.4.6 H	17.4	1.18±0.97	$1.42\times10^{-5} \pm 1.17\times10^{-5}$

It is worth noting that the values exhibit a slight variation over the sample surface. These large fluctuations in the film conductivity were also previously described for fully doped CPs, which presented an inhomogeneity of the conductivity values across the polymer surface even under perfectly controlled conditions.[74] This was attributed to the irregular distribution of the doping level over the surface. Accordingly, the variation in the current response of our system may come from the presence of the insulating TPU since there are regions with no intensity signal at all.

The vertical conductivity between the tip and the substrate electrode for TPU:P3TMA nanomembranes has been determined by applying a simple set of equations.[75] Calculations take into account both the contact area of the tip and the CP considering the Hertz theory and the average conductance values obtained from cross-sectional analyses of the current images at different regions (Table 5.4.2).[76,77] Thus, as a first step towards the evaluation of the vertical conductivity, the contact area between the tip and the film (A) should be determined according to the modified Hertz theory, which states that the contact area between two elastic and perfectly smooth solids (*i.e.* a sphere and a plain) in the presence of adhesive forces[78] can be approximated by the following relationship:

$$A = \pi \left[\frac{3}{4}\frac{R^*(F_N + F_{adh})}{E^*}\right]^{\frac{2}{3}} \quad (5.4.3)$$

where F_N corresponds to the external loading force (7 nN in this case) and F_{adh} is the adhesion force between the AFM tip and the sample surface.

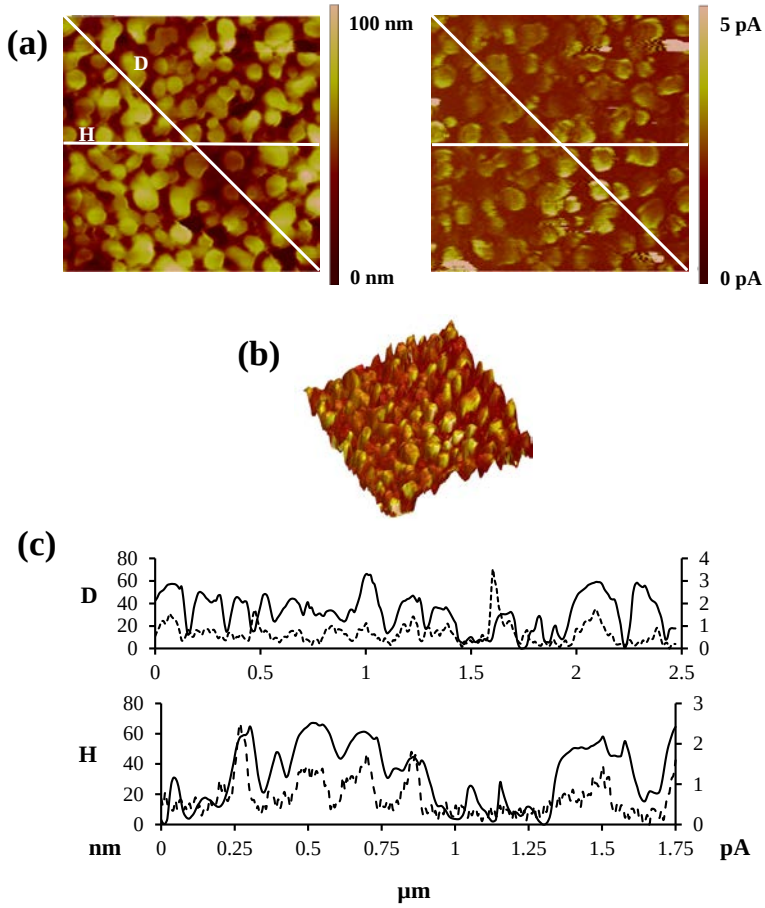

Figure 5.4.4. (a) Simultaneous 1.75 µm x 1.75 µm topographical image (left) and C-AFM current image (right) for the same 40:60 TPU:P3TMA sample. (b) 3D image superimposing height and current. (c) Dual cross-section profile of above images indicating variations in height (solid line) and current (dashed line) for the horizontal (H) and diagonal (D) lines.

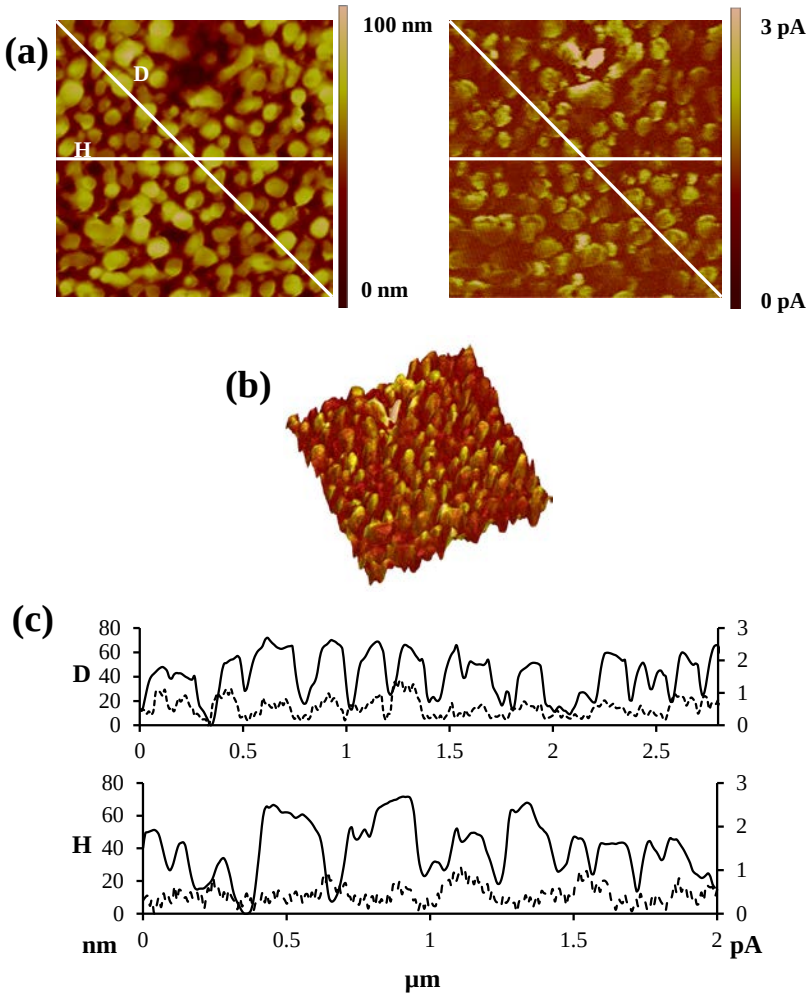

Figure 5.4.5. (a) Simultaneous 2 µm x 2 µm topographical image (left) and C-AFM current image (right) for the same 40:60 TPU:P3TMA sample. (b) 3D image superimposing height and current. (c) Dual cross-section profile of above images indicating variations in height (solid line) and current (dashed line) for the horizontal (H) and diagonal (D) lines.

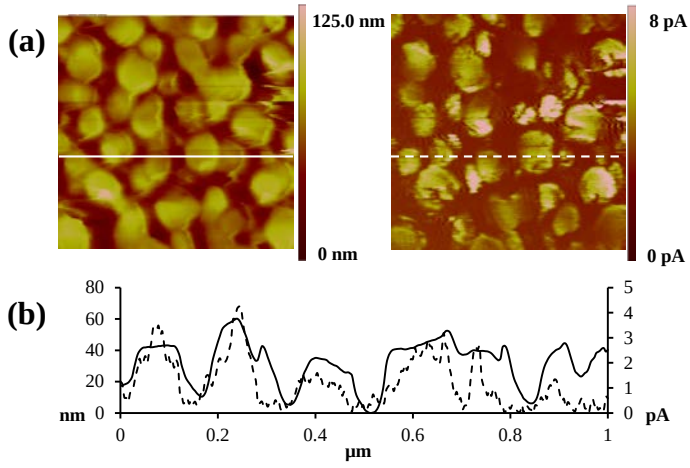

Figure 5.4.6. (a) Simultaneous 1 µm x 1 µm topographical image (left) and C-AFM current image (right) for 40:60 TPU:P3TMA sample. (b) Dual cross-section profile of above images indicating variations in height (solid line) and current (dashed line).

In our previous work, we found that the adhesion force between the tip and the TPU:P3TMA surface depends on the phase distribution, even though homogeneous values were determined for the whole surface of individual TPU and P3TMA films (*i.e.* average values: 7.2 and 5.0 nN, respectively).[26] For that reason, an average value of 6 nN has been considered for F_{adh} in the conductivity calculations. R^* is the effective radius of curvature of the tip and the sample surface contact, which is expressed as:

$$\frac{1}{R^*} = \frac{1}{R_{tip}} + \frac{1}{R_{sample}} \tag{5.4.4}$$

where R_{sample} is the radius of the sample. Thus, the resulting $R^* \approx R_{tip}$ was found to be between 5 and 10 nm. Hence, the value of R^* used for the calculations is 8 nm. E^* is the effective Young's Modulus determined by:

$$\frac{1}{E^*} = \frac{(1-\sigma_t^2)}{E_t} + \frac{(1-\sigma_s^2)}{E_s} \tag{5.4.5}$$

where E_t and E_s correspond to the Young's Modulus of the tip (168 GPa) and the sample, respectively. The nanomembrane modulus depends on the thickness of the film, values of 0.9 and 1.7 GPa being found for the thicker (80–140 nm) and the thinner (10–40 nm) regions.[26] Accordingly, the average value, E_s = 1.3 GPa, has been assigned for the calculations. The values of the Poisson's ratio for the tip and

the sample are σ_t = 0.39 and σ_s = 0.38, respectively.[79] Therefore, the contact area obtained between the tip and the sample calculated by applying 5.4.3 is 43.1 nm^2. Finally, the average conductivity has been calculated using the following equation,

$$\sigma = \frac{I_{av}}{V}\frac{l}{A} \tag{5.4.6}$$

where I_{av} is the average current, V the bias voltage applied (1.0 V), l the thickness of the film and A the contact area.

The average conductivity values were obtained by taking into account the thickness of the TPU:P3TMA films reported in our previous work (*i.e.* 52 nm),[26] and are displayed in Table 5.4.2. for the scanned lines from Figures 5.4.2–5.4.6. The obtained values, which range from 2.23 × 10^{-5} to 5.19 × 10^{-6} S/cm, represent an approximation of the global electrical behaviour of the sample. Furthermore, these values are fully consistent with a semiconductor behaviour.

***I/V* curve measurement.** In order to assess the electrical properties of the supported nanomembrane, *I/V* curves were recorded at 65 random spots throughout the TPU:P3TMA surface. As previously occurred for the current image measurements, not all the spots analyzed gave an *I/V* response. Specifically, 41 out of 65 evaluated points showed an *I/V* response curve (*i.e.* 63%). Typical *I/V* curves obtained for the semiconductive points, together with their corresponding dI/dV signals, are displayed in Figure 5.4.7a. For the measurement of *I/V* curves solid P_t AFM probes were used to improve current sensing. Amplifiers were then changed to 1 nA per div (higher current detected: 10 nA) for TPU and some regions of the TPU:P3TMA nanomembranes and 100 nA per div (higher current detected: 1000 nA) for P3TMA and TPU:P3TMA nanomembranes.

Curves were obtained by scanning the voltage in the range from -3.0 to +3.0 V and a typical semiconductor behaviour was observed. Differences among the *I/V* curves may arise from the polymer film inhomogeneity[80] and the spikes near -1 and +1 V may be attributed to the irregular distribution of P3TMA across the nanomembrane.[81] The *I/V* curves that showed no current in the applied potential range have been ascribed to TPU-rich region domains. These results are in complete agreement with the conductivity results previously discussed.

In efforts to confirm these observations, *I/V* curves were also obtained at 30 random points throughout the surface of a P3TMA supported nanomembrane. Results were similar to those obtained for the blend ultra-thin nanofilm, even though in this case all of the spots analyzed gave an *I/V* curve response since the

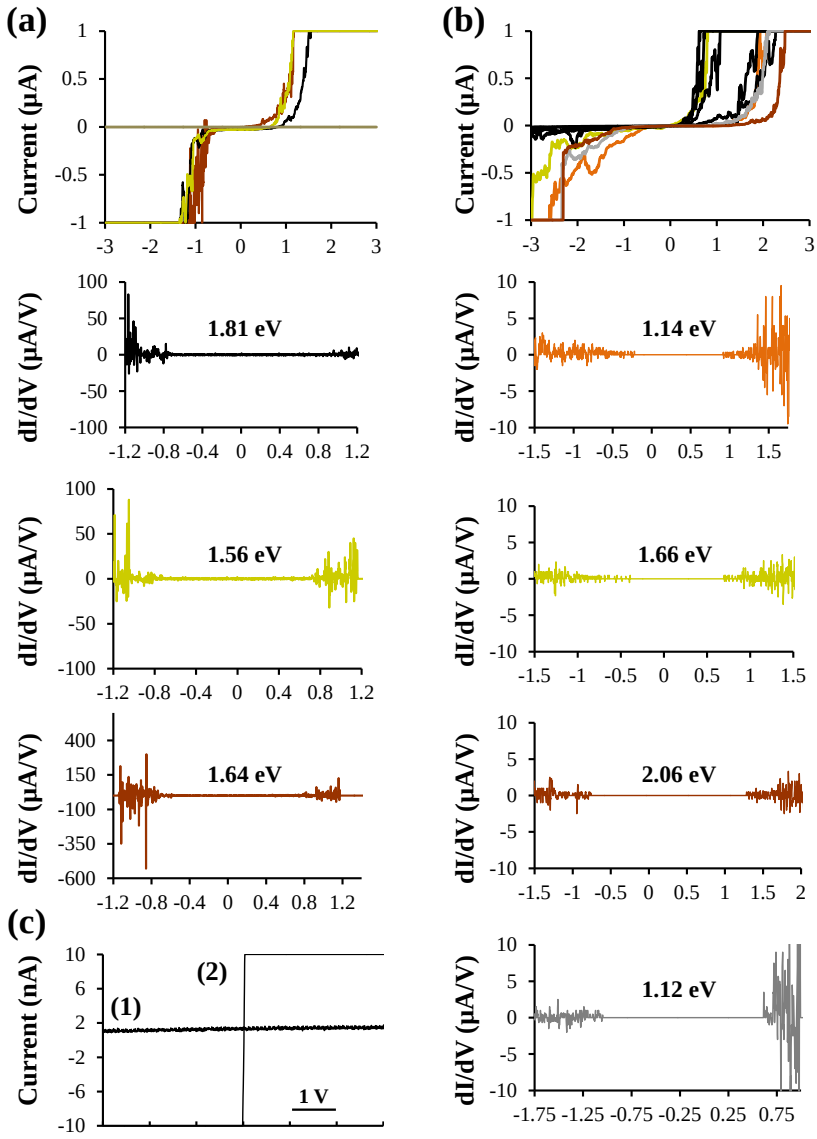

Figure 5.4.7. Typical current–voltage (*I/V*) curves (100 nA per div amplifier; max top current: 1 mA) and their corresponding d*I*/d*V* signals for: (a) TPU:P3TMA nanomembrane; (b) P3TMA nanomembrane; and (c) *I/V* curves for TPU (1) and ITO (2) in a scan range from -3 to +3 V using a more sensitive amplifier.

current path between the tip and the ITO was not blocked by an insulating polymer. Figure 5.4.7b shows four typical curves for P3TMA scanning from -3.0 to +3.0 V using the 100 nA per div amplifier. TPU nanomembrane *I/V* curves were also assessed as reference, showing no response (Figure 5.4.7c).

Band gap calculations: correlation between C-AFM and UV-vis results

The correlation of the band gap energy values obtained from the electrical and optical measurements has been examined. It is possible to assign the band gap energy values from the *I/V* curves obtained by C-AFM by measuring the distance between the first two points showing response.[82,83] Figure 5.4.7a depicts a total of three dI/dV curves obtained from the *I/V* curves for TPU:P3TMA nanomembranes registered by C-AFM. By these means, the obtained E_g values ranged from 0.72 to 1.98 eV, depending on the spot analyzed since the P3TMA distribution among the granules varies from spot to spot. Besides, polymer chains are not equally organized at all the spots and the insulating effect of TPU varies along the film surface. Applying the same procedure, E_g values obtained from four *I/V* curves for P3TMA (Figure 5.4.7b) were found to vary between 1.12 and 2.06 eV.

E_g values for the supported nanomembranes are higher when evaluated by UV-vis spectroscopy than by C-AFM. The E_g value determined by UV-vis spectroscopy corresponds to the average over the entire area of the supported nanomembrane reached by the beam. Therefore, while UV-vis spectroscopy results expose the bulk properties of the sample considering the influence of both P3TMA and TPU, C-AFM allows the direct evaluation of those points that exhibit a semiconducting response. As it was stated by Han *et al*.,[77] it has to be taken into account that the E_g value resulting from *I/V* curves measured at a specific spot on the sample surface may not represent all the electrical characteristics of the sample.

The combination of both techniques becomes essential. Although both techniques are appropriate to measure electrical properties and evaluate doping levels of CPs, UV-vis measurements provide an average value that corresponds to a more macroscopic description,[76,78] giving the general semiconductive characteristics of the whole film, while C-AFM gives the information corresponding to the distribution of the semiconducting properties at the nanoscale over the nanomembrane surface, that may be of relevance when processes at this scale, like cell adhesion and migration, are to be considered.

Overall results for the TPU:P3TMA system are very promising, even though the conformation of polymer chains, the formation of molecular aggregates, and the

discontinuities in the P3TMA path between the tip and the electrode affect the nanomembrane conductivity. For example, TPU:P3TMA electrical response can be useful when electrically active interfaces are needed to electrostimulate living tissues for regenerating purposes.

Electrochemical properties

An electrochemical study was conducted on the TPU, P3TMA and TPU:P3TMA nanomembranes to understand their response to oxidation–reduction chemical processes since they are frequently involved in cellular applications when electrical stimulation is applied. Hence, the electrochemical response of 20:80, 40:60, and 60:40 TPU:P3TMA nanomembranes supported on steel was studied in different electrolytic media by cyclic voltammetry (CV), and compared with that obtained for individual P3TMA and TPU. Figure 5.4.8a shows the first and 10^{th} control voltammograms (20 mV/s) recorded in acetonitrile, while those obtained in PBS are displayed in Figure 5.4.8b.

In acetonitrile, P3TMA shows an oxidation process that begins at 0.796 V and a second oxidation process seen as a shoulder at 0.926 V, which indicates the formation of polarons and bipolarons in the P3TMA chains. The cathodic scan in acetonitrile shows a single reduction peak at 0.766 V, indicating that polarons and bipolarons reduce at the same potential. After 10 oxidation-reduction cycles, the oxidation peaks shift to lower potentials (0.77 and 0.87 V, respectively), and the shoulder becomes more pronounced. The voltammogram of the blank (steel) reflects that the oxidation and reduction peaks are not affected by the organic solvent.

The voltammograms recorded for TPU:P3TMA nanomembranes share the characteristics of those obtained for P3TMA: the oxidation processes, as well as the reduction of polarons and bipolarons, are clearly identified in the three TPU:P3TMA compositions. Specifically, TPU:P3TMA 40:60 shows an oxidation peak with an anodic peak potential of 0.813, the corresponding reduction peak being detected in the cathodic scan at 0.758 V. Furthermore, an oxidation shoulder is identified at 0.936 V, which corresponds to the oxidation of P3TMA chains in the blend.

Moreover, voltammograms indicate that the electroactivity decreases with the concentration of P3TMA for the three TPU:P3TMA compositions. However, the influence of P3TMA is very remarkable in all cases, as the electroactivity of the

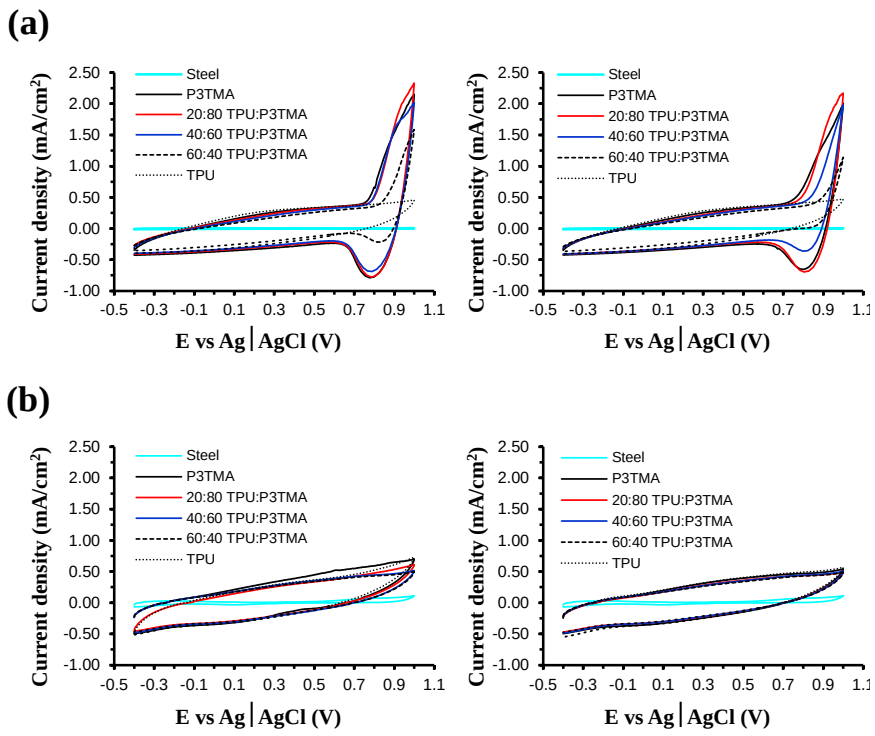

Figure 5.4.8. First (left) and 10th (right) control voltammograms for P3TMA (solid black line), TPU (dotted black line), 20:80 TPU:P3TMA (red line), 40:60 TPU:P3TMA (blue line), 60:40 TPU:P3TMA (slashed black line) and uncoated steel (cyan) in (a) acetonitrile and (b) PBS. Scan rate: 20 mV/s. Initial and final potential: -0.4 V; reversal potential: 1.0 V.

20:80, 40:60, and 60:40 TPU:P3TMA nanomembranes is lower than that of individual P3TMA by only 9%, 15%, and 24%, respectively. After 10 oxidation−reduction cycles, the 20:80, 40:60, and 60:40 TPU:P3TMA nanomembranes show similar LEA values (38%, 31%, and 35%, respectively), lower than that for P3TMA, which is 48% after 10 cycles.

In opposition, voltammograms recorded for TPU in acetonitrile do not show well-defined oxidation or reduction processes in the potential range from -0.40 to 1.00 V. However, comparison of the voltammograms recorded for bare steel and TPU indicates that the former substrate is completely inactive from an electrochemical point of view within the scanned interval of potentials, whereas the latter shows some electrochemical activity. Thus, the voltammograms recorded for

TPU are consistent with the formation of charged species at unspecific positions, representing a significant difference with respect to P3TMA in which polarons and bipolarons are formed at preferred positions. Inspection of the anodic and cathodic areas indicates that the electroactivity of TPU is 65% lower than that of P3TMA in the first control voltammogram, this value decreasing to 58% after 10 redox cycles. These results indicate that the formation of charged species in TPU through oxidation and reduction processes does not occur at the preferred position, as it is observed for P3TMA.

On the other hand, in PBS the anodic scan of P3TMA presents an anodic shoulder at 0.858 V, while the cathodic scan shows a weak reduction shoulder at 0.095 V. Comparison of the current densities reached in acetonitrile and PBS indicates that the amount of oxidized molecules is significantly higher in the former than in the latter environment. In addition, the ability to store charge is 30% higher in PBS than in acetonitrile. Similarly, the electrochemical stability of TPU:P3TMA nanomembranes is significantly high, as it is evidenced by the estimated LEA values: 21%, 24%, and 23% for the 20:80, 40:60, and 60:40 compositions, respectively. Thus, the LEA for the blends is around 15% lower in PBS than in acetonitrile.

Finally, the LEA is only 23% after 10 redox cycles in PBS, about half of the value observed in acetonitrile. The voltammogram of TPU in PBS is relatively similar to that recorded for P3TMA, showing oxidation and reduction processes at 0.780 and 0.100 V, respectively. The former has been attributed to the irreversible oxidation of polymer chains, while the latter corresponds to the reduction of PBS.

5.4.3. Conclusions

The electronic, electric and electrochemical properties of TPU:P3TMA supported nanomembranes have been examined. Results indicate that the two components of the blend are essential for obtaining nanofilms with suitable properties. TPU plays a crucial role in the film forming step during the spin-coating procedure, providing mechanical integrity to the nanomembranes.

In solution, the band gap is higher for the TPU:P3TMA mixture than for the individual P3TMA, independently of the concentration. In THF, the E_g value of the mixture and P3TMA decreases from 2.59 to 2.28 eV and from 2.62 to 1.89 eV, respectively, when the concentration increases from 0.01 mg/mL to 5 mg/mL. In contrast, the E_g values of the nanomembranes are similar: 2.32 and 2.35 eV for TPU:P3TMA and P3TMA, respectively. This feature has been attributed to the conformational distortions undergone by the P3TMA molecules during the spin-

coating process, which affect not only the packing of the π-conjugated backbone but also the π-conjugation length. Despite this, TPU:P3TMA nanomembranes exhibit semiconductor behaviour similar to that reported for many polythiophene derivatives, which is consistent with the current response observed upon application of a voltage.

C-AFM measurements have been used to characterize the distribution of P3TMA regions in the nanomembranes. The current response across the nanomembrane reflects that the two components are not homogeneously distributed. Furthermore, the electron conduction decreases in some P3TMA-rich regions, which has been attributed to the conformational distortions mentioned above and/or the presence of insulating TPU chains. The average current and conductivity of TPU:P3TMA nanomembranes have been found to range from 0.43 to 1.85 pA and from 2.23×10^{-5} to 5.19×10^{-6} S/cm, respectively. These wide intervals of variation are not only due to an irregular distribution of the doped chains, as typically occurs in CPs, but also due to the inhomogeneous presence of the insulating TPU. Inhomogeneity is also fully consistent with the *I/V* curves associated with the P3TMA-rich domains.

The voltammetric response of TPU:P3TMA nanomembranes is similar to that of P3TMA, the electroactivity of both systems being higher in PBS than in acetonitrile. Consecutive oxidation–reduction cycles produce electrochemical degradation, which is reflected by the loss of electroactivity. This effect is more pronounced in acetonitrile than in PBS in all cases. However, in the former medium the loss of electroactivity is lower for the TPU:P3TMA nanomembrane than for the P3TMA one, while the electrochemical stability of the two systems is similar in the latter medium.

In summary, the results obtained in this work indicate that TPU:P3TMA nanomembranes are excellent candidates for the fabrication of active substrates able to promote cell regeneration through electrical or electrochemical stimuli, which is very useful for different advanced biomedical applications. This represents a significant advance with respect to their recently described application as simple bioactive matrix for cellular adhesion and proliferation.

5.5. Biomedical and Biotechnological Applications

The design of electrically conducting devices for biomedical and biotechnological applications has become a topic of growing interest.[84] For tissue engineering purposes, conducting scaffolds are intended to display similar features (chemical, mechanical, and topological) to those characteristic of the extracellular matrix (ECM) in native tissues, thus performing as an adequate substrate onto which cells are able to attach and communicate. Furthermore, their electrical properties can regulate cellular functions such as adhesion, migration, proliferation, and differentiation via electrical stimulation.[67]

Therefore, this last section summarizes the results obtained from studies conducted to further explore TPU:P3TMA nanomembranes behaviour as biointerfaces. In particular, properties associated with potential biomedical applications (*i.e.* swelling, degradation, biocompatibility, and ability to adsorb extra cellular matrix proteins) have been examined. In an effort to relate the influence of the composition for tailoring purposes, 20:80, 40:60, and 60:40 weight ratios have been compared.

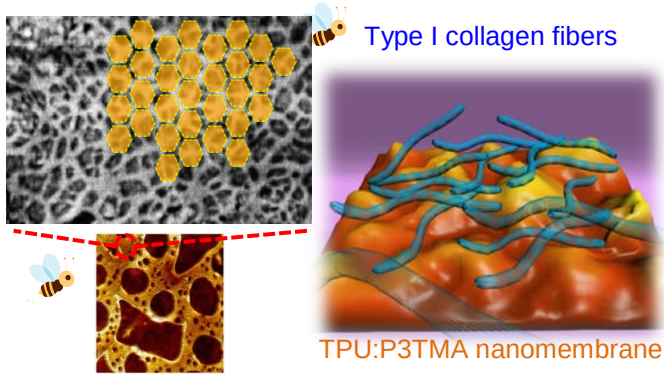

Graphical abstract

5.5.1. Experimental Section

Materials

Lipase F-AP15 (from *Rhizopus oryzae*) was purchased from Sigma (U.S.A.) and used in the enzymatic degradation experiments. For cell culture experiments, Vero and Cos-7 cells were purchased from ATCC (U.S.A.). Dulbecco's phosphate buffered saline solution (PBS) without calcium chloride and magnesium chloride, Dulbecco's modified Eagle's medium (DMEM, with 4500 mg/L of glucose, 110 mg/L of sodium pyruvate, and (2 mM) L-glutamine), penicillin-streptomycin, 3-(4,5-dimethylthiazol-2-yl)-2,5-diphenyltetrazolium bromide (MTT, 97.5%), and trypsin-EDTA solution (0.05% trypsin, 0.02% EDTA) were all purchased from Sigma-Aldrich (USA). Fetal bovine serum (FBS) and trypan blue stain (0.4%) were purchased from Gibco, U.K. Dimethyl sulfoxide (99.0%) was purchased from Panreac Quimica S.A.U. (Spain) and sodium azide (NaN_3, ≥99.5%) from Sigma-Aldrich (U.S.A.).

For the protein adsorption assessment, Type I collagen solution from calf skin (0.1% solution in 0.1 M acetic acid) and Lowry reagent were purchased from Sigma-Aldrich.

Uptake of water

For the swelling experiments, TPU and TPU:P3TMA films were solvent-cast from THF solutions onto Teflon® sheets and slowly dried under vacuum for 3 days. The resulting films were easily separated from the Teflon® sheets and cut into 1 cm × 1 cm pieces. The thickness, which was assessed by profilometry, was ~3 μm in the inner region and ~6 μm on the edges. P3TMA films could not be prepared due to poor film forming characteristics.

Swelling was evaluated by recording the weight increase of the samples placed in vessels filled with 5 mL of PBS solution at 37 °C (four samples for each system). Vessels were closed and sealed with parafilm to prevent water loss by evaporation. Measurements were run over 6 days. At each immersion time, samples were taken out from the oven, carefully dried with delicate task wipers in order to remove water from the surface, and finally weighed on an analytical balance. The percentage of water uptake (WU) was obtained by the ratio between the weight of the samples before and after immersion:

$$WU\ (\%) = \frac{m_w - m_D}{m_D} \times 100 \quad (5.5.1)$$

where m_D is the dried sample mass and m_w the wet sample mass.

Hydrolytic and enzymatic degradation

Degradation studies were carried out on TPU and TPU:P3TMA films prepared by solvent casting onto Teflon® sheets and cut to approximately 1 cm × 1 cm. Films were placed in vials containing 10 mL of phosphate buffered saline solution (PBS) supplemented with 0.1 mg/mL of sodium azide (to prevent contamination) with and without 4 mg/mL of Lipase F-AP15 to evaluate enzymatic and hydrolytic degradation, respectively. Incubation at 37 °C in a shaking incubator set at 100 rpm lasted for a total of 12 weeks. Vials were closed and sealed with parafilm to avoid loss of solution by evaporation, even though the PBS solution was replaced every 48 h. Samples were analyzed after 1, 2, 4, 6, 8, 10, and 12 weeks.

After each immersion time, samples were removed from the solution and gently washed with distillated water. After drying under vacuum for several days at room temperature, films were weighed. Degradation was quantitatively monitored as weight loss (WL, in %) of the films by applying the following formula:

$$WL = \frac{m_0 - m_t}{m_0} \times 100 \quad (5.5.2)$$

where m_0 is the weight of the film before the degradation assay and m_t is the weight of the film after exposure to the degradation medium.

Cellular adhesion and viability

All cellular assays were performed using Vero and Cos-7 cells, which are epithelial- and fibroblast-like, respectively, from African green monkey kidney tissue. These carcinogenic cells were selected because they can be cultured easily in the presence of serum. Cells were cultured in DMEM high glucose supplemented with 10% FBS, penicillin (100 units/mL), and streptomycin (100 µg/mL). The cultures were maintained in a humidified incubator with an atmosphere of 5% CO_2 and 95% O_2 at 37 °C. Culture media were changed every 2 days. When the cells reached 80 − 90% confluence, they were detached using 1−2 mL of trypsin (0.25% trypsin/EDTA) for 5 min at 37 °C. Finally, cells were re-suspended in 5 mL of fresh medium, and their concentration was determined by counting with a Neubauer camera using 0.4% trypan blue as a vital dye.

TPU, P3TMA, and TPU:P3TMA (20:80, 40:60, and 60:40 compositions) nanomembranes were prepared by spin-coating on steel AISI 316 pieces of 1 cm^2, and then they were placed in plates of 24 wells and sterilized using UV light for 15 min in a laminar flux cabinet. Controls were simultaneously performed by culturing cells on the surface of the tissue culture polystyrene (TCPS) plates and steel plates. For adhesion assays, an aliquot of 50 µL containing 5×10^4 cells was deposited on the nanomembrane of each well. Then, cell attachment to the nanomembrane surface was promoted by incubating under culture conditions for 30 min. Finally, 500 µL of the culture medium were added to each well. After 24 h, nonattached cells were washed out, while attached cells were quantified. For viability assays, the 50 µL aliquots deposited on each well contained 2×10^4 cells. Quantification of viable cells was performed after 7 days of culture.

Cell adhesion and viability were evaluated by the colorimetric MTT [3-(4,5-dimethylthiazol-2-yl)-2,5-diphenyltetrazolium bromide] assay, which determines the cell viability.[46] Specifically, 50 µL of MTT solution (5 mg/mL in PBS) was added to each well. After 3 h of incubation, samples were washed twice with PBS and stored in clean wells. In order to dissolve formazan crystals, 1 mL of DMSO/methanol/water (70/20/10% v/v) was added. Finally, the absorbance at 540 mm was measured using a UV−vis spectrophotomether (UV-3600, Shimadzu). The resulting viability results were normalized to TCPS control as relative percentages. Results were derived from the average of four replicates (n = 4) for each independent experiment.

Type I collagen adsorption: sample preparation and quantitative test

ITO (0.5×1.0 cm^2) and glass (square pieces of 1.3 cm^2 area) supported nanomembranes were incubated with type I collagen following the next procedure, which is based on the producer recommendations. A water drop (100 µL) was deposited onto the substrate to hydrate its surface and allow uniform protein dispersion. Then, 10 µL of as-received 1 g/L type I collagen weak acid solution was added, thus diluting the solution 10-fold as recommended by the producer (0.1 g/L) in situ on the nanomembrane surface. The low concentration collagen solution was not used directly because by following our procedure we could hydrate the nanomembrane surface before the protein binding step and expect to get a more uniform collagen dispersion throughout the sample.

Collagen adsorption was allowed to take place for 1 h at room temperature. After, 400 µL of water were added to prevent evaporation during the prolonged incubation step, and nanomembranes were incubated in the collagen solution

overnight at room temperature. Then, the samples were thoroughly washed with distilled water to remove any not adsorbed collagen. Type I collagen adsorption was quantitatively determined by the Lowry microassay. Samples were prepared in triplicate.

Contact angle

Contact angle measurements were obtained using the water drop method. Images of 0.4 µL distillated water drops on the nanomembrane surfaces were recorded after stabilization with the equipment OCA 15EC (DataPhysics Instruments GmbH, Filderstadt), six times for each sample. The software SCA20 was used to analyze the images and acquire the contact angle value.

ANOVA and Tukey tests were performed to determine the statistical significance of contact angle, cell viability, and collagen adsorption results. A confidence level of 95% ($p < 0.05$) was considered.

Scanning electron microscopy (SEM)

Cells and collagen fibrils adsorption were observed using a Focused Ion Beam Zeiss Neon40 scanning electron microscope equipped with an energy dispersive X-ray (EDX) spectroscopy system and operating at 5 kV. All samples were previously coated with a carbon layer of 6 − 10 nm thickness using a K950X Turbo Evaporator to prevent sample charging problems. Before the carbon coating, samples covered with cells were fixed in a 2.5% glutaraldehyde PBS solution (pH = 7.2) overnight at 4 °C. Then, they were dehydrated by washing in an alcohol battery (30°, 50°, 70°, 90°, 95°, and 100°) at 4 °C for 30 min per wash. Finally, samples were air-dried and sputter-coated with carbon.

5.5.2. Results and Discussion

Swelling

Generally, transfer processes can occur at the material−tissue interface when materials contact biological systems. For instance, fluid can move into the biomaterial device thus leading to an increase of volume, a process known as swelling. The study of this phenomenon is of high importance since water is the most important and primary driver for biointeractions, and the scaffold water absorption capacity is crucial in cell regeneration applications. Besides, swelling can

affect profoundly the behaviour of the biomaterial, causing large and continual deformations and deterioration of its mechanical properties. Therefore, the water uptake test has been used to evaluate the TPU:P3TMA films swelling properties from a quantitative point of view, special attention being paid to the influence of the composition.

Figure 5.5.1 displays the variation of the water uptake values against the immersion time for TPU and TPU:P3TMA solvent-casted films. Films with the higher content of P3TMA, that is, 20:80 and 40:60 TPU:P3TMA, displayed a swelling rate that increased almost linearly for the first 24 h, reaching values that are slightly constant for the rest of the swelling period (*i.e.* 24% ± 2% and 18% ± 2%, respectively). During the first 24 h, the water uptake curve for 60:40 TPU:P3TMA films rises up to a swelling ratio of 9% ± 2%, and from that point onward, the water uptake occurs at a much slower pace. It is important to remark that the speed at which the saturation is reached depends mostly on the thickness of the sample, the kinetics of diffusion, and the temperature. Interestingly, TPU films show the highest swelling ratio during the first 3 h, with a maximum at 11% ± 2%. However, the value decreases to 7% ± 1% after 16 h and remains practically constant and similar to the water uptake displayed by 60:40 TPU:P3TMA films.

A linear relationship between the water uptake value and the immersion time is linked to the diffusion of water in the amorphous zones of the polymer. As calorimetric results evidenced, all TPU:P3TMA blends samples exhibited the formation of two amorphous phases with different compositions. In addition to that, water molecules penetrate to void spaces left at the boundaries of the phases.

TPU films undertake severe water absorption at the earlier stages of the swelling process, which induces rupture of intramolecular hydrogen bonds, leading to relaxation movements within TPU polymeric chains. Before reaching the final equilibrium plateau, these movements resulted in a structural rearrangement of the polymeric chains during a transition step in which water can be ejected.

It can be noted that for all samples the equilibrium plateau is well established after 36 h. In general, swelling increases with P3TMA content. Indeed, at the end of the swelling period, water absorption is approximately twice for 40:60 and 20:80 TPU:P3TMA (21% ± 1% and 24% ± 1%, respectively) than for TPU and 60:40 TPU:P3TMA (9% ± 2% and 13% ± 1%, respectively). These results suggest that, in general, the swelling ability of TPU:P3TMA blends is suitable for their use as biomaterials. Accordingly, the three investigated compositions show a water uptake ability that is expected to affect favourably cellular regeneration through the formation of biointeractions in which water plays a crucial role. Furthermore,

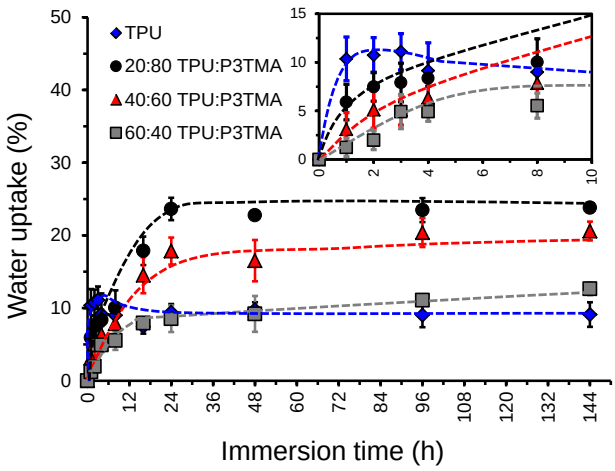

Figure 5.5.1. Variation of the water uptake (in %) against the immersion time (in hours) for TPU and TPU:P3TMA films. Inset shows the swelling during the first 10 hours of immersion. Dashed lines were added manually to help following data progression.

measured water absorption capacities indicate that the all blends will undergo hydrolytic degradation, even though this is expected to be higher for the 20:80 and 40:60 blends than for the 60:40 and pure TPU compositions (as it has been corroborated in the next section). The process of swelling and its mechanism are decisive to design biomaterial devices with a proper subsequent degradation which relies on the molecular processes involved, that is, penetration of water molecules to void spaces and relaxation of the polymeric matrix segments. By tailoring the TPU:P3TMA composition, several degradation rates can be expected according to the water uptake ratio.

Hydrolytic and enzymatic degradation

Effective mimicking of the extracellular matrix (ECM) requires CP-based tissue scaffolds to be both biodegradable and biocompatible to minimize the inflammatory reaction in a tissue that hosts the biomaterial device. TPU:P3TMA films have been subjected to degradation processes, which can provoke scissions at the backbone of the polymer chains, to assess their suitability for clinical applications as tissue scaffolds.

Figure 5.5.2a represents the temporal evolution of the weight loss (WL) measured for TPU and TPU:P3TMA films during 12 weeks of immersion in PBS

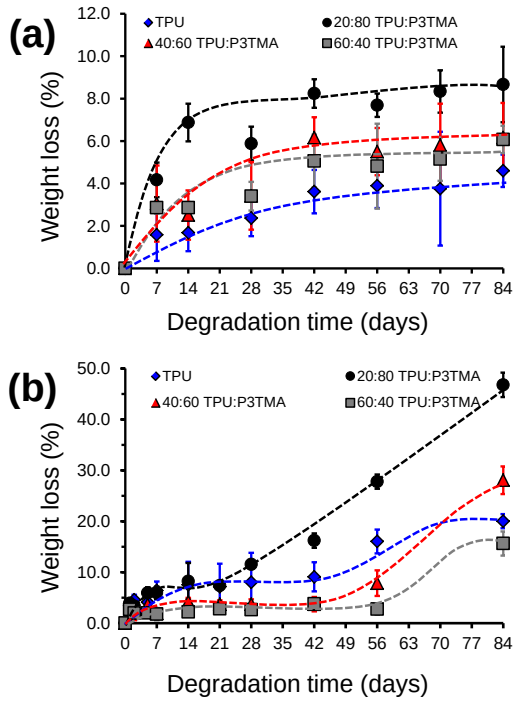

Figure 5.5.2. Weight loss of pure TPU and TPU:P3TMA films immersed in (a) PBS solution and (b) Lipase-containing PBS solution. Dashed lines were added manually to help following data progression.

solution. The hydrolytic degradation of TPU:P3TMA samples proceeds at a higher rate than that of TPU samples and depends on the P3TMA content. Thus, degradation of the 20:80 blend, which exhibits WL=9% ± 2% after 12 weeks of immersion in PBS, occurs significantly faster than that of the 40:60 and 60:40 films, both with a WL=6% ± 1% after 12 weeks. This behaviour is fully consistent with the water uptake results discussed in the previous subsection (Figure 5.5.1.) and should be attributed to the relatively partial miscibility between TPU and P3TMA.

On the contrary, the weight of TPU films decreases slowly during the first 6 weeks of immersion, remaining practically unaltered at WL ≈ 4% after such a period of time. The hydrolytic stability of TPU indicates that penetration of water into films is very limited and the weight loss displayed in Figure 5.5.2a corresponds to the first stages of surface degradation rather than to the bulk degradation processes. Moreover, the hydrolytic resistance shown by the commercial TPU used in this work is fully consistent with that recently observed for other thermoplastic

polyurethanes tuned by incorporating higher concentration of biodegradable soft segments.[85,86] Thus, the hydrolytic degradation of TPU is known to take place through the hydrolysis of the ester groups of the polyester soft segment.[87] Figure 5.5.2b displays the temporal evolution of the weight loss measured for TPU and TPU:P3TMA films during 12 weeks of immersion in the Lipase-containing solution. As it can be seen, the enzyme clearly enhances significantly the degradation process for all the compositions. Again, the P3TMA content influences the enzymatic degradation rate.

The 20:80 TPU:P3TMA blend exhibits the higher weight loss during the degradation period, escalating from WL=8% ± 4% at week 2 to WL=47% ± 2% after 12 weeks of immersion in PBS solution with Lipase. Interestingly, the weight loss evolution for 20:80 TPU:P3TMA films is similar to that shown by TPU films during the first quarter of the immersion period. However, the blend starts a severe fragmentation process after only 3 weeks, which leads to a dramatic increase in the weight loss value that is ascribed to a critical loss of mechanical properties. Although TPU films also evidence a rising trend, this is much steadier since films are able to retain their mechanical properties. The final WL value for TPU is 20% ± 1% after 12 weeks of immersion.

Within this context, it should be emphasized that 40:60 and 60:40 blends present a similar weight loss behaviour during the first half of the immersion period by showing practically equal WL values, even though this is slightly lower than those reported for TPU and 20:80 TPU:P3TMA films. Similarly, at week 6 there is a considerable increase in the weight loss for 40:60 and 60:40 TPU:P3TMA films, which rise from 4% ± 1% each to 28% ± 3% and 16% ± 2%, respectively.

TPU films behaviour is consistent with the surface mechanism reported for TPUs when exposed to lipase,[88] typical of enzymatic attack,[89] whereas for TPU:P3TMA films it depends on the amount of P3TMA. Specifically, the presence of P3TMA hinders the degradation processes for 40:60 and 60:40 blends by possibly preventing the access to cleavage points in the TPU molecular chains during the enzymatic attack, until a point is reached at which the loss of mechanical properties prevails. On the other hand, the degradation process is fully controlled by the loss of mechanical features in the case of the 20:80 TPU:P3TMA films.

Therefore, biodegradation results reveal that the TPU matrix is essential to provide mechanical integrity to CP-based tissue scaffolds, while specific compositions of TPU:P3TMA films behave not only as a semiconductor but also as a biodegradable material.

Biocompatibility

A key factor when developing CP-based devices to be attractive candidates as tissue scaffolds is their biocompatibility and immunogenity. Bearing that requirement in mind, the biocompatibility of TPU:P3TMA nanomembranes has been assessed by cell adhesion and viability tests. Moreover, the response of 20:80, 40:60, and 60:40 TPU:P3TMA towards Vero and Cos-7 cellular lines has been compared with those of TPU and P3TMA. Two substrates, TCPS and steel, were used as control in all adhesion and viability assays.

Quantitative results for cell adhesion assays are displayed in Figure 5.5.3a. The number of Vero and Cos-7 cells adhered to the surface of the TPU:P3TMA nanomembranes is higher than that of P3TMA thin films. Indeed, cellular adhesion onto TPU:P3TMA increases with decreasing content of P3TMA. This tendency is more evident in the case of Vero cells. The adhesion of both Vero and Cos-7 on the surface of TPU nanomembranes is the most favoured, comparable to the TCPS control result, whereas steel shows the worst behaviour as supportive matrix for cellular adhesion.

After 7 days of culture, the cellular activity on the materials was re-evaluated. Cellular viability results, which are included in Figure 5.5.3b, show an appreciable increment in the cellular colonization for all the TPU:P3TMA compositions. Evaluation of this increment with respect to the viability of the adhered cells indicates that the preference of Vero and Cos-7 cells is higher for the 20:80 and 60:40 compositions, respectively, even though in absolute terms the biocompatibility exhibited by TPU:P3TMA blends increases with the concentration of TPU. In contrast, P3TMA inhibits cell viability, which may be attributed to the presence of $FeCl_3$ in the polymeric matrix. This oxidizing agent, which is in excess during the polymerization process, has been reported to provoke cytotoxicity in MCF-7 cells[63] and to induce lipid peroxidation in cell membranes.[64] Finally, the viability of Vero and Cos-7 cells in TPU increases slightly, while that of steel remains practically unaltered (Cos-7 cells) or increases (Vero cells). In order to corroborate the cytotoxicity of $FeCl_3$, viability assays were performed using TPU films previously immersed in an aqueous solution containing 20 μg/mL $FeCl_3$. Results showed that viability of Vero and Cos-7 cells decreases by 23% ± 3% and 31% ± 6%, respectively, in relation with the values obtained for TPU without $FeCl_3$.

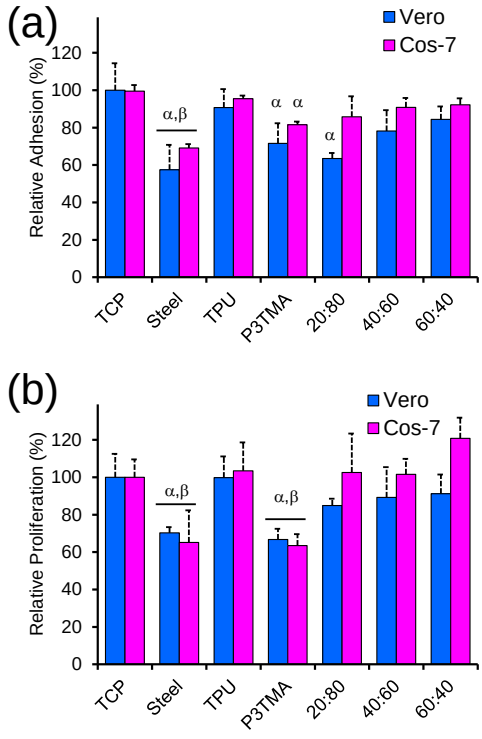

Figure 5.5.3. Relative cellular (a) adhesion and (b) viability of Vero (blue bars) and Cos-7 (purple bars) cell lines on TPU, P3TMA and TPU:P3TMA (20:80, 40:60 and 60:40) nanomembranes. Greek letters on the columns refer to significant differences ($p < 0.05$) using the ANOVA and Tukey's test: α *vs*. TCPS; β *vs*. steel.

Viability results obtained for TPU:P3TMA blends can be related with the surface structure of the nanomembranes through two key features. The first refers to the roughness, in general cell viability after 24 h and 7 days increases with the surface roughness. Thus, the formation of connection sites between the cells and the surface of TPU:P3TMA nanomembrane becomes easier on nanomembranes with higher roughness. Second, cell viability increases with the miscibility of the two components in the nanomembranes. Thus, results indicate that the partial miscibility is higher for the 60:40 and 40:60 compositions than for the 20:80, which is fully consistent with quantitative results obtained for cell adhesion and viability assays. Overall, TPU:P3TMA interfaces can be considered as effective bioactive platforms.

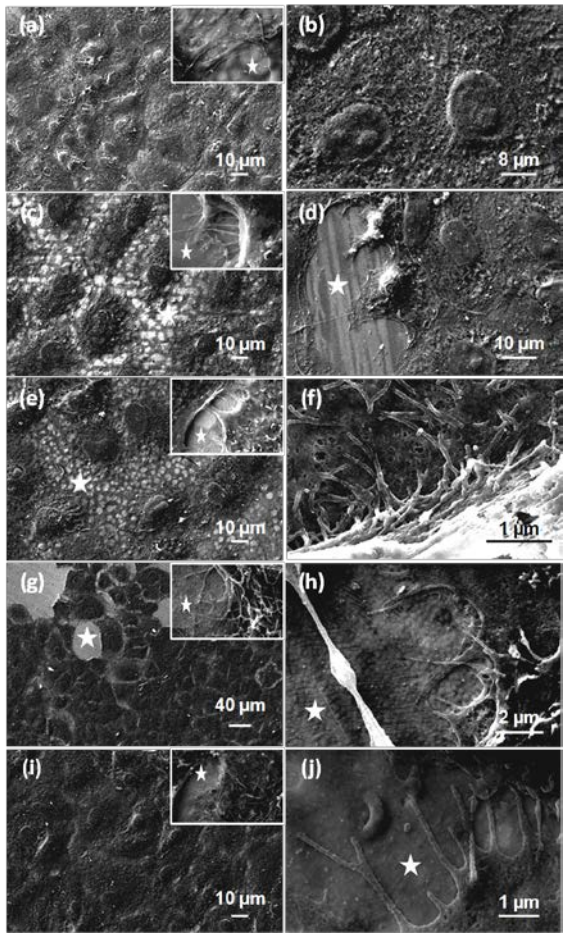

Figure 5.5.4. SEM micrographs of Vero cells cultured on the surface of TPU (a and b), P3TMA (c and d), 20:80 TPU:P3TMA (e and f), 40:60 TPU:P3TMA (g and h) and 60:40 TPU:P3TMA (i and j) substrates. Left images show adhesion results (inset: interactions between cells and the substrate surface) and right images show colonization results after 7 days. Surface without cells is indicated with a star (★).

SEM micrographs displayed in Figure 5.5.4 show the characteristics of Vero cells cultured onto the surface of TPU, P3TMA, and TPU:P3TMA nanomembranes. Inspection of the SEM micrographs for TPU:P3TMA nanomembranes (Figure 5.5.4e−j) indicates that the receptivity of the surface to colonization through cellular viability of adhered cells increases with the content of TPU. Although large microdomains without cells are identified on the surface of 20:80 TPU:P3TMA thin films, cells are widely spread on the surface of 40:60 and, especially, on 60:40

TPU:P3TMA nanomembranes. In addition, the connection sites between the cells and the surface of TPU:P3TMA are clearly identified in Figure 5.5.4h and j. These consist of actin filaments, which are known as filopodia, oriented toward the film surface for local adhesion. It is worth noting their similarities with the formation of cellular monolayers on the surface of TPU (Figure 5.5.4a-b). In general, there is a broad spreading of cells on TPU, even though very small domains without cells are occasionally detected (Figure 5.5.4a, inset). In contrast, bare P3TMA frequently shows micrometric surface areas without cells (Figure 5.5.4c,d), which is consistent with the relatively low cell viability found for this P3TMA as compared to that of TPU and TPU:P3TMA nanomembranes. Indeed, the biological behaviour of P3TMA is considerably worse than that observed for other biocompatible polythiophene derivatives, as, for example, PEDOT.[90] SEM micrographs of Cos-7 adhered to the surface of the different substrates (not shown) were fully consistent with these trends. In all, these results indicate that TPU:P3TMA nanomembranes are not only biocompatible but also stimulate the cellular viability.

At this stage, a close examination of the results described so far designate the 40:60 TPU:P3TMA composition the most adequate composition for further assays since it achieved a balance between good electrochemical properties and suitable swelling, biodegradation, and biocompatible features. Besides, it presents good mechanical and conducting properties, exhaustively studied at the nanometric scale (previous sections). Concretely, the next subsection discusses the behaviour of 40:60 TPU:P3TMA nanomembranes as bioactive platforms by analyzing their protein adsorption response.

Type I collagen adsorption

Protein adsorption onto surfaces is the first stage that takes place in cell adhesion and viability processes when biomaterials contact living cells in the appropriated media. Type I collagen is the most common collagen isotype. In addition, type I collagen is one of the most abundant extra cellular matrix (ECM) proteins, which is known to bind fibronectin, another important ECM protein, for early adhesion.[91] Various types of interactions may influence the adsorption of collagen, which depend both on the protein and the surface of the sample. Surface properties like wettability, linked to topography, roughness, and chemistry, have been shown to alter protein adsorption and conformation, influencing the cellular response of a material.[92,93]

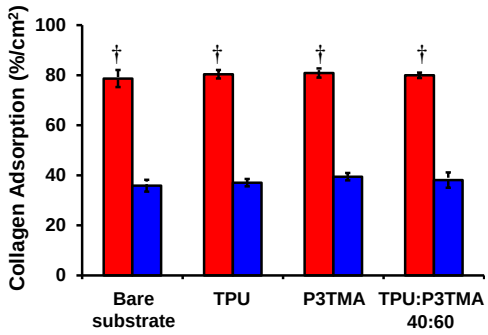

Figure 5.5.5. Type I collagen adsorption quantitative data (%/cm²). Ultrathin nanomembranes spin-coated onto ITO (red bars) and glass coverslips (blue bars). (†) Tukey's test, $p < 0.05$ *vs* respective glass support.

Quantitative data on type I collagen adsorption onto ITO and glass supported TPU, P3TMA, and 40:60 TPU:P3TMA nanomembranes are displayed in Figure 5.5.5. Protein adsorption onto bare ITO, glass coverslips, and TCPS were used as control. As depicted, no significant difference on the collagen adsorption (79−81 %/cm²) was obtained regardless of the sample surface when ITO was employed as substrate. Surprisingly, the adsorption of collagen on the bare glass coverslip, which was also used as the control substrate, is 36% ± 2%/cm², less than the half of the value obtained for ITO substrate. This value is similar to that obtained for TCPS, 29% ± 1%/cm² (not included in Figure 5.5.5). In order to further understand this difference, contact angle measurements were carried out. The contact angles determined for the bare substrates are 75° ± 3° and 68° ± 2° for ITO and glass, respectively, showing a difference of 7°.

Following these observations, the protein adsorption test was repeated for nanomembranes spin-coated onto glass coverslips to determine the influence of the substrate. Again, values of adsorbed collagen showed no significant difference regardless of the nanomebmrane composition, but all were almost half the values obtained for ITO-supported nanomembranes (37 – 39 %/cm²). This behaviour could be attributed to the differences in the surface wettability of the different substrates. Contact angle values determined for TPU, P3TMA, and 40:60 TPU:P3TMA nanomembranes spin-coated onto ITO are 81°± 1°, 82°± 1°, and 81°± 2°, respectively; whereas when spin-coated onto glass, values slightly decrease to 78°± 2°, 79° ± 2°, and 79° ± 1°, respectively. All these values are higher than the corresponding bare substrate contact angle value, regardless the nanomembrane.

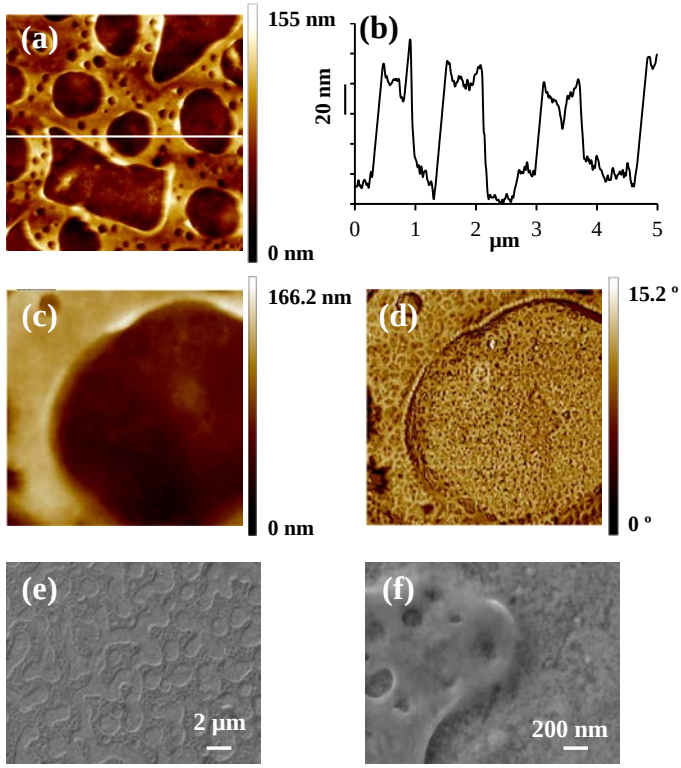

Figure 5.5.6. SEM-AFM images of type I collagen adsorbed onto 40:60 TPU:P3TMA nanomembrane: (a) height image 5×5 µm²; (b) cross-sectional data from (a); (c) height image 1×1 µm²; (d) phase image 1×1 µm² of (c); (e) and (f) SEM images (14 kX and 150 kX, respectively).

Therefore, TPU, P3TMA, and TPU:P3TMA supported nanomembranes exhibit the same degree of wettability when spin-coated onto the same substrate. Once type I collagen was adsorbed onto a glass substrate, the contact angle test was repeated and the value dropped from 68° ± 2° to 36° ± 2°. The same decreasing tendency was observed for the nanomembranes, although in a lower extent for the TPU (69° ± 4°), and in a greater extent for P3TMA and 40:60 TPU:P3TMA (50° ± 2° for both materials). Finally, it is important to highlight that TPU, P3TMA, and 40:60 TPU:P3TMA nanomembranes behave as active surfaces for the adsorption of collagen.

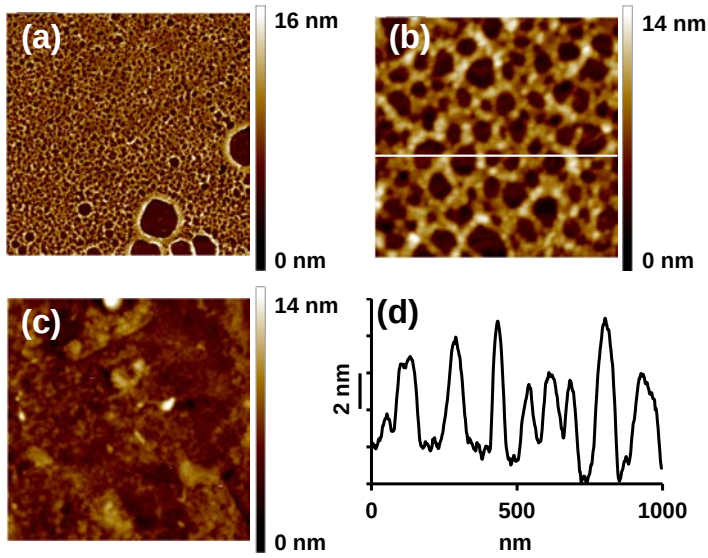

Figure 5.5.7. AFM images of type I collagen adsorbed onto TPU: (a) height image 5×5 μm²; (b) height image 1 μm²; (c) height image ×1 μm²; and (d) cross-sectional data from (b).

In general, factors that monitor the ECM protein adsorption mechanism, such as the substrate wettability, are not understood completely yet.[94-97] Inspection of the bare substrates (ITO and glass) response indicates that the amount of adsorbed protein decreases with the contact angle value (*i.e.* hydrophobicity promotes adsorption of type I collagen). Nevertheless, analysis of the TPU, P3TMA, and 40:60 TPU:P3TMA responses evidence that such simple and direct correlation cannot be applied. It becomes evident that other factors apart from wettability can affect the protein adsorption mechanism.

SEM and AFM images were recorded for type I collagen adsorbed onto ITO supported nanomembranes (TPU, P3TMA, and 40:60 TPU:P3TMA) and bare ITO substrate to evaluate the influence of the topography on the adsorbed collagen structures. Type I collagen adsorbed onto 40:60 TPU:P3TMA nanomembranes surface forms at least two layers (Figure 5.5.6). More specifically, the top layer exhibits a pseudoregular honeycomb 2D network (Figure 5.5.6a) that shows cavities with different sizes. The larger pits present diameters of 1.2 ± 0.7 μm, while the smaller ones, which are uniformly distributed throughout the surface, exhibit a diameter of 194 ± 55 nm. Besides, cross-section profile data (Figure 5.5.6b) indicate depths of about 73 nm. A careful inspection of a smaller area of the surface (Figure

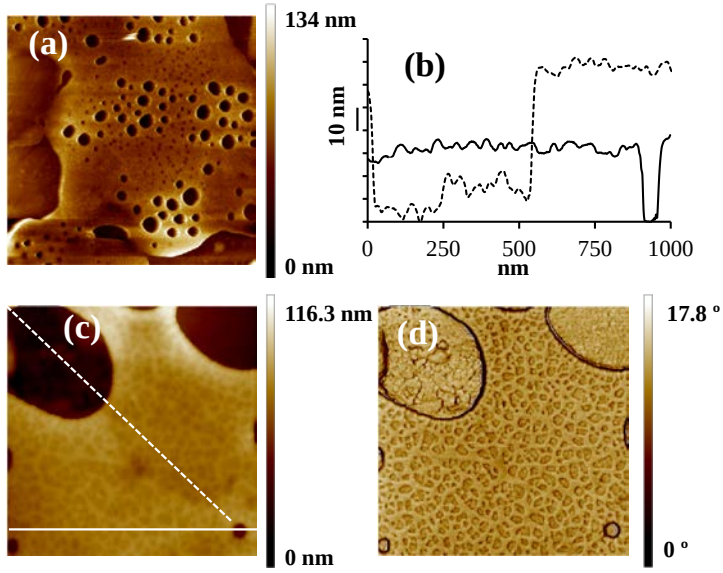

Figure 5.5.8. AFM images of type I collagen adsorbed onto P3TMA: (a) height image 5×5 μm²; (b) cross-sectional data from (c); (c) height image 1×1 μm²; and (d) phase image 1×1 μm² of (c).

5.5.6c,d) reveals a fibril structure on the top layer. The bottom layer is similar to the top one although collagen adopts a much more compact configuration.

Type I collagen topography adsorbed onto 40:60 TPU:P3TMA nanomembranes shares some similarities with that adsorbed on TPU and P3TMA nanomembranes surfaces (Figure 5.5.7 and 5.5.8, respectively). Specifically, it also adopts a two layer arrangement. However, type I collagen adsorbed onto TPU results in a matrix with a regular distribution of pits on the top layer (Figure 5.5.7a-b), whereas the bottom layer is more uniform and adsorbed collagen is closely packed together (Figure 5.5.7c). Cross-section profile data show that the depth of such pits ranges from 5 to 8 nm (Figure 5.5.7d). On the contrary, for the P3TMA nanomembrane, the collagen adsorbed top layer is more dense and with smaller cavities, which display height steps of 46.4 nm in some regions, and diameters of 227 ± 46 nm and are distributed throughout the surface (Figure 5.5.8a-b). Moreover, the fibrous collagen matrix on the top layer (Figure 5.5.8c-d) resembles that for 40:60 TPU:P3TMA, while the bottom layer is comparable in all three samples, regardless of the nanomembrane composition.

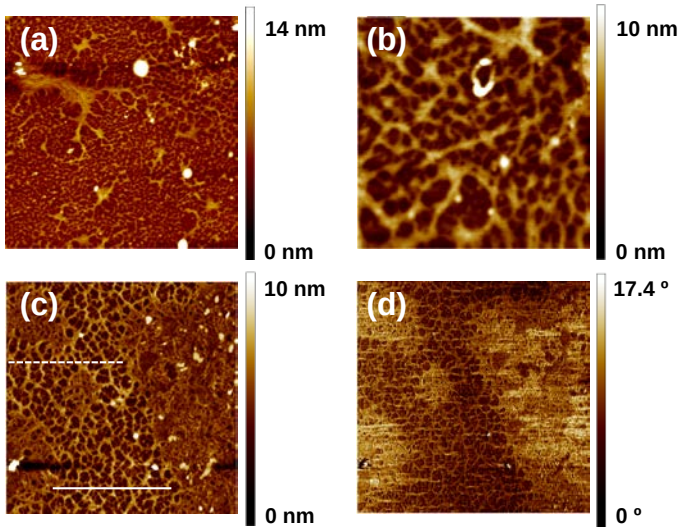

Figure 5.5.9. AFM images of type I collagen adsorbed onto ITO: (a) height image 5×5 μm^2; (b) height image 1×1 μm^2; (c) height image 3×3 μm^2; and (d) phase image 3×3 μm^2 of (c).

Finally, Figure 5.5.9 displays images for type I collagen deposited onto bare ITO. In this case, type I collagen topography differs from the one observed for the TPU:P3TMA supported nanomembranes. Particularly, fibrils appear to be arranged on branching structures and the collagen matrix does not cover the entire surface since ITO substrate is detected (dark regions in phase images, Figure 5.5.9d). Moreover, these fibrils result in a porous collagen matrix with several high density regions, in which collagen shows a more compacted structure and fibrils are not distinguished. Cross-section profiles reveal that the diameter and height of the fibrils varied from 40 to 140 nm and from 1 to 4 nm, respectively.

Furthermore, SEM images (Figure 5.5.10) allowed us to identify the type I collagen fibrous structures adsorbed onto the several surfaces.

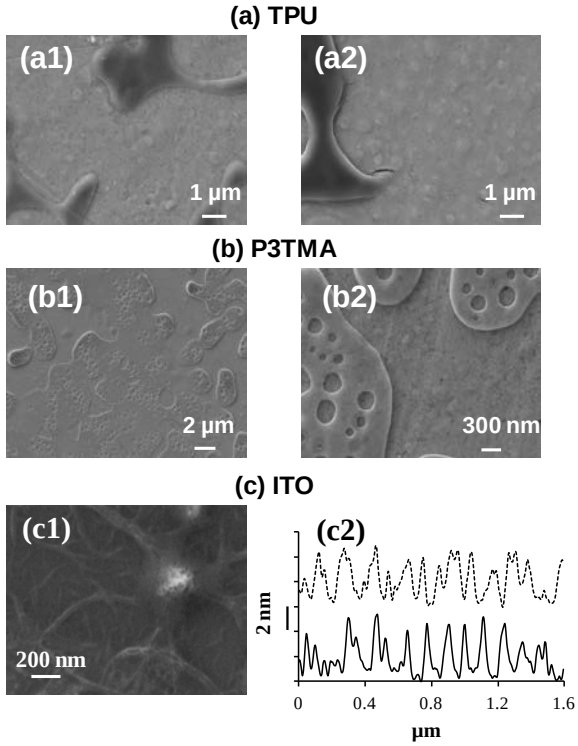

Figure 5.5.10. SEM images of type I collagen adsorbed onto (a) TPU, (b) P3TMA nanomembranes and (c) bare ITO. For TPU: (a1) and (a2) images at 30 kX. For P3TMA: images at (b1) 14 kX and (b2) 80 kX. For bare ITO: (c1) image at 152 kX and (c2) cross-sectional data from Figure 5.5.9c.

Results are in good agreement with the previous AFM observations. As a general consideration, morphological observations by SEM and AFM showed that the sample surface affects the adsorbed type I collagen structure and distribution. Type I collagen adsorbed onto the nanomembranes hides the original surface by entirely covering it. The final adsorption topography varies slightly depending on the nanomembrane film, which may be influenced by both the chemical composition and also the roughness of the nanomembranes.[98] In general terms, collagen matrix presents a 2D honeycomb-like morphology when adsorbed onto TPU, P3TMA, and 40:60 TPU:P3TMA nanomembranes, in opposition to the results obtained for the bare ITO substrate. As it has been stated elsewhere,[99,100] honeycombed collagen matrixes are suitable scaffolds for biological and biomedical purposes.

5.5.3. Conclusions

The influence of the composition on the properties, especially those oriented toward biomedical applications, of TPU:P3TMA nanomembranes has been examined. The water uptake observed for TPU:P3TMA films decreases with the concentration of TPU, even though it is relatively high in all cases. Consistently, hydrolytic and enzymatic degradation increase with the P3TMA content. This behaviour should be attributed to the phase separation between TPU and P3TMA regions, which facilitates the access of water molecules to the bulk. The response of TPU:P3TMA to lipase-containing PBS solutions is that expected from biodegradable materials. Furthermore, viability assays show that TPU:P3TMA are biocompatible blends, the viability of cells increasing with the concentration of TPU in the composition.

Studies on type I collagen reveal that the amount of adsorbed protein does not depend on the chemical composition of the organic nanomembranes, but on the substrate used as support. However, the surface that contacts the protein affects the morphology of adsorbed collagen matrices. Collagen onto bare ITO forms fibrils, while honeycomb-like structures are observed when the protein is in contact with organic nanomembranes, the dimension and regularity of such organization depending on the chemical nature of the nanomembrane.

The behaviour of TPU:P3TMA nanomembranes, especially the 40:60, as electroactive substrates for biomedical applications is very good. Thus, these hydrophilic blend nanomembranes are biodegradable and promote cell growth. In addition, adsorption of collagen results in the formation of honeycomb protein matrices with potential applications. Current research is oriented toward cell regeneration onto 40:60 TPU:P3TMA bioactive substrates through electrical stimulation for different advanced biomedical applications.

5.6. References

[1] L. Moroni, J. R. de Wijn, C.A. van Blitterswijk, *J. Biomater. Sci., Polym. Ed.* **2008**, *19*, 543.
[2] K. M. Nampoothiri, N.R. Nair, R. P. John, *Bioresour. Technol.* **2010**, *101*, 8493.
[3] M.A. Woodruff, D. W. Hutmacher, *Prog. Polym. Sci.* **2010**, *35*, 1217.
[4] K. Odelius, P. Plikk, A.-C. Albertsson, *Biomacromolecules* **2005**, *6*, 2718.
[5] F. Khan, S.R. Ahmad, *Macromol. Biosci.* **2013**, *13*, 395.
[6] R. Parenteau-Bareil, R. Gauvin, Berthod, *Materials* **2010**, *3*, 1863.
[7] R. D. Breukers, K. J. Gilmore, M. Kita, K. K. Wagner, M. J. Higgins, S. E. Moulton, G. M. Clark, D. L. Officer, R. M. I. Kapsa, G. G. Wallace, *J. Biomed. Mater. Res., Part A* **2010**, *95A*, 256.
[8] S. Lee, G. D. Moon, U. Jeong, *J. Mater. Chem.* **2009**, *19*, 743.

[9] A. Subramanian, U. Krishnan, S. Sethuraman, *J. Mater. Sci.: Mater. Med.* **2012**, *23*, 1797.
[10] L. J. del Valle, F. Estrany, E. Armelin, R. Oliver, C. Alemán, *Macromol. Biosci.* **2008**, *8*, 1144.
[11] M. R. Abidian, D. H. Kim, D. C. Martin, *Adv. Mater.* **2006**, *18*, 405.
[12] L. Xia, Z. Wei, M. Wan, *J. Colloid Interface Sci.* **2010**, *341*, 1.
[13] A.-D. Bendrea, L. Cianga, I. Cianga, *J. Biomater. Appl.* **2011**, *26*, 3.
[14] N. K. Guimard, N. Gomez, C. E. Schmidt, *Prog. Polym. Sci.* **2007**, *32*, 876.
[15] J. Matovic, Z. Jaksic, P. Grober, D. Bruckner, C. Hellmich, H. B. Schmiedmayer, H Stachelberger, I. C. Gebehuber, *in "Bionic (Nano)Membranes" in "Biomimetic – Material, Structures and Processes"*, Springer-Verlag, Berlin, **2011**.
[16] R. Vendamme, A. Onoue, A. Nakao, T. Kunitake, *Natur. Mater.* **2006**, *5*, 494.
[17] H. Watanabe, T. Muto, T. Ohzono, A. Nakao,T. Kunitake, *J. Mater. Chem.* **2009**, *19*, 2425.
[18] H. Watanabe, T. Ohzono, T. Kunitake, *Macromolecules* **2007**, *40*, 1369..
[19] H. Watanabe, Kunitake, *Adv. Mater.* **2007**, *19*, 909.
[20] H. Watanabe, T. Ohzono, T. Kunitake, *Polym. J.* **2008**, *40*, 379.
[21] T. Fujie, N. Matsutani, M. Kinoshita, Y. Okamura, A. Saito, S. Takeoka, *Adv. Funct. Mater.* **2009**, *19*, 2560.
[22] C. Y. Jiang, X. Y. Wang, R. Gunawidjaja, Y. H. Lin, M. K. Gupta, D. L. Kaplan, R. R. Naik, V. V. Tsukruk, *Adv. Funct. Mater.* **2007**, *17*, 2229.
[23] F. Toshinori, O. Yosuke, T. Shinji, *Adv. Mater.* **2007**, *19*, 3549.
[24] Y. Okamura, K. Kabata, M. Kinoshita, D. Saitoh, S. Takeoka, *Adv. Mater.* **2009**, *21*, 4388.
[25] E. Armelin, A. L. Gomes, M. M. Pérez-Madrigal, J. Puiggalí, L. Franco, L. J. del Valle, A. Rodíguez-Galán, J. S. de C. Campos, N. Ferrer-Anglada, C. Alemán, *J. Mater. Chem.* **2012**, *22*, 585.
[26] M. M. Pérez-Madrigal, E. Armelin, L. J. del Valle, F. Estrany, C. Alemán, *Polym. Chem.* **2012**, 3, 979.
[27] G. Oertel, L. Abele, *in "Polyurethane Handbook: Chemistry, Raw Materials, Processing, Application, Properties"*, 2nd ed. Munich etc.: Hanser; **1994**.
[28] B. Pukánszky Jr., K. Bagdi, Z. Tóvölgyi, J. Varga, L. Botz, S. Hudak, T. Doczi, B Pukánszky, *Eur. Polym. J.* **2008**, *44*, 2431.
[29] M. Kotal, S. K. Srivastava, B. Paramanik, *J. Phys. Chem. C.* **2011**, *115*, 1496.
[30] P. S. O. Patrício, H. D. R. Callado, F. A. C. de Oliveira, A. Righi, B. R. A. Neves, G. G. Silva, L. A. Cury, *J. Phys: Condens. Matter.* **2006**, *18*, 7529.
[31] J. Njuguna, K. Pielichowski, *J. Mater. Sci.* **2004**, *39*, 4081.
[32] H. Deligöz, B. Tieke, *Macromol. Mater. Eng.* **2006**, *291*, 793.
[33] A. L. Gomes, J. Casanovas, O. Bertran, J. S. C. C. Campos, E. Armelin, C. Alemán, *J. Polym. Res.* **2011**, *18*, 1509.
[34] L. Gomes, M. B. P. Zakia, J. G. Filho, E. Armelin, C. Alemán, J. S. C. C. Campos, *Polym. Chem.* **2012**, *3*, 1334.
[35] N. Mechau, R. Groeger, A. Prodi-Schwab, R. Schmechel, *J. Appl. Phys.* **2009**, *105*, 054318.
[36] D. Wang, S. Fujinami, K. Nakajima, S. Inukai, H. Ueki, A. Magario, T. Noguchi, M. Endo, T. Nishi, *Polymer* **2010**, *51*, 2455.
[37] D. Wang, X.-B. Liang, Y.-H. Liu, S. Fujinami, T. Nishi, K. Nakajima, *Macromolecules,* **2011**, *44*, 8693.
[38] O. Sahin, N. Erina, *Nanotechnology* **2008**, *19* 445717.
[39] H. Liu, S. Fujinami, D. Wang, K. Nakajima, T. Nishi, *Macromolecules* **2011**, *44*, 1779.
[40] P. Schön, K. Bagdi, K. Molnár, P. Markus, B. Pukánszky, G. J. Vancso, *Eur. Polym. J.* **2011**, *47*, 692.
[41] H. E. Kissinger, *Anal. Chem.* **1957**, *29*, 1702.
[42] T. Akahira, T. Sunose, *Res. Report Chiba Inst. Technol.* **1971**, *16*,22.

[43] M. Stafford, B. D. Vogt, C. Harrison, D. Julthongpiput, R. Huang, *Macromolecules* **2006**, *39*, 5095.
[44] Tahk, H. H. Lee ,D.-H. Khang, *Macromolecules* **2009**, *42*, 7079.
[45] B. O'Connor, E. P. Chan, C. Chan, B. R. Conrad, L. J. Richter, R. J. Kline, M. Heeney, I. McCulloch, C. L. Soles, D. M. DeLongchamp, *ACSNano* **2010**, *4*, 7538.
[46] T. Mosmann, *J. Immunol. Methods* **1983**, *65*, 55.
[47] R. McNeill, N. C. Greenham, *Adv. Mater.* **2009**, *21*, 3840.
[48] J. Jaczewska, A. Budkowski, A. Bernasik, E. Moons, J. Rysz, *Macromolecules* **2008**, *41*, 4802.
[49] X. Han, X. Chen,S. Holdcroft, *Adv. Mater.* **2007**, *19*, 1697.
[50] X. Han, X. Chen, S. Holdcroft, *Chem. Mater.* **2009**, *21*, 4631.
[51] M. E. Nicho, D. Peña-Salgado, P. Altuzar-Coello, *Thin Solid Films* **2010**, *518*, 1799.
[52] Y. Lee, J. K. Kim, C.-H. Chiu, Y.-K. Lan, C.-I. Huang, *Polymer* **2009**, *50*, 4944.
[53] A. Charas, Q. Ferreira, J. Farinhas, M. Matos, L. Alcacer, J. Morgado, *Macromolecules* **2009**, *42*, 7903.
[54] M. A. Ruderer, S. Guo, R. Meier, H.-Y. Chiang, V. Körstgens, J. P. Wiedersich, S. V. Roth, P. Müller-Buschbaum, *Adv. Funct. Mater.* **2011**, *21*, 3382.
[55] J.-S. Kim, P. K. H. Ho, C. E. Murphy, R. H. Friend, *Macromolecules* **2004**, *37*, 2861.
[56] A. C. Arias, N. Corcoran, M. Banach, R. H. Friend, J. D. MacKenzie, W. T. S. Huck, *Appl. Phys. Lett.* **2002**, *80*, 1695.
[57] M. Higgins, S. J. Martin, R. J. Thompson, J. Chappell, M. Voigt, D. G. Lidzey, R. A. L. Jones,M. Geoghegan, *J. Phys.: Condens. Matter* **2005**, *17*, 1319.
[58] C. Lin, E. K. Dimitriadis, *J. Biomech. Eng.* **2007**, *129*, 904.
[59] M. E. Dokukin, I. Sokolov, *Macromolecules* **2012**, *45*, 4247.
[60] A. V. Tivanski, J. E. Bemis, B. B. Akhremitchev, H. Liu, G. C. Walker, *Langmuir* **2003**, *19*, 1929.
[61] S. E. Morgan, R. Misra, P. Jones, *Polymer* **2006**, *47*, 2865.
[62] D. Wang, S. Fujinami, H. Liu, K. Nakajima, T. Nishi, *Macromolecules* **2010**, *43*, 9049.
[63] E. Laqué-Rupérez, M. J. Ruiz-Gómez, L. de la Peña, L. Gil, M. Martínez-Morillo, *Bioelectrochemistry* **2003**, *60*, 81.
[64] K. J. Woollard, S. Sturgeon, J. P. F. Chin-Dusting, H. H. Salem, S. P. Jackson, *J. Biol. Chem.* **2009**, *284*, 13110.
[65] P.R. Bidez, S. Li, A. G. MacDiarmid, E.C. Venancio, Y. Wei, P.I. Lelkes, *J. Biomater. Sci., Polym. Ed.* **2006**, *17*, 199.
[66] C. Rincón, J. C. Meredith, *Macromol. Biosci.* **2010**, *10*, 258.
[67] I. Jun, S. Jeong, H. Shin, *Biomaterials* **2009**, *30*, 2038.
[68] G. Shi, M. Rouabhia, Z. Wang, L. H. Dao, Z. Zhang, *Biomaterials* **2004**, *25*, 2477.
[69] L. Huang, X. Zhuang, J. Hu, L. Lang, P. Zhang, Y. Wang, X. Chen, Y. Wei, X. Jing, *Biomacromolecules* **2008**, *9*, 850.
[70] J. Y. Lee, C. A. Bashur, C. A.Milroy, L. Forciniti, A.S. Goldstein, C. E. Schmidt, *IEEE T. NanoBiosci.* **2012**, *11*, 15.
[71] C. R. Broda, J. Y. Lee, S. Sirivisoot, C. E. Schmidt, B.S. Harrison, *J. Biomed. Mater. Res., Part A* **2011**, *98A*, 509.
[72] J. M. de Souza, E. C. Pereira, *Synth. Met.* **2001**, *118*, 167.
[73] Y. Jiang, Y. Shen, P. Wu, *J. Colloid Interface Sci.* **2008**, *319*, 398.
[74] J. Kim, S. Cho, S. Choi, S. Baek, D. Lee, O. Kim, S. -M. Park, M. Ree, *Langmuir* **2007**, *23*, 9024.
[75] E. Riedo, H. Brune, *Appl. Phys. Lett.* **2003**, *83*, 1986.
[76] G. G. Min, S.-J. Choi, S. B. Kim, S. -M. Park, *Synth. Met.* **2009**, *159*, 2108.
[77] D.-H. Han, J.-W. Kim, S.-M. Park, *J. Phys. Chem. B* **2006**, *110*, 14874.

[78] A. Fogden, L. R. White, *J. Colloid Interface Sci. 1990*, *138*, 414.
[79] J. Brandrup, E. Immergut, in *Polymer Handbook* 2nd ed. (Eds: John Wiley & Sons), New York, **1997**.
[80] C.-G. Wu, S.-S. Chang, *J. Phys. Chem. B* **2005**, *109*, 825.
[81] H. J. Lee, J. Lee and S.-M. Park, *J. Phys. Chem. B* **2010**, *114*, 2660.
[82] B. Alperson, S. Cohen, I. Rubinstein, G. Hodes, *Phys. Rev. B* **1995**, *52*, R17017
[83] B. Alperson, I. Rubinstein, G. Hodes, *Phys. Rev. B* **2001**, *63*, R081303.
[84] G. G. Wallace, M. J. Higgins, S. E. Moulton, C. Wang, *Nanoscale* **2012**, *4*, 4327.
[85] K. Zukiene, V. Jankauskaite, V Betingyte, A. Baltuanikas, *J. Appl. Polym. Sci.* **2013**, *128*, 2186.
[86] C. Lluch, G. Lligadas, J. C. Ronda, M. Galia, V. Cádiz, *Macromol. Biosci.* **2013**, *13*, 614.
[87] L. A: Bosworth, S. Downes, *Polym. Degrad. Stab.* **2010**, *95*, 2269.
[88] X. G. Gu, J. Wu, P. T. Mather, *Biomacromolecules* **2011**, *12*, 3066.
[89] E. M. Christenson, S. Patel, J. M. Anderson,A. Hiltner, *Biomaterials* **2006**, *27*, 3920.
[90] G. Fabregat, G. Ballano, E. Armelin, L. J. del Valle, C. Cativiela, C. Alemán, *Polym. Chem.* **2013**, *4*, 1412.
[91] J. S. Tjia, B. J. Aneskievich, P. V. Moghe, *Biomaterials* **1999**, *20*, 2223.
[92] N. M. Coelho, C. González-García, M. Salmerón-Sánchez, G. Altankov, *Biotechnol. Bioeng*. **2011**, *108*, 3009.
[93] N. M. Coelho, M. Salmerón-Sánchez, G. Altankov, *Biomater. Sci.* **2013**, *1*, 494.
[94] E. Gurdak, P. G. Rouxhet, C. C. Dupont-Gillain, *Colloids Surf. B* **2006**, *52*, 76.
[95] Z. Liang, C. Zhou, R. Zeng, H. Cai, Z. Guo, *Scanning* **2010**, *32*, 104.
[96] E. Gurdak, J. Booth, C. J. Roberts, P. G. Rouxhet, C. C. Dupont-Gillain, *J. Colloid Interface Sci.* **2006**, *302*, 475.
[97] E. Gurdak, C. C. Dupont-Gillain, J. Booth, C. J. Roberts, P. G. Rouxhet, *Langmuir* **2005**, *21*, 10684.
[98] S. E. Woodcock, W. C. Johnson, Z. Chen, *J. Colloid Interface Sci.* **2005**, *292*, 99.
[99] J. George, J. Onodera, T. Miyata, *J. Biomed. Mater. Res., Part A* **2008**, *87A*, 1103.
[100] G. George, Y. Kuboki, T. Miyata, *Biotechnol. Bioeng*. **2006**, *95*, 404.

CHAPTER 6

SENSITIVE THERMAL TRANSITIONS OF P3TMA NANOINTERFACE USING THE BIMETALLIC EFFECT

Summary

The phase separation observed in both P3TMA:PE44 and TPU:P3TMA systems has been attributed to the conventional parameters typically found in thin films (*e.g.* polymer–polymer interactions, solubility of the polymers in the solvent and, especially, the spin-coating process) and also to the crucial role played by the substrate–film–air interfaces due to the ultra-thin nature of the membranes.

Inspired by this fact, the present chapter explains the studies carried out to provide understanding and rationalize the thermal results described in the previous chapters.

For that, a sensitive nanocalorimetric technology based on microcantilever sensors has been used to determine the glass transition of P3TMA interfaces. These thermal measurements were performed at *Mecwins S.L.*[1] In addition, the study has been completed with atomistic molecular dynamics simulations on models that represent the bulk powder and the ultra-thin films, which were implemented by Dr. D. Curcó[2].

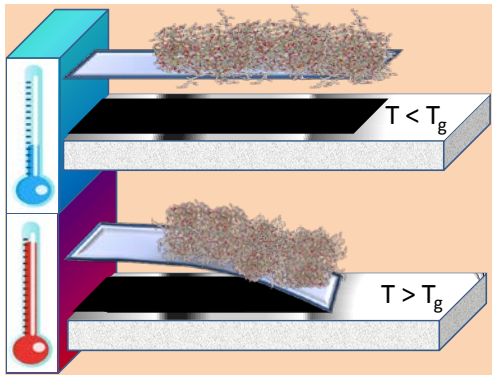

Graphical abstract

Publication derived from this work:

O. Ahumada, M. M. Pérez-Madrigal, J. Ramirez, D. Curcó, C. Esteves, A. Salvador-Matas, G. Luongo, E. Armelin, J. Puiggalí, C. Alemán, *Rev. Sci. Instrum.* **2013**, *84*, 053904.

[1]Parque Científico de Madrid PTM, Tres Cantos, Madrid.

[2]Departament d'Enginyeria Química, UPC.

6.1. Introduction

Miniaturized calorimeters (*i.e.* nanocalorimeters), which are predominantly based on silicon chips, are designed to perform nanoscale thermal analysis with high sensitivity on extremely small amounts of sample (nanograms, picoliters) under very fast operating rates.[1–3] Reduced sample size means reduced sample consumption, which demands higher resolution and better thermal isolation. Temperature can be measured using integrated thermocouples or by determining changes in the temperature coefficient of resistance of the heater element.[4] An optical technique has been recently developed to calibrate the thermal response of the chips, avoiding errors in the extrapolation from low to high temperatures.[5] Although the use of nanocalorimetry started in the 1970s by determining the heat capacity of very thin films,[6] essential progress in both development and applications has been made in the last decade. Therefore, nanocalorimetry is still considered as an emerging field. Recently, nanocalorimetry has been applied to a variety of materials including metal, ceramics, polymers, and biomolecules.[4,7,8] Thus, nanocalorimeters have been adapted to carry out unusual small-scale measures, for example, interfacial reactions,[9,10] phase transitions,[7] nanoscale biologial reactions,[2] folding-unfolding processes in proteins,[11] and absorption phenomena in ultra-thin films.[12]

Sensitive calorimeters based on the cantilever technology represent an alternative to the chip-based nanocalorimeters. Thus, the cantilever deflection resulting from the absorption of heat, either at a localized spot on the cantilever or along its entire length, can be modeled to determine thermal transitions. The small size and heat capacity of microcantilevers make them remarkable nanocalorimeters with picojoule sensitivities and milliseconds time resolution.[13] This represents a significant improvement with respect to conventional differential scanning calorimeters (DSCs) and infrared detection techniques, which typically show sensitivities of 0.2 mJ and 6 nJ, respectively, and time resolutions on the order of the second.[14] For example, cantilever-based nanocalorimetry has been used to measure enthalpy changes in picoliter volumes of solid samples during phase transitions of *n*-alkanes,[13] to detect molecules adsorbed on the layer coating of the cantilever when it is catalytically active,[15] and to determine the thermo-mechanical properties of polymeric samples in the vicinity of their glass transition temperature (T_g).[16]

Regarding the latter, Jung *et al.*[16] used the variations in the resonance frequency and deflection of the cantilever with the temperature to determine the change in the effective modulus and volume of polystyrene when the temperature was close to the T_g.

In this work, we present a technology developed to determine thermal transitions, in particular the T_g of ultra-thin polymeric samples with a mass scale lower than the picogram. This promising technology named SCALA CAL, which opens the door to measure thermal transitions at the molecular level, represents a significant improvement in relation to currently available nanocalorimetric techniques. The work has been organized as follows. In section 6.2, the technology is described after providing a brief theoretical background. After this, the technology is evaluated at the proof concept level using nylon 6 (section 6.3). Finally, in section 6.4 the new technology has been used to evaluate the T_g of P3TMA, a soluble semiconducting polymer with important applications in nanotechnology. Specifically, section 6.4 has been distributed in three parts. The first provides a description of the experimental methods, the second compares the glass transition determined in samples with a mass of $\sim 10^{-13}$ g with that obtained from samples with $\sim 10^{-3}$ g, and the last part shows a comprehensive Molecular Dynamics (MD) simulation study to rationalize the experimental observations at the molecular level.

6.2. Theoretical Background and Technology

Cantilever-based sensing technologies are emerging platforms with the advantage of being relatively cheap to mass-produce. Micro-fabrication technologies have facilitated not only the design of microcantilevers optimized for various types of sensing applications but also the manufacturing of large arrays of cantilevers, making it possible to use various sensors in parallel. These cantilever-based sensors have been proved to be quite competitive with current sensing technologies because of their high sensitivity, fast response time, and small size (*i.e.* from μm to nm).[17–20]

SCALA is the acronym for "Scanning Laser Analyzer," a recently developed technology for the optical read-out of cantilevers.[21,22] The aim of this work consists of the application of this technique, which allows the user to readout the profiles of microcantilever arrays using a picometric mass-scale and a processing speed of about ten cantilevers per second, on the analysis of the thermal properties of ultra-thin polymeric samples. The application has ended up with a new technology based on SCALA named SCALA CAL. The improvement in the scanning laser analyzer

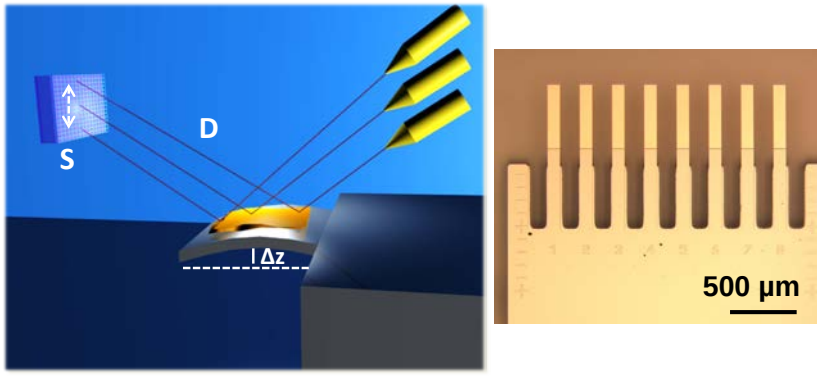

Figure 6.2.1. Schematic representation of the experimental setup used to determine thermal properties, and optical image of a microcantilever chip.

consists in the implementation of a calorimetric chamber containing a thermoelectric cooler and a cartridge heater. These elements are capable of sweeping the chamber's temperature from −50 up to 220 °C by flowing thermostatized N_2 to the sample. A holder, with multiple thermometer probes, is placed inside the chamber for a better mapping of the temperature. All the measurements are performed in nitrogen environment to avoid the oxidation of the sample. The temperature control is regulated by software realized in a LabVIEW environment, which allows to acquire data and to send commands to hardware.

The readout technique combines the optical beam deflection method and the automated two-dimensional scanning of a single laser beam by voice-coil actuators. Figure 6.2.1 shows a schematic representation of the experimental setup. A 1 mW laser diode is mounted on two perpendicular linear voice coil actuators, which allow two-dimensional non-hysteretic displacement over a range of several millimeters at speeds up to 10 mm/s and with an accuracy of 100 nm. One of the scanning axes is oriented parallel to the cantilever longitudinal axis. The cantilever array is illuminated by the laser beam and a two-dimensional linear position detector (PSD) is arranged to collect the reflected beams. A convergent lens is used to decrease the spot size of the laser on the cantilevers to 5–10 µm, approximately.

Location and characterization of cantilever sensors is carried out using TRACKER, an algorithm based on the recognition of reflected intensity patterns. This capability of SCALA allows the user to characterize a single sensor or an array of them in a fully automated process. Moreover, the algorithm is able to recognize both commercial and self-made mechanical sensors.

A change in the local slope at the cantilever surface results into a displacement of the reflected laser spot on the PSD, which is denoted *S* (Figure 6.2.1). Thus, the displacement recorded by the PSD during the scan of the cantilever is described by

$$S(x) \cong 2D\frac{dz}{dx}(x) + x\cos\beta \tag{6.2.1}$$

where *z(x)* is the cantilever profile along its longitudinal axis, *D* is the distance between the cantilever and the PSD, and β is the angle between the incident laser beam and the cantilever normal at its rest position. The second summand in equation (6.2.1) accounts for the effect of the laser beam displacement, which is generally small compared to the first summand associated to the slope variations. The cantilever profiles are obtained by integrating equation (6.2.1):

$$z(x) = \frac{1}{2D}\int_0^x S(x')dx' - \frac{1}{4}\frac{x^2}{D}\cos\beta \tag{6.2.2}$$

This technology is attracting a growing interest due to their capabilities for high sensitivity, label-free detection, and small sample consumption.[23,24] These properties are inherent in the nature of the nanomechanical response and the tiny size of the microcantilevers, with areas of ~1000 μm². In addition, these sensors are scalable as the microfabrication techniques admit routine fabrication of arrays with tenths of cantilevers, which is very convenient for platforms devoted to complex chemical and biological analyses.

Cantilevers can be used as precise thermometers or calorimeters by exploiting the *bimetallic effect*.[25] This phenomenon refers to the measurable bending produced by temperature changes in bimaterial systems, like a substrate covered on one side by another material coating.[26,27] Similarly, coated microcantilevers undergo a deflection (*i.e.* differential stress) as a result of temperature changes due to the thermal expansion coefficient difference between the coating material of the cantilever and the cantilever itself.[28] The deflection of a rectangular cantilever, Δz, produced by a change in temperature, ΔT, is expressed as[29]

$$\Delta z = \frac{3}{t_c^2 K}(\alpha_b - \alpha_c)(t_b + t_c)l^2\Delta T \tag{6.2.3}$$

where l is the rectangular cantilever's length, α_b/α_c and t_b/t_c are the thermal expansion coefficient and the thicknesses of the cantilever beam/cantilever's coating, respectively.

K is expressed as:

$$K = 4 + 6\left(\frac{t_b}{t_c}\right) + 4\left(\frac{t_b}{t_c}\right)^2 + \frac{E_b}{E_c}\left(\frac{t_b}{t_c}\right)^3 + \frac{E_c}{E_b}\left(\frac{t_c}{t_b}\right) \quad (6.2.4)$$

where E_b and E_c are the Young's modulus of the cantilever and of the coating, respectively.

The application of micromechanical sensors to thermal phase transition analyses of phase transitions is based on its compact size combined with very high sensitivity and short response times. The sensitivity of a bimaterial micromechanical sensor is ~1 pJ, while the response time is ~1 ms.[30] Accordingly, the limit of this application corresponds to enthalpy changes within attomolar quantities of material.

When a polymeric coating is heated around a thermodynamic transition (*i.e.* the temperature of the film is close to the T_g or the melting temperature, T_m), parameters such as the Young's modulus and the thermal expansion coefficients undergo abrupt changes. The effects produced by such changes on the mechanical deflection of the cantilever are recognized as the thermodynamic transitions fingerprints using equations 6.2.3 and 6.2.4.

6.3. Proof of Concept: Nylon 6

The effect of changes in the Young's modulus and the thermal expansion coefficient on the deflection of the cantilever has been evaluated using equation (6.2.3). Figure 6.3.1 represents the deflection curve calculated using the technical data sheet of commercial nylon 6 from DSM Engineering Plastics (PA6, Aukulon F-9183). The T_g and T_m of nylon 6 are visualized as changes in the slope at 57 °C and 217 °C, respectively. In region I of the curve, the cantilever bends linearly due to the fact that the thermal expansion coefficient of the polymer and the silicon are different.

The slope of the deflection curve changes at the glass transition temperature (region II), which combines pronounced jump of the thermal expansion coefficient and a decay of the Young's modulus. Finally, the Young's modulus practically vanishes at the melting temperature (region III), producing another drastic change in the deflection. The T_g and T_m values obtained from the deflection curve are in good agreement with those reported in the technical data sheet of Aukulon F-9183 (67 and 207 °C, respectively), which were determined from the bulk using conventional DSC methods.

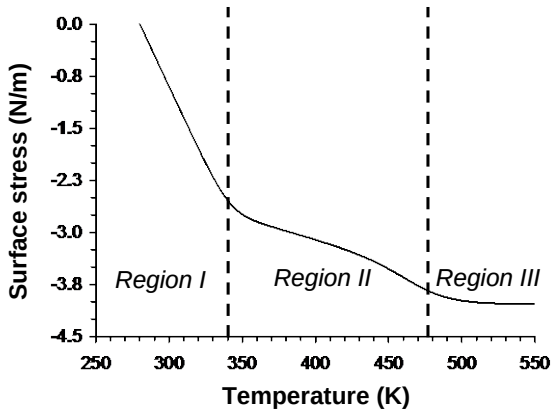

Figure 6.3.1. Calculation of the deflection curve against the temperature (Eq. 6.2.3) for commercial nylon 6.

6.4. Application to P3TMA

The technology described above has been applied to poly(3-thiophene methyl acetate) (P3TMA), a soluble polythiophene derivative. The choice of this semiconducting material is based on its already described nanotechnological application as bioactive platforms for tissue engineering when combined with PE44 and TPU polymers (Chapters 4 and 5, respectively). Furthermore, P3TMA dispersed as nanoparticles was found to be a powerful anticorrosive additive of organic coating, showing better protecting abilities than zinc phosphate compounds.[31] As a result, this material was patented for its application as anticorrosive pigment to low volatile organic compounds solvent-based epoxy and alkyd formulations.[32,33] Accordingly, comparison of the thermal properties between bulk P3TMA powder and samples in which the P3TMA chains are organized in nanometric length-scales deserves consideration.

6.4.1. Experimental and Computational Methods

P3TMA was synthesized by oxidative coupling following the procedure described by Kim *et al*.[34] After removal of residual oxidant and oligomers, P3TMA was a power soluble in different organic and polar solvents at room (25 °C) and high temperature (60 °C).[35]

Conventional DSC measurements were obtained using a TA Instruments Q100 series equipped with a refrigerated cooling system (RCS) operating at temperatures

between −90 °C and 600 °C. Experiments were conducted under a flow of dry nitrogen with a sample weight of approximately 5 mg, calibration being performed with indium. Heating runs were performed at different temperatures, ranging from 1 to 20 °C/min, with samples previously quenched from the melt state by cooling at the maximum rate allowed by the equipment. Determination of the T_g was carried out with the TA-Universal Analysis software furnished with the instrument.

Samples for nanocalorimetric measurements were prepared by spin-coating a solution of P3TMA in THF onto previously cleaned microcantilevers. In order to achieve the maximum affinity between the polymer and the surface of the substrate, different cleaning procedures and spinning conditions (*i.e.* concentration of the solution, spin-coater speed and time, and temperature) were tested using silicon squares obtained from silicon wafer as substrate. The main characteristics of this silicon substrate, which is cheaper than cantilevers, are similar to those of the chips (*i.e.* 99.9% Si), resulting very appropriate for all trials. Four different cleaning procedures were tested: (i) immersion in a piranha solution (*i.e.* a mixture of sulfuric acid and hydrogen peroxide) for 30 min; (ii) immersion in water mixed with detergent from Procter & Gamble for 30 min; (iii) exposure to UV ozone cleaner from Novascan; and (iv) immersion in acetone, a heavy duty degreaser, and then into isopropanol, 15 min in each solvent. Optimal microscopy analysis indicated that (ii) produced the most homogeneous and continuous films. The cleaning action of the detergent, which acts as surfactant in conjunction with water, should be attributed to the micelles that surround grease particles causing them to disperse in water. Regarding the spinning conditions, they were optimized to get a thickness lower than 100 nm at both the center and border regions of the microcantilevers. After trial experiments, cantilevers for calorimetric measurements were coated at room temperature applying a spin-coater speed of 1200 rpm for 60 s to a 5 mg/mL P3TMA solution. Accordingly, SCALA CAL has been used for thermal characterization of P3TMA, which was deposited using such spinning conditions on commercial arrays of 8 cantilevers from Concentris GmbH cleaned with a mixture of water and detergent. Nine chips, which represent a total of 72 different sensors, were measured. The rate of heating was 1 °C/min. Together with every functionalized sensor, a control (*i.e.* a cantilever where no polymer has been deposited) was measured.

Optical microscopy observations were performed using a Zeiss Axioskop 40 Pol light polarizing microscope equipped with a Linkam temperature control system configured by a THMS 60. Micrographs were taken with a Zeiss Axios MRC digital camera. Scanning electron microscopy (SEM) studies were carried out using a

Focused Ion Beam Zeiss Neon40 scanning electron microscope equipped with an energy dispersive X-ray (EDX) spectroscopy system operating at 3.0 kV. Samples were mounted on a double-sided adhesive carbon disc and sputter-coated with a thin layer of carbon to prevent sample charging problems. Atomic force microscopy (AFM) images were obtained in tapping mode with a Molecular Imaging PicoSPM using a NanoScope IV controller under ambient conditions. RMS roughness was determined using the statistics application and tools of the NanoScope Analysis software version 1.20. The scan window size was 5×5 μm^2 and the row scanning frequency was set to 1 Hz.

MD simulations were carried out with the NAMD program[36] using a molecular system constituted by 40 identical chains, each one involving 15 repeating units with head-to-tail polymer linkages and an alternated disposition (*i.e. anti*-conformation). Periodic boundary conditions using the nearest image convention were applied in the three (*i.e.* x-, y-, and z-edges of the simulation box) and two directions (*i.e.* x- and y-edges of the simulation box) to represent the bulk powder (BP model) and the ultra-thin coating (UTC model) samples, respectively. The potential energy was computed using the AMBER force-field,[37] all the bonding and van der Waals parameters required for the DPs under study being taken from Generalized AMBER force-field (GAFF).[38] Atomic charges were adjusted using the Restrained Electro-Static Potential (RESP) strategy.[39] Atom-pair distance cutoffs were applied at 12 Å to compute van der Waals and electrostatic interactions. Bond lengths involving hydrogen atoms were constrained using the SHAKE algorithm with a numerical integration step of 2 fs.[40]

Initial microstructures for the BP and UTC models were constructed using a recently developed computational tool to represent the packing of polythiophene derivatives.[41] In order to identify the changes induced by the glass transition at the microscopic level, each system was simulated at three temperatures, T=20 °C, 40 °C, and 80 °C. Before running the production trajectories at such temperatures, the starting microstructures were equilibrated using the following strategy: 1×10^4 steps of steepest descent energy minimization were performed in order to relax conformational and structural tensions. Next, different consecutive rounds of MD runs were performed in order to equilibrate the density, temperature, and pressure. Specifically, all atoms of the system were submitted to 2 ns of steady heating until the target temperature was reached (*i.e.* 20 °C, 40 °C, or 80 °C), 4 ns of *NVT*-MD at the desired temperature (thermal equilibration) followed by 10 ns of density relaxation (*NPT*-MD). Both temperature and pressure were controlled by the weak coupling method of the Berendsen thermobarostat,[42] using a time constant for the

heat bath coupling and a pressure relaxation time of 1 ps. After this, each *NPT*-MD production run at the desired temperature and 1 atm was 10 ns long. The numerical integration step was set to 1 fs, while the coordinates of the production run were saved every 2000 steps (2 ps interval).

6.4.2. Determination of the Glass Transition

Figure 6.4.1a displays the heating trace of P3TMA samples (5 mg) at a heating rate of 1 °C/min. Before DSC measurement, samples were quenched from the melt state in order to increase the amorphous content and the glass transition signal. This is critical due to the low heating rate and the semicrystalline character of the material directly obtained from synthesis (melting point: 111.3 °C; X-ray diffraction peak at 1.17 nm). The DSC heating trace shows a clear change on the base line allowing us to unambiguously determine the glass transition temperature at T_g = 61.8 °C.

On the other hand, P3TMA was solubilized in THF and deposited by spin-coating onto the surface of cantilever sensors for measurements. The thickness of the coating, which was determined by scratch AFM, was found to be 47 nm. The densities measured for the bulk powder and the nanofilm samples, which were determined by the flotation method from water+ethanol mixtures, were 0.976 and 1.000 g/cm^3, respectively. Thus, the change from three mesoscopic dimensions to one nano-dimension combined with two macroscopic dimensional produces an increment of 2.5% in the density of P3TMA. This effect, which is expected to increase with the reduction of the nanomembrane thickness, should be attributed to the influence of the film-air interface in the molecular chains. Finally, the surface of the sensor covered by P3TMA was estimated to be around ~10 000 μm^2 in average (Figure 6.4.2a). According to these parameters, the mass of polymer deposited on each cantilever sensor is ~10^{-13} g, which represents a mass reduction of ten orders of magnitude with respect to conventional DSC measurements.

Figure 6.4.1b displays the deflection curves recorded using three different microcantilever sensors. As it can be seen, the three show a change in the slope at approximately the same temperature reflecting the reproducibility of the technique. Moreover, Figure 6.4.1b displays the second run recorded for two of the sensors, which evidence a variation in the slope of the profile just at the same position. A control sensor has been also included in Figure 6.4.1b to show the behaviour of a non-functionalized cantilever. Figure 6.4.1c shows the ramp during the heating process (*i.e.* 1 °C/min).

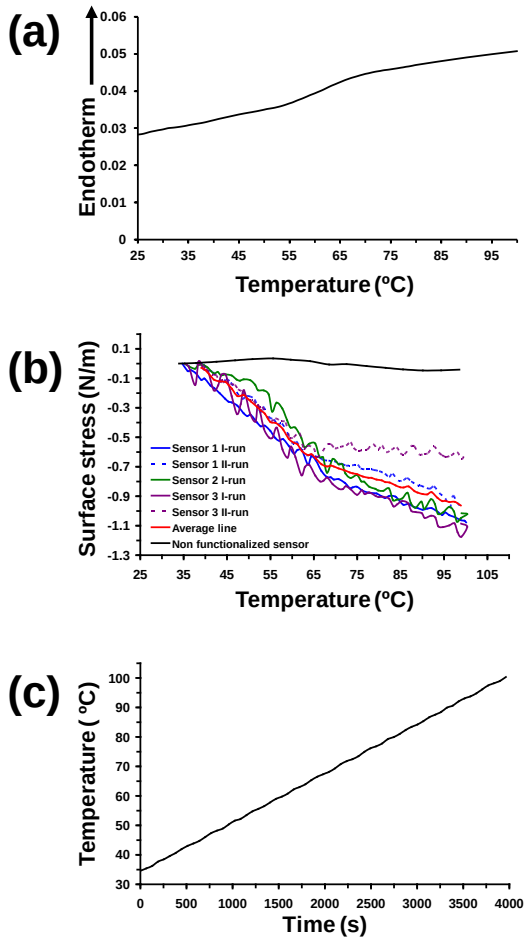

Figure 6.4.1. (a) DSC heating trace (1 ºC/min) showing the glass transition associated with P3TMA bulk powder samples. (b) Deflection curve measured using microcantilever sensors for ultra-thin P3TMA samples. The graphic includes the first run for tree sensors, the second run for two sensors, the average profile and a control sensor where no functionalization has been performed (c) ramp of temperature.

The value of the glass transition of P3TMA at the nanometric scale, T_g=67 °C, has been determined using the average curve (Figure 6.4.1b). This represents an increment of 5.2 °C with respect to the bulk samples used for conventional DSC measurements at the same heating rate.

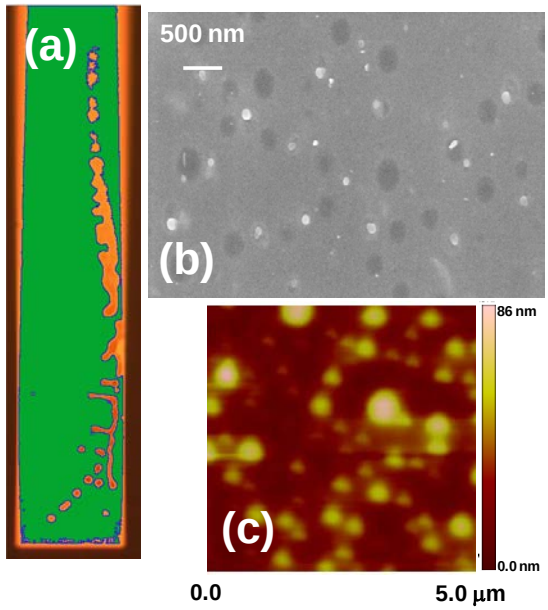

Figure 6.4.2. (a) Optical image showing the surface of the microcantilever covered by P3TMA. P3TMA ultra-thin coating: SEM (b) and AFM (c) images.

The effect of cantilever-polymer film interface on measurements of surface stress values has not been considered in this work. This is because such interface has been considered to behave ideally. More specifically, the molecular weight of P3TMA is high enough to transmit the stress along the contact points between the substrate and the polymer chains (*i.e.* formed crystals or entanglements), generating the force to bend of the cantilever. Above the percolation threshold, this behaviour will be maintained even with few contact points. Indeed, the bending of the cantilevers with the temperature through biomaterial effect indicates by itself a good affinity between the polymer and the substrate. Accordingly, despite neglecting the interface effects, the stress transmitted by the cantilever allows to distinguish two regimes, below and above the T_g. Moreover, it should be mentioned that the surface stress versus temperature trend displayed in Figure 6.4.1b has been tested in more than 70 sensors, a very similar shape being obtained in all cases.

Powder sample used for DSC experiments and ultra-thin film deposited in the cantilever sensors present very different morphologies. Figure 6.4.3 displays optical

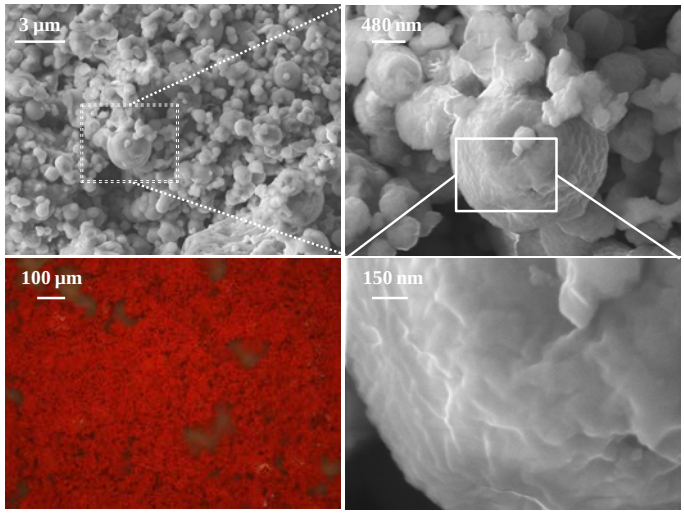

Figure 6.4.3. Optical image (20 X, bottom left) and SEM micrographs (15 kX top left; 60 kX top right; and 220 kX (bottom right) of P3TMA bulk powder samples.

and SEM images of powder samples, which present a granular morphology made of spherical particles with diameters ranging from ~0.5 to ~2.0 µm. On the other hand, SEM micrographs (Figure 6.4.2b) and AFM images (Figure 6.4.2c) of the ultra-thin films evidence spherical nanoaggregates of small (40–70 nm) and medium (250–340 nm) size, bigger particles detaching from the polymer surface. The RMS roughness measured for the P3TMA film is 47 nm. These morphological differences suggest that the 5.2 °C increment in the T_g produced by the reduction of the mass scale from ~10^{-3} g to~10^{-13} g is due to a change in the microscopic organization of the polymer molecules. In order to investigate this feature at the atomistic level, MD simulations on model systems mimicking both the bulk and the ultra-thin coating have been carried out.

6.4.3. Molecular Dynamics Simulations

Analysis of the density (Table 6.4.1) reveals significant differences between the BP and UTC models. The density predicted for the BP model varies less than 3% with the temperature, remaining within the 0.989–0.963 g/cm^3 interval. These densities are fully consistent with the value obtained by flotation at room temperature for bulk powder samples (*i.e.* 0.976 g/cm^3). In contrast, the densities calculated for the UTC model at $T < T_g$ were ~1.22 g/cm^3, this value being

significantly higher than that determined for the BP model. This feature is in qualitative agreement with experimental observations (*i.e.* the density of bulk samples was found to be lower than that of nanometric film), even though the theoretical value is overestimated because of the nanodimensional simplicity of the model used for the simulations. Thus, the contribution of the interface effects in the UTC model is over-valued with respect to the nanofilm because the nanodimension is significantly smaller in the former than in the latter. Furthermore, the density predicted for the UTC model decreases ~10% at T=80 °C (*i.e.* 1.148 g/cm^3). These results suggest not only some structural differences between the BP and UTC models, but also some temperature-induced changes in the latter when $T > T_g$.

Differences between the two models are also reflected by the averaged atomic mean square displacement, $\langle \bar{x}_a^2 \rangle$, which is represented in Figure 6.4.4 for the 10 ns of the production simulations at T=20 °C and 80 °C. For the BP model, the values $\langle \bar{x}_a^2 \rangle$ are smaller and similar at the two temperatures. In contrast, this property is one order of magnitude higher for the UTC model at T=20 °C, increasing significantly at T=80 °C.

Table 6.4.1. Average density and end-to-end distance for the BP and UTC models obtained from MD simulations at T=20 ºC, 40 ºC and 80 ºC.

		Bulk powder	**Ultra-thin coating**
Density (g/cm^3)	20 ºC	0.989 ± 0.005	1.275 ± 0.243
	40ºC	0.982 ± 0.007	1.281 ± 0.029
	80ºC	0.963 ± 0.005	1.169 ± 0.027
End-to-end distance (Å)	20ºC	27.86 ± 0.09	27.90 ± 0.11
	40ºC	27.80 ± 0.10	27.84 ± 0.13
	80ºC	26.78 ± 0.10	25.34 ± 0.13

Analysis of the inter-ring S–C^{α}–C^{α}–S (χ_1) and side group C^{β}–C(H_2)–C(=O)–O (χ_2) dihedral angles reveals that the differences between the BP and UTC models essentially refer to χ_1. This is reflected in Table 6.4.2, which summarizes the distribution of χ_1 and χ_2 at T=20 °C and 80 °C. As expected, the most populated conformation at T=20 °C for χ_1 is the *anti*-one, independent of the model (*i.e.* 84.9% and 85.1% for BP and UTC, respectively), even though the population of the *syn*-arrangement is relatively high (*i.e.* 10.9% and 9.0% for BP and UTC, respectively). These results are fully consistent with the rotational profile predicted by quantum mechanical methods for the inter-ring dihedral angle,[43–47] which indicated that the

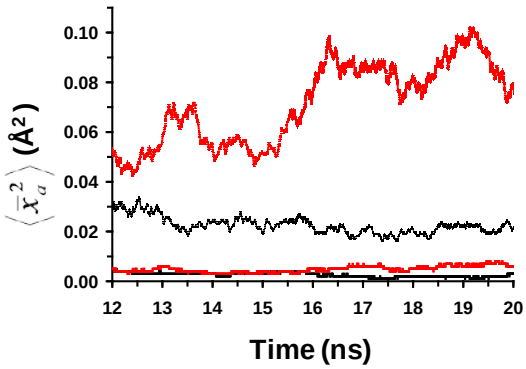

Figure 6.4.4. Temporal evolution of the averaged atomic mean square displacement, $\langle \bar{x}_a^2 \rangle$, for the BP (solid lines) and UTC (dashed lines) models at T= 0 ºC and 80 ºC (black and red, respectively).

syn- conformation is severely destabilized when adjacent substituted thiophene rings show a head-head linkage, but energetically accessible for head-tail and tail-tail linkages. From an electronic point of view, the distortion of the inter-ring dihedral angle from *anti-* to *syn-* destroys the extent of the π-conjugation along the polymer chain. Results obtained from the simulations at T=40 °C (not shown) were practically the same than those at T=20 °C. The population of the *anti* and *syn-*conformations decreases and increases, respectively, upon heating to T=80 °C, even though this change is significantly more important for the UTC model than for the BP one (*i.e.* the population of *syn-* at T=80 °C is 34.2% and 17.8% for the BP and UTC model, respectively).

Table 6.4.2. Distribution of the dihedral angles χ_1 and χ_2 for the BP and UTC models as obtained from MD simulations at T= 20 ºC and 80 ºC.

	Bulk powder				**Ultra-thin coating**			
	T= 20 ºC		T= 80 ºC		T= 20 ºC		T= 80 ºC	
	χ_1	χ_2	χ_1	χ_2	χ_1	χ_2	χ_1	χ_2
30º / 90º	0.5	13.0	0.9	11.0	1.0	14.7	0.9	7.6
90º / 150º	1.4	23.3	1.3	24.3	1.8	23.3	1.6	30.4
150º / -150º	84.9	25.1	76.9	26.6	85.1	24.1	61.1	40.7
-150º / -90º	1.5	25.3	2.2	28.2	2.3	22.6	1.7	22.9
-90º / -30º	0.8	12.4	0.9	8.8	0.8	14.1	0.5	8.3
-30º / 30º	10.9	0.9	17.8	1.1	9.0	1.2	34.2	1.1

Despite such conformational change, the influence of the temperature in the average end-to-end distance, which was calculated using the backbone atoms of the thiophene rings, is relatively small (Table 6.4.1). Thus, the value obtained for the BP and UTC models decreases 1.08 and 2.56 Å, respectively, when the temperature increases from 20 °C to 80 °C.

Independently of the model, the dihedral angle χ_2 is able to adopt a wide range of values at T=20 °C and 40 °C, as it is indicated in Table 6.4.2. Thus, populations are higher than 12% for all the intervals with exception of that comprised between −30° and 30°, which is sterically precluded. The conformational behaviour of the two models at T=80 °C is different (Table 6.4.2). For the BP model, the populations of the intervals comprised between 90° and −90° increase slightly with respect to T=20 °C (*i.e.* from 23.3%–25.3% to 24.3%–28.2% when the temperature increases from 20 °C to 80 °C). In contrast, for the UTC model the population of the interval comprised between 150° and −150° increases to 40.7% at T=80 °C, evidencing that the conformational variability of the latter model is higher than that of the BP one.

MD results indicate that the film-air interface, which has been induced in the UTC model by eliminating the periodic boundary conditions along the z-axis, affects the packing and distribution of the polymer chains. This interface breaks the isotropy of the BP model, in which periodic boundary conditions were applied in the three axes. The phase rupture imposed in the UTC model affects the density and the conformation of the molecular chains.

6.5. Conclusions

A sensing technology based on microcantilevers has been developed to study the thermal transitions of polymers. The technology has been used to investigate the glass transition of a polythiophene, P3TMA, with different applications in nanotechnology. The T_g determined for ultra-thin samples of $\sim 10^{-13}$ g is 5.2 °C higher than that obtained for 5 mg of bulk powder using conventional differential scanning calorimetry. SEM images reflect important morphological differences between the bulk powder and ultra-thin samples, suggesting a different microscopic organization of the polymer molecules. Atomistic MD simulations on models with periodic boundary conditions applied along three and two directions have been used to examine such differences. Calculations indicate that the film-air interface affects not only the density, which is in agreement with experimental observations, but also the conformation of the polymer molecules. The overall of these results

reflect how important is the development of new technologies to investigate the thermal transitions in samples similar to those used in nanotechnology.

6.6. References

[1] D. R. Queen, F. Hellman, *Rev. Sci. Instrum.* **2009**, *80*, 063901.
[2] W. Lee, W. Fon, B. W. Axelrod, M. L. Roukes, *Proc. Natl. Acad. Sci. USA* **2009**, *106*, 15225.
[3] S. L. Lai, J. Y. Guo, V. Petrova, G. Ramanath, L. H. Allen, *Phys. Rev. Lett.* **1996**, **77**, *99*.
[4] F. Yi, D. A. La Van, *Nanomed. Nanobiotechnol.* **2012**, *4*, 31.
[5] P. Swaminathan, B. G. Burke, A. E. Holness, B. Wilthan, L. Hanssen, T. P. Weihs, D. A. LaVan, *Thermochim Acta* **2011**, *522*, 60.
[6] R. L. Greene, C. N. King, R. B. Zubeck, *Phys. Rev. B* **1972**, *6*, 3297.
[7] J. L. Garden, H. Guillou, A. F. Lopeandia, J. Richard, J. S. Heron, G. M. Souche, F. R. Ong, B. Vianay, O. Bourgeois, *Thermochim. Acta* **2009**, *492*, 16.
[8] J. Lerchner, T. Maskow, G. Wolf, *Chem. Eng. Process.* **2008**, *47*, 991.
[9] R. K. Kummamuru, L. De La Rama, L. Hu, M. D. Vaudin, M. Y. Efremov, M. L. Green, D. A. LaVan, L. H. Allen, *Appl. Phys. Lett.* **2009**, *95*, 181911.
[10] L. P. Cook, R. E. Cavicchi, M. L. Green, C. B. Montgomery, W. F. Egelhoff, *Front. Character. Metrol. Naneletron.* **2007,** *31*, 151.
[11] L. Wang, B. Wang, Q. Lin, *Sens. Actuators B Chem.* **2008**, *134*, 953.
[12] J. Lerchner, R. Kirchner, J. Seidel, D. Waehlisch, G. Wolf, *Thermochim. Acta* **2004**, *415*, 27.
[13] E. Meyer, J. K. Gimzewski, Ch. Gerber, R. R. Schlittler, in *The Ultimate Limits of Fabrication and Measurement*, (Eds: M. E. Welland, J. K. Gimzewski), Kluwer, Dordrecht, **1995**, pp. 89-95.
[14] C. E. Borroni-Bird, N. Al-Sarraf, S. Andersoon, D. A. King, *Chem. Phys. Lett.* **1991**, *183*, 516.
[15] J. R. Barnes, R. J. Stephenson, M. E. Welland, Ch. Gerber, J. K. Gimzewski, *Nature*, **1994,** 372, 79.
[16] N. Jung, H. Seo, D. Lee, C. Y. Ryu, S. Jeon, *Macromolecules* **2008**, *41*, 6873.
[17] A. Mader, K. Gruber, R. Castelli, B. A. Hermann, P. H. Seeberger, J. O. Radler, M. Leisner, *Nano Letters* **2012**, *12*, 420.
[18] K. Gruber, T. Horlarcher, R. Castelli, A. Mader, P. H. Seeberger, B. A. Hermann, *ACS Nano* **2011**, *5*, 3670.
[19] A. Anne, C. Demaille, C. Goyer, *ACS Nano* **2009**, *3*, 819.
[20] G. Yoshikawa, T. Akiyama, S. Gautsch, P. Vettiger, H. Roher, *Nano Lett.* **2011**, *11*, 1044.
[21] L. Lechuga Gómez, V. Álvarez-Sanchéz, F. J. Tamayo De Miguel, Patent: US 7,646,494 B2.
[22] F. J. Tamayo De Miguel, J. Mertens, M. Calleja-Gómez, Patent: US 7,978,344 B2.
[23] N. F. Martinez, P. M. Kosaka, J. Tamayo, J. Ramirez, O. Ahumada, J. Mertens, T. D. Hien, C. V. Rijn, M. Calleja, *Rev. Sci. Instrum.* **2010**, *81*, 125109.
[24] J. Tamayo, V. Pini, P. M. Kosaka, N. F. Martinez, O. Ahumada, M. Calleja, *Nanotechnology* **2012**, *23*, 315501.
[25] R. Berger, Ch. Gerber, J. K. Ginzewski, E. Meyer, H. J. Güntherodt, *Appl. Phys. Lett.* **1996**, *69*, 40.
[26] W.-H. Chu, M. Mehregany, R. L. Mullen, *J. Micromech. Microeng.* **1993**, *3*, 4.
[27] D. Ramos, J. Mertens, M. Calleja, J. Tamayo, *Sensors* **2007**, *7*, 1757.

[28] N. Jung, H. Seo, D. Lee, C. Y. Ryu, S. Jeon, *Macromolecules* **2008**, *41*, 6873.
[29] J. R. Barnes, R. J. Stephenson, C. N. Woodburn, S. J. O'Shea, M. E. Welland, T. Rayment, J. K. Gimzewski, Ch. Gerber, *Rev. Sci. Instrum.* **1994**, *65*, 3793.
[30] K. Gimzewski, Ch. Gerber, E. Meyer, R. R. Schlittler, *Chem. Phys. Lett.* **1994**, *217*, 589.
[31] M. Martí, G. Fabregat, D. S. Azambuja, C. Alemán, E. Armelin, *Prog. Org. Coat.* **2012**, *73*, 321.
[32] E. Armelin, C. Alemán, J. I. Iribarren, F. Liesa, F. Estrany, Patent Cooperation Treaty PCT/ES2010070820, 2010.
[33] E. Armelin, C. Alemán, J. I. Iribarren, F. Liesa, F. Estrany, Patent Cooperation Treaty U.S. Application nº 13/138925.
[34] B. Kim, L. Chen, J. Gong, Y. Osada, *Macromolecules* **1999**, *32*, 3964.
[35] A. L. Gomes, J. Casanovas, O. Bertran, J. S. de C. Campos, E. Armelin, C. Alemán, *J. Polym. Res.* **2011**, *18*, 1509.
[36] J. C. Phillips, R. Braun, W. Wang, J. Gumbart, E. Tajkhorshid, E. Villa, C. Chipot, R. D. Skeel, L. Kale, K. Schulten, *J. Comput. Chem.* **2005**, *26*, 1781.
[37] W. D. Cornell, P. Cieplak, C. I. Bayly, I. R. Gould, K. M. Merz, D. M. Ferguson, D. C. Spellmeyer, T. Fox, J. W. Caldwell, P. A. Kollman, *J. Am. Chem. Soc.* **1995**, *117*, 5179.
[38] J. Wang, R. M. Wolf, J. W. Caldwell, D. A. Case, *J. Comput. Chem.* **2004**, *15*, 1157.
[39] P. Cieplak, W. Cornell, C. I. Bayly, P. A. Kollman, *J. Comput. Chem.* **1995**, *16*, 1357.
[40] J. P. Ryckaert, G. Ciccotti, H. J. C. Berendsen, *J. Comput. Phys.* **1977**, *23*, 327.
[41] D. Curcó, C. Alemán, *J. Comput. Chem.* **2007**, *28*, 1743.
[42] H. J. C. Berendsen, J. P. M. Postma, W. F. van Gunsteren, A. Dinola, J. R. Haak, *J. Chem. Phys.* **1984**, *81*, 3684.
[43] C. Alemán, L. Juliá, *J. Phys. Chem.* **1996**, *100*, 1524.
[44] C. Alemán, V. M. Domingo, L. Fajarí, L. Juliá, A. Karpfen, *J. Org. Chem.* **1998**, *63*, 1041.
[45] O. Bertran, E. Armelin, J. Torras, F. Estrany, M. Codina, C. Alemán, *Polymer* **2008**, *49*, 1972.
[46] E. Armelin, O. Betran, F. Estrany, R. Salvatella, C. Alemán, *Eur. Polym. J.* **2009**, *45*, 2211.
[47] O. Bertran, P. Pfeiffer, J. Torras, E. Armelin, F. Estrany, C. Alemán, *Polymer* **2007**, *48*, 6955.

CHAPTER 7

FIBROUS BIOINTERFACES BASED ON POLYTHIOPHENE DERIVATIVE AND BIODEGRADABLE POLYLACTIDE

Summary

The second part of this Thesis approaches the fabrication of CP-based biointerfaces as fibrous mats by blending P3TMA with biodegradable polymers by applying the electrospinning technique.

Specifically, chapter 7 describes the fabrication of a hybrid scaffold using polylactide (PLA). Both polymers were soluble in a common organic solvent, and thus easily electrospun. The optimization of the electrospinning parameters, and the morphological, thermal and compositional characterization of PLA:P3TMA fibrous biointerfaces was performed by Dr. E. Llorens.

Hence, the assessment of the electroactivity and electrostability of the samples, and their suitability for biotechnological applications (*i.e.* tissue engineering scaffolds) is presented in section 7.1.

Later, the PLA:P3TMA system was further applied to perform as drug carrier platforms (section 7.2). In this case, four different drugs were tested and successfully entrapped in the fibre matrix. Hence, biocompatible PLA:P3TMA scaffolds combine an excellent response towards cellular adhesion and proliferation, while behaving as drug delivery systems.

PLA was kindly supplied by Nupik International (Polinyà, Spain). Thermal measurements were run by Dr. L. Franco[1]. Biological assays were done in collaborative working with Dr. L. J. del Valle[1]. Dr. Elena Bailo[2] assisted in the Raman spectroscopy characterization.

Publications derived from this work:

E. Llorens, M. M. Pérez-Madrigal, E. Armelin, L. J. del Valle, J. Puiggalí, C. Alemán, *RSC Adv.* **2014**, *4*, 15245.

M. M. Pérez-Madrigal, E. Llorens, L. J. del Valle, J. Puiggalí, E. Armelin, C. Alemán, Submitted work to *J. Mater. Chem. B*

[1]Departament d'Enginyeria Química, E.T.S. d'Enginyers Industrials de Barcelona, UPC.
[2]Area Manager España & Portugal; WITec GmbH.

7.1. PLA:P3TMA Electrospun Nanofibers as Tissue Engineering Scaffolds

7.1.1. Introduction

Polymeric materials with both biodegradable and electrically conducting properties have growing interest in biomedical applications because of both the lack of long-term health risk and their good behaviour as the supportive matrix for tissue regeneration. The electrochemical response of conducting polymers makes feasible the local stimulation of desired tissue and the enhancement of either the proliferation or differentiation of various cell types.[1–4] Nevertheless, it remains a considerable challenge to synthesize an ideal electroactive polymer that meets the biocompatibility and biodegradability requirements to minimize the inflammatory reaction in the host tissue that could be raised by the use of non-degradable materials. An alternative strategy is the use of conducting polymer/biopolymer blends since unique properties that justify their potential technological applications in biomedical devices can be achieved.

In addition to biocompatibility and biodegradability, the architecture of the biomaterial used in tissue engineering applications is also very important and, specifically, scaffolds constituted by electrospun nanofibers have promising features, such as big surface area for absorbing proteins and abundance of binding sites for cell membrane receptors.

As it is addressed in Chapter 2 in more detail (section 2.2), ultrathin fibers from a wide range of polymer materials can be easily prepared by electrospinning.[5–11] Different approaches can be followed to develop scaffolds constituted by conducting and biodegradable polymers. The one used in this work is based on the direct electrospinning of a conducting/biodegradable polymer mixture, which is easy to perform, but requires a good solubility of the conducting polymer in the electrospinning solution. In opposition, it can give rise to scaffolds with low conductivity.

First works providing novel conductive materials well suited as biocompatible scaffolds for tissue engineering involved PAni–gelatin blend nanofibers.[12] Picciani *et al*.[13] considered the use of poly(L-lactide) as the support polymeric matrix for the preparation of PAni-based conducting nanofibers and evaluated the influence of operational parameters on the morphology of electrospun fibers. Several PAni and poly(D,L-lactide) mixtures at different weight percent were also successfully electrospun from 1,1,1,3,3,3-hexafluoroisopropanol solutions and their conductivity

and biocompatibility evaluated.[14] Nanofibrous blends of HCl-doped poly(aniline-*co*-3-aminobenzoic acid) copolymer and polylactide (PLA) were fabricated by electrospinning solutions of the polymers in a DMSO-THF mixture.[15]

Scarce works concern the electrospinning of mixtures based on PPy, and those reported basically deal with scaffolds constituted by PPy/PCL/gelatin nanofibers.[16] Specifically, conductive nanofibers containing 15% PPy exhibited the most suitable balance of electrical conductivity, mechanical properties and biodegradability, matching the requirements for the regeneration of cardiac tissue. Furthermore, such scaffold promoted cell attachment and proliferation as well as the interaction and expression of cardiac-specific proteins.

Polythiophenes constitute a group of conducting polymers with high technological potential due to their optical, electroluminescents, electronic and, specially, electrochemical properties.[17,18] Different derivatives can be considered and, specifically, several works were focused on the preparation of nanofibers from mixtures of poly(3-hexylthiophene) (P3HT) and PCL or poly(lactic-*co*-glycolic acid) (PLGA) as biodegradable polymers.[19,20]

On the one hand, polylactide (PLA) is a 100% biodegradable biopolymer extensively investigated and used in different applications, such as automotive parts, clothing and carpet fibers, food packaging, among others. Regarding the biomedical field, PLA and its copolymers are chosen due to their excellent properties (*i.e.* good mechanical integrity, biodegradability and biocompatibility) and its wide use in the biomedical field. On the other, the good solubility of P3TMA in organic solvents like chloroform makes it a suitable candidate for being processed by electrospinning.

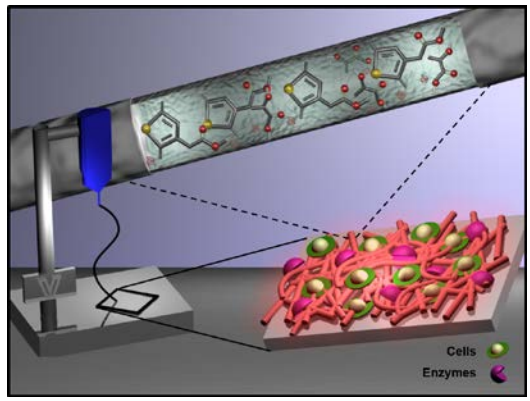

Graphical abstract

Therefore, the main goal of the present section is to establish the electrospun conditions required to get continuous micro/nanofibers from mixtures of P3TMA and PLA, as well as to perform a basic characterization of the morphology and properties (*e.g.* ability to store charge and biocompatibility) of the derived scaffolds.

7.1.2. Experimental Section

Materials

3-Thiophene acetic acid (3TAA) (98.0%) was purchased from Fluka (Sigma-Aldrich). Iron chloride anhydrous (97.0%), dry methanol (99.5%), chloroform (99.9%) were purchased from Panreac Quimica S.A.U. (Spain) and used as received without further purification. PLA, a product of Natureworks (polymer 2002D), was kindly supplied by Nupik International (Polinyà, Spain). According to the manufacturer, this PLA has a D content of 4.25%, a residual monomer content of 0.3%, a density of 1.24 g/cm^3, a glass transition temperature (T_g) of 58 °C and a melting point of 153 °C. Kidney epithelial cells derived from African green monkey (Vero) were purchased from ATCC (USA).

Synthesis of P3TMA

3-thiophene methyl acetate (3TMA) monomer was obtained with a 74% yield by refluxing 3TAA in dry methanol for 24 hours at a temperature of 90 °C.[21] The polythiophene derivative, P3TMA, was subsequently prepared by a chemical oxidative coupling in dry chloroform following the procedure described by Kim *et al.*[21] Anhydrous ferric chloride ($FeCl_3$) was used as oxidant and dopant. The polymerization yield was *ca.* 61% after removing the residual oxidant and oligomers.

Molecular weights and polydispersity index (PDI) were estimated by size exclusion chromatography (SEC) using a liquid chromatograph (Shimadzu, model LC-8A) equipped with an Empower computer program (Waters). A PL HFIP gel column (Polymer Lab) and a refractive index detector (Shimadzu RID- 10A) were employed. Polymers were dissolved and eluted in 1,1,1,3,3,3-hexafluoroisopropanol at a flow rate of 0.5 mL/min (injected volume 100 mL, sample concentration 1.5 mg/mL). The number and weight average molecular weights were calculated using poly(methyl methacrylate) standards, and were [M_n=59 300 g/mol and M_w=117 500 g/mol] and [M_n=10 700 g/mol and M_w=22 500 g/mol] for PLA and P3TMA, respectively.

Electrospinning

Mixtures of PLA and P3TMA were electrospun from different solvents such as chloroform, acetone and chloroform–acetone mixtures at polymer concentrations of 5 w/v% and 1–5 w/v% for PLA and P3TMA, respectively. Samples will be named indicating only the PLA weight percentage (*e.g.* PLA:P3TMA-100 and PLA:P3TMA-67 correspond to PLA alone and a mixture with 67%PLA and 33% P3TMA, respectively).

The electrospun fibers were collected on a target, which was placed at different distances (10–20 cm) from the syringe tip (inside diameter of 0.84 mm). The voltage was varied between 10 and 30 kV, and applied to the collecting target using a high-voltage supply (Gamma High Voltage Research, ES30-5W). The polymer solutions were delivered via a KDS100 infusion syringe pump (KD Scientific) to control the mass-flow rate (from 0.5 to 10 mL/h). All electrospinning experiments were carried out at room temperature.

Composition, morphology and properties of electrospun PLA:P3TMA

^{1}H-NMR spectra were acquired with a Bruker AMX-300 spectrometer operating at 300.1 MHz. Chemical shifts were calibrated using tetramethylsilane as an internal standard. Deuterated chloroform was used as the solvent.

Infrared absorption spectra were recorded with a Fourier Transform FTIR 4100 Jasco spectrometer in the 4000–600 cm^{-1} range. A Specac model MKII Golden Gate attenuated total reflection (ATR) with a heated Diamond ATR Top-Plate was used.Optical morphologic observations were performed using a Zeiss Axioskop 40 microscope. Micrographs were taken with a Zeiss AxiosCam MRC5 digital camera.

Inspection of the morphology of electrospun samples was conducted by scanning electron microscopy using a Focus Ion Beam Zeiss Neon 40 instrument (Carl Zeiss, Germany). Carbon coating was accomplished by using a Mitec K950 Sputter Coater fitted with a film thickness monitor *k*150x. Samples were visualized at an accelerating voltage of 5 kV. Diameter of electrospun fibers was measured with the SmartTiff software (Carl Zeiss SMT Ltd.).

Calorimetric data were obtained by DSC with a TA Instruments Q100 series equipped with a refrigeration cooling system (RCS). Experiments were conducted under a flow of dry nitrogen with a sample weight of approximately 5 mg and calibration was performed with indium. Heating runs were carried out at a rate of 20 °C/min with both electrospun and samples slowly cooled (10 °C/min) from the melt state. Thermal degradation was studied at a heating rate of 20 °C/min with

around 5 mg samples in a Q50 thermogravimetric analyzer of TA Instruments and under a flow of dry nitrogen. Test temperatures ranged from 50 to 600 °C.

X-ray powder diffraction patterns were obtained with a PANalytical X'Pert diffractometer with CuK_α radiation (λ=0.1542 nm) and a silicium monocrystal sample holder.

Electrochemical characterization

In order to assess the electrochemical behaviour of the PLA:P3TMA scaffolds, cyclic voltammetry (CV) studies were conducted with an Autolab PGSTAT302N galvanostat equipped with the ECD module (Ecochimie, The Netherlands). Measurements were performed on fiber mats, which were deposited by electrospinning on both sides of steel AISI 316 sheets of 1x1cm². All electrochemical assays were performed using a three-electrode one compartment cell under nitrogen atmosphere and at room temperature.

The cell was filled with 50 mL of phosphate buffered saline (PBS, pH = 7.4) with 0.1 M $LiClO_4$ as supporting electrolyte. Steel sheets were used as working electrode, while an Ag|AgCl electrode containing KCl saturated aqueous solution was the reference electrode (offset potential versus the standard hydrogen electrode, E_0=0.222 V at 25 °C). Steel AISI 316 sheets of 1x1cm² were used as counter electrode. Electrochemical measurements were carried out from -0.4 V to 1.1 V, at scan rate of 50 mV/s. Five consecutive oxidation–reduction cycles were conducted to assess the loss of electrochemical activity, which was determined as:

$$LEA\ (\%) = \frac{\Delta Q}{Q_1} \times 100 \qquad (7.1.1)$$

where ΔQ is the difference of anodic voltammetric charge between the first cycle and the last cycle and Q_1 is the anodic voltammetric charge corresponding to the first cycle.

Wettability

Contact angle measurements were performed using the water drop method at room temperature. Images of 0.5 μL distilled water drops were recorded after stabilization (30 s) using a OCA 15EC (DataPhysics Instruments GmbH, Filderstadt). The contact angle values were obtained as the average of eight independent measures for each sample. The software SCA 20 was used to analyze the images and acquire the contact angle values.

Cellular adhesion and proliferation assays

Vero cells were cultured in Dulbecco's modified eagle medium (DMEM) supplemented with 10% fetal bovine serum, 1%penicillin/streptomycin and 2 mM L-glutamine at 37 °C in a humidified atmosphere with 5% CO_2 and 95% air. The culture medium was changed every two days and, for sub-culture, the cell monolayers were rinsed with phosphate buffered saline (PBS) and detached by incubation with trypsin–EDTA (0.25%) for 2–5 min at 37 °C. Cell concentration was established by counting with the Neubauer camera using 4% trypan-blue as dye vital. The detached cells with viability ≥ 95% were used for cultures following the conditions for biocompatibility assays.

PLA:P3TMA electrospun nanofibers were collected on circular coverslips (diameter 1.5 cm). These samples were placed into the wells of a multiwell culture plate and then sterilized by UV-radiation for 15 min in a laminar flux cabinet. For fixing the samples on the well, a small drop of silicone (Silbione® MED ADH 4300 RTV, Bluestar Silicones France SAS, Lyon, France) was used as adhesive. Samples were incubated with 1 mL of culture medium during 30 min under culture conditions to equilibrate the material. Finally, the medium was aspired, and the material was evaluated for cell adhesion and proliferation by exposing cells to direct contact with the material surface.

For the cellular adhesion assay, aliquots of 50–100 µL containing $5x10^4$ cells were seeded onto the electrospun samples placed in each well. The plate was incubated under culture conditions for 30 min to allow cellular attachment onto the material surface. Then, 1 mL of the culture medium was added to each well, and the plate was incubated during 24 h. Finally, the cell viability was determined by the MTT assay. The controls were realized considering TCPS surfaces.

For the cellular proliferation assay, the procedure was similar to the adhesion assay, but the aliquot of 50–100 µL contained $2x10^4$ cells. Cultures were maintained during 7 days to allow the cellular growth and an adequate cellular confluence in the well. The media were renewed each two days; and finally, the viability was determined by the MTT assay.

Each sample was evaluated using five replicates, results being averaged and graphically represented. The statistical analysis was performed by one-way ANOVA test to compare the means of all groups. The *t*-test was applied to determine a statistically significant difference between different groups. The tests were performed with a confidence level of 95% ($p < 0.05$).

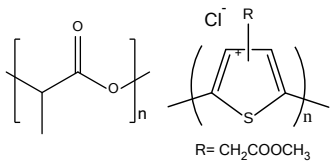

PLA **P3TMA**

Scheme 7.1.1. Chemical structures of PLA and P3TMA.

7.1.3. Results and Discussion

Electrospinning of PLA:P3TMA mixtures

In order to select the most appropriate conditions to obtain continuous PLA:P3TMA microfibers, several solvents and binary mixtures were tested at different voltages, flows, polymer concentrations and needle tip-collector distances. Although the chemical structure (Scheme 7.1.1) of both polymers was quite different, their solubility characteristics were similar and, consequently, a common solvent could be selected for the electrospinning process. In fact, solvent plays a fundamental role for the continuous micro/nanofiber production[22,23] and, in general, a relatively high polymer concentration is required to avoid the formation of droplets and electrospun beads when a good solvent is selected.[24] Both PLA and P3TMA are highly soluble in chloroform and, therefore, this solvent was selected as a starting point in the optimization of the processing conditions. However, quality of fibers improved over a wide range of polymer compositions when chloroform–acetone mixtures were employed. Although chloroform seems more appropriate for PLA considering the reported Hildebrand solubility parameters[25] (*i.e.* 18.83 $MPa^{0.5}$, 19.98 $MPa^{0.5}$ and 17.64 $MPa^{0.5}$ for chloroform, acetone and PLA, respectively), the best results were achieved when a small percentage of acetone was added. In fact, Hansen parameters[26] determined for dispersion, polar and hydrogen-bonding components suggests that the addition of acetone improves polar interactions (Table 7.1.1). Thus, a chloroform–acetone (70:30 *v/v*) mixture had closer parameters to PLA than the individual solvents and gave good electrospun fibers for all assayed PLA:P3TMA polymer blends. In fact, this solvent mixture was also previously selected as the best solution for electrospinning other PLA/polymer mixtures.[27]

Table 7.1.1. Hansen parameters of PLA and selected electrospinning solvents.

	δ_d (MPa$^{0.5}$)	δ_p (MPa$^{0.5}$)	δ_h (MPa$^{0.5}$)	δ_T (MPa$^{0.5}$)
Chloroform	17.8	3.1	7.0	18.9
Acetone	15.0	10.4	5.5	19.9
Chloroform/Acetone 70:30 *v*/*v*	17.0	5.3	6.5	19.2
PLA	17.6	5.3	5.8	19.3

The low molecular weight of P3TMA precluded its processability into micro/nanofibers since chain entanglements were insufficient to stabilize the jet. Therefore spraying of droplets that coalesced into ill-defined shapes was observed (data not shown). PLA was essential to both render a scaffold with biodegradable properties and improve processability by increasing the average molecular weight of the polymer mixture. In fact, a PLA content higher than 50% was necessary even in the most favourable electrospinning conditions to completely avoid the formation of droplets. Figure 7.1.1 illustrates the optimization process when a deposition distance of 12 cm was chosen according to a first screening. It can be observed that big drops corresponding to the CP were obtained when a relatively high flow (*i.e.* 10 mL/h) and low voltage (*i.e.* 15 kV) were employed. At an intermediate voltage (25 kV) the drop size decreased and at a high voltage (30kV) beads were characteristic.

The decrease of the flow up to 4 mL/h improved considerably the morphology and, specifically, a low voltage led to small beads, whereas continuous and homogeneous size fibers could be attained at an intermediate voltage. The selected electrospinning conditions for the different conducting/biodegradable polymer mixtures are summarized in Table 7.1.2.

Table 7.1.2. Optimal electrospinning conditions for the different studied samples.[a]

Sample	Voltage (kV)	Flow Rate (mL/h)
PLA:P3TMA-100	15-**20**	**4**-10
PLA:P3TMA-83	20-**25**	**4**-10
PLA:P3TMA-67	20-**25**	4
PLA:P3TMA-50	20-**25**	4

[a]The applied parameter is indicated in bold characters when a range of spinnability is given. In all cases, the optimal distance between syringe tip and collector was 12 cm.

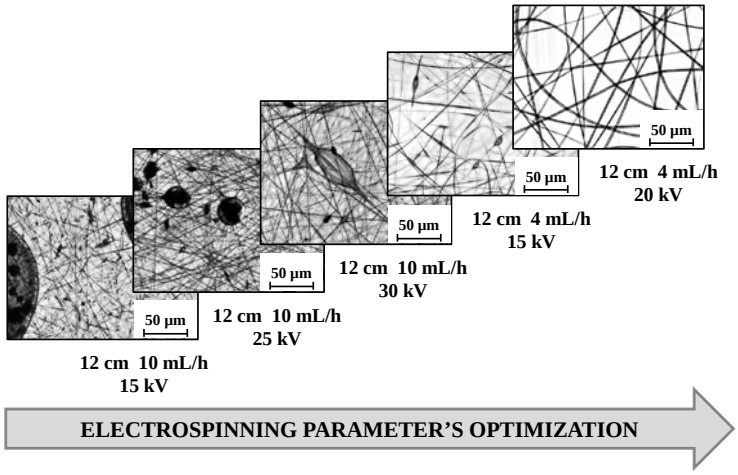

Figure 7.1.1. Optical micrographs showing typical morphologies obtained by electrospinning a PLA:P3TMA-67 mixture from a chloroform/acetone (70:30 v/v) solution and a deposition distance of 12 cm.

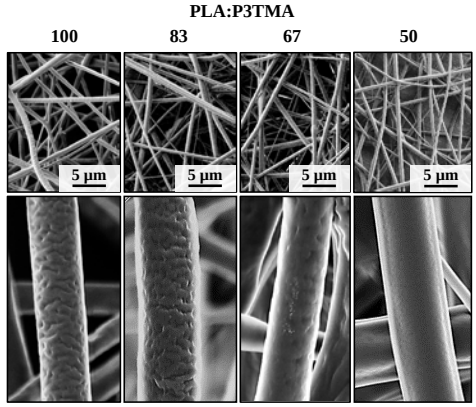

Figure 7.1.2. SEM micrographs taken at low (top) and high (bottom) magnification of electrospun nanofibers of PLA:P3TMA-x samples obtained from a chloroform/acetone (70:30 v/v) solution using optimized concentration, voltage, needle-collector distance and flow.

Morphology of PLA:P3TMA nanofibers

Figure 7.1.2 shows representative SEM micrographs of electrospun samples with different compositions. In general, long micro/nanofibers with a cylindrical morphology and randomly distributed in the fibrous mats could be attained. Fibers were adhered to each other forming a dense but porous structure. Diameter distribution was relatively wide. This feature was particularly remarkable for the PLA:P3TMA-50 sample, in which significant amounts of fibers with diameters so different as 250 nm and 2 mm were clearly distinguished. However, in all cases the most predominant size was in the 600–900 nm range. Figure 7.1.3 shows the monomodal distributions observed for the samples prepared under the optimized conditions. It is interesting to note that the increase on the P3TMA ratio in the electrospinning mixture led to a slight decrease on the average diameter (*i.e.* values progressively decreased from 864 to 633 when P3TMA content increased from 0 to 50 wt%).

Surface texture of fibers changed also gradually with composition as depicted in the high magnification images of Figure 7.1.2. It is clear that the typical rough/porous surface of PLA fibers progressively became smooth as the P3TMA content increased (*e.g.* an almost completely smoother texture was observed for PLA:P3TMA-50).

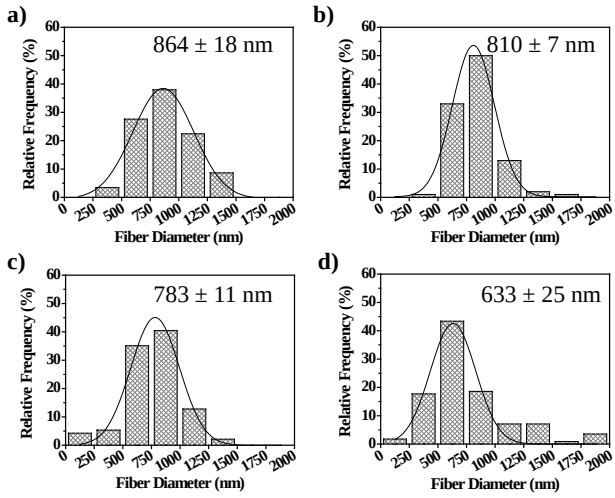

Figure 7.1.3. Diameter distribution of electrospun nanofibers of PLA:P3TMA-*x* samples obtained from a chloroform/acetone (70:30 *v*/*v*) solution using optimized concentration, voltage, needle-collector distance and flow: a) -100; b) -83, c) -67 and d) -50.

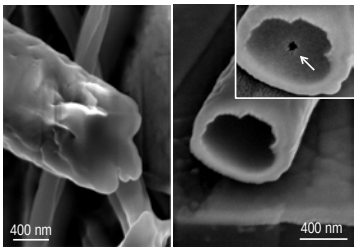

Figure 7.1.4. High magnification SEM micrographs showing the cross section of electrospun PLA (left) and PLA:P3TMA-50 (right) nanofibers. The inset shows the corresponding cross section after being exposed to a water jet.

Nanofibers were cut with the focused ion beam in order to evaluate their homogeneity through the visualization of the generated cross sections. Figure 7.1.4 clearly shows that PLA nanofibers had an irregular shape as expected from their rough surface texture and also that the section was relatively homogeneous. However, the cross sections of fibers prepared from polymer mixtures (*i.e.* PLA:P3TMA 50 shown in Figure 7.1.4) were completely different since in some cases a relative thick and bright outer part could be clearly distinguished. It is possible that the inner part was constituted by some clusters richer in a conductive P3TMA phase, giving place to the observed contrast. In order to verify that fibers were not hollow, a water jet was headed towards their cross section center. The inset of Figure 7.1.4 illustrated the apparition of a small hole caused by the impact of the jet and consequently demonstrated a compact fiber structure. It should be pointed out that cross sections taken at different places of the microfibers were rather variable since homogeneous and heterogeneous distributions were detected, suggesting that the indicated aggregates are randomly distributed along the micro/nanofibers.

Characterization of PLA:P3TMA fibers

^{1}H-NMR and FTIR spectroscopies were used to assess the composition of the electrospun hybrid scaffolds. Thus, ^{1}H-NMR spectra revealed the presence of characteristic signals of each homopolymer (Figure 7.1.5), the corresponding areas being in agreement with the theoretical composition of the sample. Spectra always showed the characteristic quadruplet at 5.21, 5.19, 5.17 and 5.15 ppm associated to the proton of the PLA methine group and the doublet at 1.60 and 1.58 ppm associated to the protons of the PLA methyl group. In addition, complex signals, which reflect sequence sensitivity, were also observed and attributed to P3TMA.

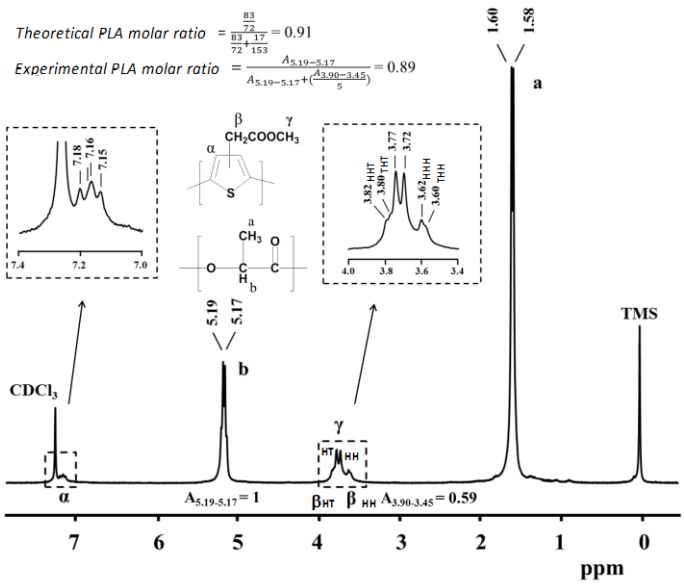

Figure 7.1.5. ^{1}H-NMR spectra of a representative electrospun PLA:P3TMA-83 sample.

Thus, thiophene protons gave rise to an isolated multiplet (7.18–7.15 ppm), whereas signals of methylene and methyl lateral groups appeared overlapped as a double duplet (3.82–3.80 ppm and 3.62–3.60 ppm) and a duplet (3.77 and 3.72 ppm), respectively. Splitting of the CH_3 signal reflects the head-to-head (HH) and head-to-tail (HT) dyads produced during the chemical polymerization, as it has been previously reported.[21] Areas of dyad signals were practically identical, demonstrating a non-regioregular structure with a statistical disposition of the monomer units. HT and HH dyads corresponding to the methylene protons were splitted again demonstrating triad sensitivity (*e.g.* splitting of HH dyad gave rise to HHT and THH triads, whereas THT and HHT triads were derived for the HT dyad). The complex signal associated to the CH group can be interpreted in a similar way, the highest chemical shifts corresponding to the TH dyad.

FTIR spectra of P3TMA samples coming directly from synthesis and from electrospinning were identical and showed a single C=O signal at 1732 cm^{-1} (Figure 7.1.6). Therefore, ester groups were not cleaved during processing, supporting the interpretation of the complex ^{1}H-NMR spectra on the basis of sequence sensitivity. Furthermore, a broad band associated to OH groups could not be detected in the 3300–2500 cm^{-1} FTIR region (not shown).

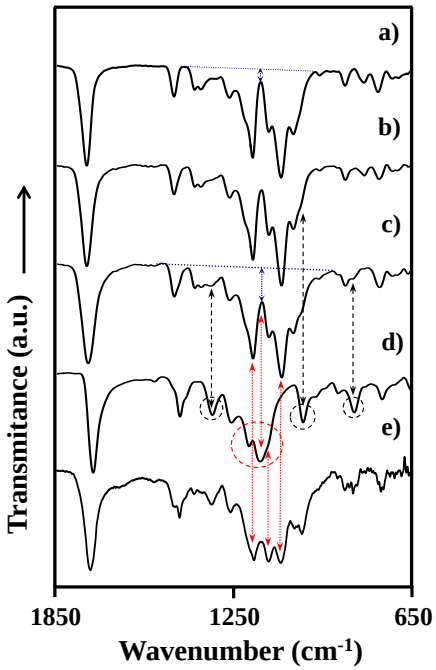

Figure 7.1.6. FTIR (1850-650 cm^{-1}) spectra of electrospun PLA (a), PLA:P3TMA-67 (b), PLA:P3TMA-50 (c) and P3TMA (d). For comparison purposes, the spectrum of a blend containing 50 wt.% of each homopolymer is shown in (e).

The spectra of P3TMA (Figure 7.1.6d) showed also typical signals at 1435 cm^{-1} (thiophene ring stretching), 1322 cm^{-1} (methyl deformation), 1198 and 1167 cm^{-1} (asymmetric and symmetric C–O stretching), 1012 cm^{-1}, 839 cm^{-1} (aromatic CH out of plane deformation) and 741 cm^{-1} (methyl rocking). On the other hand, the spectra of the scaffold samples were highly similar to that corresponding to neat PLA (Figure 7.1.6a), the C=O streching vibration at 1759 cm^{-1} and the asymmetric and symmetric C–O stretching at 1183 and 1082 cm^{-1}, respectively, being the most intense bands. The intensity of the characteristic signals of P3TMA decreased with its ratio in the scaffold (*e.g.* bands at 1322 and 839 cm^{-1}). It should be pointed out that the strong P3TMA band at 1167 cm^{-1} could not be observed in the spectra of scaffolds even for the highest P3TMA content. This suggests a change in the environment of the ester groups when the P3TMA was processed together with PLA. However, it is also significant that the transmittance measured at 1167 cm^{-1} was clearly lower for the hybrid scaffold than for the neat PLA (see blue arrows in

Figure 7.1.6), even though this wavenumber still corresponded to a transmittance maximum.

For the sake of completeness, Figure 7.1.6e shows the spectrum of a powder mixture composed by 50 wt% of each polymer where the two strong PLA bands at 1183 and 1082 cm^{-1} can be clearly observed together with the strongest P3TMA band. However, the latter appears slightly shifted due to its overlapping with a medium intensity PLA band at 1129 cm^{-1}. Differences between the spectra of electrospun samples and polymer mixtures are evident and suggest the occurrence of some specific interactions in the processed samples.

Table 7.1.3 contains the main calorimetric data (*i.e.* glass transition, cold crystallization and melting temperatures as well as crystallization and melting enthalpies) obtained from the heating run of all electrospun scaffolds, whereas heating traces of representative samples can be seen in Figure 7.1.7.

Table 7.1.3. Selected calorimetric data from the heating scan performed with the different PLA:P3TMA-*x* electrospun samples.

	T_g (°C)	T_c (°C)	ΔH_c (J/g)	T_m (°C)	ΔH_m (J/g)	$\Delta H_m - \Delta H_c$ (J/g)	X_c[a]
PLA[b]	60.0	-	-	149.8	33.4	33.4	31.5
PLA:P3TMA-100	61.7	96.6	17.4	146.2	22.0	4.6	4.3, 20.7
PLA:P3TMA-83	59.5	96.4	14.0	147.2	17.5	3.5	4.0, 19.9
PLA:P3TMA-67	59.4	96.5	14.3	147.5	17.8	3.5	4.9, 25.1
PLA:P3TMA-50	60.4	94.1	12.0	145.7	16.2	4.2	7.9, 30.6
P3TMA	67.2	-	-	111.3	11.6	11.6	-

[a]Degree of crystallinity referred to the PLA content (heat of fusion=106 J/g for a 100% crystalline sample)[28] for electrospun samples (left) and attained during the heating scan (right).

Several features deserve attention: (a) A broad exothermic peak (70–130 °C) corresponding to the cold crystallization of PLA is always observed. The high molecular orientation attained in the electrospinning process facilitated the PLA crystallization, as previously reported.[28] On the contrary, amorphous samples (Figure 7.1.7c) were always attained when samples were slowly cooled from the melt due to the lack of orientation and the difficulty of PLA to crystallize. (b) The degree of crystallinity referred to the PLA content tends to increase when nanofibers are obtained from mixtures with a higher P3TMA content, which is probably due to the higher orientation attained when the fiber diameter decreased. This trend was observed in both samples from direct electrospun (*i.e.* calculated

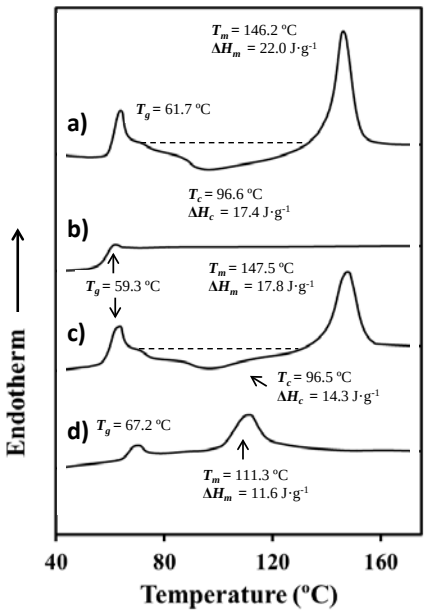

Figure 7.1.7. DSC heating (a,c) and cooling (b) scans performed with electrospun PLA:P3TMA-100 (a,b) and PLA:P3TMA-67 (c) samples obtained under the corresponding optimized processing conditions. For comparison purposes the heating scan of a P3TMA powder sample is shown in (d).

through the difference between melting and crystallization enthalpies) and samples obtained after cold crystallization (*i.e.* considering only the melting enthalpy). (c) All samples show a clear glass transition, as could be presumed for amorphous samples, and a typical relaxation endothermic peak, which indicates that metastable PLA glassy material achieves equilibrium thermodynamic conditions with a lower specific volume, enthalpy and entropy.[29] (d) Incorporation of P3TMA has a scarce influence on the characteristic glass transition, crystallization and melting temperatures of the final scaffold. In fact, neither the glass transition nor the melting peak of P3TMA (Figure 7.1.7d) were detected in the heating runs of the resulting scaffolds.

It is interesting to note that P3TMA obtained from chemical polymerization was semicrystalline despite the random disposition of its repeating unit. The X-ray diffraction profile (Figure 7.1.8) is characterized by a strong and well defined peak at 1.17 nm that is related to the interchain distance (inset of Figure 7.1.8). Profiles of electrospun samples showed only amorphous halos without Bragg reflections

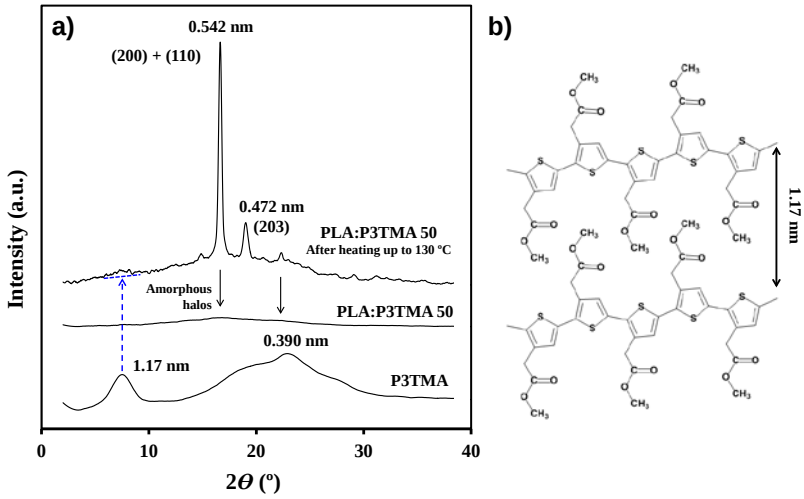

Figure 7.1.8. a) X-ray power difractograms of a P3TMA powder sample and an electrospun PLA:P3TMA-50 scaffold before and after being heated up to 130 ºC. b) Scheme of the molecular arrangement where for the sake of simplicity only a heat-to-heat distribution has been represented.

assigned to any of the two homopolymers. However, crystallization took place when the sample was heated up to 130 °C and the diffraction profile clearly showed the two strongest reflections of the *α*-form of PLA (*i.e.* those appearing at 0.542 and 0.472 nm that correspond to the (200) + (110) and (203) indices, respectively).[30,31] Therefore, crystallization involved only PLA since the main reflection of P3TMA can only be guessed.

Scaffolds were thermally stable up to more than 200 °C, as deduced from TGA and DTGA curves (Figure 7.1.9). Incorporation of P3TMA slightly modified the degradation process, leading to a regular increase of both the char yield at 600 °C and the onset degradation temperature. Thermal degradation of PLA has previously been explained according to a complex reaction process with the participation of at least two different mechanisms.[32] The DTGA curve of PLA is clearly asymmetric showing a shoulder in the low temperature region, which is associated with a minor degradation process. This shoulder disappears in the DTGA curves of scaffolds suggesting that the first degradation step is hindered by the presence of P3TMA. It is also clear that the DTGA maximum is slightly shifted to a lower temperature, which coincides with one of the two degradation processes observed also for P3TMA.

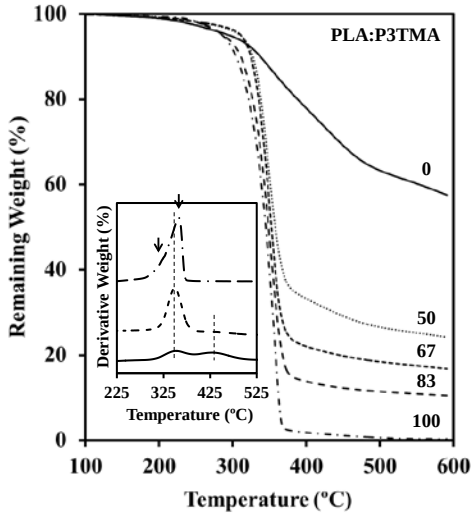

Figure 7.1.9. TGA degradation curves of the different electrospun PLA:P3TMA-*x* samples. Inset compares DTGA curves of PLA (dashed), PLA:P3TMA-50 (dotted) and P3TMA (solid).

In addition, the scaffold has a hardly observed minor decomposition process that corresponds to the higher temperature degradation step of P3TMA.

Electrochemical characterization of PLA:P3TMA fibers

The low molecular weight of P3TMA makes unfeasible to get electrospun mats and to carry out the corresponding CV measurements from the neat CP. Processability into fibers has been demonstrated to be possible only when a high molecular weight polymer (in our case, PLA) is incorporated.

The control voltammogram recorded for PLA fibers (Figure 7.1.10a) shows an oxidation shoulder with anodic potential $E_p^a(O_1)$ of 0.86 V and an oxidation peak with E_p^a (O_2) higher than 1.1 V. Both peaks have been assigned to the formation of irreversible polarons and bipolarons. Besides, the cathodic scan shows a weak reduction shoulder R_1 with a cathodic peak potential E_p^c (R_1) of -0.08 V. The voltammogram recorded for the PLA:P3TMA-83 hybrid was highly similar to that obtained for PLA (Figure 7.1.10a, curves 3 and 4), but interestingly the hybrids with a lower PLA content (*i.e.* PLA:P3TMA-50 and 67 samples) showed clearly improved electrochemical properties (Figure 7.1.10a, curves 1 and 2). Thus, $E_p^a(O_1)$ and E_p^a (O_2) anodic potentials shifted to 0.75 and 1.40 V for the 67 wt% sample, and to 0.82 and

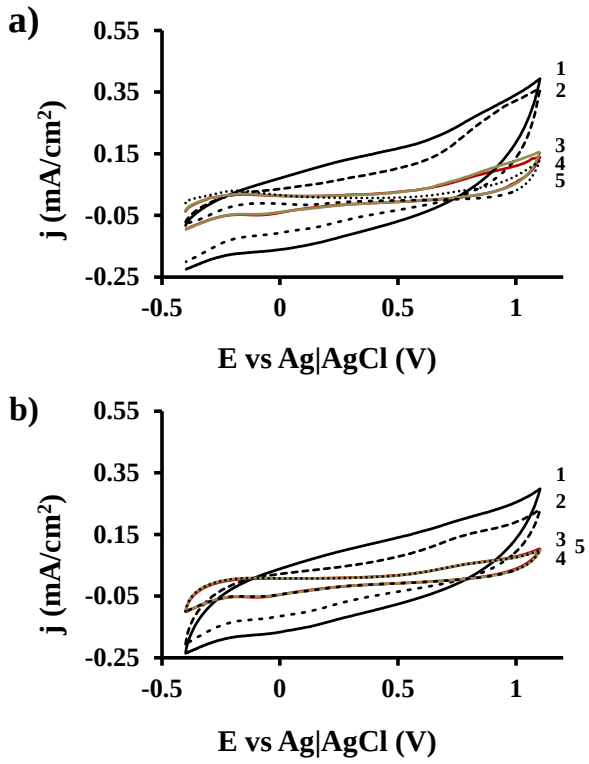

Figure 7.1.10. a) Control voltammograms collected using scan rates of 50 mV/s for electrospun mats of PLA (curve 4, red) and PLA:P3TMA-50 (curve 1, solid black), -67 (curve 2, dashed black) and -83 (curve 3, brown) in a PBS solution containing 0.1M $LiClO_4$. Curve 5 (pointed black) corresponds to a steel sheet used as control. b) Cyclic voltammograms of the same species after 5 consecutive oxidation–reduction cycles.

1.08 V for the 50 wt% sample, respectively, and pointed out an increased irreversibility for the oxidation process. Furthermore, the weak R_1 reduction shoulder was always observed (*i.e.* cathodic peak potentials of -0.04 V and -0.05 V for the PLA:P3TMA-50 and 67, respectively). Current densities (*j*) determined at 1.10 V were 0.152 mA/cm² and 0.394 mA/cm² for PLA:P3TMA-83 and 50 samples, respectively.

The electroactivity, which refers to the ability to store charge, was evaluated by integrating the cathodic and anodic areas of the voltammograms displayed in Figure 7.1.10. Specifically, the electroactivity increases with the similarity between such areas. Results indicate that the electroactivity increases significantly upon the

incorporation of P3TMA, especially when the concentration of the CP is higher than 30% wt. Thus, the electroactivity measured for PLA:P3TMA-83, 67 and 50 is 17%, 190% and 289%higher than that of PLA. In order to investigate the electrochemical stability of the samples, five consecutive cycles were applied by varying the potential in the interval defined by -0.4 V (initial and final potential) and 1.1 V (reversal potential) at 50 mV/s. The electroactivity decreases with the oxidation and reduction areas of consecutive voltammograms. The voltammograms recorded after such five cycles, which are shown in Figure 7.1.10b, indicate that the oxidation–reduction peak distributions are highly similar. As it can be seen, the reduction of the cathodic and anodic areas, which reflects a loss of electroactivity, depends on the P3TMA content. More specifically, the LEA determined for PLA:P3TMA-50 and PLA:P3TMA-83 samples is 27% and 38%, respectively, evidencing that the electrostability increases with the P3TMA content.

Table 7.1.4 summarizes the electrochemical behaviour for all samples including the values of the current densities measured at 1.10 V for the first and fifth cycles. Major differences in the electrochemical behaviour were found when the integrated area and the current density were considered. Thus, independently of the number of cycle, charge and current density increased when the P3TMA content did. Results indicate that the incorporation of P3TMA into the PLA matrix provided fibers with interesting electrochemical features since an increase in both the electroactivity and electrostability were clearly observed.

Table 7.1.4. Electrochemical behaviour of PLA and PLA:P3TMA-83, -67, and -50 samples: current density at 1.1 V and charge for the 1st cycle and the 5th oxidation-reduction cycles, and electrostability after 5 consecutive cycles.

	***j* at 1.1 V (mA/cm^2)**		***Q* (mC)**		**LEA (%)**
	1st cycle	5th cycle	1st cycle	5th cycle	
PLA	0.138	0.102	2.9	2.0	31
PLA:P3TMA-83	0.152	0.098	3.1	1.9	38
PLA:P3TMA-67	0.355	0.223	8.4	5.5	34
PLA:P3TMA-50	0.394	0.290	11.3	8.3	27

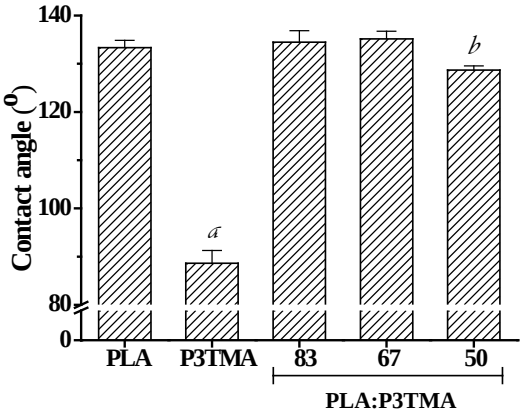

Figure 7.1.11. Graphical representation of the contact angles measured for PLA, P3TMA and PLA:P3TMA mixtures with 83 wt%, 67 wt% and 50 wt%. Tukey's test, $p < 0.05$; *a*, *b* *vs.* other materials.

Wettability of PLA:P3TMA fibers

Figure 7.1.11 compares the contact angle measured for the different systems studied in this work. The average value of the contact angle determined for PLA (133.4° ± 1.5°) and P3TMA (88.6° ± 2.6°) reflects the hydrophobic character of the polyester and the slightly hydrophilic nature of the polythiophene derivative. It should be noted that the contact angle found for PLA is similar to that recently reported by Liu *et al.* for PLA nanofibers prepared using a similar technique.[33] The very low wetting ability of electrospun PLA nanofibers should be attributed to the combined effect of the surface roughness and morphology for these particular nanostructures. The addition of P3TMA to PLA does not produce relevant changes in the contact angle of the latter, values obtained for PLA:P3TMA-83, -67 and -50 mixtures being 134.5° ± 2.4°, 135.1° ± 1.6° and 128.7° ± 0.8°, respectively. The similarity between the contact angles of PLA and PLA:P3TMA combined with the electrochemical results displayed in the previous subsection suggest that the behaviour of the mixtures as supportive matrix for the cell growth should be better than that of the homopolymer. Thus, the incorporation of P3TMA to the PLA matrix is expected to mainly affect the hydrophilicity of the surface, which in fact remains practically unaltered, and the ability of exchange ions across cell membranes, which was shown to be enhanced.

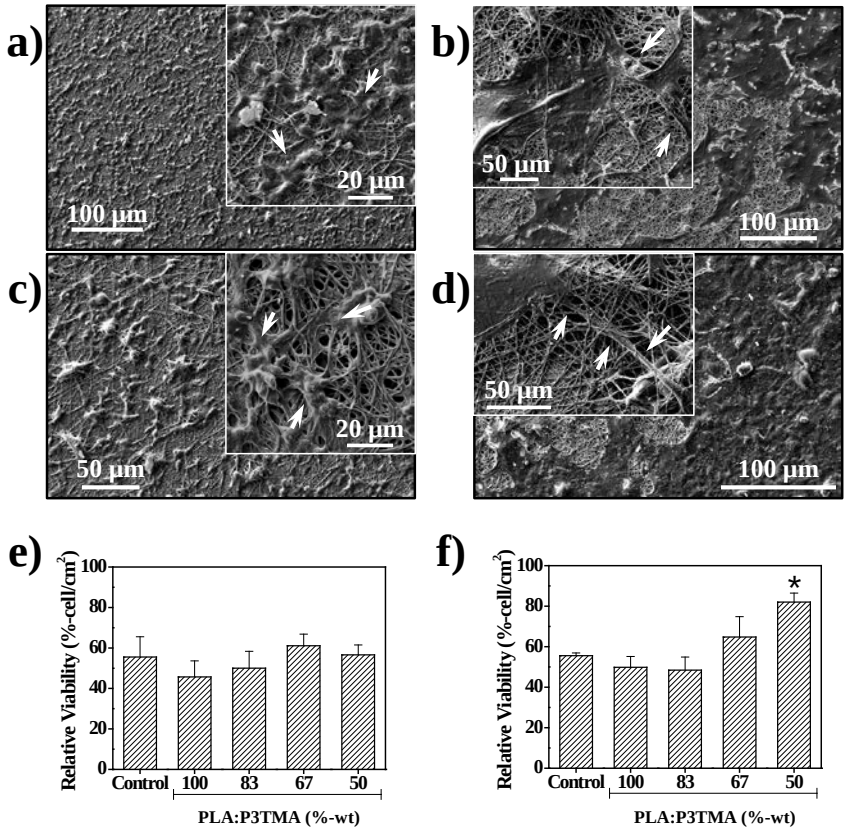

Figure 7.1.12. SEM images of Vero cells adhering (a and c) and growing (b and d) on electrospun fibers of PLA (a and b) and PLA:P3TMA-50 (c and d). The arrows indicate morphological details of the cellular extensions. Quantitative data of the relative adhesion (e) and proliferation (f) of cells onto the fibers mats. * $p < 0.05$ vs others fibers mats and control (tissue culture plate), Tukey's test for $n = 4$ replicates.

Cell adhesion and growth in PLA:P3TMA hybrid scaffolds

SEM images of Vero cells adhered and grown on the PLA (control) and PLA:P3TMA matrices were qualitatively very similar (Figure 7.1.12). Vero cells cultured during 24 h on the 3D surfaces led always to a homogeneous distribution and rounded morphologies (Figure 7.1.12a and c), which should correspond to individual cells or small groups of a few cells (insets of Figure 7.1.12a and c). Cells appeared also adhered to the fibers by small filopodia. Cells cultured during 7 days on the mats surface were able to form monolayers (Figure 7.1.12b and d), a typical

indicator of cell viability and proliferation. The surface colonization progressed through a suitable cellular extension, which apparently was facilitated and guided by the fiber array (inset in the Figure 7.1.12b and d).

In quantitative terms, the P3TMA content in the fibers did not affect the cell adhesion (Figure 7.1.12e) but interestingly the cellular proliferation was slightly improved in the scaffolds with a higher P3TMA content (Figure 7.1.12f). In this way, the new electrospun micro/nanofibers constituted by the hybrid materials may improve the electrochemical properties and the cellular response (frequently mediated by ionic channels) to several physiological processes, such as membrane depolarization during cell division.[34]

In conclusion, PLA:P3TMA micro/nanofibers were well suited to provide a good substrate for cell adhesion and cell proliferation and offered an appropriate 3D environment. Furthermore, cells developed in the PLA:P3TMA matrices showed always a healthy morphology.

7.1.4. Conclusions

Mixtures of PLA and P3TMA can be effectively electrospun to render hybrid micro/nanofibers that combine the biocompatibility and electrochemical properties of each homopolymer. Processing conditions (solvent, concentration, flow, voltage, collector distance) were optimized to allow incorporating up to 50 wt% of P3TMA and keeping continuous fiber morphology. Increasing contents of the conducting polymer gave rise to smoother fiber surfaces, smaller diameters, higher orientation of PLA chains and the sporadic formation of cluster aggregates inside the fibers.

Incorporation of P3TMA into the PLA matrix provided an increase of the electroactivity and electrostability, both charge and current intensity clearly increasing with the P3TMA content. Current density determined at 1.10 V was so high as 0.394 mA/cm^2 for fiber mats containing 50 wt% of P3TMA, while the electroactivity of such hybrid was 289% higher than that of PLA. The electrostability of samples was probed since the average charge loss was less than 27% after performing five consecutive oxidation–reduction cycles. New hybrid scaffolds were good substrates for cell adhesion and cell proliferation, and even the last was clearly enhanced respect to the parent PLA scaffolds. Cellular response to physiological processes seemed to be improved by the incorporation of P3TMA.

7.2. PLA:P3TMA Electrospun Nanofibers as Drug Delivery Systems

7.2.1. Introduction

Polylactide (PLA), which is the biodegradable polymer chosen to be blended with P3TMA to render fibrous biointerfaces (section 7.1), has been also widely studied for its drug loading and release behaviour, and it has already been commercialized in surgical sutures and microspheres for drug delivery.[35-38] Also, it has been used to fabricate scaffolds for nerve regeneration.[39] In addition, PLA displays good resistance to degradation, and thus researchers have used PLA microfilaments as structural support for long lesion nerve gap regeneration.[40]

On the other hand, electrically conducting polymers (CPs) represent another important family of organic materials with proved biocompatibility. Specifically, CPs have attracted the attention of biomedical engineers in the last few years because many cell types (*e.g.* neurons, osteoblasts and fibroblasts) respond to external electrical and/or electrochemical stimuli *in vitro* and *in vivo* when in contact with CPs.[41,42] Several researchers have demonstrated that cellular adhesion, proliferation and stimulation are promoted upon the application of external potentials.[43] One of the pioneers in the study of the effect of electrical stimulation (ES) on cell growth and cell regeneration employing CPs was Schmidt's group.[44] Schmidt and co-workers proved that PC-12 cells cultured on polypyrrol (PPy) films and subjected to ES through the film showed a significant increase in neurite lengths compared to those PPy films that were not electrically stimulated or tissue culture polystyrene controls.

Moreover, Albertsson and co-workers have vastly studied the combination of biodegradable polymers with CPs for bioengineering applications. Recently, they studied the degradability and cytotoxicity of blends made of caprolactone and hyperbranched degradable CPs as good candidates for neural tissue engineering applications.[45] In another example, the same group developed PLA films with an hydrophilic and electroactive surface for future biomedical uses.[46] Comparatively, interesting reviews focusing on several kinds of biomaterials and blended systems have been published in the field of tissue engineering.[47-49] Nevertheless, most of the investigations on nanofiber PLA:CPs are related to the use of biodegradable

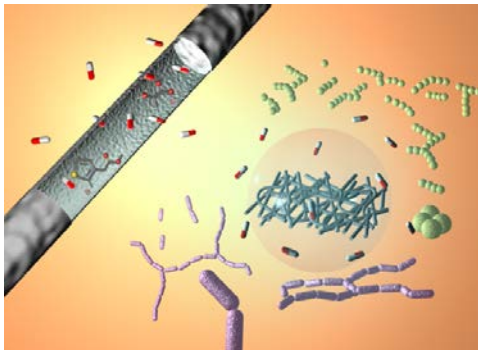

Graphical abstract

polymers combined with electroactive oligomer units as for example, oligothiophene,[50] or oligoaniline,[51,52] and mainly polyaniline (PAni) and PPy derivatives.[48,53-55]

Hence, rationally designed nanofibers with conducting and electroactive features could play an important role as tissue engineering scaffolds and efficient systems for drug targeting and delivery.[56-58] Inspired by this consideration, nanofibers composed by mixing different ratios of polylactide (PLA) and poly(3-thiophene methyl acetate) (P3TMA) for tissue engineering applications were fabricated (section 7.1).[59] Scaffolds containing P3TMA exhibited enhanced cellular proliferation and adhesion in comparison to pristine PLA. The improvement was attributed to the electrochemical and wettability properties provided by the CP.

The overall of the results was a remarkable stimulus to continue investigating the synergistic combination of PLA and P3TMA as a fibrous biointerface. Thus, the aim of the work summarized in this section is to combine the cellular response of PLA:P3TMA biocompatible scaffolds with essential properties as drug carrier and delivery platform. For this purpose, the encapsulation and release of different drugs (*i.e.* ciprofloxacin, chlorhexidine, triclosan and ibuprofen) in PLA:P3TMA systems have been investigated by controlling the nanofiber morphology and CP content inside the PLA polymer matrix. Regarding drug delivery systems fabricated with biodegradable polymers and CP nanofibers, antecedents are very scarce. Martin and co-workers[60] developed electrospun poly(lactide-*co*-glycolide)-poly(3,4-ethylenedioxythiophene) conductive core-sheath nanofibers (PLGA-PEDOT) capable of modulating dexamethasone mass release upon electrical stimulation of 1 V. Dexamethasone is an anti-inflammatory drug which reduces inflammation in the central nervous system. After electrical excitation, a significant increase in the amount of released dexamethasone was observed.

7.2.2. Experimental Section

Materials

3-Thiophene acetic acid (3TAA) (98.0%) was purchased from Fluka (Sigma-Aldrich). Iron chloride anhydrous (97.0%), dry methanol (99.5%) and chloroform (99.9%) were purchased from Panreac Quimica S.A.U. (Spain) and used as received without further purification. PLA, a product of Natureworks (polymer 2002D), was kindly supplied by Nupik International (Polinyà, Spain). According to the manufacturer, this PLA has a D-lactide content of 4.25%, a residual monomer content of 0.3%, a density of 1.24 g/cm^3, a glass transition temperature (T_g) of 58 °C and a melting point of 153 °C. The number-average molecular weight (M_n) and weight-average molecular weight (M_w) were measured by gel permeation chromatography (GPC) at 25 °C with a Waters 1525 chromatograph equipped with a Waters 2414 refractive index detector. GPC measurements were carried out using tetrahydrofuran (THF) as eluent with a flow rate of 1 mL/min, respectively. Polystyrene standards were used for calibration. For PLA, M_n = 59300 g/mol and M_w = 117500 g/mol. Ciprofloxacin (CIP) (≥ 98% HPLC), chlorhexidine dihydrochloride (CHX) (≥ 98%), triclosan (TCS) (≥ 97% HPLC), and ibuprofen sodium salt (IBU) (≥ 98% GC) were purchased from Sigma-Aldrich. *Escherichia coli* CECT 101 and *Staphylococcus epidermidis* CECT 231 bacterial strains were obtained from the Spanish Collection of Type Culture (Valencia, Spain), and culture media were purchased from Difco (Detroit, MI, USA).

Synthesis of poly(3-thiophene methyl acetate)

The monomer 3-thiophene methyl acetate (3TMA) was obtained with a 74% yield by refluxing 3TAA in dry methanol for 24 hours at a temperature of 90 °C.[61] Polythiophene derivative, P3TMA, was subsequently prepared by a chemical oxidative coupling polymerization in dry chloroform following the procedure described by Kim *et al*.[21] Anhydrous ferric chloride ($FeCl_3$) was used as oxidant and dopant. The polymerization yield was ca. 61% after removing the residual oxidant and oligomers. Molecular weights were estimated by GPC using 1,1,1,3,3,3-hexafluoroisopropanol as eluent. The number and weight average molecular weights found were M_n = 10700 g/mol and M_w = 22500 g/mol for P3TMA. ^{1}H-NMR (400MHz, $CDCl_3$) δ = 7.28-7.07 (m, 1H, Ar-H), 3.68(s, 2H, -CH_2-), 3.63 (s, 3H, O-CH_3); ^{13}C-NMR (100MHz, $CDCl_3$) δ = 170.8 (C=O), 136-124 (Ar-C), 52.1 (O-CH_3), 34.3 (CH_2); FTIR-ATR (cm^{-1}): 3095-3010 (=C-H β, thiophene ring), 2998 (C-H aliphatic),

1735 (C=O, ester), 1436 (-CH_2-), 1375 (-O-CH_3, ester), 1255-1160 (C-O-CH_3, ester), 840 (C-H β, thiophene ring). Data are in good agreement with previous results.[59,61,62]

Preparation of PLA:P3TMA nanofibers

For the nanofiber preparation, mixtures of PLA and P3TMA were electrospun from chloroform/acetone (70:30 *v/v*) at polymer concentrations of 5 *w/v*-% and 0-5 *w/v*-% for PLA and P3TMA, respectively. Samples will be identified indicating the PLA and P3TMA weigth ratio. According to our previous optimization of processing conditions,[59] PLA electrospun fibers were collected on a target with a deposition distance of 12 cm, applying a voltage of 15 kV (Gamma High Voltage Research, ES30-5W) and a flow rate of 4 mL/h, whereas blends of PLA:P3TMA were prepared using 20-25 kV of voltage and flow rate of 4-10 mL/h. Polymer solutions were delivered via a KDS100 infusion syringe pump (KD Scientific) to control the mass-flow rate, and the tip used had an inside diameter of 0.84 mm (syringe needle, 18G). All electrospinning experiments were carried out at room temperature. Fiber diameters varied from 600 to 800 nm under such conditions.

PLA:P3TMA nanofibers drug-loading

PLA (0.5 g) was dissolved in 5 mL of chloroform-acetone mixture (2:1 *v/v*) and P3TMA (0.25 g) in 4 mL of the same solvent mixture. Then, 1 mL of dimethylsulfoxide (DMSO) containing the drug (0.1 g) was added, and the mixture was homogenized by vortexing to obtain an electrospinable solution of 5 *w/v*-% PLA, 2.5 *w/v*-% P3TMA and 1 *w/v*-% drug. The drugs loaded in the electrospun nanofibers were ciprofloxacin (CIP), chlorhexidine dihydrochloride (CHX), triclosan (TCS) and ibuprofen sodium salt (IBU) (Scheme 7.2.1) The electrospinning process was conducted at room temperature. Electrospun fibers were collected at a distance of 12 cm from the needle (18G, inside diameter of 0.84 mm). The applied voltage was of 25 kV, and the solution was moved with a flow rate of 4 mL/h.

Characterization

^{1}H and ^{13}C-NMR spectra were acquired with a Bruker AMX-300 spectrometer operating at 300.1 MHz. Chemical shifts were calibrated using tetramethylsilane as internal standard. Deuterated chloroform was used as the solvent. Infrared absorption spectra were recorded with a Fourier Transform FTIR 4100 Jasco spectrometer in the 4000-600 cm^{-1} range. A Specac model MKII Golden Gate attenuated total reflection (ATR) with a heated Diamond ATR Top-Plate was used.

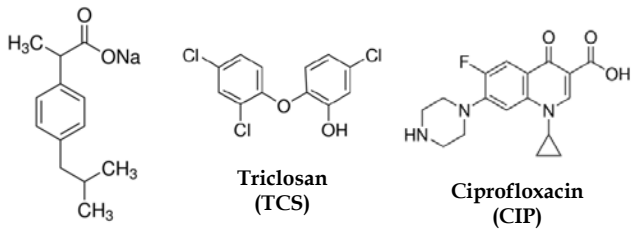

Ibuprofen sodium salt (IBU) **Triclosan (TCS)** **Ciprofloxacin (CIP)**

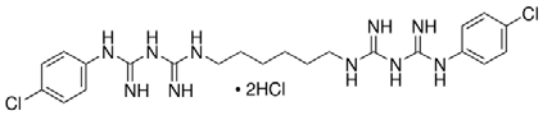

Chlorhexidine dihydrochloride (CHX)

Scheme 7.2.1. Chemical strcuture of the drugs loaded in PLA:P3TMA electrospun nanofibers: ibuprofen sodium salt (IBU), triclosan (TCS), ciprofloxacin (CIP) and chlorhexidine dihydrochloride (CHX).

Atomic force miscroscopy (AFM) images were obtained for all the samples in tapping mode with an AFM Dimension 3100 microscope and a NanoScope IV controller (Veeco) under ambient conditions. A silicon probe Tap150-G (Budget Sensors) with a resonant frequency and spring constant of 150 kHz and 5 N/m, respectively, was used. The row scanning frequency was set at 0.8 Hz and the scan window size varied from 1×1 μm^2 to 20×20 μm^2. Data were acquired using the Reasearch NanoScope software (v. 7.30) and, afterwards, they were analyzed using the NanoScope Analysis software (v. 1.20).

Confocal Raman-AFM microscope a300R+ from WITec (GmbH, Germany) was used to collect single Raman spectra from the homopolymers (*i.e.* PLA and P3TMA), PLA:P3TMA fibrous blends and drug loaded samples. For excitation, a laser with wavelength of 785 nm was used. The integration time was between 0.3 and 2.1 seconds depending on the scan, and high resolution Raman images were obtained by collecting complete Raman spectra at less than 3 cm^{-1} per pixel. Nanofibers were analyzed as obtained after the electrospining process, without any additional preparation, at room temperature and after the exposure time necessary to decay the fluorescence.

Optical morphologic observations were performed using a Zeiss Axioskop 40 microscope. Micrographs were taken with a Zeiss AxiosCam MRC5 digital camera. Morphological characterization of the electrospun samples was conducted by scanning electron microscopy (SEM) using a Focus Ion Beam Zeiss Neon 40

instrument (Carl Zeiss, Germany). Prior sample observation, carbon coating was accomplished by using a Mitec K950 Sputter Coater. Samples were visualized at an accelerating voltage of 5 kV. Diameter of electrospun fibers was measured with the SmartTiff software from Carl Zeiss SMT Ltd.

Contact angle measurements were performed with an OCA 15EC (DataPhysics Instruments GmbH, Filderstadt) equipment and using the droplet sessile method at room temperature. Three different polar solvents were tested: ultrapure water, formamide and ethylene glycol (Table 7.2.1). For the static contact angle (sCA) measurements, solvent droplets of volume 0.5 µL were dispensed on the respective surfaces. Images were recorded after drop stabilization (30 s) using the SCA 20 software. Contact angle values were obtained as the average of fourteen independent measures for each sample.

Table 7.2.1. Surface energy components of the liquids used in sCA measurements.

Liquid	γ_L^d	γ_L^p	γ_L
Water	29.1	43.7	72.8
Formamide	35.1	23.1	58.2
Ethylene Glycol	29.3	18.9	48.2

The surface energy (SE) of PLA:P3TMA samples was calculated based on the sCA data by applying several mathematical approaches: Equation-of-State (EoS),[63] Fowkes,[64] Owens-Wendt-Rabel-Kaelble (OWRK)[65,66] and Wu[67] models, which will be described in detail below. Surface phenomena (wetting, adsorption and adhesion) are controlled by the SE of materials. Generally, organic polymers show low SE values.[68,69] SE can be related to the contact angle via Young's equation:[70]

$$\gamma_S = \gamma_{SL} + \gamma_L \times \cos\theta \tag{7.2.1}$$

where θ is the contact angle, γ_S the SE of the solid-gas interface, γ_{SL} the SE of the solid-liquid interface and γ_L the SE of the liquid-gas interface. Each model defines an expression for γ_{SL}, which is combined with the Young's equation (Table 7.2.2). Therefore, the solid's SE (γ_S) can be obtained from this relation since the contact angle and the liquid's surface tension (γ_L) can be easily measured.[71] Table 7.2.1 contains the SE components of the liquids used. Researchers neglect the influence of γ_{SL} (value still unknown) in systems containing a solid polymer and a measuring liquid because it is insignificant.[72] M. Żenkiewicz analyzed the most commonly

applied methods for the calculation of the surface energy of solids, utilizing the results of the contact angle measurements.[72]

The main difference between the models mentioned above is the component composition of the SE (γ_S). The simplest model is the EoS model because it is based on an empirical approach, which only uses the total surface tension of the test liquid. Therefore, this approach does not consider any interface component, namely polar or disperse, and it is practically less accurate than others, being only applicable to mainly disperse systems.[63,71] For instance, Fowkes considers the SE of a solid or a liquid as the sum of independent components, each one of them related to specific interactions.[64] Therefore, the SE of a solid (γ_S) is broken into its components:

$$\gamma_S = \gamma_S^d + \gamma_S^p + \gamma_S^h + \gamma_S^i + \gamma_S^{ab} + \gamma_S^0 \tag{7.2.2}$$

where γ_S^d, γ_S^p, γ_S^h, γ_S^i and γ_S^{ab} are the dispersion, polar, hydrogen (related to hydrogen bonds), induction, and acid-base components, respectively, while γ_S^0 refers to all remaining interactions. In spite of this, Fowkes' model uses an expression for γ_S which only takes into account the dispersive component. Other interaction components are neglected. Thus, from the Fowkes method only the dispersive contribution to the SE can be extracted (*i.e.* especially convenient when applied to nonpolar polymers and polymeric materials)[72]. Nevertheless, since this method is based on the independence and additivity of the dispersion and polar interactions, γ_S^p can be calculated from Eq. 7.2.9 knowing the Fowkes' γ_S^d value and the θ_p values obtained using a liquid with a strong polar component (*i.e.* water).

On the contrary, an important modification to Fowkes' model was done by Owens and Wendt (OWRK) who considered that all the interface components in Eq. 7.2.2, except the dispersive component of the SE, can be associated to the polar component.[65,66] Therefore, the SE of a solid (γ_S) is broken into its components, the dispersive (γ_S^d) and the polar component (γ_S^p). Both components are independent and additive in nature. Thus, the polar component includes all the remaining interactions. Consequently, a distinction between the polar and the dispersive component of the SE is obtained from the OWRK approach. Besides, the γ_S expression includes a geometric mean of these components. Because of the difference when defining the polar interaction in the Fowkes and OWRK models, $\gamma_L^p$and γ_S^p in Eq. 7.2.2 are not comparable with those in Eq. 7.2.10. When applying the OWRK method, at least two measuring liquids have to be used to determine the contact angle, and thus yield two set of equations in the form of Eq. 7.2.11 from which calculate $\gamma_S^p$and γ_S^d. Generally, water, glycerol, formamide, diiodomethane or

α-bromonaphthalene are chosen for this purpose. Lastly, the Wu model also discerns between the polar and the dispersive component of the SE as the OWRK model does, but it substitutes the geometric mean used in the γ_S expression by a harmonic mean.[67]

To sum up, the SE components of a solid surface can be related to its sCA value (θ) determined with a liquid which surface energy components (γ_L^d and γ_L^p) are known. In addition, the work of adhesion (W_A) was determined to quantify the wettability of a liquid droplet on the sample.[69] As defined in [73], W_A is the work required to separate the drop from the solid surface, while leaving behind on that solid surface the adlayer adsorbed from equilibration with the vapour of the liquid at saturation pressure, and it is defined as:

$$W_A = \gamma_L(1 + \cos\theta) \tag{7.2.3}$$

Based on the OWRK model, W_A was calculated according to the following equation:

$$W_A = 2\left(\sqrt{\gamma_S^d\gamma_L^d} + \sqrt{\gamma_S^p\gamma_L^p}\right) \tag{7.2.4}$$

Table 7.2.2. Main mathematical models used to obtain the surface energy (γ_S) of PLA:P3TMA nanofibers.

Model	Equations	
Equation of State (EoS)	$\gamma_{SL} = f(\gamma_S, \gamma_L)$	(7.2.5)
	$\gamma_{SL} = \gamma_S + \gamma_L - 2(\gamma_L\gamma_S)^{0.5}[\beta_2(\gamma_L - \gamma_S)^2]$	(7.2.6)
	β_2 = 1.057× 10^{-4} Determined experimentally for several standard solids and various measuring liquids.[72]	
Fowkes	$\gamma_{SL} = \gamma_S + \gamma_L - 2(\gamma_S^d\gamma_L^d)^{0.5}$	(7.2.7)
	$\gamma_S = \gamma_S^d = \frac{\gamma_L^2(1 + \cos\theta)^2}{4\gamma_L^d}$	(7.2.8)
	$\gamma_S^p = \frac{\left[0.5\gamma_L(1 + \cos\theta_p) - (\gamma_S^d\gamma_L^d)^{0.5}\right]^2}{\gamma_L^p}$	(7.2.9)
OWRK	$\gamma_{SL} = \gamma_S + \gamma_L - 2(\gamma_S^d\gamma_L^d)^{0.5} - 2\left(\gamma_S^p\gamma_L^p\right)^{0.5}$	(7.2.10)
	$\left(\gamma_S^p\gamma_L^p\right)^{0.5} + (\gamma_S^d\gamma_L^d)^{0.5} = 0.5\gamma_L(1 + \cos\theta)$	(7.2.11)
Wu	$\gamma_{SL} = \gamma_S + \gamma_L - 4\left[\frac{\gamma_S^d\gamma_L^d}{\gamma_S^d + \gamma_L^d} + \frac{\gamma_S^p\gamma_L^p}{\gamma_S^p + \gamma_L^p}\right]$	(7.2.12)

Electrochemical impedance spectroscopy (EIS)

EIS measurements were performed using an AUTOLAB PGSTAT302N in the 10 kHz to the 10 mHz frequency range with an sinusoidal voltage amplitude of 10 mV. All experiments were carried at room temperature. Fiber mats were cut in a disc shape (1.766 cm^2) and were sandwiched between two stainless steel electrodes assembled into an isolating resin holder.[74] The cell was tightened with screws to ensure constant pressure fastening. The thickness of the films, which was determined by a micrometer, varied between 18.9 and 26.0 µm. Prior cell closing, samples were immersed in phosphate buffer saline (PBS, pH 7.4) at room temperature for 24h, and the water excess wiped out with a tissue. After data collection, EIS results were then processed and fitted to an electrical equivalent circuit (EEC).

Drug-release experiments

Drug-loaded mats were cut into small square pieces (20×20×0.1 mm^3) which were weighed and placed into polypropylene tubes. PBS and PBS supplemented with 70 *v/v*-% of ethanol (PBS-EtOH) were considered as release media. PBS was considered as a hydrophilic medium in comparison to the PBS-EtOH medium, which is less hydrophilic than PBS. Hence, the PBS-EtOH medium was considered appropriate to simulate the usual release medium supplemented with serum.[28] Drug-release assays were carried out by immersing the sample mats in 50 mL of the release medium at 25 °C for 1 week. Aliquots (1 mL) were drawn from the release medium at predetermined intervals, and an equal volume of fresh medium was added to the release vessel. The drug concentration in the release medium was evaluated by UV-vis spectroscopy using a UV-3600 (Shimadzu, Japan). Finally, the mats were dissolved in chloroform and the residual drug was extracted in ethanol for quantification. Calibration curves were obtained by plotting the absorbance measured at the corresponding wavelengths (*i.e* 322, 254, 281 and 260 nm for CIP, CHX, TCS and IBU, respectively) against drug concentration. All tests were performed in triplicate to control the homogeneity of the release, and the results were averaged.

Agar diffusion test

Escherichia coli and *Staphylococcus epidermidis* were cultured aerobically overnight in 15 mL of brain–heart infusion (BHI) broth at 37 °C. The bacterial suspension was spread on Plate Count Agar (PCA) (Difco, MI, USA) using a nylon swab. Uniform

disks of 1 mm thick and 5 mm in diameter were prepared by perforating the drug-loaded PLA:P3TMA electrospun mats. Then, samples were placed on the surface of the agar plates and incubated at 37 °C. After 24h, the inhibition zone around each specimen was observed to determine the activity of the drug.

7.2.3. Results and Discussion

Topography and RAMAN analyses of PLA:P3TMA nanofibers

In our previous work (section 7.1),[59] a first approach was carried out to characterize and optimize the electrospinning conditions and morphology of PLA:P3TMA nanofiber mats. The presence of P3TMA in the electrospinning solution induced a slightly decrease in the PLA fiber diameter, led to smoother fiber surfaces and gave rise to some heterogeneous clusters inside the fibers, which corresponded to P3TMA aggregates. Furthermore, both the electroactivity and the bioactivity of the fibers increased with the content of P3TMA. In particular, incorporation of the CP provoked a significant enhancement of the cellular proliferation, which increased around 50% with respect to PLA.

AFM analyses of electrospun fibers provided more precise information about the roughness of PLA and nanofiber blends (Figure 7.2.1). The average roughness of PLA nanofibers, which exhibit remarkable irregularities on its surface (Figure 7.2.1a), is 41.4 nm ± 3.8 nm. The addition of P3TMA decreases the surface roughness to 34.8 nm ± 2.5 nm, 39.9 nm ± 3.0 nm and 35.6 nm ± 4.5 nm for 5:1, 2:1 and 1:1 PLA:P3TMA ratios, respectively (Figures 7.2.1b-d). On the other hand, the thickness of the fibers also decreases upon the addition of P3TMA. Moreover, AFM phase images allow us to distinguish a phase contrast for those samples containing P3TMA, which is not observed for PLA fibers. Although this is a strong indication of the P3TMA presence in the fibers, it is not possible to associate each region (*i.e.* dark or bright areas) to a specific polymer-rich phase, or detect P3TMA aggregation.

Further studies were carried out to understand P3TMA compositional distribution on PLA:P3TMA fibers by means of Raman spectroscopy. Figures 7.2.2a and b depict optical images taken with the Raman confocal microscope of PLA fibers and its Raman spectrum. As it can be seen, the PLA spectrum presents identifiable peaks at well-known positions.[75] However, as it is highlighted in Figure 7.2.2b, the most intense line is located at *ca.* 874 cm^{-1}, which corresponds to the νC-COO stretching. Optical images of PLA:P3TMA nanofibers are displayed in Figure 7.2.2c and e. P3TMA powder was analyzed by Raman spectroscopy and the

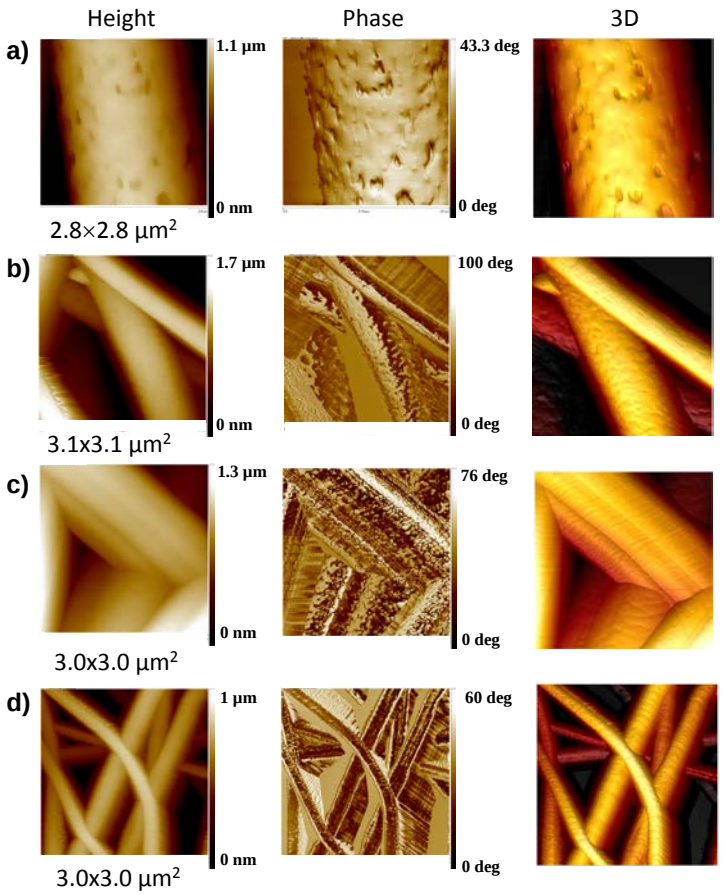

Figure 7.2.1. AFM micrographs from PLA and PLA:P3TMA nanofibers scaffolds: a) PLA, b) PLA:P3TMA 5:1, c) PLA:P3TMA 2:1 and d) PLA:P3TMA 1:1.

resulting spectrum is depicted in Figure 7.2.2d (dotted line). It has to be mentioned that P3TMA showed a great amount of fluorescence when using the laser at 532 nm, which was the one used with PLA fibers. Therefore, P3TMA-containing samples were analyzed using the laser at 785 nm instead, leading to less fluorescence overlapping but also to a lower peak resolution. In this case, the most intense line for the P3TMA spectra is found at *ca.* 1480 cm^{-1}, which corresponds to the totally symmetric in–phase vibration of the bulk thiophene rings spread over the whole polymeric chains linkages.[76] Raman spectra were taken at three different spots of

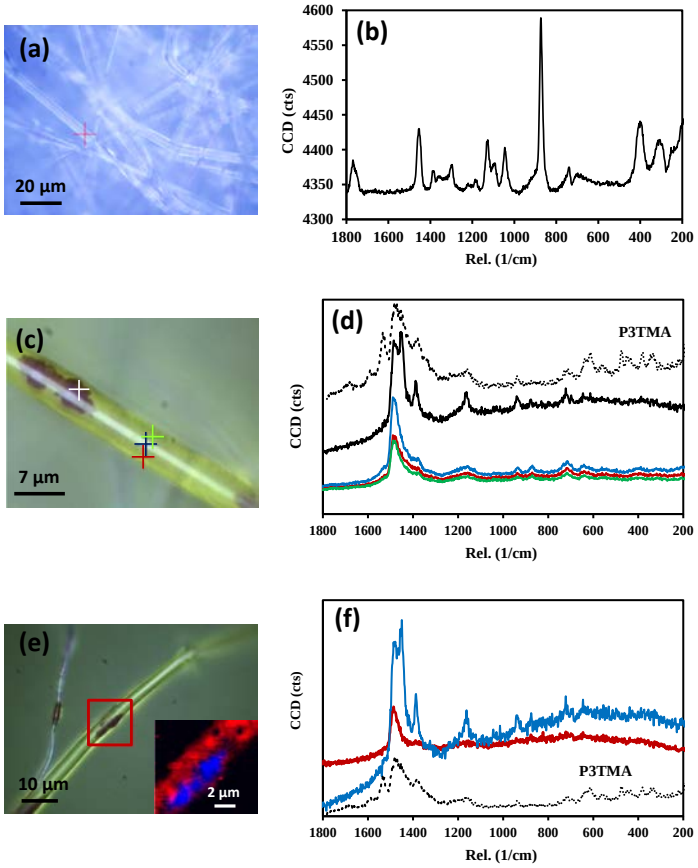

Figure 7.2.2. (a) PLA fiber optical image. (b) PLA Raman spectra at the cross point in (a). (c) PLA:P3TMA 2:1 fiber optical image. (d) Raman spectra at the cross points in (c). The solid black line corresponds to the white cross in (c) and the pointed line to P3TMA powder. (e) PLA:P3TMA 2:1 fiber optical image. Inset: scanned area (red box). (f) Raman spectra associated to the inset in (e).

the PLA:P3TMA fibers (Figures 7.2.2c) as well as in P3TMA particles, which are clearly visible as dark spots inside the fibers (Figures 7.2.2c and e). These results corroborate the homogenous distribution of P3TMA among the PLA fibers, even though some P3TMA agglomerations are also detected. Moreover, PLA:P3TMA (2:1) fibers loaded with drugs were also evaluated by Raman spectroscopy (discussed later).

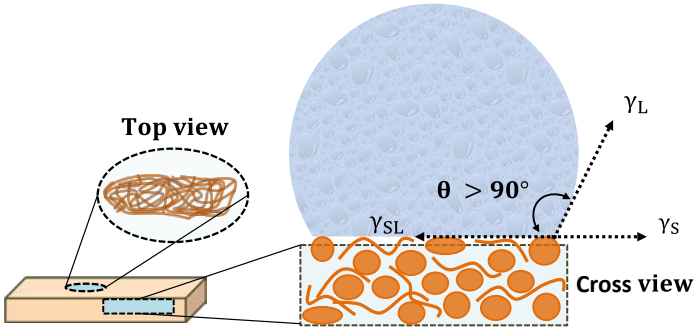

Scheme 7.2.2. Expected wetting behaviour of PLA:P3TMA scaffolds where air pockets avoid the liquid infiltration. SE can be related to the contact angle (θ) via Young's equation (Eq. 7.2.1)

Wettability and surface energy determination

Understanding wetting of hydrophobic and rough surfaces relies on the question if there is a complete liquid penetration into the roughness grooves (homogeneous wetting regime) *versus* the entrapment of air bubbles inside the grooves underneath the liquid, and preventing penetration (heterogeneous wetting regime) (Scheme 7.2.2). These two states are referred as Wenzel and Cassie-Baxter cases, respectively.[77] A composite surface (*i.e.* air and solid) is considered to follow the Cassie-Baxter equations. For drug-delivery applications, the entrapped air in the 3D fibrous scaffolds acts as a barrier avoiding water penetration, and thus affecting the drug-release. Nevertheless, a wetting transition from the Cassie-Baxter state to the Wenzel state occur whenever the air regions are no longer thermodynamically stable, and liquid starts to infiltrate the surface. Generally, the chemical, physical and mechanical features of the drug-loaded systems are controlled to better tune the drug-release rate.[78]

Table 7.2.3 gives the sCA values for the PLA and PLA:P3TMA scaffold samples for the three different liquids evaluated (*i.e.* water, formamide and ethylene glycol). These results have been contrasted with the same PLA:P3TMA blend films prepared by solvent casting, and using $CHCl_3$ as solvent. Results indicate that samples exhibit a different wetting behaviour depending on the microscopic film morphology. Scaffolds with fiber diameters varying from 600 to 800 nm increase and stabilize the PLA sCA values, being more hydrophobic than samples prepared by solvent evaporation. Hence, it is considered that the nanofiber matrix, which

presents a rougher surface and air pockets, is able to stop and retain the liquid phase, and results in a more hydrophobic surface (Scheme 7.2.2). However, the exact final frontier of the three-phase contact line is unclear since the liquid may penetrate the porous matrix through the space left between adjacent fibers. Therefore, it is not possible to affirm which set of state equations (Wenzel, Cassie-Baxter or transition) can be applied to adjust the wetting behaviour of the porous scaffold samples.

In addition to this observation, the incorporation of P3TMA in PLA nanofibers does not alter the hydrophobicity of the later to a great extent, as proved by sCA measurements (Table 7.2.3). On the other hand, the wettability of PLA:P3TMA 2:1 is the most similar to PLA nanofiber films (PLA:P3TMA 1:0), except for ethylene glycol.

Table 7.2.3. Contact angle values (in degrees) for PLA:P3TMA samples prepared by electrospinning (fibrous scaffold, FS) and by solvent casting[b)] (SC).

	Water[a)]		**Formamide**		**Ethylene Glycol**	
PLA:P3TMA	FS	SC	FS	SC	FS	SC
1:0	132.0±2.2	76.1±3.1	121.8±5.4	55.3±2.2	110.5±2.7	50.0±2.4
5:1	130.5±2.1	90.5±3.4	118.7±3.2	56.0±2.3	123.8±3.8	55.8±2.1
2:1	135.3±1.5	86.9±5.2	121.6±4.7	55.4±3.2	130.1±2.0	55.0±3.4
1:1	134.6±2.4	87.7±3.8	127.4±2.4	68.6±5.6	126.7±2.0	54.9±1.6

[a)] Previously reported.[59] [b)] PLA and PLA:P3TMA films were solvent casted from a solution of 16 mg/mL of polymer in $CHCl_3$ solvent. The mean values are the average of at least 14 droplets.

Overall, this is a very attractive response for drug-release applications since little wetting and, in turn, slow release, can be achieved by the nanofiber scaffold in contact with these solvents. Our results are in good accordance with other works which apply sCA to determine the wettability of PLA-based samples. For instance, Kaplan *et al.* studied the superhydrophobicity of biodegradable poly(lactide-*co*-glycolide) electrospun meshes,[78] while Singh *et al.* characterized the modification of the surface properties of poly(lactic acid)-perfluoropolyether block copolymeric films.[69]

Surface phenomena, like wetting, adsorption and adhesion, are controlled by the SE of the materials used for deposition. Therefore, an exhaustive surface tension study using the sCA data obtained for ultrapure water, formamide and ethylene glycol (Table 7.2.3), have been performed using the theoretical models previously described (Table 7.2.2). As each model considers different physical assumptions and interactions for the calculation of the SE components, comparison among such approaches is not recommended. However, as it is observed in Table 7.2.4, a general behaviour can be extracted from the results. Values for γ_S and its components, γ_S^d and γ_S^p, which refer to dispersive and polar interactions, respectively, decrease with increasing P3TMA content. Samples with high SE, like PLA:P3TMA (1:0) nanofibers, are more readily to interact with liquids because of their bonding potential. Results allow us to conclude that a small percentage of P3TMA adequately dispersed in the electrospinning process is able to reduce the SE parameters, helping the system to avoid rapid drug release in polar solvents.

Table 7.2.4. Surface energy parameters (mJ/m^2) for PLA:P3TMA fibrous scaffolds.

	EoS	**Fowkes**	**OWRK**		
PLA:P3TMA	γ_S	γ_S^d	γ_S^d	γ_S^p	γ_S
1:0	7.07±0.26	7.00±0.23	10.99±0.00	0.62±0.00	11.61±0.00
5:1	6.53±0.36	5.05±0.21	3.95±0.00	0.11±0.00	4.06±0.00
2:1	5.02±0.38	3.51±0.28	3.61±0.00	0.00±0.00	3.62±0.00
1:1	4.43±0.18	3.61±0.14	2.52±0.00	0.13±0.00	2.65±0.00

Moreover, the effect of PLA:P3TMA fibrous morphology on the SE values was also compared with the same blend films prepared by solvent casting from $CHCl_3$ solutions (Table 7.2.5). Results demonstrated that γ_S values obtained from the latter are one order of magnitude higher than those from samples prepared by electrospinning. In the literature, γ_S values for PLA films have been determined to be between 35.1-40.2 mJ/m^2 (up to 50 mJ/m^2), with γ_S^d *ca.* 26.9-29.7 mJ/m^2, and γ_S^p *ca.* 8.2-10.5 mJ/m^2, which are in good agreement with our results for solvent casted films. Hence, the SE values of fibrous PLA:P3TMA interfaces, and thus their wetting response, are influenced by the morphology displayed.

Table 7.2.5. Surface energy parameters (mJ/m²) for PLA:P3TMA solvent casted films.

	EoS	Fowkes	OWRK		
PLA:P3TMA	γ_S	γ_S^d	γ_S^d	γ_S^p	γ_S
1:0	37.65±0.24	35.99±0.02	33.99±0.03	4.42±0.01	38.41±0.03
5:1	33.79±0.77	53.67±0.10	73.08±0.00	2.31±0.01	75.39±0.00
2:1	34.75±0.69	54.6±0.10	58.2±0.02	0.10±0.00	58.31±0.02
1:1	32.04±0.38	47.93±0.10	37.66±0.02	0.95±0.00	39.62±0.02

Finally, the highest work of adhesion (W_A) was obtained for PLA scaffolds, which was attributed to the fact that PLA exhibits the highest SE calculated using the OWRK model (Table 7.2.6). Accordingly, this surface is less repellent to liquid than the systems with P3TMA. In conclusion, the surface energy and adhesion work of PLA:P3TMA scaffolds prepared by electrospinning are substantially lower than those obtained for solvent-casted blends, thus the surface of the fibrous mats are more repellent to polar liquids.

Table 7.2.6. W_A values (mJ/m²) for PLA:P3TMA scaffolds based on the data obtained applying the OWRK model (Eq. 7.2.4).

PLA:P3TMA	Water	Formamide	Ethylene Glycol
1:0	49.08	49.02	44.72
5:1	34.68	33.18	30.23
2:1	33.72	33.13	29.26
1:1	30.37	28.45	25.91

Nanofiber characterization by EIS analysis

The presence of the CP moiety in the PLA nanofiber mat accomplishes two purposes. Firstly, as it has been discussed previously, a small percentage of P3TMA adequately dispersed is able to reduce the SE parameters, thus decreasing the wetting behaviour and slowing down the rapid drug release in polar solvents. Secondly, it is expected that cells will respond to an external electrical or electrochemical stimuli when in contact with the CP. Therefore, before the drug-loading step, the bulk conductivity of PLA:P3TMA nanofiber mats was evaluated by EIS. Samples were prepared by electrospinning and cut in disc-shaped formats for adaptation to the capacitor cell (Figure 7.2.3).[74]

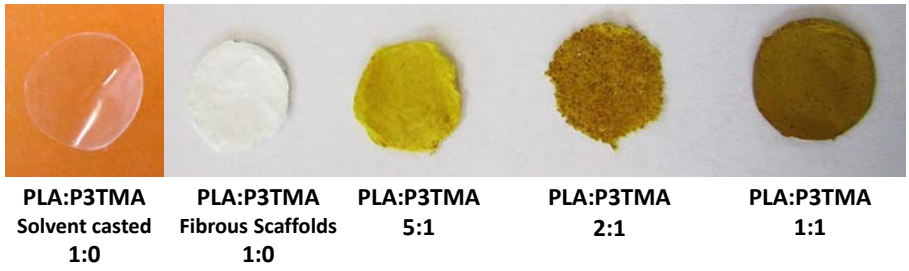

Figure 7.2.3. Photographs of PLA:P3TMA nanofiber scaffolds and PLA:P3TMA 1:0 solvent casted film, which were prepared for EIS analyses.

The Nyquist and Bode plots provided information about the homogenous distribution or, by contrary, the collapse of P3TMA in the biopolymeric matrix when it is not well distributed. As it is reflected in Figure 7.2.3, scaffolds become darker with increasing content of CP in comparison to the PLA pristine films. Figure 7.2.4a indicates that PLA:P3TMA (1:0) scaffolds exhibit similar resistance and capacitance than PLA:P3TMA (5:1), proving that the incorporation of a very low concentration of CP does not alter the electrochemical response of PLA fibers.

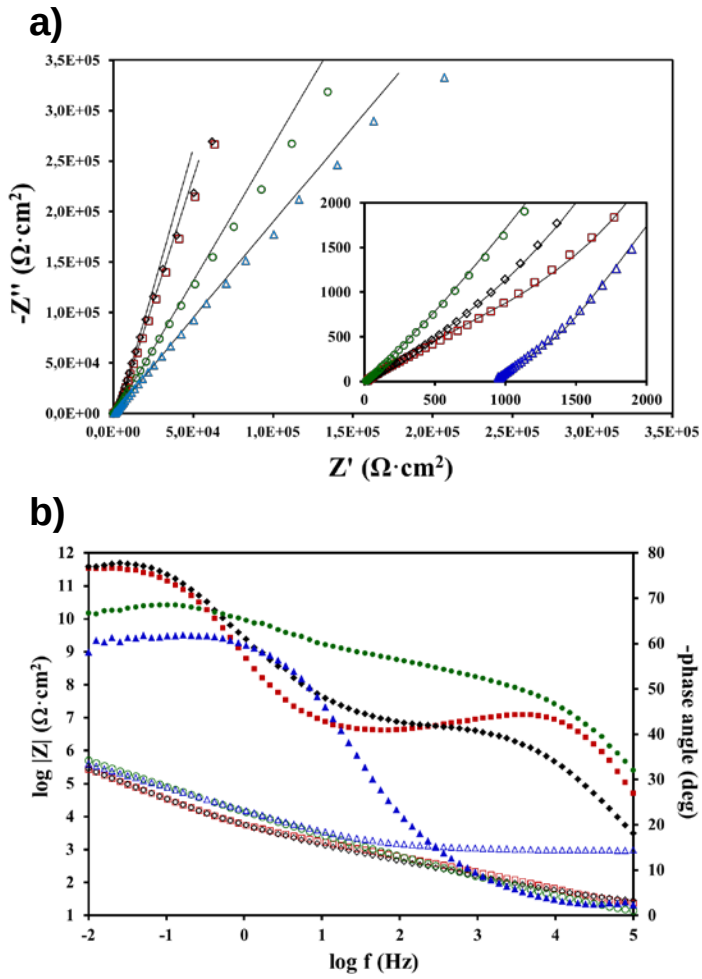

Figure 7.2.4. a) Nyquist plots of PLA (red square) and 5:1, 2:1 and 1:1 PLA:P3TMA (black diamond, green circle and blue triangle, respectively) fiber matrices. The inset shows the impedance plot with magnified scale axes. Continuous lines correspond to the fitting of experimental data using the EEC in Figure 7.2.5c. b) Bode diagram from Nyquist plot. Filled figures refer to the angle phase axis, while empty figures refer to the log|Z| axis.

Results for the three replicated samples of each system were alike and, therefore, only one curve has been represented. As it can be seen, each spectrum shows a very compressed and small beginning of a semicircle in the high frequency range, and an inclined straight line in the low frequency range. It is well known that the high frequency semicircle is associated to the bulk relaxation of the film and its irregular thickness and morphology, while the straight line refers to the migration of ions and the surface inhomogeneity of the electrodes.[79]

On the other hand, the spectrum for the PLA:P3TMA 1:1 scaffolds, which contains the highest P3TMA concentration, shows a slightly different behaviour as it is observed in the Bode plot (Figure 7.2.4b). The phase angle for these samples is very low in the high frequency region, which only can be explained by the presence of defects caused by an irregular distribution of P3TMA aggregates inside the nanofibers, thus provoking the rapid penetration and conduction of the electrolyte across the scaffold. In contrast, P3TMA seems to be homogenously distributed in PLA:P3TMA 2:1 nanofibers, thus showing a Nyquist plot (Figure 7.2.4a) with the lowest resistance and capacitance values (Table 7.2.7), whereas the Bode plot (Figure 7.2.4b) presents the highest phase angle (32.1º) and the lowest log $|Z|$ (1.15) at the high frequency zone (10^5 Hz), in comparison to nanofibers made of PLA:P3TMA (1:0) or the other ratios.

Quantitative analyses of these results required fitting with an adequate electrical equivalent circuit (EEC), which provides a simple understanding of each nanofiber system. In our experiment, PLA:P3TMA samples were placed between two stainless steel electrodes forming a through-plane cell geometry for bulk resistance and capacitance measurements across the film (*i.e.* forming a capacitor cell).[74] Basically, it means that under polarization, an electrical double layer will be formed at the electrodes interface. This charged ion monolayer includes the electrolyte ions arranged in a monolayer at the electrode surface since they cannot trespass the electrode, and the layer of opposite ionic charge at the electrode surface.[79]

As it is carefully explained by Soboleva *et. al.*,[80] the idealized circuit for such a system has several elements and can be represented by the EEC displayed in Figure 7.2.5a. Briefly, each film/blocking electrode interface is represented by the parallel combination of a capacitance, which models the capacitance of the double layer (C_1 and C_2), and the resistance of the blocking electrode (R_1 and R_2). Besides, the bulk properties of the polymer film are represented by means of a bulk membrane capacitance (C_b) and a bulk resistance (R_b). However, after taking into account several considerations (*i.e.* the electrode/electrolyte interface is merely capacitive,

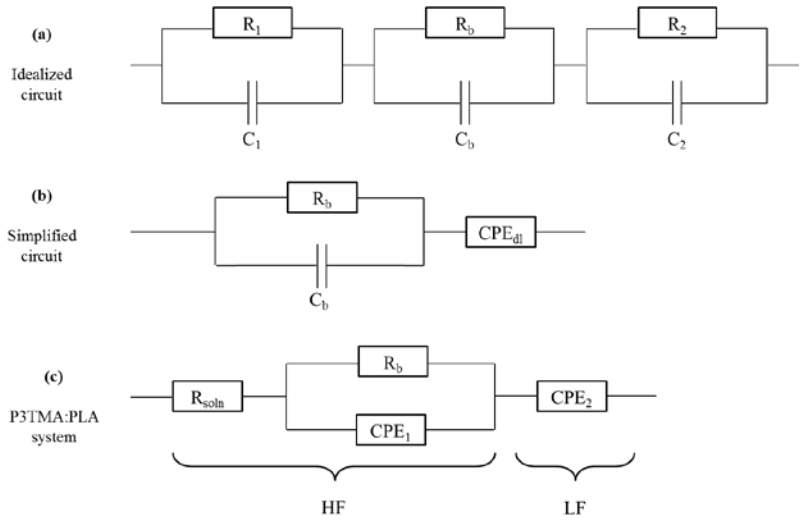

Figure 7.2.5. EEC for a film sample between two blocking electrodes: (a) Ideal circuit, (b) simplified circuit and (c) EEC adjusted to PLA:P3TMA scaffolds. HF stands for high frequency range and LF for low frequency range.

therefore resistances R_1 and R_2 can be omitted, and also that the dominant process at the proton conducting electrode can be considered as a double layer capacitance[80]), the above circuit can be simplified into the one shown in Figure 7.2.5b. The elements of this equivalent electric circuit are C_{dl}, which models the interfacial capacitance that arises from the double layer capacitance at the film/electrode interface, and R_b and C_b, associated in parallel, which represent the bulk resistance and the geometrical capacitance of the film/electrode interface, respectively.

However, as the real system is much more complicated and the capacitance at solid electrodes does not show an ideal behaviour, two constant phase elements substitute C_{dl} and C_b, thus considering the heterogeneity of the system and the roughness and irregularities of the electrode surface.[81,82] The impedance of a CPE (Z_{CPE}), which models the behaviour of a double layer, that is an imperfect capacitor, can be expressed as:

$$Z_{CPE} = \frac{1}{C\omega^n} e^{-\frac{\pi}{2}ni} \tag{7.2.13}$$

$$\alpha = (1-n)\frac{\pi}{2} \tag{7.2.14}$$

where ω is the frequency and n is related to α, which is the deviation from the vertical of the line in the Nyquist plot. Both C and n are frequency independent. Thus, n = 1 equals an ideal capacitance, lower n values reflect the roughness of the electrode employed, and n = 0 a pure resistor.[79]

After fitting the experimental data to an EEC, it was found that PLA and PLA:P3TMA 5:1 and 2:1 wt.% ratio adjust to the circuit depicted in Figure 7.2.5c, while the fitting of the EEC for PLA:P3TMA 1:1 was more difficult to achieve. It is thought that the increasing concentration of P3TMA in the 1:1 sample results in a complex interface distribution caused by the formation of P3TMA agglomerates inside the polymer matrix. Only the experimental data of one tested sample was properly fitted with the previous circuit. Therefore, in terms of the EEC elements analysis, data shown for the PLA:P3TMA 1:1 system are not the averaged values. The EEC satisfactorily used for fitting the EIS data for PLA and PLA:P3TMA blends was $R_{soln}(R_bCPE_1)CPE_2$. It only differs from the general circuit described before (Figure 7.2.5b) in that it includes R_{soln}, which models the PBS electrolyte resistance. The parallel combination of R_b and CPE_1 results in the high frequency semicircle, while the CPE_2 represents the double layer capacitance. Averaged data is summarized in Table 7.2.7.

Table 7.2.7. EEC values obtained after fitting EIS data to the circuit displayed in Figure 7.2.5c for PLA:P3TMA systems. [a)] Only one sample (Sample 1) properly fitted to EEC proposed in Figure 7.2.5c.

PLA:P3TMA	Rsoln (Ω)	CPE_1 (F)	n_1	R_b (kΩ)	CPE_2 (F)	n_2
1:0	8.24 ± 3.34	5.00×10^{-5} ± 1.71×10^{-5}	0.50 ± 0.08	2.47 ± 0.09	2.27×10^{-5} ± 1.82×10^{-5}	0.73 ± 0.13
5:1	11.73 ± 3.91	1.55×10^{-4} ± 3.02×10^{-5}	0.51 ± 0.02	2.74 ± 0.54	4.21×10^{-5} ± 1.90×10^{-6}	0.87 ± 0.03
2:1	11.62 ± 5.58	1.47×10^{-4} ± 5.76×10^{-5}	0.50 ± 0.03	1.75 ± 0.82	1.51×10^{-5} ±8.83×10^{-6}	0.73 ± 0.05
1:1[a)]	939	1.32×10^{-5}	0.66	1.456	4.88×10^{-6}	0.80

EIS results showed that when increasing the P3TMA content in the scaffold matrices, the density of the charge carriers and the mobility of the fiber matrix are also enhanced, improving the bulk conductivity. Concretely, the bulk conductivity of the fiber matrix films can be calculated by applying the following equation:

$$\sigma = \frac{1}{R_b}\frac{t}{A} \tag{7.2.15}$$

where σ is the bulk conductivity, t is the thickness of the fiber film, A is the area of the polymer discs and R_b is the bulk resistance.

The good dispersion of P3TMA particles in the polymeric matrix, under electrospinning conditions, is critical to obtain good electrical properties in the insulating nanofiber blends. The bulk conductivity determined for PLA and the 2:1 PLA:P3TMA were 4.33×10^{-7} and 8.26×10^{-7} S/cm, respectively. Thus, the addition of 33 wt.% of P3TMA in the PLA nanofiber (PLA:P3TMA 2:1) results in an increment in the bulk conductivity of 91%. EIS analyses demonstrated that PLA:P3TMA 2:1 exhibits the highest bulk conductivity and the best dispersion of the CP in the PLA matrix. Table 7.2.8 summarizes the bulk conductivity values for all systems, while Figure 7.2.6 shows the behaviour of all tested samples. Therefore, PLA:P3TMA 2:1 nanofiber mats were chosen for drug-loading and release assays since they accomplish the two-fold purpose described before: suitable wettability properties and good bulk conductivity features.

Table 7.2.8. Thickness and bulk conductivity values for PLA:P3TMA nanofiber scaffolds obtained by EIS measurements. [a)] Only one sample fitted properly to the EEC proposed.

PLA:P3TMA	Thickness (μm)	σ (×10^{-7} S/cm)
1:0	18.9 ± 4.2	4.33± 0.91
5:1	26.0 ± 5.9	5.39 ± 0.72
2:1	25.2 ± 10.6	8.26 ± 0.59
1:1[a)]	24.8 ± 5.8	8.16

Similarly, bulk conductivities were recently reported for other CP-biodegrable polymer systems. For example, PLA was blended with undoped polyaniline (PAni) or doped with camphorsulfonic acid (PAni-CSA) by electrospinning.[83] The conductivity determined by EIS of PLA:PAni and PLA:PAni-CSA was reported to be 1.5×10^{-5} S/cm and 8.4×10^{-2} S/cm, respectively.[83]

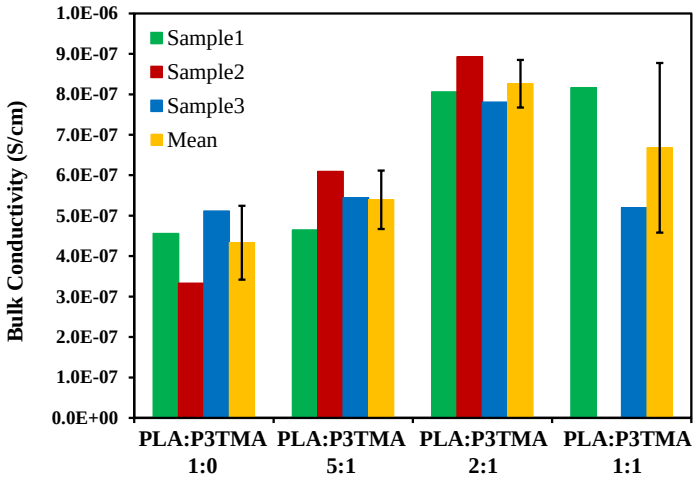

Figure 7.2.6. Bulk conductivity of PLA:P3TMA samples obtained after fitting the EEC to the experimental EIS data. For PLA:P3TMA 1:1, only data from Sample 1 fitted to the EEC proposed in Figure 7.2.5c. It was not possible to fit any EEC for Sample 2, and although data from Sample 3 fitted to an EEC, it was not equivalent to the one proposed for the rest of systems.

The system PLA:PAni was also satisfactorily studied in previous works.[84,14] For instance, McKeon *et al.* electrospun several polyaniline and poly(D,L-lactide) (PDLA:PANi) mixtures at different weight percent values. Only the 25:75 electrospun scaffold was able to conduct a current of 5 mA. The calculated electrical conductivity for this scaffold was 4.37×10^{-2} S/cm.[14]. In another work, PAni-CSA was blended with poly(L-lactide-*co*-ε-caprolactone) (PLCL) to obtain uniform nanofibers with good electrical properties.[85] Recently, incorporation of PAni into PCL fibers significantly increased the electrical conductivity from a non-detectable level for PCL fibers to $63.6 \times 10^{-3} \pm 6.6 \times 10^{-3}$ S/cm for the fibers containing 3 wt.% of PAni.[86] Forciniti *et al.* prepared another biomaterial by blending poly(lactic-*co*-glycolic acid) (PLGA) and chloride-doped polypyrrole (PPy-Cl).[87] Results suggested that PPy-Cl synthesized on the PLGA films inherited the same electrical properties as the homopolymer PPy-Cl film. Conductive polyamide 6 nanofibers were prepared by polymerizing Py molecules directly on the fiber surface (*i.e.* PPy coating of the PA6 fibers).[88] The electrical conductivity of iodine doped poly(3-hexylthiophene-2,5-diyl) (P3HT) electrospun fibers, which was determined using the four-point probe measurement, ranged from 30 S/cm to 60 S/cm.[89]

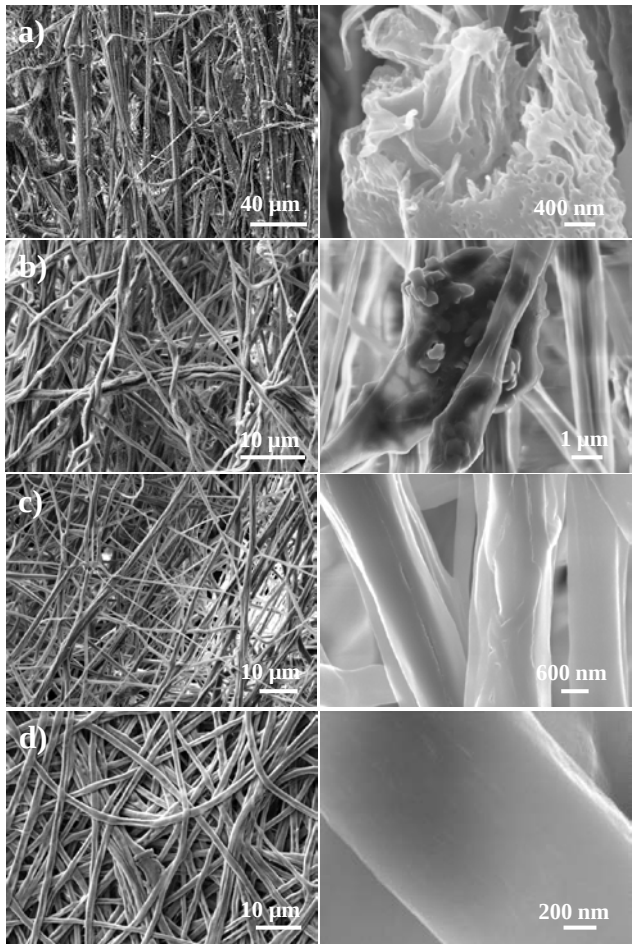

Figure 7.2.7. SEM images of PLA:P3TMA 2:1 samples loaded with: (a) IBU, (b) CIP, (c) CHX and (d) TCS. Left images correspond to low magnification and right images to high magnification.

Topography and RAMAN analyses of PLA:P3TMA 2:1 nanofibers loaded with drugs

Once the PLA:P3TMA:drug (2:1:0.4 *w/w*) samples were prepared considering CIP (antibiotic), CHX and TCS (both biocides), and IBU (anti-inflammatory) as drugs, SEM micrographs were taken to identify the morphological changes induced by the drug-loading. The surface of the loaded fibers was not as smooth and homogeneous as that of the unloaded fiber samples. More specifically, Figure 7.2.7a

and b reflect the lack of uniformity for IBU- and CIP-loaded PLA:P3TMA 2:1 fibers, respectively. These fibers exhibit high flexibility and their diameters are not homogeneous, varying from 1.58 to 5.09 µm. Besides, fibers tend to agglomerate forming disorganized branches without directional preference with diameters between 11 and 40 µm, which in turn are composed of several individual fibers. Figure 7.2.7a (right) shows the interior of a broken IBU-loaded fiber. As it can be seen, the fiber morphology is highly porous, either in the outer or inner side. Figure 7.2.7b (right), which displays a CIP-loaded fiber, allow us to distinguish drug particles embedded into the PLA:P3TMA 2:1 matrix.

Morphological changes are less severe for CHX-loaded samples in comparison to fibrous mats containing IBU and CIP. Particularly, a well formed and homogeneous scaffold made of fibers with similar structure, diameter and surface roughness is obtained (Figure 7.2.7c). Finally, TCS-containing samples provide the most homogenous fibers, exhibiting a highly smooth surface that largely resembles the one obtained for unloaded PLA:P3TMA 2:1 fibers (Figure 7.2.7d).

AFM analyses are in good agreement with SEM observations indicating that, in general, fibers show a great range of diameters and structures. In addition to slight variations in the surface roughness, drug-loading alters the entire fiber distribution in the matrix. For instance, PLA:P3TMA:TCS fibers formed the most compact and regular matrix (Figure 7.2.8). Nevertheless, the incorporation of TCS into PLA:P3TMA 2:1 resulted in "ribbon"-like structures more than in fibers. In contrast, PLA:P3TMA:CHX, PLA:P3TMA:CIP and PLA:P3TMA:IBU fiber matrices were radically different. In these cases, both the random distribution of the fibers and the large spaces between them made AFM observation more difficult (Figure 7.2.9).

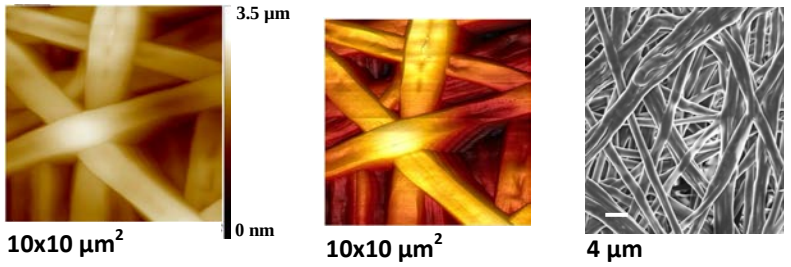

Figure 7.2.8. AFM micrographs from PLA:P3TMA:TCS nanofibers: (a) 2D height image, (b) 3D image (10×10 µm²) and (c) SEM micrograph (scale bar: 4 µm).

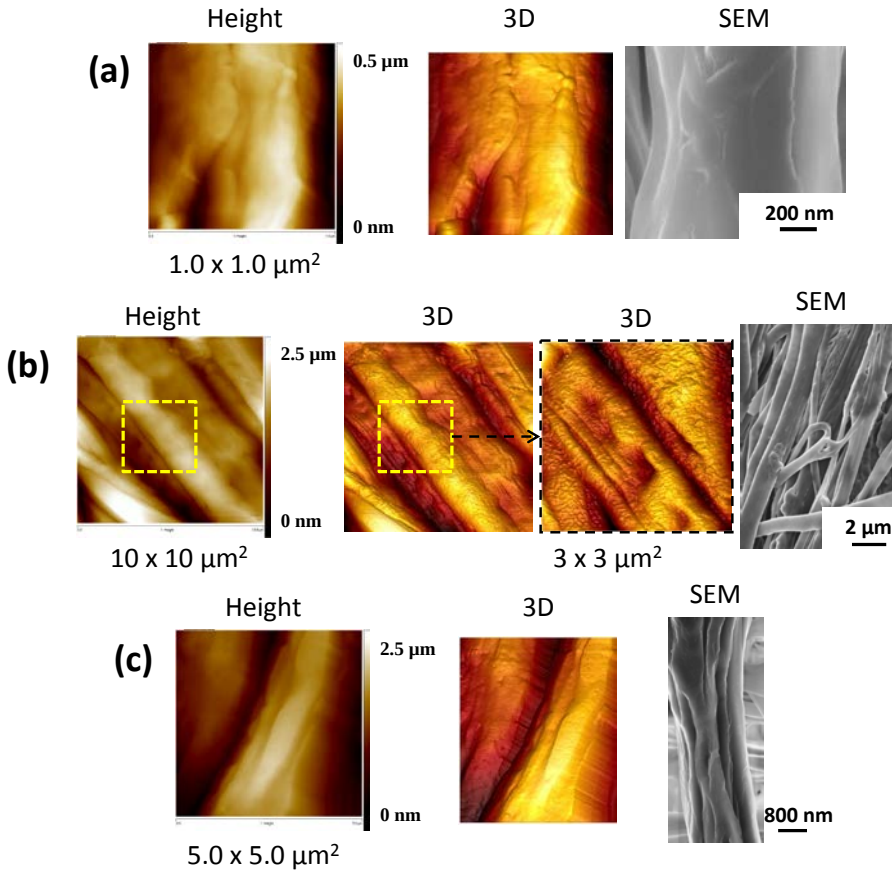

Figure 7.2.9. AFM micrographs from PLA:P3TMA 2:1 loaded with CHX (top), IBU (middle) and CIP (bottom): 2D height image, 3D images and SEM micrograph.

Confocal Raman spectroscopy was also used to examine the drug-loading into PLA:P3TMA samples. Unfortunately, the amount of drug loaded, which was very small (12 *wt.* %), was difficult to identify in some cases. Figure 7.2.10, which shows the spectrum for the PLA:P3TMA:CIP samples, reflects the presence of several peaks (brown-shadowed) coming from the drug and the main absorption band from P3TMA at about 1480 cm^{-1}. Moreover, the corresponding optical image allows us to observe a white shine along the fiber that was attributed to the drug. However, identification of the presence of the drug in the spectra of the other three drug-loaded samples (Figure 7.2.11) was not clear, which was attributed to the very small amount of loaded drug (12 *wt.*%). In spite of this, it should be noted that

morphology changes observed by SEM and optical microscopy of PLA:P3TMA:drug nanofibers suggested the presence of the drug inside the fibers.

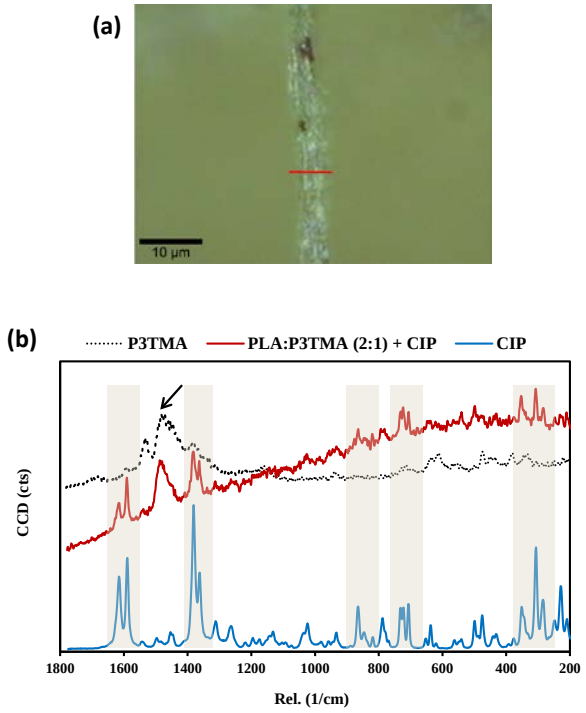

Figure 7.2.10. (a) Optical image of PLA:P3TMA:CIP fiber. The red line shows the spot in which the Raman spectrum was taken. (b) Raman spectra: the dotted line corresponds to P3TMA powder, the blue line to CIP powder and the red line to the PLA:P3TMA:CIP sample.

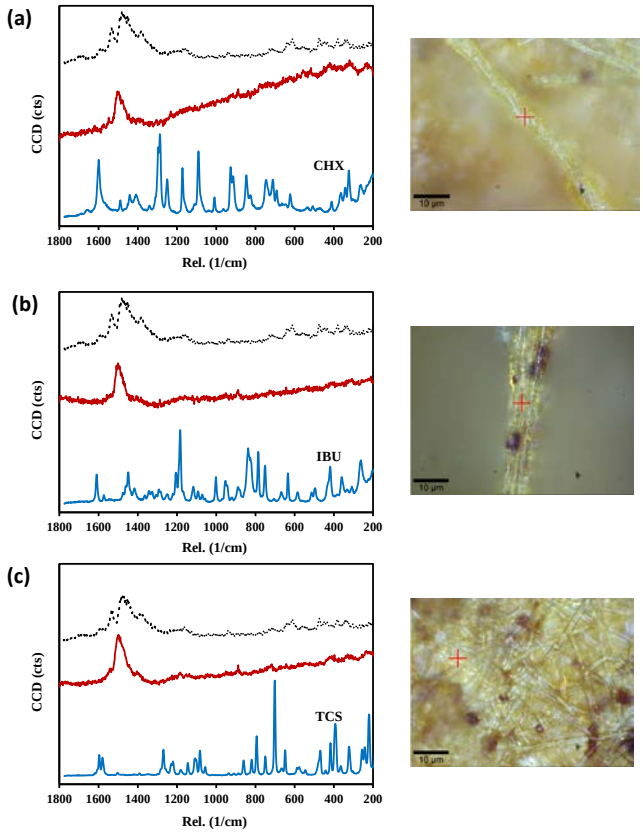

Figure 7.2.11. Raman spectra of: (a) PLA:P3TMA:CHX, (b) PLA:P3TMA:IBU and (c) PLA:P3TMA:TCS. The dotted line corresponds to P3TMA powder spectrum, the blue line to the drug powder spectrum and the red line to the PLA:P3TMA:drug spectrum.

Drug release study

Drug release from electrospun fibers in a given medium is intimately related to the morphology and crystallinity of such fibers and also to the intermolecular interactions that can be established between drugs and the polymeric matrix. Quantitative release studies were performed considering PLA:P3TMA matrices loaded with CIP, CHX, TCS and IBU (Scheme 7.2.1). Both PBS and PBS-EtOH were used as release media. According to previous studies,[28] the ethanol supplement facilitates the release of highly hydrophobic molecules, such as TCS and IBU,

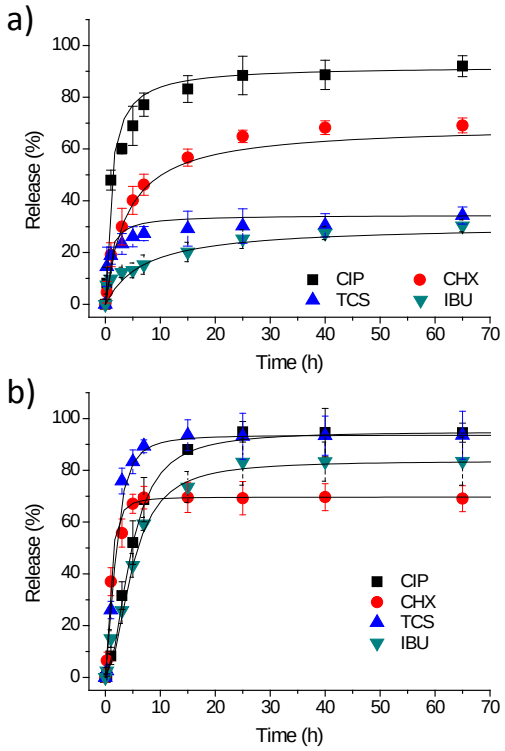

Figure 7.2.12. Drug release profile from PLA:P3TMA:drug scaffolds in (a) PBS (a) and (b) PBS-EtOH medium.

avoiding the establishment of early equilibrium conditions that typically limit their release in PBS. Figure 7.2.12a shows the release profiles of all four drugs loaded in PLA:P3TMA matrices in the PBS medium. The lower values were obtained for TCS (30%) and IBU (25%) indicating that these drugs were better retained into the polymer crystalline domains. However, the release of TCS and IBU increases to 90% and 80%, respectively, when the release was performed in a more hydrophobic medium (*i.e.* in PBS-EtOH medium) (Figure 7.2.12b).

Comparing the release of CIP and CHX from loaded matrices with that displayed by TCS and IBU drugs, higher release percentages are attained for PLA:P3TMA scaffolds loaded with the formers (*i.e.* 90% and 70%, respectively) in the PBS medium. Moreover, the initial release of CHX in the PBS-EtOH medium was very fast and reached values of 70% after only seven hours of exposure (Figure 7.2.12b). Previous studies[90-92] indicated that the release kinetics of these drugs

loaded into polymer matrices can be explained by the Higuchi and first-order models, which are usually combined to describe the first (0-60%) and second (40-100%) parts of the release,[93] respectively. In both cases, the release process is explained by the diffusion of the drug through the polymer matrix, which is facilitated by the ethanol-induced swelling of PLA.[28]

Thus, from the drug-release profiles of CIP, CHX, TCS and IBU from PLA:P3TMA fibrous interfaces, some important conclusions can be drawn: a) the electrospun hybrid fibers of PLA and P3TMA can be successfully used to load either hydrophilic and hydrophobic drugs, b) the release profiles for PLA:P3TMA 2:1 scaffolds depend on the release environment (*i.e.* less hydrophilic medium, higher velocity of drug release).

Evaluation of bactericide activity of drug-loaded PLA:P3TMA 2:1 scaffolds

Agar diffusion tests were conducted to demonstrate qualitatively the biological activity of the antimicrobial drugs (CIP, CHX and TCS) loaded into PLA:P3TMA 2:1 fibrous scaffolds. *E. coli* and *S. epidermidis* bacteria were chosen as representative Gram negative and Gram positive bacteria groups, respectively. There was no inhibition halo in the growth plate of *E. coli* and *S. epidermidis* (Figures 7.2.13a and b, respectively) around the tested samples for unloaded and IBU loaded PLA:P3TMA matrices. The obtained result was expected because no bactericidal activity has been described for PLA, P3TMA and IBU.

In contrast, halos of inhibition were observed for PLA:P3TMA electrospun matrices loaded with TCS, CHX and CIP according to their antimicrobial activity.[28,87,94] The formation of halos corresponds to the drug released from the scaffold and, subsequently, diffused through the agar. The diameters of the three halos are similar (Figure 7.2.13b) suggesting that the susceptibility of *S. epidermidis* towards TCS, CHX and CIP is similar. However, the response of *E. coli* towards the drugs is completely different, as it is reflected by the different size of the halos. Although the agar diffusion test can also be used as a quantitative method, the diameter of the halos is only indicative of bacterial susceptibility towards the drug. In summary, these results clearly prove that the biological activity of the drugs is not affected by the electrospinning process or by the interactions established between the drugs and the PLA:P3TMA matrix, and thus they are feasible to be released from the fibrous biointerface by electrical stimulation.

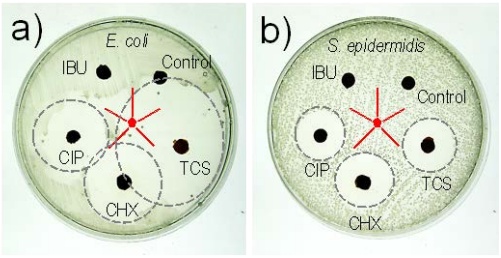

Figure 7.2.13. Growth inhibition of (a) *Escherichia coli* and (b) *Staphylococcus epidermidis*. Unloaded PLA:P3TMA 2:1 scaffold were used as control disk. TCS, CHX, CIP and IBU disks refer to PLA:P3TMA:drug fibers loaded with the corresponding drug. Red lines indicate the areas of the plates occupied by each sample. Inhibition zones are circled with dashed lines.

7.2.4. Conclusions

PLA:P3TMA fibrous interfaces have been obtained to perform as scaffold platforms and drug-delivery systems. For this purpose, after optimization of the electrospinning parameters, PLA:P3TMA samples with different ratios were obtained and further characterized by AFM and SEM microscopies, RAMAN spectroscopy, contact angle measurements, and electrochemical impedance spectroscopy. The overall of the results indicate that the presence of P3TMA in the PLA scaffold matrices induces changes in the fiber surface morphology, although maintaining the fiber integrity, and decreases its bulk resistance. Wettability studies have demonstrated that a small percentage of P3TMA adequately dispersed in the electrospinning process is able to reduce the surface energy parameters, helping the system to avoid rapid drug release in polar solvents.

PLA:P3TMA 2:1 is the most appropriate system for drug-loading since it combines a suitable wetting behaviour with a good electrochemical response (*i.e.* an increment in the bulk conductivity compared to PLA scaffolds). Therefore, in the future, the electrical stimulated response of drug delivery would be explored for this optimized ratio. In this way, drug release experiments proved that the release kinetics depends on the hydrophilicity of the release medium, being faster for a less polar medium (*i.e.* in the PBS-EtOH medium). On the other hand, CHX showed a stable release behaviour in PBS, combined with a good fiber formation by electrospinning. As expected, neither IBU loaded fibers, PLA nor P3TMA homopolymers show antibacterial activity against *E. coli* and *S. epidermidis* bacteria.

On the contrary, PLA:P3TMA electrospun matrices loaded with TCS, CHX or CIP showed normal antibacterial activity, proving that these bioactive molecules have not been destroyed by the electrospinning process, and also demonstrating that they are well mixed in the PLA:P3TMA scaffold matrices.

7.3. References

[1] Y. Wei, P. I. Lelkes, A. G. MacDiarmid, E. Guterman, S. Cheng, K. Palouian, in *Contemporary Topics in Advanced Polymer Science and Technology*. Peking University Press, Beijing, **2004**, pp. 430.

[2] P. Bidez, S. Li, A. G. MacDiarmid, E. C. Venancio, Y. Wei, P.I. Lelkes, *J. Biomater. Sci., Polym. Ed*. **2006**, *17*, 199.

[3] A. Kotwal, C. E. Schmidt, *Biomaterials* **2001**, *22*, 1055.

[4] R. F. Valentini, in *Nerve Guidance Channels in The Biomedical Engineering HandBook*, CRC Press LLC, Boca Raton, **2000**.

[5] D. H. Reneker, I. Chun, *Nanotechnology*. **1996**, **7**, 216.

[6] A. Frenot, I. S. Chronakis, *Curr. Opin. Colloid Interface Sci*. **2003**, *8*, 64.

[7] Y. Dzenis, *Science* **2004**, *304*, 1917.

[8] D. Li, Y. Xia, *Adv. Mater*. **2004**, *16*, 1151.

[9] K. Jayaraman, M. Kotaki, Y. Zhang, X. Mo, S. Ramakrishna, *J. Nanosci. Nanotechno*. **2004**, *4*, 52.

[10] R. Dersch, M. Steinhart, U. Boudriot, A. Greiner, J. H. Wendorff, *Polym. Advan. Technol*. **2005**, *16*, 276.

[11] J. M. Deitzel, J. Kleinmeyer, D. Harris, N. C. B. Tan, *Polymer*. **2001**, *42*, 261.

[12] M. Li, Y. Guo, Y. Wei, A. G. MacDiarmid, P. I. Lelkes, *Biomaterials* **2006**, *27*, 2705.

[13] P. H. S. Picciani, E.S. Medeiros, Z. Pan, W. J. Orts, L. H. C. Mattoso, B. G. Soares, *J. Appl. Polym. Sci*. **2009**, *112*, 744.

[14] K. D. McKeon, A. Lewis, J. W. Freeman, *J. Appl. Polym. Sci*. **2010**, *115*, 1566.

[15] M. Gizdavic-Nikolaidis, S. Ray, J. R. Bennett, A. J. Easteal, Cooney R. P., *Macromol. Biosci*. **2010**, *10*, 1424.

[16] D. Kai, M. P. Prabhakaran, G. Jin, S. Ramakrishna, *J. Biomed. Mater. Res., Part A* **2011**, *99*, 376.

[17] J. Roncali, *Chem. Rev.*, 1997, **97**, 173.

[18] O. Bertran, E. Armelin, F. Estrany, A. Gomes, J. Torras, C. Alemán., *J. Phys. Chem. B* **2010**, *114*, 6281.

[19] S. Lee, G. D. Moon, U. Jeong, *J. Mater. Chem.* **2009**, *19*, 743.

[20] A. Subramanian, U. M. Krishnan, S. Sethuraman, *J. Mater. Sci.: Mater. Med*. **2012**, *23*, 1797.

[21] B. Kim. L. Chen, J. Gong, Y. Osada, *Macromolecules* **1999**, *32*, 3964.

[22] S. V. Fridrikh, J. H. Yu, M. P. Brenner, G. C. Rutledge, *Phys. Rev. Lett.* **2003**, *90*, 144502.

[23] M. G. McKee, C. L. Elkins, T. E. Long, *Polymer* **2004**, *45*, 8705.

[24] C. J. Luo, M. Nangrejo and M. Edirisinghe, *Polymer* **2010**, *51*, 1654.

[25] D. W. van Krevelen, in *Properties of Polymers*, Elsevier, Amsterdam, **1990**.

[26] C. M. Hansen. *Hansen Solubility Parameters - a User's Handbook*. CRC Press, Florida, **2000**, pp. 168-195.

[27] A. Agrawal, A. D. Saran, S. S. Rath, A. Khanna, *Polymer* **2004**, *45*, 8603.

[28] L. J. del Valle, R. Camps, A. Díaz, L. Franco, A. Rodríguez-Galán, J. Puiggalí, J. *Polym. Res*. **2011**, *18*, 1903.

[29] J. R. Sarasua, R. E. Prud'homme, M. Wisniewski, A. Le Borgne, N. Spassky, *Macromolecules* **1998**, *31*, 3895.
[30] P. de Santis, A.J. Kovacs, *Biopolymers* **1968**, *6*, 299.
[31] W. Hoogsteen, A. R. Postema, A. J. Pennings, G. ten Brinke, P. Zugenmaier, *Macromolecules* **1990**, *23*, 634.
[32] K. Chrissafis, *Thermochim. Acta*. **2010**, *511*, 163.
[33] W. Liu, J. Wei, Y. Chen, P. Huo, Y. Wei, *ACS Appl. Mater. Interfaces* **2013**, *5*, 680.
[34] M.H. Bolin, K. Svennersten, X. Wang, I. S. Chronakis, A. Richter-Dahlfors, E. W. H. Jager, M. Berggren, *Sens. Actuators, B* **2009**, *142*, 451.
[35] H. Okada, H. Toguchi, *Crit. Rev. Ther. Drug Carrier Syst.* **1995**, *12*, 1.
[36] J. Kitchell, D. Wise, *Methods Enzymol.* **1985**, *112*, 436.
[37] J. M. Kane, M. Eerdekens, J. P. Lindenmayer, S. J. Keith, M. Lesem, K. Karcher, *Am. J. Psychiatry* **2003**, *160*, 1125.
[38] M. Hans, K. Shimoni, D. Danino, S. J. Siegel, A. Lowman, *Biomacromolecules* **2005**, *6*, 2708.
[39] M.S. Widmer, P.K. Gupta, L. Lu, R.K. Meszlenyi, G.R.D. Evans, K. Brandt, T. Savel, A. Gukrlek, C.W. Patrick, A.G. Mikos, *Biomaterials* **1998**, *19*, 1945.
[40] N. Rangappa, A. Romero, K.D. Nelson, R.C. Eberhart, G.M. Smith, *J. Biomed. Mater. Res.* **2000**, *51*, 625.
[41] J. Y. Lee, C. A. Bashur, C. A. Milroy, L. Forciniti, A. S. Goldstein, C. E. Schmidt. *IEEE Trans. Nanobiosci.* **2012**, *11*, 15.
[42] M. Gizdavic-Nikolaidis, S. Ray, J.R. Bennett, A.J. Easteal, R.P. Cooney, *Macromol. Biosci.* **2010**, *10*, 1424.
[43] N.K. Guimard, N. Gomez, C.E. Schmidt. *Prog. Polym. Sci.* **2007**, *32*, 876.
[44] C.E. Schmidt, V.R. Shastri, J.P. Vacanti, R. Langer, *Proc. Natl. Acad. Sci.* **1997**, *94*, 8948.
[45] B. Guo, Y. Sun, A. Finne-Wistrand, K. Mustafa, A-C. Albertsson. *Acta Biomater.* **2012**, *8*, 144.
[46] B. Guo, A. Finne-Wistrand, A-C. Albertsson, *Macromolecules* **2012**, *45*, 652.
[47] Y. Wei, P.I. Lelkes, A.G. MacDiarmid, E. Guterman, S. Cheng, K. Palouian, P.R. Bidez, *Electroactive polymers and nanostructured materials for neural tissue engineering in contemporary topics in advanced polymer science and technology*. Zhou QF, Cheng ZD, editors. Beijing China: Peking University Press; **2004**. pp. 430-6.
[48] B. Guo, L. Glavas, A-C. Albertsson, *Prog. .Polym. Sci.* **2013**, *38*, 1263.
[49] D. Bennet, S. Kim, *J. Mater. Sci.* **2011**, *46*, 4723.
[50] N.K.E. Guimard, J.L. Sessler, C.E. Schmidt, *Macromolecules* **2009**, *42*, 502.
[51] W. Zhao, L. Glavas, K. Odelius, U. Edlund, A-C. Albertsson, *Chem. Mater.* **2014**, *26*, 4265.
[52] L. Glavas, K. Odelius, A-C. Albertsson, *Soft Matter* **2014**, *10*, 4028.
[53] G.X. Shi, M. Rouabhia, Z.X. Wang, L.H. Dao, Z. Zhang, *Biomaterials* **2004**, *25*, 2477.
[54] H. Xu, J.M. Holzwarth, Y. Yan, P. Xu, H. Zheng, Y. Yin, S. Li, P.X. Ma, *Biomaterials* **2014**, *35*, 225.
[55] S.I. Jeong, I.D. Jun, M.J. Choi, Y.C. Nho, Y.M. Lee, H. Shin, *Macromol. Biosci.* **2008**, *8*, 627.
[56] D. Svirskis, J. Travas-Sejdic, A. Rodgers, S. Garg. *J. Controlled Release* **2010**, *146*, 6.
[57] G. Bidan, C. Lopez, F. Mendes-Viegas, E. Vieil, *Biosens. Bioelectron.* **1994**, *10*, 219.
[58] R.T. Richardson, A.K.Wise, B.C. Thompson, B.O. Flynn, P.J. Atkinson, N.J. Fretwell, J.B. Fallon, G.G. Wallace, R.K. Shepherd, G.M. Clark, S.J. O'leary, *Biomaterials* **2009**, *30*, 2614.
[59] E. Llorens, M.M. Pérez-Madrigal, E Armelin, L.J. del Valle, J. Puiggalí, C. Alemán, *RSC Adv.*, **2014**, *4*, 15245.

[60] M.R. Abidian, D-H. Kim, D.C. Martin. *Adv. Mater.* **2006**, *18*, 405.
[61] E. Armelin, A.L. Gomes, M.M. Pérez-Madrigal, J. Puiggalí, L. Franco, L.J. del Valle, A. Rodríguez-Galán, J.S. de C. Campos, N. Ferrer-Anglada, C. Alemán, *J. Mater. Chem.* **2012**, *22*, 585.
[62] A.C. Carreon, W.L. Santos, J.B. Matson, R.C. So, *Polym. Chem.* **2014**, *5*, 314.
[63] A. W. Neumann, R. J. Good, C. J. Hope, M. Sejpal, *J. Colloid Interface Sci.* **1974**, *49*, 291.
[64] F. M. Fowkes, *J. Phys. Chem.* **1963**, *67*, 2538.
[65] D. K. Owens, R. C. Wendt, *J. Appl. Polym. Sci.* **1969**, *13*, 1741.
[66] D. H. Kaelble, *J. Adhes.* **1970**, *2*, 66.
[67] S. Wu, *J. Polym. Sci., Part C: Polym. Symp.* **1971**, *34*, 19.
[68] M. K. Chaudhury, *Mater. Sci. Eng.* **1996**, *R16*, 97.
[69] A. Singh, A. K Naskar, D. Haynes, M. J Drews, D. W Smith Jr, *Polym. Int.* **2010**, *60*, 507.
[70] T. Young, *Phil. Trans. R. Soc. Lond.* **1805**, *95*, 65.
[71] D. Janssen, R. De Palma, S. Verlaak, P. Heremans, W. Dehaen, *Thin Solid Films*, **2006**, *515*, 1433.
[72] M. Żenkiewicz, *Journal of Achievements in Materials and Manufacturing Engineering*, **2007**, *24*, 137.
[73] M. E. Schrader, *Langmuir* **1995**, *11*, 3585.
[74] F. Mu̇ller, C.A. Ferreira, D.S. Azambuja, C. Alemán, E. Armelin, *J. Phys. Chem. B* **2014**, *118*, 1102.
[75] G. Kister, G. Cassanas, M. Vert, *Polymer* **1998**, *39*, 267.
[76] G. Shi , J. Xu, M. Fu, *J. Phys. Chem. B* **2002**, *106*, 288.
[77] A. Marmur, *Langmuir* **2003**, *19*, 8343.
[78] J.A. Kaplan, H. Lei, R. Liu, R. Padera, Y.L. Colson, M.W. Grinstaff , *Biomacromolecules* **2014**, *15*, 2548.
[79] X. Quian, N. Gu, Z. Cheng, X. Yang, E. Wang, S. Dong, *Electrochim. Acta* **2001**, *46*, 1829.
[80] T. Soboleva, Z. Xie, Z. Shi, E. Tsang, T. Navessin, S. Holdcroft, *J. Electroanal. Chem.* **2008**, *622*, 145.
[81] I. R. Rodrigues, M. M. de Camargo Forte, D. S. Azambuja, K. R. L. Castagno, *React. Funct. Polym.* **2007**, *67*, 708.
[82] E. F. Douglass Jr., P. F. Driscoll, D. Liu, N. A. Burnham, C. R. Lambert, W. G. McGimpsey, *Anal. Chem.* **2008**, *80*, 7670.
[83] S. Peng, P. Zhu, Y. Wu, S.G. Mhaisalkar, S. Ramakrishna, *RSC Adv.* **2012**, *2*, 652.
[84] M.P. Prabhakaran, L. Ghasemi-Mobarakeh, G. Jin, S. Ramakrishna, *J. Biosci. Bioengin.* **2011**, *112*, 501.
[85] S.I. Jung, E. Ko, J. Yum, C.H. Jung, Y.M. Lee, H. Shin, *Macrom. Biosci.* **2008**, *8*, 627.
[86] M-C. Chen, Y-C. Sun, Y-H. Chen, *Acta Biomater.* **2013**, *9*, 5562.
[87] L. Forciniti, N.K. Guimard, S. Lee, C.E. Schmidt, *J. Mater. Chem.* **2010**, *20*, 8865.
[88] F. Granato, A. Bianco, C. Bertarelli, G. Zerbi, *Macromol. Rap. Comm.* **2009**, *30*, 453.
[89] K.H.K. Chan, T. Yamao, M. Kotaki, S. Hotta, *Synth. Met.* **2010**, *160*, 2587.
[90] R. Zurita, J. Puiggalí, A. Rodríguez-Galán, Macromol. Biosci. **2006**, *6*, 58.
[91] L.J. Del Valle, M. Roa, A. Díaz, M.T. Casas, J. Puiggalí, A. Rodríguez-Galán, *J. Polym. Res.* **2012**, *19*, 9792.
[92] L. J. del Valle, D. Roca, L. Franco, J. Puiggalí, A. Rodríguez-Galán, *J. Appl. Polym. Sci. 2011*, **122**, 1953.
[93] R. Baker in *Controlled release of biologically active agents*. Wiley & Sons, New York, **1987**, Chap. 4.
[94] M.C.Bottino, K. Kamocki, G.H. Yassen, J.A. Platt, M. M. Vail, Y. Ehrlich, K. J. Spolnik, R. L. Gregory. *J. Dent. Res.* **2013**, *92*, 963.

CHAPTER 8

FIBROUS BIOINTERFACES BASED ON POLYTHIOPHENE DERIVATIVE AND BIODEGRADABLE POLY(ESTER UREA)-*CO*-POLY(ESTER AMIDE)

Summary

Following the approach described in chapter 7, a copolymer derived from L-leucine, which bears ester, urea and amide groups, poly(ester urea)-*co*-poly(ester amide) (PEU-*co*-PEA), has been used to prepare P3TMA-based fibrous scaffolds, and appears to be an ideal carrier for the CP.

The resulting scaffolds are practically amorphous and thermally stable, and present a pronounced electrochemical activity. Thus, the formation of polarons and bipolarons at specific positions, the ability to exchange charge reversibly and the electrical stability of hybrid PEU-*co*-PEA:P3TMA electrospun scaffolds are practically the same as those displayed by P3TMA alone.

PEU-*co*-PEA was synthesized by Dr. S. Kobauri and Dr. R. Katsarava[1]. Dr. M. Planellas optimized the preparation of the hybrid scaffolds. Thermal measurements were run by Dr. L. Franco[2].

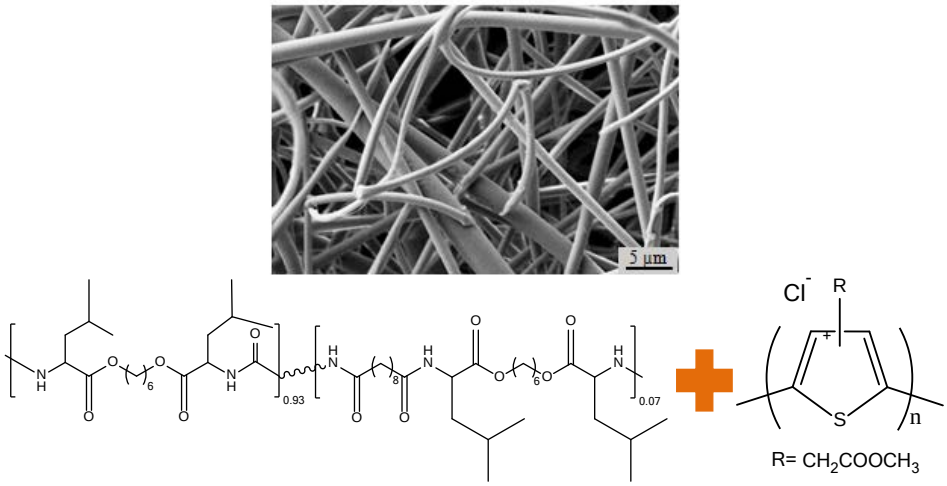

Graphical abstract

Publication derived from this work:

M. Planellas, M. M. Pérez-Madrigal, L. J. del Valle, S. Kobauri, R. Katsarava, C. Alemán, J. Puiggalí, *Polym. Chem.* **2015**, *6*, 925.

[1]Institute of Chemistry and Molecular Engineering, Agricultural University of Georgia, Tblisi, Georgia.
[2]Departament d'Enginyeria Química, E.T.S. d'Enginyers Industrials de Barcelona, UPC.

8.1. Introduction

Materials able to combine biodegradable and conducting properties have highly promising applications in biomedicine. Among conducting materials, conducting polymers (CPs) are potential candidates for the preparation of scaffolds because the intrinsic electrical and electrochemical (*i.e.* electroactivity) properties of these organic materials enhance cell proliferation at the polymer–tissue interface through electrochemical stimulation and an ion-exchange mechanism, respectively.[1–3]

As CPs are non-degradable materials, different strategies have been explored to ensure their biodegradability when used in CP-containing scaffolds. For example, some effort has been focused on the synthesis of hybrid polymers that combine conducting and degradable units.[4,5] Other alternatives are based on the use of degradable polymers as templates for a subsequent deposition of CPs[6–8] or the development of nanostructured blends of conducting and biodegradable polymers.[9,10]

Electrospinning is a versatile technique that offers great potential for the fabrication of hybrid scaffolds with the porosity required for effective tissue regeneration applications.[11] Unfortunately, the preparation of conductive micro/nanofibers by direct electrospinning of CPs is not an easy task due to their low solubility, fast crystallization and low molecular weight. As a result, fiber morphology usually becomes discontinuous showing many beads[12] that, in some cases, can be minimized using a coaxial setup to prevent crystallization at the nozzle tip.[13]

These morphological problems can be overcome by blending the CP with another electrospinnable polymer (used as a carrier). The detriment of the electronic properties is the major inconvenience of this strategy, while the specific properties contributed by the carrier (*e.g.* biodegradability and biocompatibility) represent the new advantages for the development of biomedical materials.

Poly(3-thiophene methyl acetate) (P3TMA) is an electroactive polythiophene derivative with good solubility in some organic solvents such as $CHCl_3$, THF or DMSO. This characteristic has been exploited to prepare a common solution with high molecular weight biodegradable polymers, for example poly(tetramethylene succinate) (Chapter 4) and polylactide (Chapter 7), and fabricate stable FsNM and nanofiber scaffolds.[14–17] The bioactivity of such P3TMA-containing scaffolds as well as of individual P3TMA interfaces was repeatedly proved through cellular adhesion and proliferation assays.

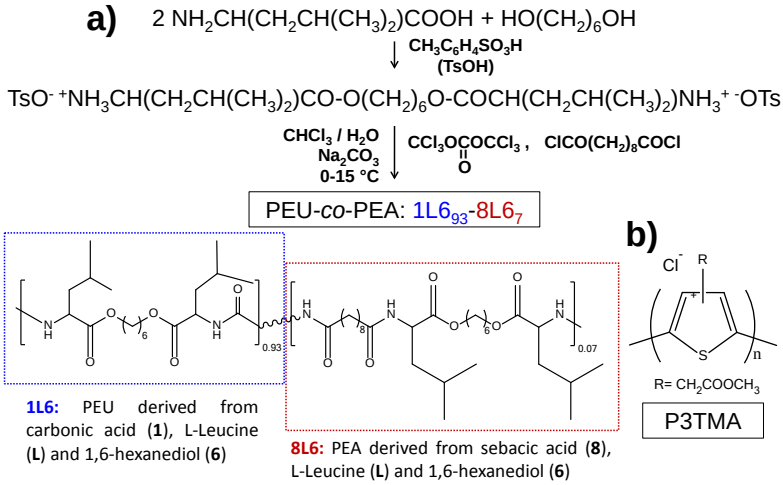

Scheme 8.1.1. a) Synthesis of the biodegradable 1L6$_{93}$-8L6$_{7}$ PEU-*co*-PEA. b) Chemical structure of the conducting polymer P3TMA.

α-Amino acid-based polymers (AABPs) have been receiving great attention as new biodegradable materials for biomedical applications due to their favourable combination of properties. Among AABPs poly(ester amide)s,[18–23] (PEAs) are the most studied. A relatively new and less investigated class of AABPs is the one that includes poly(ester urea)s (PEUs) obtained for the first time by Katsarava and co-workers via solution active polycondensation.[24] Later, this team showed that high-molecular weight PEUs with desirable material properties could be synthesized via interfacial polycondensation using phosgene or triphosgene as starting monomers.[25] In this way, a L-leucine based PEU was successfully used for preparing nanofibers loaded with anti-bacterials drugs,[26] while L-phenylalanine based PEUs were employed to develop high-strength materials as promising bone substitutes.[27,28] In general, PEAs and PEUs are promising materials since strong intermolecular hydrogen bond interactions can be established between amide or urea groups, giving rise to good thermal and mechanical properties. Furthermore, the degradability of these materials can also be guaranteed by the presence of hydrolysable ester groups, whereas the selection of adequate constitutive units may provide biocompatibility and nontoxic hydrolysis by-products. Hence, a tremendous variety of materials with easily customized properties can be obtained due to (i) the high versatility of natural *α*-amino acids with different pendent groups, and (ii) the possibility of using diols along with dicarboxylic acid units with aliphatic segments of different lengths.

The PEU derived from carbonic acid, L-leucine and 1,6-hexanediol (named 1L6 in Scheme 8.1.1a) showed interesting properties and appeared suitable as implantable surgical devices (*e.g.* vascular stents and hard tissue replacement implants). Specifically, a tensile strength at yield, elongation at break and Young's modulus of 21 MPa, 114% and 622 MPa, respectively, were reported together with a melting temperature of 114 °C and a glass transition temperature of 47 °C.[25] Solubility in organic solvents and properties like molecular flexibility can be easily improved by incorporating a small ratio of dicarboxylic acid units with high methylene content (*e.g.* sebacic acid). In this case, copolymers contain both urea and amide groups (PEU-*co*-PEA copolymers) in a proportion that can be easily tuned following a simple two step procedure based on the interfacial polycondensation method previously reported for PEUs (Scheme 8.1.1a).[25]

The goal of the present chapter is to develop hybrid scaffolds with the maximum load of P3TMA using a new biodegradable PEU-*co*-PEA polymer as the electrospinnable carrier. Intermolecular interactions between the polar moieties of the two polymers are expected to play a crucial role and might achieve a high concentration of the CP in the electrospinnable solution. P3TMA has been selected not only because of its high biocompatibility, but also because of its electrochemical activity, the latter being responsible for its excellent behaviour as a bioactive matrix (*i.e.* cellular adhesion and proliferation are significantly enhanced by the ion-exchange ability of this CP at the cell–polymer interface).[14–16,29]

8.2. Experimental Section

8.2.1. Materials

All chemicals were of ACS grade and used without further purification. The di-*p*-toluenesulfonic acid salt of bis-L-leucine-hexane-1,6-diester (L6) was prepared, as reported previously,[30] by direct condensation of 26.24 g (0.2 mol) of L-leucine with 11.8 g (0.1 mol) of 1,6-hexanediol in refluxing benzene (500 mL) in the presence of a slight excess of 39.95 g (0.21 mol) of *p*-toluenesulfonic acid monohydrate. The reaction was prolonged for 16 h until 7.4 mL (0.41 mol) of water was collected in a Dean–Stark trap. The reaction mixture was then cooled to room temperature and filtered off. The obtained white solid was dried using benzene, washed with water to remove excess *p*-toluenesulfonic acid, recrystallized from water and dried at 100 °C in an oven equipped with a fan. Yield 59.25 g (86%), m.p. 189–191 °C, reported m.p. 190–192.30 °C.

8.2.2. Polymer Synthesis

PEU-*co*-PEA copolymer

To a suspension of 13.78 g (0.02 mol) of L6 in 150 mL of water, 6.36 g of anhydrous sodium carbonate (0.06 mol, 3.0 equiv.) was added and stirred at room temperature for about 30–40 min (1st solution). In parallel, 5.52 g (0.0186/3 mol, 93.0 mol%) of triphosgene (purity 98.5%) and 0.335 g (0.0014 mol, 7.0 mol%) of sebacoyl chloride (purity 98.5%) were dissolved in 65.0 mL of chloroform stabilized by amylene (2nd solution). The 1st solution was placed in a reactor for interfacial polycondensation and the 2nd solution was quickly added at one go at room temperature (20 °C) and the water–organic mixture was stirred vigorously for about 15–20 min. The stirring was stopped, and then the mixture was transferred to a separatory funnel and a two layered system was allowed to form. The lower layer, that represents the polymer solution in chloroform, was collected and washed 3 times (3 x 0.6 L – the chloroform layer was separated after each portion of washing water was added) with distilled water to remove the salts (*i.e.* sodium chloride, sodium carbonate/bicarbonate, and sodium *p*-toluenesulfonate). After washing, the chloroform layer was separated again, dried over anhydrous Na_2SO_4 (100.0 g) and filtered off. The obtained chloroform solution was placed in a glass vessel and chloroform (*ca.* 55–60 mL) was removed by distillation under atmospheric pressure. Afterwards, 600 mL of hot water (*ca.* 70 °C) was added to the viscous polymer solution and the rubbery mass formed was removed from the glass vessel and placed onto the Teflon® plate and squeezed to remove and pour out the residual water. The plate was then placed in an oven equipped with a fan and dried at 100 °C. Finally, the polymer was vacuum-dried at 100 °C up to constant weight, and a yield of 95% was obtained with this procedure.

The copolymer PEU-*co*-PEA composed of 93 mol% of poly-(ester urea) 1L6 and 7 mol% of poly(ester amide) 8L6 is labelled as $1L6_{93}$-$8L6_7$ (1 for carbonyl, 8 for sebacoyl, L for L-leucine, and 6 for 1,6-hexanediol units).

P3TMA conducting polymer

The 3-thiophene methyl acetate (3TMA) monomer was obtained with a 74% yield by refluxing 3TAA in dry methanol for 24 hours.[14] The polythiophene derivative, P3TMA (Scheme 8.1.1b), was subsequently prepared by a chemical oxidative coupling polymerization in dry chloroform following the procedure described by Kim *et al.*[31] Anhydrous iron chloride ($FeCl_3$) was used as oxidant and

dopant agent. The polymerization yield was *ca.* 61% after removing the residual oxidant and oligomers.

Molecular weight was estimated by gel permeation chromatography (GPC) using a liquid chromatograph (Shimadzu, model LC-20AD) equipped with a LC solution GPC software (Shimadzu). A PL HFIP gel 9 µm column (Polymer Lab 300 x 7.5 mm) at 40 °C and a refractive index detector (Shimadzu RID-10A) were employed. The polymer was dissolved and eluted in 1,1,1,3,3,3-hexafluoroisopropanol (HFIP) containing CF_3COONa (0.05 M) at a flow rate of 1 mL/min (injected volume 20 µL, sample concentration 2–6 mg/mL). The number and weight average molecular weights and molar-mass dispersities were calculated using poly(methyl methacrylate) standards. Deconvolution of GPC curves was performed with the PeakFit v4 program of the Jandel Scientific Software using an asymmetric function known as "asymmetric double sigmoidal".

8.2.3. Electrospinning

Electrospun fibers were collected on a target placed at different distances (10–25 cm) from the needle tip (inside diameter of 0.84 mm). The voltage was varied between 10 and 30 kV and applied to the target using a high-voltage supply (Gamma High Voltage Research, ES30-5W). Polymer solutions were delivered via a KDS100 infusion syringe pump (KD Scientific, USA) to control the mass-flow rate (from 0.5 to 4 mL/h). All electrospinning experiments were carried out at room temperature. Electrospun fiber scaffolds were prepared using optimized parameters (*i.e.* needle tip–collector distance, voltage and flow rate) and solvent conditions (*i.e.* solvent ratio and polymer concentrations).

8.2.4. Characterization Techniques

FTIR spectroscopy and thermal characterization

Infrared absorption spectra were recorded with a FTIR 4100 Fourier Transform spectrometer from Jasco. A MKII Golden Gate attenuated total reflection (ATR) accessory from Specac was employed. ^{1}H-NMR spectra were acquired with a Bruker AMX-300 spectrometer operating at 300.1 MHz. Chemical shifts were calibrated using tetramethylsilane as an internal standard. Deuterated chloroform ($CDCl_3$) was used as the solvent at room temperature. X-Ray powder diffraction patterns were obtained with a PANalytical X'Pert PRO MPD θ/θ powder

diffractometer with CuK_α radiation (λ = 1.5418 Å) and a silicon monocrystal sample holder. Operating voltage and current were 40 kV and 50 mA, respectively. Thin samples sandwiched between low absorbing films were used.

Calorimetric data were obtained by differential scanning calorimetry with a TA Instruments Q100 series. Experiments were conducted at a heating rate of 10 °C/min under a flow of dry nitrogen with a sample weight of approximately 5 mg, while calibration was performed with indium. Thermal degradation was studied at a heating rate of 10 °C/min with around 5 mg samples in a Q50 thermogravimetric analyzer of TA Instruments and under a flow of dry nitrogen. Test temperatures ranged from 50 to 600 °C.

Morphology of electrospun scaffolds

Optical microscopy studies were performed with a Zeiss Axioskop 40 microscope. Micrographs were taken with a Zeiss AxiosCam MRC5 digital camera. Detailed inspection of texture and morphology of electrospun samples was conducted by SEM using a Focus Ion Beam Zeiss Neon 40 instrument (Carl Zeiss, Germany). Carbon coating was accomplished using a Mitec K950 Sputter Coater fitted with a film thickness monitor k150x. Samples were visualized at an accelerating voltage of 5 kV. Diameters of electrospun fibers were measured with the SmartTiff software (Carl Zeiss SMT Ltd.).

Determination of P3TMA doping level

The doping level (DL) of chemically synthesized P3TMA was determined electrochemically by carrying out chronopotentiometry assays under a constant cathodic current intensity that varied from −0.1 mA to −2 mA (current density: −0.025 to −0.5 mA/cm^2). This procedure aimed to reduce the P3TMA film completely. Electrochemical experiments were conducted on a PGSTAT302N AUTOLAB potentiostat using a three-electrode one-compartment cell under a nitrogen atmosphere at room temperature. The cell was filled with 25 mL of acetonitrile with 0.1 M $LiClO_4$.

Steel sheets, which were used as working electrodes, were cleaned with acetone and their edges were carefully protected with an epoxy resin. Thus, only controlled areas (2 × 2 cm^2) were covered with P3TMA and exposed to the electrochemical medium. A P3TMA solution of 0.1 g/mL was obtained by dissolving P3TMA powder in chloroform. As a pre-treatment, P3TMA underwent mild sonication for 10 minutes before (as a powder) and after its dissolution. Following the pre-

treatment, the solution was filtered with cotton as a separation barrier. Then, the resulting solution was used for solvent-casting deposition. Specifically, 35 µL of the P3TMA solution were solvent cast onto each side of the steel substrate, which was then allowed to dry under vacuum at room temperature for 24 h. The weight of P3TMA deposited was determined as the difference between the masses of the coated and the uncoated working electrodes using a CPA26P Sartorius analytical micro-balance with a precision of 10^{-6} g. The exact amount of P3TMA covering the steel sheet was 6.4 ± 0.4 mg. The reference electrode was an Ag|AgCl electrode containing a KCl saturated aqueous solution (E^0 = 0.222 V at 25 °C) and steel sheets were also used as counter electrodes. For statistical purposes, samples were run in triplicate for each current density tested.

$FeCl_3$ was used as the oxidant and dopant agent in the P3TMA polymerization reaction. Therefore, the counter-ions neutralizing the positive charges in the polymer backbone are mostly Cl^- or $[FeCl_4]^-$ anions. The doping level (DL), which is defined as the number of moles of anions per monomeric unit (MU) of CP, was determined using the following expressions:

$$DL = \frac{mol\ (Cl^-)}{mol\ (MU)} \tag{8.2.1}$$

$$mol\ (Cl^-) = \frac{Q_{red}}{F \times n} = \frac{i_{red} \times t_{red}}{F \times n} \tag{8.2.2}$$

$$mol\ (MU) \approx \frac{m_{P3TMA}}{MW_{MU}} \tag{8.2.3}$$

where Q_{red} is the reduction charge (C), i_{red} (A) is the current intensity applied, t_{red} (s) is the reduction time, F is the Faraday constant (C/mol), n is the electron charge involved in the electrochemical process (n = 1), m_{P3TMA} (g) is the mass of P3TMA deposited onto each working electrode, and MW_{MU} is the molecular weight of the monomeric unit of P3TMA (g/mol).

Electrochemical characterization of PEU-*co*-PEA:P3TMA hybrid scaffolds

In order to assess the electrochemical behavior of the PEU-*co*-PEA:P3TMA scaffolds, cyclic voltammetry (CV) studies were conducted with an Autolab PGSTAT302N galvanostat equipped with the ECD module (Ecochimie, The Netherlands). Measurements were performed on fiber mats, which were deposited

by electrospinning on both sides of steel AISI 316 sheets of 1 cm^2. All electrochemical assays were performed using a three-electrode one compartment cell under a nitrogen atmosphere and at room temperature.

The cell was filled with 50 mL of PBS solution containing 0.1 M $LiClO_4$ as a supporting electrolyte (pH = 7.4). Steel AISI 316 sheets of 1 × 1 cm^2 were used as the working and the counter electrodes, while an Ag|AgCl electrode containing KCl saturated aqueous solution was the reference electrode (offset potential *versus* the standard hydrogen electrode, E^0 = 0.222 V at 25 °C). Ten cyclic voltammograms were registered in the potential range from −0.4 to +1.1 V at a scan rate of 50 mV/s.

The electroactivity, which indicates the ability to exchange charge reversibly, was evaluated by examining the similarity between the anodic and cathodic areas of the control voltammograms. The electrochemical stability (*i.e.* loss of electroactivity, LEA) was determined using the following expression:

$$LEA\ (\%) = \frac{\Delta Q}{Q_1} \times 100 \tag{8.2.4}$$

where ΔQ is the difference in anodic voltammetric charge between the first cycle and the last cycle, and Q_1 is the anodic voltammetric charge corresponding to the first cycle.

8.3. Results and Discussion

8.3.1. Electrospinning of PEU-*co*-PEA

Several solvents and binary solvent mixtures were tested at different voltages, flow rates, polymer concentrations and needle tip–collector distances to obtain continuous electrospun microfibers. PEU-*co*-PEA is soluble in most organic solvents (*e.g.* chloroform, methanol, ethanol and dimethylformamide), the best solubility being attained in a $CHCl_3$–MeOH 10:1 *v/v* mixture. Usually the electrospinning process requires a relatively high polymer concentration to avoid the formation of droplets and electrospun beads.[32] In this case, the minimum value needed to obtain continuous microfibers under a wide range of processing conditions was 18% (w/v). In fact, the high molecular weight of the copolymer facilitated the electrospinning process, and good fibers were obtained under most test conditions.

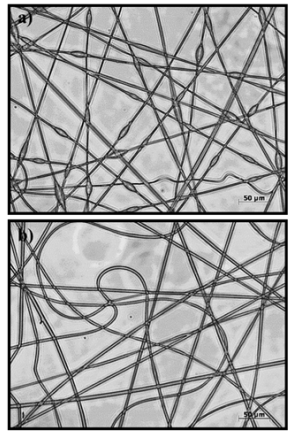

Figure 8.3.1. Optical micrographs of $1L6_{93}$-$8L6_7$ PEU-*co*-PEA electrospun microfibers obtained at a flow rate of 1.5 mL/h, needle tip-collector distance of 24 cm and applied voltages of 20 kV (a) and 25 kV (b).

Table 8.3.1. Optimization of the electrospinning conditions.[a] Both the voltage and rate conditions are optimized to avoid the presence of broken fibers and beads.

Sample[b]	Voltage (kV)	Rate (mL/h)	Morphological characteristics
PEU-*co*-PEA/P3TMA 100	20	1.5	Fibers with beads
	25	**1.5**	Homogeneous fibers
PEU-*co*-PEA/P3TMA 10	20	1.0	Highly broken fibers with beads
	20	1.5	Broken fibers with beads
	25	1.5	Broken fibers with beads
	15	2.5	Broken fibers with beads
	20	2.5	Broken fibers with beads
	20	3.5	Slightly broken fibers with beads
	25	**3.5**	Continuous fibers

[a]The concentration of PEU-*co*-PEA ($1L6_{93}$-$8L6_7$) was 18% (*w/v*). Solvent was a mixture of $CHCl_3$/MeOH (10:1 *v/v*). The optimal parameters are indicated in bold characters. In all cases, the optimal distance between syringe tip and collector was 24 cm. [b] The number after abbreviatures indicates the *wt%* of the PEU-*co*-PEA component in the mixture.

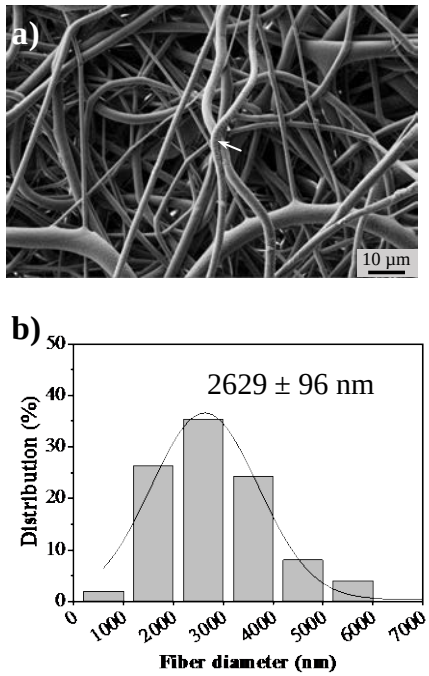

Figure 8.3.2. (a) SEM micrograph of $1L6_{93}$-$8L6_7$ PEU-*co*-PEA electrospun microfibers obtained under optimized processing conditions. Striations are indicated by white arrows. (b) Diameter distribution of the above indicated microfibers.

Nevertheless, the applied voltage was essential to minimize the dramatic effect of the bead formation. This effect is illustrated in Figure 8.3.1, which compares fibers obtained under voltages of 25 kV and 20 kV. Optimal processing conditions (*i.e.* those that avoid the formation of broken fibers and beads) are indicated in Table 8.3.1, while a representative SEM micrograph is given in Figure 8.3.2. Fibers are continuous and tortuous and, in general, have a smooth surface, although striations (white arrow) and porous regions can also be detected. Analysis of the fibers' diameters (Figure 8.3.2b) shows a unimodal distribution with an average value close to 2.63 µm.

8.3.2. Phase Separation of PEU-*co*-PEA:P3TMA mixtures

PEU-*co*-PEA and P3TMA were independently dissolved in $CHCl_3$–MeOH 10:1 *v/v* mixtures to reach a concentration of 36% (w/v). Equal volumes of the two solutions were subsequently mixed in order to obtain a single solution with

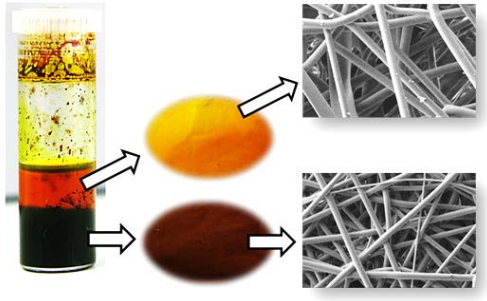

Figure 8.3.3. Image showing the spontaneous phase separation produced by mixing equal volumes of 36% (w/v) solutions of $1L6_{93}$-$8L6_7$ and P3TMA in $CHCl_3$:MeOH 10:1 *v/v* and the resulting macroscopic textures obtained after the electrospinning of each phase.

18%(w/v) concentration of each polymer. The complex system (two solvents and two polymers) spontaneously evolved towards a phase separation with a dense and brown colored P3TMA rich phase (60 v%) and a lighter and yellowish PEU-*co*-PEA rich phase (Figure 8.3.3). This induced phase separation is expected to facilitate the preparation of CP-enriched fibers.

The polymer composition of each phase was ascertained by means of ^{1}H NMR spectra (Figure 8.3.4). P3TMA signals are predominant in the spectrum of the dense phase (Figure 8.3.4a). Specifically, signals of methylene and methyl lateral groups appear overlapped as a double duplet (3.82–3.80 ppm and 3.62–3.60 ppm) and a duplet (3.77 and 3.72 ppm), respectively. Splitting of these signals is interpreted as a consequence of the different arrangements of thiophene rings during chemical polymerization and the corresponding triad and dyad (*e.g.* head-to-head and head-to-tail) sensitivities.[17,31] In addition, the spectrum also shows multiple peaks that can be easily assigned to the predominant PEU unit of the copolymer.

Composition was determined considering the area of the signal at 4.20–4.10 ppm (O–CH_2 protons of the hexanediol unit of both PEA and PEU moieties) and the area of the above mentioned signals corresponding to the lateral groups of P3TMA:

$$\mathrm{PEU} - co - \mathrm{PEA\ mol\%} = 100 \times \frac{\left(\frac{A_{4.20-4.10}}{4}\right)}{\left(\frac{A_{4.20-4.10}}{4}\right) + \frac{A_{3.82-3.60}}{5}} \qquad (8.2.5)$$

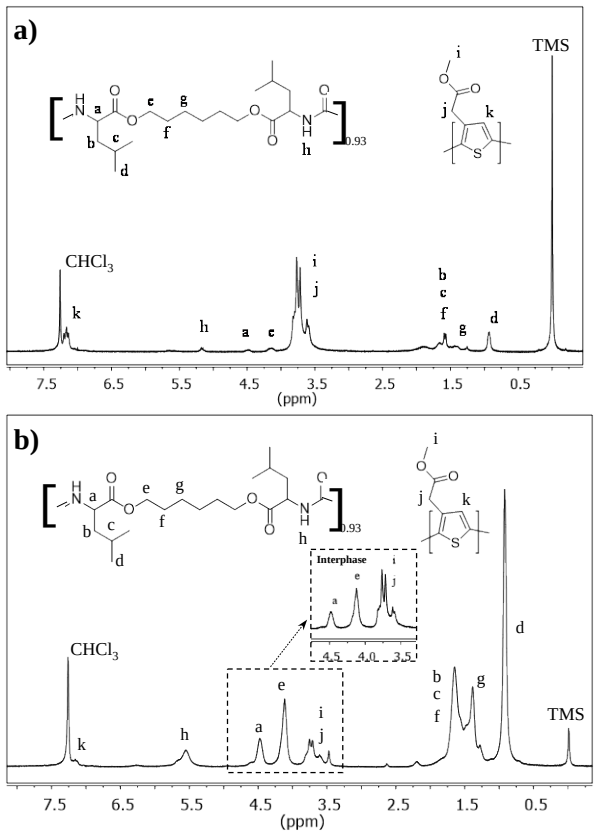

Figure 8.3.4. ^{1}H NMR spectra of the PEU-*co*-PEA:P3TMA mixture obtained from the dense (P3TMA-enriched) brown phase (a) and the light yellowish phase (b). The inset shows the 4.5-3.5 ppm region of the interphase.

The spectrum of the light phase (Figure 8.3.4b) clearly shows predominant signals attributed to the biodegradable copolymer. In addition, the small peak at 2.62 ppm associated to the CO–CH_2 protons of the sebacoyl unit of the PEA moiety can also be appreciated. The spectrum recovered from the interphase shows an intermediate composition, as deduced from the signals appearing in the 4.5–3.5 ppm region (inset of Figure 8.3.4b).

Molar percentages of PEU-*co*-PEA are 5.2, 33 and 61% for the dense, the interphase and the light phase, respectively. These values correspond to 10, 50 and 76 wt% when the molecular weight of the corresponding repeat units is considered. The global polymer concentration (*i.e.* PEU-*co*-PEA plus P3TMA) estimated from a

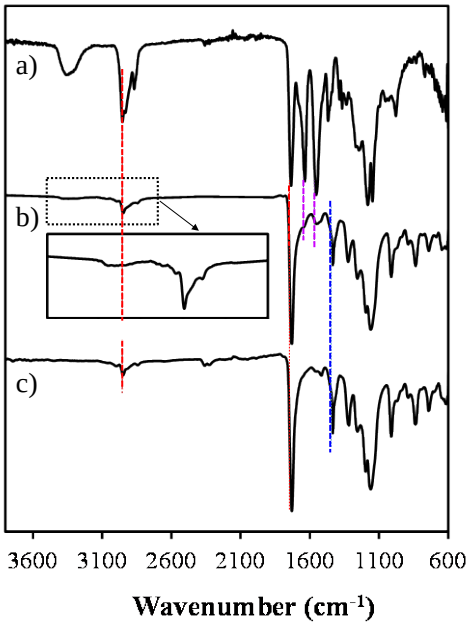

Figure 8.3.5. FTIR spectra of $1L6_{93}$-$8L6_7$ PEU-*co*-PEA (a), the PEU-*co*-PEA:P3TMA mixture from the dense phase (b) and P3TMA (c). The inset corresponds to a magnification for signals corresponding to CH_2 and CH_3 stretching vibrations. Red dashed lines point out common signal for the three samples, whereas black and blue dashed lines indicate common signals between the mixture and PEU-*co*-PEA and P3TMA, respectively.

simple mass balance is 24% and 54% (w/v) for the dense and light phases, respectively. These percentages were experimentally corroborated by weighing the residues recovered after solvent evaporation for each phase.

Figure 8.3.5 compares the FTIR spectra of the biodegradable PEU-*co*-PEA and the conducting P3TMA samples. The spectrum of the polymer mixture coming from the dense phase, which is also displayed, is practically identical to the P3TMA spectrum (*i.e.* peaks do not shift as a consequence of new intermolecular interactions). Specifically, bands at 2950–2840 cm^{-1} (CH stretching), 1732 cm^{-1} (C=O), 1435 cm^{-1} (thiophene ring stretching), 1322 cm^{-1} (methyl deformation), 1198 and 1167 cm^{-1} (asymmetric and symmetric C–O stretching), 1012 cm^{-1}, 839 cm^{-1} (aromatic CH out of plane deformation) and 741 cm^{-1} (methyl rocking) are characteristic of the P3TMA rich sample. The spectrum of PEA-*co*-PEU shows the typical CH_2 (2955 and 2871 cm^{-1}), hydrogen bonded NH (3339 and 1558 cm^{-1}), C=O ester (1734 cm^{-1}), C=O urea (1633 cm^{-1}) and C–O ester (1243 and 1183 cm^{-1}) groups.

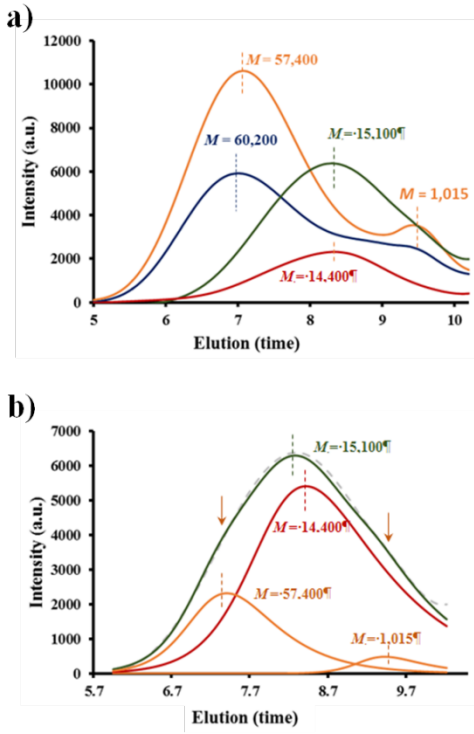

Figure 8.3.6. a) GPC chromatograms of $1L6_{93}$-$8L6_7$ PEU-*co*-PEA (orange), P3TMA (garnet) and polymer mixtures from dense (green) and light (blue) phases. b) Deconvolution of the GPC curve of the dense phase (green) into typical curves of P3TMA (red) and $1L6_{93}$-$8L6_7$ PEU-*co*-PEA (orange). The addition of deconvoluted profiles corresponds to the gray curve.

Note that the absorption of the C=O ester groups appeared at the same wavelength in all samples.

Figure 8.3.6 compares the GPC curves of both the initial biodegradable polymer and the CP and of those recovered from the dense and light phases. P3TMA presents a narrow and unimodal distribution with a maximum at 14400 g/mol. PEU-*co*-PEA shows a broader distribution and two peaks centered at 60200 and 1015 g/mol. Although the peak corresponding to the lower molecular weight fraction is small, it has been used to evaluate the possible existence of fractionation processes during phase separation. This feature may occur if strong interactions can be established between P3TMA and the terminal groups of PEU-*co*-PEA. The chromatogram of the polymer coming from the light phase presents a predominant peak that corresponds to 60200 g/mol and a long tail that should include both the P3TMA fraction and the low molecular weight copolymer fraction. The GPC curve

of the polymer coming from the dense phase is very broad and corresponds to a low molecular weight, as expected from a P3TMA rich fraction. Deconvolution of the curve allowed us to observe two additional peaks associated with PEU-*co*-PEA (Figure 8.3.6b). It is interesting to note that the low molecular fraction of the copolymer is detected in both dense and light phases, allowing us to discard a significant molecular weight fractionation.

8.3.3. P3TMA Doping Level

Electrochemical assays were performed to assess the doping level (DL) of as-synthesized P3TMA, which in fact may also be useful to evaluate the capability to form intermolecular interactions with charged low molecular weight oligomers. Figure 8.3.7 displays a representative chronopotentiometry curve of P3TMA submitted to a reduction process under a constant cathodic current intensity of −2 mA. Although other current intensities of growing values from −0.1 mA to −2 mA were tested, only samples reduced at −2 mA resulted in a complete dedoping of the CP.

The curve shows that the system's potential gradually decreases to more negative values, which is indicative of a dedoping process. The potential value rapidly reduces before stabilizing abruptly at around 500 seconds. Interestingly, the system's potential starts to increase towards more positive values at t_{red}=601.5 seconds (inset of Figure 8.3.7). Therefore, the reduction charge applied up to that minimum equals −1.203 C. This response is interpreted as the completion of the dedoping process. The electrochemical process has reduced completely the polymer backbone, closing the polymer structure up to a point that results in the film break. These fractured regions expose the steel support surface and open new paths for the intensity to flow easily. Thus, the DL determination reveals that each monomeric unit of P3TMA contains 0.27 ± 0.01 counter-ions (one positive hole per 3.7 thiophene rings), which corresponds to 6.0 wt% ± 0.29 wt% of Cl^- counter-ions in the as-synthesized P3TMA samples. This DL is in good agreement with those determined for other CPs.[33–35] Aradilla *et al.*[33] prepared poly[1-(2-cyanoethyl)pyrrole] in acetonitrile using $LiClO_4$ as a dopant agent, while Gök *et al.*[34] synthesized polythiophene in chloroform using $FeCl_3$ as an oxidant. In both cases, it was stated that because of structural disorder in the CP chains and crosslinking, one positive charge is generated per approximately three monomeric units, the measured DLs being 0.35[33] and 0.33.[34] In an earlier work,[35] a reaction of 2,2-bithiophene with

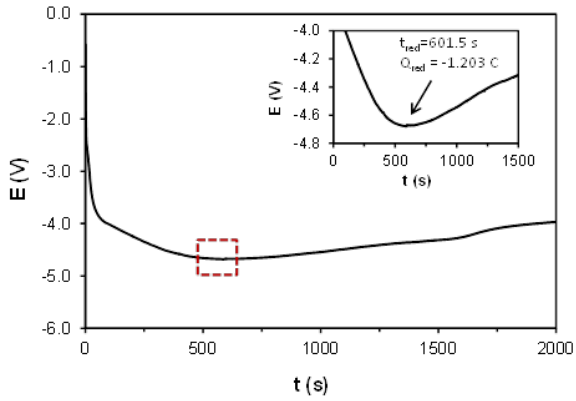

Figure 8.3.7. Chronopotenciometry curve for P3TMA submitted to an electrochemical reduction process at -2 mA. Inset: t_{red} = 601.5 s; Q_{red} = -1.203 C.

copper (II) perchlorate in acetonitrile was conducted and yielded polymers with a DL of ~0.17.

For CPs, such as PTh and its derivatives, the DL and the extension of the π-conjugated system along the polymer backbone are closely related with their electronic properties.[36] The conductivity increases with the amount of dopant until a saturation limit is reached. Comparative studies of polyalkylthiophenes doped with different agents showed that materials doped with $FeCl_3$ presented higher stability in comparison with other dopants. However, even for the doping saturation (*i.e.* one charge per thiophene monomeric unit), the conductivity of substituted polythiophene derivatives is around 10^{-6} S/cm.[36]

In a previous work, the electronic and electric responses of nanomembranes prepared using a spin-coated mixture of P3TMA and thermoplastic polyurethane (TPU) were exhaustively examined by UV-vis spectroscopy, conductive AFM and current/voltage measurements.[37] Both TPU:P3TMA and P3TMA nanomembranes showed semiconductor behavior with very similar band gap energy values (2.35 and 2.32 eV, respectively). In addition, current and conductivity values determined for the composite nanomembranes at P3TMA-rich domains ranged from 0.43 to 1.85 pA and from 2.23×10^{-5} to 5.19×10^{-6} S/cm, respectively.

8.3.4. Electrospinning of the Dense PEU-*co*-PEA:P3TMA Phase

The electrospinning process was optimized again for the dense phase since polymer composition was modified and also the total polymer concentration varied

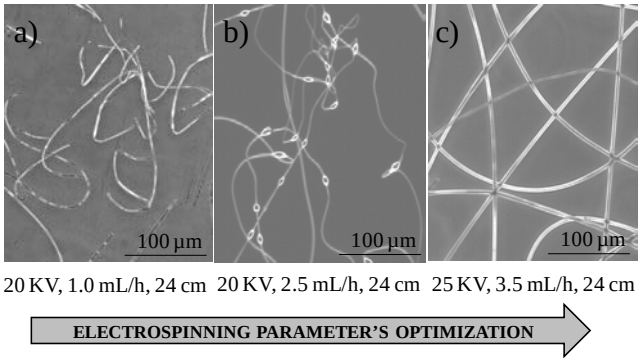

Figure 8.3.8. Optical micrographs showing the optimization sequence for the electrospinning parameters and typical morphologies produced by electrospinning the dense phase obtained from the spontaneous separation of 36% (w/v) solution of $1L6_{93}$-$8L6_{7}$ PEU-*co*-PEA plus P3TMA in $CHCl_3$:MeOH 10:1 *v/v*: a) highly broken fibers, b) fibers with beads, and c) continuous fibers. The systematic optimization procedure is described in Table 8.3.1.

considerably (*i.e.* from 36% w/v to 24% w/v). It should be pointed out that the presence of a small fraction of PEU-*co*-PEA is essential since electrospinning of P3TMA alone was unfeasible, even at such a high concentration, since its low molecular weight leads to abundant bead formation.

Figure 8.3.8 is an example of the optimization process for a given tip–collector distance followed by optical microscopy observation. Although beads and broken fibers were attained under most test conditions (Table 8.3.1), the increase in the flow rate up to 3.5 mL/h and the applied potential to 25 kV allowed us to obtain homogeneous and continuous microfibers. SEM images (Figure 8.3.9a) reveal a smooth surface texture, beads and broken fibers being relatively infrequent. The average diameter (Figure 8.3.9b) is close to 1.47 µm but values extended over a relatively wide range (from 500 nm to 2.50 µm). The hybrid fibers are clearly less tortuous than those prepared from PEU-*co*-PEA and also have a significantly lower diameter (1.47 µm with respect to 2.63 µm). Although the latter observation is consistent with the decrease of the global polymer concentration in the electrospinnable solution (*i.e.* from 36% w/v to 24% w/v), the increase in the flow rate (*i.e.* from 1.5 mL/h to 3.5 mL/h) indicates the opposite behaviour.

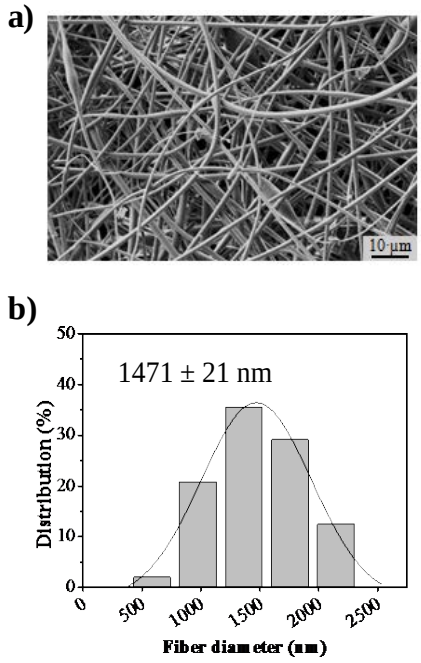

Figure 8.3.9. (a) SEM micrograph of electrospun microfibers derived from the P3TMA rich phase under optimized processing conditions. (b) Diameter distribution of the above indicated microfibers.

8.3.5. Characterization of PEU-*co*-PEA:P3TMA Electrospun Scaffolds

Physicochemical characterization

Figure 8.3.10 compares the heating run of the electrospun hybrid scaffold, the electrospun PEU-*co*-PEA scaffold and the P3TMA powder sample. P3TMA derived from chemical polymerization is semicrystalline despite the random disposition of its repeating unit, and consequently a small melting peak at 110.9 °C can be observed. Nevertheless, the sample has a high amorphous content since a clear glass transition is detected at 68.7 °C. The electrospun PEU-*co*-PEA scaffold is amorphous and renders only a clear glass transition at a lower temperature (*i.e.* 41.9 °C) due to the increased chain flexibility. The incorporation of a small percentage of PEA units

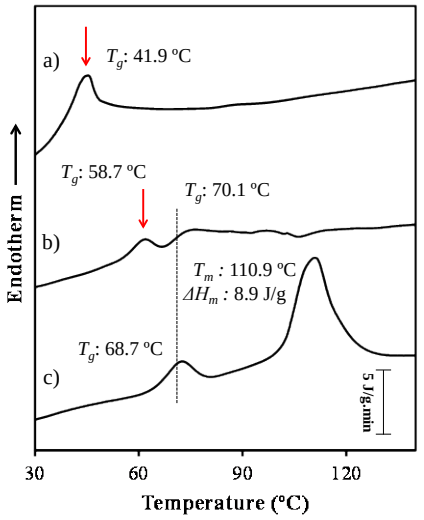

Figure 8.3.10. DSC 1st heating scans performed with $1L6_{93}$-$8L6_7$ PEU-*co*-PEA electrospun scaffold (a), PEU-*co*-PEA/P3TMA electrospun scaffold (b) and P3TMA powder sample (c). Red arrows point out endothermic processes detected for $1L6_{93}$-$8L6_7$:P3TMA electrospun scaffold and the low temperature relaxation peak observed in $1L6_{93}$-$8L6_7$ PEU-*co*-PEA and PEU-*co*-PEA:P3TMA electrospun scaffolds. The dashed black line related the relaxation peaks associated with P3TMA.

affects its crystallinity since the parent 1L6 PEU was reported to be semicrystalline.[25] In addition, it should be pointed out that the applied electrical potential tends to induce molecular orientation and probably favours crystallization.[38,39] However, this effect is clearly insufficient for PEU-*co*-PEA, the sample remaining amorphous after electrospinning.

Typical relaxation endothermic peaks are detected for both P3TMA and PEU-*co*-PEA samples, indicating that metastable equilibrium thermodynamic conditions with a lower specific volume, enthalpy and entropy are achieved in the glassy state. The PEU-*co*-PEA:P3TMA electrospun scaffold shows a complex thermal behaviour with different endothermic peaks. Thus, two relaxation peaks at 58.7 and 70.1 °C can be detected and, therefore, the presence of two amorphous phases is inferred. The greatest change in the specific heat capacity corresponds to the transition that occurred at a temperature intermediate between those observed for P3TMA and PEU-*co*-PEA. Hence, this transition can be associated with a miscible phase where both polymers were present. The second phase can only be associated with P3TMA since the transition is detected at practically the same temperature found for the CP

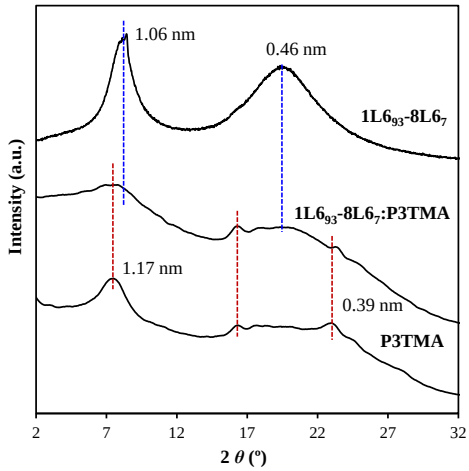

Figure 8.3.11. X-Ray powder diffractograms of the 1L6$_{93}$-8L6$_7$ PEU-*co*-PEA powder sample (top), PEU-*co*-PEA:P3TMA electrospun scaffold (middle) and P3TMA powder sample (bottom). Blue and red dashed lines point out typical reflections of the biodegradable copolymer and the CP, respectively.

sample. The composition of the miscible phase was determined by considering the T_g value predicted by the Fox equation:[40]

$$\frac{1}{T_g} = \frac{w_1}{T_{g1}} + \frac{w_2}{T_{g2}} \tag{8.3.6}$$

where w_i and T_{gi} represent the weight fraction and the glass transition temperature of each component, respectively, and T_g the glass transition temperature of the miscible phase.

The miscible phase was composed of 35% of the copolymer and represented a 28.6% of the global sample as it can be deduced taking into account the global composition determined by ^{1}H-NMR, and assuming that the crystalline phase was negligible.

The X-ray diffraction profile of the PEU-*co*-PEA:P3TMA electrospun scaffold (Figure 8.3.11) reveals a practically amorphous character, although some minor crystalline reflections could be detected. Note that the DSC heating run is complex and that melting and recrystallization peaks can be assumed. Basically, the X-ray diffraction profile shows the typical reflections of P3TMA (*e.g.* a strong and well defined peak at 1.17 nm that is related to the interchain distance[17]), amorphous halos and also some incipient signals that correspond to the reflections detected for the PEU-*co*-PEA powder sample (see blue dashed lines in Figure 8.3.11).

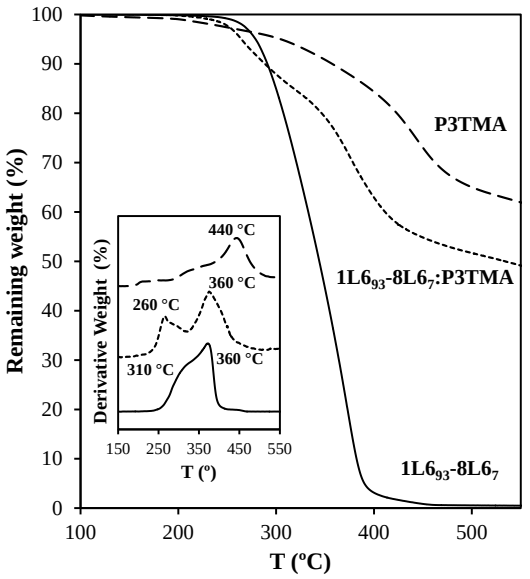

Figure 8.3.12. TGA degradation curves of 1L6$_{93}$-8L6$_7$ PEU-*co*-PEA electrospun scaffold (solid line), PEU-*co*-PEA:P3TMA electrospun scaffold (dotted line) and P3TMA powder sample (dashed line). Inset compares DTGA curves of the indicated samples.

PEU-*co*-PEA:P3TMA scaffolds were thermally stable up to more than 200 °C, as deduced from TGA and DTGA curves (Figure 8.3.12). The decomposition of this hybrid sample is different from those of the biodegradable and conducting components, and specifically the degradation process is slightly enhanced. Thus, the biodegradable PEU-*co*-PEA sample displays a two-step degradation process with DTGA peaks at 310 and 360 °C, which reflects the complex constitution of the repeat unit. The polymer is completely degraded at a temperature of 500 °C. In contrast, P3TMA gives rise to a char yield of 60% at 550 °C and degrades also following a two-step process with a predominant DTGA peak at 440 °C.

The hybrid scaffold gives rise to a remarkable char yield at 550 °C (*i.e.* 50%) that is consistent with its high P3TMA content. Nevertheless, the decomposition shows an unexpected behaviour since the first DTGA peak appears at 260 °C, which is lower than the temperature observed for the first peak of the two components. Thus, the presence of P3TMA has a slightly negative influence on the thermal stability of the copolymer. Degradation of the hybrid scaffold finishes at a lower temperature than that observed for the P3TMA sample (*i.e.* DTGA peaks at 360 °C and 440 °C), due to the accelerated decomposition process caused by the previous

decomposition of the PEU-*co*-PEA component. In summary, the incorporation of a small amount of the copolymer sample has a negative influence on the thermal stability of P3TMA, but this feature is not essential to discard the use of the new scaffold at reasonably high temperatures.

Electrochemical Characterization

Figure 8.3.13a compares the first control voltammogram in PBS with 0.1 M $LiClO_4$ of PEU-*co*-PEA:P3TMA electrospun scaffolds having 90 and 24 wt% of the CP, which were obtained from the dense and light phases, respectively. The voltammogram of the hybrid with 90 wt% of P3TMA shows an oxidation process O_1 that begins at 0.55 V and an oxidation peak O_2, indicating the formation of both polarons and bipolarons in the CP chains. The anodic peak potential of O_1 is $E_p^a(O_1)$ = 0.81 V, while O_2 is expected to reach an anodic peak potential at $E_p^a(O_2) \approx 1.3$ V (*i.e.* ~0.2 V above the reversal potential).

On the other hand, the cathodic scan shows a weak reduction peak, R_1, with a cathodic reduction potential $E_p^c(R_1)$ = 0.21 V, which reflects the fact that the O_1 and O_2 oxidation processes are highly irreversible. Similarly, the control voltammogram recorded for the hybrid having 24 wt% of P3TMA presents two oxidation processes with $E_p^a(O_1)$ = 0.90 V and $E_p^a(O_2)$ higher than 1.10 V. Moreover, the reduction peak is identified at $E_p^c(R_1)$ = 0.12 V. It is worth noting that the voltammograms recorded for the two hybrid scaffolds resemble that recently recorded for individual P3TMA using the same experimental conditions.[15] The voltammogram of the sample without P3TMA, which is included in Figure 8.3.13a, shows a weak oxidation shoulder O_1 with an anodic peak potential $E_p^a(O_1)$ = 0.91 V, while no reduction peak is detected at a cathodic reduction potential. Accordingly, the electrochemical activity of PEU-*co*-PEA electrospun scaffolds is consistent with the formation of charged species at unspecified positions, representing a significant difference with respect to PEU-*co*-PEA:P3TMA scaffolds in which polarons and bipolarons are formed at preferred positions. Current densities (j) determined at 1.10 V were 0.11, 0.44 and 0.51 mA/cm² for samples containing 0, 24 and 90 wt% of P3TMA, respectively.

The electroactivity, which increases with the similarity between the anodic and cathodic areas, was determined using the voltammograms displayed in Figure 8.3.13a. Results indicate that the ability to store charge increases upon the addition of P3TMA.

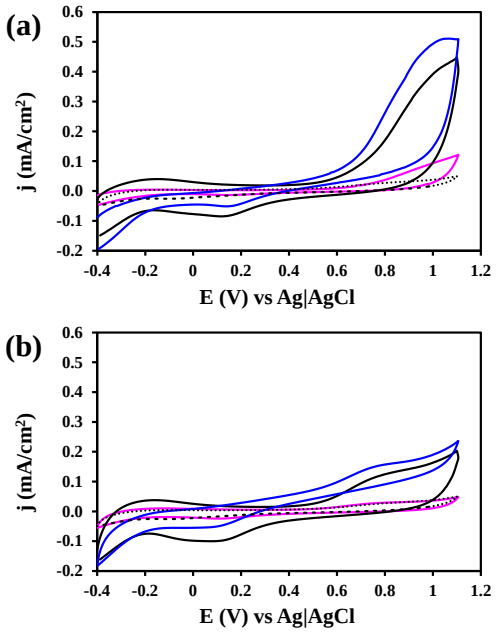

Figure 8.3.13. Cyclic voltammograms for $1L6_{93}$-$8L6_7$ PEU-*co*-PEA (purple line) and PEU-*co*-PEA:P3TMA electrospun scaffolds having 24 wt-% (blue line) and 90% wt-% (black line) of P3TMA in PBS with 0.1 M $LiClO_4$ (dotted line): (a) first control voltammogram; and (b) voltammogram after 10 consecutive oxidation-reduction cycles. Initial and final potential: -0.40 V; reversal potential: 1.10 V. Scan rate: 50 mV/s.

Specifically, the anodic charges of hybrid scaffolds having a 24 and 90 wt% of the CP are 2.05 mC/cm² and 3.08 mC/cm², respectively, while that of PEU-*co*-PEA scaffold decreases to 0.37 mC/cm². Figure 8.3.13b represents the cyclic voltammograms recorded for the two hybrids and PEU-*co*-PEA electrospun scaffolds after 10 consecutive oxidation–reduction cycles. The reduction of the areas associated with the cathodic and anodic scans with respect to the control voltammograms displayed in Figure 8.3.13a indicates that the ability to exchange charge reversibly decreases with the number of redox processes. This loss of electroactivity is typically related with the structural changes provoked by the redox processes in the CP.[41] Thus, the compactness of P3TMA increases with the number of redox cycles, hindering the access and escape of dopant ions during the oxidation and reduction processes, respectively. The LEA measured after 10 redox cycles for the PEU-*co*-PEA scaffolds is 46%, decreasing to 39% and 24% for the hybrids with 24

and 90 wt% of P3TMA. These values clearly indicate that electrochemical stability increases with the P3TMA content.

The overall electrochemical results indicate that the electroactivity and electrostability of electrospun microfibers made of P3TMA supported on biodegradable PEU-*co*-PEA are similar to those reported for isolated P3TMA.[15] As expected, the electrochemical responses of these hybrid scaffolds improve with the P3TMA content. This feature combined with the fact that such CP behaves as a bioactive matrix[14–17,29] support the view that PEU-*co*-PEA:P3TMA electrospun microfibers are promising candidates for biotechnological and biomedical applications.

8.4. Conclusions

Electrospun scaffolds having a high content of P3TMA have been successfully prepared using a novel poly(ester urea) as a carrier. This should contribute to specific properties like biocompatibility and biodegradability, leading to a material with clear advantages for the biomedical field. The designed poly(ester urea) contains α-amino acid units (L-leucine) and a small ratio of amide groups in a random disposition to improve solubility in organic solvents, which is an essential requirement for the electrospinning technique.

The selected biodegradable polymer can be easily electrospun over a wide range of conditions, giving rise to homogeneous and continuous microfibers. These good properties guarantee the electrospinnability of the low molecular weight P3TMA by the addition of a small percentage of PEU-*co*-PEA and specifically, the preparation of electrospun scaffolds with a 90 wt% of CP.

Hybrid microfibers are continuous and show lower diameters than those prepared from the degradable polymer, which has been attributed to the formation of strong intermolecular interactions. In fact, as prepared P3TMA revealed exceptional doping level characteristics since each monomeric unit was able to interact with 0.27 counter-ions. Thermal analyses have indicated that microfibers present a phase in which conducting and biodegradable polymers are well mixed. Physicochemical characterization of the hybrid scaffolds has revealed low crystallinity, high thermal stability and a remarkable electrochemical response. The formation of charged species at specific positions and the electroactivity and electrochemical stability of PEU-*co*-PEA:P3TMA hybrid scaffolds are very similar to those of the as prepared P3TMA.

8.5. References

[1] B. Guo, L. Glavas, A.-C. Albertsson, *Prog, Polym. Sci.* **2013**, *38*, 1263.

[2] E. Llorens, E. Armelin, M.M. Pérez-Madrigal, L. J. del Valle, C. Alemán, J. Puiggalí, *Polymers* **2013**, *5*, 1115.

[3] D. Bendrea, L. Cianga, I. Cianga, *J. Biomater. Appl.* **2011**, *26*, 3.

[4] Y. Guo, M. Y. Li, A. Mylonakis, J. J. Han, A. G. MacDiarmid, X. S. Chen, P. I. Lelkes, Y. Wei, *Biomacromolecules* **2007**, *8*, 3025.

[5] Y. Liu, J. Hu, X. Zhuang, P. Zhang, X. Chen, Y. Wei, X. Wang, *Macromol. Biosci.* **2011**, *11*, 806.

[6] H. H. Kuhn, A. D. Child, in *Electrically Conducting Textiles. Handbook of Conducting Polymers*, 2nd ed. (Eds: T. A. Skotheim, R. L. Elsenaumer, J. R. Reynolds) Marcel Dekker: New York, NY, USA, **1998**; pp. 993–1104.

[7] S. Nair, S. Natarajan, S. H. Kim, *Macromol. Rapid Commun.* **2005**, *26*, 1599.

[8] S. Aznar-Cervantes, M. I. Roca, J. G. Martinez, L. Meseguer-Olmo, J. L. Cenis, J. M. Moraleda, T. F. Otero, *Biochemistry* **2012**, *85*, 36.

[9] M. Li, Y. Guo, Y. Wei, A. G. MacDiarmid, P. I. Lelkes, *Biomaterials* **2006**, *27*, 2705.

[10] D. Kai, M. P. Prabhakaran, G. Jin, S. Ramakrishna, *J. Biomed. Mater. Res., Part A* **2011**, *99*, 376.

[11] C. Sharma, S. Gautam, A. K. Dinda, N. C. Mishra, *Adv. Mater. Lett.* **2011**, *2*, 90.

[12] H. Liu, C. H. Reccius, H. G. Craighead, *Appl. Phys. Lett.* **2005**, *87*, 253106:1.

[13] S. Lee, G. D. Moon, U. Jeong, *J. Mater. Chem.* **2009**, *19*, 743.

[14] E. Armelin, A. L. Gomes, M. M. Pérez-Madrigal, J. Puiggalí, L. Franco, L. J. del Valle, A. Rodríguez-Galán, J. S. de C. Campos, N. Ferrer-Anglada, C. Alemán, *J. Mater. Chem.* **2012**, *22*, 585.

[15] M. M. Pérez-Madrigal, E. Armelin, L. J. del Valle, F. Estrany, C. Alemán, *Polym. Chem.* **2012**, *3*, 979.

[16] M. M. Pérez-Madrigal, M. I. Giannotti, G. Oncins, L. Franco, E. Armelin, J. Puiggalí, F. Sanz, L. J. del Valle, C. Alemán, *Polym. Chem.* **2013**, *4*, 568.

[17] E. Llorens, M. M. Pérez-Madrigal, E. Armelin, L. J. del Valle, J. Puiggalí, C. Alemán, *RCS Adv.* **2014**, *4*, 15245.

[18] R. Katsarava, Z. Gomurashvili, in *Biodegradable Polymers composed of naturally occurring a-amino acids. In Handbook of Biodegradable Polymers - Isolation, Synthesis, Characterization and Applications*, (Eds: A. Lendlein, A. Sisson) Wiley-VCH, Verlag GmbH & Co. KGaA. **2011**, Chapter 5, p. 107.

[19] M. Okada, *Progr. Polym. Sci.* **2000**, *27*, 87.

[20] P. A. M. Lips, P. J. Dijkstra, in *Biodegradable polyesteramides. In Biodegradable Polymers for Industrial Applications*; (Ed: R. Smith) CRC Press, Boca Raton, **2005**; Chapter 5, pp. 109–139.

[21] A. Rodríguez-Galán, L. Franco, J. Puiggalí, *Polymers* **2011**, *3*, 65.

[22] S. K. Murase, J. Puiggalí, in *Poly(Ester Amide)s: Recent Developments on Synthesis and Applications. In Natural and synthetic biomedical polymers*, (Eds: S. G. Kumbar, C. T. Laurencin, M. Deng) Elsevier: Burlington-San Diego, USA, **2014**. Chapter 8, pp. 145–163.

[23] A. Diaz, R. Katsarava, J. Puiggalí, *Int. J. Mol. Sci.* **2014**, *15*, 7064.

[24] T. Kartvelishvili, G. Tsitlanadze, L. Edilashvili, N. Japaridze, R. Katsarava, *Macromol. Chem. Phys.* **1997**, *198*, 1921.

[25] Z. D. Gomurashvili, R. Katsarava, D. Tugushi, Poly(ester urea) polymers and methods of use. WO 2007050415 A2. 3 May 2007.

[26] A. Díaz, L. J. del Valle, D. Tugushi, R. Katsarava, J. Puiggalí, *Mater. Sci. Eng. C: Mater. Biol. Appl.* **2015,** *46*, 450.
[27] K. S. Stakleff, F. Lin, L. A. Smith Callahan, M. B. Wade, A. Esterle, J. Miller, M. Graham, M. L. Becker, *Acta Biomater.* **2013**, *9*, 5132.
[28] J. Yu, F. Lin, P. Lin, Y. Gao, M. L. Becker, *Macromolecules* **2014**, *47*, 121.
[29] M. M. Pérez-Madrigal, M. I. Giannotti, L. J. del Valle, L. Franco, E. Armelin, J. Puiggalí, F. Sanz, C. Alemán, *ACS Appl. Mater. Interfaces* **2014**, *6*, 9719.
[30] R. Katsarava, V. Beridze, N. Arabuli, D. Kharadze, C. C. Chu, C. Y. Wen, *J. Polym. Sci. Part A: Polym. Chem.* **1999**, *37*, 391.
[31] B. Kim. L. Chen, J. Gong, Y. Osada, *Macromolecules* **1999**, *32*, 3964.
[32] C. J. Luo, M. Nangrejo, M. Edirisinghe, *Polymer* **2010**, *51*, 1654.
[33] D. Aradilla, F. Estrany, E. Armelin, R. Oliver, J. I. Iribarren, C. Alemán, *Macromol. Chem. Phys.* **2010**, *211*, 1663.
[34] A. Gök, M. Omastová, A. G. Yavuz, *Synth. Met.* **2007**, *157*, 23.
[35] M. B. Inoue, E. F. Velazquez, M. Inoue, *Synth. Met.* **1988**, *24*, 223.
[36] D. Fichou, in *Handbook of oligo- and polythiophenes*; Wiley-VCH: Weinheim ; New York, **1999**; p 534.
[37] M. M. Pérez-Madrigal, M. I. Giannotti, E. Armelin, F. Sanz, C. Alemán, *Polym. Chem.* **2014**, *5*, 1248.
[38] J. Zeng, X. Chen, Q. Liang, X. Xu, X. Ping, *Macromol. Biosci.* **2004**, *4*, 1118.
[39] L. J. del Valle, R. Camps, A. Díaz, L. Franco, A. Rodríguez-Galán, J. Puiggalí, *J. Polym. Res.* **2011**, *18*, 1903.
[40] T. G. Fox., *Bull. Am. Phys. Soc.* **1956**, *1*, 123.
[41] D. Aradilla, F. Estrany, C. Alemán, *J. Phys. Chem. C* **2011**, *115*, 8430.

CHAPTER 9

POLYPYRROLE-MEMBRANE PROTEIN SUPPORTED INTERFACE:

BIOINSPIRED CHANNELS

Summary

The last part of this dissertation covers the design of CP-based biointerfaces with nanometric thickness prepared by electropolymerization. Inspired by cell biology, we immobilized a membrane protein in a synthetic polymeric matrix, being aware that the structure and function of proteins are affected by environmental conditions.

The work reported in this chapter includes the preparation of an operative composite that regulates the diffusion of alkali ions by functionalizing a supporting matrix made of poly(*N*-methylpyrrole) (PNMPy) with a *β*-barrel membrane protein (Omp2a) that forms channels and pores. The protein has been identified in the composite, and its structure has been shown to remain unaltered. The PNMPy−Omp2a platform fulfills properties typically associated with functional biointerfaces for biomedical applications (*e.g.* biocompatibility, biodegradability, and hydrophilicity). The functionality of the immobilized protein has been examined by studying the passive ion transport response in the presence of electrolytic solutions with Na^+ and K^+ concentrations close to those found in blood.

Expression, purification and refolding of the trimeric outer membrane protein (Omp2a) from *Brucella melitensis* was performed by Dr. C. Michaux[1], Dr. G. Roussel[1] and Dr. E. A. Perpète[1]. Biological assays were done in collaborative working with Dr. L. J. del Valle[2].

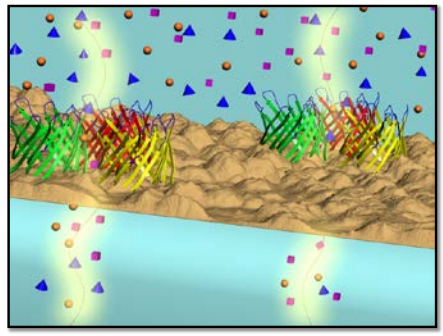

Graphical abstract

Publication derived from this work:

M.M. Pérez-Madrigal, L.J. del Valle, E. Armelin, C. Michaux, G. Roussel, E.A. Perpète, C. Alemán, *ACS Appl. Mater. Interfaces* **2015**, *7*, 1632.

[1]Unité de Chimie, Physique Théorique et Structurale (UCPTS) at the University of Namur, Belgium.
[2]Departament d'Enginyeria Química, E.T.S. d'Enginyers Industrials de Barcelona, UPC.

9.1. Introduction

The development of hybrid surfaces made of synthetic polymers and biomolecules for biomedical applications has the potential to revolutionize the treatment of a wide variety of medical conditions. Due to their excellent electrochemical, chemical, and optical properties,[1–3] conjugated conducting polymers (CPs) are promising candidates for biomolecule immobilization and subsequent formation of one- and two-dimensional composites for biomedical devices (*e.g.* bio-sensors, electrochemical actuators, substrates for tissue engineering, and nanowires).[4–10]

On the other hand, biological membranes (lipid bilayers) are unique natural interfaces with exceptional solute transport selectivity and permeability properties, which are mainly due to the embedded membrane proteins (MPs). MPs participate in various cellular processes, such as signalling biochemical cascades, cell-to-cell communication, membrane fusion, and ion transport.[11,12] MPs play a central role in controlling a wide array of gradients such as chemical, electrical, and mechanical gradients and are responsible for cell structure during key events such as cellular division. Furthermore, many signal transduction processes between cells, such as neurons and muscle tissue, rely on the gating of ion channels (passive transport) and pumps (active transport), which allow the flow of ions across the biomembrane. In these processes, MPs act as channels that move specific molecules and ions into and out of the membrane, and their function is triggered by ligand binding or changes in the transmembrane potential.[13]

Considering that folding processes in MPs of lipid bilayers represent an important challenge in structural biology,[14,15] it is not surprising that the proper immobilization of purified MPs in platforms for biomedical applications, for example, micro-and nanoarrays, results in a very difficult task. Thus, drastic changes in natural environmental conditions affect MPs structure, influencing their activity.[16] In addition, the complex nature of proteins, their insolubility in aqueous solutions, and their instability in the presence of detergents strongly complicate the fabrication of protein-integrated devices based on MPs. Despite these limitations and following biomimicking approaches, some advances have been reported using polymers as soft substrates,[17–25] even though only a few of them involved CPs.[24,25] In a recent study, Arun and Narayan[24] anchored bacteriorhodopsin, a MP that functions as a light-driven proton pump, onto conducting surfaces of poly(3,4-ethylenedioxythio-phene) (PEDOT) and polyaniline (PAni). More recently, Della Pia *et al.*[25] used electropolymerization and amphipatic polymers to functionalize micro-

and nanosurfaces with MPs. Specifically, these authors used gold surfaces selectively modified by electrogeneration of polypyrrole (PPy) in the presence of biotin, and the strong affinity of biotin for avidin was exploited to immobilize streptavidin proteins.[25] These hybrid platforms were proposed to be particularly suited to fabricate specific antibody bionanosensors. Because of these recent advances, composites combining CPs and MPs are expected to be functional materials with advanced properties and applications.

In this work, a CP−MP nanocomposite with regulated channeling activity has been prepared and characterized. The trimeric outer MP Omp2a from *Brucella melitensis*[26] has been selected for this purpose. This β-barrel protein forms pores that allow the diffusion not only of ions but also of molecules as large as 667 Da (*e.g.* nutrients and antibiotics). Indeed, pores are larger in Omp2a than in its homologue Omp2b (85% sequence identity and both encoded in the same genetic locus).[27] Although the function of Omp2a is still poorly understood at the structural level, as the 3D structure of *Brucella* β-barrel MPs is not known yet, very recent refolding studies suggested that Omp2a first refolds under a monomeric form and then self-associates into a trimeric state.[28,29] On the other hand, poly(*N*-methylpyrrole) (PNMPy) is the CP chosen to act as the supporting matrix for Omp2a. This PPy derivative displays a compact structure[30] and relatively infrequent formation of chemical cross-links when prepared under controlled conditions.[31] PNMPy has been successfully used in different biomedical and biotechnological applications, as for example the detection of glucose,[32] neurotransmitters,[6] and opioids.[33]

Herein, we describe the procedure to successfully prepare PNMPy-supported MP composites, and the characterization of their surface, electrochemical, and biomedical related properties. Subsequently, we demonstrate the potential of this new material to be used as electroactive stable synthetic membranes with enhanced ion permeability for biomedical applications by means of electrochemical impedance spectroscopy (EIS), and using different electrolytic solutions with K^+ and Na^+ concentrations similar to those found in blood. The observed passive ion transport properties indicate that PNMPy−Omp2a system is well suited for the preparation of smart bioinspired interfaces. Specifically, the ionic transport exerted by PNMPy−Omp2a has wide potential applications in nanofluidics, energy conversion, and biosensors.

9.2. Experimental Section

9.2.1. Materials

All chemicals used in this work were of analytical grade, purchased from commercial suppliers (Sigma Aldrich) and used as received without any further purification. Lipase F-AP15 (from *Rhizopus oryzae*) was purchased from Sigma (USA) and used in the enzymatic degradation experiments.

9.2.2. Expression, Purification and Refolding of the Trimeric Outer Membrane Protein (Omp2a) from *Brucella Melitensis*

Cells of *Escherichia coli* BL21 (DE3) carrying pLysS and pET2a plasmids (containing the gene Omp2a without peptide signal) were grown in Lysogeny broth (LB) medium at 37 °C with constant shaking. Log cultures (OD 0.6) of 500 mL were stimulated with isopropyl-beta-D-thiogalactopyranoside (IPTG) (0.2 mg/mL) for 3 h. Cells were then harvested by centrifugation at 4000 g for 30 min, and the resulting bacterial pellets were stored at -20 °C.

The bacterial pellets were thawed and treated with 8 mL of TEN lysis buffer (50 mM Tris–HCl pH 8, 1 mM EDTA, 17 mM NaCl, 125 mM PMSF, 250 mg/mL lysozyme) for 20 min at 25 °C. Harvested cells were further broken by addition of 10 mg of sodium deoxycholate for 60 min at 37 °C with constant shaking, and 2 mg of DNase I for 60 min at 25 °C. The suspension was then centrifuged at 14000 g for 20 min at 4 °C. The resulting pellet underwent a washing buffer (2 M urea, 20 mM Tris–HCl pH 8, 500 mM NaCl, 2% Triton X-100) and centrifuged at 14000 g for 20 min at 4 °C. The inclusion bodies were solubilized with 8 mL of TEN buffer (50 mM Tris–HCl pH 8, 1 mM EDTA, 17 mM NaCl, 8 M urea). The solubilized proteins were then applied onto an anion-exchange DEAE column previously equilibrated with 25 mL of buffer (50 mM Tris–HCl pH 8, 17 mM NaCl, 8 M urea). Omp2a was eluted with a 50 mL linear gradient of NaCl from 17 to 500 mM, whereas the protein profile was further analyzed using SDS–PAGE. Fractions containing 39 kDa proteins were then pooled and stored at 4 °C.

9.2.3. Refolding of the Trimeric Omp2a

To refold Omp2a, the protein solution (1 mg/mL protein, 250 mM NaCl, 50 mM Tris–HCl pH 8 and 8 M urea) was eluted onto a PD-10 column to exchange the buffer (150 mM NaCl, 50 mM Tris–HCl pH 8, and 120 mM sodium dodecyl sulfate (SDS), which is 15 times the critical micellar concentration). SDS-unfolded samples were then diluted 1:1 in a refolding solution (50 mM Tris–HCl pH 8, 150 mM NaCl, 3 M 2-methyl-2,4-pentanediol (MPD)). The protein solution was then incubated at room temperature. The samples were stored at -20 °C to stop the refolding reaction. Hereafter, Omp2a protein at this procedure stage is named as obtained Omp2a. The protein sequence is:

Accepted sequence (triple letter code) of Omp2a protein (367 amino acids).

Met - Asn - Ile - Lys - Ser - Leu - Leu - Leu - Gly - Ser - Ala - Ala - Ala - Leu - Val - Ala - Ala - Ser - Gly - Ala - Gln - Ala - Ala - Asp - Ala - Ile - Val - Ala - Pro - Glu - Pro - Glu - Ala - Val - Glu - Tyr - Val - Arg - Val - Cys - Asp - Ala - Tyr - Gly - Ala - Gly - Tyr - Phe - Tyr - Ile - Pro - Gly - Thr - Glu - Thr - Cys - Leu - Arg - Val - His - Gly - Tyr - Val - Arg - Tyr - Asp - Val - Lys - Gly - Gly - Asp - Asp - Val - Tyr - Ser - Gly - Thr - Asp - Arg - Asn - Gly - Trp - Asp - Lys - Gly - Ala - Arg - Phe - Ala - Leu - Met - Phe - Asn - Thr - Asn - Ser - Glu - Thr - Glu - Leu - Gly - Thr - Leu - Gly - Thr - Tyr - Thr - Gln - Leu - Arg - Phe - Asn - Tyr - Thr - Ser - Asn - Asn - Ser - Arg - His - Asp - Gly - Gln - Tyr - Gly - Asp - Phe - Ser - Asp - Asp - Arg - Asp - Val - Ala - Asp - Gly - Gly - Val - Ser - Thr - Gly - Thr - Asp - Leu - Gln - Phe - Ala - Tyr - Ile - Thr - Leu - Gly - Gly - Phe - Lys - Val - Gly - Ile - Asp - Glu - Ser - Glu - Phe - His - Thr - Phe - Thr - Gly - Tyr - Leu - Gly - Asp - Val - Ile - Asn - Asp - Asp - Val - Val - Ala - Ala - Gly - Ser - Tyr - Arg - Thr - Gly - Lys - Ile - Ala - Tyr - Thr - Phe - Thr - Gly - Gly - Asn - Gly - Phe - Ser - Ala - Val - Ile - Ala - Leu - Glu - Gln - Gly - Gly - Glu - Asp - Val - Asp - Asn - Asp - Tyr - Thr - Ile - Asp - Gly - Tyr - Met - Pro - His - Val - Val - Gly - Gly - Leu - Lys - Tyr - Ala - Gly - Gly - Trp - Gly - Ser - Ile - Ala - Gly - Val - Val - Ala - Tyr - Asp - Ser - Val - Ile - Glu - Glu - Trp - Ala - Thr - Lys - Val - Arg - Gly - Asp - Val - Asn - Ile - Thr - Asp - Arg - Phe - Ser - Val - Trp - Leu - Gln - Gly - Ala - Tyr - Ser - Ser - Ala - Ala - Thr - Pro - Asn - Gln - Asn - Tyr - Gly - Gln - Trp - Gly - Gly - Asp - Trp - Ala - Val - Trp - Gly - Gly - Ala - Lys - Phe - Ile - Ala - Pro - Glu - Lys - Ala - Thr - Phe - Asn - Leu - Gln - Ala - Ala - His - Asp - Asp - Trp - Gly - Lys - Thr - Ala - Val - Thr - Ala - Asn - Val - Ala - Tyr - Gln - Leu - Val - Pro - Gly - Phe - Thr - Ile - Thr - Pro - Glu - Val - Ser - Tyr - Thr - Lys - Phe - Gly - Gly - Glu - Trp - Lys - Asp - Thr - Val - Ala - Glu - Asp - Asn - Ala - Trp - Gly - Gly - Ile - Val - Arg - Phe - Gln - Arg - Ser – Phe

9.2.4. Synthesis of Poly(*N*-methylpyrrole)

PNMPy control films were prepared by chronoamperometry (CA) using an Autolab PGSTAT302N equipped with the ECD module (Ecochimie, The Netherlands). Polymerization was carried out in a standard three-electrode one compartment cell at room temperature. The cell was filled with 10 mL of a 15 mM NMPy solution in deionized water containing 10 mM of SDS (pH= 7.3-7.4). Steel AISI 316 sheets of 1.0 ×1.0 cm^2 were used as working and counter electrodes, while the reference electrode was an Ag|AgCl electrode containing KCl saturated aqueous solution (E^0 = 0.222 at 25 ^oC). PNMPy-Omp2a films were prepared following the same procedure, although in that case the solution also contained Omp2a protein (1 mg/mL). Prior its use, Omp2a was unfrozen and submitted to dialysis, which resulted in the suspension of the protein in a solution that contained only 10 mM SDS. Hereafter, Omp2a protein at this procedure stage is named dialyzed Omp2a.

The cyclic voltammogram recorded in steel electrodes for the anodic oxidation of the NMPy solution without MP (Figure 9.3.1) shows an anodic process with a peak potential of 1.089 V (O_1). This peak shifts to 1.119 V (O_1') upon the addition of 1 mg/mL Omp2a to the solution. In order to maximize the polymerization process without damaging the resulting materials by overoxidation, both PNMPy and PNMPy-Omp2a films were prepared under a constant potential of 1.10 V, which is between O_1 and O_1'. In order to reach the desired thickness, the polymerization time, θ, was adjusted to 20 s.

9.2.5. Methods

The thickness of the films was determined by optical profilometry using a surface profilometer Dektak 150 (Veeco). Generally, scratches were intentionally done in the surface of the films, and the step at several positions along the scratches was measured by the computer software Dektatk (version 9.2, Veeco Instruments Inc.). At least five samples were tested for each system.

Electrochemical properties

The electroactivity (charge storage ability) and the electrochemical stability (electrostability) were determined by cyclic voltammetry (CV) assays. Fifteen consecutive oxidation-reduction cycles were conducted in an aqueous solution containing 0.1 M of $LiClO_4$. The initial and final potential was -0.4 V, while the

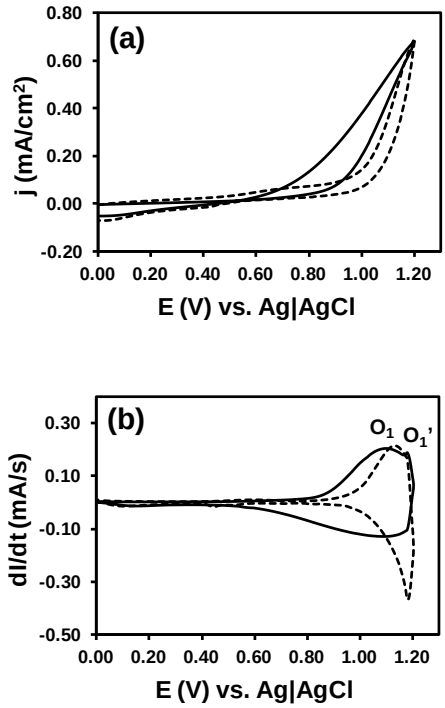

Figure 9.3.1. (a) Control voltammogram for the oxidation of a 15 mM NMPy solution in deionized water with 10 mM SDS and with (dashed line) / without (solid line) Omp2a (1 mg/mL). Initial and final potential: 0.0 V; reversal potential 1.2 V. Scan rate: 50 mV/s. The derivatives of the current for the voltammograms are displayed in (b). The anodic peak potential of the anodic processes O_1 (without Omp2a) and O_1' (with Omp2a) is 1.089 and 1.119 V, respectively.

reversal potential was 1.1 V. All measurements were performed at 25 ^{o}C using scan rates of 25 and 50 mV/s. The electrostability was quantified by calculating the loss of electroactivity (LEA; in %):

$$LEA = \frac{\Delta Q}{Q_I} \times 100 \tag{9.2.1}$$

where ΔQ is the difference between the oxidation charge (in C) of the first and the last oxidation-reduction cycle, and Q_I is the oxidation charge corresponding to the first cycle. Data was obtained as the average of three samples for each system.

Spectroscopic characterization

Circular dichroism (CD) measurements in the far-UV region were measured between 190 and 350 nm at 20 ºC, with a Jasco J-815 equipment, using a protein concentration of approximately 50 μg/mL and a 0.1 cm cell path. Spectra were acquired at a scan speed of 100 nm/min with a 0.2 nm data pitch using a 1 nm bandwidth and a 4 second digital integration time. Spectra were averaged after two accumulations and corrected by subtraction of the background spectrum. Several PNMPy-Omp2a films were incubated in water overnight and carefully removed from the steel substrate prior to their characterization.

X-ray photoelectron spectroscopy (XPS) analyses were performed in a SPECS system equipped with a non-monochromated twin anode X-ray source XR50 of Mg/Al (1253 eV/1487 eV). Specifically, the Al anode was used as X-ray source operating at 150 W, and a Phoibos 150 MCD-9 XP as detector. The pass energy was set to 25 and 0.1 eV for the survey and the narrow scans, respectively. The C 1s peak was used as an internal reference with a binding energy of 284.5 eV. High-resolution XPS spectra were acquired by Gaussian–Lorentzian curve fitting after S-shape background subtraction.

UV-vis absorption spectra were obtained using a UV-vis-NIR Shimadzu 3600 spectrophotometer equipped with a tungsten halogen visible source, a deuterium arc UV source, a photomultiplier tube UV-vis detector, and a InGaAs photodiode and cooled PbS photocell NIR detectors. Protein solutions spectra were recorded in the absorbance mode, whereas spectra of PNMPy and PNMPy-Omp2a films deposited onto steel sheets were recorded in the reflectance mode and converted to absorbance using the integrating sphere accessory (model ISR-3100). The wavelength range was 200-750 nm in all cases. The interior of the integrating sphere was coated with highly diffuse BaO reflectance standard. Measurements, data collection and data evaluation were controlled by the computer software UVProbe version 2.31.

Morphological and topographical properties

The morphology of PNMPy and PNMPy-Omp2a films was examined by scanning electron microscopy (SEM) using a Focused Ion Beam Zeiss Neon40 scanning electron microscope equipped with an energy dispersive X-ray (EDX) spectroscopy system and operating at 5 kV. Samples were sputter-coated with a thin carbon layer of 6-10 nm using a K950X Turbo Evaporator to prevent electron charging problems.

Atomic force microscopy (AFM) was conducted in the tapping mode to obtain topographic images of the films surface using a silicon TAP 150-G probe (Budget Sensors, Bulgaria) with a frequency of 150 kHz and a force constant of 5 N/m. Images were obtained with a AFM Dimension microscope using a NanoScope IV controller under ambient conditions (Veeco). The row scanning frequency was set between 0.8 and 1 Hz. The Root Mean Square (RMS) roughness, which is the average height deviation taken from the mean data plane, was determined using the statistical application of the NanoScope Analysis software (Veeco, v. 1.20).

The porosity was quantified through the parameter Δ calculated as follows:[34]

$$\Delta = \frac{l_0 - l_{15}}{l_0} \times 100 \tag{9.2.2}$$

where l_0 and l_{15} refer to thickness before applying any redox cycles and after 15 consecutive oxidation-reduction cycles.

Wettability

Contact angle measurements were carried out using the water drop method. Images of 0.5 µL distillated water drops were recorded after stabilization with the equipment OCA 15EC (Data-Physics Instruments GmbH, Filderstadt). SCA20 software was used to analyze the images and determine the contact angle value, which was obtained as the average of at least six independent measures for each sample.

Enzymatic degradation

PNMPy−Omp2a films were immersed in 1 mL of phosphate buffered saline solution (PBS) supplemented with 0.1 mg/mL of sodium azide (which allowed us to prevent contamination) and 50 µg/mL of Lipase F-AP15 to examine the enzymatic degradation of the protein. Incubation took place at 37 °C in a shaking incubator set at 100 rpm. Samples were analyzed after 1, 4, 8, 24, 48, and 72 h. After each immersion time, samples were removed from the solution and gently washed with distillated water. Then, samples were dried under vacuum for several days at room temperature before being observed by SEM.

Cellular adhesion

Vero cells (African green monkey kidney epithelial cell line) and Cos-7 cells (African green monkey kidney fibroblast cell line) were cultured in Dulbecco's

modified Eagle medium (DMEM) supplemented with 10% fetal bovine serum, 1%penicillin/streptomycin, and 2 mM L-glutamine at 37 °C in a humidified atmosphere of 5% CO_2 in air. The cultured medium was changed every 2 days, and for subculture, cell monolayers were rinsed with phosphate buffered saline (PBS) and detached by incubation with 0.25% trysin/EDTA for 5 min at 37 °C. Cell concentration was determined by counting at the Neubauer camera using 4% trypan blue as dye vital. The detached cells with viability ≥95% were used for cultures following the conditions for the adhesion assays.

PNMPy−Omp2a and PNMPy films deposited onto steel AISI 316 sheets of 1 cm^2 were placed in plates of 24 wells and sterilized using UV irradiation for 15 min in a laminar flux cabinet. Samples were incubated with 1 mL of culture medium during 30 min under culture conditions to equilibrate the material. Finally, the medium was aspired, and the material was evaluated for cell adhesion by exposing cells to direct contact with the material surface. An aliquot of 50 µL containing 5×10^4 cells was deposited on the substrate of each well. The plate was incubated under culture conditions for 60 min to promote the cell attachment to the film surface. Finally, 1 mL of the culture medium was added to each well. Controls of adhesion were simultaneously performed by culturing cells on the surface of the tissue culture polystyrene (TCPS) plates and uncoated steel. Cell adhesion was evaluated after 24 h of culture using the MTT [3-(4,5-dimethylthiazol- 2-yl)-2,5-diphenyltetrazolium bromide] assay, which determines the cell viability. The viability results were normalized to TCPS control as relative percentages.

Results were derived from the average of four replicates (n = 4) for each independent experiment. ANOVA and Tukey's tests were performed to determine the statistical significance, which was considered at a confidence level of 95% ($p < 0.05$).

Electrochemical impedance spectroscopy (EIS)

Spectra were taken at open circuit potential (OCP) over the frequency range of 10 kHz−10 mHz with a potential amplitude of 0.05 V using an AUTOLAB-302N potentiostat/galvanostat. Typical potassium and sodium blood concentrations vary from 3.5 to 5.2 mM and 135 to 145 mM, respectively. Besides, K^+ is at a higher concentration in intracellular regions than outside the membrane by 2 orders of magnitude, whereas the opposite is true for Na^+ or Cl^- ions. Therefore, EIS spectra were collected using different aqueous electrolyte mediums at low and high ionic concentrations for KCl (5 and 100 mM) and NaCl (5 and 140 mM).

9.3. Results and Discussion

9.3.1. Synthesis and Characterization of PNMPy−Omp2a

The Omp2a protein was expressed, purified, and refolded using the procedure described in the section 9.2.2. The molecular weight and isoelectric point of trimeric Omp2a (367 amino acids) are 113.4 kDa and 4.47, respectively. PNMPy−Omp2a films were prepared by the anodic polymerization of *N*-methylpyrrole (NMPy), and introducing Omp2a (1 mg/mL) in the generation medium, which consisted of a 15 mM monomer solution in deionized water with 10 mM of sodium dodecyl sulfate (SDS). Cyclic voltammograms recorded for the anodic oxidation of NMPy monomer with and without the MP in the generation medium (Figure 9.3.1) reflected an anodic process with anodic peak potentials of 1.119 and 1.089 V, respectively. According to these results, PNMPy−Omp2a and PNMPy films were deposited onto steel AISI 316 sheets using a potential of 1.10 V and a polymerization time of 20 s. The thickness of PNMPy−Omp2a and PNMPy films, as determined by optical profilometry, is 219 ± 71 nm and 298 ± 72 nm, respectively. The chemical composition of PNMPy−Omp2a composite was initially characterized by XPS, as shown in Table 9.3.1 and Figure 9.3.2. Spectra associated with control PNMPy are provided in Figure 9.3.3. As expected, the oxygen content in the atomic percent composition is higher for PNMPy− Omp2a than for PNMPy due to the presence of the MP. Deconvolution of the high-resolution XPS spectrum in the C 1s region for the composite led to three Gaussian curves that have been attributed to the saturated and conjugated C−C/C = C bonds[35,36] (284.5 eV) of NMPy units, the C = O bond (287.5 eV) of oxidized NMPy units[35,37] (*i.e. N*-substituted PPy derivatives typically undergo an oxidation process), and the C−N, $C-NH_3^+$, and C = O from peptide bonds (286.3 eV) in the protein.[38,39]

Table 9.3.1. Atomic and Mass Percent Composition of PNMPy and PNMPy-Omp2a.

		C 1s	N 1s	O 1s	S 2p
PNMPy	Atomic composition	70.7	7.9	18.9	2.5
	Mass composition	63.3	8.3	22.5	5.9
PNMPy-Omp2a	Atomic composition	53.9	3.6	39.4	3.1
	Mass composition	45.4	3.5	44.2	6.9

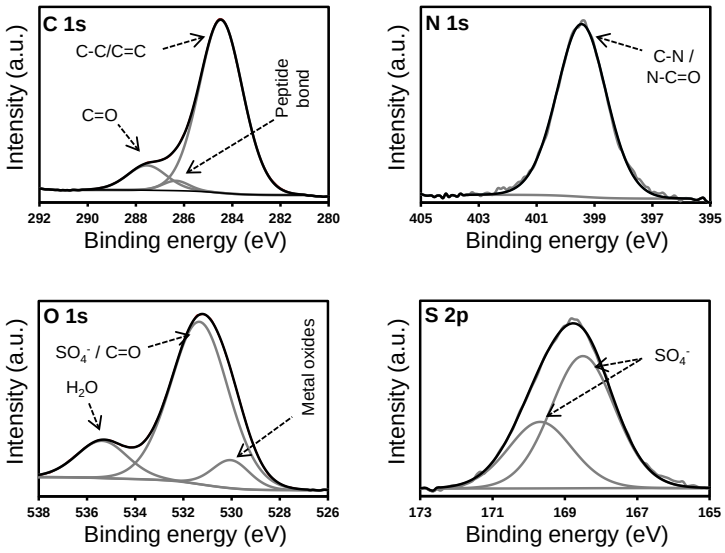

Figure 9.3.2. High-resolution C 1s, N 1s, O 1s and S 2p XPS spectra for PNMPy-Omp2a. Peaks from deconvolution are also displayed (grey lines). Intensity is displayed in arbitrary units.

The high-resolution N 1s spectrum of control PNMPy (Figure 9.3.3) shows two peaks centered at 399.9 eV (6.9%) and 401.4 eV (1.0%), which have been assigned to the C−N bonds of NMPy units involving neutral and charged nitrogen, respectively.[35,40] The ratio 1.0/(6.9 + 1.0) = 0.13 (Table 9.3.2) represents the fraction of charged nitrogen, which can be associated with the doping level of the electropolymerized material. In contrast, PNMPy− Omp2a presents a single peak at 399.5 eV due to the overlapping of the binding energies associated with the C−N bond of NMPy units and the N−C = O (amide) of the protein, the latter being also around 400 eV.[38,41] The annihilation of the peak associated with the charged nitrogen atom indicates that the doping level of the CP in the composite is lower than that in the control, which is fully consistent with the low polymerization charge registered for the composite during the electrogeneration process. Furthermore, the absence of a peak at around 401.5 eV reflects that the amount of positively charged residues in Omp2a is very low.[38,39] Thus, Arg and Lys are essentially present in the composite as uncharged species, photoemitting at the same region that amides in high-resolution N 1s spectra.

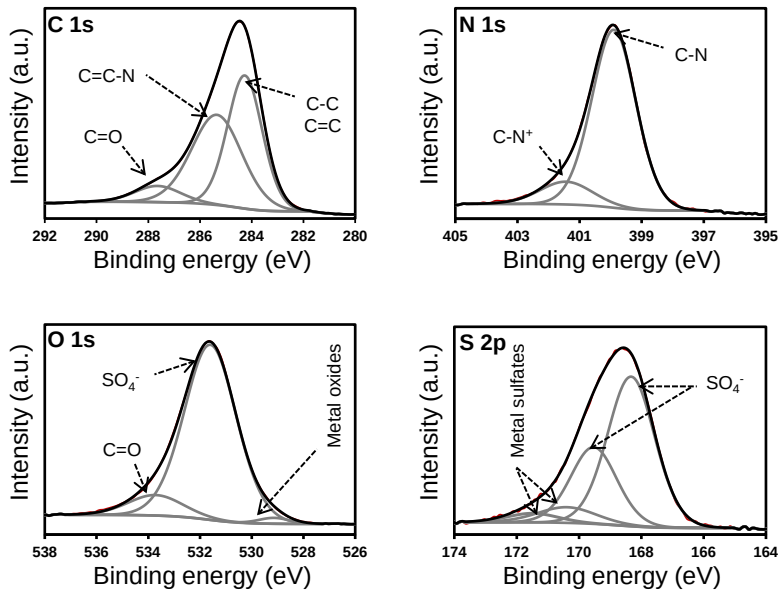

Figure 9.3.3. High-resolution C 1s, N 1s, O 1s and S 2p XPS spectra for control PNMPy samples. Peaks from deconvolution are also displayed (grey lines). Intensity is displayed in arbitrary units.

The high-resolution O 1s spectra of both control PNMPy and PNMPy−Omp2a samples show three peaks. Those of PNMPy have been attributed to the sulfate groups of SDS (531.6 eV), the C = O of oxidized NMPy units (533.7 eV), and the metallic oxides on the steel substrate (529.1 eV). The $C/O_{531.6}$ and $N/O_{531.6}$ composition ratios, where C and N refer to the total compositions displayed in Table 9.3.1, and $O_{531.6}$ corresponds to the relative contribution to the total atomic O percent composition of the peak at 531.6 eV (Table 9.3.2), are 4.3 and 0.5, respectively. For PNMPy−Omp2a, the peaks detected in the high-resolution O 1s spectra appear at 531.3, 535.4, and 530.0 eV. The first one involves not only the sulfate groups of SDS but also the C = O from the peptide bond.[38,39] Accordingly, the $C/O_{531.3}$ and $N/O_{531.3}$ ratios are 1.8 and 0.1, respectively, which are lower than in control PNMPy. The peak at 535.4 eV has been attributed to the water oxygen from moisture of the samples,[42,43] while the peak at 530.0 eV corresponds to metallic oxides at the substrate surface.

Finally, the S 2p high resolution spectrum registered for PNMPy and PNMPy−Omp2a samples are very similar. Both show the spin-split sulfur coupling at 168.3 eV ($S\ 2p_{3/2}$) and 169.5 eV ($S\ 2p_{1/2}$), which is associated with the sulfate

groups of the surfactant. Moreover, the S 2p spectrum for PNMPy also present small peaks at 170.4 eV (S $2p_{3/2}$) and 171.5 eV (S $2p_{1/2}$), which correspond to metallic sulfates at the steel surface.

Table 9.3.2. Assignment of the peaks obtained in the high-resolution XPS spectra recorded for PNMPy and PNMPy-Omp2a, and atomic percent composition (C 1s, O 1s, N 1s and S 2p).

Sample	#Atom	Position (eV)	%	
PNMPy	C 1s	284.3	33.0	C–C / C=C
		285.4	32.4	C=C–N
		287.6	5.3	C=O (oxidized NMPy units)
	N 1s	399.9	6.9	C–N
		401.4	1.0	$C–N^+$
	O 1s	529.1	0.3	Metal oxides
		531.6	16.6	SO_4^- from SDS
		533.7	2.0	C=O
	S $2p_{3/2}$ – S $2p_{1/2}$	168.3 – 169.5	2.2	SO_4^- from SDS
		170.4 -171.5	0.3	Metallic sulfates at steel
PNMPy-Omp2a	C 1s	284.5	46.3	C–C / C=C
		286.3	1.6	Peptide bond
		287.5	6.0	C=O (oxidized NMPy units)
	N 1s	399.5	3.6	C–N and N–C=O
	O 1s	530.0	3.4	Metal oxides
		531.3	29.9	SO_4^- from SDS and C=O from protein
		535.4	6.1	Adsorbed water
	S $2p_{3/2}$ – S $2p_{1/2}$	168.3 – 169.5	3.1	SO_4^- from SDS

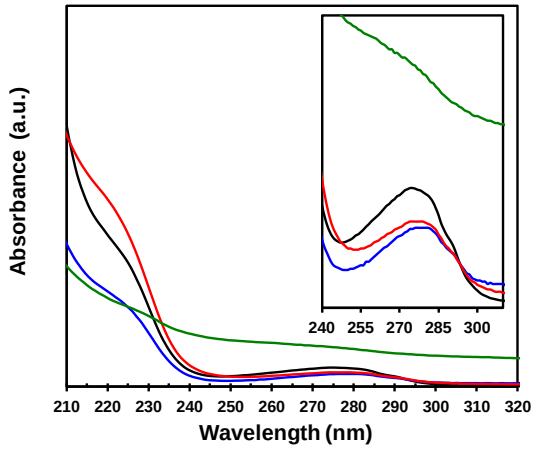

Figure 9.3.4. UV-vis spectra for as obtained Omp2a (black), dialyzed Omp2a (blue), the Omp2a-containing polymerization medium (red) and a PNMPy-Omp2a suspension (green).

UV−vis absorption spectra were registered in the 200−350 nm range to further confirm the presence of Omp2a in the PNMPy−Omp2a composite, which was achieved by identifying the bands associated with the absorption of the peptide group and side groups of aromatic amino acids. PNMPy−Omp2a films were removed from the steel substrate and suspended in water to conduct the UV−vis measurements. Comparison of recorded spectra, which are displayed in Figure 9.3.4, indicate that the typical absorptions of the peptide group and the aromatic side chains of tryptophan (Trp), tyrosine (Tyr), and phenylalanine (Phe) residues were detected as shoulders in the spectrum of PNMPy−Omp2a suspensions when compared to the spectra recorded for the control protein mediums (Figure 9.3.4). Thus, peptide groups typically absorb between 180 and 230 nm, while the aromatic side chains of Trp, Tyr, and Phe amino acids absorb in the 240−300 nm range.[44] Accordingly, spectra of as obtained Omp2a, dialyzed Omp2a and the Omp2a-containing polymerization medium show absorption maxima at such regions. More specifically, the shoulders detected at 289 and 260 nm come from the Trp (10 residues) and Phe (18 residues) residues, respectively.[44] The absorbance of the disulfide bond formed by the two Cys residues at 260 nm also contributes to the latter shoulder. All these peaks appear as shoulders in the spectrum of PNMPy−Omp2a suspension. Protein absorbance was zero above 310 nm.

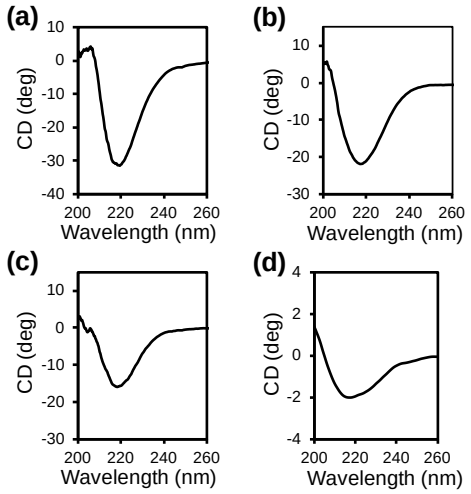

Figure 9.3.5. CD spectra for (a) as-obtained Omp2a; (b) dialyzed Omp2a; (c) Omp2a-containing polymerization medium; and (d) PNMPy-Omp2a composite. Protein concentration is 0.05 mg/mL in all cases with the exception of PNMPy-Omp2a composite.

Although XPS and UV−vis results confirm the correct immobilization of Omp2a into the PNMPy matrix during the electrogeneration process, the native structure of the protein in the PNMPy−Omp2a composite was successfully corroborated by circular dichroism (CD) spectroscopy. Figure 9.3.5 compares the CD spectra for the expressed protein as obtained, after dialysis, and once incorporated into the NMPy-containing polymerization medium. In all cases, the profile exhibits a band at ~217 nm, which is typically found in β-stranded proteins.[45] This characteristic band is preserved in the CD spectra of the composite (Figure 9.3.5d), evidencing that the native β-sheet secondary structure is preserved when the pore-forming protein is immobilized into the polymeric matrix. Therefore, the operative and functional state of the PNMPy−Omp2a interface is ensured by having Omp2a in its folded and/or assembled form.

On the other hand, the UV−vis absorption spectra of steel-supported control PNMPy and PNMPy−Omp2a films (Figure 9.3.6) indicate that the protein affects the oxidation process of the CP during the electrochemical polymerization, as it has already been mentioned. The first absorption band corresponds to the π−π* transition of aromatic rings (λ_{max}= 338 and 377 nm for PNMPy and PNMPy−Omp2a, respectively). The band gap energy, which was determined from the onset wavelength,[46] is 2.44 and 2.30 eV for PNMPy and PNMPy−Omp2a, respectively.

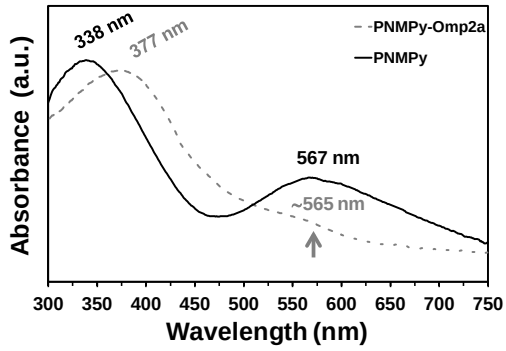

Figure 9.3.6. UV-vis spectra for control PNMPy and PNMPy-Omp2a films deposited onto steel sheets. The values of λ_{max} are indicated.

The second absorption band is related to the first stages of the oxidation process and has been assigned to the formation of polarons. This band is clearly defined for PNMPy at λ_{max}= 567 nm, whereas for PNMPy−Omp2a samples this oxidation process is only identified as a weak shoulder at ~565 nm in the UV−vis spectrum. This feature is fully consistent with XPS results, which suggested that the doping level of the composite was lower than that of PNMPy. Neither system displays an absorption band in the range of 650−700 nm, which is typically assigned to very high oxidation levels (bipolaric states).[37]

9.3.2. Surface Properties

To better understand the passive ion transport response of PNMPy−Omp2a composite, its surface properties were evaluated. Surface morphology and topography of PNMPy−Omp2a were deeply examined by SEM and AFM, respectively. Control PNMPy films (Figure 9.3.7) show a very compact and dense globular structure that is consistent with a homogeneous distribution of the polymer chains. RMS roughness of PNMPy (23 ± 9 nm) is similar to that of steel substrate (18 ± 5 nm). These features indicate a multidirectional growing of polymers that is only possible through the formation of some chemical couplings involving the β- and β'-positions of the repeat units. Accordingly, the transport of ions through this partially cross-linked polymeric matrix is expected to be hindered by the densely packed structure.

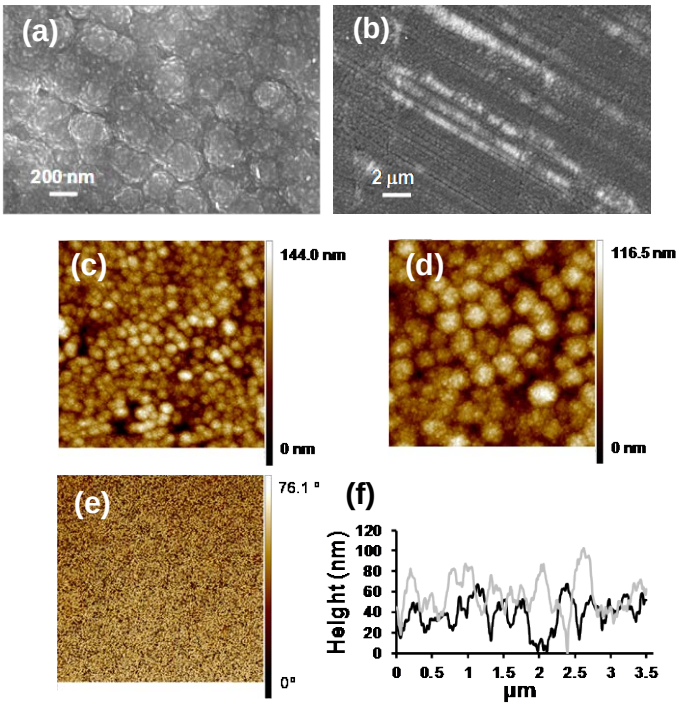

Figure 9.3.7. PNMPy surface characterization: SEM micrograph at (a) 100 kX and (b) 10 kX; (c) 5.0×5.0 and (d) 2.5×2.5 µm² AFM height images; (e) 2.5×2.5 µm² AFM phase image corresponding to (d); and (f) cross-section profiles obtained from (d). In the cross sectional profiles the black line corresponds to the diagonal drawn from the down left corner to the up right corner, while the grey line corresponds to the diagonal drawn from the up left corner to the down right corner.

Incorporation of the protein provokes significant changes in the surface morphology. SEM micrographs and AFM height images of PNMPy−Omp2 (Figure 9.3.8) show elements of both submicrometric and micrometric dimensions with a very homogeneous and smooth texture and without the nodular outcrops typically found in PNMPy aggregates. These particles correspond to folded protein molecules, as evidenced by comparison with SEM micrographs derived from dialyzed Omp2a solutions (Figure 9.3.9).

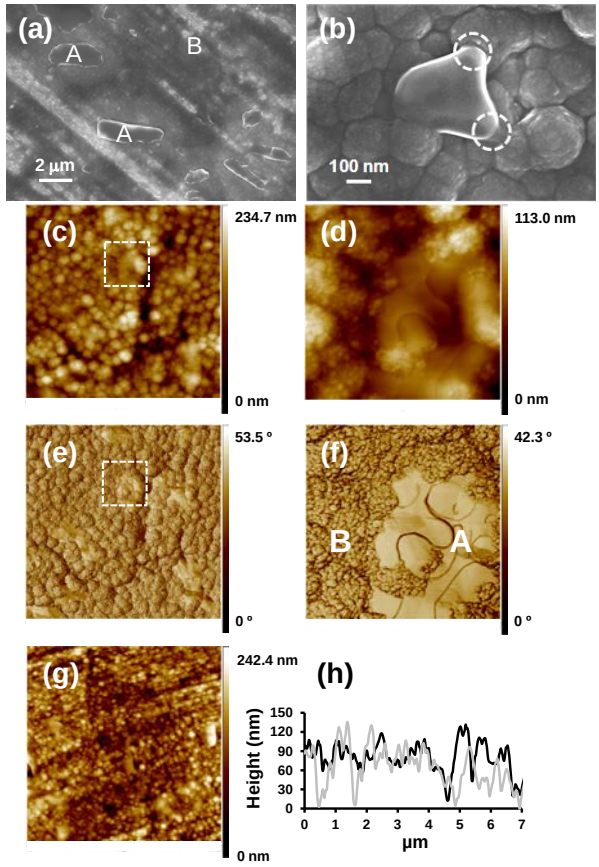

Figure 9.3.8. PNMPy-Omp2a surface characterization: (a) Low and (b) high magnification SEM micrographs; (c) 5.0×5.0 µm² and (d) 1.0×1.0 µm² AFM height images; (e) 5×5 µm² and (f) 1.0×1.0 µm² AFM phase images corresponding to (c) and (d), respectively; (g) 10.0×10.0 µm² AFM height image; and (h) cross-section profiles obtained from (c). Dashed circles in (b) illustrate the connection between PNMPy and Omp2a particles. Squares in (c) and (e) indicate the regions displayed in (d) and (f), respectively. Labels A and B in (f) indicate the Omp2a and PNMP phase, respectively. In the cross sectional profiles the black line corresponds to the diagonal drawn from the down left corner to the up right corner, while the grey line corresponds to the diagonal drawn from the up left corner to the down right corner.

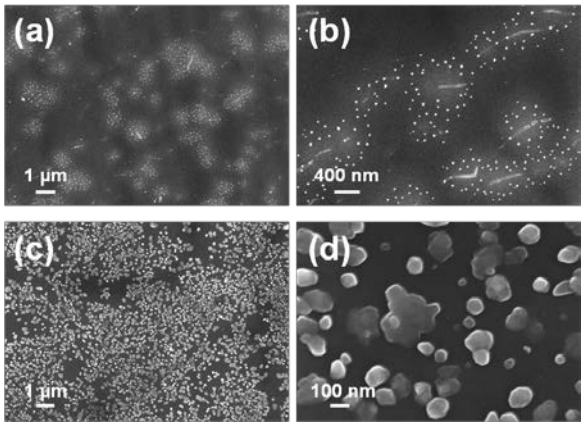

Figure 9.3.9. Low and high magnification SEM micrographs of (a, b) SDS (10 mM) and (c, d) Omp2a (1 mg/mL, 3.6 mM SDS) aqueous solutions solvent casted onto steel.

Although PNMPy and Omp2a proteins are interconnected in the composite (Figure 9.3.8b), well-defined morphological and texture differences reveal a complete phase separation. The latter fact is corroborated by the high contrasts observed in AFM phase images, which enable us to distinguish between the two phases in the composite. The smooth areas in Figure 9.3.8f (labeled A) correspond to the Omp2a phase, whereas the rough and irregular areas (labeled B) represent the PNMPy phase. The mean RMS roughness, which was measured considering several 5 × 5 µm windows, increases to 31 ± 5 nm upon the incorporation of the Omp2a protein.

Overall, morphological and topographical observations reveal that Omp2a proteins are well-distributed throughout the PNMPy-OMP2a composite surface, thus establishing pore structures. Although the PNMPy phase is characterized by a dense and compact matrix, MP functionality is expected to enhance the passive ion transport across the artificial membrane creating permanent ion channels.

Furthermore, contact angle measurements indicate that the surface of both steel ($\theta = 74° \pm 7°$) and PNMPy ($\theta = 67° \pm 4°$) shows some hydrophilicity, while PNMPy−Omp2a water-wettability increases significantly upon the incorporation of the MP ($\theta = 32° \pm 8°$). This effect is noticeably more pronounced for PNMPy−Omp2a than for composites prepared using PNMPy and other proteins (Figure 9.3.10), as for example bovine serum albumin (BSA). This indicates that not only is Omp2a immobilized on the CP matrix, but it retains its natural disposition where the protein hydrophilic regions are positioned toward the outer region of the

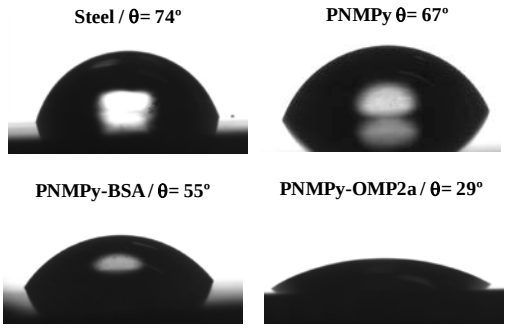

Figure 9.3.10. Contact angle values measured for steel, PNMPy, PNMPy-BSA and PNMPy-Omp2a substrates. Average contact angle values are: 74º ± 7º (steel), 67º ± 4º (PNMPy), 54º ± 7 º (PNMPy-BSA) and 32º ± 8º (PNMPy-Omp2a). The hydrophilicity of PNMPy increases 19 % and 52 % upon the incorporation of bovine serum albumin (BSA) and Omp2a, respectively.

membrane, just as in biological environments. Although the isoelectric point of BSA (4.7) is very similar to that of Omp2a (4.5),[47] the contact angle value for PNMPy−BSA films prepared under similar experimental conditions (θ = 54° ± 7°) represents a reduction of only 20% with respect to PNMPy.

9.3.3. Electrochemical Properties

Cyclic voltammetry studies were run to determine the influence of these new formed ion channels in the electrochemical properties of the PNMPy− Omp2a composite. First, as occurred for the monomer (Figure 9.3.1), the anodic process at around ~1.1 V is less marked for PNMPy−Omp2a than for PNMPy (Figure 9.3.11). The ability to exchange charge reversibly, hereafter denoted electroactivity, increases with the similarity between the anodic and cathodic areas of the first control voltammogram. Thus, the electroactivity of PNMPy−Omp2a is 10% higher than that of PNMPy. Besides, the electrochemically induced reduction of the thickness has been used to evaluate the relative porosity (Por) of PNMPy−Omp2a and PNMPy systems. Specifically, Por (in %) has been estimated as the difference between the thicknesses of the films as prepared and after 15 consecutive redox cycles (193 nm ± 51 and 253 nm ± 93 nm for PNMPy− Omp2a and PNMPy, respectively) relative to the thickness of the as-prepared film. The values obtained for Por are very similar for the two systems (*i.e.* 12 and 15%, respectively). Therefore, the difference observed in electroactivity and LEA values between

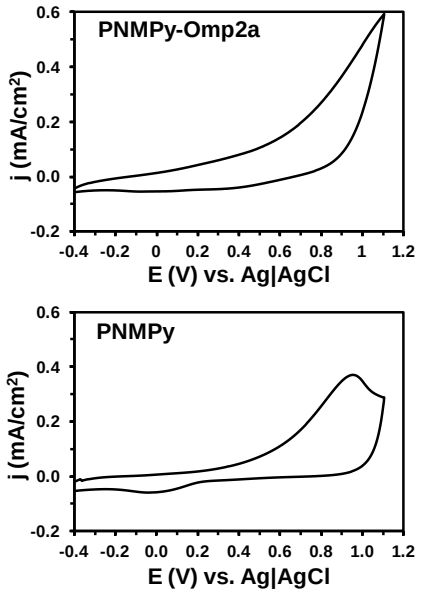

Figure 9.3.11. Cyclic voltammograms of PNMPy-Omp2a and PNMPy in aqueous solution with 0.1M $LiClO_4$. Initial and final potentials: -0.40 V; reversal potential: 1.10 V. Scan rate: 25 mV/s.

PNMPy and PNMPy−Omp2a systems are mainly due to the operative state of Omp2a.

SEM micrographs recorded for PNMPy−Omp2a samples submitted to 15 redox cycles (Figure 9.3.12) reveal significant structural changes, which mainly affect the elements associated with the protein phase. Specifically, after a certain number of cycles, the smooth homogeneous particles (Figure 9.3.12a,b) disaggregate into a heterogeneous distribution of small spherical aggregates that have been associated with unfolded protein molecules. Accordingly, AFM images suggest that the 3D structure of the protein collapses, and only the space once occupied by the Omp2a remains in the PNMPy surface. However, this aggressive electrochemically induced degradation process is not expected to occur when assessing the ion transport response of PNMPy−Omp2a by EIS because it is a nondestructive technique. Consequently, the functionality of the biomolecule in the composite is assured for passive ion transport applications.

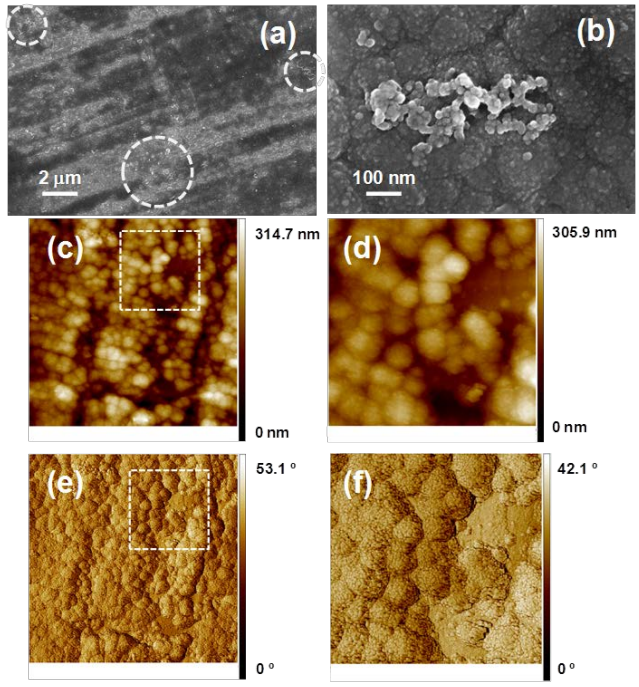

Figure 9.3.12. Surface characterization of PNMPy-Omp2a after 15 consecutive oxidation-reduction cycles: (a) Low and (b) high magnification SEM micrographs; (c) 5×5 µm² and (d) 2.0×2.0 µm² AFM height images; (e) 5×5 µm² and (f) 2.0×2.0 µm² AFM phase images corresponding to (c) and (d), respectively. Dashed circles in (a) illustrate the regions with unfolded protein. Squares in (c) and (e) indicate the regions displayed in (d) and (f), respectively.

9.3.4. Biodegradability and Biocompatibility

CP-based platforms for biotechnological and biomedical applications typically require biodegradability and/or biocompatibility to minimize their impact on the environment and/or the adverse reaction of the body. Accordingly, bearing those requirements in mind, and before performing EIS measurements, we conducted both enzymatic degradation and cell viability tests to validate the integrated-protein composite for biointerface applications.

In the particular case of PNMPy−Omp2a, excessively rapid enzymatic degradation of the MP could greatly influence the applicability of the composite when used in physiological mediums. Consequently, the enzymatic biodegradability of Omp2a in the composite was investigated by monitoring the

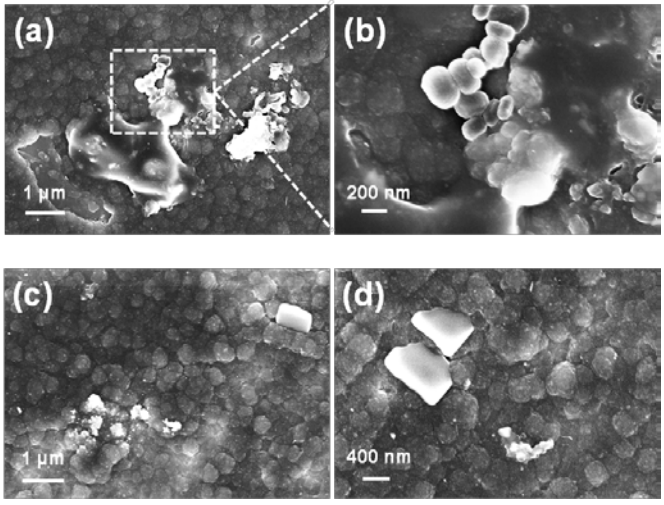

Figure 9.3.13. Low (a, c) and high (b, d) magnification SEM micrographs for PNMPy-Omp2a composite after 8 h (a, b) and 24 h (c, d) of immersion in a Lipase F-AP15 solution.

protein morphology change induced during 72 h of continuous immersion in a Lipase-containing solution. Samples extracted after 1, 4, 8, 24, and 72 h were observed by SEM, and results indicated severe degradation of the protein, which started after 24 h of immersion in the enzymatic solution (Figure 9.3.13). Thus, the protein retained the initial aspect and texture in samples extracted after 1, 4, and 8 h. This feature suggests that the CP matrix protects Omp2a aggregates from the action of the enzyme at the earlier stages of degradation. Micrographs of samples extracted after 72 h revealed that the degraded protein is mostly detached from the surface of the films (Figure 9.3.14), indicating that the benefits provided by the protein to the composite are expected to be null after this time of exposure to aggressive bioconditions.

Quantitative results for cell adhesion assays are displayed in Figure 9.3.15a. The number of Vero and Cos-7 cells adhered to the surface of the PNMPy−Omp2a is significantly higher than that of PNMPy. This tendency is more evident in the case of Vero cells. On the other hand, the adhesion of both Vero and Cos-7 cells on the surface of PNMPy and PNMPy−Omp2a is favoured with respect to the TCPS and steel control substrates, which show similar relative viabilities.

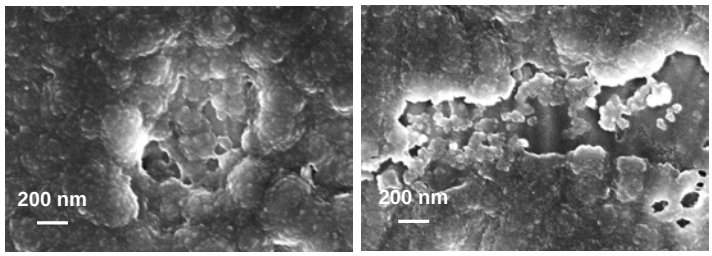

Figure 9.3.14. SEM micrographs for PNMPy-Omp2a composite after 72 h of immersion in a Lipase F-AP15 solution.

On the other hand, SEM micrographs show the significant spreading of Cos-7 cells, which form cellular monolayers on the surface of PNMPy−Omp2a (Figure 9.3.15b), whereas large domains without cells appear on the surface of PNMPy (Figure 9.3.15c). The actin filaments emerging from the cells and with the barbed ends oriented toward the surface of PNMPy−Omp2a (Figure 9.3.15d), which are known as filopodia, are responsible for local adhesion. The grouping of these filaments results in stress fibers, denoted lamellipodia, that are used by cells to move along the substrate. Figure 9.3.15e shows typical connections between two Cos-7 cells to establish communication, which is a crucial step in the coordination of differentiation processes in eukaryotic cells. Similar features are displayed in Figure 9.3.16 for cultured Vero cells. Overall, the results presented in this section indicate that PNMPy−Omp2a is a potential candidate for biotechnological and biomedical applications in which biocompatibility is a requisite.

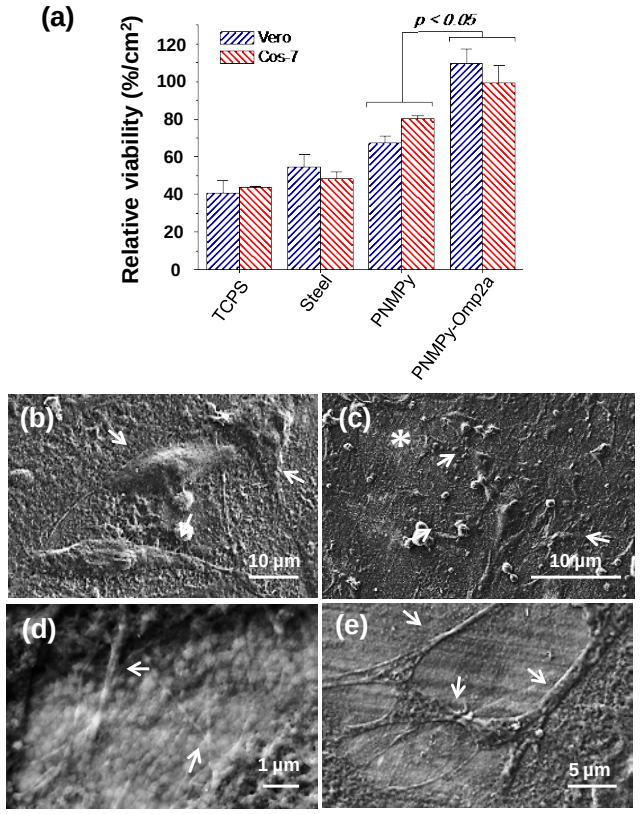

Figure 9.3.15. (a) Cellular adhesion onto PNMPy-Omp2a, PNMPy and steel surfaces using Vero (epithelial-like) and Cos-7 (fibroblast-like) cells. The relative viability was established in relation to the TCPS control (tissue culture polystyrene). ANOVA-Tukey's test, $p<0.05$. SEM micrographs of Cos-7 cells seeded for 24 h onto (b) PNMPy-Omp2a and (c) PNMPy surfaces. The asterisk in (c) indicates substrate surface, while arrows in (b) and (c) indicate the cells adhered onto the surface. Micrographs showing cellular interactions (arrows) at cultured PNMPy-Omp2a films: (d) connection sites (filopodia) between Cos-7 cells and the substrate; and (e) intercellular junctions used for cell-cell communication processes.

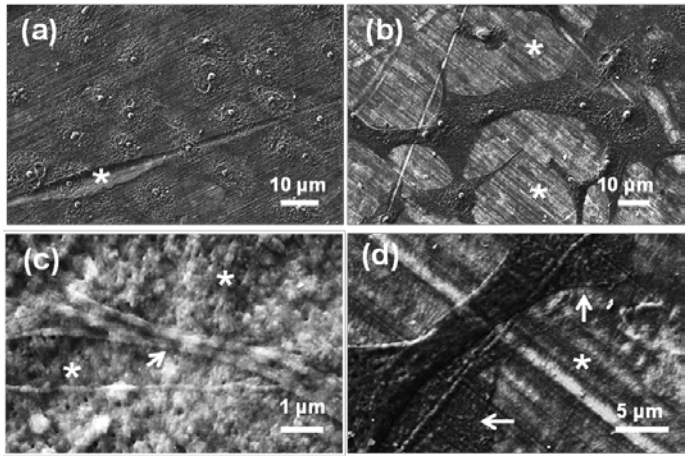

Figure 9.3.16. SEM micrographs of Vero cells seeded for 24 h onto (a) PNMPy and (b) PNMPy-Omp2a surfaces. The asterisks indicate substrate surface. Micrographs showing cellular interactions (arrows) in PNMPy-Omp2a films covered by Vero cells: (c) intercellular junctions used for cell-cell communication processes and (d) connection sites (lamellipodia) between Vero cells and the substrate.

9.3.5. Ion Channels

EIS measurements have been carried out to evaluate the proper function of ion channels and pores formed by the MP in the PNMPy−Omp2a composite.[48−52] This methodology provides information not only of the ion transport, but also a complete description of the investigated system, as was recently discussed in a comparative study.[53]

Impedance was measured as a function of frequency for steel-supported PNMPy and PNMPy−Omp2a films. EIS spectra were registered using different aqueous electrolyte mediums: 5 and 100 mM KCl solutions and 5 and 140 mM NaCl solutions. It should be noted that Na^+ and K^+ are two main blood electrolytes, their normal blood levels being 135−145 and 3.5− 5.2 mM, respectively. Moreover, the concentration of K^+ is 2 orders of magnitude higher in intracellular regions than outside the membrane, while the opposite occurs for Na^+.

Figure 9.3.17a−e compares representative Nyquist plots obtained for PNMPy and PNMPy−Omp2a in different Na^+- and/or K^+-containing media. In all cases, Nyquist spectra show a semicircle in the high-frequency range and a straight ascending line in the low-frequency range.

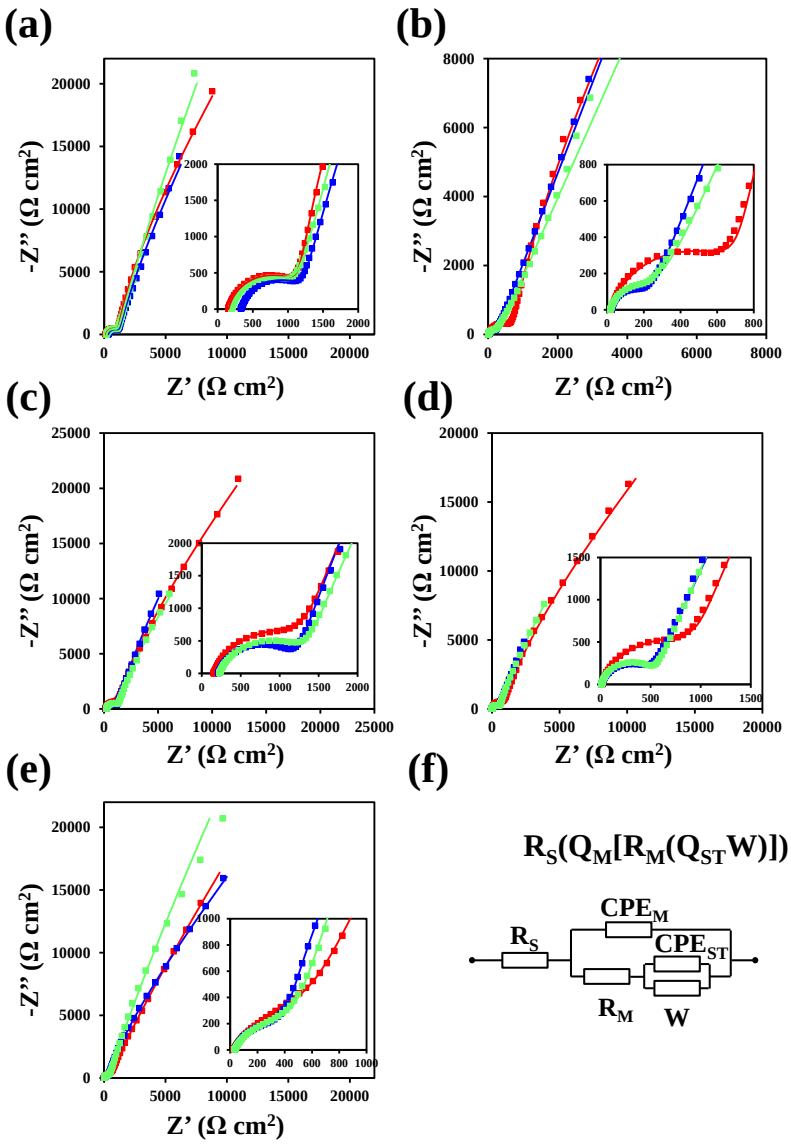

Figure 9.3.17. Nyquist plots for PNMPy (red) and PNMPy-Omp2a (blue and green) in an aqueous solution containing: (a) 5 mM K^+; (b) 100 mM K^+; (c) 5mM Na^+; (d) 140 mM Na^+; and (e) 5 mM K^+ + 140 mM Na^+. (f) Electrical equivalent circuit (EEC) used for fitting experimental data for PNMPy and PNMPy-Omp2a. R_S is the electrolyte resistance, CPE_M and R_M are the membrane constant phase element and resistance, respectively, CPE_{ST} is the steel constant phase element, and finally, W is the Warburg impedance.

The electrical equivalent circuit (EEC) used to fit the experimental data is shown in Figure 9.3.17f, where R_S corresponds to the electrolyte solution resistance and R_M represents the ability of the PNMPy−Omp2a system to impede ion transport at the interface between the electrolyte and the membrane. The ECC also includes double layer capacitances from both the membrane and steel (Q_M and Q_{ST}, respectively) and a Warburg impedance element (W), corresponding to the diffusion of water molecules. Therefore, both R_M and Q_M are associated with the overall contribution of the protein-integrated interface. It should be noted that the incorporation of ion channels through the immobilization of the MP is expected to alter the membrane resistance value, R_M. Accordingly, channel activity can be monitored by comparing the membrane resistance of PNMPy and PNMPy−Omp2a in the different media.

Table 9.3.3 lists the contribution of each element for PNMPy and PNMPy−Omp2a. Both capacitances were replaced by a constant phase element (CPE) that describes a nonideal capacitor when the phase angle is different from −90°. The CPE impedance is attributed to the surface reactivity, surface heterogeneity and roughness, which in turn are related to the electrode geometry and porosity. Also, the CPE impedance accounts for the nonuniform diffusion among the films adhered to the electrode surface. The CPE impedance, which has been expressed as $Z_{CPE} = [Q\,(j\omega)^n]^{-1}$, represents an ideal capacitor and a pure resistor for n = 1 and n = 0, respectively, while it is associated with a diffusion process when n = 0.5. The fitting quality was judged based on the error percentage associated with each circuit component, showing errors lower than 5% in most of the elements.

EIS results evidence that the pore-forming MP is properly immobilized in the PNMPy matrix, retaining the functionality associated with the β-barrel structure. More specifically, the response of PNMPy and PNMPy−Omp2 films is very similar for both the 5 mM K^+ and the 5 mM Na^+ electrolytic media (Figure 9.3.17a,c). Accordingly, the RM values (Table 9.3.3), which indicate the facility to exchange ions between the system and the electrolyte solution, are very similar for the control PNMPy and the MP-containing composite. Similarly, the ability to store electrical charge and the diffusion impedance of PNMPy, which are defined by Q_M and W, respectively, are not significantly affected by the incorporation of the protein when the concentration of ions is low. In spite of this, the diffusion of hydrated Na^+ is slightly higher for the MP-composite than for the CP, suggesting that Omp2a is more efficient for the transport of Na^+ than for K^+.

In contrast, R_M values are lower for PNMPy−Omp2a than for PNMPy in the 100 mM K^+ and 140 mM Na^+ solutions (Figure 9.3.17b,d). Accordingly, PNMPy−Omp2a promotes the passive ion transport in solutions with high ionic concentrations, thus

Table 9.3.3. Fitting parameters used to simulate the EIS spectra displayed in Figures 9.3.17a-d using the electrical equivalent circuit represented in Figure 9.3.17f: R_S (Ω cm^2), R_M (Ω cm^2), Q_M (F cm^{-2} s^{n-1}), n, Q_S (F cm^{-2} s^{n-1}) and W (Ω cm^2). For PNMPy-Omp2a, the first and second values provided for each element correspond to the blue and green spectra, respectively. The error percentage associated to each circuit element is included in parenthesis. Fitting parameters used to simulate the EIS spectra displayed in Figure 9.3.17e are listed in Table 9.3.4.

	PNMPy				**PNMPy-Omp2a**			
	5 mM K^+	**100 mM K^+**	**5 mM Na^+**	**140 mM Na^+**	**5 mM K^+**	**100 mM K^+**	**5 mM Na^+**	**140 mM Na^+**
R_S	154 (0.2)	21.2 (1.0)	156 (0.4)	19.1 (1.0)	336 (0.4) 201 (0.4)	22.1 (0.6) 18.2 (1.3)	217 (0.3) 229 (0.2)	14.7 (0.7) 14.5 (0.6)
R_M	1158 (0.7)	821 (2.5)	1553 (1.7)	1249 (3.6)	1005 (0.6) 1074 (1.4)	243 (2.1) 328 (4.3)	1096 (0.8) 1282 (0.6)	589 (1.7) 589 (1.3)
$Q_M \cdot 10^5$	3.749 (1.6)	5.158 (4.5)	4.732 (2.5)	5.137 (4.4)	4.941 (3.7) 3.788 (3.3)	3.683 (5.5) 5.906 (7.9)	3.964 (2.0) 5.006 (1.3)	4.853 (3.1) 2.886 (2.8)
n	0.8500 (0.3)	0.8254 (0.8)	0.8497 (0.5)	0.8597 (0.8)	0.8291 (0.9) 0.8363 (0.7)	0.8884 (0.9) 0.8363 (0.7)	0.8460 (0.5) 0.8161 (0.3)	0.8494 (0.5) 0.8931 (0.4)
$Q_S \cdot 10^4$	3.787 (0.6)	4.229 (2.7)	2.227 (1.3)	2.441 (4.0)	5.406 (1.2) 4.013 (1.4)	4.844 (0.7) 4.533 (1.4)	7.385 (0.9) 5.852 (0.6)	7.790 (3.4) 5.580 (2.5)
n	0.9787 (0.5)	0.9579 (2.2)	0.9740 (1.2)	0.9869 (3.3)	0.9017 (1.3) 0.8720 (1.1)	0.7626 (0.4) 0.7286 (0.8)	0.8921 (1.0) 0.9292 (0.7)	0.8169 (2.3) 0.8628 (1.7)
$W \cdot 10^5$	9.356 (2.6)	9.579 (12.5)	10.76 (2.9)	13.89 (7.2)	9.040 (8.9) 3.626 (17.2)	2.369 (.89) 1.630 (5.7)	12.16 (7.8) 17.39 (2.7)	10.37 (19.5) 13.77 (11.1)

the MP functionality is enhanced when the concentration of ions in the medium is high. EIS spectra recorded in a solution containing 5 mM K^+ + 140 mM Na^+, which correspond to the concentrations of such ions in blood, evidence a similar behaviour (Figure 9.3.17e). Thus, the ion transport resistance of PNMPy (1037 Ω cm^2) decreases 1 order of magnitude when the MP is immobilized in the PNMPy− Omp2a composite (~600 Ω cm^2), which activates the transport of ions.

Inspection of the Q_M values obtained for the 5 mM K^+ and 140 mM Na^+ solutions indicates that, as occurred for the solutions with lower concentrations of ions, the MP does not alter significantly the ability to store charge of the CP. Indeed, inspection of results displayed in Table 9.3.4 evidence that such ability is intrinsic to PNMPy because it is practically independent of the concentration and nature of the ions as well as of the Omp2a presence. Comparison of the diffusional impedance values obtained for more concentrated solutions also suggest that Omp2a favours the diffusion of Na^+ with respect to that of K^+. Thus, results for PNMPy indicate that the bulk ionic diffusion through the CP interface is practically independent of both the concentration and nature of ions. Accordingly, although ions affect the R_M of PNMPy, the diffusional activity of this material is not selective. In contrast, the impedance behaviour observed for PNMPy−Omp2a evidence that R_M is very sensitive to the ionic concentration, while W is affected by the nature of ions. These features indicate that the MP brings not only ion transport capacity, but also sensitivity and selectivity to the PNMPy-Omp2a biointerface.

Table 9.3.4. Fitting parameters used to simulate the EIS spectra displayed in Figure 9.3.17e: R_S (Ω cm^2), R_M (Ω cm^2), Q_M (F cm^{-2} s^{n-1}), n, Q_S (F cm^{-2} s^{n-1}) and W (Ω cm^2). For PNMPy-Omp2a, the first and second values provided for each element correspond to the blue and green spectra, respectively. The error percentage associated to each circuit element is included in parenthesis.

	PNMPy	**PNMPy-Omp2a**
R_S (Ω cm^2)	26.6 (1.2)	30.6 (0.9) / 24.5 (0.8)
R_M (Ω cm^2)	1037 (8.5)	622 (4.1) / 579 (2.8)
$Q_M \cdot 10^4$ (F cm^{-2} s^{n-1})	1.223 (6.6)	1.079 (5.3) / 1.223 (3.6)
n	0.6880 (1.4)	0.7223 (1.1) / 0.7231 (0.7)
$Q_S \cdot 10^4$ (F cm^{-2} s^{n-1})	1.972 (8.9)	1.773 (3.8) / 3.822 (2.6)
n	0.8448 (5.0)	0.9959 (1.9) / 0.9452 (1.4)
$W \cdot 10^5$ (Ω cm^2)	7.052 (22.4)	12.02 (4.5) / 242.9 (26.9)

Overall, we have successfully produced a protein-integrated system that preserves the native structure and functionality of the MP. The combination of biological elements with synthetic materials is a challenging research field that requires further understanding of interactions and compatibility between materials. However, as a first step, PNMPy−Omp2a approach has resulted in a biointerface with proven passive ion transport. Interestingly, as Omp2a allows the passive transport of other molecules such as nutrients and antibiotics, PNMPy−Omp2a composite can also be exploited to design bio-hybrid materials with multifunctional artificial channels for bioapplications.

9.4. Conclusions

In this work, novel CP−MP biocomposites have been prepared using PNMPy, which shows a very compact structure, and Omp2a from *Brucella melitensis*, a β-barrel protein that forms trimeric pores. The MP has been successfully immobilized onto the surface of PNMPy during the electrochemical polymerization, which has been proven by XPS and UV−vis spectroscopy analyses. Furthermore, Omp2a retained its native-state β-sheet structure, thus preserving its folded operative form. SEM and AFM characterization techniques enabled us to identify the PNMPy−Omp2a composite surface properties, which are related to the passive ion transport. As a result, Omp2a pore-forming structures are distributed throughout the compact PNMPy matrix. Additionally, PNMPy−Omp2a biocomposites are hydrophilic, electroactive, and biocompatible biointerfaces.

Although the porosity of PNMPy and PNMPy−Omp2a are very similar, their responses toward electrolyte solutions are completely different. Thus, the behaviour of PNMPy is independent of the electrolyte concentration, while PNMPy−Omp2a promotes the exchange of ions between the systems and the electrolyte solution. This passive transport ability, which is associated with the β-barrel structure of the immobilized protein, is regulated by the concentration of ions in the electrolyte solution.

PNMPy−Omp2a behaves as a smart bioinspired ion-channel, which has potential applications in different areas of the biomedical field, such as nanofluidics, energy conversion and biosensoring. Furthermore, changing the concentration of ions in the electrolyte solution regulates the activity of Omp2a nanochannels integrated in the PNMPy−Omp2a composite. This has been proved by examining the ion transport process using K^+ and Na^+ concentrations around those typically found in blood. Furthermore, results suggest that Omp2a is more efficient for the

diffusion of Na^+ than for the diffusion of K^+. In addition to the above-mentioned applications, Omp2a immobilized onto PNMPy can be used to simulate the process of ions and small molecules transport in living organisms, enabling the investigation of the chemistry, size, and conformational states of β-barrel nanochannels.

9.5. References

[1] C. Li, C.; H. Bai, G. Shi, *Chem. Soc. Rev.* **2009**, *38*, 2397.
[2] E. C. S. Coelho, V. B. Nascirnento, A. S. Ribeiro, M. Navarro, *Electrochim. Acta* **2014**, *123*, 441.
[3] Y.-Z. Longa, M.-M. Lia, C. Gub, C.; M. Wanc, J.-L. Duvaild, Z. Liue, Z. Fanf, *Prog. Polym. Sci.* **2011**, *36*, 1415.
[4] B. Guo, L. Glavas, A.-C. Albertsson, *Prog. Polym. Sci.* **2013**, *38*, 1263.
[5] I. S. Romero, M. L. Schurr, J. V. Lally, M. Z. Kotlik, A. R. Murphy, *ACS Appl. Mater. Interfaces* **2013**, *5*, 553.
[6] M. Martí, G. Fabregat, F. Estrany, C. Alemán, E. Armelin, *J. Mater. Chem.* **2010**, *20*, 10652.
[7] M. Bongo, O. Winther-Jensen, S. Himmelberger, X. Straskosas, M. Ramuz, A. Hama, E. Stavrinidou, G. G. Malliaras, A. Salleo, B. Winther-Jensen, R. M. Owens, *J. Mater. Chem. B* **2013**, *1*, 3860.
[8] R. Hassanien, M. Al-Hinai, S. A. F. Al-Said, R. Little, L. Siller, N. G. Wright, A. Houlton, B. R. Horrocks, *ACS Nano* **2010**, *4*, 2149.
[9] Y. Ma, P. L. Chiu, A. Serrano, S. R. Ali, A. M. Chen, H. He, *J. Am. Chem. Soc.* **2008**, *130*, 7921.
[10] I. S. Romero, N. P. Bradshaw, J. D. Larson, S. Y. Severt, S. J. Roberts, M. Schiller, J. M. Leger, A: R. Murphy, *Adv. Funct. Mater.* **2014**, *24*, 3866.
[11] J. W. Taraska, *Curr. Opin. Struct. Biol.* **2012**, *22*, 507.
[12] N. P. Barrera, M. Zhou, C. V. Robinson, *Trends Cell Biol.* **2013**, *23*, 1.
[13] T. Stora, J. H. Lakey, H. Vogel, *Angew. Chem. Int. Ed.* **1999**, *38*, 389.
[14] J. U. Bowie, *Nature* **2005**, *438*, 581.
[15] A. Jungbauer, W. Kaar, *J. Biotechnol.* **2007**, *128*, 587.
[16] R. Valiokas, S. Vaitekonis, G. Klenkar, G. Trinkūnas, B. Liedberg, *Langmuir* **2006**, *22*, 3456.
[17] M. Kumar, J. E. O. Habel, Y.-X. Shen, W. P. Meier, T. Walz, *J. Am. Chem. Soc.* **2012**, *134*, 18631.
[18] K. Kita-Tokarczyk, J. Grumelard, T. Haefele, W. Meier, *Polymer* **2005**, *46*, 3540.
[19] A. González-Pérez, K. B. Stibius, T. Vissing, C. H. Nielsen, O. G. Mouritsen, *Langmuir* **2009**, *25*, 10447.
[20] A. Graff, M. Sauer, P. Van Gelder, W. Meier, *Proc. Natl. Acad. Sci. U.S.A.* **2002**, *99*, 5064.
[21] K. Yao, C. Liu, Y. Chen, L. Chen, F. Li, K. Liu, R. Sun, P. Wang, C. Yang, *J. Mater. Chem.* **2012**, *22*, 7342.
[22] Y.-X. Shen, P. O. Saboe, I. T. Sines, M. Erbakan, M. Kumar, *J. Membr. Sci.* **2014**, *454*, 359.
[23] A. Mecke, C. Dittrich, W. Meier, *Soft Matter* **2006**, *2*, 751.
[24] N. Arun, K. S. Narayan, *J. Phys. Chem. B* **2008**, *112*, 1564.
[25] E. A. Della Pia, J. V. Holm, N. Lloret, C. Le Bon, J.-L. Popot, M. Zoonens, J. Nygård, K. L. A. Martinez, *ACS Nano* **2014**, *8*, 1844.

[26] M.-L. Boschiroli, V. Foulongne, D. O'Callaghan, *Curr. Opin. Microbiol.* **2001**, *4*, 58.
[27] J.-Y. Paquet, M. A. Diaz, S. Genevrois, M. Grayon, J.-M. Verger, X. De Bolle, J. H. Lakey, J.-J. Letesson, A. Cloeckaert, *J. Bacteriol.* **2001**, *183*, 4839.
[28] G. Roussel, A. Matagne, X. De Bolle, E. A. Perpète, C. Michaux, *Protein Expression Purif.* **2012**, *83*, 198.
[29] G. Roussel, E. A. Perpète, E. Tinti, C. Michaux, *Biotechnol. Bioeng.* **2013**, *110*, 417.
[30] D. Aradilla, F. Estrany, C. Alemán, *J. Phys. Chem. C* **2011**, *115*, 8430.
[31] D. Aradilla, F. Estrany, E. Armelin, C. Alemán, *Thin Solid Films* **2010**, *518*, 4203.
[32] D. T. McQuade, A. E. Pullen, T. M. Swager, *Chem. Rev.* **2000**, *100*, 2537-.
[33] B. Teixeira-Dias, C. Alemán, F. Estrany, D. S. Azambuja, E. Armelin, *Electrochim. Acta* **2011**, *56*, 5836.
[34] E. Pál, V. Hornok, D. Sebök, A. Majzik, I. Dékány, *Colloids Surf., B* **2010**, *79*, 276.
[35] N. Anwar, M. Vagin, F. Laffir, G. Armstrong, C. Dickinson, T. McCormac, *Analyst* **2012**, *137*, 624.
[36] A.-D. Bendrea, G. Fabregat, L. Cianga, F. Estrany, L. J. del Valle, I. Cianga, C. Alemán, *Polym. Chem.* **2013**, *4*, 2709.
[37] G. Fabregat, C. Alemán, M. T. Casas, E. Armelin, *J. Phys. Chem. B* **2012**, *116*, 5064.
[38] D. M. Eby, K. Artyushkova, A. K. Paravastu, G. R. Johnson, *J. Mater. Chem.* **2012**, *22*, 9875.
[39] J. S. Stevens, A. C. de Luca, M. Pelendritis, G. Terenghi, S. Downes, S. L. M. Schroeder, *Surf. Interface Anal.* **2013**, *45*, 1238.
[40] N. Cioffi, L. Torsi, I. Losito, C. Di Franco, I. De Bari, L. Chiavarone, G. Scamarcio, V. Tsakova, L. Sabbatini, P. G. Zambonin, *J. Mater. Chem.* **2001**, *11*, 1434.
[41] D. Bhattacharyya, K. K. Gleason, *Chem. Mater.* **2011**, *23*, 2600.
[42] S. Tougaard, *J. Vac. Sci. Technol. A* **1996**, *14*, 1415.
[43] A. V. Naumkin, A. Kraut-Vass, S. W. Gaarenstroom, C. J. Powell, NIST X-ray Photoelectron Spectroscopy Database,
http://srdata.nist.gov/xps/XPSDetailPage.aspx?AllDataNo=21109, accessed: April, 2014.
[44] F.-X. Schmid, Biological Macromolecules: UV-visible Spectrophotometry, in *Encyclopedia of Life Sciences*, John Wiley & Sons, Ltd. **2001**.
[45] S. Y. Venyaminov, J. T. Yang, in *Circular dichroism and the conformational analysis of biomolecules*, (Ed: G. D. Fasman), Plenum Press, New York **1996**, pp. 69–104.
[46] H. Meng, J. Zheng, A. J. Lovinger, B.-C. Wang, P. G. Van Patten, Z. Bao, *Chem. Mater.* **2003**, *15*, 1778.
[47] S. Ge, K. Kojio, A. Takahara, T. Kajiyama, *J. Biomater. Sci. Polym. Ed.* **1998**, *9*, 131.
[48] J. Lin, J. Motylinski, A. J. Krauson, W. C. Wimley, P. C. Searson, K. Hristova, *Langmuir* **2012**, *28*, 6088.
[49] B. P. G. Silva, D. Z. de Florio, S. Brochsztain, *J. Phys. Chem. C* **2014**, *118*, 4103.
[50] S. Smeazzetto, A. Sacconi, A. L. Schwan, G. Margheri, F. Tadini-Buoninsegni, *Langmuir* **2014**, *30*, 10384.
[51] G. Valincius, T. Meskauskas, F. Ivanauskas, *Langmuir* **2012**, *28*, 977.
[52] G. W. de Groot, S. Demarche, M. G. Santonicola, L. Tiefenauer, G. J. Vancso, *Nanoscale* **2014**, *4*, 2228.
[53] F. Müller, C. A. Ferreira, D. S: Azambuja, C. Alemán, E. Armelin, *J. Phys. Chem. B* **2014**, *118*, 1102.

CHAPTER 10

BIOACTIVE INTERFACE CONTAINING TERTHIOPHENE, CARBOXYL AND SCHIFF BASE FUNCTIONALITIES

Summary

A new bis-thienyl type monomer (AzbT) was synthesized and polymerized electrochemically with 2,2′:5′,2″-terthiophene (Th_3) mixtures - in different molar ratios (*i.e.* 50:50, 60:40 and 80:20) - to render random copolymers, P(AzbT-*co*-Th_3)s, as ultra-thin films. Spectroscopic analyses confirmed that the content of AzbT structural units in the copolymers increases with the increasing of AzbT:Th_3 molar ratio in the electropolymerization medium.

The morphology of the films evolved from a porous multi-level surface to a more compact and flat globular structure with increasing AzbT content, which also resulted in a reduction of the electrochemical activity and stability. Cytotoxicity and cell adhesion and proliferation tests revealed that P(AzbT-*co*-Th_3) matrices can be potentially applied as bioactive substrates. The 80:20 copolymer biointerface, which combines biocompatibility, optical and electrochemical properties in the range of semiconducting PTh derivatives, results into a promising functional biomaterial.

The bis-thienyl monomer, AzbT, was synthesized and characterized by Dr. L. Cianga[1] and Dr. I. Cianga[1]. Biological and biodegradation assays were done in collaborative working with Dr. L. J. del Valle[2].

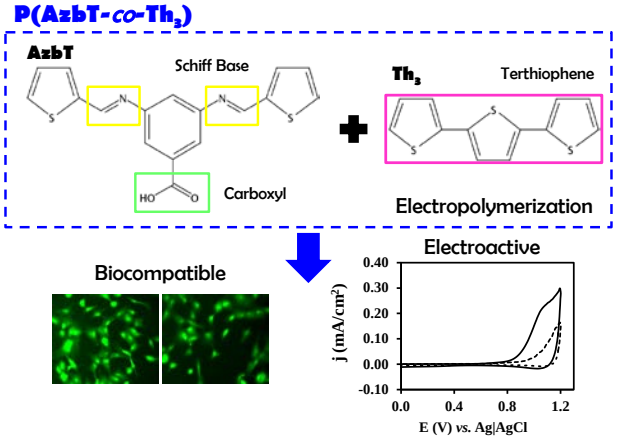

Graphical abstract

Publication derived from this work:

M.M. Pérez-Madrigal, L. Cianga, L.J. del Valle, I. Cianga, C. Alemán, *Polym. Chem.* **2015**, DOI: 10.1039/c5py00480b.

[1]"Petru Poni" Institute of Macromolecular Chemistry, Iasi, Romania.
[2]Departament d'Enginyeria Química, E.T.S. d'Enginyers Industrials de Barcelona, UPC.

10.1. Introduction

Compounds that contain the –C=N– functional linkage in their structure, which are known as Schiff bases (imine or azomethine), are usually synthesized by the condensation of primary amines with compounds bearing active carbonyl groups (*e.g.* an aldehyde). Schiff bases have been applied in a great number of different fields including reactants for organic synthesis,[1-2] inhibition of corrosion[3] and, specifically, biological chemistry. Thus, the azomethine functional group exhibits antibacterial and antifungal,[4,5] pesticidal,[6] antitubercular,[7,8] analgesic,[9] antioxidant,[10] anti-inflammatory,[9,10] antidyslipidemic,[11,12] antiviral,[13] antiglycation,[14] and antitumor[15] activities.

In the field of polymers, poly(Schiff base)s or polyazomethines are considered very important materials as long as all the above mentioned properties for Schiff bases are preserved in the polymer counterpart.[16] Furthermore, the presence of –C=N– conjugated double bonds in the main polymeric chain represents a highly attractive alternative to vinylene linkages to display semiconducting properties.[17-18] Thus, polyazomethine-based materials have been exploited for the fabrication of solar cells,[19] fluorescent sensors for explosive or environmentally toxic metal ions,[20,21] electrochromic devices,[22,23] organic field-effect transistors (OFET)s,[24] and organic non-volatile memories (ONVM)s for the next generation of data storage devices.[25]

Another important aspect concerning the azomethine bond is related to its reversibility, a property which was efficiently exploited in the J. M. Lehn's concept of molecular dynamers.[26-28] In that context, dynamic covalent chemistry is a powerful concept for the construction of adaptive and responsive molecular systems. Conjugated polyazomethines can undergo constitutional exchange resulting in materials with tuneable properties induced by external stimuli.[29,30]

Aromatic polyazomethines can be obtained by different chemical procedures: classical polycondensation between aromatic/heterocyclic dialdehydes with aromatic/heterocyclic diamines;[18-20,23-25] polymerization of monomers containing preformed azomethine linkages;[22-36] and self-polycondensation of an automer.[32] Among these synthetic approaches, the one employing monomers that contain preformed azomethine bonds seems to be more versatile, provided that it permits the introduction in the conjugated main chain of different moieties (*e.g.* thienyl, pyrrolyl, naphtyl and aryl) or well-defined polymeric side chains in a controlled manner, thus allowing for a fine tuning of the electrical and/or optical properties of the final materials.

In recent years, different research strategies have been followed to enhance the behaviour of polythiophenes (PThs) as bioactive cellular matrices for tissue engineering applications. For example, soluble PTh derivatives have been combined with biodegradable and biocompatible insulating polymers to fabricate 2D (*e.g.* free-standing nanomembranes, Chapters 4 and 5)[37-41] and 3D (*e.g.* nanofibers, Chapters 7 and 8)[42-44] scaffolds. Other approaches are based on hydrophilic and biocompatible poly(ethylene glycol) (PEG) chains which have been grafted to PTh chains to fabricate amphiphilic PTh bottle-brush copolymers;[45-47] and biomolecules, such as small peptides[48] or proteins,[49-51] which have been immobilized into PTh matrices using *in situ* polymerization approaches.

In this chapter, the main aim is to fabricate a new functional synthetic biointerface with optical properties similar to those displayed by semiconducting PThs. For this purpose, an azomethine-containig bis-thienyl (AzbT) monomer has been synthesized and electrochemically copolymerized with 2,2′:5′,2′′-therthiophene (Th_3). After investigation of the chemical and physical properties of the resulting P(AzbT-*co*-Th_3) copolymers, which were obtained using different AzbT:Th_3 molar ratios, their behaviour as cellular matrices for tissue engineering applications has also been examined. The advantages and drawbacks provoked with the incorporation of the Schiff base functionality have been determined by comparing systematically the properties of P(AzbT-*co*-Th_3) with those of polyterthiophene (PTh_3).

10.2. Experimental Section

10.2.1. Materials

2-Thiophenecarboxaldehyde (Aldrich,98%) was distilled under reduced pressure before use. Benzene was dried over sodium wire and distilled before use. *p*-Toluenesulfonic acid (99%), and 3,5-diaminobenzoic acid (98%), Th_3 (99%), tetrabutylammonium tetrafluoroborate (TBATFB) (99.0%,) were purchased from Aldrich and used as received. The rest of the solvents were purchased from Panreac Quimica S.A.U. (Spain), and used as received.

For cell culture experiments, human osteosarcoma (MG-63) and African green monkey kidney epithelial (Vero) cell lines were purchased from ATCC (USA). Dulbecco's phosphate buffered saline solution (PBS) without calcium chloride and magnesium chloride, Dulbecco's modified Eagle's medium (DMEM, with 4500 mg

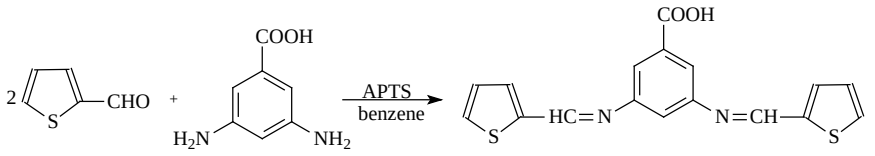

Scheme 10.2.1. Synthetic path followed to obtain the AzbT monomer.

of glucose/L, 110 mg of sodium pyruvate/L and 2 mM L-glutamine), penicillin-streptomycin, 3-(4,5-dimethylthiazol-2-yl)-2,5-diphenyltetrazolium bromide (MTT, 97.5%) and trypsin-EDTA solution (0.05% trypsin, 0.02% EDTA) were all purchased from Sigma-Aldrich (USA). Fetal bovine serum (FBS) and trypan blue stain (0.4%) were purchased from Gibco, UK. Dimethyl sulfoxide (99.0%) was purchased from Panreac Quimica S.A.U. (Spain). Phalloidin-TRITC (for F-actin staining; 1:100 in 0.1% Bovine Serum Albumin (BSA)/PBS) and Hoechst 33342 (1:2000 in 0.1% BSA/PBS) was purchased from Sigma Chemical.

10.2.2. Synthesis of the AzbT monomer

3,5-Bis([2-thienylmethylene]amino)benzoic acid (AzbT) was synthesized as follows (Scheme 10.2.1): a 250 mL three necks round bottom flask equipped with a condenser, a Dean-Stark trap, nitrogen inlet-outlet and magnetic stirrer was charged with 2-thiophene-carboxaldehyde (5.68 mL; 0.062 mol), 3,5-diaminobenzoic acid (4.56 g, 0.03 mol), *p*-toluenesulfonic acid (0.015 g) and benzene (150 mL). Nitrogen was purged through the reaction mixture for 15 minutes. The mixture was heated to reflux with stirring for 15 hours, continuously removing the benzene-water azeotrope. After cooling the reaction mixture, the formed solid product was filtered, dried, and purified by precipitation from acetone in toluene and filtration. Further purification was achieved by using the column chromatography method (aluminum oxide - Fluka Type 507c) and 1,2-dichloroethane as eluent. The solution was concentrated by evaporation under reduced pressure, and the solid obtained after cooling was filtrated and dried. An orange-brownish solid was obtained. Yield: 38%; m.p.: 176-178 °C.

10.2.3. Chemical Characterization of the AzbT monomer

^{1}H-NMR spectra were recorded at room temperature on a Bruker Avance DRX-400 spectrometer (400 MHz), using DMSO-d6 as solvent. Chemical shifts are reported in ppm and referenced to tetramethylsilane (TMS), the internal standard.

The melting point of the synthesized monomer was determined by using Melt-Temp II (USA Laboratory Devices). FTIR spectra of the synthesized monomer and the starting chemicals were recorded on a Bruker Vertex 70 FTIR spectrometer equipped with a diamond ATR device (Golden Gate, Bruker) in transmission mode, by using KBr pellets. Measurements of UV-vis absorption and fluorescence emission of the synthesized monomer dissolved in DMSO (1×10^{-3} M) were carried out by using a Specord 200 Analytik Jena spectrophotometer and Perkin Elmer LS 55 apparatus, respectively.

10.2.4. Electropolymerization

P(AzbT-*co*-Th_3) and PTh_3 films were prepared by chronoamperometry (CA) using an Autolab PGSTAT302N equipped with the ECD module (Ecochimie, The Netherlands). Polymerization was carried out in a standard three-electrode one-compartment cell at room temperature. ITO substrates of approximately 1.0 x 0.5 cm^2 were used as working electrodes, while Pt sheets of the same area were used as counter electrode. The reference electrode was an Ag|AgCl electrode containing KCl saturated aqueous solution (E^0=0.222 V at 25 °C).

Stock solutions of Th_3 and AzbT monomers (2 mM) were prepared in acetronitrile containing 0.1 M TBATFB as dopant agent. For the preparation of PTh_3 films, the cell was filled with 5 mL of the 2 mM Th_3 solution. Polymerization was carried out applying a constant potential of 1.0 V during a polymerization time of θ=150 seconds. P(AzbT-*co*-Th_3) films were prepared considering 50:50, 60:40 and 80:20 AzbT:Th_3 molar ratios. For this purpose, the cell was filled with the corresponding monomer solution prepared after mixing the appropriate amount of each stock solution. The applied potential was varied with the copolymer composition (1.05 V for PTh_3, the 50:50 and 60:40 copolymers; and 1.15 V was used for the 80:20 copolymer), while the polymerization time was 180 seconds in all cases. It should be noted that films obtained using $\theta \geq 300$ s were extremely brittle and peeled off easily from the ITO electrodes. As the behaviour of the 50:50 and 60:40 copolymers was found to be very similar, some of the results obtained for the latter will be briefly addressed.

10.3.5. Characterization Techniques

X-Ray photoelectron spectroscopy

XPS analyses were performed in a SPECS system equipped with a non-monochromated twin anode X-ray source XR50 of Mg/Al (1253 eV/1487 eV). Specifically, the Al anode was operated at 150 W. The pass energy was set to 25 and 0.1 eV for the survey and the narrow scans, respectively. The C 1s peak was used as an internal reference with a binding energy of 284.5 eV. High-resolution XPS spectra were acquired by Gaussian–Lorentzian curve fitting after S-shape background subtraction.

FTIR and UV-vis spectroscopy

Spectra of electropolymerized polymers were recorded on a FTIR Nicolet 6700 spectrophotometer equipped with the Smart SAGA accessory, which is designed for the analysis of thin films on reflective substrates. As samples were adhered onto ITO substrates, gold-coated glass was placed as reflective substrate on top. Thus, background spectrum was collected using uncoated ITO. Samples were placed on the plate using the 5 mm aperture, and 64 scans were performed between 4000 and 600 cm^{-1} with a resolution of 2 cm^{-1}.

UV-vis absorption spectra were obtained using a UV-vis-NIR Shimadzu 3600 spectrophotometer equipped with a tungsten halogen visible source, a deuterium arc UV source, a photomultiplier tube UV-vis detector, and a InGaAs photodiode and cooled PbS photocell NIR detectors. Spectra of PTh_3 and P(AzbT-*co*-Th_3) films deposited onto ITO were recorded between 300 and 800 nm in the absorbance mode using the integrating sphere accessory (model ISR-3100). The interior of the integrating sphere was coated with highly diffuse BaO reflectance standard. Measurements, data collection and data evaluation were controlled by the computer software UVProbe (version 2.31).

Optical profilometry

The thickness of the electropolymerized films was determined using a surface profilometer Dektak 150 (Veeco). Several scratches (minimum 6) were intentionally made throughout the surface of the polymer samples (n=4), and the step at several positions along the scratches was measured by the computer software Dektatk (Veeco Instruments Inc., version 9.2.) to allow statistical analysis of data.

Scanning electron microscopy

The morphology of the prepared films was examined by SEM using a Focused Ion Beam Zeiss Neon40 scanning electron microscope equipped with an energy dispersive X-ray (EDX) spectroscopy system and operating at 5 kV. All samples were sputter-coated with a thin carbon layer using a K950X Turbo Evaporator to prevent electron charging problems. Prior to SEM observation, samples covered with cells were fixed in a 2.5% glutaraldehyde PBS solution (pH= 7.2) overnight at 4 °C. Then, they were dehydrated by washing in an alcohol battery (30º, 50º, 70º, 90º, 95° and 100º) at 4 ºC for 30 min per wash and air-dried.

Atomic force microscopy

AFM was conducted to obtain topographic images of the films surface using a silicon TAP 150-G probe (Budget Sensors, Bulgaria) with a frequency of 150 kHz and a force constant of 5 N/m. Images were obtained with a AFM Dimension microscope using a NanoScope IV controller under ambient conditions in tapping mode. The row scanning frequency was set between 0.6 and 0.8 Hz. The Root Mean Square roughness (RMS R_q), which is the average height deviation taken from the mean data plane, was determined using the statistical application of the NanoScope Analysis software (Veeco, version 1.20).

Similarly to the procedure adopted during the profilometry technique, a scratch was intentionally made throughout the surface of the polymer. After scratching, a topographic image was then obtained in tapping mode, and used to determine the film thickness from the depth of the scratch.

Electrochemical properties

The electroactivity (charge storage ability) and electrostability (loss of electroactivity with consecutive oxidation-reduction cycles) of PTh_3 and P(AzbT-*co*-Th_3) films were determined by cyclic voltammetry (CV) assays. Ten consecutive oxidation-reduction cycles were conducted in acetonitrile containing 0.1 M of TBATFB from 0.0 to 1.2 V at scan rates of 25, 50 and 100 mV/s. The electrostability (LEA, %) was evaluated as:

$$LEA\ (\%) = \frac{\Delta Q}{Q_I} \times 100 \tag{10.3.1}$$

where ΔQ is the difference between the oxidation charge (in C) of the first and the last cycle, and Q_I is the oxidation charge corresponding to the first cycle.

Biological studies

MG-63 and Vero cells were cultured in DMEM high glucose supplemented with 10% FBS, penicillin (100 units/mL), and streptomycin (100 μg/mL). The cultures were maintained in a humidified incubator with an atmosphere of 5% CO_2 and 95% O_2 at 37 ºC. Culture media was changed every two days. When the cells reached 80-90% of confluence, they were detached using 1-2 mL of trypsin (0.25% trypsin/EDTA) for 5 min at 37 °C. Finally, cells were re-suspended in 5 mL of fresh medium, and their concentration was determined by counting with a Neubauer camera using 0.4% trypan blue as a vital dye.

PTh_3 and P(AzbT-*co*-Th_3) films deposited onto ITO were placed in plates of 24 wells and sterilized using UV-light for 15 min in a laminar flux cabinet. For adhesion assays, an aliquot of 50 μL containing $5x10^4$ cells was deposited onto each polymer surface. Then, cell attachment was promoted by incubating under culture conditions for 30 min. Finally, 500 μL of the culture medium were added to each well. After 24 h, non-attached cells were washed out, while attached cells were quantified. For proliferation assays, the 50 μL aliquots deposited on each well contained $2x10^4$ cells. Quantification of proliferated cells was performed after 7 days of culture. Controls were simultaneously performed by culturing cells on the surface of the tissue culture polystyrene (TCPS) plates and uncoated ITO sheets. Cytotoxicity was also determined after 24 h and 7 days of culture. All viability measures were relative to the TCPS control (*i.e.* 100%).

Viability for cytotoxicity, cellular adhesion and cellular proliferation were evaluated by the colorimetric MTT assay. This assay measures the ability of the mitochondrial dehydrogenase enzyme of viable cells to cleave the tetrazolium rings of the MTT and form formazan crystals, which are impermeable to cell membranes and, therefore, are accumulated in healthy cells. This process is detected by a color change: the characteristic pale yellow of MTT transforms into the dark-blue of formazan crystals. Specifically, 50 μL of MTT solution (5 mg/mL in PBS) were added to each well. After 3 h of incubation, samples were washed twice with PBS and stored in clean wells. In order to dissolve formazan crystals, 1 mL of DMSO/methanol/water (70/20/10% *v/v*) was added. Finally, the absorbance at 540 mm was measured using a UV-vis spectrophotomether (UV-3600, Shimadzu). The resulting viability results were normalized to TCPS control as relative percentages. Results were derived from the average of four replicates (n=4) for each independent experiment. ANOVA and Tukey's tests were performed to determine statistical significance, which was considered at a confidence level of 95% ($p < 0.05$).

Fluorescence microscopy

The protocol for the immunofluorescence staining study was as follows: MG-63 and Vero cells cultured onto materials for 7 days were fixed in 2.5% paraformaldehyde/PBS during 15 min. Then, samples were washed with PBS, and a permeabilizing buffer (0.1% Triton X-100 in 1% BSA/PBS) was added for 5 min. Next, samples were incubated for 5 min in 1% BSA/PBS and washed with 0.1% BSA/PBS for other 5 min. After this, Phalloidin-Atto 488 (Sigma-Aldrich) was sequentially added for 1 hour. Then, samples were washed twice in 0.1% BSA/PBS for 5 min, and Hoechst 33342 (1:2000 in 0.1% BSA/PBS) (Sigma-Aldrich) was added for 10 min to stain the nucleus of the cells Samples were washed one more time before air-drying for 24 h. After that period of time, samples were ready for epifluorescence microscopy observations. The entire fluorescent staining protocol was performed at room temperature. Fluorescence microscope (BA410 Model, Motic Spain S.L.) was used to examine the fluorescently-labelled cells onto the material substrates. Hoechst and Phalloidin images were acquired sequentially using an excitation/emission filters of 350/460 nm and 480/535 nm, respectively. The final analysis of the images was performed using the Image-J software.

10.4. Results and Discussion

10.4.1. Synthesis and Characterization of AzbT Monomer

In the literature, both 2-thiophene carboxaldehyde and 3,5-diaminobenzoic acid have been used to synthesize different Schiff bases in conjunction with naturally occurring aminoacids,[52] 2-aminobenzoic acid,[53] or several aromatic monoaldehydes.[54-56] These compounds show interesting properties like antibacterial,[53,54] or anticancer activity,[55] and can also act as useful regents for poisonous metal ions depollution.[56] Moreover, due to the presence of three functional groups in its structure, 3,5-diaminobenzoic acid has been employed in the synthesis of polyamides,[57] polyimides[58] and polyazometines[59] with carboxylic pendant groups. Therefore, inspired by these previous results, we combined 2-thiophene carboxaldehyde and 3,5-diaminobenzoic into a new structure (Scheme 10.2.1) that, to the best of our knowledge, has not been reported to date.

FTIR and ^{1}H-NMR spectroscopy were complementarily used to confirm the chemical structure of the new-formed AzbT monomer.

Figure 10.4.1, which compares the FTIR spectrum of the synthesized monomer with that of 3,5-diaminobenzoic acid confirms the presence of the thienyl rings in the AzbT monomer by the following characteristic peaks: 3097 cm^{-1} (aromatic α-CH stretching); 3073 cm^{-1} (aromatic β-CH stretching); 1450 cm^{-1} (symmetric C=C stretching vibration); 836 cm^{-1} (ring β(C-H) out-of-plane bending vibration); 762 cm^{-1} (out-of-plane α(C-H) ring deformation); 710 cm^{-1} (ν C–S); 572 cm^{-1} (γ ring deformation); and 473 cm^{-1} (C–S–C ring deformation). Moreover, absorption peaks attributed to the vibration of NH_2 functional groups, which are present in the IR spectrum of starting 3,5-diaminobenzoic acid, disappear in the spectrum of the AzbT monomer. Specifically, these peaks are observed at 3339 cm^{-1} (asymmetric ν N–H), 3216 cm^{-1} (symmetric ν N–H) and 1352 cm^{-1}(ν C–N). For the new-formed azomethine bond, a shoulder at 1638 cm^{-1} is discernible. A shallow peak centred at 1910 cm^{-1} appeared in the spectrum of AzbT that could be attributable to the 1,3,5-trisubstituted benezene ring.[60] In addition, the C=O stretching vibration of the carboxylic function characteristic of dimerized benzoic acids appears at 1689 cm^{-1} in both spectra.

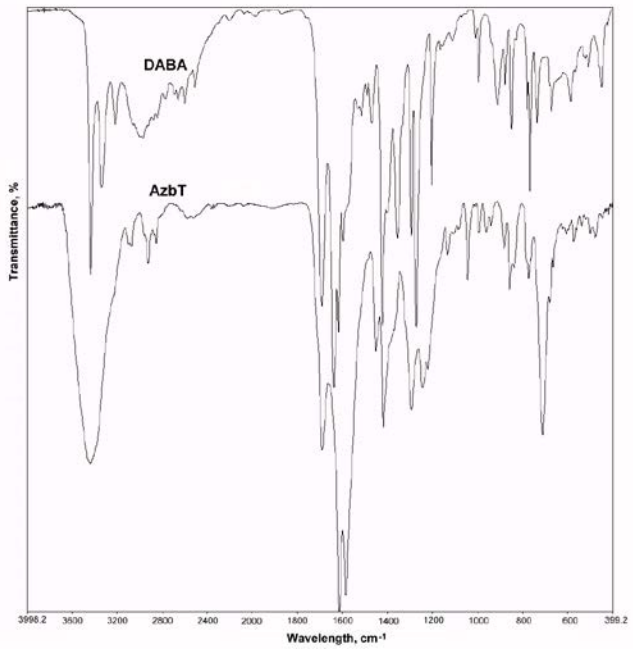

Figure 10.4.1. FTIR spectra of azomethine-containing bis-thienyl (AzbT) monomer and 3,5-diamonobenzoic acid (DABA).

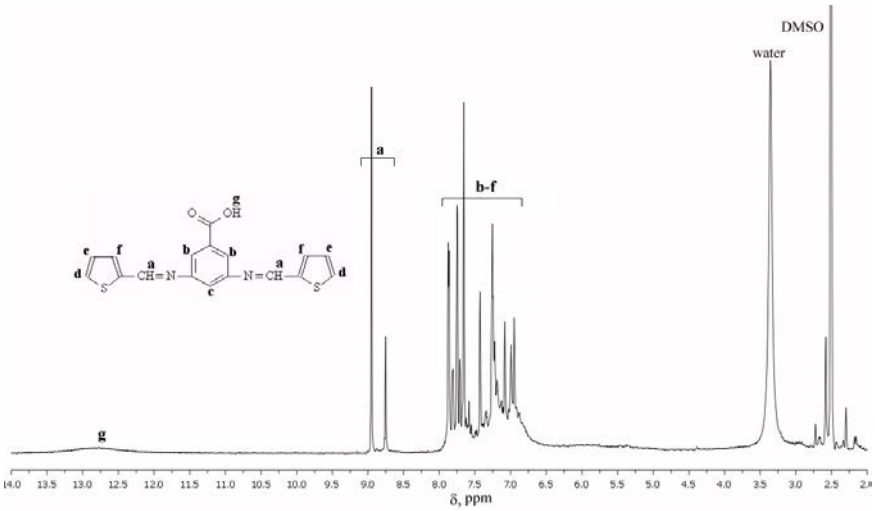

Figure 10.4.2. ^{1}H-NMR spectrum of azomethine-containing bis-thienyl monomer (AzbT).

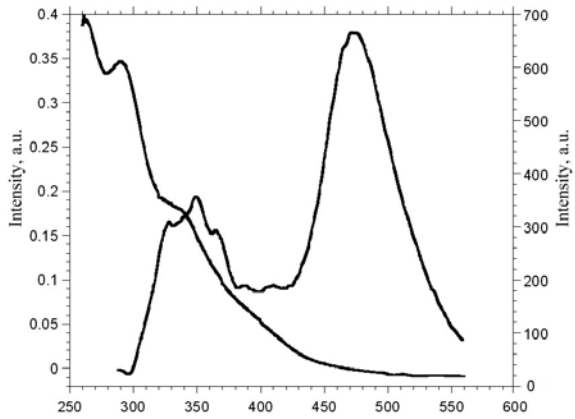

Figure 10.4.3. UV-vis absorption (left) and fluorescence (right; λ_{ex} = 298 nm) spectra of azomethine-containing bis-thienyl monomer (AzbT).

Finally, the presence of the thiophene (Th) rings as well as of the trisubstituted benzene ring in the synthesized monomer was also confirmed by the multiplet in the interval comprised between 6.8 and 7.8 ppm of the ^{1}H-NMR spectrum (Figure 10.4.2). The two singlets at 8.75 ppm and at 8.9 ppm have been assigned to the *syn*- and *anti*-isomers of the azomethine group.[61,62]

UV-vis absorption and fluorescence emission (λ_{ex}= 298 nm) spectra of the new monomer dissolved in DMSO are presented in Figure 10.4.3. The UV-vis spectrum shows one sharp absorption maximum centered at 289 nm and a shallow one centered at 340 nm. The first peak has been assigned to the π-π^* transition in the tri-substituted benzene ring, while the second one has been attributed to the π-π^* transition of the conjugated sequence formed between the thienyl moieties and the benzene ring, which are connected by the –C=N–bond. On the other hand, AzbT emits in both violet and blue regions with peaks at 360 nm and 490 nm, respectively

10.4.2. Synthesis of Random Copolymers P(AzbT-*co*-Th$_3$)s

P(AzbT-*co*-Th$_3$)s and PTh$_3$ films were prepared by chronoamperometry (CA) using acetonitrile and tetrabutylammonium tetrafluoroborate (TBATFB) as solvent and dopant agent, respectively. Even though a number of different experimental conditions were tested for the electropolymerization of AzbT alone (*i.e.* varying the solvent, electrolyte, electrode and/or potential), no polymer was obtained. For this behaviour of AzbT in the given conditions several explanations could be possible. The first one is related to the presence of carboxyl as electron-withdrawing group and, the second, the conjugated short chain-like structure that could hinder electrochemical polymerization by a high oxidation potential.

Thus, radicals derived from monomers of high oxidation potentials undergo rapid reactions with the solvent or anions to form soluble products rather than to electropolymerize.[63] Moreover, the anodic polymerization of thiophenes with reactive functional groups (*e.g.* -NH$_2$, -OH and –COOH) has been reported to be difficult due to their substantial nucleophilicity, which allows the functional groups to attack on the radical cations formed during electropolymerization, hence inhibiting the polymerization process.[64]

On the other hand, in acetonitrile–TBATFB mixture, during the electropolymerization process, a protonation of this medium could take place most probably by ionic dissociation of the carboxyl group.[65] In our case, the ionization process could be favoured and enhanced by the presence in the medium of TBATFB. Into an organic medium of higher acidity, the azomethine linkages can

undergo a dynamical exchange that possibly could compete with the polymerization reaction.[29]

In order to overcome this limitation, Th_3 was added to the polymerization medium, the presence of which allowed the incorporation of AzbT structural units in the main chain of the copolymers, a strategy already known as a successful one for the obtainment of polymeric materials with functional, reactive groups.[64]

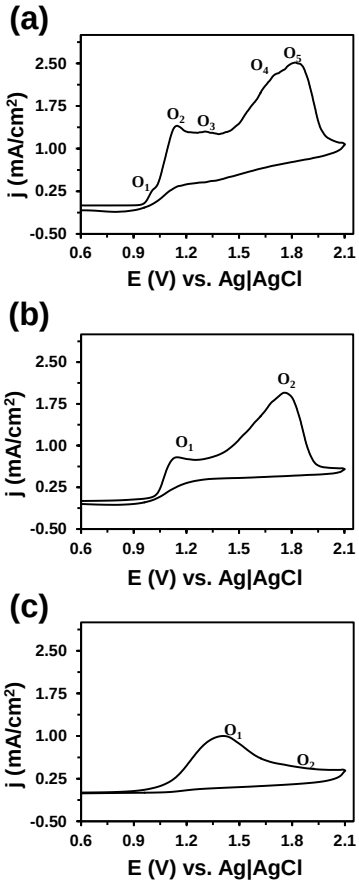

Figure 10.4.4. Control voltammograms for the oxidation of (a) Th_3, (b) 50:50 AzbT:Th_3 and (c) 80:20 AzbT:Th_3 in acetonitrile containing 0.1 M TBATFB. Voltammograms were recorded using 1.0×0.5 cm^2 ITO substrates as working electrodes. Initial and final potentials: 0.6 V; reversal potential: 2.1 V. Scan rate: 50 mV/s. The anodic processes (O) are indicated for each case.

Figure 10.4.4 shows the cyclic voltammograms recorded for the anodic oxidation of Th_3 solution and for solutions of AzbT:Th_3 mixtures (molar ratios 50:50 and 80:20) in acetonitrile in the presence of 0.1 M TBATFB. Five anodic processes with anodic peak potentials at 1.01 (O_1), 1.14 (O_2), 1.31 (O_3), 1.70 (O_4) and 1.82 V (O_5) are detected in the voltammogram of the Th_3 solution, whereas two anodic processes appear at 1.15 / 1.40 (O_1) and 1.76 / 1.82 V (O_2) in the voltammograms of the 50:50/80:20 AzbT:Th_3 solutions. The cyclic voltammogram obtained from the 60:40 AzbT:Th_3 solution was practically identical to that of the 50:50 mixture. According to these results, a potential of 1.00 V was considered for the anodic generation of PTh_3 film.

The polymerization potential for film generation of P(AzbT-*co*-Th_3)s was established at 1.05 V when AzbT:Th_3 molar ratios were 50:50 and 60:40, while 1.15 V was appropriate for film generation at 80:20 molar ratio. These polymerization potentials, which are very close to the oxidation potential O_1 discussed above (Figure 10.4.4), allowed us to (1) maximize the velocity of polymerization process and (2) avoid the undesirable over-oxidation of the electrogenerated materials, which were deposited onto ITO electrodes. The polymerization time used to prepare the PTh_3 and the three P(AzbT-*co*-Th_3) copolymer films was set at θ =150 and 180 s, respectively. These values for the polymerization time were found to be the most appropriate to obtain high quality films without compromising the optical properties of the resulting systems.

Table 10.4.1. Optical properties of PTh_3 and P(AzbT-*co*-Th_3) copolymers electropolymerized during θ = 50, 100, 200 and 400 seconds obtained from UV-vis spectra displayed in Figure 10.4.5: onset wavelength (λ_{onset}, in nm) and lowest π-π^* transition energy (E_g, in eV).

θ (seconds)	PTh_3		P(AzbT-*co*-Th_3)					
			50:50		60:40		80:20	
	λ_{onset}	E_g	λ_{onset}	E_g	λ_{onset}	E_g	λ_{onset}	E_g
50	685	1.81	803	1.54	667	1.86	685	1.81
100	914	1.36	678	1.83	632	1.96	637	1.95
200	764	1.62	673	1.84	690	1.80	635	1.95
400	892	1.39	697	1.78	648	1.91	654	1.90

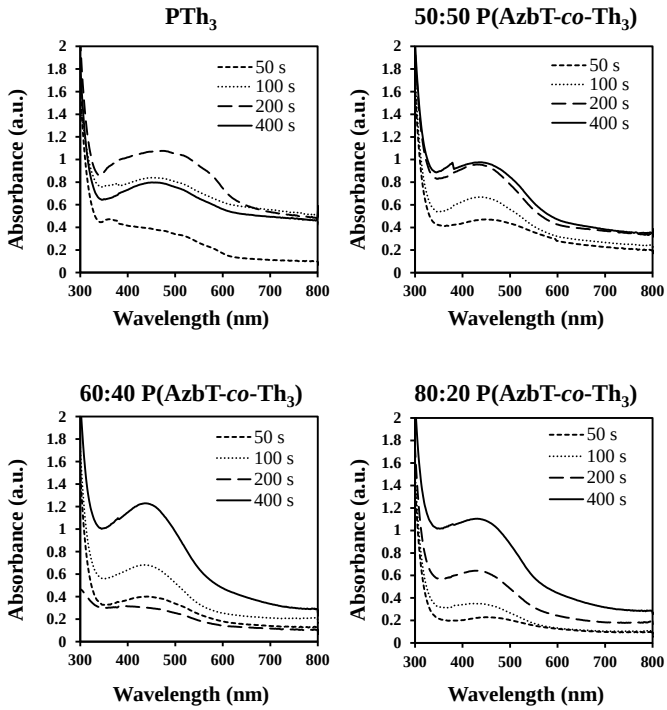

Figure 10.4.5. UV-vis spectra of PTh_3 and P(AzbT-*co*-Th_3) films prepared using polymerization times of 50, 100, 200 and 400 seconds at their corresponding polymerization potential.

By analyzing Figure 10.4.5, which compares the UV-vis spectra of copolymers film obtained for different polymerization times (θ = 50, 100, 200 and 400 s) and at their corresponding polymerization potential (*i.e.* 1.0, 1.05 or 1.15 V, depending on the composition), it can be concluded that the estimated optical lowest π-π^* transition energy (E_g) values (Table 10.4.1) for P(AzbT-*co*-Th_3) copolymers do not vary considerable with the polymerization time.

On the contrary, E_g values for PTh_3 films fluctuate, this phenomenon being an indication that the polymerization time affects the π-conjugation length of the polymeric chains in a greater extent for this system. However, P(AzbT-*co*-Th_3) and PTh_3 films obtained using $\theta \geq 300$ s were extremely fragile and peeled off easily from the ITO electrodes in comparison with those produced using θ comprised between 150 and 200 s.

10.4.3. XPS Spectroscopy

The films surface composition of P(AzbT-*co*-Th_3) copolymers was evaluated by XPS spectroscopy in an attempt to assess the proportion of the AzbT structural units in the copolymers. Spectra in the B 1s and F 1s regions (not shown) for PTh_3 and the three compositions of P(AzbT-*co*-Th_3) films show a sharp peak at 193.8 - 194.3 eV and 685.8 - 686.2 eV, respectively, which correspond to the B–F bonds of the dopant agent.[66,67] Table 10.4.2 summarizes the atomic percent composition of PTh_3 and the three copolymers as resulted by XPS. The B/S ratios obtained using such atomic percent compositions were directly associated to the doping level (DL in Table 10.4.3), which corresponds to the number of positive charges per thiophene ring. The doping level is relatively high for PTh_3, DL= 0.71, indicating that the formula of the oxidized polymer produced by CA is: $\{[(Th^{0.71+})_3]_n\ (BF_4^-)_{0.71\cdot 3n}\}_{solid}$. However, the doping level decreases drastically upon the incorporation of AzbT in the polymerization medium, as it is revealed by the very low value of DL (0.19) obtained for the 50:50 copolymer. This effect is accompanied by a reduction in the charge consumed during the polymerization process (Q_{pol} in Table 10.4.3). Thus, the value of Q_{pol} determined for PTh_3, which was directly obtained from the chronoamperogram recorded during the polymerization process, decreases by ~25% for 50:50 AzbT:Th_3 composition. Results obtained for the copolymer prepared using 60:40 AzbT:Th_3 composition were fully coherent with the previous observations, as it is reflected in Table 10.4.3.

Table 10.4.2. Atomic percent composition (B 1s, C 1s, N 1s, O 1s, F 1s and S 2p) of PTh_3 and P(AzbT-*co*-Th_3) copolymers based on XPS and copolymers composition obtained from FTIR spectroscopy.

	B 1s	**C 1s**	**N 1s**	**O 1s**	**F 1s**	**S 2p**	**AzbT:Th_3 (%)[a]**
PTh_3	3.8	66.7	3.7	3.8	16.6	5.4	-
50:50 P(AzbT-*co*-Th_3)	1.3	69.6	1.4	14.0	6.8	6.8	16/84
60:40 P(AzbT-*co*-Th_3)	1.2	73.3	1.6	3.2	6.6	14.3	59/41
80:20 P(AzbT-*co*-Th_3)	2.2	64.4	5.1	14.9	9.7	3.7	61/39

[a]Copolymer composition based on FTIR spectroscopy.

These phenomena could take place based on the following two possible scenarios. First, AzbT hinders the electropolymerization of Th_3 promoting the formation of a closed cross-linked structure in which the presence of long linear Th-chains seems to be unfavourable (*i.e.* α-β and β-β linkages are formed between the

Th rings rather than α-α linkages). Consequently, the penetration of the dopant agent (BF_4^-) into such structure is hampered, thus explaining the low doping level. Second, the ionized form of the AzbT (*i.e.* AzbT-COO$^-$) present in the medium could work as a doping agent in competition with BF_4^-. Moreover, while BF_4^- doping is a conventional diffusion-controlled slow process, "*rapid doping*" could be achieved by the release of protons from the ionizable carboxyl function of AzbT, resulting in so-called "*self- or autodoping polymers*".[64] As a result, all of these trends, could have induced the experimentally observed decrease in the DL value.

Table 10.4.3. Properties of PTh_3 and P(AzbT-*co*-Th_3) copolymers: Doping level (DL, in number of positive charges per Th ring), polymerization charge (Q_{pol}, in mC/cm^2), thickness determined by profilometry and AFM inspection of scratched regions (ℓ_{prof} and ℓ_{AFM}, in nm), respectively), Root Mean Square roughness (RMS R_q, in nm) and lowest π-π* transition energy (E_g, in eV).

	DL	**Q_{pol}**	**ℓ_{profil}**	**ℓ_{AFM}**	**RMS R_q**	**E_g**
PTh_3	0.71	54.3 ± 8.1	2.26 ± 0.37 μm	-	380 ± 67	1.64
50:50 P(AzbT-*co*-Th_3)	0.19	40.4 ± 10.9	415 ± 78 nm	254 ± 16	111 ± 10	1.83
60:40 P(AzbT-*co*-Th_3)	0.08	38.4 ± 5.7	388 ± 86 nm	291 ± 23	78 ± 8	1.94
80:20 P(AzbT-*co*-Th_3)	0.59	49.4 ± 10.3	451 ± 91 nm	253 ± 53	60 ± 11	2.03

The above described situation is changing when the AzbT:Th_3 is increased. Thus, the DL in relation with BF_4^- increases noticeably for the 80:20 copolymer (DL=0.59). Consistently, the Q_{pol} is only ~9% lower than that of PTh_3 (Table 10.4.3). These features suggest that, although AzbT seems to preclude the incorporation of Th_3 monomers, the molar ratio of the latter in the polymerization medium is low enough to reduce significantly the formation of cross-links with respect to 50:50 P(AzbT-*co*-Th_3). This results in an opened structure that facilitates the incorporation of dopant anions and the oxidation of polyaromatic fragments.

On the other hand, if the existence and presence of AzbT-COO$^-$ in the reaction medium are accepted in equilibrium with unionized AzbT, experimental results can also be interpreted in another way: the amount of the more reactive Th_3 in the mixture affects and shifts the equilibrium between the two forms of AzbT. Hence, it

seems that a higher AzbT:Th_3 molar ratio would shift the equilibrium towards AzbT polymerization into a linear chain, while a higher amount of Th_3 in the reaction medium displaces this equilibrium toward the AzbT-COO^- form. As previously assumed, this ionized form could work as a better dopant than BF_4^- for the PTh_3 growing chains that are developing faster due to the higher reactivity of Th_3.

For PTh_3, the C/S and B/F ratios, 4.6 and 0.23, respectively, are very close to those theoretically expected (*i.e.* 4.0 and 0.25, respectively). The detection of oxygen in this homopolymer, with a C/O ratio of 17.5, was attributed to the oxidation of some Th rings, which also explains the small difference between the observed and theoretical C/S ratios. In the case of the 50:50 copolymer, the B/F ratio (0.19) and C/O ratio (5.0) are smaller than expected, while the N/B ratio (1.1) is not consistent with the incorporation of AzbT units into the copolymer chains. The same trends were founded from the calculated B/F, N/B and C/O ratios for the 60:40 copolymer (Table 10.4.2). These experimental data confirm the previous supposition about the multiple processes that can take place in the polymerization mixture of the above-mentioned copolymers. Generally, when a film is forming from solution the moieties with the lower surface energy are naturally migrating toward the upper layers of it. In our particular case, the use of acetonitrile (polar and hydrophilic) as solvent could favour the migration toward these upper layers of the more hydrophilic and polar groups such as COOH groups. When considering 50:50 and 60:40 polymerization mediums, if AzbT works as dopant, rather than as comonomer, most of it will remain attached by electrostatic forces to the more hydrophobic PTh_3 chains in the deep layers of the film, fact that could explain the low values of N/B and C/O calculated ratios for these copolymers.

Finally, 80:20 P(AzbT-*co*-Th_3) presents a N/B ratio of 2.3, which reflects the incorporation of AzbT units into the copolymer chains. This feature is consistent with the C/N and C/O ratios (12.6 and 4.3, respectively), which indicates that the sources of N and O on the surface films are not only the BF_4^- dopant and the oxidation of Th rings, respectively, but also the incorporation of AzbT units.

Figure 10.4.6 depicts the characteristic XPS spectra in the C 1s, O 1s and N 1s regions for PTh_3 and both 50:50 and 80:20 P(AzbT-*co*-Th_3). Deconvolution of the C 1s peak led to two or three Gaussian curves, depending on the sample. The component at ~284.5 eV, which is present in all samples, corresponds to the C–C/C=C (284.8 eV) linkages of the Th_3 and AzbT units.[68-70] The spectra recorded for PTh_3 and 50:50 P(AzbT-*co*-Th_3) (also for the 60:40 copolymer, Figure 10.4.7) show a component centered at ~286.4 eV, which has been attributed to the C–S bond of polarized Th rings.[68-71] This component is apparently absent in the 80:20 copolymer.

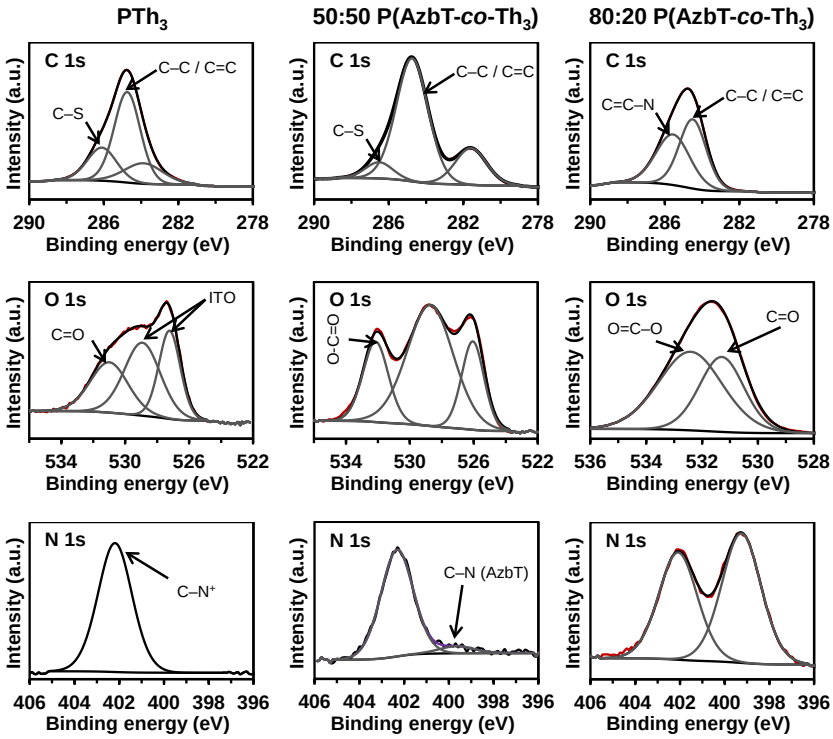

Figure 10.4.6. High-resolution XPS spectra (black line) for PTh_3 and both 50:50 and 80:20 P(AzbT-*co*-Th_3): C 1s (top), O 1s (middle) and N 1s (bottom) regions. Peaks from deconvolution (grey lines) are also displayed.

Furthermore, the latter is the only composition that presents the component associated to the aromatic C=C–N groups from the AzbT units at 285.6 eV.[72] These features are fully consistent with the assumptions derived from the atomic compositions, according to which the amount of AzbT units in the 50:50 and 60:40 copolymers is very low, while AzbT is the main constituent of the 80:20 copolymer. The assignment of the components detected at 283.9 and 281.6 eV for PTh_3 and 50:50 P(AzbT-*co*-Th_3), respectively, is not so clear, even though they probably belong to the tetrabutylammonium cations and the substrate. The values of N/B ratios corroborated with the uniqueness of C–S bond of polarized Th rings in 50:50 and 60:40 copolymers and that of aromatic C=C–N groups in 80:20 copolymer sustain the supposition that AzbT could work not only as a comonomer, but as the dopant as well.

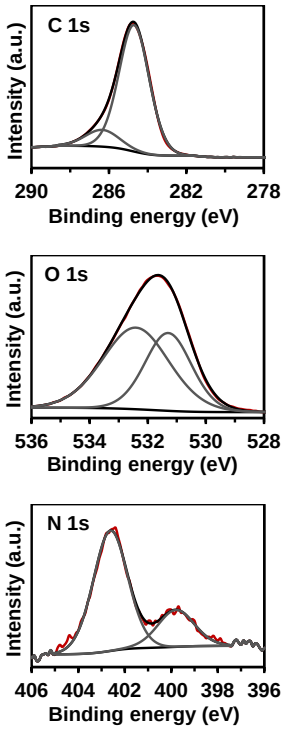

Figure 10.4.7. High-resolution XPS spectra (black line) for the 60:40 P(AzbT-*co*-Th_3) copolymer: C 1s (top), O 1s (middle) and N 1s (bottom) regions. Peaks from deconvolution (in grey) are also displayed.

Deconvolution of the O 1s peak obtained from PTh_3 (Figure 10.4.6) led to three Gaussian curves that have been attributed to the C=O arising from the oxidation of the Th rings (531.0 eV) and the inorganic oxides of the ITO electrode (528.9 and 527.2 eV).[73-75] For the 50:50 copolymer, the component of highest energy changes to 532.1 eV, and has been associated to the O=C–O bonding,[45,76,77] while the other two components correspond to the oxides of ITO electrodes. The spectrum of the 80:20 copolymer shows two components centered at 532.4 and 531.3 eV that correspond to O=C–O and C=O bonds, respectively. The high resolution XPS spectrum of the S 2p region for PTh_3 and all P(AzbT-*co*-Th_3) compositions (Figure 10.4.8) is very similar to that recently reported for different PTh derivatives.[45,69,78] The main observations refer to the spin-split sulphur coupling, S $2p_{3/2}$ (163.6 - 163.9 eV) and S $2p_{1/2}$ (164.8 - 165.1eV), with a separation of 1.2 eV, and to the relatively high energy broad tail produced by positively charged sulphur within the Th rings.

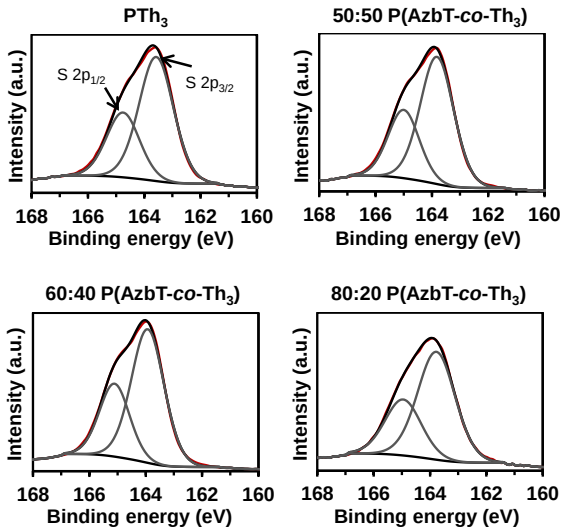

Figure 10.4.8. High-resolution XPS spectra in the S 2p region for PTh_3 and the three different P(AzbT-*co*-Th_3) compositions.

Finally, the high resolution N 1s spectrum of PTh_3 in Figure 10.4.6 shows a single peak centred at 402.2 eV, which has been attributed to the C–N^+ bond of tetrabutylammonium counterions.[79] The N 1s spectra recorded for the three P(AzbT-*co*-Th_3) compositions present two peaks centered at 402.1 - 402.6 and 399.3 - 399.8 eV. The former corresponds to the tetrabutylammonium counter-ion,[79] as it was identified for PTh_3, while the latter has been assigned to the C–N bond of AzbT units.[80] Although the amount of AzbT units is relatively low in the 50:50 and 60:40 copolymers (atomic percent composition of N associated to AzbT units: 0.1% and 0.4%, respectively), it is significantly higher for the 80:20 copolymer (2.8%).

The overall of the XPS analyses reveals some difficulties in determining the composition of the copolymer chains obtained using 50:50, 60:40 and 80:20 AzbT:Th_3 ratios in the generation medium. However, the morphologies and topographies of the three prepared copolymers are not only completely different when compared among them, but also with regard to those of PTh_3 (see next sub-section), which is consistent with different chemical compositions. On the basis of these results, we have concluded that the content of AzbT units in P(AzbT-*co*-Th_3) increases with the concentration of the corresponding monomer in the generation medium, as it is clearly evidenced by the N 1s XPS spectra.

10.4.4. FTIR Spectroscopy

Another attempt for assessing the composition of the synthesized copolymers was done by using FTIR spectroscopy. Unlike XPS spectroscopy, which is a surface sensitive quantitative technique, FTIR measurement is a "through the sample" technique. By analysing all the spectra displayed Figure 10.4.9, it can be noticed that they are approximately similar in their shape in the range from 400 to 1280 cm^{-1}. The most evident peaks in this range appeared as follows: the peak at around 568 cm^{-1} attributable to γ thiophene ring vibration[60]; that at 695 $cm^{-1} \pm 4$ cm^{-1} due to C–S–C ring deformation; and the peak at 793 cm^{-1} due to CH out-of-plane bending vibration (δ C–H) of 2,5-substituted thiophene rings.[81,82] A strong doublet-like band centred at 1260 cm^{-1} and at 1050 ± 10 cm^{-1} is also present in this range, which could be due to the β C–H bending in doped PTh chains.[81]

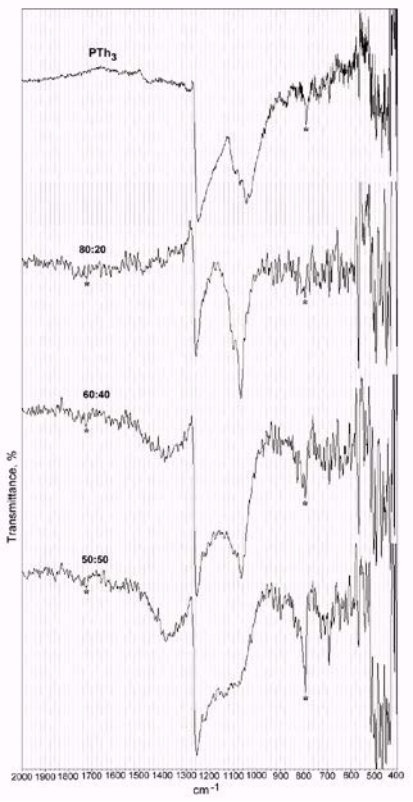

Figure 10.4.9. FTIR spectra of PTh_3 and 50:50, 60:40 and 80:20 P(AzbT-*co*-Th_3) copolymers.

An absorption band centered at 1660 $cm^{-1} \pm 20$ cm^{-1} can be seen in the spectra of all the investigated materials due to the conjugation between the thiophene rings along the polymer chains.

Unlike PTh_3, P(AzbT-*co*-Th_3)s present in the range 1650-1800 cm^{-1} a discernible peak centred at approximately 1730 cm^{-1} that was attributed to the vibration of carbonyl (ν C=O) in carboxyl groups, which is shifted by 40 cm^{-1} toward higher wavenumbers when compared to that observed in the FTIR spectrum of AzbT monomer, in a similar manner as observed before.[83] It should be noted that between this position and 1800 cm^{-1}, in all spectra, there are several peaks that could be due to the presence of other carbonyl moieties, as it was already revealed by XPS analysis. There are several plausible explanations that would motivate the presence of these peaks in the spectra: *(i)* Despite all the precautions taken during the experiments, traces of moisture could be present in AzbT structural units due to its inherent molecular association with carboxyl groups.[84] Thus, several works have shown that the presence of water traces results in the incorporation of carbonyl groups in the polymer chains when they are obtained by electropolymerization;[63] *(ii)* During the handling of the sample, a photo-oxidation process could occur. There are several possible mechanisms that could lead to the formation of carbonyl groups within a PTh backbone due to photo-oxidation,[85] but formation of carboxylic acids was ruled out by Holdcroft,[86] and recently it was reiterated for unsubstituted PTh.[87]

Based on the IR spectra presented in Figure 10.4.9, the copolymers composition was calculated by using the ratio of the integrated area of the peak at 1730 cm^{-1} (belonging only to the AzbT comonomer) and the integrated area of the peak at 793 cm^{-1} (belonging to both comonomers). The obtained results are presented in Table 10.4.2. The use for this calculation of one of the characteristic absorption peaks from the 1,3,5-trisubstituted benzene ring was hindered by the overlapping of its characteristic bands with those arising from the thiophene ring.

From the results showed in Table 10.4.2, it can be concluded that the results of XPS analysis correlate well with those from IR investigation, reflecting that the highest amount of the AzbT comonomer is present in the 80:20 copolymer. Furthermore, the AzbT:Th_3 ratio values obtained from IR spectra are almost the same for the 60:40 and 80:20 copolymers. Unfortunately, from IR analysis, it was not possible to further discriminate between enchained AzbT units and AzbT-COO^- present in copolymers as dopant, due to the fact that the asymmetrical and symmetrical carbonyl stretching vibration in the ionized COO^- at approximately 1550 and 1425 cm^{-1},[84] respectively, merged with those of asymmetric and

symmetric stretching vibrations of the thiophene ring. However, taking into account the XPS results and also the difference in shape of IR spectra it could be claimed that the highest amount of the enchained AzbT units are found in 80:20 copolymer.

10.4.5. Thickness, Morphology and Topography

Micrometric PTh_3 films were obtained using a polymerization time of 150 s. The incorporation of AzbT monomer into the generation medium resulted in a drastic reduction in the thickness of the electropolymerized films. Thus, the thickness of all P(AzbT-*co*-Th_3) copolymers determined by profilometry was around ~400 nm (Table 10.4.3). In addition to that, scratched regions were further scanned by AFM. Although the thicknesses determined by analyzing the recorded AFM images (Figure 10.4.10) were in good agreement with the profilometry estimations, the values determined using the former technique were ~100 - 200 nm lower. These results are fully consistent with our previously discussed interpretations according to which the presence of AzbT obstructs the polymerization of Th_3 units and favours the formation of compact cross-linked structures.

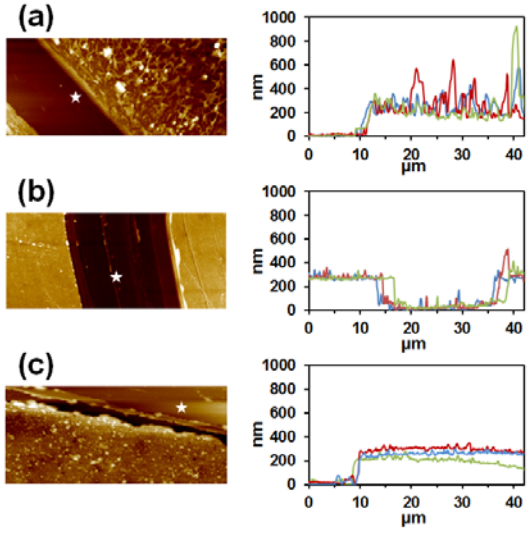

Figure 10.4.10. AFM steps of (a) 50:50, (b) 60:40 and (c) 80:20 P(AzbT-*co*-Th_3) copolymers. Stars indicate the ITO surface.

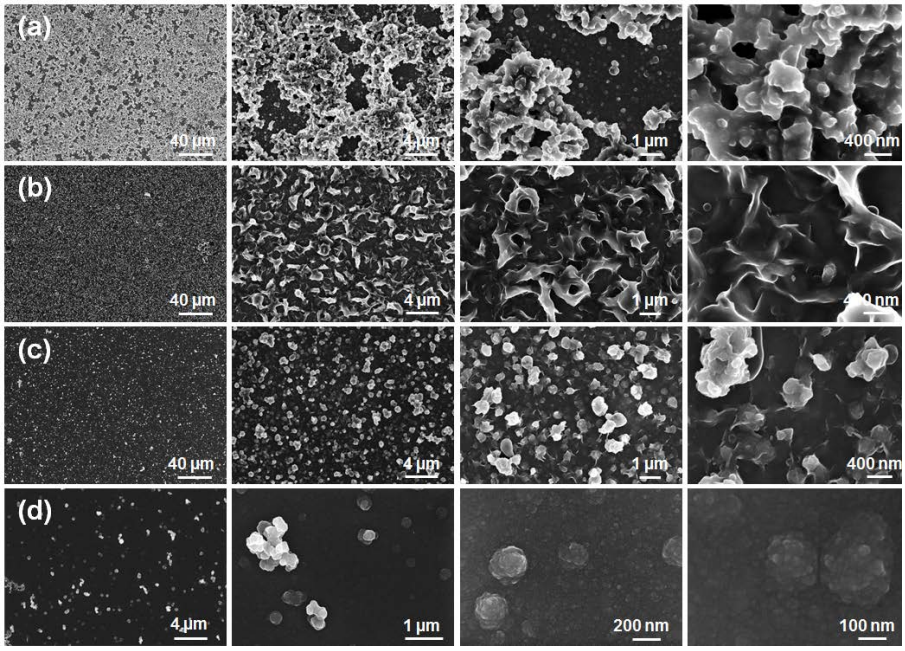

Figure 10.4.11. SEM micrographs with different magnifications for PTh_3 and P(AzbT-*co*-Th_3): (a) PTh_3, (b) 50:50 P(AzbT-*co*-Th_3), (c) 60:40 P(AzbT-*co*-Th_3) and (d) 80:20 P(AzbT-*co*-Th_3).

Figure 10.4.11 shows low, medium and high magnification SEM micrographs of all prepared materials, while AFM images are provided in Figures 10.4.12. PTh_3 presents a porous structure made of sub-micrometric sheets that aggregate at different levels. The topography derived from such multileveled surface consists on a dense distribution of abundant peaks emerging from deep and narrow valleys. This particular distribution results in a relatively rough surface with a root mean square roughness (RMS R_q) value of 380 ± 67 nm.

The presence of AzbT in the polymerization medium drastically affects the structure, as it is evidenced in Figures 10.4.11 and 10.4.12. Thus, the surface morphology and topography of P(AzbT-*co*-Th_3) copolymers vary progressively with the content of AzbT in the polymerization medium. More specifically, the porous multi-leveled morphology of 50:50 P(AzbT-*co*-Th_3) largely reminds that of PTh_3, even though the surface of the former is significantly more flat than the one of the latter. The sheets become smaller and show folds in 60:40 P(AzbT-*co*-Th_3), resulting into a more compact morphology and smooth topography. Finally, the 80:20 copolymer presents a dense globular morphology, in which the sheets completely

disappear, and are organized in a plane surface. The progressive reduction in the RMS roughness with the increasing content of AzbT in the polymerization medium is displayed in Table 10.4.3. Thus, the RMS R_q value decreases from 111 ± 10 nm to 60 ± 11 nm when the AzbT content increases in the polymerization medium.

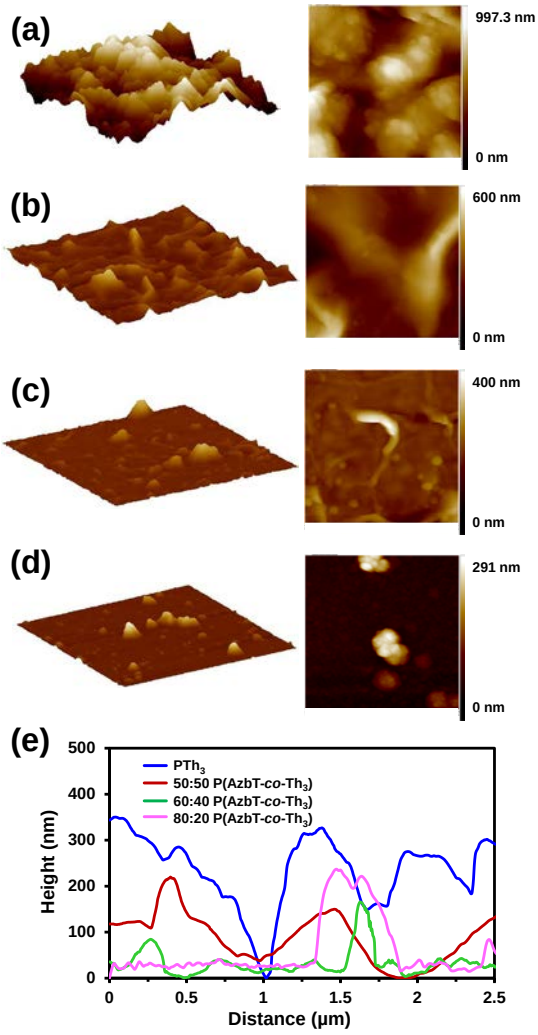

Figure 10.4.12. 3D and 2D AFM height images for: (a) PTh_3, (b) 50:50 P(AzbT-*co*-Th_3), (c) 60:40 P(AzbT-*co*-Th_3) and (d) 80:20 P(AzbT-*co*-Th_3). Left column: 10 µm × 10 µm; right column 2 µm × 2 µm. (e) Cross-section profiles of a diagonal line for 2D images (a) to (d): PTh_3 (blue), 50:50 P(AzbT-*co*-Th_3) (red), 60:40 P(AzbT-*co*-Th_3) (green) and 80:20 P(AzbT-*co*-Th_3) (pink).

10.4.6. Electrochemical and Optical Properties

Cyclic voltammetry studies were run to assess the influence of the presence of AzbT units on the electrochemical properties of P(AzbT-*co*-Th_3) films. Hence, the amount of exchanged charge reversibly (*i.e.* electroactivity) and the electrochemical stability (*i.e.* electrostability) of the electropolymerized copolymers were evaluated by submitting the samples to ten consecutive oxidation-reduction cycles in acetonitrile (0.1 M TBATFB) from 0.0 to 1.2 V at different scan rates.

Figure 10.4.13a represents the first control voltammogram of PTh_3 and P(AzbT-*co*-Th_3) copolymers recorded at a scan rate of 100 mV/s. As it can be seen, the amount of exchanged charge (*i.e.* electroactivity) decreases with increasing the AzbT content in the polymerization medium.

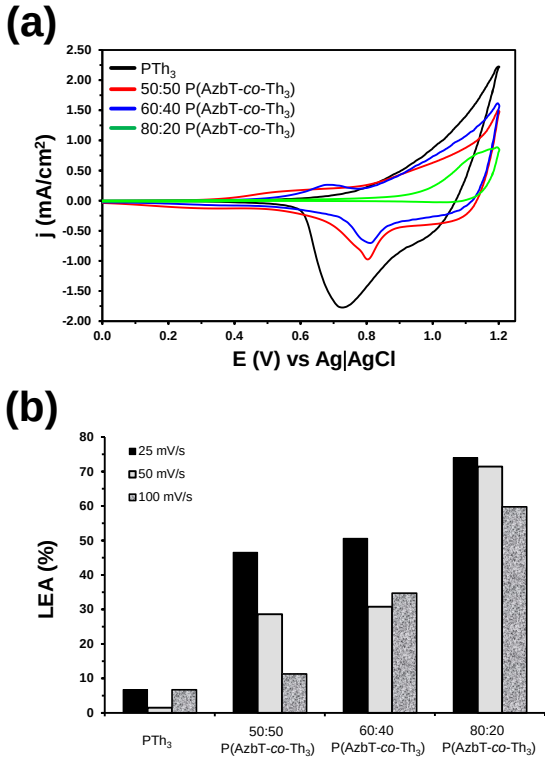

Figure 10.4.13. (a) First control voltammogram for PTh_3 (black) and P(AzbT-*co*-Th_3) 50:50 (red), 60:40 (blue) and 80:20 (green) in acetonitrile with 0.1M TBATFB. Initial and final potential: 0.0 V; reversal potential: 1.2 V. Scan rate: 100 mV/s. (b) Variation of the LEA value for PTh_3 and P(AzbT-*co*-Th_3) as a function of the scan rate.

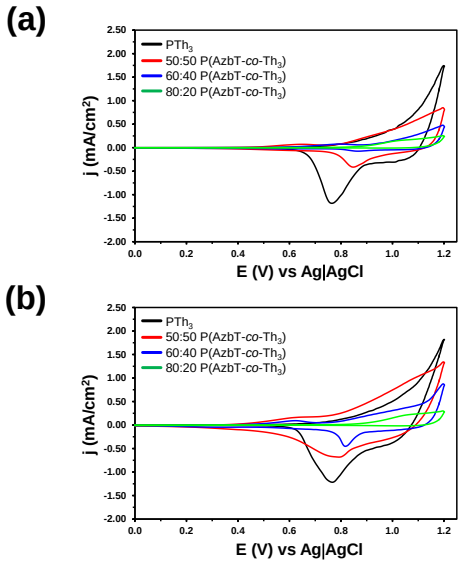

Figure 10.4.14. First control voltammograms for PTh_3 and P(AzbT-*co*-Th_3) films in acetonitrile with 0.1M TBATFB. Initial and final potential: 0.0 V; reversal potential: 1.2 V. Scan rate: (a) 25 mV/s and (b) 50 mV/s.

More specifically, the electroactivity of 50:50, 60:40 and 80:20 copolymers, which was determined by evaluating the oxidation and reduction charges from the corresponding voltammograms, is smaller than that of PTh_3 by 42%, 67% and 84%, respectively. Differences between PTh_3 and the three copolymers are independent of the scan rate, as it is evidenced in the control voltammograms recorded at 25 and 50 mV/s (Figure 10.4.14).

Although consecutive oxidation and reduction cycles provoked a reduction of electroactivity in all cases, the behaviour of the copolymers differs from that of PTh_3 in terms of electrostability. Figure 10.4.15 compares the voltammogram recorded after 10 redox processes with that of the as prepared material (scan rate 50 mV/s), while Figure 10.4.13b depicts the variation of the electrostability (LEA in equation 10.3.1) with the scan rate for PTh_3 and P(AzbT-*co*-Th_3) samples.

The LEA value is lower than 7% for PTh_3, independently of the scan rate. The electrochemical stability decreases upon the incorporation of AzbT units, thus LEA values increase systematically with the content of AzbT in the polymerization medium. On the other hand, the low electrochemical stability of 80:20 P(AzbT-*co*-Th_3) is practically independent of the scan rate, whereas low scan rates affect negatively the electrochemical behaviour of 50:50 and 60:40 copolymers.

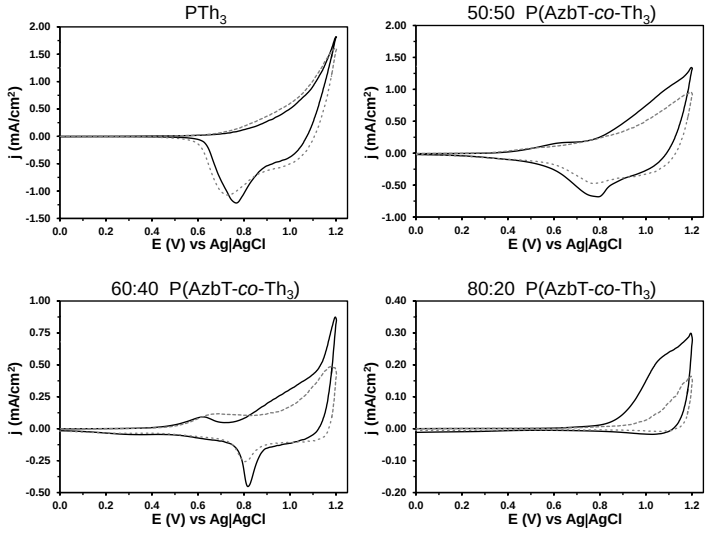

Figure 10.4.15. Voltammograms of PTh_3 and P(AzbT-*co*-Th_3) films recorded in acetonitrile with 0.1M TBATFB for the as prepared materials and after 10 consecutive oxidation-reduction cycles (1st cycle solid line; 10th cycle dashed line). Initial and final potential: 0.0 V; reversal potential: 1.2 V. Scan rate: 50 mV/s.

Figure 10.4.16a represents the UV-vis spectra recorded for PTh_3 and P(AzbT-*co*-Th_3) films prepared using the experimental conditions described in section 10.3.5. For PTh_3, the broad absorption band centered at 475 nm, which corresponds to the π-π^* transition, was used to approximate the optical lowest π-π^* transition energy (E_g=1.64 eV) by estimating the onset wavelength (λ_{onset} = 758 nm). The spectrum of the 80:20 copolymer is very similar to that of PTh_3, and also displays a broad band centered at 447 nm (λ_{onset} = 677 nm). The resulting E_g value is 1.83 eV, which is slightly higher than that obtained for PTh_3. Accordingly, the extension of the π-conjugation is lower for 80:20 P(AzbT-*co*-Th_3) than for PTh_3. However, this reduction is more notable for the 50:50 and 60:40 copolymers, which show broad absorption bands at 392 and 400 nm, respectively. The E_g estimated for 50:50 and 60:40 P(AzbT-*co*-Th_3) are 1.94 (λ_{onset} = 634 nm) and 2.03 eV (λ_{onset} = 610 nm), respectively. It should be noted that these results are in excellent agreement with the doping level calculated from XPS interpretations.

Lastly, as polyazomethine-based materials have been reported to be used in electrochromic devices,[22,23] electrochromism was also examined for P(AzbT-*co*-Th_3) materials.

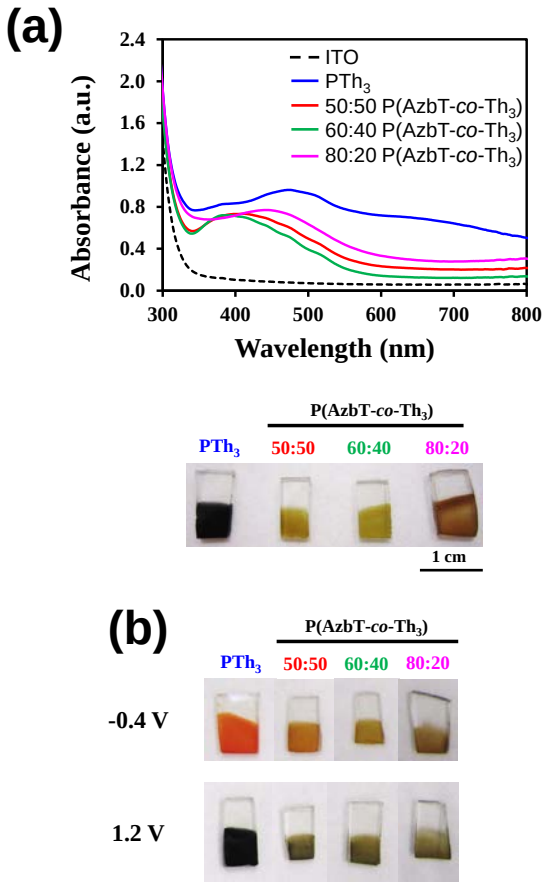

Figure 10.4.16. (a) UV-vis spectra and color of as prepared PTh_3 and P(AzbT-*co*-Th_3) films. (b) Color of PTh_3 and P(AzbT-*co*-Th_3) films after applying a potential of 1.20 and -0.40 V during 100 s (oxidized and reduced samples, respectively).

The colour of the as prepared films (Figure 10.4.16a) is dark blue for PTh_3, yellow-brownish for 50:50 and 60:40 copolymers, and earthy brown for 80:20 P(AzbT-*co*-Th_3). After being submitted to potentials of -0.40 (reduction process) and 1.20 V (oxidation process) during 100 s, PTh_3 and P(AzbT-*co*-films) exhibit a colour change (Figure 10.4.16b). As it can be seen, the dark blue colour of as prepared oxidized PTh_3 changes to bright orange upon reduction. The contrast is less marked for the three copolymers, which present brown and matt orange in the oxidized and reduced states, respectively. This feature suggests that the applicability of P(AzbT-*co*-Th_3) for the fabrication of electrochromic devices is limited if compared with PTh_3 and other PTh derivatives previously reported.[88-90]

10.4.7. Biological Studies

Biocompatibility is a requisite when designing bioactive matrices for biotechnological and biomedical applications. Consequently, the interface in contact with cells is expected to guarantee no toxic or injurious effects on biological systems. To ensure that, biological studies were firstly performed by culturing MG-63 and Vero cells (human osteosarcoma and monkey kidney epithelial cell lines, respectively) in wells that contained ITO electrodes coated with PTh_3 and P(AzbT-*co*-Th_3) films. The 60:40 copolymer was not involved in such study since, as it was evidenced in previous subsections, its properties were very similar to those exhibited by 50:50 P(AzbT-*co*-Th_3). By culturing cells in wells that contained uncoated ITO electrodes or only tissue culture polystyrene (TCPS) (*i.e.* no ITO electrode in the wells), controls were simultaneously performed.

The potential cytotoxicity of the systems was evaluated after 24 h and 7 days of culturing by using the MTT assay. All viable cells in the wells were quantified, which enabled us to consider the toxic effects associated not only to the polymeric matrix, but also to small molecules (*e.g.* acetonitrile, TBATFB, Th_3 and AzbT) or oligomers that could be eventually released from the polymeric matrix. Figure 10.4.17 indicates that PTh_3 and 50:50 copolymer reduce cell viability with respect to TCPS control after 24 h of culturing, thus exhibiting some cytotoxic effect for both MG-63 and Vero cell lines. In contrast, these negative effects are not observed for the 80:20 copolymer that shows viabilities slightly higher than those of the control. After 7 days, the cytotoxic effect of all studied systems on MG-63 cells disappears, while PTh_3 and 50:50 P(AzbT-*co*-Th_3) samples remain toxic to Vero cells.

The cytotoxicity of PTh_3 and 50:50 copolymer should be attributed to harmful molecules, especially Th_3 monomers entrapped into the polymeric matrix, which are leaching out from the films. In a recent study, we found that Th_3 reaches a maximum of cytotoxicity when the concentration is ~10^{-5} M becoming stable at higher concentrations.[47] Although such observation is fully supported with the lack of negative effects for the copolymer obtained using the lowest concentration of Th_3 in the polymerization medium (Figure 10.4.17), the cytotoxicity of the AzbT monomer cannot be completely discarded yet, and it should be specifically analysed in future studies.

Figure 10.4.18 displays quantitative results for cell adhesion and proliferation assays. In this case, cellular viability was exclusively determined onto the surface of uncoated (control) or coated ITO electrodes. General inspection of the results clearly evidence that Th_3 inhibits cell viability, which is fully consistent with the cytotoxic effect discussed above. The biocompatibility of the three examined organic

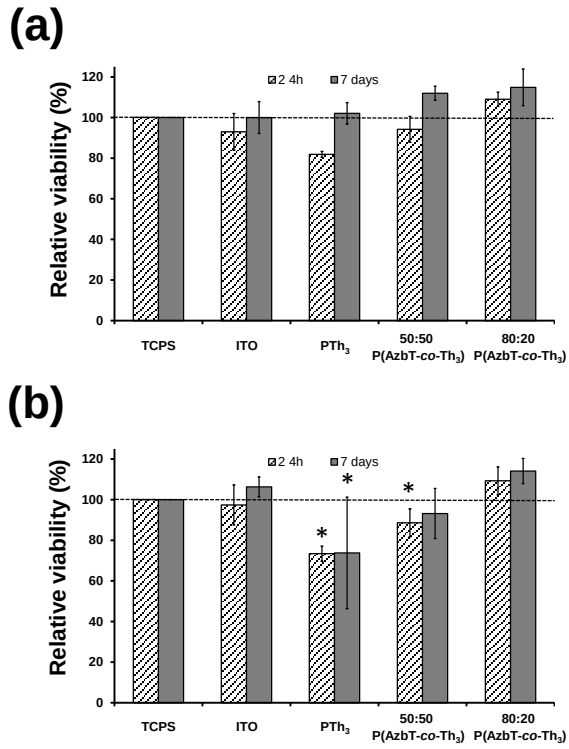

Figure 10.4.17. Cytotoxicity of PTh_3 and P(AzbT-*co*-Th_3) films after 24 h and 7 days: (a) MG-63 and (b) Vero cells. Four samples were analyzed for each group. Bars represent the standard deviation. The relative viability of MG-63 and Vero cells was established in relation to the TCPS control (tissue culture polystyrene). ITO was also considered as a control substrate because PTh_3 and P(AzbT-*co*-Th_3) were deposited onto this material. The asterisk (*) indicates a significant difference with the TCPS control, Tukey's test ($p < 0.05$).

materials clearly increases with the content of AzbT. Thus, the number of cells adhered to the surface of the 80:20 copolymer is considerably higher than that of PTh_3 and 50:50 P(AzbT-*co*-Th_3) films. Moreover, the adhesion and proliferation of MG-63 cells on the surface of 80:20 P(AzbT-*co*-Th_3) are also higher when compared to the results obtained for the control substrates (*i.e.* TCPS and uncoated ITO).

In contrast, MG-63 cells activity on 50:50 P(AzbT-*co*-Th_3) is comparable to that observed for ITO, while PTh_3 shows the worst behaviour as supportive matrix for cellular adhesion and proliferation. Regarding Vero cells, the biocompatibility of ITO, PTh_3 and 50:50 P(AzbT-*co*-Th_3) substrates is very poor, especially in terms of

cell proliferation, whereas the cell response towards the 80:20 copolymer and control TCPS substrates is comparable.

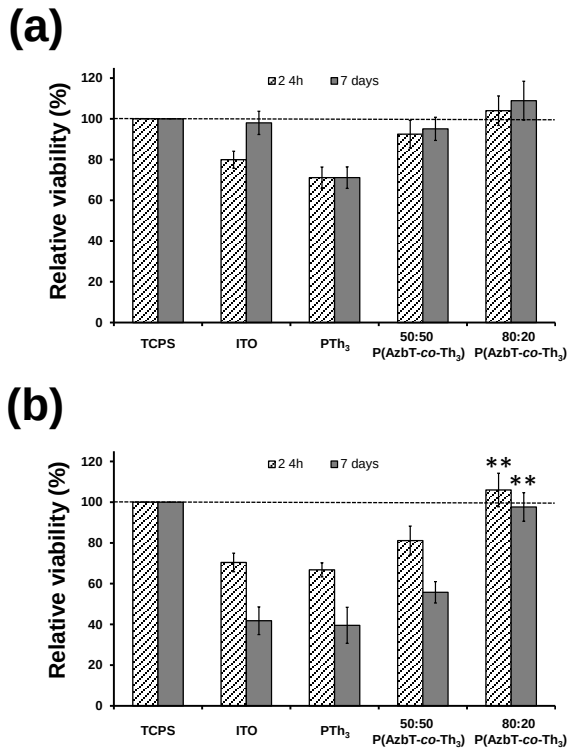

Figure 10.4.18. Relative cellular adhesion (viability onto the material after 24 h) and cellular proliferation (viability onto the material after 7 days) of PTh_3 and P(AzbT-*co*-Th_3) films: (a) MG-63 and (b) Vero cells. Four samples were analyzed for each group. Bars represent the standard deviation. The relative viability of MG-63 and Vero cells was established in relation to the TCPS control (tissue culture polystyrene). ITO was also considered as a control substrate because PTh_3 and P(AzbT-*co*-Th_3) were deposited onto this material. The double asterisk (**) indicates a significant difference with the PTh_3 result, Tukey's test ($p < 0.05$).

Furthermore, the different ability exhibited by PTh_3 and the two examined P(AzbT-*co*-Th_3) copolymers to behave as cellular matrices is clearly reflected in the fluorescence microscopy images displayed in Figure 10.4.19. The densities of MG-63 and Vero cells adhered onto the substrate after 7 days of culturing, which are relatively low for PTh_3, increase considerably for the copolymers. In addition, the spreading of cells onto the surface of PTh_3 and 50:50 P(AzbT-*co*-Th_3) matrices is relatively inhomogeneous, becoming more uniform for the 80:20 copolymer. Details about the actin organization of cultured cells onto the investigated substrates are evidenced in the high magnification fluorescence images displayed in Figure 10.4.20.

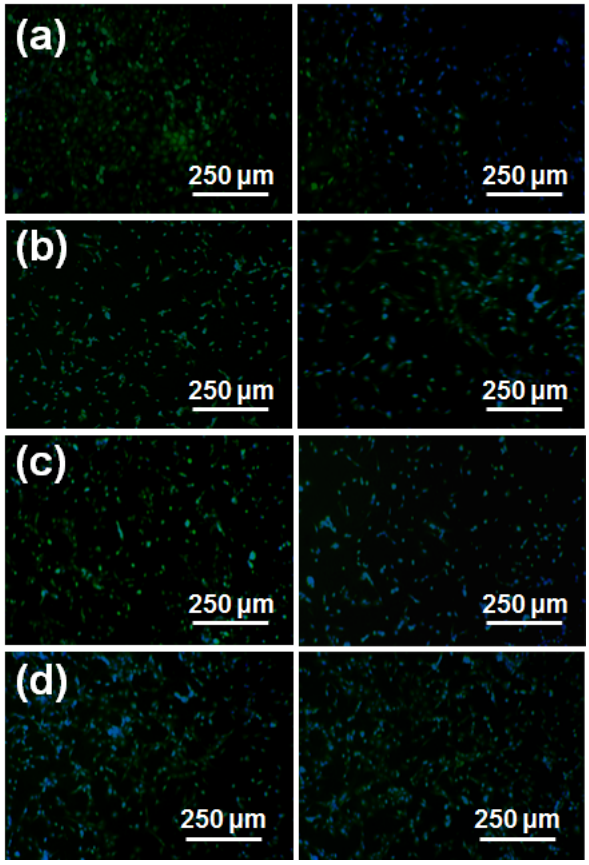

Figure 10.4.19. Fluorescence images of MG-63 and Vero cells (left and right, respectively) adhered onto: (a) ITO, (b) PTh_3, (c) 50:50 P(AzbT-*co*-Th_3) and (d) 80:20 P(AzbT-*co*-Th_3).

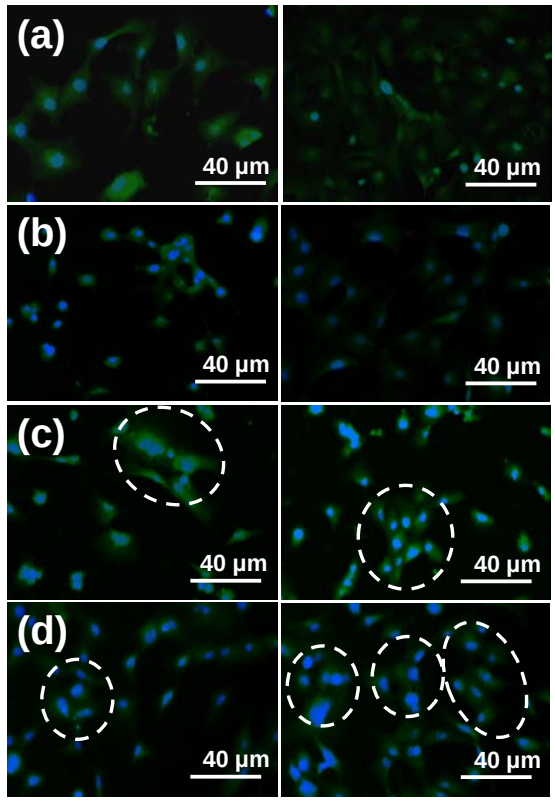

Figure 10.4.20. High magnification fluorescence images of MG-63 and Vero cells (left and right, respectively) adhered onto: (a) ITO, (b) PTh_3, (c) 50:50 P(AzbT-*co*-Th_3) and (d) 80:20 P(AzbT-*co*-Th_3). Networks of cell-to-cell connections are displayed in (c) and (d) (dashed circles).

As it can be seen, cells tend to establish a large spreading of the cytoplasm in all cases, actin filaments being visible within the cells. Besides, cell-to-cell contact tends to be formed onto the copolymers surfaces, and thus the density of such connections increases with the content of AzbT units in the substrate. Hence, dense and large networks are obtained for both MG-63 and Vero cell lines adhered onto the 80:20 P(AzbT-*co*-Th_3) film.

SEM micrographs show MG-63 and Vero cells adhered and proliferated onto the surface of PTh_3 and P(AzbT-*co*-Th_3) films (Figure 10.4.21). Inspection of the images indicates that, in general, the receptivity of the polymeric surfaces to be colonized through cellular viability is higher for MG-63 cells than for Vero cells.

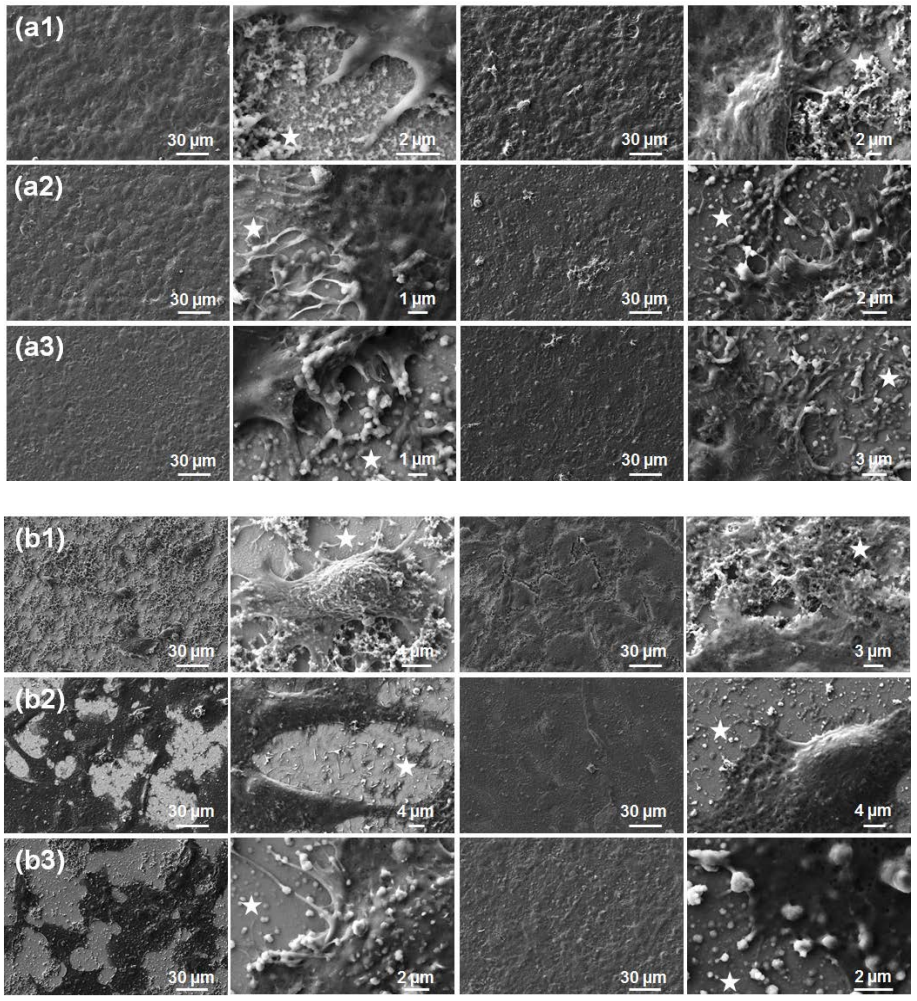

Figure 10.4.21 SEM images for PTh_3 and P(AzbT-*co*-Th_3) covered with (a) MG-63 and (b) Vero cells: (#1) PTh_3, (#2) 50:50 P(AzbT-*co*-Th_3) and (#3) 80:20 P(AzbT-*co*-Th_3). From right to left columns: adhesion (1 kX), adhesion details, proliferation (1 kX) and proliferation details. Stars indicate the polymer surface.

Even though large microdomains without adhered Vero cells are identified on the surface of polymeric films proliferated Vero cells are widely spread. In contrast, the spreading of viable MG-63 cells indicates a homogeneous colonization for both adhered and proliferated cells. These observations are fully consistent with the cell viability results and the fluorescence images recorded. On the other hand, high magnification SEM micrographs provide details on the connection sites established

between cells and the polymeric surfaces. These consist on long and thin actin filaments, which are known as filopodia, oriented towards the film surface for local adhesion. Filopodial protrusions play an important role in sensing, thus act as feelers of the substrate surface and participate in cell-cell interactions, which in turn control the adhesion of cells to the substrate and their migration through the surface (*i.e.* cellular motility). Overall, the good results obtained for 80:20 P(AzbT-*co*-Th_3) films ensures its applicability as scaffolds in the field of tissue engineering.

10.5. Conclusions

A novel azomethine-containig bis-thienyl monomer, AzbT, has been synthesized by a simple chemical route. In spite of the easiness for its obtainment, the AzbT's structural peculiarities are responsible for both the impossibility of its electrochemical homopolymerization and the concomitant and complex phenomena that take place in the reaction medium when its copolymerization with Th_3 was applied.

XPS analyses as well as FTIR measurements of P(AzbT-*co*-Th_3) films evidenced that, near to copolymerization, other secondary processes are also developing in the reaction medium depending on AzbT:Th_3 molar ratios. The experimental results clearly corroborated that the content of AzbT in the copolymer chains increase with the content of AzbT in the electropolymerization medium and that, in the case of a higher amount of Th_3, AzbT works mostly as a dopant than as a comonomer. Differences in the structural, electrochemical and optical properties of the copolymers derived from the different AzbT:Th_3 molar ratio support this feature.

From a structural point of view, the thickness and roughness of P(AzbT-*co*-Th_3) films decrease with the content of AzbT. Furthermore, the porous multi-level surface morphology of the 50:50 copolymer, which is very similar to that of PTh_3, changes to a compact globular morphology in the 80:20 copolymer. On the other hand, the electroactivity and electrostability values of P(AzbT-*co*-Th_3)s decrease with the content of AzbT, while the E_g depends on the molecular architecture of the copolymer chains, which is also affected by the AzbT content. Thus, the E_g of the 80:20 copolymer and PTh_3 are similar and lower than those of 50:50 and 60:40 P(AzbT-*co*-Th_3), which has been attributed to the cross-linked structure of the latters.

The potential application of P(AzbT-*co*-Th_3) films as bioactive substrates has been evaluated. Results obtained using human osteosarcoma and monkey kidney epithelial cell lines (MG-63 and Vero, respectively) indicated that the cytotoxicity of

the examined systems increases with the content of Th_3, which has been attributed to the release of harmful Th_3 monomers entrapped into the polymeric matrix. The same tendency was observed for the cellular adhesion and proliferation assays. The 80:20 copolymer showed the best behaviour as bioactive matrix. Indeed, cell viability has been found to be higher than for the control TCPS substrate. Furthermore, the spreading of cells cultured onto the surface of 80:20 P(AzbT-*co*-Th_3) is very homogeneous.

In summary, this new copolymer promotes cellular viability, most probably due to the presence of the carboxyl groups. More specifically, we hypothesize that such favourable response is essentially due to the recognition of fibronectin and integrins (cell membrane-spanning receptor proteins) by the imine and carboxylate groups of AzbT units. It should be noted that, in a very recent study, such recognition mechanism was found to be responsible of the bioactive response of a polythiophene:peptide composite.[48] Thus, the sequence of such short peptide, Cys-Arg-Glu-Lys-Ala (CREKA), was reported to contain a similar spatial distribution of the same functionalities.

On the other hand, if the antibacterial activity is *a priori* taken into account due to the presence of the Schiff base functionalities in its structure, 80:20 P(AzbT-*co*-Th_3) should be considered as a suitable bioactive platform for advanced biomedical applications in which optical properties similar to those displayed by semiconducting PTh derivatives are required.

10.6. References

[1] K. Maruoka, T.Doi, *Chem.Rev.* **2003**, *103*, 3013.
[2] T. Ooi, K. Maruoka, *Angew .Chem. Int. Ed.*, **2007**, *46*, 4222
[3] S. Li, S. Chen, S. Lei, H. Ma, R. Yu, D. Liu, *Corrosion Sci.* **1999**, *41*, 1273.
[4] P. Mishra, H. Rajak, A. Mehta, *J. Gen. Appl. Microbiol.* **2005**, *51*, 133.
[5] B.C. Revanasiddappa, M.A. Jayamol, D. Satyanarayana, *Universal J. Pharm.* **2013**, *2*, 145.
[6] M. M. Ali, M. Jesmin, S. M. A. Salam, J. A. Khanam, M. F. Islam, M. N. Islam, *J. Sci. Res.* **2009**, *1*, 641.
[7] M. de L. Ferreira, T. R. A. Vasconcelos, E. M. de Carvalho, M. C. S. Lourenço, S. M. S. V. Wardell, J. L. Wardell, V. F. Ferreira, M. V. N. de Souza, *Carbohydr. Res.* **2009**, *344*, 2042.
[8] F. Martins, S. Santos, C. Ventura, R. Elvas-Leitão, L. Santos, S. Vitorino, M. Reis, V. Miranda, H. F. Correia, J. Aires-de-Sousa, V. Kovalishyn, D. A. R. S. Latino, J. Ramos, M. Viveiros, *Eur. J. Med. Chem.* **2014**, *81*, 119.
[9] Y. Zhou, M. Zhao, Y. Wu, C. Li, J. Wu, M. Zheng, L. Peng, S. Peng, *Bioorg. Med. Chem.* **2010**, *18*, 2165.
[10] M. S. Alam , J.-H. Choi, D.-U. Lee, *Bioorg. Med. Chem.* **2012**, *20*, 4103.

[11] K. V. Sashidhara, A. Kumar, G. Bhatia, M.M. Khan, A.K. Khanna, J.K. Saxena, *Eur.J. Med.Chem.* **2009**, *44*,1813.
[12] S. Ganguli, M. Firdous, T. S. Maity, R.K. Bera, M. Panigrahi, *Int. J. Pharm. Pharm. Sci.*, **2012**, *4*, 175..
[13] K. S. Kumar, S. Ganguly, R. Veerasamy, E. De Clercq, *Eur.J. Med.Chem.* **2010**, *45*, 5474.
[14] K. M. Khan, M. Khan, M. Ali, M. Taha, S. Rasheed , S. Perveen, M. Iqbal Choudhary, *Bioorg. Med. Chem.* **2009**, *17*, 7795.
[15] M. Jesmin, M.M. Ali, J.A. Khanam, *Thai J. Pharm. Sci.* **2010**, *34*, 20.
[16] A. Iwan, D. Sek, *Prog. Polym Sci.* **2008**, *33*, 289.
[17] S. Barik, W.G. Skene, *Polym. Chem.* **2011**, *2*, 1091.
[18] S. Barik, T. Bletzacker, W.G. Skene, *Macromolecules* **2012**, *45*, 1165
[19] A. Iwan, E. Schab-Balcerzak, K. P. Korona, S. Grankowska, M. Kaminska, *Synth. Met.* **2013**, *185– 186*, 17.
[20] C. Mallet, M. Le Borgne, M. Starck, W. G. Skene, *Polym. Chem.* **2013**, *4*, 250.
[21] I. Kaya, M. Kamaci, *J. Fluoresc.* **2013**, *23*, 115.
[22] S. Tarkuc, E. Sahin, L. Toppare, D. Colak, I. Cianga, Y. Yagci, *Polymer* **2006**, *47*, 2001.
[23] A. Bolduc, W. G. Skene, *Polym. Chem.* **2014**, *5*, 1119.
[24] D. Isık, C. Santato, S. Barik, W.G. Skene, *Org. Electron.* **2012**, *13*, 3022.
[25] B. Hu, X. Zhu, X. Chen, L. Pan, S. Peng, Y. Wu, J. Shang, G. Liu, Q. Yan, R.-W. Li, *J. Am. Chem. Soc.* **2012**, *134*, 17408..
[26] J.-M. Lehn, *Prog. Polym. Sci.* **2005**, *30*, 814.
[27] T. Maeda, H. Otsuka, A. Takahara, *Prog. Polym. Sci.* **2009**, *34*, 581.
[28] E. Moulin, G. Cormos, N. Giuseppone, *Chem. Soc. Rev.* **2012**, *41*, 1031.
[29] N. Giuseppone, G. Fuks, J.-M. Lehn, *Chem. Eur. J.* **2006**, *12*, 1723.
[30] D. Janeliunas, P. van Rijn, J. Boekhoven, C.B. Minkenberg, J. van Esch, R. Eelkema, *Angew. Chem. Int. Ed.* **2013**, *52*, 1998.
[31] C.I. Simionescu, I. Cianga, M. Ivanoiu, Al. Duca, I. Cocarla, M. Grigoras, *Eur.Polym. J.* **1999**, *35*, 587.
[32] C.I. Simionescu, I. Cianga, M. Ivanoiu, A. Airinei, M. Grigoras, I. Radu, *Eur. Polym. J.* **1999**, *35*, 1895.
[33] C.I. Simionescu, M. Grigoras, I. Ciang, N. Olaru, *Eur.Polym. J.* **1998**, *34*, 891.
[34] M. Grigoras, I. Cianga, A. Farcas, G. Nastase, M. Ivanoiu, *Rev. Roum. Chim.* **2000**, *45*, 703.
[35] D. Colak, I. Cianga, A.E. Muftuoglu, *J. Polym. Sci. Part A: Polym. Chem.* **2006**, *44*, 724.
[36] I. Cianga, M. Ivanoiu, *Eur. Polym. J.* **2006**, *42*, 1922.
[37] E. Armelin, A. L. Gomes, M. M. Pérez-Madrigal, J. Puigalí, L. Franco, L. J. del Valle, A. Rodríguez-Galán, J. S. de C. Campos, N. Ferre-Anglada and C. Alemán, *J. Mat. Chem.* **2012**, *22*, 585.
[38] M. M. Pérez-Madrigal, E. Armelin, L. J. del Valle, F. Estrany and C. Alemán, *Polym. Chem.* **2012**, *3*, 979.
[39] M. M. Pérez-Madrigal, M. I. Giannotti, G. Oncins, L. Franco, E. Armelin, J. Puiggalí, F. Sanz, L. J. del Valle and C. Alemán, *Polym. Chem.* **2013**, *4*, 568.
[40] M. M. Pérez-Madrigal, M. I. Giannotti, E. Armelin, F. Sanz, C. Alemán, *Polym. Chem.* **2014**, *5*, 1248.
[41] M. M. Pérez-Madrigal, M. I. Giannoti, L. J. del Valle, L. Franco, E. Armelin, J. Puiggalí, F. Sanz, C. Alemán, *ACS Appl. Mater. Interfaces* **2014**, *6*, 9719.
[42] E. Llorens, E. Armelin, M. M. Pérez Madrigal, L. J. del Valle, C. Alemán and J. Puiggalí, *Polymers* **2013**, *5*, 1115.
[43] E. Llorens, M. M. Pérez-Madrigal, E. Armelin, L. J. del Valle, J. Puiggalí, C. Alemán, *RSC Adv.* **2014**, *4*, 15245.

[44] M. Planellas, M. M. Pérez-Madrigal, L. J. del Valle, S. Kobauri, R. Katsarava, C. Alemán and J. Puiggalí, *Polym. Chem.* **2015**, *6*, 925.
[45] A. D. Bendrea, G. Fabregat, L. Cianga, F. Estrany, L. J. del Valle, I. Cianga, C. Alemán, *Polym. Chem.* **2013**, *4*, 2709.
[46] A. D. Bendrea, G. Fabregat, J. Torras, S. Maione, L. Cianga, L. J. del Valle, I. Cianga, C. Alemán, *J. Mater. Chem. B* **2013**, *1*, 4135.
[47] S. Maione, G. Fabregat, L. J. del Valle, A. D. Bendrea, L. Cianga, F. Estrany, C. Alemán, J. Polym. Sci.: Part B: Polym. Phys. **2015**, *53*, 239.
[48] G. Fabregat, B. Teixeira-Dias, L. J. del Valle, E. Armelin, F. Estrany, C. Alemán, *ACS Appl. Mater. Interfaces* **2014**, *6*, 11940.
[49] D. E. López-Pérez, D. Aradilla, L. J. Del Valle, C. Alemán, *J. Phys. Chem. C* **2013**, 117, 6607.
[50] J. Soto-Delgado, J. Torras, L. J. del Valle, F. Estrany, C. Alemán. *RSC Adv.* **2015**, *5*, 9189.
[51] M. M. Pérez-Madrigal, L. J. del Valle, E. Armelin, C. Michaux, G. Roussel, E. A. Perpète, Carlos Alemán, *ACS Appl. Mater. Interfaces* **2015**, *7*, 1632.
[52] N. Sarı, P. Gürkan, *Z. Naturforsch.* **2004**, *59b*, 692.
[53] G. G. Mohamed, M.M. Omar, A. M.M. Hindy, *Spectrochimica Acta Part A* **2005**, *62*, 1140.
[54] M. Tumer, E. Akgu, S. Toroglu, A. Kayraldiz, L. Donbak, *J. Coord. Chem.* **2008**, *61*, 2935.
[55] Z. Zhang, C. Bi, D. Buac, Y. Fan, X. Zhang, J. Zuo, P. Zhang, N. Zhang, L. Dong, Q. Ping Dou, *J. Inorg. Biochem.* **2013**, *123*, 1.
[56] C. I. Ezugwu, O. T. Ujam, P. O. Ukoha, N. N. Ukwueze, *Chem Sci Trans.* **2013**, *2*, 1118.
[57] M. Onciu, *J. Appl. Polym. Sci.* **2007**, *103*, 2013.
[58] E. Hamciuc, C. Hamciuc, V.E. Musteata, Y. Kalvachev, A.Wolinska-Grabczyk, *High Perform. Polym.* **2014**, *26*, 175.
[59] Y. Ozaytekin, *Polym. Compos.* **2014**, *35*, 372.
[60] M. Avram, G. D. Mateescu, "Spectroscopia în infraroşu aplicaţii în chimia organică", Editura Tehnică Bucureşti, **1966**.
[61] S. Destri, I. A. Khotina, W. Porzio, *Macromolecules* **1998**, *31*, 1079.
[62] L. Marin, M.D. Damaceanu, D. Timpu, *Soft Matter* **2009**, *7*, 1.
[63] R. Kiebooms, R. Menon, K. Lee, "Synthesis, Electrical and Optical Properties of Conjugated Polymers" in Handbook of Advanced Electronic and Photonic Materials and Devices, vol. 8, Conducting Polymers, (Eds: H.S. Nalwa), Academic Press, **2001**, p. 15.
[64] G. Li, G. Koßmehl, H.- P. Welzel, G. Engelmann, W.- D. Hunnius, W. Plieth, H. Zhu, *Macromol. Chem. Phys.* **1998**, *199*, 525.
[65] J. Li, K. Aoki, *J. Electroanal. Chem.* **1998**, *458*, 155.
[66] D. N. Hendrickson, J. M. Hollander, W. L. Jolly, *Inorg. Chem.* **1970**, *9*, 612.
[67] R. Benoit, Y. Durand, B. Narjoux, G. Quintana and Y. Georges, LaSurface X-ray Photoelectron Spectroscopy Database, http://www.lasurface.com/database/liaisonxps.php (accessed December 2014).
[68] S. A. Spanninga, D. C. Martin, Z. Chen, *J. Phys. Chem. C* **2010**, *114*, 14992.
[69] C. D. Grande, M. C. Tria, G. Jiang, R. Ponnapati, R. Advincula, *Macromolecules* **2011**, *44*, 966.
[70] S. Ahmad, M. Deepa, S. Singh, *Langmuir* **2007**, *23*, 11430.
[71] T. R. Dillingham, D. M. Cornelison, S. W. Townsend, *J. Vac. Sci. Technol., A* **1996**, *14*, 1494.
[72] J. S. Stevens, A. C. de Luca, M. Pelendritis, G. Terenghi, S. Downes, S. L. M. Schroeder, *Surf. Interface Anal.* **2013**, *45*, 1238.
[73] S. Sharma, R. W. Johnson, T. A. Desai, *Appl. Surf. Sci.* **2003**, *206*, 218.
[74] K. L. Purvis, G. Lu, J. Schwartz, S. L. Bernasek, *J. Am. Chem. Soc.* **2000**, *122*, 1808.
[75] J. Chastain, C. Roger, Handbook of X-ray Photoelectron Spectroscopy, **1995**.

[76] E. Kiss, I. Bertoti, E. I. Vargha-Butler, *J. Colloid Interf. Sci.* **2002**, *245*, 91.
[77] V. I. Nefedoc, D. Gati, B. F. Dzhurinskii, N. P. Sergushin, V. Ya, Russ. *J. Inorg. Chem.* **1975**, *20*, 2307.
[78] D. Aradilla, D. Azambuja, F. Estrany, J. I. Iribarren, C. A. Ferreira, C. Alemán, *Polym. Chem.* **2011**, *2*, 2548.
[79] A. S. Vanini, J. P. Audouard, P. Marcus, *Corr. Sci.* **1994**, *36*, 1825.
[80] F. Beguin, I.Rashkov, N. Manolova, R. Benoit, R. Erre, S. Delpeux, *Eur. Polym. J.* **1998**, *34*, 905.
[81] X.-G. Li, J. Li, Q.-K. Meng, M.-R. Huang, *J. Phys. Chem. B* **2009**, *113*, 9718. See also Electronic Supporting information.
[82] H. Peng, L. Zhang, J. Spires, C. Soeller, J. Travas-Sejdic, *Polymer* **2007**, *48*, 3413.
[83] O. Bertran, E. Armelin, F. Estrany, A. Gomes, J. Torras, C. Aleman, *J. Phys. Chem B* **2010**, *114*, 6281.
[84] L. Cianga, *High Perform. Polym.* **2005**, *17*, 117.
[85] T. K. Kunz, M.O. Wolf, *Polym. Chem.* **2011**, *2*, 640.
[86] M. S. A. Abdou, S. Holdcroft, *Macromolecules* **1993**, *26*, 2954.
[87] M. Manceau, A. Rivaton, J.-L. Gardette, S. Guillerez, N. Lemaitre, *Polym. Degrad. Stab.* **2009**, *94*, 898.
[88] R. Berridge, S. P.Wright, P.J. Skabara, A. Dyer, T. Steckler, A. A. Argun, J. R. Reynolds, W.H. Ross, W. J. Clegg, *Mater. Chem.* **2007**, *17*, 225.
[89] M. Krompiec, I. Gridzka, M. Filapek, L. Shorka, S. Krompiec, M. Lapkowski, M. Kania, W. Danikiewicz, *Electrochim. Acta* **2011**, *56*, 8108.
[90] D. Aradilla, J. Casanovas, F. Estrany, J. I. Iribarren, C. Alemán, *Polym. Chem.* **2012**, *3*, 436.

General Conclusions

Conclusions

This chapter summarizes the main conclusions drawn from this Thesis.

Part A: P3TMA-Based FsNM

- Very stable free-standing nanomembranes are obtained combining P3TMA, a soluble polythiophene derivative, with a biodegradable polyester (PE44) or a thermoplastic polyurethane (TPU) using the spin-coating technique. In both cases, the optimization of experimental parameters resulted in robust and flexible nanofilms. Blending with a conventional polymer is crucial to provide mechanical integrity to the CP.
- P3TMA is entrapped as spherical nanoaggregates of small (40–70 nm) and medium (250–340 nm) size in the polyester matrix, whereas the morphology of TPU:P3TMA FsNM depends on the composition. Specifically, the surface of TPU:P3TMA 40:60 consists of a homogeneous distribution of granules, which are associated with the P3TMA-rich phase.
- The phase separation observed is understood by considering both the conventional parameters typically found in thin films (*e.g.* polymer–polymer interactions, solubility of the polymers in the solvent and, especially, the spin-coating process) and the crucial role of the substrate–film–air interfaces.
- Although the thermal stability of the blends is highly dependent on the composition, P3TMA:PE44 blends are very stable with degradation temperatures ranging between 320 and 385 °C. For the TPU:P3TMA system, thermal degradation is determined by the low energy processes associated with each individual polymer, namely, P3TMA at the beginning and TPU at the end.
- The irregular distribution of P3TMA doped chains and the presence of the insulating polymer in P3TMA-based interfaces affect their electrical conductivity, although it is found within the range typically for semiconductor materials. As the concentration of P3TMA reduces, the conductivity value decreases. Electrical conductivity values range from ~10^{-4} to ~10^{-5} S/cm and from ~10^{-5} to ~10^{-6} S/cm, for P3TMA:PE44 80:20 and TPU:P3TMA 40:60, respectively.
- P3TMA-based interfaces retain the electrochemical features of P3TMA. The oxidation and reduction processes found in the individual CP are also present in P3TMA:PE44 and TPU:P3TMA systems. After consecutive oxidation–reduction

cycles, samples experience a reduction of the electroactivity in both acetonitrile and PBS mediums.

- After blending, PE44 and TPU induce biodegradability to the P3TMA-based interfaces, thus facilitating the detachment of the P3TMA domains. Hydrolytic and enzymatic degradation increase with the P3TMA content.
- The Youngs' modulus (*E*) of the TPU:P3TMA 40:60, which depends on the thickness of the different regions examined, is half-way between those found for the individual components. In contrast, the adhesion force depends on the composition of the domains, being higher for the TPU-rich domains.
- P3TMA:PE44 and TPU:P3TMA behave as potent cellular biointerfaces since they are biocompatible, electrobioactive and adequate substrates for type I collagen adsorption (honeycomb-like structures). In general, the viability of cultured cells is significantly higher for the blend than for the insulating matrix and, especially, the CP, since the presence of $FeCl_3$ (doping agent) inhibits cell viability.
- The morphological differences between bulk P3TMA powder and the ultra-thin film induce a change in the microscopic organization of the polymer molecules that affect the glass transition temperature of P3TMA: the T_g value for the ultra-thin samples (~10^{-13} g) is 5.2 °C higher than that obtained for the bulk powder (5 mg) using conventional DSC.

Part B: P3TMA-Based Fibrous Interfaces

- Hybrid micro/nanofibers are prepared by blending P3TMA with PLA or PEU-*co*-PEA using the electrospinning technique, without compromising the characteristic properties of each homopolymer. In the case of PEU-*co*-PEA, only a small percentage (10 wt%) was needed to produce homogeneous and continuous hybrid microfibers with 90 wt% of P3TMA.
- Some specific interactions occur in the processing of the samples. The presence of P3TMA in the electrospinning solution influences the morphology of the hybrid fibers. For PLA:P3TMA, increasing content of P3TMA produces smoother fiber surfaces with smaller diameters, and a higher orientation of PLA chains; while for PEU-*co*-PEA:P3TMA, fibers with lower diameters are obtained.
- The P3TMA content does not affect the characteristic glass transition, crystallization and melting temperatures of the final PLA:P3MTA hybrid scaffolds, whereas it slightly modifies the degradation process. PEU-*co*-PEA

microfibers present low crystallinity, high thermal stability and a phase in which the CP and the biodegradable copolymer are well mixed.

- P3TMA displays a good doping level, and retains its electrochemical features in the hybrid fibrous samples, which are electroactive and stable after performing consecutive oxidation–reduction cycles. In particular, the electroactivity and electrochemical stability of PEU-*co*-PEA:P3TMA interfaces are similar to those displayed by P3TMA.
- PLA:P3TMA 2:1 fibrous interface can perform as scaffold and drug-delivery platform since it combines a suitable wetting behaviour, biocompatibility and electrochemical features. Drug-loaded matrices with TCS, CHX or CIP are antibacterial active, and the drug-release kinetics is faster for a more hydrophobic medium (*i.e.* PBS-EtOH medium).

Part C: Electropolymerized CP-based Biointerfaces

- Electropolymerization has been applied to prepare thin CP-based biointerfaces with special functionalities. Both systems result in interfaces suitable for bioapplications despite the fact that their electropolymerizing process differs since each one follows a specific modification strategy to adapt their properties. On the one hand, PNMPy-Omp2a has been designed adopting the entrapment approach: Omp2a, a β-barrel protein that forms trimeric pores, was immobilized into PNMPy, thus rendering a biocomposite. On the other, P(AzbT-*co*-Th_3)s interfaces, which contain terthiophene, carboxyl and Schiff base moieties, are obtained as a combination of the doping and/or covalent linkage methods.
- The native structure of the protein (β-sheet secondary structure) is preserved in the PNMPy−Omp2a composite, which ensures its operative and functional state in the PNMPy−Omp2a interface. In fact, as PNMPy and PNMPy-Omp2a show similar porosity, the improved electrochemical behaviour of PNMPy-Omp2a interfaces has been attributed to the protein operative state.
- The entrapment of Omp2a affects the oxidation process of PNMPy during polymerization (*i.e.* the doping level of PNMPy in the composite decreases), and alters the morphology and topography of the PNMPy matrix.
- PNMPy−Omp2a behaves as a biocompatible interface: the number of adhered Vero and Cos-7 cells on its surface is higher than for the control PNMPy.
- The passive ion transport ability of PNMPy-Omp2a interfaces depends on the electrolyte concentration, which regulates the activity of Omp2a channels

integrated in the composite. Omp2a is more efficient for the diffusion of Na^+ than for the diffusion of K^+.

- The electrochemical homopolymerization of AzbT, which contains the azometine functional group that induces particular features to the CP-based biointerface, is not feasible due to its structural peculiarities. In addition, when it is copolymerized with Th_3, the complex phenomena that occur in the reaction medium, which depend on the AzbT:Th_3 molar ratio, also influence the formation of P(AzbT-*co*-Th_3)s and determine the content of AzbT in the copolymer chains.
- The AzbT monomer adopts a dual role when copolymerized with Th_3 depending on the AzbT:Th_3 molar ratio. Thus, AzbT acts mostly as a dopant agent (*i.e.* doping approach), rather than as a comonomer (*i.e.* covalent linkage method), when the amount of Th_3 is high in the electropolymerization medium (*i.e.* 50:50 or 60:40).
- The AzbT:Th_3 molar ratio in P(AzbT-*co*-Th_3) thin films affects their structure (the thickness and roughness decrease with the content of AzbT), electrochemical response (the electroactivity and electrostability decrease with the content of AzbT) and optical properties (the E_g value depends on the molecular architecture of the copolymer chains, which is also affected by the AzbT content).
- 80:20 P(AzbT-*co*-Th_3) shows the best behaviour as bioactive platform with a homogeneous spreading of cells onto its surface because of a the minor release of harmful Th_3 monomer entrapped into the polymeric matrix and the presence of AzbT's distinctive groups in its structure (*i.e.* carboxyl and Schiff base moieties).

Annex. List of Publications

Scientific Papers

1. P. Kaali, M. M. Pérez-Madrigal, E. Strömberg, R. E. Aune, Gy. Czél, S. Karlsson, *eXPRESS Polymer Letters* **2011**, *5*, 1028.

2. E. Armelin, A. L. Gomes, M. M. Pérez-Madrigal, J. Puiggalí, L. Franco, L. J. del Valle, A. Rodríguez-Galán J. S. de C. Campos, N. Ferrer-Anglada, C. Alemán, *J. Mater. Chem.* **2012**, *22*, 585.

3. M. M. Pérez-Madrigal, E. Armelin, L. J. del Valle, F. Estrany, C. Alemán, *Polym. Chem.* **2013**, *3*, 979.

4. M. M. Pérez-Madrigal, M. I. Giannotti, G. Oncins, L. Franco, E. Armelin, J. Puiggalí, F. Sanz, L. J. del Valle, C. Alemán, *Polym. Chem*. **2013**, *4*, 568.

5. D. Aradilla, M. M. Pérez-Madrigal, F. Estrany, D. S. Azambuja, J. I. Iribarren, C. Alemán, *Org. Electron.* **2013**, *14*, 1483.

6. O. Ahumada, M. M. Pérez-Madrigal, J. Ramirez, D. Curcó, C. Esteves, A. Salvador-Matas, G. Luongo, E. Armelin, J. Puiggalí, C. Alemán, *Rev. Sci. Instrum.* **2013**, *84*, 053904.

7. E. Llorens, E. Armelin, M. M. Pérez-Madrigal, L. J. del Valle, C. Alemán, J. Puiggalí, *Polymers* **2013**, *5*, 1115.

8. M. M. Pérez-Madrigal, M. I. Giannotti, E. Armelin, F. Sanz, C. Alemán, *Polym. Chem*. **2014**, *5*, 1248.

9. M. M. Pérez-Madrigal, M. I. Giannotti, L. J. del Valle, L. Franco, E. Armelin, J. Puiggalí, F. Sanz, C. Alemán, *ACS Appl. Mater. Interfaces* **2014**, *6*, 9719.

10. E. Llorens, M. M. Pérez-Madrigal, E. Armelin, L. J. del Valle, J. Puiggalí, C. Alemán, *RSC Adv.* **2014**, *4*, 15245.

11. M. M. Pérez-Madrigal, E. Armelin, D. S. Azambuja, F. Estrany, C. Alemán, *Polym. Compos.* **2014**, *Accepted*. DOI. 10.1002/pc.23230

12. M. Planellas, M. M. Pérez-Madrigal, L. J. del Valle, S. Kobauri, R. Katsarava, C. Alemán, J. Puiggalí, *Polym. Chem.* **2015**, *6*, 925.

13. M. M. Pérez-Madrigal, L. J. del Valle, E. Armelin, C. Michaux, G. Roussel, E. A. Perpète, C. Alemán, *ACS Appl. Mater. Interfaces* **2015**, *7*, 1632.

14. M. Häring, M. M. Pérez-Madrigal, D. Kühbeck, A. Pettignano, F. Quignard, D. Díaz-Díaz, *Molecules* **2015**, *20*, 4136.

15. M. M. Pérez-Madrigal, L. Cianga, L.J. del Valle, I. Cianga, C. Alemán, *Polym. Chem.* **2015**, DOI: 10.1039/c5py00480b.

16. M. M. Pérez-Madrigal, E. Llorens, L. J. del Valle, J. Puiggalí, E. Armelin, C. Alemán, "Development of New Scaffolds Based on Biodegradable Polylactide and Soluble Polythiophene for Drug Delivery", Submitted work to *J. Mater. Chem. B*

17. J. Torras, M. M. Pérez-Madrigal, D. Curcó and C. Alemán. Organization of collagen adsorbed onto soft polymeric surfaces. Submitted work to *Chem. Comun*.

18. M. M. Pérez-Madrigal, E. Armelin, J. Puiggalí, C. Alemán, "Review: From Insulating to Semiconducting Polymeric Free Standing Nanomembranes for Biomedical Applications", Submitted to *J. Mater. Chem. B*

19. E. Mayans, G. Ballano, J. Casanovas, A. Díaz, M. M. Pérez-Madrigal, F. Estrany, J. Puiggalí, C. Cativiela, C. Alemán, "Self-Assembly of Tetraphenylalanine Peptides", Submitted to *ACS Nano.*

Conference Proceedings

1. M.M Pérez-Madrigal, E. Armelin, A. Puiggalí, L. J. del Valle, C. Michaux, G. Roussel, E. A. Perpète, C. Alemán, *Polypyrrole-Supported Membrane Proteins for Bio-Inspired Ion Channels,* European Polymer Congress, Dresden (Germany), June 2015.

2. M.M. Pérez-Madrigal, E. Armelin, M. I. Giannotti, L. J. del Valle, F. Sanz, C. Alemán, *Thermoplastic polyurethane: Polythiophene nanomembranes for biomedical applications.* Fourth International Conference on Multifunctional, Hybrid and Nanomaterials, Sitges (Spain), March 2015.

3. M. M. Pérez-Madrigal, M. I. Giannotti, G. Oncins, L. Franco, E. Armelin,J. Puiggalí, F. Sanz, L. J. del Valle, C. Alemán, *Characterization of thermoplastic polyurethane:polythiophene nanomembranes for biomedical and biotechnological applications.* International Conference on Scanning Probe Microscopy on Soft and Polymeric Materials, Toronto (Canada), September 2014.

4. M. M. Pérez-Madrigal, E. Llorens, E. Armelin, L. J. del Valle, J. Puiggali, C. Alemán, *Electroactive nanofibers for drug release devices and cellular substrates*. RSC 11th International Conference on Materials Chemistry, Warwick (UK), 2013 [Poster awarded].

5. O. Ahumada, M. M. Pérez-Madrigal, D. Curcó, C. Alemán, *Sensitive thermal transitions of polymers for nanotechnology using femtogram mass-scale samples*. Frontiers in Polymer Science, Sitges (Spain), 2013.
6. M. M. Pérez-Madrigal, E. Armelin, M. I. Giannotti, F. Sanz, L.J. del Valle, C. Alemán, *Conducting polymer:thermoplastic blends for the fabrication of flexible free-standing ultra-thin membranes: nanomeasures and biomedical applications*. E-MRS 2012 Spring Meeting, Strasbourg (France), May 2012.
7. E. Armelin, A. L. Gomes, M. M. Pérez-Madrigal, L. J. del Valle, J. Puiggalí, C. Alemán, *Free-standing nanomembranes of conducting polymer and biodegradable polyester*. Second International Conference on Multifunctional, Hybrid and Nanomaterials, Strasbourg (France), 2011.
8. C. Alemán, M. M. Pérez-Madrigal, G. Fabregat, E. Armelin, *Nanotechnology for detection of biomolecules and fabrication of bioactive platforms*, 12th Mediterranean Congress of Chemical Engineering, Barcelona (Spain), 2011.